Advances in
QUANTUM CHEMISTRY

VOLUME **61**

Editors

JOHN R. SABIN
Quantum Theory Project
University of Florida
Gainesville, Florida

ERKKI BRÄNDAS
Department of Quantum Chemistry
Uppsala University
Uppsala, Sweden

ELSEVIER

Amsterdam • Boston • Heidelberg • London • New York • Oxford
Paris • San Diego • San Francisco • Singapore • Sydney • Tokyo

Academic Press is an imprint of Elsevier

Academic Press is an imprint of Elsevier
525 B Street, Suite 1900, San Diego, CA 92101-4495, USA
225 Wyman Street, Waltham, MA 02451, USA
32 Jamestown Road, London NW1 7BY, UK

First edition 2011

ISBN: 978-0-12-386013-2
ISSN: 0065-3276

Printed and bounded in USA
11 12 13 10 9 8 7 6 5 4 3 2 1

PREFACE

The present volume of *Advances in Quantum Chemistry* contains the first 6 chapters out of 12 on various aspects of quantum chemistry, ranging from the mathematical to the biological. We hope that there is something here for many theorists with a wide range of interests.

The first chapter reviews information theoretic methods applied to determination of molecular electronic structure in the context of the Orbital Communication Theory of the chemical bond. The molecule is treated as an information network from which structural information can be obtained. The results of probing molecular charges and bond orders using this method are compared with results obtained by more commonly used means.

In Chapter 2, the author revisits the notorious quantum mechanical measurement problem. In this regard, a different emphasis on the fundamental understanding of a quantum state is introduced. The weirdness usually put into the accounts of quantum mechanics is reviewed and criticized; for instance, one might refer to a commendable appraisal in connection with the quantum eraser. The author compares current developments in the modern studies of basic quantum concepts from the Gimo Nobel Conference (Ref. [13] of Chapter 2) in 1997 to the present. Although present results do not indicate that any original and new results have been obtained during the last decade, except a very startling and exciting technological development, Chapter 2 represents a new approach beyond the orthodox interpretation for quantum chemists that differs significantly from standard textbook treatments.

Addressing large molecular systems is the aim of Chapter 3, which reviews a recently developed model based on the combined use of quantum mechanics and molecular mechanics (QM/MM). This approach uses a fully self-consistent polarizable embedding (PE) scheme described in the paper. The PE model is generally compatible with any quantum chemical method, but this review is focused on its combination with density functional theory (DFT) and time-dependent density functional theory (TD-DFT). The PE method is based on the use of an electrostatic embedding potential resulting from the permanent charge distribution of the classically treated part of

the system. However, the electrostatic embedding potential only accounts for the permanent charge distribution of the environment, and in order to account for many-body induction effects, a set of localized anisotropic dipole polarizability tensors at the expansion centers is introduced. The strength of the PE scheme is the ability to describe excited states and general molecular properties on the same footing as the ground state.

In Chapter 4, the author describes important theory developments in signal processing within medical applications, the latter exposed in more detail in Chapter 12. The author elucidates the state-of-the-art of signal processing from the perspective of quantum physics and chemistry. The connections between important approaches due to Lanczos, Krylov, Padé, etc. are considered, compared, appraised, and computationally assessed. The rich mathematical structure of one of the most popular multipurpose strategy, the Fast Padé Transform, FPT, is shown to perform an optimal synthesis and decomposition in connection with the Froissart filter for exact signal–noise separation. The main characteristics of FPT in the quantification of the time signal, for example, equivalent to the harmonic inversion problem, are reviewed, theoretically analyzed, and numerically illustrated as well as tested for stability and robustness.

A brief introduction to the nonequilibrium Green's function method is discussed in the Chapter 5. Two examples where nonequilibrium Green's functions can be used are presented: (1) electric current calculations in molecular tunneling devices and (2) in quantum dot-sensitized solar cells. These applications require development of sophisticated computational methods to perform predictive calculations of conduction properties. The success of the electron propagator methodology applied to molecules provides a hope that this method will be also successful in systems combined from finite and infinite electron subsystems. In tunneling junctions, the molecular bridge electrons interact with electrons from the leads, and therefore the electronic levels of the molecular subsystem are modified by this interaction. Even if this interaction is small, there is finite dissipation resulting in the broadening of molecular levels. In the case of an isolated molecule, however, the imaginary part of the molecular Green's functions is infinitesimally small. The most systematic approach is to use many-body theory with a diagrammatic expansion with respect to the perturbation. In a many-electron system, this perturbation is usually the Coulomb interaction. In tunneling junctions, an interaction picture is different; there are two interactions: (1) the interaction between the lead electrons and the electrons in the bridge and (2) the Coulomb interaction within the bridge. The interaction between the bridge and lead electrons makes this problem substantially more complicated than molecular electronic structure calculations because of nonequilibrium conditions determined by the difference in chemical potentials of the leads. In this case, the nonequilibrium Green's function method has to be applied to find electric current in molecular devices.

In Chapter 6, the authors discuss calculation of electron impact inner-shell ionization cross section (EIICS) from the *K*-, *L*-, and *M*-shells of neutral atoms with atomic numbers $Z = 6$–92. The evaluations of the EIICS are discussed using recently propounded, easy-to-use models that are found to be adequately successful in describing the experimental cross sections. The selection of the range of atomic number Z for different inner-shells was guided by the availability of the EIICS data either from experiments or from rigorous quantal calculations. Details of the models are presented and their results are compared with the experimental and other theoretical values. The models describe experimental results nicely for *K*-, *L*-, and *M*-shell ionization for $Z \leq 92$ in the energy range $E \leq 2\,\text{GeV}$.

We offer this volume of *Advances in Quantum Chemistry* to the readers with the belief that it will be both interesting and informative.

John R. Sabin and Erkki Brändas
Editors

CONTRIBUTORS

A. K. Fazlul Haque, Department of Physics, University of Rajshahi, Rajshahi, Bangladesh.

Arun K. Basak, Department of Physics, University of Rajshahi, Rajshahi, Bangladesh.

Bidhan C. Saha, Department of Physics, Florida A & M University, Tallahassee, Florida, USA.

Dariusz Szczepanik, Department of Computational Methods in Chemistry, Jagiellonian University, Cracow, Poland.

Dževad Belkić, Nobel Medical Institute, Karolinska Institute, Department of Oncology and Pathology, Stockholm, Sweden.

Grigory Kolesov, Department of Physics and Astronomy, University of Wyoming, Laramie, WY, USA.

Jacob Kongsted, Department of Physics and Chemistry, University of Southern Denmark, Odense M, Denmark.

Janusz Mrozek, Department of Computational Methods in Chemistry, Jagiellonian University, Cracow, Poland.

Jógvan Magnus Haugaard Olsen, Department of Physics and Chemistry, University of Southern Denmark, Odense M, Denmark.

M. Alfaz Uddin, Department of Physics, University of Rajshahi, Rajshahi, Bangladesh.

M. Rashid Talukder, Department of Applied Physics and Electronic Engineering, University of Rajshahi, Rajshahi, Bangladesh.

M. Shahjahan, Department of Physics, University of Rajshahi, Rajshahi, Bangladesh.

O. Tapia, Department of Physical Chemistry and Analytical Chemistry, Uppsala University, Uppsala, Sweden.

Roman F. Nalewajski, Department of Theoretical Chemistry, Jagiellonian University, Cracow, Poland.

Yuri Dahnovsky, Department of Physics and Astronomy, University of Wyoming, Laramie, WY, USA.

CHAPTER 1

Bond Differentiation and Orbital Decoupling in the Orbital-Communication Theory of the Chemical Bond

Roman F. Nalewajski[a], **Dariusz Szczepanik**[b], and **Janusz Mrozek**[b]

Contents

1. Introduction 3
2. Molecular Information Channels in Orbital Resolution 6
3. Decoupled (Localized) Bonds in Hydrides Revisited 11
4. Flexible-Input Generalization 15
5. Populational Decoupling of Atomic Orbitals 21
6. Bond Differentiation in OCT 29
7. Localized σ Bonds in Coordination Compounds 34
8. Restricted Hartree–Fock Calculations 36
   8.1. Orbital and condensed atom probabilities of diatomic fragments in molecules 37
   8.2. Average entropic descriptors of diatomic chemical interactions 40
9. Conclusion 44
References 45

Abstract *Information-theoretic* (IT) probe of molecular electronic structure, within the *orbital-communication theory* (OCT) of the chemical bond, uses the standard entropy/information descriptors of the Shannon theory of communication

[a] Department of Theoretical Chemistry, Jagiellonian University, Cracow, Poland
[b] Department of Computational Methods in Chemistry, Jagiellonian University, Cracow, Poland

Advances in Quantum Chemistry, Volume 61
ISSN 0065-3276, DOI: 10.1016/B978-0-12-386013-2.00001-2

to characterize the scattering of electron probabilities and their information content throughout the system network of chemical bonds generated by the occupied *molecular orbitals* (MOs). Thus, the molecule is treated as information network, which propagates the "signals" of the electron allocation to constituent *atomic orbitals* (AOs) or general basis functions between the channel AO "inputs" and "outputs." These orbital "communications" are determined by the *two*-orbital conditional probabilities of the output AO events given the input AO events. It is argued, using the quantum-mechanical superposition principle, that these conditional probabilities are proportional to the squares of corresponding elements of the first-order density matrix of the AO *charges and bond orders* (CBO) in the standard *self-consistent field* (SCF) theory using *linear combinations of AO* (LCAO) to represent MO. Therefore, the probability of the interorbital connections in the molecular communication system is directly related to the Wiberg-type quadratic indices of the chemical bond multiplicity. Such probability propagation in molecules exhibits the communication "noise" due to electron delocalization via the system chemical bonds, which effectively lowers the information content in the output signal distribution, compared with that contained in probabilities determining its input signal, molecular or promolecular. The orbital information systems are used to generate the entropic measures of the chemical bond multiplicity and their covalent/ionic composition. The average conditional-entropy (communication noise, electron delocalization) and mutual-information (information capacity, electron localization) descriptors of these molecular channels generate the IT covalent and IT ionic bond components, respectively. A qualitative discussion of the mutually decoupled, localized bonds in hydrides indicates the need for the *flexible*-input generalization of the previous *fixed*-input approach, in order to achieve a better agreement among the OCT predictions and the accepted chemical estimates and quantum-mechanical bond orders. In this extension, the input probability distribution for the specified AO event is determined by the molecular conditional probabilities, given the occurrence of this event. These modified input probabilities reflect the participation of the selected AO in all chemical bonds (AO communications) and are capable of the continuous description of its decoupling limit, when this orbital does not form effective combinations with the remaining basis functions. The occupational aspect of the AO decoupling has been shown to be properly represented only when the separate communication systems for each occupied MO are used, and their occupation-weighted entropy/information contributions are classified as bonding (positive) or antibonding (negative) using the extraneous information about the signs of the corresponding contributions to the CBO matrix. This information is lost in the purely probabilistic model since the channel communications are determined by the squares of such matrix elements. The performance of this MO-resolved approach is then compared with that of the previous, overall (fixed-input) formulation of OCT for illustrative π-electron systems, in the Hückel approximation. A qualitative description of chemical bonds in octahedral complexes is also given. The bond differentiation trends in OCT have been shown to agree with both the

chemical intuition and the quantum-mechanical description. The numerical *Restricted Hartree–Fock* (RHF) applications to diatomic bonds in representative molecular systems are reported and discussed. The probability weighted scheme for diatomic molecular fragments is shown to provide an excellent agreement with both the Wiberg bond orders and the intuitive chemical bond multiplicities.

1. INTRODUCTION

The techniques and concepts of *information theory* (IT) [1–8] have been shown to provide efficient tools for tackling diverse problems in the theory of molecular electronic structure [9]. For example, the IT definition of *Atoms-in-Molecules* (AIM) [9–13] has been reexamined and the information content of electronic distributions in molecules and the entropic origins of the chemical bond has been approached anew [9–18]. Moreover, the Shannon theory of communication [4–6] has been applied to probe the bonding patterns in molecules within the *communication theory of the chemical bond* (CTCB) [9, 19–28] and thermodynamic-like description of the electronic "gas" in molecular systems has been explored [9, 29–31]. The CTCB bonding patterns in both the ground and excited electron configurations have been tackled and the valence-state promotion of atoms due to the orbital hybridization has been characterized [28]. This development has widely explored the use of the average communication noise (delocalization, indeterminacy) and information-flow (localization, determinacy) indices as novel descriptors of the overall IT covalency and ionicity, respectively, of all chemical bonds in the molecular system as a whole, as well as the internal bonds present in its constituent subsystems and the external interfragment bonds.

The electron localization function [32] has been shown to explore the nonadditive part of the Fisher information [1–3] in the *molecular orbital* (MO) resolution [9, 33], whereas a similar approach in the *atomic orbital* (AO) representation generates the so-called contragradience (CG) descriptors of chemical bonds, which are related to the matrix representation of the electronic kinetic energy [34–38]. It should be recalled that the molecular quantum mechanics and IT are related through the Fisher (locality) measure of information [34–41], which represents the gradient content of the system wavefunction, thus being proportional to the average kinetic energy of electrons. The stationary Schrödinger equation indeed marks the optimum probability amplitude of the associated Fisher information principle, including the additional constraint of the fixed value of the system potential energy [34, 39–41]. Several strategies for molecular subsystems have been designed [9, 22, 25, 26] and the atomic resolution of bond descriptors has been proposed [24]. The relation between CTCB and the *Valence Bond* (VB) theory has

been examined [23, 27] and the molecular similarities have been explored [9, 42]. Moreover, the orbital resolution of the "stockholder" atoms and the configuration-projected channels for excited states have been developed [43–45].

The key concept of CTCB is the molecular information system, which can be constructed at alternative levels of resolving the electron probabilities into the underlying elementary "events" determining the channel inputs $\boldsymbol{a} = \{a_i\}$ and outputs $\boldsymbol{b} = \{b_j\}$, for example, of finding an electron on the basis set orbital, AIM, molecular fragment, *etc*. They can be generated within both the local and the condensed descriptions of electronic probabilities in a molecule. Such molecular information networks describe the probability/information propagation in a molecule and can be characterized by the standard quantities developed in IT for real communication devices. Because of the electron delocalization throughout the network of chemical bonds in a molecule the transmission of "signals" from the electron assignment to the underlying events of the resolution in question becomes randomly disturbed, thus exhibiting the communication "noise." Indeed, an electron initially attributed to the given atom/orbital in the channel "input" $\boldsymbol{a}$ (molecular or promolecular) can be later found with a nonzero probability at several locations in the molecular "output" $\boldsymbol{b}$. This feature of the electron delocalization is embodied in the conditional probabilities of the outputs given inputs, $\mathbf{P}(\boldsymbol{b}|\boldsymbol{a}) = \{P(b_j|a_i)\}$, which define the molecular information network.

Both *one*- and *two*-electron approaches have been devised to construct this matrix. The latter [9] have used the simultaneous probabilities of two electrons in a molecule, assigned to the AIM input and output, respectively, to determine the network conditional probabilities, whereas the former [38, 46–48] constructs the orbital-pair probabilities using the projected superposition-principle of quantum mechanics. The two-electron (correlation) treatment has been found [9] to give rise to rather poor representation of the bond differentiation in molecules, which is decisively improved in the one-electron approach in the AO resolution, called the *orbital-communication theory* (OCT) [38, 46–48]. The latter scheme complements its earlier orbital implementation using the effective AO-promotion channel generated from the sequential cascade of the elementary orbital-transformation stages [43–45, 49, 50]. Such consecutive cascades of elementary information systems have been used to represent the underlying orbital transformations and electron excitations in the resultant propagations of the electron probabilities, determining the orbital promotions in molecules. The information cascade approach also provides the probability scattering perspective on atomic promotion due to the orbital hybridization [28].

In OCT the conditional probabilities determining the molecular communication channel in the basis-function resolution follow from the quantum-mechanical superposition principle [51] supplemented by the "physical" projection onto the subspace of the system-occupied MOs, which determines

the molecular network of chemical bonds. Both the molecule as a whole and its constituent subsystems can be adequately described using the OCT bond indices. The internal and external indices of molecular fragments (groups of AO) can be efficiently generated using the appropriate *reduction* of the molecular channel [9, 25, 46, 48] by combining selected outputs and larger constituent fragment(s).

In this formulation of CTCB the off-diagonal orbital communications have been shown to be proportional to the corresponding Wiberg [52] or related quadratic indices of the chemical bond [53–63]. Several illustrative model applications of OCT have been presented recently [38, 46–48], covering both the localized bonds in hydrides and multiple bonds in CO and CO_2, as well as the conjugated π bonds in simple hydrocarbons (allyl, butadiene, and benzene), for which predictions from the one- and two-electron approaches have been compared; in these studies the IT bond descriptors have been generated for both the molecule as whole and its constituent fragments.

After a brief summary of the molecular and MO-communication systems and their entropy/information descriptors in OCT (Section 2) the mutually decoupled, localized chemical bonds in simple hydrides will be qualitatively examined in Section 3, in order to establish the input probability requirements, which properly account for the nonbonding status of the lone-pair electrons and the mutually decoupled (noncommunicating, closed) character of these localized σ bonds. It will be argued that each such subsystem defines the *separate* (externally closed) communication channel, which requires the individual, unity-normalized probability distribution of the input signal. This calls for the variable-input revision of the original and fixed-input formulation of OCT, which will be presented in Section 4. This extension will be shown to be capable of the continuous description of the orbital(s) decoupling limit, when AO subspace does not mix with (exhibit no communications with) the remaining basis functions.

Additional, occupational aspect of the orbital decoupling in the OCT description of a diatomic molecule will be described in Section 5. It introduces the separate communication channels for each occupied MO and establishes the relevant weighting factors and the crucial sign convention of their entropic bond increments, which reflects the bonding or antibonding character of the MO in question, in accordance with the signs of the associated off-diagonal matrix elements of the CBO matrix. This procedure will be applied to determine the π-bond alternation trends in simple hydrocarbons (Section 6) and the localized bonds in octahedral complexes (Section 7). Finally, the weighted-input approach for diatomic fragments in molecules will be formulated (Section 8). It will be shown that this new AO-resolved description using the flexible-input (bond) probabilities as weighting factors generates bond descriptors exhibiting excellent agreement with both the chemical intuition and the quantum-mechanical bond orders formulated in the standard SCF-LCAO-MO theory.

Throughout this article, the bold symbol $\mathbf{X}$ represents a square or rectangular matrix, the bold-italic $\boldsymbol{X}$ denotes the row vector, and italic X stands for the scalar quantity. The entropy/information descriptors are measured in *bits*, which correspond to the base 2 in the logarithmic (Shannon) measure of information.

2. MOLECULAR INFORMATION CHANNELS IN ORBITAL RESOLUTION

In the standard MO theory of molecular electronic structure the network of chemical bonds is determined by the system-occupied MO in the electron configuration in question. For simplicity, let us first assume the *closed-shell* (cs) ground state of the $N=2n$ electronic system in the *Restricted Hartree–Fock* (RHF) description, involving the n lowest (real and orthonormal), doubly occupied MO. In the LCAO-MO approach, they are given as linear combinations of the appropriate (orthogonalized) basis functions $\boldsymbol{\chi}=(\chi_1,\chi_2,\ldots,\chi_m)=\{\chi_i\}$, $\langle\boldsymbol{\chi}|\boldsymbol{\chi}\rangle=\{\delta_{i,j}\}\equiv\mathbf{I}$, for example, Löwdin's symmetrically orthogonalized AO, $\boldsymbol{\varphi}=(\varphi_1,\varphi_2,\ldots,\varphi_n)=\{\varphi_s\}=\boldsymbol{\chi}\mathbf{C}$, where the rectangular matrix $\mathbf{C}=\{C_{i,s}\}$ groups the relevant LCAO-expansion coefficients.

The system electron density $\rho(\boldsymbol{r})$ and hence the one-electron probability distribution $p(\boldsymbol{r})=\rho(\boldsymbol{r})/N$, that is, the density per electron or the *shape* factor of ρ, are determined by the first-order density matrix $\boldsymbol{\gamma}$ in the AO representation, also called the *charge and bond order* (CBO) matrix,

$$\rho(\boldsymbol{r})=2\boldsymbol{\varphi}(\boldsymbol{r})\boldsymbol{\varphi}^{\dagger}(\boldsymbol{r})=\boldsymbol{\chi}(\boldsymbol{r})[2\mathbf{C}\mathbf{C}^{\dagger}]\boldsymbol{\chi}^{\dagger}(\boldsymbol{r})\equiv\boldsymbol{\chi}(\boldsymbol{r})\boldsymbol{\gamma}\boldsymbol{\chi}^{\dagger}(\boldsymbol{r})=Np(\boldsymbol{r}). \tag{1}$$

The latter represents the projection operator $\hat{P}_{\varphi}=|\boldsymbol{\varphi}\rangle\langle\boldsymbol{\varphi}|=\sum_s|\varphi_s\rangle\langle\varphi_s|\equiv\sum_s\hat{P}_s$ onto the subspace of all doubly occupied MO,

$$\boldsymbol{\gamma}=2\langle\boldsymbol{\chi}|\boldsymbol{\varphi}\rangle\langle\boldsymbol{\varphi}|\boldsymbol{\chi}\rangle=2\mathbf{C}\mathbf{C}^{\dagger}\equiv2\langle\boldsymbol{\chi}|\hat{P}_{\varphi}|\boldsymbol{\chi}\rangle=\{\gamma_{i,j}=2\langle\chi_i|\hat{P}_{\varphi}|\chi_j\rangle\equiv2\langle i|\hat{P}_{\varphi}|j\rangle\}, \tag{2a}$$

thus, satisfying the appropriate idempotency relation

$$(\boldsymbol{\gamma})^2=4\langle\boldsymbol{\chi}|\hat{P}_{\varphi}|\boldsymbol{\chi}\rangle\langle\boldsymbol{\chi}|\hat{P}_{\varphi}|\boldsymbol{\chi}\rangle=4\langle\boldsymbol{\chi}|\hat{P}_{\varphi}^2|\boldsymbol{\chi}\rangle=4\langle\boldsymbol{\chi}|\hat{P}_{\varphi}|\boldsymbol{\chi}\rangle=2\boldsymbol{\gamma}. \tag{3}$$

The CBO matrix reflects the promoted, valence state of AO in the molecule, with the diagonal elements measuring the effective electron occupations of the basis functions, $\{\gamma_{i,i}=N_i=Np_i\}$. The AO-probability vector in this state, $\boldsymbol{p}=\{p_i=N_i/N\}$, groups the probabilities of the basis functions being occupied in the molecule.

The information system in the (condensed) orbital resolution involves the AO events $\boldsymbol{\chi}$ in its input $\boldsymbol{a}=\{\chi_i\}$ and output $\boldsymbol{b}=\{\chi_j\}$. It represents the effective promotion of these basis functions in the molecule via the probability/information scattering described by the conditional probabilities of AO outputs given AO inputs, with the input (*row*) and output (*column*) indices, respectively. In the one-electron approach [46–48], these AO-communication connections $\{P(\chi_j|\chi_i) \equiv P(j|i)\}$ result from the appropriately generalized superposition principle of quantum mechanics [51],

$$\mathbf{P}(\boldsymbol{b}|\boldsymbol{a}) = \left\{P(j|i) = \mathcal{N}_i|\langle i|\hat{P}_{\boldsymbol{\varphi}}|j\rangle|^2 = (2\gamma_{i,i})^{-1}\gamma_{i,j}\gamma_{j,i}\right\}, \quad \sum_j P(j|i) = 1, \tag{4}$$

where the closed-shell normalization constant $\mathcal{N}_i = (2\boldsymbol{\gamma}_{i,i})^{-1}$ follows directly Eq. (3). These (physical) one-electron probabilities explore the dependencies between AOs resulting from their participation in the system-occupied MO, that is, their involvement in the entire network of chemical bonds in a molecule. This molecular channel can be probed using both the promolecular ($\boldsymbol{p}^0 = \{p_i^0\}$) and molecular ($\boldsymbol{p}$) input probabilities, in order to extract the IT multiplicities of the *ionic* and *covalent* bond components, respectively.

In the *open-shell* (os) case [48] one partitions the CBO matrix into contributions originating from the closed-shell (doubly occupied) MO $\boldsymbol{\varphi}^{\mathrm{cs}}$ and the open-shell (singly occupied) MO $\boldsymbol{\varphi}^{\mathrm{os}}$, $\boldsymbol{\varphi} = (\boldsymbol{\varphi}^{\mathrm{cs}}, \boldsymbol{\varphi}^{\mathrm{os}})$:

$$\boldsymbol{\gamma} = \langle\boldsymbol{\chi}|\boldsymbol{\varphi}^{\mathrm{os}}\rangle\langle\boldsymbol{\varphi}^{\mathrm{os}}|\boldsymbol{\chi}\rangle + 2\langle\boldsymbol{\chi}|\boldsymbol{\varphi}^{\mathrm{cs}}\rangle\langle\boldsymbol{\varphi}^{\mathrm{cs}}|\boldsymbol{\chi}\rangle \equiv \langle\boldsymbol{\chi}|\hat{P}_{\boldsymbol{\varphi}}^{\mathrm{os}}|\boldsymbol{\chi}\rangle + 2\langle\boldsymbol{\chi}|\hat{P}_{\boldsymbol{\varphi}}^{\mathrm{cs}}|\boldsymbol{\chi}\rangle \equiv \boldsymbol{\gamma}^{\mathrm{os}} + \boldsymbol{\gamma}^{\mathrm{cs}}. \tag{5}$$

They satisfy separate idempotency relations,

$$(\boldsymbol{\gamma}^{\mathrm{os}})^2 = \left\langle\boldsymbol{\chi}\middle|\hat{P}_{\boldsymbol{\varphi}}^{\mathrm{os}}\middle|\boldsymbol{\chi}\right\rangle\left\langle\boldsymbol{\chi}\middle|\hat{P}_{\boldsymbol{\varphi}}^{\mathrm{os}}\middle|\boldsymbol{\chi}\right\rangle = \left\langle\boldsymbol{\chi}\middle|(\hat{P}_{\boldsymbol{\varphi}}^{\mathrm{os}})^2\middle)\boldsymbol{\chi}\right\rangle = \left\langle\boldsymbol{\chi}\middle|\hat{P}_{\boldsymbol{\varphi}}^{\mathrm{os}}\middle|\boldsymbol{\chi}\right\rangle = \boldsymbol{\gamma}^{\mathrm{os}}, \tag{6}$$

and $(\boldsymbol{\gamma}^{\mathrm{cs}})^2 = 2\boldsymbol{\gamma}^{\mathrm{cs}}$ (Eq. [3]). Hence,

$$P(j|i) = \mathcal{N}_i|\langle i|\hat{P}_{\boldsymbol{\varphi}}|j\rangle|^2 = (\gamma_{i,i}^{\mathrm{os}} + 2\gamma_{i,i}^{\mathrm{cs}})^{-1}\gamma_{i,j}\gamma_{j,i}, \tag{7a}$$

The conditional probabilities of Eqs. (4 and 7a) define the probability scattering in the AO-promotion channel of the molecule, in which the "signals" of the molecular (or promolecular) electron allocations to basis functions are transmitted between the AO inputs and outputs. Such information system constitutes the basis of OCT [46–48]. The off-diagonal conditional probability of jth AO output given ith AO input is thus proportional to the squared element of the CBO matrix linking the two AOs, $\gamma_{j,i} = \gamma_{i,j}$. Therefore, it is also proportional to the corresponding AO contribution $\mathcal{M}_{i,j} = \gamma_{i,j}^2$ to the Wiberg

index [52] of the chemical bond covalency between two atoms A and B, $\mathcal{M}(\mathrm{A,B}) = \sum_{i\in\mathrm{A}}\sum_{j\in\mathrm{B}} \mathcal{M}_{i,j}$, or to generalized quadratic descriptors of molecular bond multiplicities [53–63].

By separating the CBO contributions due to each occupied MO one similarly defines the information system for each orbital. For example, in the closed-shell system, each doubly occupied MO $\boldsymbol{\varphi} = \{\varphi_s\}$ generates the corresponding contributions to the CBO matrix of Eq. (2):

$$\boldsymbol{\gamma} = 2\sum_s \langle \boldsymbol{\chi}|\varphi_s\rangle\langle\varphi_s|\boldsymbol{\chi}\rangle \equiv \sum_s \boldsymbol{\gamma}_s^{\mathrm{cs}}, \quad \boldsymbol{\gamma}_s^{\mathrm{cs}} = \left\{\gamma_{i,j}^{\mathrm{cs}}(s) = 2\langle i|\hat{P}_s|j\rangle\right\}, \tag{2b}$$

In the open-shell configuration, one separately partitions the contribution of $\boldsymbol{\gamma}^{\mathrm{cs}} = \sum_s^{\mathrm{cs}} \boldsymbol{\gamma}_s^{\mathrm{cs}}$, due to the doubly occupied MO $\boldsymbol{\varphi}^{\mathrm{cs}}$, and the remaining part $\boldsymbol{\gamma}^{\mathrm{os}} = \sum_s^{\mathrm{os}} \boldsymbol{\gamma}_s^{\mathrm{os}}$, $\boldsymbol{\gamma}_s^{\mathrm{os}} = \{\gamma_{i,j}^{\mathrm{os}}(s) = \langle i|\hat{P}_s|j\rangle\}$, generated by the singly occupied MO $\boldsymbol{\varphi}^{\mathrm{os}}$. They satisfy the corresponding idempotency relations (see Eqs. [3 and 6]): $(\boldsymbol{\gamma}_s^{\mathrm{cs}})^2 = 2\boldsymbol{\gamma}_s^{\mathrm{cs}}$ and $(\boldsymbol{\gamma}_s^{\mathrm{os}})^2 = \boldsymbol{\gamma}_s^{\mathrm{os}}$. One then determines the corresponding communication connections for each occupied MO,

$$\mathbf{P}_s^{\mathrm{os}}(\boldsymbol{b}|\boldsymbol{a}) = \left\{P_s^{\mathrm{os}}(j|i) = \frac{\gamma_{i,j}^{\mathrm{os}}(s)\gamma_{j,i}^{\mathrm{os}}(s)}{\gamma_{i,i}^{\mathrm{os}}(s)}\right\} \quad \text{and} \quad \mathbf{P}_s^{\mathrm{cs}}(\boldsymbol{b}|\boldsymbol{a}) = \left\{P_s^{\mathrm{cs}}(j\,|i) = \frac{\gamma_{i,j}^{\mathrm{cs}}(s)\gamma_{j,i}^{\mathrm{cs}}(s)}{2\gamma_{i,i}^{\mathrm{cs}}(s)}\right\}, \tag{7b}$$

were obtained using Eqs. (4a and 7a) with the normalization constants appropriately modified to satisfy the normalization condition for the conditional probabilities:

$$\sum_j P_s^{\mathrm{cs}}(j|i) = \sum_j P_s^{\mathrm{os}}(j|i) = 1. \tag{7c}$$

In OCT, the entropy/information indices of the covalent/ionic components of all chemical bonds in a molecule represent the complementary descriptors of the average communication noise and the amount of information flow in the molecular information channel. The molecular input $\boldsymbol{p}(\boldsymbol{a}) \equiv \boldsymbol{p}$ generates the same distribution in the output of the molecular channel,

$$\boldsymbol{p}\mathbf{P}(\boldsymbol{b}|\boldsymbol{a}) = \left\{\sum_i p_i P(j|i) \equiv \sum_i P(i,j) = p_j\right\} = \boldsymbol{p} \tag{8}$$

and thus identifying $\boldsymbol{p}$ as the *stationary* probability vector for the molecular state in question. In the preceding equation we have used the partial normalization of the molecular joint, two-orbital probabilities $\mathbf{P}(\boldsymbol{a},\ \boldsymbol{b}) = \{P(i,j) = p_i P(j|i)\}$ to the corresponding one-orbital probabilities. It should be observed at this point that the promolecular input $\boldsymbol{p}(\boldsymbol{a}^0) \equiv \boldsymbol{p}^0$ in general produces different output probability $\boldsymbol{p}^0\mathbf{P}(\boldsymbol{b}|\boldsymbol{a}) = \boldsymbol{p}^*(\boldsymbol{a}^0) = \{p_j^*\} = \boldsymbol{p}^* \neq \boldsymbol{p}$.

The purely molecular communication channel [9, 38, 46–48], with $\boldsymbol{p}$ defining its input signal, is devoid of any reference (history) of the chemical bond formation and generates the average noise index of the molecular IT bond covalency, measured by the *conditional entropy* $S(\boldsymbol{b}|\boldsymbol{a}) \equiv S$ of the system outputs given inputs:

$$S(\boldsymbol{b}|\boldsymbol{a}) = -\sum_i \sum_j P(i,j)\log_2[P(i,j)/p_i]$$
$$= -\sum_i p_i \sum_j P(j|i)\log_2 P(j|i) \equiv S[\boldsymbol{p}|\boldsymbol{p}] \equiv S[\mathbf{P}(\boldsymbol{b}|\boldsymbol{a})] \equiv S. \quad (9a)$$

Thus, this average noise descriptor expresses the difference between the Shannon entropies of the molecular one- and two-orbital probabilities,

$$S = H[\mathbf{P}(\boldsymbol{a},\boldsymbol{b})] - H[\boldsymbol{p}];$$
$$H[\boldsymbol{p}] = -\sum_i p_i \log_2 p_i,$$
$$H[\mathbf{P}(\boldsymbol{a},\boldsymbol{b})] = -\sum_i \sum_j P(i,j)\log_2 P(i,j). \quad (9b)$$

For the independent input and output events, when $\mathbf{P}^{\text{ind.}}(\boldsymbol{a},\boldsymbol{b}) = \{p_i p_j\}$, $H[\mathbf{P}^{\text{ind.}}(\boldsymbol{a},\boldsymbol{b})] = 2H[\boldsymbol{p}]$ and hence $S^{\text{ind.}} = H[\boldsymbol{p}]$.

The molecular channel with $\boldsymbol{p}^0$ determining its input signal refers to the initial state in the bond formation process, for example, the atomic *promolecule*—a collection of nonbonded free atoms in their respective positions in a molecule or the AO basis functions with the atomic ground-state occupations, before their mixing into MO [9, 38, 46–48]. The AO occupations in this reference state are fractional in general. However, in view of the exploratory character of the present analysis, we shall often refer to the simplest description of the promolecular reference by a single (ground-state) electron configuration, which exhibits the integral occupations of AO. It gives rise to the average information-flow descriptor of the system IT bond ionicity, given by the *mutual information* in the channel inputs and outputs:

$$I(\boldsymbol{a}^0:\boldsymbol{b}) = \sum_i \sum_j P(i,j)\log_2[P(i,j)/(p_j p_i^0)] = H[\boldsymbol{p}] + H[\boldsymbol{p}^0] - H[\mathbf{P}(\boldsymbol{a},\boldsymbol{b})]$$
$$= H[\boldsymbol{p}^0] - S = I[\boldsymbol{p}^0:\boldsymbol{p}] \equiv I[\mathbf{P}(\boldsymbol{b}|\boldsymbol{a})] = I, \quad (10)$$

This quantity reflects the fraction of the initial (promolecular) information content $H[\boldsymbol{p}^0]$, which has not been dissipated as noise in the molecular communication system. In particular, for the molecular input, when $\boldsymbol{p}^0 = \boldsymbol{p}$,

$I(\boldsymbol{a}:\boldsymbol{b}) = \sum_i \sum_j P(i,j)\log_2[P(i,j)/(p_j p_i)] = H[\boldsymbol{p}] - S = I[\boldsymbol{p}:\boldsymbol{p}]$. Thus, for the independent input and output events, $I^{\text{ind.}}(\boldsymbol{a}:\boldsymbol{b}) = 0$.

Finally, the sum of these two bond components,

$$\mathcal{N}(\boldsymbol{a}^0;\boldsymbol{b}) = S + I \equiv \mathcal{N}[\boldsymbol{p}^0;\boldsymbol{p}] \equiv \mathcal{N}[\mathbf{P}(\boldsymbol{b}|\boldsymbol{a})] \equiv \mathcal{N} = H[\boldsymbol{p}^0], \tag{11}$$

measures the overall IT bond multiplicity of all bonds in the molecular system under consideration. It is seen to be conserved at the promolecular-entropy level, which marks the initial information content of orbital probabilities. Again, for the molecular input, when $\boldsymbol{p}^0 = \boldsymbol{p}$, this quantity preserves the Shannon entropy of the molecular input probabilities: $\mathcal{N}(\boldsymbol{a};\boldsymbol{b}) = S(\boldsymbol{b}|\boldsymbol{a}) + I(\boldsymbol{a}:\boldsymbol{b}) = H[\boldsymbol{p}]$.

It should be emphasized that these entropy/information descriptors and the underlying probabilities depend on the selected basis set, for example, the *canonical* AO of the isolated atoms or the *hybrid orbitals* (HOs) of their promoted (valence) states, the *localized MO* (LMO), etc. In what follows we shall examine these IT descriptors of chemical bonds in illustrative model systems. The emphasis will be placed on the orbital decoupling in the molecular communication channels and the need for appropriate changes in their input probabilities, which weigh the contributions to the average information descriptors from each input.

There are two aspects of the orbital decoupling in chemical bonds. On one side, the two chemically interacting AOs becomes decoupled, when they do not mix into MO, for example, in the extreme MO-polarization limit of the electronic *lone* pair, when two bonding electrons occupy a single AO. On the other side, the two AOs are also effectively decoupled, no matter how strong is their mutual mixing, when the bonding and antibonding MO combinations are completely occupied by electrons, since such MO configuration is physically equivalent to the Slater determinant of the doubly occupied (original) AO. We shall call these two facets the *mixing* (shape) and *occupation* (population) decouplings, respectively.

It is of vital interest for a wider applicability of CTCB to examine how these two mechanisms can be accommodated in OCT. In Section 3, we shall argue that the mutual decoupling status of several subsets of basis functions, manifesting itself by the absence of any external communications (bond orders) in the whole system, calls for the separate unit normalization of its input probabilities since such fragments constitute the mutually nonbonded (closed) building blocks of the molecular electronic structure. It will be demonstrated, using simple hydrides as an illustrative example, that the fulfillment of this requirement dramatically improves the agreement with the accepted chemical intuition and the alternative bond multiplicity concepts formulated in the MO theory.

To conclude this section, we observe that by propagating the AO probabilities through the information channels of the separate MO, defined by the conditional probabilities of Eq. (7b), one could similarly determine the

IT bond increments for each occupied MO. We shall implement this idea in Section 5, when tackling the *populational* decoupling of atomic orbitals, as a result of an increased occupation of the antibonding MO.

3. DECOUPLED (LOCALIZED) BONDS IN HYDRIDES REVISITED

In the ground-state the chemical interaction between two (singly occupied) orthonormal AOs $\boldsymbol{\chi} = (a, b)$ originating from atoms A and B, respectively, gives rise to the doubly occupied, *bonding* MO $\varphi_{\text{bond.}}$ and the unoccupied antibonding MO $\varphi_{\text{anti.}}$,

$$\varphi_{\text{bond.}} = \sqrt{P}a + \sqrt{Q}b, \quad \varphi_{\text{anti.}} = -\sqrt{Q}a + \sqrt{P}b, \quad P + Q = 1. \tag{12}$$

Their shapes are determined by the complementary (conditional) probabilities: $P(a|\varphi_{\text{bond.}}) = P(b|\varphi_{\text{anti.}}) = P$ and $P(b|\varphi_{\text{bond.}}) = P(a|\varphi_{\text{anti.}}) = Q$, which control the bond polarization, covering the symmetrical bond combination for $P = Q = 1/2$ and the limiting lone-pair (nonbonding) configurations for $P = (0, 1)$. The associated model CBO matrix,

$$\boldsymbol{\gamma} = 2\begin{bmatrix} P & \sqrt{PQ} \\ \sqrt{PQ} & Q \end{bmatrix}, \tag{13}$$

then generates the information system for such a two-AO model, shown in Scheme 1.1a.

In this diagram one adopts the molecular input $\boldsymbol{p} = (P, Q = 1 - P)$, to extract the bond IT covalency index measuring the channel average communication noise, and the promolecular input $\boldsymbol{p}^0 = (1/2, 1/2)$, to calculate the IT ionicity relative to this *covalent* promolecule, in which each basis function contributes a single electron to form the chemical bond. The bond IT covalency $S(P)$ is then determined by the *binary entropy function* $H(P) = -P\log_2 P - Q\log_2 Q = H[\boldsymbol{p}]$. It reaches the maximum value $H(P = 1/2) = 1$ for the symmetric bond $P = Q = 1/2$ and vanishes for the lone-pair configurations, when $P = (0, 1), H(P = 0) = H(P = 1) = 0$, marking the alternative ion-pair configurations A^+B^- and A^-B^+, respectively, relative to the initial AO occupations $\boldsymbol{N}^0 = (1, 1)$ in the assumed promolecular reference. The complementary descriptor of the IT ionicity, determining the channel (mutual) information *capacity* $I(P) = H[\boldsymbol{p}^0] - H(P) = 1 - H(P)$, reaches the highest value for these two limiting electron-transfer configurations $P = (0, 1) : I(P = 0, 1) = 1$. Thus, this ionicity descriptor is seen to identically vanish for the purely covalent, symmetric bond, $I(P = 1/2) = 0$.

Both components yield the conserved overall bond index $\mathcal{N}(P) = 1$ in the whole range of bond polarizations $P \in [0, 1]$. Therefore, this model properly accounts for the competition between the bond covalency and ionicity, while

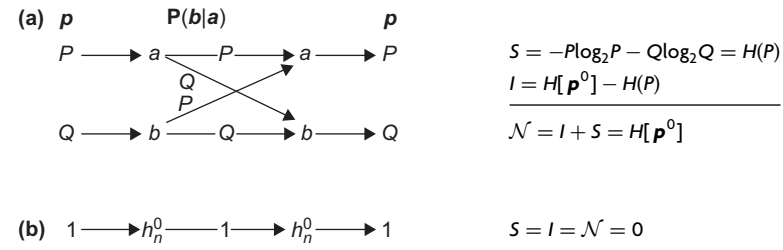

Scheme 1.1 The molecular information system modeling the chemical bond between two basis functions $\chi = (a, b)$ and its entropy/information descriptors. In Panel *b*, the corresponding *non*bonding (deterministic) channel due to the lone-pair hybrid h_n^0 is shown. For the molecular input $\boldsymbol{p} = (P, Q)$, the orbital channel of Panel *a* gives the bond entropy-covalency represented by the binary entropy function $H(P)$. For the promolecular input $\boldsymbol{p}^0 = (1/2, 1/2)$, when both basis functions contribute a single electron each to form the chemical bond, one thus predicts $H[\boldsymbol{p}^0] = 1$ and the bond information ionicity $I = 1 - H(P)$. Hence, these two bond components give rise to the conserved (P-independent) value of the single overall bond multiplicity $\mathcal{N} = I + S = 1$.

preserving the single measure of the overall IT multiplicity of the chemical bond. Similar effects transpire from the two-electron CTCB [9] and the quadratic bond indices formulated in the MO theory [53–63].

This localized bond model can be straightforwardly extended to the system of r localized bonds in simple hydrides XH_r [49], for example, CH_4, NH_3, or H_2O, for $r = 4, 3, 2$, respectively. Indeed, a single σ bond X–H_α, for $X = C$, N, O and $\alpha = 1, \ldots, r$, can then be approximately regarded as resulting from the chemical interaction of a pair of two orthonormal orbitals: the bonding sp^3 hybrid h_α of the central atom, directed towards the hydrogen ligand H_α, and the $1s_\alpha \equiv \sigma_\alpha$ orbital of the latter. The localized bond X–H_α then originates from the double occupation of the corresponding bonding MO $\varphi_{\text{bond.}}(\alpha)$, with the antibonding MO $\varphi_{\text{anti.}}(\alpha)$ remaining empty:

$$\varphi_{\text{bond.}}(\alpha) = \sqrt{P}h_\alpha + \sqrt{Q}\sigma_\alpha, \quad \varphi_{\text{anti.}}(\alpha) = -\sqrt{Q}h_\alpha + \sqrt{P}\sigma_\alpha \quad P + Q = 1. \tag{14}$$

In the $\boldsymbol{\chi}_\alpha = (h_\alpha, \sigma_\alpha)$ representation, the corresponding CBO matrix $\boldsymbol{\gamma}_\alpha$ for a single σ bond X–$H_\alpha\{\gamma_{\alpha,\beta}\}$ then includes the following nonvanishing elements:

$$\gamma_{h_\alpha,h_\alpha} = 2P, \quad \gamma_{\sigma_\alpha,\sigma_\alpha} = 2Q, \quad \gamma_{h_\alpha,\sigma_\alpha} = \gamma_{\sigma_\alpha,h_\alpha} = 2\sqrt{PQ}, \tag{15}$$

while for each of $4 - r$ nonbonded hybrids $\{h_n\}$, describing the system lone-electronic pairs,

$$\gamma_{h_n,h_n} = 2 \quad \text{and} \quad \gamma_{h_n,j} = 0, \quad j \neq h_n. \tag{16}$$

The corresponding conditional probabilities (see Eq. [4]), which determine the nonvanishing communication connections, then read:

$$P(h_\alpha|h_\alpha) = P, \quad P(\sigma_\alpha|\sigma_\alpha) = Q, \quad P(h_\alpha|\sigma_\alpha) = Q, \quad P(\sigma_\alpha|h_\alpha) = P, \quad P(h_n|h_n) = 1. \tag{17}$$

Therefore, the electron probability is not scattered by the lone-pair hybrids. As a result such *decoupled* subchannels $\{h_n = h_n^0\}$ representing two lone pairs of oxygen atom in H_2O or a single nonbonding electron pair of nitrogen in NH_3, introduce the exactly vanishing contributions to both bond components and hence to the overall bond index of these molecules in OCT.

It follows from these expressions that each localized bond X–H_α in this HO representation defines the separate communication system of Scheme 1.1a, consisting of inputs and outputs $\boldsymbol{\chi}_\alpha = (h_\alpha, \sigma_\alpha)$, which does not exhibit any external communications with AO involved in the system remaining bonds. Therefore, such orbital pairs constitute the externally closed (nonbonding) subsystems, determining the mutually decoupled information systems defined by the diagonal blocks

$$\mathbf{P}_\alpha(\boldsymbol{b}_\alpha|\boldsymbol{a}_\alpha) \equiv \mathbf{P}_\alpha[\boldsymbol{\chi}_\alpha|\boldsymbol{\chi}_\alpha] = \begin{bmatrix} P & Q \\ P & Q \end{bmatrix}, \quad \mathbf{P}_\alpha(\boldsymbol{a}_\alpha, \boldsymbol{b}_\alpha) \equiv \mathbf{P}_\alpha[\boldsymbol{\chi}_\alpha, \boldsymbol{\chi}_\alpha] = \begin{bmatrix} P^2 & PQ \\ QP & Q^2 \end{bmatrix}, \tag{18}$$

of the associated overall probability matrices in the $\boldsymbol{\chi} = \{\boldsymbol{\chi}_\alpha\}$ basis set: $\mathbf{P}(\boldsymbol{b}|\boldsymbol{a}) = \{\mathbf{P}_\alpha(\boldsymbol{b}_\alpha|\boldsymbol{a}_\alpha)\delta_{\alpha,\beta}\}$ and $\mathbf{P}(\boldsymbol{a}, \boldsymbol{b}) = \{\mathbf{P}_\alpha(\boldsymbol{a}_\alpha, \boldsymbol{b}_\alpha)\delta_{\alpha,\beta}\}$. Such mutually closed (isolated) subchannels correspond to the *separate* input/output probability distributions, $\boldsymbol{p}_\alpha^0 = (1/2, 1/2)$ or $\boldsymbol{p}_\alpha = \boldsymbol{p}_\alpha^* = (P, Q)$, each satisfying the unit normalization [9, 26]. These separate molecular subsystems give rise to the additive bond contributions $S_\alpha(\boldsymbol{b}_\alpha|\boldsymbol{a}_\alpha) \equiv S_\alpha$, $I_\alpha(\boldsymbol{a}_\alpha^0 : \boldsymbol{b}_\alpha) \equiv I_\alpha$ and $\mathcal{N}_\alpha(\boldsymbol{a}_\alpha^0 : \boldsymbol{b}_\alpha) = S_\alpha + I_\alpha \equiv \mathcal{N}_\alpha$ to the system overall bond descriptors in OCT:

$$S(P) = \sum_\alpha S_\alpha = rH(P), \quad I(P) = \sum_\alpha I_\alpha = r[1 - H(P)], \quad \mathcal{N} = \sum_\alpha \mathcal{N}_\alpha = r. \tag{19}$$

We have recognized in these expressions that each lone-pair (doubly occupied) hybrid h_n of the central atom, which does not form any chemical bonds (communications) with the hydrogen ligands, generates the decoupled deterministic subchannel of Scheme 1.1b, thus exhibiting the unit input probability. Therefore, it does not contribute to the resultant entropy/information index of all chemical bonds in the molecule.

The same result follows from another, delocalized representation of chemical bonds in these prototype systems. Consider, as an illustration, the canonical valence-shell MO in CH_4, with four hydrogen ligands in the alternating corners of the cube placed in such a way, that the three axes of the Cartesian coordinate system pass through the middle of its opposite walls. In such an arrangement, the four delocalized bonds are described by the four (mutually decoupled) orbital-pair interactions between the specified canonical AO of carbon atom and the corresponding symmetry combination of four hydrogen orbitals. Again, the net result is the four decoupled bonds in the system giving rise to overall IT bond index $\mathcal{N} = 4$, with $S = 4H(P)$ and $I = 4[1 - H(P)]$.

One observes, however, a change in the bond covalent/ionic composition resulting from this transformation from the localized MO description to the canonical MO perspective [48]. As an illustration of this entropic effect, let us briefly examine the bonding pattern in the linear BeH_2. In the localized bond representation, the two bonding MOs result from the mutually decoupled interactions between two-orbital pairs, each including one *sp* hybrid of Be and 1*s* orbital of the corresponding hydrogen. This localized approach thus gives $\mathcal{N} = 2$, with $S = 2H(P)$ and $I = 2[1 - H(P)]$, and hence for the maximum orbital mixing ($P = 1/2$), the IT bond composition reads $S^{\text{max.}} = 2$ and $I^{\text{max.}} = 0$. In the delocalized description, the two doubly occupied canonical MO, expressed in the basis set $\boldsymbol{\chi} = (h_1, h_2, \sigma_1, \sigma_2)$ used to generate the localized MO of Eq. (12), read as follows:

$$\psi_1 = \sqrt{U}s + \sqrt{\frac{V}{2}}(\sigma_1 + \sigma_2) = \sqrt{\frac{U}{2}}(h_1 + h_2) + \sqrt{\frac{V}{2}}(\sigma_1 + \sigma_2), \quad U + V = 1,$$
$$\psi_2 = \sqrt{T}p + \sqrt{\frac{W}{2}}(\sigma_1 - \sigma_2) = \sqrt{\frac{T}{2}}(h_1 - h_2) + \sqrt{\frac{W}{2}}(\sigma_1 - \sigma_2), \quad T + W = 1. \tag{20}$$

The associated CBO matrix,

$$\boldsymbol{\gamma} = \begin{bmatrix} U+T & U-T & \sqrt{UV}+\sqrt{TW} & \sqrt{UV}-\sqrt{TW} \\ U-T & U+T & \sqrt{UV}-\sqrt{TW} & \sqrt{UV}+\sqrt{TW} \\ \sqrt{UV}+\sqrt{TW} & \sqrt{UV}-\sqrt{TW} & V+W & V-W \\ \sqrt{UV}-\sqrt{TW} & \sqrt{UV}+\sqrt{TW} & V-W & V+W \end{bmatrix}, \tag{21}$$

indicates that all these basis orbitals in fact exhibit the nonvanishing communications to all outputs in this delocalized representation of the system electronic structure. In the maximum mixing limit of $U = V = T = W = 1/2$

it is only partly decoupled,

$$\boldsymbol{\gamma}^{\text{max.}} = \begin{bmatrix} 1 & 0 & 1 & 0 \\ 0 & 1 & 0 & 1 \\ 1 & 0 & 1 & 0 \\ 0 & 1 & 0 & 1 \end{bmatrix}, \tag{22}$$

and so is the associated matrix $\mathbf{P}(\boldsymbol{b}|\boldsymbol{a}) = 1/2\boldsymbol{\gamma}^{\text{max.}}$ of molecular communications (see Eq. [4]). Thus, this delocalized channel is characterized by the input distributions $\boldsymbol{p} = \boldsymbol{p}^0 = \{1/4\}$, which give rise to the overall unit normalization. The associated entropy/information indices for this channel read as follows: $S^{\text{max.}} = I^{\text{max.}} = 1$ and hence $\mathcal{N}^{\text{max.}} = 2$.

The variable-input norm description of the decoupled chemical bonds gives the full agreement with the chemical intuition, of r bonds in XH_r, with changing covalent/ionic composition in accordance with the actual MO polarization and the adopted basis set representation. The more the probability parameter P deviates from the symmetrical bond (maximum covalency) value $P = 1/2$, due to the electronegativity difference between the central atom and hydrogen, the lower is the covalency (the higher ionicity) of this localized, diatomic bond. Therefore, in this IT description the total bond multiplicity $\mathcal{N} = r$ bits is conserved for changing proportions between the overall covalency and ionicity of all chemical bonds in the system under consideration.

In the orbital-communication theory, this "rivalry" between bond components reflects a subtle interplay between the electron delocalization ($S_\alpha = H(P)$) and localization ($I_\alpha = 1 - H(P)$) aspects of the molecular scattering of electron probabilities in the information channel of a separated single chemical bond, decoupled from the molecular remainder. The more deterministic is this probability propagation, the higher the ionic component. Accordingly, the more delocalized is this scattering, the higher the "noise" descriptor of the underlying information system.

4. FLEXIBLE-INPUT GENERALIZATION

Thus, it follows from the analysis of the preceding section that a general agreement of IT descriptors with the intuitive chemical estimates follows only when each externally decoupled fragment of a molecule exhibits the separate unit normalization of its input probabilities; this requirement expresses its externally closed status relative to the molecular remainder. It modifies the overall norm of the molecular input to the number of such mutually closed, noncommunicating fragments of the whole molecular system. This requirement was hitherto missing in all previous applications of CTCB and OCT to polyatomic systems.

In the generalized approach the probabilities $\boldsymbol{p}_\alpha^0 = \{p_a^\alpha\}$ of the constituent inputs in the given *externally* decoupled (noncommunicating and nonbonded) subchannel α^0 of the system "promolecular" reference $\mathrm{M}^0 = (\alpha^0|\beta^0|\ldots)$ should thus exhibit the *internal* (intrasubsystem) normalization, $\sum_{a\in\alpha} p_a^\alpha = 1$; we have denoted the externally closed status of each fragment in M^0 by separating it with the vertical *solid* lines from the rest of the molecule. Therefore, these subsystem probabilities are, in fact, *conditional* in character; $p_a^\alpha = P(a|\alpha) = p_a/P_\alpha$, calculated per unit input probability $P_\alpha = 1$ of the whole subsystem α in the collection of the mutually nonbonded subsystems in the reference M^0, that is, when this molecular fragment is not considered to be a part of a larger system. Indeed, the above summation over the internal orbital events then expresses the normalization of all such conditional probabilities in the separate (or isolated) subsystem α^0: $\sum_{a\in\alpha} P(a|\alpha) = 1$.

This situation changes discontinuously in the externally coupled (communicating and bonded) case, when the same subsystem exhibits non-vanishing (no matter how small) communications with the remainder of the molecule $\mathrm{M} = (\alpha|\beta|\ldots)$. Such *bonded* fragments of the molecule are mutually open, as symbolically denoted by the vertical *broken* lines separating them. They are characterized by the fractional condensed probabilities $\boldsymbol{P} = \{P_\alpha^{\mathrm{M}} < 1\}$, which measure the probabilities of the constituent subsystems in M as a whole. Therefore, the input probabilities of the bonded fragment α in M, $\boldsymbol{p}_\alpha^{\mathrm{M}} = \{p_a^{\mathrm{M}} = P_\alpha^{\mathrm{M}}\, p_a^\alpha\}$, are then subject to the *molecular* normalization: $\sum_{a\in\alpha} p_a^\alpha = P_\alpha^{\mathrm{M}} \sum_{a\in\alpha} p_a^\alpha = P_\alpha^{\mathrm{M}}$. The need for using the molecular input probabilities then causes a discontinuous change in the system covalent/ionic bond components compared with the corresponding decoupled (promolecular) values. Indeed, the former corresponds to the unit norm of input probabilities for all molecular subsystems, whereas in the latter, each decoupled fragment appears as a separate system, thus alone exhibiting the unit probability normalization.

In the previous, fixed-input determination of the IT bond indices this discontinuity in the transition from the decoupled to the coupled descriptions of the molecular fragments prevents an interpretation of the former as the limiting case of the latter, when all external communications of the subsystem in question become infinitely small. In other words, the fixed- and flexible-input approaches generate the mutually exclusive sets of bond indices, which cannot describe this transition in a continuous ("causal") fashion. As we have demonstrated in the decoupled approach of the preceding section, only the overall input normalization equal to the number of the decoupled orbital subsystems gives rise to the full agreement with the accepted chemical intuition.

Therefore, in this section we shall attempt to remove this discontinuity in the unifying, flexible-input generalization of the use of the molecular information systems. We shall demonstrate that in such an extension the above limiting transition in the communication description of the subsystem

decoupling in the molecule finds the continuous (causal) representation. In order to make this transition continuous, the separate input-dependent distributions, tailored for each ith input event, have to explicitly depend on the structure of its molecular communications, which is embodied in the ith row of the system two-orbital conditional probabilities. Indeed, they have to continuously increase the overall norm of the distribution for the given input orbital with increasing localization of the molecular scattering of this input signal to reach the unit input norm in the limit of this orbital being totally decoupled from the rest of the molecule.

The essence of the new proposition lies in a separate determination of the entropy/information contributions due to each AO input in the molecular channel specified by the conditional probabilities $\mathbf{P}(\boldsymbol{b}|\boldsymbol{a})$. This goal can be tackled by using the separate probability distributions tailored for each input. The hitherto single molecular propagation of the overall molecular input probabilities $\boldsymbol{p}$ of the previous approach, carried out to extract the IT covalent bond descriptor, will now be replaced by the series of m molecular propagations of the separate probability distributions $\{\boldsymbol{p}(i) = \{p(k;i)\}$ for each molecular input $i = 1, 2, \ldots, m$, which generate the associated covalencies: $\{S(i) = S[\boldsymbol{p}(i)]\}$. The reference promolecular probabilities, also input dependent $\{\boldsymbol{p}(i^0) = \{p(k;i^0)\}$, will be used to estimate the corresponding ionic contributions due to each input: $\{I(i) = I[\boldsymbol{p}(i^0)]\}$. Together, these input-dependent contributions generate the corresponding total indices $\{\mathcal{N}(i) = I(i) + S(i) = \mathcal{N}[\boldsymbol{p}(i^0), \boldsymbol{p}(i)]\}$. Finally, the overall IT bond descriptor of M as a whole will be generated by the summation of all such additive contributions determined in the separate propagations of the input-tailored molecular/promolecular distributions: $\mathcal{N} = \sum_i \mathcal{N}(i)$. In the average molecular quantities, these contributions must be weighted with the appropriate *ensemble* probabilities of each input, for example, the molecular probabilities $\boldsymbol{p} = \{p_i\}$.

There are obvious normalization (sum) rules to be satisfied by these input-dependent probabilities. Consider first the completely coupled molecular channel, in which all orbitals interact chemically, thus exhibiting nonvanishing direct and/or indirect communications with the system remainder. In this case all molecular inputs have to be effectively probed to the full extent of the *unit* condensed probability of the molecule as a whole:

$$\sum_k p(k;i)] = \sum_k p(k;i^0)] = 1. \tag{23}$$

This condition recognizes a general category of these input-dependent probabilities $\{p(k;i)\}$ and $\{p(k;i^0)\}$ as conditional probabilities of two-orbital events, that is, the joint probabilities per unit probability of the specified input: $p(k;i) \equiv p(k|i)$ and $p(k;i^0) \equiv p(k|i^0)$. However, it should be emphasized that these probabilities are also conditional on the molecule as a whole, since

they correspond to the unit input probability in M or M^0, $\sum_i p_i = \sum_i p_i^0 = 1$,

$$p(k|i) = p(k|i\|M) = P(k|i), \quad p(k|i^0) = p(k|i^0\|M^0) = P(k|i^0) \equiv P(k|i). \tag{24}$$

In case of the decoupled single-orbital subsystem χ_i^0, only the diagonal probability scattering $P_i(i|i) = 1$ is observed in the molecule (Scheme 1.1b). The input-tailored conditional probabilities then refer to the unit input probability of the input $i(i^0)$ alone:

$$p(k|i) = p(i|i\|i) = p(i|i)\delta_{i,k} = p(k|i^0) = p(i|i^0\|i^0) = p(i^0|i^0)\delta_{i,k} = \delta_{i,k}. \tag{25}$$

In order to make the fragment decoupling continuous in this generalized description, the input probabilities $\{\boldsymbol{p}(i), \boldsymbol{p}^0(i)\}$ have to be replaced by the separate distributions reflecting the actual participation of ith AO in the chemical bonds (communications) of the molecule. Therefore, they both have to be related explicitly to the ith row in the conditional probability matrix $\mathbf{P}(\boldsymbol{b}|\boldsymbol{a}) = \{P(j|i)\}$, which reflects all communications (bonds) between this orbital input and all orbital outputs $\{j\}$ (columns in $\mathbf{P}(\boldsymbol{b}|\boldsymbol{a})$). This link must generate the separate subsystem probabilities p_α^0, when the fragment becomes decoupled from the rest of the molecular system, $\alpha \to \alpha^0$, when $\mathbf{P}(\boldsymbol{b}|\boldsymbol{a}_\alpha) \to \{\mathbf{P}(\boldsymbol{b}_\alpha|\boldsymbol{a}_\alpha)\delta_{\alpha,\beta}\}$, where $\mathbf{P}(\boldsymbol{b}_\alpha|\boldsymbol{a}_\alpha) = \{P(a'|a)\}$. Indeed, for the decoupled subsystem $\alpha^0 = (a, a', \ldots)$ only the internal communications of the corresponding block of the molecular conditional probabilities $\mathbf{P}(\boldsymbol{b}_\alpha|\boldsymbol{a}_\alpha) = \{P(a'|a)\}$ are allowed. They also characterize the internal conditional probabilities in α^0 since

$$p(j|i\|\alpha^0) = p(i,j\|\alpha^0)/p(i\|\alpha^0) = P(i,j\|M)/p(i\|M) = p(j|i\|M) = P(j|i). \tag{26}$$

Hence, $\{p(k|a\|\alpha^0) = p_\alpha(a'|a)\delta_{\alpha,\beta} = p(k|a^0\|\alpha^0) = p_\alpha(a'|a^0)\delta_{\alpha,\beta} = P(a'|a)\delta_{\alpha,\beta}\}$; again, the AO inputs in α are to be probed with an overall unit condensed probability: $\sum_{a'\in\alpha} P(a'|a) = 1$.

In the input-dependent molecular channels, all these requirements can be shown to be automatically satisfied when one selects the input-tailored probabilities, we seek, as the corresponding rows of the molecular conditional probability matrix $\mathbf{P}(\boldsymbol{b}|\boldsymbol{a}) = \{P(j|i)\}$. Consider the conditional-entropy contribution from ith channel:

$$S(i) = -\sum_k \sum_j P(k,j;i)\log_2[P(j,k)/p_k] = -\sum_k P(k|i)\left[\sum_j P(j|k)\log_2 P(j|k)\right]. \tag{27}$$

Since this entropy-covalency corresponds to the overall unit norm of probability distribution associated with ith input, in the average molecular quantity, corresponding to all mutually open basis functions, it has to be weighted by the actual probability p_i of this input in the molecule as a

whole. It can be directly verified that such averaging indeed reproduces the molecular index of Eq. (9):

$$\begin{aligned} S_{\text{av.}} &= \sum_i p_i S(i) \equiv \sum_i S_i = -\sum_i \sum_k \sum_j [p_i P(k|i)] P(j|k) \log_2 P(j|k) \\ &= -\sum_k \sum_j \left[\sum_i P(k,i) \right] P(j|k) \log_2 P(j|k) = -\sum_k \sum_j p_k P(j|k) \log_2 P(j|k) \\ &= -\sum_k \sum_j P(j,k) \log_2 P(j|k) = S. \end{aligned} \tag{28}$$

A similar demonstration can be carried out for the mutual-information (ionic) contributions:

$$\begin{aligned} I(i) &= \sum_k \sum_j P(k^0, j|i) \log_2 [P(j,k)/(p_j p_k^0)] = -S(i) - \sum_k \sum_j P(j,k^0) \log_2 p_k^0 \\ &= -S(i) - \sum_k p_k^0 \log_2 p_k^0 = -S(i) + H[\boldsymbol{p}^0], \\ I_{\text{av.}} &= \sum_i p_i I(i) \equiv \sum_i I_i = -S + H[\boldsymbol{p}^0], \end{aligned} \tag{29}$$

Thus, it follows from these contributions that they also reproduce the overall molecular bond index as the mean value of the partial, input AO contributions:

$$\begin{aligned} \mathcal{N}(i) &= S(i) + I(i) = -\sum_k \sum_j P(k^0, j) \log_2 p_k^0, \\ \mathcal{N}_{\text{av.}} &= \sum_i p_i \mathcal{N}(i) \equiv \sum_i \mathcal{N}_i = \mathcal{N} = H[\boldsymbol{p}^0]. \end{aligned} \tag{30}$$

To summarize, in the flexible-input extension of OCT the consistent use of the molecular channel is proposed, with only the molecular inputs being used in probability propagation. However, the promolecular reference distribution is seen to enter the final determination of the ionic (difference) components relative to the initial distribution of electrons before the bond formation.

As an illustration (see Scheme 1.2a), let us again consider the two-AO channel of Scheme 1.1a. We first observe that the input-dependent distributions in this model are identical with the molecular distribution (see Eq. [18]). The partial and average IT descriptors are also reported in this diagram, relative to the reference distribution $\boldsymbol{p}^0 = (1/2, 1/2)$ of the covalent promolecule, when two AOs contribute a single electron each to form the chemical bond.

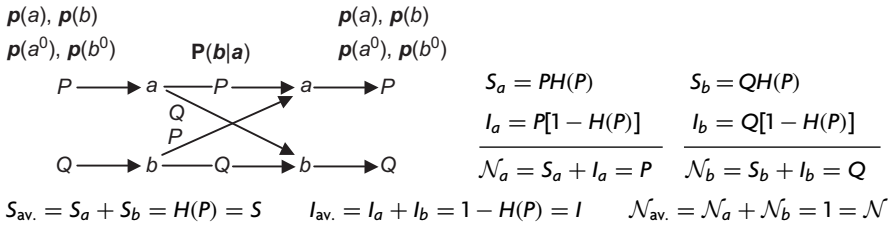

Scheme 1.2 The flexible-input generalization of the two-AO channel of Scheme 1.1a for the promolecular reference distribution $\boldsymbol{p}^0 = (1/2, 1/2)$. The corresponding partial and average entropy/information descriptors of the chemical bond are also reported.

The flexible-norm generalization of the previous OCT completely reproduces the overall IT bond order and its components reported in Scheme 1.1.

It follows from the input probabilities in Scheme 1.2 that in the limit of the decoupled (lone-pair) orbital $\varphi_{\text{bond.}} = a(P = 1)$ or $\varphi_{\text{bond.}} = b(Q = 1)$ its input probability becomes 1, while that of the other (empty) orbital identically vanishes, as required. The unit input probability of the doubly occupied AO in the channel input is then deterministically transmitted to the same AO in the channel output, with the other (unoccupied) AO not participating in the channel communications, so that both orbitals do not contribute to the resultant bond indices. Therefore, the flexible-input approach correctly accounts for the MO *shape* decoupling in the chemical bond, which was missing in the previous, fixed-input scheme.

It is also of interest to examine the dissociation of this model molecule A–B into (one-electron) atoms A and B, which determine the promolecule. Such decoupled AO corresponds to the molecular configuration $[\varphi^1_{\text{bond.}}\ \varphi^1_{\text{anti.}}]$ since the Slater determinant $|\varphi_{\text{bond.}}\ \varphi_{\text{anti.}}| = |ab|$. Indeed, using the orthogonal transformations between $\boldsymbol{\chi} = (a, b)$ and $\boldsymbol{\varphi} = (\varphi_{\text{bond.}}, \varphi_{\text{anti.}})$,

$$\boldsymbol{\chi} = \boldsymbol{\varphi}\begin{bmatrix} \sqrt{P} & \sqrt{Q} \\ -\sqrt{Q} & \sqrt{P} \end{bmatrix} \equiv \boldsymbol{\varphi}\mathbf{C}^{\mathrm{T}} \quad \text{and} \quad \boldsymbol{\varphi} = \boldsymbol{\chi}\mathbf{C}, \quad \mathbf{C}^{\mathrm{T}}\mathbf{C} = \mathbf{C}\mathbf{C}^{\mathrm{T}} = \mathbf{I},$$

one can directly verify that $\boldsymbol{\gamma}[\varphi^1_{\text{bond.}}\ \varphi^1_{\text{anti.}}] = \mathbf{C}\mathbf{C}^{\mathrm{T}} = \mathbf{I} = \mathbf{P}(\boldsymbol{b}|\boldsymbol{a})$, so that the decoupled AO inputs become $\boldsymbol{p}(a) = \boldsymbol{p}(a^0) = (1, 0)$ and $\boldsymbol{p}(b) = \boldsymbol{p}(b^0) = (0, 1)$, each is separately unity normalized.

Therefore, while still retaining the essence of the previous approach, the new proposition introduces in OCT of the chemical bond that is the desired input flexibility generating the continuity in the IT description of the fragment decoupling process. This generalization covers in a common framework both the completely coupled AO in the molecule and the limiting cases of its subsystems being effectively decoupled in the molecular channel. In the former case, the resultant input signal corresponds to the unit norm of the condensed probability distribution. In the case of n-mutually separated fragments, this flexible normalization is automatically increased

to n by the choice of the flexible probabilities for each input represented by the conditional two-orbital probabilities. As we have shown in the previous section, such an approach dramatically improves the agreement with the accepted chemical intuition. It also has the conceptual and interpretative advantages by providing a unifying description capable of tacking both the coupled and decoupled molecular fragments in a single theoretical framework and generating the continuous description of the shape-decoupling limit, so that the decoupled subsystems appear naturally as those exhibiting infinitely small communications with the molecular remainder.

It should be emphasized that in calculating the "ensemble" average bond components of Eq. (28), the product $\sum_k p_i P(k|i)P(j|k) = \sum_k P(i,k)$ $P(j|k) \equiv P^{\text{ens.}}(i,j)$ represents an effective joint probability of orbitals χ_i and χ_j in a molecule. Indeed, the amplitude interpretation of Eq. (4) gives $\sum_k p_i P(j|k)$ $P(k|i) \propto p_i \sum_k \langle j|\boldsymbol{\varphi}\rangle\langle\boldsymbol{\varphi}|k\rangle\langle k|\boldsymbol{\varphi}\rangle\langle\boldsymbol{\varphi}|i\rangle = p_i\langle j|\hat{P}_{\boldsymbol{\varphi}}\hat{P}_{\boldsymbol{\chi}}\hat{P}_{\boldsymbol{\varphi}}|i\rangle = p_i\langle j|\hat{P}_{\boldsymbol{\varphi}}|i\rangle \propto p_i P(j|i)$, since $\hat{P}_{\boldsymbol{\chi}}\hat{P}_{\boldsymbol{\varphi}} = \hat{P}_{\boldsymbol{\varphi}}$ and $\hat{P}_{\boldsymbol{\varphi}}\hat{P}_{\boldsymbol{\varphi}} = \hat{P}_{\boldsymbol{\varphi}}$. Therefore, this probability product in fact measures an ensemble probability of simultaneously finding an electron on orbitals χ_i and χ_j. In Section 8, we shall use such *diatomic* (bonding) probability weights, when $\chi_{i\in\text{A}}$ and $\chi_{j\in\text{B}}$, in determining the effective IT descriptors of chemical interactions in diatomic fragments of the molecule.

5. POPULATIONAL DECOUPLING OF ATOMIC ORBITALS

The previous formulation of CTCB in atomic resolution was shown to fail to predict a steady decrease in the resultant bond order with increasing occupation of the antibonding MO [9, 43–45]. The same shortcoming is observed in the fixed-input OCT. For example, in the $N = 3$, electron system described by the two-AO model, $[\text{M}(3)] = [\varphi^2_{\text{bond.}}\ \varphi^1_{\text{anti.}}]$, one obtains $S = 0.47$, $I = 0.48$, and $\mathcal{N} = 0.95$. Therefore, despite a half occupation of $\varphi_{\text{anti.}}$, MO the overall bond multiplicity remains almost the same as in the completely bonding configuration of the two-electron system $[\text{M}(2)] = [\varphi^2_{\text{bond.}}]$. Moreover, this probabilistic approach cannot distinguish between the two bonding configurations for $N = 1$, $[\text{M}(1)] = [\varphi^1_{\text{bond.}}]$, and $N = 2$, $[\text{M}] = [\varphi^2_{\text{bond.}}]$, predicting the same bond indices, reported in Scheme 1.1a. Similarly, for the total population decoupling in the $N = 4$ electron system, $[\text{M}(4)] = [\varphi^2_{\text{bond.}}\ \varphi^2_{\text{anti.}}]$, one predicts $S = 0$, $I = \mathcal{N} = 1$. This is because the probabilistic models loose the "memory" about the relative phases of AO in MO [43–45], which is retained by the elements of the quantum-mechanical CBO matrix and density of the nonadditive Fisher information [34–38]. Therefore, in this approach only the covalent index reflects the nonbonding (noncommunicating) status of AO in this limit. This diagnosis indicates a need for introducing into the MO-resolved scheme the information about the bonding/antibonding character of specific (occupied) MO, which is not reflected by their condensed electron probabilities in atomic resolution.

Let us now put to the test the performance of the flexible-input channels, which were shown to properly account for the MO shape decoupling. In the limiting case of the complete population decoupling in the two-AO model, when both doubly occupied basis functions remain effectively nonbonding in the molecule, $\boldsymbol{\gamma} = 2\mathbf{I}$ and hence $\mathbf{P}(\boldsymbol{b}|\boldsymbol{a}) = \mathbf{I}$. Therefore, the two completely occupied AOs remain effectively closed (noncommunicating and decoupled) for any level of their mixing measured by the AO-probability parameter P. Again, the input-dependent probabilities separately exhibit the unit probability norm, completely localized on a single orbital: $\boldsymbol{p}(a) = \boldsymbol{p}(a^0) = (1,0)$ and $\boldsymbol{p}(b) = \boldsymbol{p}(b^0) = (0,1)$. Thus, this scheme correctly predicts the *nonbonding* (*nb*) character of such a hypothetical electronic structure: $S^{\rm nb} = I^{\rm nb} = \mathcal{N}^{\rm nb} = 0$. Obviously, the same result follows from the flexible-input contributions to the system average entropy/information descriptors. However, the problem of distinguishing between the two bonding cases, a half-bond for $N = 1$ and the full single bond for $N = 2$, still remains, and the descriptors of the $N = 3$ channel also grossly contradict the chemical intuition.

This failure to properly reflect the intuitive MO-population trends by the IT bond indices calls for a thorough revision of the hitherto used overall communication channel in AO resolution, which combines the contributions from all occupied MOs in the electron configuration in question. Instead, one could envisage a use of the separate MO channels introduced in Section 2 (Eq. [7b]). As an illustration, let us assume for simplicity the two-AO model of the chemical bond A–B originating from the quantum-mechanical interaction between two AOs: $\boldsymbol{\chi} = (a \in \mathrm{A}, b \in \mathrm{B})$. The bond contributions between this pair of AO in the information system of sth MO,

$$\begin{aligned} \mathcal{S}_{a,b}(\varphi_s) &= S[\mathbf{P}_s(\boldsymbol{b}\,|\boldsymbol{a})], \\ \mathcal{I}_{a,b}(\varphi_s) &= H[\boldsymbol{p}_s^0] - \mathcal{S}(\varphi_s), \\ \mathcal{N}_{a,b}(\varphi_s) &= \mathcal{S}_{a,b}(\varphi_s) + \mathcal{I}_{a,b}(\varphi_s) = H[\boldsymbol{p}_s^0], \end{aligned} \tag{31}$$

would then be straightforwardly recognized as *bonding* (positive), when $\gamma_{a,b}(\varphi_s) > 0$, or *antibonding* (negative), when $\gamma_{a,b}(\varphi_s) < 0$, and *nonbonding* (zero), when $\gamma_{a,b}(\varphi_s) = 0$. Here, $\boldsymbol{p}_s^0$ denotes the input probability in the φ_s information channel. Alternatively, the purely molecular estimate of the mutual information $\mathcal{I}_s[\boldsymbol{p}_s:\boldsymbol{p}_s]$ can be used to index the localized bond ionicity.

In combining such MO contributions into the corresponding resultant bond indices for the specified pair (i,j) of AO, these increments should be subsequently multiplied by the MO-occupation factor $\boldsymbol{f}^{\rm MO} = \{f_s = n_s/2\}$, which recognizes that the full bonding/antibonding potential of the given MO is realized only when it is completely occupied, and by the corresponding MO probability $\boldsymbol{P}^{\rm MO} = \{P_s = n_s/N\}$. The resultant A–B descriptors would then be obtained by summation of such occupation/probability-weighted bonding or antibonding contributions from all occupied MOs, which

determine the system chemical bonds:

$$\mathcal{S}(i,j) = \sum_s \text{sign}[\gamma_{i,j}(\varphi_s)]P_s f_s \mathcal{S}_{i,j}(\varphi_s), \quad \mathcal{I}(i,j) = \sum_s \text{sign}[\gamma_{i,j}(\varphi_s)]P_s f_s \mathcal{I}_{i,j}(\varphi_s),$$
$$\mathcal{N}(i,j) = \sum_s \text{sign}[\gamma_{i,j}(\varphi_s)]P_s f_s \mathcal{N}_{i,j}(\varphi_s). \tag{32}$$

As shown in Scheme 1.3, these resultant IT indices from the MO-resolved OCT do indeed represent adequately the population-decoupling trends for $N = 1 \div 4$ electrons in the two-AO model.

Consider now another model system of the π electrons in allyl, with the consecutive numbering of $2p_z = z$ orbitals in the carbon chain. In the Hückel approximation, it is described by two occupied (canonical) MOs:

$$\varphi_1 = \frac{1}{\sqrt{2}}\left[\frac{1}{\sqrt{2}}(z_1 + z_3) + z_2\right] \quad \text{(doubly occupied) and}$$
$$\varphi_2 = \frac{1}{\sqrt{2}}(z_1 - z_3) \quad \text{(singly occupied)}, \tag{33}$$

which generate the corresponding MO and molecular CBO matrices,

$$\boldsymbol{\gamma}_1 = \frac{1}{2}\begin{bmatrix} 1 & \sqrt{2} & 1 \\ \sqrt{2} & 2 & \sqrt{2} \\ 1 & \sqrt{2} & 1 \end{bmatrix}, \quad \boldsymbol{\gamma}_2 = \frac{1}{2}\begin{bmatrix} 1 & 0 & -1 \\ 0 & 0 & 0 \\ -1 & 0 & 1 \end{bmatrix},$$
$$\boldsymbol{\gamma} = \boldsymbol{\gamma}_1 + \boldsymbol{\gamma}_2 = \frac{1}{2}\begin{bmatrix} 2 & \sqrt{2} & 0 \\ \sqrt{2} & 2 & \sqrt{2} \\ 0 & \sqrt{2} & 2 \end{bmatrix}, \tag{34}$$

and the molecular information system shown in Scheme 1.4. The corresponding MO information systems, generated by the partial CBO matrices $\{\boldsymbol{\gamma}_s\}$, using the MO-input probabilities of AO, $\boldsymbol{p}_s = \{p(i|s) = \gamma_{ij}(s)/n_s\}$, are reported in Scheme 1.5; their normalization requires that $\sum_i p(i|s) = 1$.

It follows from Eqs. (2b, 7a, and 7a) that there are no analytical combination formulas [9] for grouping the partial MO bond indices of Scheme 1.5 into their overall analogs of Scheme 1.4. Indeed, the MO channels are determined by their own CBO structure, and a variety of their nonvanishing communication connections between AOs generally differ from that for the system as a whole. Moreover, the input (conditional) probabilities used in Scheme 1.5 do not reflect the two MO channels being a part of the whole molecular channel. The latter requirement is only satisfied when the two networks are parallely coupled [42] into the combined information system, in which the input probabilities are given by the corresponding products $\{\bar{\boldsymbol{p}}_s = P_s \boldsymbol{p}_s\}$, where the MO probabilities $\boldsymbol{P}^{\text{MO}} = \{P_s\} = (2/3, 1/3)$. In allyl such molecular inputs give the following IT descriptors of the two MO channels: $\bar{S}_1 = P_1 S_1 = 1$,

(a)

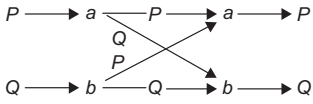

$$\boldsymbol{\gamma}_b = n_b \begin{bmatrix} P & \sqrt{PQ} \\ \sqrt{PQ} & Q \end{bmatrix}$$

$$\mathcal{S}(\varphi_b) = H(P)$$

$$\mathcal{I}(\varphi_b) = H\left(\tfrac{1}{2}\right) - H(P) = 1 - H(P)$$

$$\mathcal{I}(\varphi_b) = \mathcal{S}(\varphi_b) + \mathcal{I}(\varphi_b) = 1$$

(b)

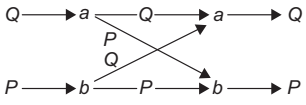

$$\boldsymbol{\gamma}_a = n_a \begin{bmatrix} Q & -\sqrt{PQ} \\ -\sqrt{PQ} & P \end{bmatrix}$$

$$\mathcal{S}(\varphi_a) = H(P)$$

$$\mathcal{I}(\varphi_a) = H\left(\tfrac{1}{2}\right) - H(\mathrm{P}) = 1 - H(\mathrm{P})$$

$$\mathcal{M}(\varphi_a) = \mathcal{S}(\varphi_a) + \mathcal{I}(\varphi_a) = 1$$

(c)

$$\boldsymbol{\gamma} = \begin{bmatrix} P & \sqrt{PQ} \\ \sqrt{PQ} & Q \end{bmatrix} \qquad \mathbf{P}(b|a) = \begin{bmatrix} P & Q \\ P & Q \end{bmatrix} \qquad \boldsymbol{P}^{\mathrm{MO}} = (1, 0)$$

$$\mathcal{S} = \tfrac{1}{2}\mathcal{S}(\varphi_b) = \left(\tfrac{1}{2}\right)H(P) \qquad \mathcal{I} = \tfrac{1}{2}\mathcal{I}(\varphi_b) = \left(\tfrac{1}{2}\right)[1 - H(P)] \qquad \mathcal{N} = \tfrac{1}{2} \quad \mathcal{M}(\varphi_b) = \tfrac{1}{2}$$

$$\boldsymbol{\gamma} = 2\begin{bmatrix} P & \sqrt{PQ} \\ \sqrt{PQ} & Q \end{bmatrix} \qquad \mathbf{P}(b|a) = \begin{bmatrix} P & Q \\ P & Q \end{bmatrix} \qquad \boldsymbol{P}^{\mathrm{MO}} = (1, 0)$$

$$\mathcal{S} = \mathcal{S}(\varphi_b) = H(P) \qquad \mathcal{I} = \mathcal{I}(\varphi_b) = [1 - H(P)] \qquad \mathcal{N} = \mathcal{M}(\varphi_b) = 1$$

$$\boldsymbol{\gamma} = \begin{bmatrix} 2P + Q & \sqrt{PQ} \\ \sqrt{PQ} & 2Q + P \end{bmatrix} \qquad \mathbf{P}(b|a) = \begin{bmatrix} (P+1)^2/(3P+1) & PQ/(3P+1) \\ QP/(3Q+1) & (Q+1)^2/(3Q+1) \end{bmatrix} \boldsymbol{P}^{\mathrm{MO}} = \left(\tfrac{2}{3}, \tfrac{1}{3}\right)$$

$$\mathcal{S} = \left(\tfrac{2}{3}\right)\mathcal{S}(\varphi_b) - \left(\tfrac{1}{6}\right)\mathcal{S}(\varphi_a) = \tfrac{1}{2}H(P) \qquad \mathcal{I} = \left(\tfrac{2}{3}\right)\mathcal{I}(\varphi_b) - \left(\tfrac{1}{6}\right)\mathcal{I}(a) = \left(\tfrac{1}{2}\right)[1 - H(P)]$$

$$\mathcal{N} = \left(\tfrac{2}{3}\right)\mathcal{M}(\varphi_b) - \left(\tfrac{1}{6}\right)\mathcal{M}(\varphi_a) = \tfrac{1}{2}$$

$$\boldsymbol{\gamma} = \begin{bmatrix} 2 & 0 \\ 0 & 2 \end{bmatrix} \qquad \mathbf{P}(b|a) = \begin{bmatrix} 1 & 0 \\ 0 & 1 \end{bmatrix} \qquad \boldsymbol{P}^{\mathrm{MO}} = \left(\tfrac{1}{2}, \tfrac{1}{2}\right)$$

$$\mathcal{S} = \left(\tfrac{1}{2}\right)\mathcal{S}(\varphi_b) - \left(\tfrac{1}{2}\right)\mathcal{S}(\varphi_a) = 0 \qquad \mathcal{I} = \left(\tfrac{1}{2}\right)\mathcal{I}(\varphi_b) - \left(\tfrac{1}{2}\right)\mathcal{I}(\varphi_a) = 0$$

$$\mathcal{N} = \left(\tfrac{1}{2}\right)\mathcal{M}(\varphi_b) - \left(\tfrac{1}{2}\right)\mathcal{M}(\varphi_a) = 0$$

Scheme 1.3 Decoupling of atomic orbitals in the MO-resolved OCT (2-AO model) with increasing occupation of the antibonding combination of AO. Panels a and b summarize the bonding and antibonding channels, while Panel c reports the associated probability/occupation-weighted indices.

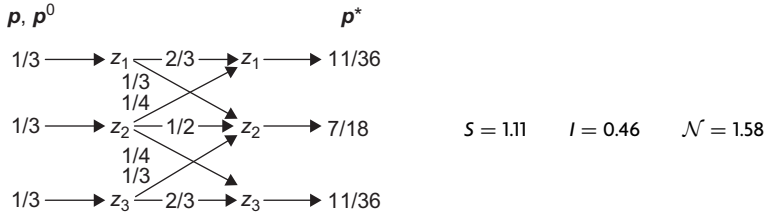

Scheme 1.4 The molecular information channel of π electrons in allyl and its overall IT bond indices.

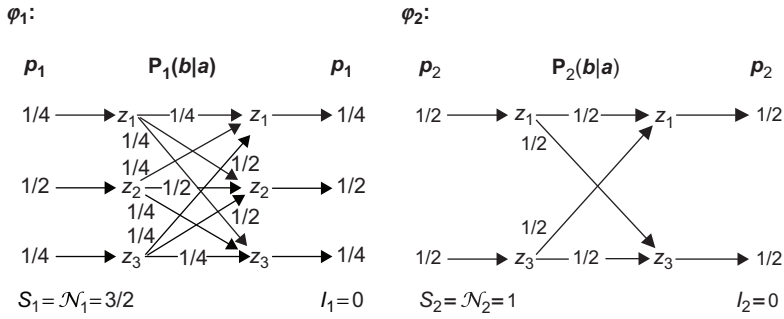

Scheme 1.5 The molecular π-electron information systems for two occupied MOs in allyl (Eq. [33]). The corresponding MO bond indices (in bits) are also reported.

$\bar{I}_1 = -P_1\log_2 P_1 = 0.39$; $\bar{S}_2 = P_2 S_2 = \frac{1}{3}$, $\bar{I}_2 = -P_2\log_2 P_2 = 0.53$. Such molecular inputs thus generate the nonvanishing IT ionicities, which sum up to the *group* entropy $\bar{I} = \bar{I}_1 + \bar{I}_2 = H[\boldsymbol{P}^{\rm MO}] = -\sum_s P_s \log_2 P_s = 0.92$.

One then observes that the overall index of Scheme 1.4, $\mathcal{N} = 1.58 = H[\boldsymbol{p}^0]$, predicting about $3/2$ π-bond multiplicity in allyl, can be reconstructed by adding to this additive-ionicity measure, the sum of the bonding (positive) entropy-covalency $\bar{S}_1$ of the first MO and the antibonding (negative) contribution $(-\bar{S}_2)$ due to the second MO:

$$\bar{S}_1 + (-\bar{S}_2) + \bar{I} = \mathcal{N}. \tag{35}$$

One also notices that the population-weighting procedure of Scheme 1.3, with $f_1 = 1$ and $f_2 = 1/2$, gives a diminished bond multiplicity:

$$\begin{aligned} \bar{\mathcal{N}} &= f_1 P_1 S_1 - f_2 P_2 S_2 + (f_1 \bar{I}_1 - f_2 \bar{I}_2) = f_1(\bar{S}_1 + \bar{I}_1) - f_2(\bar{S}_2 + \bar{I}_2) \\ &\equiv f_1 \bar{\mathcal{N}}_1 - f_2 \bar{N}_2 = 0.96, \end{aligned} \tag{36}$$

thus predicting roughly a single π bond in allyl. The latter result reflects the fact that only a single-bonding MO, φ_1, is completely occupied, whereas the antibonding combination φ_2 of AO on peripheral carbon atoms remains practically nonbonding.

In the same Hückel approximation the delocalized π bonds in butadiene are determined by two doubly occupied canonical MOs with $\boldsymbol{P}^{\mathrm{MO}} = \left(\frac{1}{2}, \frac{1}{2}\right)$ and $\boldsymbol{f}^{\mathrm{MO}} = (1,1)$,

$$\varphi_1 = a(z_1 + z_4) + b(z_2 + z_3), \quad \varphi_2 = b(z_1 - z_4) + a(z_2 - z_3), \quad 2(a^2 + b^2) = 1;$$
$$a = \frac{1}{2}\sqrt{1 - \frac{1}{\sqrt{5}}} = 0.3717, \quad b = \frac{1}{2}\sqrt{1 + \frac{1}{\sqrt{5}}} = 0.6015. \tag{37}$$

The corresponding CBO matrices,

$$\boldsymbol{\gamma}_1 = 2\begin{bmatrix} a^2 & ab & ab & a^2 \\ ab & b^2 & b^2 & ab \\ ab & b^2 & b^2 & ab \\ a^2 & ab & ab & a^2 \end{bmatrix}, \quad \boldsymbol{\gamma}_2 = 2\begin{bmatrix} b^2 & ab & -ab & -b^2 \\ ab & a^2 & -a^2 & -ab \\ -ab & -a^2 & a^2 & ab \\ -b^2 & -ab & ab & b^2 \end{bmatrix},$$
$$\boldsymbol{\gamma} = \frac{1}{\sqrt{5}}\begin{bmatrix} \sqrt{5} & 2 & 0 & -1 \\ 2 & \sqrt{5} & 1 & 0 \\ 0 & 1 & \sqrt{5} & 2 \\ -1 & 0 & 2 & \sqrt{5} \end{bmatrix}, \tag{38}$$

generate the associated AO-information channels as shown in Schemes 1.6 and 1.7.

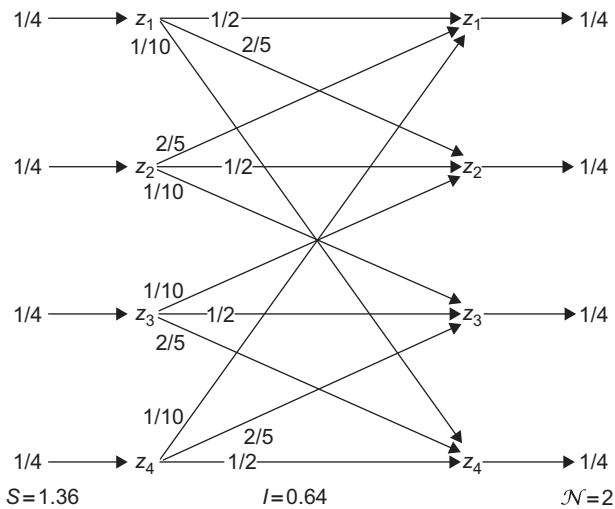

Scheme 1.6 The overall π-electron channel in OCT for butadiene derived from the Hückel MO.

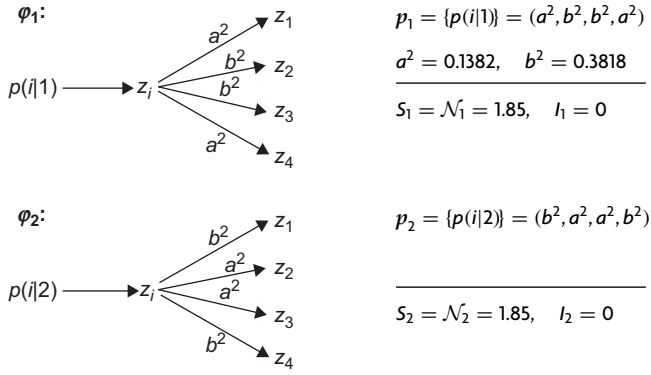

Scheme 1.7 Probability scattering in the Hückel π-MO channels of butadiene for the representative input orbital $z_i = 2p_{z,i}$ and the associated MO entropies.

The overall data correctly predict the resultant double multiplicity of all π bonds in butadiene. In the one-electron OCT treatment, they exhibit rather substantial IT ionicity [48], which indicates a high degree of determinism (localization) in the orbital probability scattering, compared with the previous two-electron approach [9]. A reference to the preceding equation indicates that a half of the reported entropy for φ_2 is associated with the antibonding interactions between AOs, as reflected by the negative values of the corresponding elements in the MO CBO matrix. Therefore, the bonding and antibonding components in S_2 cancel each other, when one attributes different signs to these AO contributions. The group ionicity $\bar{I} = \bar{I}_1 + \bar{I}_2 = H[\boldsymbol{P}^{\mathrm{MO}}] = 1$ and hence Eq. (35) now reads $\bar{S}_1 + \left(\frac{1}{2}\bar{S}_2 - \frac{1}{2}\bar{S}_2\right) + \bar{I} = 1.925$, where $\bar{S}_s = P_s S_s$, thus again predicting roughly two π bonds in the system.

In the Hückel theory the three occupied MO, which determine the π bonds in benzene, $\boldsymbol{P}^{\mathrm{MO}} = \frac{1}{3}\boldsymbol{1}$, where $\boldsymbol{1}$ stands for the unit row matrix, read

$$\begin{aligned}
\varphi_1 &= \frac{1}{\sqrt{6}}(z_1 + z_2 + z_3 + z_4 + z_5 + z_6),\\
\varphi_2 &= \frac{1}{2}(z_1 + z_2 - z_4 - z_5),\\
\varphi_3 &= \frac{1}{\sqrt{12}}(z_1 - z_2 - 2z_3 - z_4 + z_5 + 2z_6).
\end{aligned} \tag{39}$$

They give rise to the overall CBO matrix elements reflecting the π-electron population on orbital $\chi_i = z_i$, $\gamma_{i,i} = z_1$, $\gamma_{i,i} = 1$, and the chemical coupling between χ_i and its counterparts on carbon atoms in the relative *ortho*-, *meta*-, and *para*-positions, respectively, $\gamma_{i,i+1} = 2/3$, $\gamma_{i,i+2} = 0$, $\gamma_{i,i+3} = -1/3$. The resultant scattering of AO probabilities for the π electrons in benzene is shown in

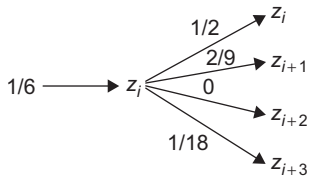

$S = 1.70$ $I_2 = 0.89$ $\mathcal{N} = 2.58$

Scheme 1.8 The probability scattering in benzene (Hückel theory) for the representative input orbital $z_i = 2p_{z,i}$ and the associated OCT entropy/information descriptors.

Scheme 1.8. The overall bond multiplicity is somewhat lower that $\mathcal{N} = 3$ predicted for the three localized π bonds in cyclohexatriene since in benzene, the π-bond alternation is prevented by the stronger σ bonds, which assume the maximum strength in the regular hexagon structure [64–67].

All matrix elements in $\boldsymbol{\gamma}_1 = 2\langle \boldsymbol{\chi}|\hat{P}_1|\boldsymbol{\chi}\rangle = (\frac{1}{3})\mathbf{1}$, where $\boldsymbol{\chi} = (z_1, z_2, z_3, z_4, z_5, z_6)$ and all elements in the square matrix $\mathbf{1}$ are equal to 1, are positive (bonding), whereas half of them in $\boldsymbol{\gamma}_2$ and $\boldsymbol{\gamma}_3$ is negative, thus representing the antibonding interactions between AOs. The nonvanishing elements in $\boldsymbol{\gamma}_2$ are limited to the subset $\boldsymbol{\chi}' = (z_1, z_2, z_4, z_5)$:

$$\boldsymbol{\gamma}_2 = 2\langle \boldsymbol{\chi}'|\hat{P}_2|\boldsymbol{\chi}'\rangle = \frac{1}{2}\begin{bmatrix} 1 & 1 & -1 & -1 \\ 1 & 1 & -1 & -1 \\ -1 & -1 & 1 & 1 \\ -1 & -1 & 1 & 1 \end{bmatrix}, \tag{40}$$

while $\boldsymbol{\gamma}_3$ explores the whole basis set $\boldsymbol{\chi}$:

$$\boldsymbol{\gamma}_3 = 2\,\langle \boldsymbol{\chi}|\,\hat{P}_3|\boldsymbol{\chi}\rangle = \frac{1}{6}\begin{bmatrix} 1 & -1 & -2 & -1 & 1 & 2 \\ -1 & 1 & 2 & 1 & -1 & -2 \\ -2 & 2 & 4 & 2 & -2 & -4 \\ -1 & 1 & 2 & 1 & -1 & -2 \\ 1 & -1 & -2 & -1 & 1 & 2 \\ 2 & -2 & -4 & -2 & 2 & 4 \end{bmatrix}. \tag{41}$$

These CBO matrices of the occupied MO give rise to the following communications and input probabilities in the associated MO channels:

$$\mathbf{P}_1(\boldsymbol{b}|\boldsymbol{a}) = \frac{1}{6}\mathbf{1},\ \boldsymbol{p}_1 = \frac{1}{6}\boldsymbol{1}; \quad \mathbf{P}_2(\boldsymbol{b}|\boldsymbol{a}) = \frac{1}{4}\begin{bmatrix} 1 & 1 & 0 & 1 & 1 & 0 \\ 1 & 1 & 0 & 1 & 1 & 0 \\ 0 & 0 & 0 & 0 & 0 & 0 \\ 1 & 1 & 0 & 1 & 1 & 0 \\ 1 & 1 & 0 & 1 & 1 & 0 \\ 0 & 0 & 0 & 0 & 0 & 0 \end{bmatrix},$$

$$\boldsymbol{p}_2 = \frac{1}{4}(1,1,0,1,1,0); \quad \mathbf{P}_3(\boldsymbol{b}|\boldsymbol{a}) = \frac{1}{12}\begin{bmatrix} 1 & 1 & 4 & 1 & 1 & 4 \\ 1 & 1 & 4 & 1 & 1 & 4 \\ 1 & 1 & 4 & 1 & 1 & 4 \\ 1 & 1 & 4 & 1 & 1 & 4 \\ 1 & 1 & 4 & 1 & 1 & 4 \\ 1 & 1 & 4 & 1 & 1 & 4 \end{bmatrix},$$

$$\boldsymbol{p}_3 = \frac{1}{12}(1,1,4,1,1,4). \tag{42}$$

The corresponding entropy/information descriptors then read as follows:

$$S_1 = \mathcal{N}_1 = 2.58,\ I_1 = 0; \quad S_2 = \mathcal{N}_2 = 2,\ I_2 = 0; \quad S_3 = \mathcal{N}_3 = 2.25,\ I_3 = 0. \tag{43}$$

The group ionicity $\bar{I} = \bar{I}_1 + \bar{I}_2 + \bar{I}_3 = H[\boldsymbol{P}^{\mathrm{MO}}] = 1.58$ and $\bar{S}_1 = S_1/3$ then also gives rise to roughly (2.5)-bond multiplicity, with the bonding (positive) and antibonding (negative) contributions in $\bar{S}_2$ and $\bar{S}_3$ approximately canceling each other.

6. BOND DIFFERENTIATION IN OCT

It has been demonstrated elsewhere that the bond alternation effects are poorly represented in both the CTCB formulated in atomic resolution [9] and in its OCT (fixed-input) extension [48]. The OCT indices from the alternative output reduction schemes have been shown to give more realistic but still far from satisfactory description of the bond alternation trends in these molecular systems [48]. This is because in purely probabilistic models, the bonding and antibonding interactions are not distinguished since conditional probabilities (squares of the MO-CBO matrix elements) loose the information about the relative phases of AO in MO. However, this distinction is retained in the off-diagonal CBO matrix elements, particularly in the separate CBO contributions $\{\boldsymbol{\gamma}_s\}$ from each occupied MO. Since the OCT analysis of the bonding patterns in molecules provides the supplementary, *a posteriori* description to the standard MO scheme in this section we shall attempt to use this extra information, directly available from the standard SCF MO calculations, to generate more realistic "chemical" trends of the π-bond alternation patterns in the three illustrative systems of the preceding section.

The problem can be best illustrated using the simplest allyl case. As discussed elsewhere [9, 22], the entropy/information indices for the given pair of atomic orbitals can be extracted from the relevant *partial* channel, which includes all AO inputs (sources of the system chemical bonds) and the two-orbital outputs in question, defining the localized chemical interaction of interest. In Scheme 1.9, two examples of such partial information systems are

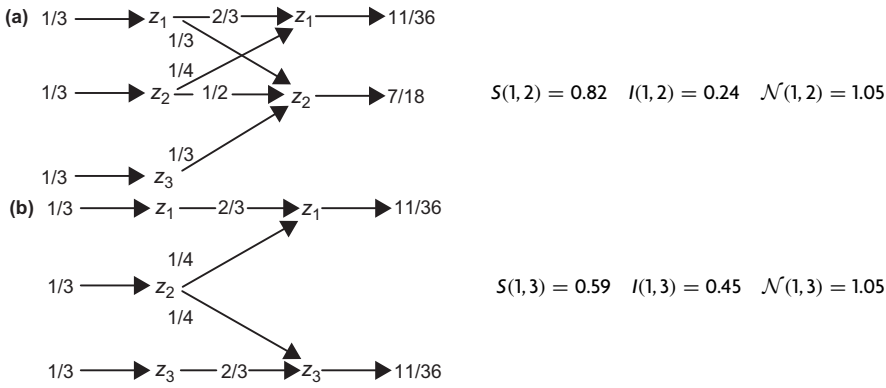

Scheme 1.9 The molecular partial information channels and their entropy/information descriptors of the chemical interaction between the adjacent (Panel a) and terminal (Panel b) AO in the π-electron system of allyl.

displayed for the nearest neighbor (z_1, z_2) and terminal (z_1, z_3) chemical interactions. They have been obtained from the molecular channel of Scheme 1.4, by removing communications involving the third, remaining AO of this minimum basis set of π AO. It follows from these illustrative sets of indices that the two partial channels give rise to identical overall index $\mathcal{N}$, with only the IT-covalent/ionic components differentiating the two bonds: the nearest neighbor interaction exhibits a higher "noise" (covalency) component and hence the lower information-flow (ionicity) content. In the Hückel theory the corresponding partial information systems in the butadiene π-electron system predict identical indices for all pairs of orbitals, $S(i,j) = 0.68$, $I(i,j) = 0.25$, and $\mathcal{N}(i,j) = 0.93$, thus failing completely to account for the π-bond alternation.

To remedy this shortcoming of the communication theory, one has to bring into play the known signs of interactions between the specified pair (i,j) of AO in the given MO φ_s, in order to recognize them as bonding (exhibiting a "constructive" interference), $\gamma_{i,j}(s) > 0$, or antibonding (involving a "destructive" interference), $\gamma_{i,j}(s) < 0$, with $\gamma_{i,j}(s) = 0$ corresponding to the nonbonding (zero communication) case. The MO-resolved channels are vital for the success of such an approach since the bonding interaction between the given pair of AOs in one MO can be accompanied by the antibonding interaction between these basis functions in another occupied MO. This extraneous information determines the signs of contributions in the weighted contributions of Eqs. (31 and 32) from the partial MO channels, including the two specified orbitals in their input and output, and using the fragment-renormalized MO probabilities [9, 26]. It should be observed that in the flexible-input approach of Section 4 the nonbonding AOs, which

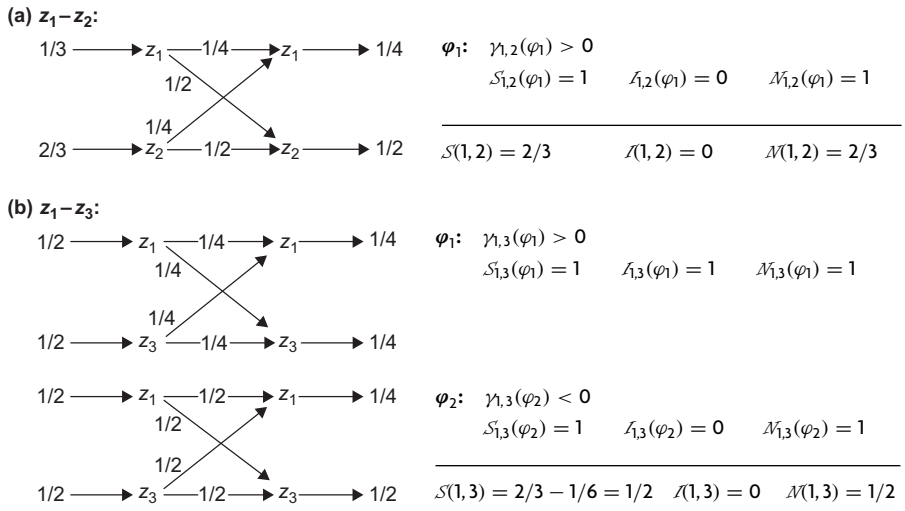

Scheme 1.10 The partial MO-information channels and their entropy/information descriptors of the chemical interactions between the nearest neighbor (Panel a) and terminal (Panel b) AO in the π-electron system of allyl.

communicate only with themselves, gives rise to the separate AO channels of Scheme 1.1b, thus not contributing to the resultant bond descriptors.

An illustrative application of such scheme to π electrons in allyl, for which $\boldsymbol{P}^{\mathrm{MO}} = \left(\frac{2}{3}, \frac{1}{3}\right), \boldsymbol{f}^{\mathrm{MO}} = \left(1, \frac{1}{2}\right), \boldsymbol{p}_1 = \left(\frac{1}{4}, \frac{1}{2}, \frac{1}{4}\right)$, and $\boldsymbol{p}_2 = \left(\frac{1}{2}, 0, \frac{1}{2}\right)$, is reported in Scheme 1.10. One observes that z_1–z_2 interaction has only the bonding contribution from φ_1, while the effective z_1–z_3 interaction combines the bonding contribution due to φ_1 and the antibonding increment originating from φ_2. This scheme is seen to generate (2/3)-bond multiplicity between the nearest neighbors and a weaker half-bond between the terminal carbon atoms. This somewhat contradicts the Wiberg's covalency indices predicting a half z_1–z_2 bond and a vanishing z_1–z_3 interaction. The reason for a finite value of this bond index in OCT is the dominating delocalization of electrons in φ_1 throughout the whole π system.

Let us similarly examine the localized π interactions in butadiene, for which $\boldsymbol{P}^{\mathrm{MO}} = \left(\frac{1}{2}, \frac{1}{2}\right), \boldsymbol{f}^{\mathrm{MO}} = (1,1), \boldsymbol{p}_1 = (a^2, b^2, b^2, a^2)$, and $\boldsymbol{p}_2 = (b^2, a^2, a^2, b^2)$. A reference to Eq. (38) indicates that the equivalent terminal pairs of AO, z_1–z_2 and z_3–z_4, exhibit only the bonding interactions in φ_1 and φ_2, while the remaining AO combinations involve the bonding contribution from φ_1 and the antibonding from φ_2. These MO increments are summarized in Scheme 1.11 (see also Scheme 1.7).

These diatomic IT indices predict the strongest terminal (1–2) or (3–4) π bonds, which exhibit somewhat diminished bond multiplicity to about 92%

of the unit value in ethylene, and the vanishing bond orders of the (1–3) and (2–4) interactions. The middle (2–3) π bond measures about 14% of the ethylene reference value, while the chemical interaction between terminal carbons (1–4) is diagnosed as being antibonding in character, in full conformity with the negative value of the corresponding off-diagonal element in the overall CBO matrix (Eq. [38]). These predictions should be compared with the associated quadratic indices $\mathcal{M}_{i,j} = \gamma_{i,j}^2$ of Wiberg, $\mathcal{M}_{1,2} = \mathcal{M}_{3,4} = 0.8$, $\mathcal{M}_{1,3} = \mathcal{M}_{2,4} = 0$, and $\mathcal{M}_{1,4} = \mathcal{M}_{2,3} = 0.2$, which unrealistically equates the partial bonding (2–3) and antibonding (1–4) interactions.

As final example let us reexamine from the present perspective a differentiation of the localized π-bonds between the two carbon atoms in the relative *ortho*-, *meta*- and *para*-positions in benzene [9, 48]. This weighted MO approach makes a separate use of the diatomic parts of the canonical MO channels, with the bonding and antibonding contributions identified by the signs of the corresponding coupling elements in the MO density matrices $\{\boldsymbol{\gamma}_s\}$. It should be realized that while the canonical (delocalized) MO completely reflect the molecular symmetry, its diatomic fragments do not. Therefore, the bond indices generated in this scheme must exhibit some dispersions so that they have to be appropriately averaged with respect to the admissible choices of the corresponding orbital pairs to ultimately generate the invariant entropy/information descriptors of the *ortho*-, *meta*-, and *para* π bonds in benzene. We further observe that in this π system, $\boldsymbol{P}^{\mathrm{MO}} = \left(\frac{1}{3}, \frac{1}{3}, \frac{1}{3}\right)$ and $\boldsymbol{f}^{\mathrm{MO}} = (1, 1, 1)$.

Scheme 1.12 summarizes the elementary entropy/information increments of the diatomic bond indices generated by the MO channels of Eq. (42). They give rise to the corresponding diatomic descriptors, which are obtained from Eq. (32). For example, by selecting $i = 1$ of the diatomic fragment consisting additionally the $j = 2, 3, 4$ carbon, one finds the following IT bond indices:

$$\mathcal{S}(1,2) = \mathcal{N}(1,2) = 0.42, \quad \mathcal{S}(1,3) = \mathcal{N}(1,3) = 0.01,$$
$$\mathcal{S}(1,4) = \mathcal{N}(1,4) = -0.25.$$

These predictions correctly identify the bonding, a practically nonbonding, and the antibonding characters of π bonds between two carbons of the benzene ring in the relative *ortho*-, *meta*-, and *para*-positions, respectively, as indeed reflected by the overall CBO matrix elements. However, due to a nonsymmetrical (fragment) use of the symmetrical MO channels, these predictions exhibit some dispersions when one explores other pairs of carbon atoms in the ring, giving rise to the following *average* descriptors:

$$\mathcal{S}(ortho) = \mathcal{N}(ortho) = 0.52, \quad \mathcal{S}(meta) = \mathcal{N}(meta) = 0.06,$$
$$\mathcal{S}(para) = \mathcal{N}(para) = -0.19.$$

(a) z_1-z_2, z_1-z_3:

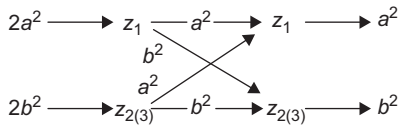

φ_1: $\gamma_{1,2}(\varphi_1) > 0$, $\gamma_{1,3}(\varphi_1) > 0$

$\mathcal{S}_{1,2}(\varphi_1) = \mathcal{N}_{1,2}(\varphi_1) = 0.925$ $\mathcal{I}_{1,2}(\varphi_1) = 0$

$\mathcal{S}_{1,3}(\varphi_1) = \mathcal{N}_{1,3}(\varphi_1) = 0.925$ $\mathcal{I}_{1,3}(\varphi_1) = 0$

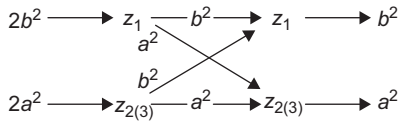

φ_2: $\gamma_{1,2}(\varphi_2) > 0$, $\gamma_{1,3}(\varphi_2) < 0$

$\mathcal{S}_{1,2}(\varphi_2) = \mathcal{N}_{1,2}(\varphi_2) = 0.925$ $\mathcal{I}_{1,2}(\varphi_2) = 0$

$\mathcal{S}_{1,3}(\varphi_2) = \mathcal{N}_{1,3}(\varphi_2) = 0.925$ $\mathcal{I}_{1,3}(\varphi_2) = 0$

$\mathcal{S}(1,2) = \mathcal{N}(1,2) = 0.925$, $\mathcal{I}(1,2) = 0$

$\mathcal{S}(1,3) = \mathcal{N}(1,3) = 0$, $\mathcal{I}(1,3) = 0$;

(b) z_1-z_4:

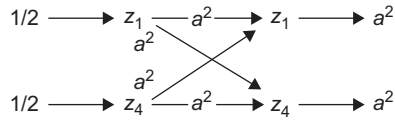

φ_1: $\gamma_{1,4}(\varphi_1) > 0$

$\mathcal{S}_{1,4}(\varphi_1) = \mathcal{N}_{1,2}(\varphi_1) = 0.789$ $\mathcal{I}_{1,4}(\varphi_1) = 0$

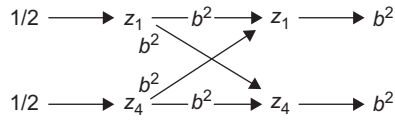

φ_2: $\gamma_{1,4}(\varphi_2) < 0$

$\mathcal{S}_{1,4}(\varphi_2) = \mathcal{N}_{1,4}(\varphi_2) = 1.061$ $\mathcal{I}_{1,4}(\varphi_2) = 0$

$\mathcal{S}(1,4) = \mathcal{N}(1,4) = -0.136$, $\mathcal{I}(1,2) = 0$

(c) z_2-z_3:

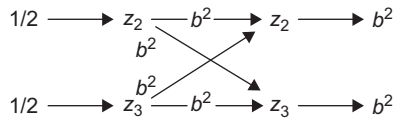

φ_1: $\gamma_{2,3}(\varphi_1) > 0$

$\mathcal{S}_{2,3}(\varphi_1) = \mathcal{N}_{2,3}(\varphi_1) = 1.061$ $\mathcal{I}_{2,3}(\varphi_1) = 0$

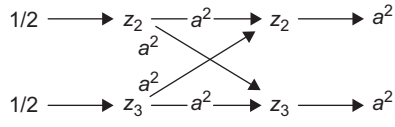

φ_2: $\gamma_{2,3}(\varphi_2) < 0$

$\mathcal{S}_{2,3}(\varphi_2) = \mathcal{N}_{2,3}(\varphi_2) = 0.789$ $\mathcal{I}_{2,3}(\varphi_2) = 0$

$\mathcal{S}(2,3) = \mathcal{N}(2,3) = 0.136$, $\mathcal{I}(2,3) = 0$

Scheme 1.11 The partial MO-information channels and their entropy/information descriptors for the two-orbital interactions in the π-electron system of butadiene.

The above *ortho* result shows that the overall IT bond multiplicity between the nearest neighbors $\mathcal{M}(ortho) \sim 0.5$ is indeed compromised in benzene, compared with $\mathcal{N} = 1$ in ethylene, due to the effect of the prohibited bond alternation, enforced by the stronger σ bonds [64–67]. Again, the magnitudes of these IT indices generally agree with the corresponding Wiberg indices: $\mathcal{M}_{\text{ortho}} = 0.44$, $\mathcal{M}_{\text{meta}} = 0$, and $\mathcal{M}_{\text{para}} = 0.11$. Note, however, that OCT properly recognizes the *para* interactions in benzene as antibonding, whereas in the Wiberg scheme, this distinction is lost.

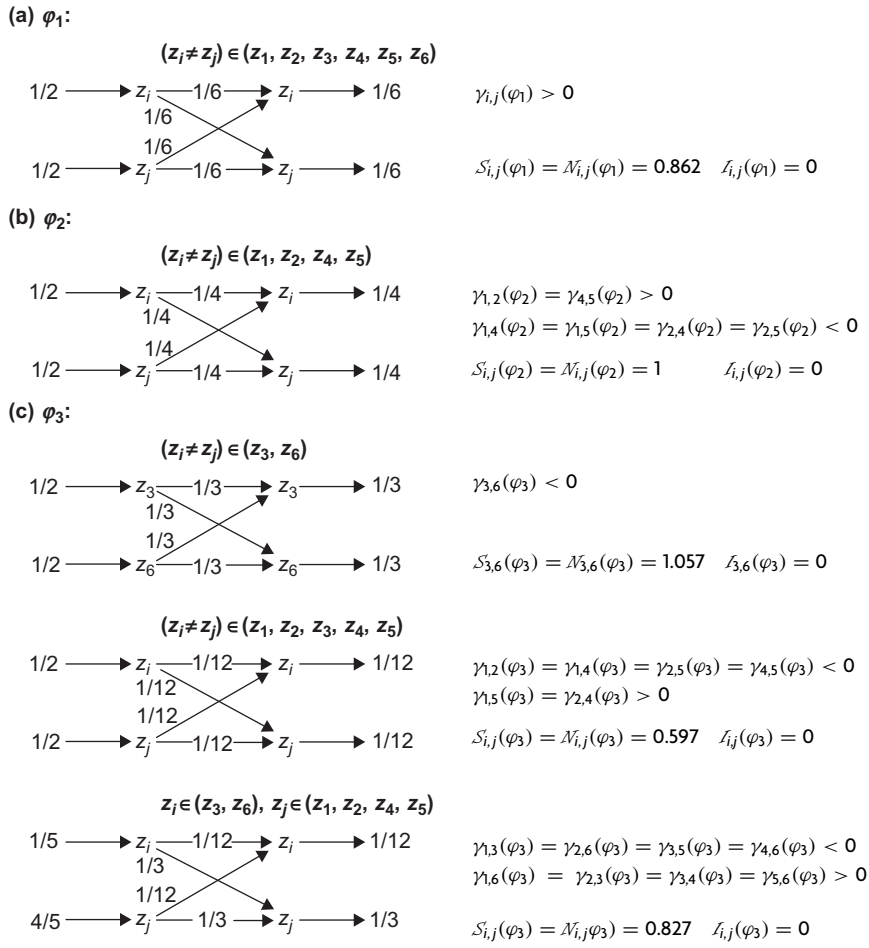

Scheme 1.12 The elementary entropy/information contributions to chemical interactions between two different AOs in the minimum basis set $\{z_i = 2p_{z,i}\}$ of the π-electron system in benzene.

7. LOCALIZED σ BONDS IN COORDINATION COMPOUNDS

The decoupled description of hydrides (Section 3) can be naturally extended into the localized σ bonds between the central atom/ion X and the coordinated ligands $\{L_\alpha\}$, for example, in the coordination compounds of transition metal ions or in SF_6. Consider, for example, the octahedral complex XL_6 with the ligands placed along the axes of the Cartesian coordinate system: $\{L_1(e), L_2(e)\}$, $e = x, y, z$. The X–L_α bond then results from the chemical interaction

between six *acceptor* (partially occupied) d^2sp^3 hybrids $\{H_\alpha\}$ of X and the corresponding *donor* (doubly occupied) $\{\sigma_\alpha\}$ orbitals of ligands. The corresponding localized MO, which determines the communication channel of the separate bond M–L_α, $\alpha = 1, 2, \ldots, 6$, now include the (doubly occupied) bonding MO $\varphi_b(\alpha)$, with the two electrons originating from the donor σ_α orbital, $n_b = N_\sigma(\alpha) = 2$, and the antibonding MO $\varphi_a(\alpha)$, in general partly occupied with $n_a = N_X(\alpha)$ electrons originating from X, which result from the two basis functions $\boldsymbol{\chi}_\alpha = (H_\alpha, \sigma_\alpha)$:

$$\varphi_b(\alpha) = \sqrt{P}H_\alpha + \sqrt{Q}\sigma_\alpha, \quad \varphi_a(\alpha) = -\sqrt{Q}H_\alpha + \sqrt{P}\sigma_\alpha, \quad P + Q = 1. \tag{44}$$

The associated CBO matrix elements and the corresponding conditional probabilities they generate now depend on the initial number of electrons n_a on H_α, which are contributed by X to the αth σ bond (see also Scheme 1.3),

$$\gamma_{H_\alpha,H_\alpha} = 2P + n_a Q, \quad \gamma_{\sigma_\alpha,\sigma_\alpha} = 2Q + n_a P, \quad \gamma_{H_\alpha,\sigma_\alpha} = \gamma_{\sigma_\alpha,H_\alpha} = (2 - n_a)\sqrt{PQ}. \tag{45}$$

Indeed, $n_a = 0$, for example, in SF_6, determines the maximum value of the magnitude of the coupling CBO element $\gamma_{H_\alpha,\sigma_\alpha} = \gamma_{\sigma_\alpha,H_\alpha} = 2\sqrt{PQ}$, and $n_a = 1$ diminishes it by a factor of 2, while the double occupation of $\varphi_a(\alpha)$ gives rise to the nonbonding state corresponding to the separate, decoupled subchannels for each orbital,

$$\gamma_{H_\alpha,H_\alpha} = \gamma_{\sigma_\alpha,\sigma_\alpha} = 2 \quad \text{and} \quad \gamma_{H_\alpha,\sigma_\alpha} = \gamma_{\sigma_\alpha,H_\alpha} = 0, \tag{46}$$

which do not contribute to the entropy/information indices of the localized chemical bond.

For $n_a = 0$, that is, the empty antibonding MO, when X–L_α channel is given by Scheme 1.1a, the IT bond indices correctly predict the overall IT multiplicity reflecting the six decoupled bonds in this molecular system:

$$S(P) = \sum_\alpha S_\alpha(\boldsymbol{b}_\alpha|\boldsymbol{a}_\alpha) = 6H(P),$$
$$I(P) = \sum_\alpha I_\alpha(\boldsymbol{a}^0_\alpha : \boldsymbol{b}_\alpha) = 6[1 - H(P)], \quad N = 6. \tag{47}$$

The highest IT covalency of the σ bond M–L_α, $S^{\max.} = 1$, predicted for the strongest mixing of orbitals $P = Q = 1/2$, is thus accompanied by the vanishing IT ionicity, $I^{\max.} = 0$.

The corresponding conditional probabilities $\mathbf{P}_\alpha(\boldsymbol{b}_\alpha|\boldsymbol{a}_\alpha) \equiv \mathbf{P}_\alpha[\boldsymbol{\chi}_\alpha|\boldsymbol{\chi}_\alpha]$ for the single and double occupations of $\varphi_a(\alpha)$ are reported in the corresponding diagrams of Scheme 1.3c. It follows from these expressions that in the latter case

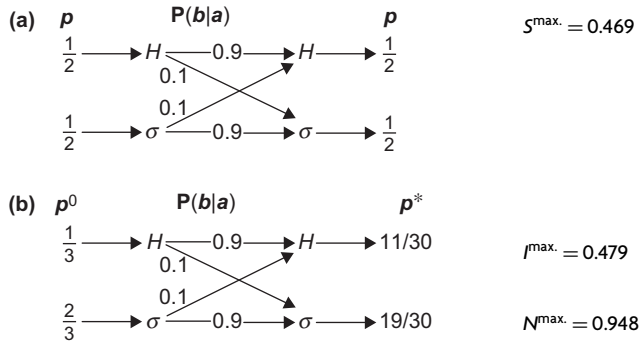

Scheme 1.13 The orbital-communication channels for the localized M–L_α bond in the fixed-input approach, for $P = Q = 1/2$, and the singly occupied antibonding MO: covalent (molecular input; Panel a) and ionic (promolecular input; Panel b).

the off-diagonal elements identically vanish, $\gamma_{H_\alpha,\sigma_\alpha} = \gamma_{\sigma_\alpha,H_\alpha} = 0$, thus giving rise to the decoupled pair of orbitals and hence to the deterministic channel of Scheme 1.1b for each of them (see the fourth diagram in Scheme 1.3c). Therefore, such separate channels do not contribute to the overall IT bond descriptors.

For the partly bonding, open-shell configuration $n_a = 1$ (the third diagram in Scheme 1.3c) and the maximum covalency combination $P = Q = 1/2$, one obtains a strongly deterministic information system as shown in Scheme 1.13. It follows from these diagrams that the fixed-input approach predicts a practically conserved overall bond order compared with the $n_a = 0$ case (the second diagram in Scheme 1.3c), with the bond weakening being reflected only in the bond composition with now roughly equal (half-bond) covalent and ionic components.

As already discussed in Scheme 1.3, the populational decoupling trends of AO in the coordination bond are properly reflected only in the flexible-input (MO-resolved) description, which recognizes the bonding and antibonding contributions to the resultant bond multiplicity from the signs of the corresponding CBO matrix elements of the system-occupied MO. It should be emphasized, however, that such treatment ceases to be purely probabilistic in character since it uses the extraneous piece of the CBO information, which is lost in the conditional probabilities.

8. RESTRICTED HARTREE–FOCK CALCULATIONS

In typical SCF-LCAO-MO calculations the lone pairs of the valence and/or inner shell electrons can strongly affect the IT descriptors of the chemical bond. Therefore, the contributions due to each AO input should be

appropriately weighted (see Eqs. [28 and 29] in Section 4) using the joint, two-orbital probabilities that reflect the actual participation of each AO in the system chemical bonds. In this section we describe such an approach to diatomic chemical interactions in molecules and present numerical results from standard RHF calculations for a selection of representative molecular systems.

8.1. Orbital and condensed atom probabilities of diatomic fragments in molecules

The molecular probability scattering in the specified diatomic fragment (A, B), involving AO contributed by these two bonded atoms, $\boldsymbol{\chi}_{AB} = (\boldsymbol{\chi}_A, \boldsymbol{\chi}_B)$, to the overall basis set $\boldsymbol{\chi} = \{\boldsymbol{\chi}_X\}$, is completely characterized by the corresponding $\mathbf{P}(\boldsymbol{\chi}_{AB}|\boldsymbol{\chi}_{AB})$ block [22, 26] of the molecular conditional probability matrix of Eq. (4), which determines the molecular communication system in OCT [46–48] of the chemical bond:

$$\begin{aligned}\boldsymbol{P}(\boldsymbol{\chi}_{AB}|\boldsymbol{\chi}_{AB}) &\equiv [\boldsymbol{P}(\boldsymbol{\chi}_Y|\boldsymbol{\chi}_X); (X, Y) \in (A, B)] \\ &\equiv \{\boldsymbol{P}(j|\boldsymbol{\chi}_{AB}); \chi_j \in \boldsymbol{\chi}_{AB}\} \equiv \{P(j|i); (\chi_i, \chi_j) \in \boldsymbol{\chi}_{AB})\}. \end{aligned} \tag{48}$$

Thus, the square matrix $\boldsymbol{P}(\boldsymbol{\chi}_{AB}|\boldsymbol{\chi}_{AB})$ contains only the intrafragment communications, which miss the probability propagations originating from AO of the remaining constituent atoms $\boldsymbol{\chi}_Z \notin \boldsymbol{\chi}_{AB}$.

The atomic *output* reduction of $\boldsymbol{P}(\boldsymbol{\chi}_{AB}|\boldsymbol{\chi}_{AB})$ [9] gives the associated *condensed* conditional probabilities of the associated molecular information system,

$$\begin{aligned}\boldsymbol{P}(X_{AB}|\boldsymbol{\chi}_{AB}) &= [\boldsymbol{P}(A|\boldsymbol{\chi}_{AB}), \boldsymbol{P}(B|\boldsymbol{\chi}_{AB})] \\ &= \left\{\boldsymbol{P}(X|\boldsymbol{\chi}_{AB}) \equiv \{P(X|i)\} = \sum_{j \in X} P(j|\,\chi_{AB}); \chi_i \in \boldsymbol{\chi}_{AB}, X = A, B\right\}, \end{aligned} \tag{49}$$

where $P(Y|i)$ measures the conditional probability that an electron on χ_i will be found on atom Y in the molecule. The sum of these conditional probabilities over all AOs contributed by the two atoms then determines the communication connections $\{P(A, B|i)\}$, linking the condensed atomic output (A, B) and the given AO input χ_i in the associated communication system of the diatomic fragment:

$$\begin{aligned}\boldsymbol{P}(A|\boldsymbol{\chi}_{AB}) + \boldsymbol{P}(B|\boldsymbol{\chi}_{AB}) &= \boldsymbol{P}(A, B|\boldsymbol{\chi}_{AB}) \\ &= \left\{P(A,B|i) = P(A|i) + P(B|i) = \sum_{j \in (A,B)} P(j|\,i) \leq 1\right\}. \end{aligned} \tag{50}$$

In other words, $P(\mathrm{A,B}|i)$ measures the probability that the electron occupying χ_i will be detected in the diatomic fragment AB of the molecule. The inequality in the preceding equation reflects the fact that the atomic basis functions participate in chemical bonds with all constituent atoms, with the equality sign corresponding only to a diatomic molecule, when $\boldsymbol{\chi}_{\mathrm{AB}} = \boldsymbol{\chi}$.

The fragment-normalized AO probabilities

$$\tilde{p}(\mathrm{AB}) = \{\tilde{p}_i(\mathrm{AB}) = \gamma_{i,i}/N_{\mathrm{AB}}\}, \quad N_{\mathrm{AB}} = \sum_{i\in(\mathrm{A,B})} \gamma_{i,i}, \sum_{i\in(\mathrm{A,B})} \tilde{p}_i(\mathrm{AB}) = 1, \tag{51}$$

where N_{AB} stands for the number of electrons in the specified diatomic fragment of the molecule and $\tilde{p}_i(\mathrm{AB})$ denotes the probability that one of them occupies $\chi_{i\in(\mathrm{A,B})}$, then determine the simultaneous probabilities of the joint two-orbital events [47]:

$$\boldsymbol{P}_{\mathrm{AB}}(\boldsymbol{\chi}_{\mathrm{AB}}, \boldsymbol{\chi}_{\mathrm{AB}}) = \{P_{\mathrm{AB}}(i,j) = \tilde{p}_i(\mathrm{AB})P(j|i) = \gamma_{i,j}\gamma_{j,i}/(2N_{\mathrm{AB}})\}. \tag{52}$$

They generate, via relevant partial summations, the joint atom-orbital probabilities in AB, $\{P_{\boldsymbol{AB}}(\mathrm{X}, i)\}$:

$$\begin{aligned}\boldsymbol{P}_{\mathrm{AB}}(\boldsymbol{X}_{\mathrm{AB}}, \boldsymbol{\chi}_{\mathrm{AB}}) &= [\boldsymbol{P}_{\mathrm{AB}}(\mathrm{A}, \boldsymbol{\chi}_{\mathrm{AB}}), \boldsymbol{P}_{\mathrm{AB}}(\mathrm{B}, \boldsymbol{\chi}_{\mathrm{AB}})] \\ &= \left\{P_{\mathrm{AB}}(\mathrm{X}, i) = \sum_{j\in\mathrm{X}} P_{\mathrm{AB}}(i,j) \equiv \tilde{p}_i(\mathrm{AB})P(\mathrm{X}|i), \mathrm{X} = \mathrm{A}, \mathrm{B}\right\}.\end{aligned} \tag{53}$$

For the closed-shell molecular systems one thus finds

$$\boldsymbol{P}_{\mathrm{AB}}(\mathrm{X}, \boldsymbol{\chi}_{\mathrm{AB}}) = \left\{P_{\mathrm{AB}}(\mathrm{X}, i) = \tilde{p}_i(\mathrm{AB}) \sum_{j\in\mathrm{X}} P(j|\, i) = \sum_{j\in\mathrm{X}} \frac{\gamma_{i,j}\gamma_{j,i}}{2N_{\mathrm{AB}}}\right\}, \quad \mathrm{X} = \mathrm{A}, \mathrm{B}. \tag{54}$$

These vectors of AO probabilities in diatomic fragment AB subsequently define the condensed probabilities $\{P_{\mathrm{X}}(\mathrm{AB})\}$ of both bonded atoms in subsystem AB:

$$P_{\mathrm{X}}(\mathrm{AB}) = \frac{N_{\mathrm{X}}(\mathrm{AB})}{N_{\mathrm{AB}}} = \sum_{i\in(\mathrm{A,B})} P_{\mathrm{AB}}(\mathrm{X}, i) = \sum_{i\in(\mathrm{A,B})} \sum_{j\in\mathrm{X}} \frac{\gamma_{i,j}\gamma_{j,i}}{2N_{\mathrm{AB}}}, \quad \mathrm{X} = \mathrm{A}, \mathrm{B}, \tag{55}$$

where the effective number of electrons $N_{\mathrm{X}}(\mathrm{AB})$ on atom $\mathrm{X} = \mathrm{A}, \mathrm{B}$ reads:

$$N_{\mathrm{X}}(\mathrm{AB}) = \sum_{i\in(\mathrm{A,B})} \sum_{j\in\mathrm{X}} \frac{\gamma_{i,j}\gamma_{j,i}}{2}. \tag{56}$$

Therefore, in diatomic molecules, for which $\boldsymbol{\chi}_{AB} = \boldsymbol{\chi}$, one finds using the idempotency relations of Eq. (3),

$$P_X(AB) = \sum_{j\in X}\left(\sum_i \frac{\gamma_{j,i}\gamma_{i,j}}{2N_{AB}}\right) = \sum_{j\in X}\frac{\gamma_{j,j}}{N_{AB}} = \sum_{j\in X}\tilde{p}_j(AB), \quad X = A, B, \tag{57}$$

and hence $P_A(AB) + P_B(AB) = 1$. Clearly, the last relation does not hold for diatomic fragments in larger molecular systems, when $\boldsymbol{\chi}_{AB} \neq \boldsymbol{\chi}$, so that in general $P_X(AB) \neq \sum_{j\in X}\tilde{p}_j$ and

$$P_A(AB) + P_B(AB) \neq 1. \tag{58}$$

We finally observe that the effective orbital probabilities of Eqs. (52–54) and the associated condensed probabilities of bonded atoms (Eq. 55) do not reflect the actual AO participation in all chemical bonds in AB, giving rise to comparable values for the bonding and nonbonding (lone-pair) AO in the valence and inner shells. The relative importance of basis functions of one atom in forming the chemical bonds with the other atom of the specified diatomic fragment is reflected by the (nonnormalized) joint *bond probabilities* of the two atoms, defined by the *diatomic* components of the simultaneous probabilities of Eqs. (52 and 53):

$$P_b(A, B) \equiv \sum_{i\in B} P_{AB}(A, i) = \sum_{i\in A} P_{AB}(B, i) = P_b(B,A) = \sum_{i\in A}\sum_{j\in B}\frac{\gamma_{i,j}\gamma_{j,i}}{2N_{AB}}. \tag{59}$$

The underlying joint atom-orbital probabilities, $\{P_{AB}(A, i), i \in B\}$ and $\{P_{AB}(B, i), i \in A\}$, to be used as weighting factors in the average conditional-entropy (covalency) and mutual-information (ionicity) descriptors of the AB chemical bond(s), indeed assume appreciable magnitudes only when the electron occupying the atomic orbital χ_i of one atom is simultaneously found with a significant probability on the other atom, thus effectively excluding the contributions to the entropy/information bond descriptors due to the lone-pair electrons. Thus, such joint bond probabilities emphasize of AOs have both atoms are simultaneously involved in the occupied MOs.

The reference bonding probabilities of AO have to be normalized to the corresponding sums $\boldsymbol{P}(A, B|\boldsymbol{\chi}_{AB}) = \{P(A, B|i)\}$ of Eq. (50). Since the bond probability concept of Eq. (59) involves symmetrically the two bonded atoms, we apply the same principle to determine the associated reference bond probabilities of AO to be used to calculate the mutual-information bond index:

$$\{p_b(i) = P(A, B|i)/2; \quad i \in (A, B)\}, \tag{60}$$

where $P(\mathrm{A,B}|i)$ denotes the probability that an electron originating from orbital χ_i will be found on atom A or B in the molecule.

8.2. Average entropic descriptors of diatomic chemical interactions

As we have already mentioned in Section 2, in OCT the complementary quantities characterizing the average *noise* (conditional entropy of the channel output given input) and the *information flow* (mutual information in the channel output and input) in the diatomic communication system defined by the conditional AO probabilities of Eq. (48) provide the overall descriptors of the fragment bond covalency and ionicity, respectively. Both molecular and promolecular reference (input) probability distributions have been used in the past to determine the information index characterizing the displacement (ionicity) aspect of the system chemical bonds [9, 46–48].

In the A–B fragment development we similarly define the following average contributions of both constituent atoms to the diatomic covalency (delocalization) entropy:

$$H_{\mathrm{AB}}(\mathrm{B}|\boldsymbol{\chi}_{\mathrm{A}}) = \sum_{i\in\mathrm{A}} P_{\mathrm{AB}}(\mathrm{B},i)\; H(\chi_{\mathrm{AB}}|i), \quad H_{\mathrm{AB}}(\mathrm{A}|\boldsymbol{\chi}_{\mathrm{B}}) = \sum_{i\in\mathrm{B}} P_{\mathrm{AB}}(\mathrm{A},i)\; H(\chi_{\mathrm{AB}}|i), \tag{61}$$

where the Shannon entropy of the conditional probabilities for the given AO input $\chi_i \in \boldsymbol{\chi}_{\mathrm{AB}} = (\boldsymbol{\chi}_{\mathrm{A}}, \boldsymbol{\chi}_{\mathrm{B}})$ in the diatomic channel:

$$H(\chi_{\mathrm{AB}}|i) = -\sum_{j\in(\mathrm{A,B})} P(j|i)\log_2 P(j|i). \tag{62}$$

In Eq. (61) the conditional entropy $S_{\mathrm{AB}}(\mathrm{Y}|\boldsymbol{\chi}_{\mathrm{X}})$ quantifies (in bits) the delocalization X→Y per electron so that the total covalency in the diatomic fragment A–B reads as follows:

$$\mathcal{S}_{\mathrm{AB}} = N_{\mathrm{AB}}[H_{\mathrm{AB}}(\mathrm{B}|\boldsymbol{\chi}_{\mathrm{A}}) + H_{\mathrm{AB}}(\mathrm{A}|\boldsymbol{\chi}_{\mathrm{B}})]. \tag{63}$$

Again, it should be emphasized that the simultaneous (diatomic) probabilities $\{P_{\mathrm{AB}}(\mathrm{X}, i \in \mathrm{Y}), \mathrm{Y} \neq \mathrm{X}\}$, used in Eq. (61) as weighting factors of the corresponding contributions due to the specified input AO, effectively eliminate contributions due to the inner- and valence-shell lone pairs, since these weighting factors reflect the actual orbital participation in the fragment chemical bonds.

Accordingly, the probability-weighted contributions to the average mutual-information quantities of bonded atoms are defined in reference to

the unbiased bond probabilities of AO (Eq. [60]):

$$I_{AB}(\chi_A : B) = \sum_{i \in A} P_{AB}(B, i) I(\chi_{AB} : i), \quad I_{AB}(\chi_B : A) = \sum_{i \in B} P_{AB}(A, i) I(\chi_{AB} : i),$$

$$I(\chi_{AB} : i) = \sum_{j \in (A,B)} P(j|i) \log_2 \left(\frac{P(j|i)}{p_b(i)} \right). \quad (64)$$

They generate the total information ionicity of all chemical bonds in the diatomic fragment:

$$\mathcal{I}_{AB} = N_{AB}[I_{AB}(\chi_A : B) + I_{AB}(\chi_B : A)]. \quad (65)$$

Finally, the sum of the above total (diatomic) entropy-covalency and information-ionicity indices determines the overall information-theoretic bond multiplicity in the molecular fragment in question:

$$\mathcal{N}_{AB} = \mathcal{S}_{AB} + \mathcal{I}_{AB}. \quad (66)$$

They can be compared with the diatomic (covalent) bond order of Wiberg [52] formulated in the standard SCF-LCAO-MO theory,

$$\mathcal{M}_{AB} = \sum_{i \in A} \sum_{j \in B} \gamma_{i,j}^2 = \sum_{i \in A} \sum_{j \in B} \mathcal{M}_{i,j}, \quad (67)$$

which has been previously shown to adequately reflect the chemical intuition in the ground state of typical molecular systems. Such a comparison is performed in Tables 1.1 and 1.2, reporting the numerical RHF data of bond orders in diatomic fragments of representative molecules for their equilibrium geometries in the minimum (STO-3G) and extended (6-31G*) basis sets, respectively.

It follows from both these tables that the applied weighting procedure gives rise to an excellent agreement with both the Wiberg bond orders and the chemical intuition. A comparison between corresponding entries in Table 1.1 and the upper part of Table 1.2 also reveals generally weak dependence on the adopted AO representation, with the extended basis set predictions being slightly closer to the familiar chemical estimates of the localized bond multiplicities in these typical molecules. In a series of related compounds, for example, in hydrides or halides, the trends exhibited by the entropic covalent and ionic components of a roughly conserved overall bond order also agree with intuitive expectations. For example, the single chemical bond between two “hard” atoms in HF appears predominantly covalent,

Table 1.1 Comparison of the diatomic Wiberg and entropy/information bond multiplicity descriptors in selected molecules: the RHF results obtained in the minimum (STO-3G) basis set

Molecule	A–B	$\mathcal{M}_{AB}$	$\mathcal{N}_{AB}$	$\mathcal{S}_{AB}$	$\mathcal{I}_{AB}$
H_2	H–H	1.000	1.000	1.000	0.000
F_2	F–F	1.000	1.000	0.947	0.053
HF	H–F	0.980	0.980	0.887	0.093
LiH	Li–H	1.000	1.000	0.997	0.003
LiF	Li–F	1.592	1.592	0.973	0.619
CO	C–O	2.605	2.605	2.094	0.511
H_2O	O–H	0.986	1.009	0.859	0.151
AlF_3	Al–F	1.071	1.093	0.781	0.311
CH_4	C–H	0.998	1.025	0.934	0.091
C_2H_6	C–C	1.023	1.069	0.998	0.071
	C–H	0.991	1.018	0.939	0.079
C_2H_4	C–C	2.028	2.086	1.999	0.087
	C–H	0.984	1.013	0.947	0.066
C_2H_2	C–C	3.003	3.063	2.980	0.062
	C–H	0.991	1.021	0.976	0.045
C_6H_6[1]	C_1–C_2	1.444	1.526	1.412	0.144
	C_1–C_3	0.000	0.000	0.000	0.000
	C_1–C_4	0.116	0.119	0.084	0.035

[1] For the sequential numbering of carbon atoms in the benzene ring.

although a substantial ionicity is detected for LiF, for which both Wiberg and information-theoretic results predict roughly (3/2)-bond in the minimum basis set, consisting of approximately one covalent and 1/2 ionic contributions; in the extended basis set, both approaches give approximately a single-bond estimate, with the information theory predicting the ionic dominance of the overall bond multiplicity. The significant information-ionicity contribution is also detected for all halides in the lower part of Table 1.2. One also finds that all carbon–carbon interactions in the benzene ring are properly differentiated. The chemical orders of the single and multiple bonds in ethane, ethylene, and acetylene are also properly reproduced, and the triple bond in CO is accurately accounted. Even more subtle bond differentiation effects are adequately reflected by the present information-theoretic results. The differentiation of the "equatorial" and "axial" S–F bonds in the irregular tetrahedron of SF_4 is reproduced, and the increase in the strength of the central bond in propellanes with increase of sizes of the bridges is correctly predicted [9].

Table 1.2 The same as in Table 1.1 for the extended 6-31G* basis set

Molecule	A–B	$\mathcal{M}_{AB}$	$\mathcal{N}_{AB}$	$\mathcal{S}_{AB}$	$\mathcal{I}_{AB}$
F_2	F–F	1.228	1.228	1.014	0.273
HF	H–F	0.816	0.816	0.598	0.218
LiH	Li–H	1.005	1.005	1.002	0.004
LiF	Li–F	1.121	1.121	0.494	0.627
CO	C–O	2.904	2.904	2.371	0.533
H_2O	O–H	0.878	0.896	0.662	0.234
AlF_3	Al–F	1.147	1.154	0.748	0.406
CH_4	C–H	0.976	1.002	0.921	0.081
C_2H_6	C–C	1.129	1.184	1.078	0.106
	C–H	0.955	0.985	0.879	0.106
C_2H_4	C–C	2.162	2.226	2.118	0.108
	C–H	0.935	0.967	0.878	0.089
C_2H_2	C–C	3.128	3.192	3.095	0.097
	C–H	0.908	0.943	0.878	0.065
C_6H_6[1]	C_1–C_2	1.507	1.592	1.473	0.119
	C_1–C_3	0.061	0.059	0.035	0.024
	C_1–C_4	0.114	0.117	0.081	0.035
LiCl	Li–Cl	1.391	1.391	0.729	0.662
LiBr	Li–Br	1.394	1.394	0.732	0.662
NaF	Na–F	0.906	0.906	0.429	0.476
KF	K–F	0.834	0.834	0.371	0.463
SF_2	S–F	1.060	1.085	0.681	0.404
SF_4	S–F_a	1.055	1.064	0.670	0.394
	S–F_b	0.912	0.926	0.603	0.323
SF_6	S–F	0.978	0.979	0.726	0.254
B_2H_6[2]	B–B	0.823	0.851	0.787	0.063
	B–H_t	0.967	0.995	0.938	0.057
	B–H_b	0.476	0.490	0.462	0.028
Propellanes[3]					
[1.1.1]	C_b–C_b	0.797	0.829	0.757	0.072
[2.1.1]	C_b–C_b	0.827	0.860	0.794	0.066
[2.2.1]	C_b–C_b	0.946	0.986	0.874	0.112
[2.2.2]	C_b–C_b	1.009	1.049	0.986	0.063

[1] For the sequential numbering of carbon atoms in the benzene ring.
[2] H_t and H_b denote the *terminal* and *bridge* hydrogen atoms, respectively.
[3] Central bonds between the *bridgehead* carbon atoms C_b.

Moreover, as intuitively expected, the C–H bonds are seen to slightly increase their information ionicity when the number of these terminal bonds increases in a series: acetylene, ethylene, and ethane. In B_2H_6, the correct $\approx$ (1/2)-bond order of the bridging B–H bond is predicted, and approximately single terminal bond multiplicity is detected. For the alkali metal fluorides the increase in the bond entropy-covalency (decrease in information ionicity) with increasing size (softness) of the metal is also observed. For the fixed alkali metal in halides, for example, in a series consisting LiF, LiCl, and LiBr (Table 1.2), the overall bond order is increased for larger (softer) halogen atoms, mainly due to a higher entropy-covalency (delocalization) and noise component of the molecular communication channel in AO resolution.

9. CONCLUSION

Until recently, a wider use of CTCB in probing the molecular electronic structure has been hindered by the originally adopted two-electron conditional probabilities, which blur a diversity of chemical bonds. We have demonstrated in the present work that the MO-resolved OCT using the flexible-input probabilities and recognizing the bonding/antibonding character of the orbital interactions in a molecule, which is reflected by the signs of the underlying CBO matrix elements, to a large extent remedies this problem. The off-diagonal conditional probabilities it generates are proportional to the quadratic bond indices of the MO theory; hence, the strong interorbital communications correspond to strong Wiberg bond multiplicities. It also covers the orbital decoupling limit and properly accounts for the increasing populational decoupling of AO when the antibonding MOs are more occupied. It should be also emphasized that the extra-computation effort of this IT analysis of the molecular bonding patterns is negligible compared with the standard computations of the molecular electronic structure, since all quantum-mechanical computations in the orbital approximation already determine the CBO data required by this generalized formulation of OCT.

We have also demonstrated that a dramatic improvement of the overall entropy/information descriptors of chemical bonds and a differentiation of diatomic bond multiplicities is obtained when one recognizes the mutually decoupled groups of orbitals as the separate information systems. Such decoupling process can be satisfactorily described only within the flexible-input approach, which links the specified AO-input distribution to its involvement in communicating (bonding) with the remaining orbitals. The other improvement of the IT description of the bond diversity in molecules and their weakening with the nonzero occupation of antibonding MO has been gained by applying the MO-resolved channels supplemented with the extra sign convention of their entropy/information bond contributions, which is linked to those of the associated MO bond orders. Indeed, the

bonding/antibonding classification, although lost in the conditional probabilities, is directly available from the corresponding CBO matrix elements, routinely generated in all LCAO-MO calculations and required to generate the information channels themselves.

This orbital IT development extends our understanding of the chemical bond from the complementary viewpoint of the information/communication theory. The purely probabilistic models have been previously shown to be unable to completely reproduce the bond differentiation patterns observed in alternative bond order measures formulated in the standard MO theory. However, as convincingly demonstrated in Section 8, the bond probability weighting of contributions due to separate AO inputs gives excellent results, which completely reproduce the bond differentiation in diatomic fragments of the molecule implied by the quadratic criterion of Wiberg. In excited states, only the recognition of the bonding/antibonding character of the orbital interactions, which is reflected by the signs of the corresponding elements of the CBO matrix, allows one to bring the IT overall descriptors to a semi-quantitative agreement with the alternative measures formulated in the SCF-LCAO-MO theory.

The OCT has recently been extended to cover many orbital effects in the chemical bond and reactivity phenomena [38, 68–70]. The orbital communications have also been used to study the bridge bond order components [71, 72] and the multiple probability scattering phenomena in the framework of the probability-amplitude channel [73]. The implicit bond-dependency origins of the indirect (bridge) interactions between atomic orbitals in molecules have also been investigated [74].

REFERENCES

[1] R.A. Fisher, On the mathematical foundations of theoretical statistics, Philos. Trans. R. Soc. (London) 222 (1922) 309.
[2] R.A. Fisher, Theory of statistical estimation, Proc. Cambridge Phil. Soc. 22 (1925) 700.
[3] R.A. Fisher, Statistical Methods and Scientific Inference, second ed., Oliver and Boyd, London, 1959.
[4] C.E. Shannon, The mathematical theory of communication, Bell System Tech. J. 27 (1948) 379, 623.
[5] C.E. Shannon, W. Weaver, The Mathematical Theory of Communication, University of Illinois, Urbana, 1949.
[6] N. Abramson, Information Theory and Coding, McGraw-Hill, New York, 1963.
[7] S. Kullback, R.A. Leibler, On Information and Sufficiency, Ann. Math. Stat. 22 (1951) 79.
[8] S. Kullback, Information Theory and Statistics, Wiley, New York, 1959.
[9] R.F. Nalewajski, Information Theory of Molecular Systems, Elsevier, Amsterdam, 2006, and refs. therein.
[10] R.F. Nalewajski, R.G. Parr, Information theory, atoms-in-molecules, and molecular similarity, Proc. Natl. Acad. Sci. USA 97 (2000) 8879.
[11] R.F. Nalewajski, R.G. Parr, Information theoretic thermodynamics of molecules and their Hirshfeld fragments, J. Phys. Chem. A 105 (2001) 7391.

[12] R.F. Nalewajski, Hirshfeld analysis of molecular densities: Subsystem probabilities and charge sensitivities, Phys. Chem. Chem. Phys. 4 (2002) 1710.
[13] R.G. Parr, P.W. Ayers, R.F. Nalewajski, What is an atom in a molecule? J. Phys. Chem. A 109 (2005) 3957.
[14] R.F. Nalewajski, E. Broniatowska, Entropy displacement analysis of electron distributions in molecules and their Hirshfeld atoms, J. Phys. Chem. A 107 (2003) 6270.
[15] R.F. Nalewajski, E. Broniatowska, Information distance approach to Hammond postulate, Chem. Phys. Lett. 376 (2003) 33.
[16] R.F. Nalewajski, E. Broniatowska, Atoms-in-molecules from the stockholder partition of molecular two-electron distribution, Theret. Chem. Acc. 117 (2007) 7.
[17] R.F. Nalewajski, E. Broniatowska, Entropy/information indices of the "stockholder" atoms-in-molecules, Int. J. Quantum Chem. 101 (2005) 349.
[18] R.F. Nalewajski, E. Świtka, A. Michalak, Information distance analysis of molecular electron densities, Int. J. Quantum Chem. 87 (2002) 198.
[19] R.F. Nalewajski, Entropic measures of bond multiplicity from the information theory, J. Phys. Chem. A 104 (2000) 11940.
[20] R.F. Nalewajski, Entropy descriptors of the chemical bond in information theory. I. Basic concepts and relations, Mol. Phys. 102 (2004) 531.
[21] R.F. Nalewajski, Entropy descriptors of the chemical bond in information theory. II. Applications to simple orbital models, Mol. Phys. 102 (2004) 547.
[22] R.F. Nalewajski, Partial communication channels of molecular fragments and their entropy/information indices, Mol. Phys. 103 (2005) 451.
[23] R.F. Nalewajski, Comparison between valence-bond and communication theories of the chemical bond in H_2, Mol. Phys. 104 (2006) 365.
[24] R.F. Nalewajski, Atomic resolution of bond descriptors in the two-orbital model, Mol. Phys. 104 (2006) 493.
[25] R.F. Nalewajski, Reduced communication channels of molecular fragments and their entropy/information bond indices, Theoret. Chem. Acc. 114 (2005) 4.
[26] R.F. Nalewajski, Entropy/information bond indices of molecular fragments, J. Math. Chem. 38 (2005) 43.
[27] R.F. Nalewajski, Communication theory perspective on valence bond theory, J. Math. Chem. 45 (2009) 709.
[28] R.F. Nalewajski, Information-scattering perspective on orbital hybridization, J. Phys. Chem. A 111 (2007) 4855.
[29] R.F. Nalewajski, Information theoretic approach to fluctuations and electron flows between molecular fragments, J. Phys. Chem. A 107 (2003) 3792.
[30] R.F. Nalewajski, Local information-distance thermodynamics of molecular fragments, Ann. Phys. (Leipzig) 13 (2004) 201.
[31] R.F. Nalewajski, Electronic chemical potential as information temperature, Mol. Phys. 104 (2006) 255.
[32] A.D. Becke, K.E.J. Edgecombe, A simple measure of electron localization in atomic and molecular systems, J. Chem. Phys. 92 (1990) 5397.
[33] R.F. Nalewajski, A.M. Köster, S. Escalante, Electron localization function as information measure, J. Phys. Chem. A 109 (2005) 10038.
[34] R.F. Nalewajski, Use of Fisher information in quantum chemistry, Int. J. Quantum. Chem. 108 (2008) 2230.
[35] R.F. Nalewajski, P. de Silva, J. Mrozek, Use of non-additive Fisher information in probing the chemical bonds, J. Mol. Struct.: Theochem 954 (2010) 57.
[36] R.F. Nalewajski, P. de Silva, J. Mrozek, Kinetic-energy/Fisher-information indicators of chemical bonds, in: A. Wang, T.A. Wesoxowski, (Eds.), Kinetic Energy Functional, World Scientific, Singapore, in press.

[37] R.F. Nalewajski, Use of non-additive information measures in exploring molecular electronic structure: Stockholder bonded atoms and role of kinetic energy in the chemical bonds, J. Math. Chem. 47 (2010) 667.
[38] R.F. Nalewajski, Information Origins of the Chemical Bond, Nova Science Publishers, New York, 2010.
[39] S.B. Sears, Applications of Information Theory in Chemical Physics. Ph. D. Thesis; University of North Carolina, Chapel Hill, 1980.
[40] S.B. Sears, R.G. Parr, U. Dinur, On the quantum-mechanical kinetic energy as a measure of information in a distribution, Isr. J. Chem. 19 (1980) 165.
[41] B.R. Frieden, Physics from the Fisher Information – A Unification, Cambridge University Press, Cambridge, 2000.
[42] R.F. Nalewajski, On molecular similarity in communication theory of the chemical bond, J. Math. Chem. 45 (2009) 607.
[43] R.F. Nalewajski, Molecular communication channels of model excited electron configurations, Mol. Phys. 104 (2006) 1977.
[44] R.F. Nalewajski, Orbital resolution of molecular information channels and stockholder atoms, Mol. Phys. 104 (2006) 2533.
[45] R.F. Nalewajski, Entropic bond indices from molecular information channels in orbital resolution: Excited configurations, Mol. Phys. 104 (2006) 3339.
[46] R.F. Nalewajski, Information origins of the chemical bond: Bond descriptors from molecular communication channels in orbital resolution, Int. J. Quantum. Chem. 109 (2009) 2495.
[47] R.F. Nalewajski, Chemical bond descriptors from molecular information channels in orbital resolution, Int. J. Quantum. Chem. 109 (2009) 425.
[48] R.F. Nalewajski, Multiple, localized and delocalized/conjugated bonds in the orbital-communication theory of molecular systems, Adv. Quant. Chem. 56 (2009) 217.
[49] R.F. Nalewajski, Entropic bond indices from molecular information channels in orbital resolution: Ground-state systems, J. Math. Chem. 43 (2008) 265.
[50] R.F. Nalewajski, Chemical bonds through probability scattering: Information channels for intermediate-orbital stages, J. Math. Chem. 43 (2008) 780.
[51] P.A.M. Dirac, The Principles of Quantum Mechanics, fourth ed., Clarendon, Oxford, 1958.
[52] K.A. Wiberg, Application of the Pople-Santry-Segal CNDO method to the cyclopropylcarbinyl and cyclobutyl cation and to bicyclobutane, Tetrahedron 24 (1968) 1083.
[53] M.S. Gopinathan, K. Jug, Valency. I. Quantum chemical definition and properties, Theoret. Chim. Acta (Berl.) 63 (1983) 497.
[54] M.S. Gopinathan, K. Jug, Valency. II. Applications to molecules with first-row atoms, Theoret. Chim. Acta (Berl.) 63 (1983) 511.
[55] K. Jug, M.S. Gopinathan, Valence in molecular orbital theory, in: Z.B. Maksić, (Ed.), Theoretical Models of Chemical Bonding, Vol. II, Springer, Heidelberg, 1990, p. 77.
[56] I. Mayer, Charge, bond order and valence in the ab initio SCF theory, Chem. Phys. Lett. 97 (1983) 270.
[57] R.F. Nalewajski, A.M. Köster, K. Jug, Chemical valence from the two-particle density matrix, Theoret. Chim. Acta (Berl.) 85 (1993) 463.
[58] R.F. Nalewajski, J. Mrozek, Modified valence indices from the two-particle density matrix, Int. J. Quantum Chem. 51 (1994) 187.
[59] R.F. Nalewajski, S.J. Formosinho, A.J.C. Varandas, J. Mrozek, Quantum mechanical valence study of a bond-breaking – bond-forming process in triatomic systems, Int. J. Quantum Chem. 52 (1994) 1153.
[60] R.F. Nalewajski, J. Mrozek, G. Mazur, Quantum-mechanical valence indices from the one-determinantal difference approach, Can. J. Chem. 100 (1996) 1121.
[61] R.F. Nalewajski, J. Mrozek, A. Michalak, Two-electron valence indices from the Kohn-Sham orbitals, Int. J. Quantum Chem. 61 (1997) 589.

[62] J. Mrozek, R.F. Nalewajski, A. Michalak, Exploring bonding patterns of molecular systems using quantum mechanical bond multiplicities, Polish J. Chem. 72 (1998) 1779.
[63] R.F. Nalewajski, Entropic and difference bond multiplicities from the two-electron probabilities in orbital resolution, Chem. Phys. Lett. 386 (2004) 265.
[64] S. Shaik, A qualitative valence bond model for organic reactions, in: J. Bertran, I.G. Czismadia, (Eds.), New Theoretical Concepts for Understanding Organic Reactions, NATO ASI Series, Vol. C267, Kluwer, Dordrecht, 1989, p. 165.
[65] S. Shaik, P.C. Hiberty, Curve crossing diagrams as general models for chemical structure and reactivity, in: Z.B. Maksić, (Ed.), Theoretical Models of Chemical Bonding, Vol. IV, Springer, Heidelberg, 1991, p. 269.
[66] S. Shaik, P.C. Hiberty, Valence bond mixing and curve crossing diagrams in chemical reactivity and bonding, Adv. Quant. Chem. 26 (1995) 100.
[67] K. Jug, A.M. Köster, Influence of σ and π electrons on aromaticity, J. Am. Chem. Soc. 112 (1990) 6772.
[68] R.F. Nalewajski, Many-orbital probabilities and their entropy/information descriptors in orbital communication theory of the chemical bond, J. Math. Chem. 47 (2010) 692.
[69] R.F. Nalewajski, Entropy/information coupling between orbital communications in molecular subsystems, J. Math. Chem. 47 (2010) 808.
[70] R.F. Nalewajski, Use of the bond-projected superposition principle in determining the conditional probabilities of orbital events in molecular fragments, J. Math. Chem. in press. 49 (2011) 592.
[71] R.F. Nalewajski, Through-space and through-bridge components of chemical bonds, J. Math. Chem. in press. 49 (2011) 371.
[72] R.F. Nalewajski, Chemical bonds from the through-bridge orbital communications in prototype molecular systems, J. Math. Chem. in press. 49 (2011) 546.
[73] R.F. Nalewajski, On interference of orbital communications in molecular systems, J. Math. Chem. in press. 49 (2011) 806.
[74] R. F. Nalewajski, P. Gurdek, On the implicit bond-dependency origins of bridge interactions, J. Math. Chem. in press.

CHAPTER 2

Quantum States for Quantum Measurements

O. Tapia[a]

Contents

1. Introduction 50
2. Quantum States for Quantum Probing 51
3. Aspects of Standard Quantum Measurement Model 55
   3.1. Preparing and recording 55
   3.2. Copenhagen view 57
   3.3. Copenhagen view challenged 58
4. View from a Fence 60
   4.1. Double-slit case 60
   4.2. Recording screens 66
   4.3. Tonomura's experiment 71
5. Quantum States for Quantum Measurement 73
   5.1. Scully et al. double-slit setup: basic elements 73
   5.2. The Einstein–Podolsky–Rosen thought experiment 78
   5.3. The Wheeler's delayed-choice experiments 83
   5.4. Particle picture and delayed-choice experiment 86
   5.5. Coherence lost and regained 87
6. Back to Quantum States for Quantum Probing 87
   6.1. The Scully et al. atom interferometer 88
   6.2. *Welcher Weg* setup 95
   6.3. Quantum eraser 96
   6.4. Entanglement issues 98
7. Discussion 100
Acknowledgments 105
References 105

[a] Department of Physical Chemistry and Analytical Chemistry, Uppsala University, Uppsala, Sweden
E-mail address: orlando.tapia@fki.uu.se

Advances in Quantum Chemistry, Volume 61
ISSN 0065-3276, DOI: 10.1016/B978-0-12-386013-2.00002-4

Abstract This work introduces a different way to understand the concept of quantum state (QS) with incidence on the concept of measurement.

The mathematical architecture is unchanged; abstract QSs are elements of a linear vector space over the field of complex numbers. Inertial frames mediate introduction of configuration space (CS); the number of degrees of freedom defining the material system characterizes the CS dimension. A rigged Hilbert space permits projecting abstract quantum states leading to generalized wavefunctions. CS coordinates do not map out particle positions, but wavefunctions retain the character of abstract quantum states; operators act on QS can yield new quantum states. Given a basis, quantum states are defined by the set of nonzero amplitudes. QSs are submitted to quantum probing; amplitudes control response to external probes. QSs are sustained by the material system, yet they are not attributes (properties) of their elementary constituents; these latter must be present yet not necessarily localized. With respect to previous views on quantum measurement, the one presented here shows characteristic differences, some of which are discussed below.

1. INTRODUCTION

This chapter deals with a quantum state–based approach to quantum measurements differing from dominant views exposed in standard quantum mechanics textbooks [1–3].

The headline hints at differences concerning the concept of quantum state as reported in [4, 5]. In a nutshell, differences are at a foundational level; one stepwise moves away from either epistemic or ontic models [6] to replace particle/wave (objects) themes underlying orthodox interpretation: (1) by an abstract grasp of quantum states (mathematics is unchanged); (2) laboratory projected physical quantum states that are *sustained* by elementary constituents of the material systems.

Quantum states belong to Hilbert space and as such they are elements of an abstract linear vector space over the field of complex numbers. Special relativity (SR) provides inertial frames and symmetry groups that help introducing abstract configuration spaces; the number of degrees of freedom associated with the corresponding material systems determines its dimension. The Coordinates label the base states of rigged Hilbert spaces. Configuration space projected quantum states are represented as usual by complex functions over the field of real numbers covered by configuration space, that is, wavefunctions.

The (inertial) I-frame is an element of ordinary 3D (real) space; it is origin localizable and can be rotated with respect to a second frame (e.g., Euler angles). Abstract quantum states are necessarily invariable to translations and rotations of such frames. Projected quantum states must be invariant to origin translations and I-frame rotations: linear and angular momentum

conservation rules hold, and quantum-mechanical phases enter the stage in a prominent way as illustrated below.

Preparation and probing of quantum states require special attention. The reason is simple: interactions involving energy exchanges are needed for. Planck's discovery in 1900 regulates this real-space exchange. Laws of energy conservation enter stage now. A fundamental interaction carrier is the quantized electromagnetic radiation incorporated through Fock space base states (see Chapter 5 in Ref. [5] for an elementary introduction). If interactions involve scattering processes of elastic type, a description as time evolution within Hilbert space holds. Otherwise, a break of Schrödinger time evolution obtains. The mixed region, where such descriptive changes are enforced, is referred to as a Fence; the alterations require physical quantum states.

Quantum-mechanical phase measurement for I-frame quantum systems provides a most direct manifestation of underlying abstract physics. Physical quantum states as projected states are to be probed at a laboratory level. Registering a resulting physical quantum state generates events with implied energy conservation rules. It can also be accomplished by further interactions leading to a detectable physical process. This is the crux of the problem.

This chapter is organized as follows: In Section 2, quantum states are briefly described. Section 3 presents aspects of standard quantum measurement model. Section 4 includes double-slit, Einstein–Podolsky–Rosen, and Tonomura's experiments. Section 5 illustrates calculations of quantum states for quantum measurements. In Section 6, atom interferometer experiment of Scully et al. is analyzed. A detailed discussion is presented in Section 7, emphasizing a physical perception of quantum mechanics.

2. QUANTUM STATES FOR QUANTUM PROBING

Basically, quantum probes stand as alternative name for measuring devices. Probing concerns responses that are characteristics of a probed quantum state.

Given the basic constituents of a material system, namely, the number of electron and nuclei and a time-independent Hamiltonian H with a complete set of basis states $\{|\mathrm{j}\rangle\}$ and eigenvalues $\{\varepsilon_\mathrm{j}\}$, an arbitrary quantum state is given as a linear superposition with complex number amplitudes:

$$|\Psi, t\rangle = \Sigma_\mathrm{j} C_\mathrm{j}(\Psi, t)|\mathrm{j}\rangle. \tag{1}$$

The amplitude $C_\mathrm{j}(\Psi)$ controls the material system response. It does it through spectral activation rooted at energy level ε_j. Zero amplitude at a base state prevents response; the set $\{C_\mathrm{j}(\Psi)\}$ of nonzero amplitudes presents the quantum state $|\Psi, t\rangle$ to probing.

Consider the excitation operator $|\mathrm{k}\rangle\langle\mathrm{k}'|$ corresponding to the elementary transition relating $|\mathrm{k}'\rangle$ (root state) to a target state $|\mathrm{k}\rangle$; $|\Psi, t\rangle$ acting from the right to commutator $[\mathrm{H}, |\mathrm{k}\rangle\langle\mathrm{k}'|]$ yields:

$$[\mathrm{H}, |\mathrm{k}\rangle\langle\mathrm{k}'|]|\Psi, t\rangle = (\varepsilon_{\mathrm{k}} - \varepsilon_{\mathrm{k}'}) \quad |\mathrm{k}\rangle\langle\mathrm{k}'|\Psi, t\rangle = |\mathrm{k}\rangle\ (\varepsilon_{\mathrm{k}} - \varepsilon_{\mathrm{k}'})C_{\mathrm{k}'}(\Psi, t). \tag{2}$$

Thus, probing the response from root state $|\mathrm{k}'\rangle$ with electromagnetic (EM) radiation *matching the gap* $(\varepsilon_{\mathrm{k}} - \varepsilon_{\mathrm{k}'})$ actually would elicit the amplitude at state $|\mathrm{k}'\rangle$. The root state is also defined as the initial state for a transition $\mathrm{k}' \to \mathrm{k}$:

$$\langle\mathrm{k}|[\mathrm{H}, |\mathrm{k}\rangle\langle\mathrm{k}'|]|\Psi, t\rangle = (\varepsilon_{\mathrm{k}} - \varepsilon_{\mathrm{k}'})\, C_{\mathrm{k}'}(\Psi, t). \tag{3}$$

Again, the amplitude at root state would control a possible physical response.

Yet actual probing is not an operation carried out in Hilbert space; this requires an appropriate external probe to be switched on. Once the probing interaction is included, the linear superposition associated to Eq. (1) stands out for a physical state to the extent it maps out all accessible root states. In so doing, the presentation stays as near standard QM as possible. Yet the amplitude has nothing to do with a probability of finding a material system occupying the $\varepsilon_{\mathrm{k}'}$-level. For measurements in intensity regime, amplitude in square modulus controls the relative intensity of the response [4, 5] (whichever it might be).

The elementary constituents of a material substrate are fixed. But, the material system is not represented by a base state in the sense that it does not occupy such state. A quantum state indicates us all *possible* responses to external probes that such system may show. The two instances are noncommensurate: one belongs to real space (material system) and the other is an element of Hilbert space (quantum state).

With a I-frame, one introduces a time axis appearing as a parameter in Eq. (1), the space component provides a mean to define a multidimensional Euclidean configuration space, $\mathbf{x} = (\mathbf{x}_1, \ldots, \mathbf{x}_n)$, that is, sets of real numbers. The space dimension is determined by the number of degrees of freedom related to constitutive elements of the material system; these coordinates belong to an abstract cartesian product space, whereas origin and relative orientations of I-frames belong to laboratory space. Spin degrees of freedom are separately handled.

At the Fence space in which laboratory and Hilbert space magnitudes are gathered, one gets projected amplitude:

$$\langle\mathbf{x}|\Psi, t\rangle = \Sigma_{\mathrm{j}} C_{\mathrm{j}}(\Psi, t)\langle\mathbf{x}|\mathrm{j}\rangle = \Sigma_{\mathrm{j}} C_{\mathrm{j}}(\Psi, t)\phi_{\mathrm{j}}(\mathbf{x}). \tag{4}$$

Note that the amplitudes are invariant elements when compared with that in Eq. (1); the configuration space is the support for the complex functions $\langle \mathbf{x}|\Psi, t\rangle$ and the set of base functions $\phi_j(\mathbf{x})$ relates to eigenfunctions of the time-independent Schrödinger equation. The Hamiltonian incorporates constitutive parameters of the material system.

The I-frame localizes a projected quantum state; this frame is a classical physics element, whereas configuration base states $\{|\mathbf{x}\rangle\}$ define a rigged Hilbert space basis [1].

Let $\mathbf{R}$ and $\mathbf{K}$ be the position vector and momentum of an I-frame with respect to another fixed one; consider the case where the former I-frame sustains the quantum state $\langle \mathbf{x}|\Psi, t\rangle \rightarrow \Psi(\mathbf{x}, t)$, and let $\langle \mathbf{x}'|\Psi, t\rangle \rightarrow \Psi(\mathbf{x}', t)$ be the same quantum state projected in the shifted I-frame. The abstract configuration space is the same; only the I-frames differ in laboratory space location, and this fact translates into a phase factor $\exp(\mathrm{i}\mathbf{R}\cdot\mathbf{K}/\hbar)$ relating states in both frames. "Internal" and "external" quantum states complete the description at a Fence, whereas abstract quantum states belong to a general formalism. In a projected state, one can introduce connections to material elements.

Thus, for projecting a quantum state in any set of inertial frames, the linear superposition given by Eq. (4) is invariant except for an overall phase that indicates to us I-frame locations.

Consider a scattering center located at $\mathbf{R}_0$, to determine the interaction project the quantum state at this position and use it to set up an I-frame to project the initial quantum state and the quantum state generated by scattering: for example, $\exp(\mathrm{i}\mathbf{R}_0\cdot\mathbf{K}/\hbar)\langle \mathbf{x}|\Psi, t\rangle$ and $\exp(\mathrm{i}(\mathbf{R}-\mathbf{R}_0)\cdot\mathbf{K}/\hbar)\langle \mathbf{x}|\Phi, t\rangle$. If one has two or more identical scattering centers interacting with one and the same quantum state, the projected states would differ in their phases. The scattered quantum states, except for phase factors, will be the same if the scattering sources are identical.

This is a moment of maximal difficulty to grasp. The material system that sustains the quantum state must be the same as the one detected at the end if the experiment is so designed. In between, it is the quantum state that describes the whereabouts of the system not as a localized material one but as presence at Fence space. It is here where one has to calculate quantum states for quantum measurements. Being infinite in number, they cover all possible behaviors. What is decisive is the presence of a Hilbert space that forces first calculations based on quantum states and at last, the laboratory requirement would impose, at the recording apparatus, the presence of the material system.

The aforementioned situation is rather perplexing. It originates in the requirement of bringing together two (or more) noncommensurable levels: Hilbert space and laboratory space. Local interaction potentials permit knitting both levels. Local sources of interaction have a place (location) in a laboratory space.

Interaction with a local potential such as a double slit yields a linear superposition of scattered states, each one being labeled with phases, for example, $\exp(\mathrm{i}(\mathbf{R}_1 + \mathbf{R}_{01}) \cdot \mathbf{K}/\hbar)$ and $\exp(\mathrm{i}(\mathbf{R}_2 + \mathbf{R}_{02}) \cdot \mathbf{K}/\hbar)$; vectors $\mathbf{R}_{01}$ and $\mathbf{R}_{02}$ indicate position for the slits 1 and 2. The vectors $\mathbf{R}_1$, and $\mathbf{R}_2$ indicate real-space location measured from slits 1 and 2, respectively.

For slit-2, for example, one gets a scattered component: $V(\mathbf{x}; \mathbf{R}_{02}) \exp(\mathrm{i}(\mathbf{R} - \mathbf{R}_{02})\mathbf{K}/\hbar)\Psi(\mathbf{x})$. Take origin between both slits, then $|\mathbf{R}_{02} - \mathbf{R}_{01}| = 2D$, and $|\mathbf{R}_{02}| = |\mathbf{R}_{01}| = D$. To simplify the writing, take the scattered state represented by the symbols $\langle \Psi(\mathbf{x})|V(\mathbf{x}; \mathbf{R}_{01})|\Psi(\mathbf{x})\rangle_{\mathrm{x}}$ and $\langle \Psi(\mathbf{x})|V(\mathbf{x}; \mathbf{R}_{02})|\Psi(\mathbf{x})\rangle_{\mathrm{x}}$ for which the "internal" degrees of freedom are integrated, and the scattered quantum states (SQS) appear as follows:

$$\begin{aligned}
\Phi_{\mathrm{SQS1}}(\mathbf{R}) &= \langle \Psi(\mathbf{x})|V(\mathbf{x}; \mathbf{R}_{01})|\Psi(\mathbf{x})\rangle_{\mathrm{x}} \exp(\mathrm{i}(\mathbf{R} - \mathbf{R}_{01}) \cdot \mathbf{K}_1/\hbar) \exp(\mathrm{i}\gamma_1) \\
\Phi_{\mathrm{SQS2}}(\mathbf{R}) &= \langle \Psi(\mathbf{x})|V(\mathbf{x}; \mathbf{R}_{02})|\Psi(\mathbf{x})\rangle_{\mathrm{x}} \exp(\mathrm{i}(\mathbf{R} - \mathbf{R}_{02}) \cdot \mathbf{K}_2/\hbar) \exp(\mathrm{i}\gamma_2). \qquad (5)
\end{aligned}$$

The phase factors $\exp(\mathrm{i}\gamma_1)$ and $\exp(\mathrm{i}\gamma_2)$ are identical if the scattering sources have such property. In general, they can signal specific differences.

The role of abstract configuration space is not easy to assay. We are used to represent particle positions thereby endowing quantum states with particle overtones. Perusal of Eq. (4) states us that, whatever model we endow to the configuration space, abstract quantum states are determined by amplitudes. The base states are fixed pillars; the same for all possible quantum states.

Scattered quantum states $\Phi_{\mathrm{SQS}i}(\mathbf{R}), i = 1, 2$, have localized sources (origin) in real space. The principle of linear superposition works for these states. These functions carry information on interactions of the internal ingoing state $\Psi(\mathbf{x})$ with the slits: $V(\mathbf{x}; \mathbf{R}_{0i})|\Psi(\mathbf{x})\rangle$; see Scully et al. case, Section 5.1. In what follows, both elastic and inelastic scattering situations are examined. Here, we hint at general cases emphasizing what differs from the standard models.

The classical concept of object dissolves in so far the configuration space for the internal degrees of freedom is concerned. The material elements such as electrons and nuclei must be present to sustain quantum states, but localizability is not a requirement; it may be a result of specific operators. The configuration space is an abstract mathematical space. Of course, one can force a representation as position vectors for particles. Consequently, one has to interpret the wavefunction. But again, Eqs. (3 and 4) demand amplitudes, energy gaps, and quantum numbers. This is spectroscopy of one type or another. The introduction of I-frames allows classical frameworks to be naturally incorporated.

Subsets of these quantum states may trap the material system into spectroscopically recognizable chemical species that might be endowed with finite lifetimes; this is the nearest one may come to the idea of objects, that are taken

as sources of interaction potentials, but we have to include the EM fields that make their production at laboratory space. Quantum mechanics handle all *possible* states; again, it does not describe the whereabouts of the constitutive elements of the material systems in specific circumstances. All possibilities accessible to a system are predicted rigorously.

Of course, life is never that simple. Poly-I-frame systems are important and must be incorporated in one way or another. See Ref. [5] for further discussions.

3. ASPECTS OF STANDARD QUANTUM MEASUREMENT MODEL

Let us first set up the stage by introducing selected topics illustrating only the dominating view in the quantum theory of measurement. The description is based on selected references. The reader is kindly asked to examine them to get further information and clarifications.

3.1. Preparing and recording

The nature of quantum superposition states and how one can sense or "see" them in our world continue to fascinate scientists. A great difficulty in teaching and grasping QM arises when coming to the topic measurement theory; a reason is that no universally accepted theoretical model exists [7–10]. To prepare or record a quantum state, an external source standing for the probing system cannot be overlooked. A probing–recording system is a quantum system too; quantized EM systems are examples thereof.

A central problem is posed by the so-called interpretation of QM [9]. Thus, for instance, Ballentine [10] discusses two cases: (1) The Copenhagen Interpretation and (2) The Statistical Interpretation.

As far as linear superpositions or quantum states are concerned, the view (1) asserts that a pure state provides a complete and exhaustive description of an individual system (e.g., an electron, molecule, and molecular objects) and the view exposed in case (2) asserts that a pure state provides a description of certain statistical properties of an ensemble of similarly prepared systems, but need not provide a complete description of an individual system. These statements correspond to those given in Refs. [7–9]. For details, the reader can go back to Refs. [1, 9, 10].

In the early view, there are correspondence rules relating the primitive concept of state and observable to empirical reality. Observables are mapped on to the set of eigenvalues of a particular class of self-adjoint operators (e.g., Hamiltonians). The individual systems would occupy only one base state; the amplitude appearing in the linear superposition in square modulus represents the probability to find one system occupying a base state when scanning the ensemble.

The reader may find a careful discussion on these issues in Ballentine's article [10], see also Ref. [1]. At this point, observe that the system is basically taken as an object or more technically an entity existent in laboratory (real) space; a res corporea, a substance that is known through anyone of its properties (attributes); in one word, an object in the sense of classical physics. Of course, observable asks for observer; thus, an object/subject philosophy underlies this particular view of QM presentation that now it becomes a representation. Note that if knowledge is defined as the relation of given representations to well-defined objects, we will also have a problem with the theory of knowledge by endorsing our views on quantum states.

The quotations and comments made above are sufficient for further discussions. Now, some criticisms voiced, for example, in Refs. [7–10].

Here, two sources of uncertainty become apparent in preparation and measurement of a quantum system; they originate precisely from *the way* the system is prepared (first aspect) and thereafter the interactions leading to the change of quantum state allows for detection (second aspect). These two aspects have not always been well acknowledged (cf. de Muynck [8]). Furthermore, the standard theory requires that each individual material system, once it is measured, be left only in one eigenstate so that the amplitude squared is assigned a statistical interpretation. This sort of transition is named as the collapse of the wavefunction [9].

The concept of observables must be excluded whenever a sequential set of measurements does not yield the same result. This is one reason to introduce the wavefunction collapse view as an axiom.

Wigner in 1963 [11] concluded that *the standard theory of measurement remains the only one that is compatible with the QM*. This is a strong statement made by one of the pioneers that should be nuanced by supplementing with another comment made in the same paper: "This is a legitimate statement if we acknowledge that the interpretation is sustained by the idea that QM describes the states of *objects* (entities) in real space. A measurement put the object in a particular eigenstate of the observable one selects: the linear superposition collapse as it were [11]."

The statements displayed above correspond to an ontic view as defined and summarized by Malin [6]; that is, it gives a meaning to an entity.

Malin's article [6] raised the question concerning the nature of quantum states and presented the strong arguments against their ontic and epistemic interpretations. Let us present a summary including his interpretation.

To get to the point, let us give three quotations from Ref. [6] concerning the ontic viewpoint first:

1. "…Einstein pointed out that the collapse, which he assumed took place on a $t =$ constant hypersurface means that the influence of the appearance of an elementary quantum leads to an instantaneous (faster that light)

propagation of the change in the value of the wave function everywhere on the hypersurface. Einstein tacitly assumed the ontic interpretation of the wave function."
2. "...the ontic interpretation is incompatible with Einstein's principle of covariance."
3. Concerning Schrödinger cat paradox one reads: "According to the ontic interpretation the cat is in a state of superposition of being alive and being dead in various proportions that change as time goes by."

For the epistemic interpretation "the superposition says nothing about the cat, it speaks about us. It says that we don't know how the cat is..."

The third interpretation tries to overcome the "knower" by saying that the quantum state is the place where the available or potential knowledge about the system is found.

Malin proposes three principles or working hypothesis:

1. QSs represent knowledge available about the potentialities of a quantum system, knowledge from the perspective of a particular location in space;
2. Collecting all such perspectives is all what there is about a quantum system;
3. "Whether or not the development of entangled systems involves *an apparent* superluminal connection, such connection can never be used for superluminal connection, such connection can never be used for superluminal transmission of information."

The ontic point of view considers the QS to represent the material system itself as if it was an object. Yet the above epistemic interpretation denies a relationship with the material system to the extent a QS says something about our knowledge about the system. The QS as perspectives on an available knowledge about potentialities is taking a step on a direction away from physics.

3.2. Copenhagen view

Following Omnès, a summary of Copenhagen theses is quoted below (see page 85 in Ref. [3] for further details):

1. The theory is concerned with individual objects.
2. Probabilities are primary.
3. The frontier separating the observed object and the means of observation is left to the choice of the observer.
4. The observational means must be described in terms of classical physics.
5. The act of observation is irreversible, and it creates a document.
6. The quantum jump taking place when a measurement is made is a transition from potentiality to actuality.
7. Complementary properties cannot be observed simultaneously.

8. Only the results of a measurement can be taken to be true.
9. Pure quantum states are objective but not real.

These statements speak for themselves. As our point of view develops, the reader will have elements to qualify the above statements.

3.3. Copenhagen view challenged

The challenges come from Refs. [1, 7, 8, 10]. The Copenhagen view on QM requires the existence of a classical macroscopic domain in order to explain the measurement process. Heisenberg uncertainty relations appear as the mathematical expression of a complementarity concept, quantifying the mutual disturbance that takes place in a simultaneous measurement of incompatible observables, say $\hat{A}$ and $\hat{B}$, that is, operators that do not commute.

The standard deviations' operators $\Delta\hat{A}$ and $\Delta\hat{B}$ can be arranged in the uncertainty relation with respect to a given quantum state $|\Psi\rangle$:

$$\Delta_\Psi \hat{A}\Delta_\Psi \hat{B} = \Delta A \Delta B \geq (1/2)|\langle[\hat{A},\ \hat{B}]\rangle|. \tag{6}$$

The symbol $\langle[\hat{A}, \hat{B}]\rangle$ is just $\langle\Psi|[\hat{A}, \hat{B}]|\Psi\rangle$, a quantum-mechanical average over the quantum state $|\Psi\rangle$. The inequality is known as Heisenberg–Kennard–Robertson relationship, which has often been interpreted as the mathematical expression of the disturbance following measurement. Ballentine noted that this relationship does not seem to have any bearing on the issue of joint measurement; instead, this relation can be traced back to the preparation process of an initial state, see Ref. [1, 10].

The reason behind this statement lies in the fact that separately measuring each standard deviation, $(\Delta A)^2$ and $(\Delta B)^2$, makes product, $\sqrt{((\Delta A)^2(\Delta B)^2)} = \Delta A \Delta B$; this relationship can be experimentally tested. Thus, for the momentum-position operators, the quantum state prepared as a plane wave, that is, an eigenstate of the momentum operator, $\Delta\mathbf{p} = 0$, so that $\Delta\mathbf{r}$ must be infinite in such a way that the product has a lower bound, namely, $\hbar/2$. Hereafter, we select the direction of the momentum along the x-axis to simplify the discussion. Including a screen perpendicular to x-direction, the possibility to define position and momentum of a system passing a slit located at the plane x_S is limited by the screen observables uncertainties

$$\Delta z_S \Delta p_{zS} \geq \hbar/2. \tag{7}$$

In our view, this inequality defines the preparation of system at the slit; note that the interaction between the ingoing quantum state and the material system that make up the slit produces a scattered quantum state component.

This state contains the characteristics of the scattering center, for example, (double) slits. The final state is a linear superposition of the ingoing quantum state with the scattered one. In the model developed in this paper, it is the production of this quantum state that will be essential to grasp phenomena beyond the slit. Whether the particle went this or that way is not an issue here when quantum states for measurements are considered.

For a particle model, the latitudes δz_S and δp_{zS} of particle position and momentum perpendicular to the propagation direction (x in our example) must satisfy Heisenberg's inequality, the product being larger or of the order

$$\delta z \delta p_z \approx \hbar/2. \tag{8}$$

This relation would represent a lower bound for the disturbing effect due to the measuring instrument on the particles. This would cause a postmeasurement state of the object that satisfies the uncertainty relation.

Inequality in Eq. (8) must be distinguished from the relationship satisfied by the standard deviations Δz and Δp_z:

$$\Delta z \Delta p_z \geq \hbar/2. \tag{9}$$

As mentioned earlier, the latter inequality concerns the (initial) quantum state preparation. Thus, Eq. (9) being an instance of Eq. (6) does not refer to a joint measurement of position and momentum. On the contrary, Eq. (8) makes sense if a particle interacts at the slit; therefore, there is no direct connection to a quantum state in this case.

It is the presence of the uncertainty products that would state us that an interaction took place between the incoming quantum state and the quantum states from the slit (not explicitly incorporated) in Hilbert space leads to a scattered state; combining both, one can easily understand the emergence of diffraction effects. It is not the particle model that will indicate us this result. The scattered quantum state suggests all (infinite) possibilities the quantum system has at disposal. One particle will only be associated with one event at best; yet, the time structure of a set of these events may be the physically significant element (see Section 4.1).

For the two-slit experiment, according to standard QM, strict completion of Eq. (7) would make impossible to determine which hole the electron or photon passes through without, at the same time, disturbing the electrons or photons enough to destroy the interference pattern. This is a puzzling situation within the particle model. Somewhere, there is a missing link (see below).

Following de Muynck [8], the problem stems from a poor distinction made between different aspects of preparation and measurement. From the Copenhagen viewpoint, a measurement is not perceived as a mean to obtain information about the initial state of the system but *as a way of preparing*

the system in some final state: a postmeasurement state. The complementarity problem according to de Muynck has actually two aspects [8]: preparation and measurement that are not sufficiently distinguished.

The concept of measurement disturbance should apply to cases given in Eqs. (7 and 8), while Eq. (6) refers to the preparation step. de Muynck concludes [8] that "[w]ith no proper distinction between preparation and measurement the Copenhagen interpretation was bound to amalgamate the two forms of complementarity, thus interpreting the Heisenberg–Kennard–Robertson uncertainty as a property of (joint) measurement." Statements such as these may appear to be unclear, but this is the state of the matter as given by de Muynck.

The elements of information summarized above are sufficient for our needs. We move on to examine the measurement problem from a perspective advanced in Refs. [4] and [5] and further developed here. Because the quantum evolution of probing and probe is entangled in Hilbert space and the events in real-space elicit results in measurements, this junction zone is a Fence.

4. VIEW FROM A FENCE

Using the example of the two-slit experiment, differences between the present approach and the standard ones can be sensed.

For atom or electron interference experiments, one material system at a time is allowed through the setup sequentially [12]. A sensitive surface located at a point beyond the two-slit surface acts as a recorder or detecting screen. The elementary result is an event (click revealing a quantized energy exchange) at a detecting screen (screen location $x = x_D$); the interaction at this Fence is local. All energy exchange interactions in real space are local; yet, they involve a change of quantum state.

For an excellent overview of basic quantum concepts and phenomena related to measurement, see Karlsson and Brändas' article [13] and those reported at Gimo's meeting appearing in book form [13].

4.1. Double-slit case

The present model allows the material system somehow to go through while focusing on changes of quantum states that cover all available possibilities. This is a completely different view: element of Hilbert space, not a representation of the material system.

This situation requires that the quantum states entering the description of a given experiment are carefully constructed:

1. Before interaction with the double slit;
2. Quantum state preparation at the slits;

3. Quantum state beyond the surface including the double slit (x_S) propagates toward a detecting screen (at $x = x_D$) or can be used for some other purposes.

Hence, the quantum state just *before* interaction at $x = x_D$ must be well defined. This is a key point.

The *quantum state incident* to the screen with a double slit is usually taken as a plane wave; this is a useful model for a coherent state, and the reciprocal vector **k** characterizes the base state.

What is the meaning assigned to the initial state? For the time being, it is a laboratory prepared state with a given initial internal quantum state. The basic (material) elements sustaining the quantum states are fixed. In chemical terms, they may belong to a molecule, atom, free electron, or electromagnetic radiation (see examples discussed later), but in QM terms (as presented here), the whereabouts of such elements are not an issue.

To examine the interactions, the origin for the slits is given on the y-axis. The plane wave propagates along the x-axis so that δp_y is zero by construction and δy must be infinite in such a way that an equivalent to inequality Eq. (9) holds (replace z-axis by y-axis only).

Note that the initial quantum state translated at x_S will interact simultaneously with full screen. The base states of interest are those originated by interaction with the slits labeled as hole states |H-1⟩ and |H-2⟩:

$$\begin{aligned} |\text{H-1}\rangle &= \exp(\mathrm{i}\gamma_1)\langle x, y, z|1\rangle \exp(\mathrm{i}(k_x x + k_{y1}(y - D) + k_{z1} z))|\Psi\rangle \\ |\text{H-2}\rangle &= \exp(\mathrm{i}\gamma_2)\langle x, y, z|2\rangle \exp(\mathrm{i}(k_x x + k_{y2}(y + D) + k_{z2} z))|\Psi\rangle. \end{aligned} \tag{10}$$

The holes centers are located on the y-axis at distance $2D$ and radius $d \ll D$. To alleviate notation, the z component is made implicit in the Fresnel integrals $\langle x, y, z|1\rangle$ and $\langle x, y, z|2\rangle$ [14]. If there are differences in the interaction at the slits, the phases γ_1 and γ_2 might differ. An internal quantum state is designated as $|\Psi\rangle$.

Let the quantum state after screen at x_S be labeled as $|\Phi\rangle$. The fundamental principle of QM allows us to write the quantum state as a linear superposition:

$$|\Phi\rangle = \{C_1|\text{H-1}\rangle + C_2|\text{H-2}\rangle\}|\Psi\rangle. \tag{11}$$

$C_1 = \langle \text{H-1}|\Phi\rangle$; $C_2 = \langle \text{H-2}|\Phi\rangle$. Because the case discussed now does not affect the internal state, focus on the pure space part designated as $\langle x, y, z|\Phi\rangle_{(x)x_S)}$ is

$$\begin{aligned} \langle (x)x_S;\, z = 0)|\Phi\rangle = {} & C_1 \exp(\mathrm{i}\gamma_1)\langle x, y|1\rangle \exp(\mathrm{i}(k_x x + k_{y1}(y - D))) \\ & + C_2 \exp(\mathrm{i}\gamma_2)\langle x, y|2\rangle \exp(\mathrm{i}(k_x x + k_{y2}(y + D))). \end{aligned} \tag{12}$$

This is a plane wave state to the extent as x-axis propagation is concerned. The quantum state includes information about interactions at the slits through amplitudes, phases, and Fresnel integrals ($\langle x, y|1\rangle$ and $\langle x, y|2\rangle$) [14]. For us, these quantities are parameters that can be controlled by one way or another. The linear superposition form is what matters. This is the form taken by the abstract factor of the physical quantum state.

The projected global quantum state $|\Phi\rangle$ propagates ($x \rangle x_{\mathrm{S}}$) until getting at a neighborhood of a detecting screen that can be located at $x_{\mathrm{D}} \rangle x_S$. The key result is a well-defined quantum state given by

$$\langle x, y, z|\Phi\rangle \rightarrow \langle (x \rangle x_{\mathrm{S}}; z = 0)|\Phi\rangle;$$

The (generalized) function in Eq. (12) is well defined at any point of a screen that can now be replaced by a recording screen thereby allowing for interactions in real space to take place. To make Planck's law effective, a mechanism for energy exchange between impinging material system and the detecting plane must be included. For the time being, we assume that Planck's law would hold now thereby introducing local energy exchange effects; this granularity is imposed by the nature of the detector. Such process belongs to a Fence region.

Note that Eq. (12) requires that the material system sustaining the quantum state went through the double slit; the way it actually does is of no concern. Why is this so? Answer: QM works on all possibilities epitomized by quantum states. Remember the Feynman scheme where all possible paths must be in the calculation of the propagated quantum state [14]. Therefore, one particle path in real space does not make sense in Hilbert space.

Thus, whatever a recording screen will record, this recording must be (co) related to the interaction with the quantum state generated at the double slit; this latter being corelated to the source quantum state.

The recording screen does not create correlations backward with events that might have happened at plane x_{S}; it records a material system interaction only. This is the place for local interactions. Of course, any correlation that might be set up at x_{S} is included in the quantum state impinging at x_{D}. This caveat may be useful later on (Cf. Section 4).

Before discussing this part of the problem, let us see whether we can glean some information from the values a quantum state has at a screen located at x_{D} that has *not* yet been sensitized as it were.

A firm result will be this: if the value of the function at a given neighborhood to a point on the surface is zero, whatever you do there will never be a spectral response derived from a quantum-mechanical interaction at that neighborhood; no imprint mediated by the quantum state. Another one is that any finite value different from zero of the quantum state function at a given neighborhood of a point opens a *possibility* for a response from a properly sensitized surface that would reflect the wavefunction at that region (Cf. Eq. (3)).

Interference effects result from coherent superposition between the *states* originated at each slit. Fresnels' functions [14] have zero overlap just after the double-slit screen. The quantum state in this region would correspond to two separate (noninteracting) beams. Using collimators, a two-channel state can be prepared if one wants to do this. Because these channels are separated in real space, experiments can be designed that will modulate each channel at will; Scully et al. [15] presents thought experiments using this type of device discussed in Section 6.

We want to emphasize one aspect that is essential to understand the workings of modulating devices required for probing (measurement). Preparation of above two-channel states spatially separated permits, if it is so required, to modulate each channel in an independent fashion. Modulation devices are local (Cf. Section 5.3 for a simple example).

A condition for interference pattern to appear is related to sameness of the quantum state that interacts at the holes; the holes are assumed to be of equal nature.

When the two-channel state is manipulated so that they come up different from each other and thereafter channeled to another two-slit device, interference cannot be necessarily expected; the relative intensity response at a given point is determined by the numeric value of the modulus square amplitude. Whenever a mechanism is set up to restore both channels' quantum state sameness, then interference effects will show up. The way one stores (or restore) such sameness is the key to elicit interferences. Coherence can be lost and regained; this issue is discussed below. For an experimental case, the reader is referred to Chapman's et al. [16].

The mathematical expression of the wavefunction $\langle (x = x_D; z = 0)|\Phi\rangle$ yields further insights.

$$\langle (x = x_D; z = 0)|\Phi\rangle = C_1 \exp(i\gamma_1)\langle x_D, y|1\rangle \exp(i(k_x x_D + k_{y1}(y - D)) + C_2 \exp(i\gamma_2)\langle x_D, y|2\rangle \exp(i(k_x x_D + k_{y2}(y + D))). \quad (13)$$

The factor $\exp(ik_x x_D)$ indicates where to look at, namely, at the detector plane surface located at x_D; k_{y1} points in the direction of interest from the frame located at hole-1; k_{y2} does it from that at hole-2.

Furthermore, if the state corresponds to $y = 0$ and $z = 0$, the values of the integrals $\langle x_D, y = 0, z = 0|1\rangle$ and $\langle x_D, y = 0, z = 0|2\rangle$ are equal (say, FI) so that approaching sameness for these channels is apparent:

$$\langle x, y, z|(x_D, y = 0, z = 0\rangle = \exp(ik_x x_D)\mathrm{FI} \times \{C_1 \exp(-ik_{y1}D)) + C_2 \exp i(\gamma_2 - \gamma_1) \exp(ik_{y2}D)\}.$$

The amplitude reflects the geometric characteristic of the holes and the physical character of the interaction cloaked in the coefficients C_1 and C_2.

A coherent response in the tensity regime leads to

$$I(x_{\mathrm{D}}, y=0, z=0) = |\mathrm{FI}|^2\{|C_1|^2 + |C_2|^2 + C_1C_2^* \exp(-\mathrm{i}(k_{\mathrm{y1}} + k_{\mathrm{y2}})D) \exp \mathrm{i}(\gamma_2 - \gamma_1) + C_2C_1^* \exp(\mathrm{i}(k_{\mathrm{y1}} + k_{\mathrm{y2}})D) \exp -\mathrm{i}(\gamma_2 - \gamma_1). \tag{14}$$

For this specific setup, $(k_{\mathrm{y1}} + k_{\mathrm{y2}}) = 0$, and if no phase effects were introduced by the interaction, namely, $(\gamma_2 - \gamma_1) = 0$, the intensity is a function of the amplitudes

$$\mathrm{I}(x_{\mathrm{D}}, y=0, z=0) = |\mathrm{FI}|^2 \times \{|C_1|^2 + |C_2|^2 + C_1C_2^* + C_2C_1^*\}. \tag{15}$$

The cross terms add up to the real part of the product: $2\mathrm{Re}\, C_1C_2^*$. The intensity at this point reflects the nature of the interactions between the ingoing quantum state and the two-slit device. The particular case, $C_1 = C_2 = 1/\sqrt{2}$ and $(\gamma_2 - \gamma_1) \neq 0$, produces the result

$$\mathrm{I}(x_{\mathrm{D}}, y=0, z=0) = |\mathrm{FI}|^2\{1 + 1/2\ (\exp \mathrm{i}(\gamma_2 - \gamma_1) + \exp -\mathrm{i}(\gamma_2 - \gamma_1))\}. \tag{16}$$

An interesting case corresponds to $(\gamma_2 - \gamma_1) = \pi/2$. For now, the real part in the interference term $\cos(\gamma_2 - \gamma_1)$ annihilates while the imaginary part of the exponentials sum cancels out. The relative response intensity being $|\langle x_{\mathrm{D}}, z = 0|1\rangle|^2$ while for $(\gamma_2 - \gamma_1) = 0$ the intensity is twice this value.

For an interaction at the slits producing a difference in phase $(\gamma_2 - \gamma_1) = \pi$ it is easy to check that the intensity at the origin of the recording screen annihilates as it is defined here. The factor $\{1 + 1/2(\exp \mathrm{i}\pi + \exp -\mathrm{i}\pi\}$ is zero.

The preceding discussions show that the amplitude at the midpoint between the slits but calculated now at the detector screen x_{D} can be modulated in different manners; this modulation should be reflected at the screen where we may place an energy conserving detector device. The quantum interactions at the two slits determine the type of response to be measured at the recording screen. The fringes may disappear if the amplitudes C_1 and C_2 are independently changed thereby breaking coherence.

The just exposed correlations then do not originate between a measuring apparatus and system being observed; as a matter of fact, there is no need for an observer. The quantum state at the recording screen is totally independent from the presence of the sensitized screen element. Bearing in mind that a quantum state does not represent a particle in laboratory space and the idea that its square modulus stands for the probability of finding the material system (particle) in a volume element is foreign to the present view, the underlined result obtained from the present theoretical approach is reasonable from a physical point of view: *It is measurement of a wavefunction that is a basic element of the theory*.

Note again that it is not the material system going through the two-slit device that is the subject of the analysis. If the interaction between the quantum state and the slits results into another quantum state the case does not qualify as an event. We keep the word event to indicate an energy exchange ruled by Planck's law and localized in real space, a Fence happening. Thus, there is no event that can be realized in two nondistinguishable ways that could impose the linear superposition state. See Section 4.3 for further details. In our case, it is the quantum interaction of the same quantum state with the two scattering centers that generate the superposition state. In this sense, what is new from the physical point of view is the concept of sameness for the ingoing state.

Notwithstanding, the kind of response at x_{D} depends upon the detector nature. The event showing the local interaction appears to be contingent to the extent both place and time are concerned. But it is a necessary correlate to the interaction between both systems: screen and material system's quantum states we are interested in probing (measuring); the way that this probing is done depend upon the type of experimental management. Implementation will be on the side of quantum technology.

It is the alteration in quantum state elicited by the event that uncovers a presence of the material system supporting the quantum state. The whereabouts of the material system in terms of particle trajectories are not described. But we are not yet there with the theoretical description.

We also have the "shadows" corresponding to the slits we place on the first screen; here for shadow-1, the wave vector component will be k_{yD1} and k_{zD1} for a circular slit; to get a simple picture, we keep $z = 0$.

If we look at the theoretical intensity pattern, we can infer a simple result, namely, a decrease in amplitude squared from the origin in the detection surface toward the origin of the (virtual) slit's shadows. For the intensity pattern, this is controlled by the overlap between Fresnel integrals. But there is need for a reference just in case we decide to close one slit for beal example.

The quantum state interacting with the open slit-1 is the same as the one we used with the open slit-2. The interaction generates a scattered state represented by Eq. (13) by taking $C_2 = 0$ to get:

$$\langle x, y, z|(x = x_{\mathrm{D}})\rangle = C_1 \exp(\mathrm{i}\gamma_1)\langle x_{\mathrm{D}}, y|1\rangle \exp(\mathrm{i}(k_{\mathrm{x}}x_{\mathrm{D}} + k_{\mathrm{y1}}(y - D)).$$

To this base state, adds the incoming initial state $\exp(\mathrm{i}k_{\mathrm{x}}x)$ to form a diffraction quantum state:

$$\begin{aligned}\langle x, y, z|(x = x_{\mathrm{D}}); \mathrm{diffraction}\rangle = {} & \exp(\mathrm{i}k_{\mathrm{x}}x) \\ & \times \{1 + C_1 \exp(\mathrm{i}\gamma_1)\langle x_{\mathrm{D}}, y|1\rangle \exp(\mathrm{i}(k_{\mathrm{y1}}(y - D)\}\end{aligned}$$

The intensity pattern obtains from $|\langle x, y, z|(x = x_D);\ \text{diffraction}\rangle|^2$. The contribution to the diffraction takes on a simple form when $C_1\langle x_D, y|1\rangle$ is the product of two real numbers:

$$2C_1\langle x_D, y|1\rangle \cos(k_x x + \gamma_1 + k_{y1}(y - D)) + C_1^2\langle x_D, y|1\rangle^2.$$

Consider a Fraunhofer diffraction case. At the detecting surface, there will be a maximum intensity at the center of the shadow slit, followed by concentric circles with decreasing intensity. The diffraction pattern will reproduce itself a shadow slit at 2 when slit-1 is closed. If there were no interference between states 1 and 2, one would expect a sum of each slit's diffraction intensity pattern. Thus, very little intensity will be found in between the shadow slits.

If two slits being simultaneously open and $(\gamma_2 - \gamma_1) = 0$, the preceding analysis shows that the intensity of the diffraction pattern at a shadow slit becomes weighted down by the small overlap between Fresnel integrals. However, the intensity increases at the middle. The interference pattern would clearly appear. The complete diffraction pattern should appear if we could measure the quantum state or something directly related to.

Such will be the patterns if one could get imprinted the quantum state in one step. Let us examine the situation at recording screens.

4.2. Recording screens

The quantum state discussed above not only must have the response spectra that are able to disclose the interaction with the measured quantum system but also must allow register it. This type of effect occurs at a Fence that is a region where different levels of description are mingled. If no register is implied, quantum interactions entangle measuring/measured quantum states keeping everything in Hilbert space (Cf. Section 6.4). You will never get funded to produce Hilbert space description only! At some point, information must be produced; this implies a change of entropy (energy dispersion). Even if we can claim that it is the evolution in Hilbert space that determines the way the quantum state sustained by the material system will change, it is at the laboratory world with its real-space elements that such effects should manifest themselves. At a Fence both spaces coexist as a matter of speaking; interestingly, as levels of complexity develop leading to the emergence of an object concept (I-frame system), it becomes apparent that quantum theory cannot be founded and be concerned with individual objects.

Information production has at least two aspects:

1. Imprint a quantum state in a material support;
2. Reading of such imprint (interpretation).

The first item concerns physics; the second has a social aspect that at the very least expresses itself through communication (cultural) channels, such as pictorial views, journalism, etc.

Let us consider some examples of how information can be produced using a toy model: a two-state I-frame quantum system. A ground base state $|0\rangle$ and an excited state $|1\rangle$ gathered in the row vector $(|0\rangle\ |1\rangle)$ are used to represent any quantum state of the quantum reading system as a linear superposition; the energy difference is $\Delta E = E_1 - E_0$.

Yet, the eigenvalues with energy dimension are elements from Hilbert space. The connection introduced by Bohr ($E_1 - E_0 = \hbar\omega$) is not that innocent. As the sources and sinks of electromagnetic energy are located in real space and $(E_1 - E_0)$ is a magnitude from Hilbert space, we must connect two noncommensurate levels. Bohr's equality looks more as a postulate than a law of Nature. This is the locus in which we transform as it were an abstract magnitude $(E_1 - E_0)$ belonging to an abstract space into an information datum belonging to laboratory (real) space. In fact, the connection must be done with Eq. (3), viz. $(\varepsilon_k - \varepsilon_o)\ C_o(\Psi, t)$ that clearly includes significant elements of Hilbert space. If the amplitude at root state ($C_o(\Psi, t)$ in the present example) is different from zero, then frequency ω identifies a system external to Hilbert space endowed with sources (sinks) of energy. Planck's law provides the connection introducing quantized exchanges of energy: $h\nu = \hbar\omega$. Thus, the electromagnetic field must be quantized as well to get Niels Bohr's postulate right: $E_{1k} - E_0 = h\nu = \hbar\omega$. Implicit now is the requirement of nonzero amplitude in the probed quantum state.

Let us continue with the simple toy model. In the base $(|0\rangle\ |1\rangle)$, the quantum state given as column vector $[C(0)\ \ C(1)]$ for which $C(0) = 1$ and $C(1) = 0$ corresponds to the ground state: $|1, 0\rangle \rightarrow (1\ \ 0)$. Off-resonance frequencies ω' set the system in a linear superposition state once an interaction operator is switched on; normalization leads to amplitudes proportional to $[\cos\omega' t\ \ \sin\omega' t]$; the parameter ω' can reflect coupling between base states and probed system.

Consider a resonance case: $\omega' = \omega$. For the global system, there are two states: $|0\rangle|n_\omega = 1\rangle$ and $|1\rangle|n_\omega = 0\rangle$ with equal energy; note the qualitative difference: for $|0\rangle|n_\omega = 1\rangle$ the energy is in the field; while $|1\rangle|n_\omega = 0\rangle$, energy localizes at the material system; the photon field has not available energy (it is "empty").

But now you know something about this system. For example, if the amplitude at base state $|1\rangle|n_\omega = 0\rangle$ is near one, the interaction with the vacuum may prompt for *spontaneous* emission in any arbitrary direction; the I-frame system "return" to the ground state $C(0, n_\omega = 1) \approx 1$, while $C(1, n_\omega = 0) \approx 0$. We do not want this because a full control of the energy is required to construct a theoretic recorder; thus, select adequate material systems to sustain this type of states with minimal spontaneous emission. Assume we

have it. A premise that required for a quantum system to be transformed into a detector is laid down. For a finite time interval, one can consider the energy localized at the I-frame system. Connect this I-frame to a secondary system able to get hold of (trap) that energy and use it in activating a cascade process, now we have the premises of an *event*. A trapping event can be amplified and stored elsewhere; the actual mechanism of recording may well enter into complex devices is not now the focus for the elementary measurement model we are discussing. An important point is that the recording subsystem is left in a "ground" state, probably ready to act again. More fundamental is the local character of such event borrowed from the local nature of the I-frame and SR theory.

There is not a quantum jump in the description given above. The import of this situation can be appraised with respect to thesis 6 from Copenhagen view [3]. The physical situation is subtler.

A new fundamental feature pops up: the event leading to an actual energy transfers between the measuring I-frame system and the amplifier device. This kind of event discloses an interaction with the measured system albeit indirectly. At any rate, energy conservation is required because this is a Fence event between two different material systems.

To stay in Hilbert space would imply the measuring/measured quantum systems to remain in an entangled state unknown to people at the Fence. But all *possible* changes are there anyway. To disclose them, energy must be exchanged, and consequently, entropy must vary. One is coming close to thermodynamics as soon as the *description* of phenomena forces to take the systems away Hilbert space arena. In other words, Hilbert space alone is not adequate to handle this type of physics because it is an abstract formalism only. This implies that actual emergence of a particular outcome cannot be accounted for by a quantum theory: the space-time occurrence of one click is not predictable by the theory.

So far, a photon field makes part of the Fence quantum system of interest. We do this because not only it is easier to construct the formalism but also EM radiation is an energy carrier allowing for sensing the sources of such radiation. The photon field transports information in a world from external to Hilbert space; you do not have an elephant at the retina but a coded quantum state; the information is there to be decoded, we call it an image and assign a name (label) to that which is the case. Thus, at the end of the day, the material system that sustains the quantum states must have energy to exchange with the I-frame detector system or the probing (measuring) field; it can appear as an energy source or it can be a sink, or both at different field frequencies.

Therefore, clicks have a cause as discussed earlier. That at the Fence, the theory is not able to predict the position and time of appearance for a particular click does not mean that it is produced without cause, this result contradicts the tenets of Ref. [17].

A quantum state sustained by a material system describes all possibilities; the mapping discussed (N. Bohr's postulate) is used to introduce the concepts of imprint and reading. In this mixed space, we live and die. In Hilbert space, we don't; see also Ref. [4].

Retain the two-state model idea for the photon field and define the operator

$$\hat{\aleph} = |-\rangle\langle -| + |+\rangle\langle +|. \tag{17}$$

This is a unit operator in this new space. The energy quantum state can be written as a linear superposition:

$$|\Delta E\rangle = |-\rangle\langle -|\Delta E\rangle + |+\rangle\langle +|\Delta E\rangle. \tag{18}$$

Prepare the system in the particular state $\langle +|\Delta E\rangle = 1$ and $\langle -|\Delta E\rangle = 0$. This means the system can deliver energy ΔE sustained by the transition $|+\rangle \rightarrow |-\rangle$. The energy states are used in conjunction with the scattered quantum state.

The total wavefunction after interaction with the double slit including energy states is given by

$$\begin{aligned}\langle x, y, z|(x\ \rangle\ x_S)\rangle|\Delta E\rangle &= \{C_1 \exp(i\gamma_1)\langle x, y|1\rangle \exp(i(k_x x + k_{y1}(y - D))) \\ &\quad + C_2 \exp(i\gamma_2)\langle x, y|2\rangle \exp(i(k_x x - k_{y2}(y + D)))\}|\Delta E\rangle \\ &= A(C_1, C_2, \gamma_1, \gamma_2,\ \langle x, y|1\rangle, \langle x, y|2\rangle)|\Delta E\rangle. \end{aligned} \tag{19}$$

The operator $\hat{\aleph}$ permits mapping a possible energy exchange into the abstract formalism in a simple manner. Using the I-frame energy basis, the quantum state can be written as

$$\begin{aligned}\langle x, y, z|(x\rangle x_S)\rangle|\Delta E\rangle &= A(C_1, C_2, \gamma_1, \gamma_2, \langle x, y|1\rangle, \langle x, y|2\rangle) \\ &\quad \{\langle -|\Delta E\rangle|-\rangle + \langle +|\Delta E\rangle|+\rangle\}. \end{aligned} \tag{20}$$

From the perspective of a photon field, the interaction information embedded in the function $A(C_1, C_2, \gamma_1, \gamma_2, \langle x, y|1\rangle, \langle x, y|2\rangle)$ would imprint at both channels.

Now, look at quantum state for an I-frame system prepared as $\langle +|\Delta E\rangle = 1$ and $\langle -|\Delta E\rangle = 0$, the propagating quantum state is the linear superposition:

$$\begin{aligned}\{C_1 \exp(i\gamma_1)\langle x, y|1\rangle \exp(i(k_x x + k_{y1}(y - D))) + C_2 \exp(i\gamma_2)\langle x, y|2\rangle \\ \exp(i(k_x x - k_{y2}(y + D)))\}|+\rangle. \end{aligned} \tag{21}$$

The base component $|-\rangle$ has zero amplitude. Surreptitiously, the quantum side of the energy exchange is hidden. One should keep track of this point.

The coherent response in intensity at the detecting screen is just the equation

$$|\{C_1 \exp(\mathrm{i}\gamma_1)\langle x, y|1\rangle \exp(\mathrm{i}(k_x x + k_{y1}(y - D))) + C_2 \exp(\mathrm{i}\gamma_2)\langle x, y|2\rangle \times \exp(\mathrm{i}(k_x x - k_{y2}(y + D)))\}|^2. \tag{22}$$

This simply means that for the relative response intensity, a change of state involving a photon release would reflect the interference pattern. If Eq. (22) is zero in a neighborhood of a surface point, there will be no change of state that would trigger a detector chain. If only one energy quantum could exchange, the spot may appear anywhere except at nodal regions.

Thus, *at whatever space point where an amplification event might take place, the system would be measuring the interference pattern at given neighborhood*.

Such is a translation of Eq. (22). A local detector permits calculating the amplitude just there so that the amplifier may or may not be triggered.

Actual *localization* of a triggering process does not belong to the present model. Once it happens, a spot (click) becomes visible (localized), and we can use Eq. (22) to rationalize the result.

The spot produced by the material I-frame system (if there is any) is given a particulate property. However, there is no compelling quantum-mechanical reason that would permit to identify the real-space event to a particle, although in the particle model philosophy such assignment would seem natural. In this case, the I-frame kinetic energy would play the role of energy carrier.

Anyway, the click/spot may be fully related to the quantum state at the neighborhood in real space to the extent the material system sustains the quantum state. Thus, a view from outside (without the Fence walls) that counts such spots will reflect the quantum state and nothing else; wouldn't it?

The orthodox and standard quantum measurement theory uses a probability density view focused on the particle conception. The physical nature of the interaction that may lead to an event (click) is not central. Generally, it is true that a click will be eliciting the quantum state, but due to external factors, a click can be related to noise or any source of systematic error (lousy detectors); from the QM viewpoint developed here such events have no direct QM-related cause; see Ref. [17]. *The probabilities cannot be primary*. They can be useful as actually they are. One thing is sure: the clicks do have a cause. But causality is a concept more related to a particle description: it belongs to classical physics.

In a way of speaking, the particle picture hides the quantum state by directing the view to the I-frame instead of the quantum state. We come back to this issue below.

4.3. Tonomura's experiment

The feature we have just found at the Fence is the activation of a detection screen. It appears as an event localized in real space that can be timed once the system is clocked at when action initiates. Thus, an arrival time can be registered. Then, all these events occur in laboratory (real) space.

There is more. Tonomura reports experiments on electron interference using field-emission electron microscope equipped with an electron biprism and two-dimensional, position-sensitive, electron-counting system [12]. Events could be counted one-by-one on a TV monitor. Let us describe some results from the present perspective.

1. The first event may happen anywhere on the TV screen; you can prepare the system as many times as you want and check that the first event appears localized (almost) at random; this randomness is only apparent if you use the theory presented here. What has happened was a change in amplitudes for a transition from state $|+\rangle$ to $|-\rangle$ by capturing energy from the I-frame system; the relative coherent intensity response being:

$$|\{C_1 \exp(\mathrm{i}\gamma_1)\langle x, y|1\rangle \exp(\mathrm{i}(k_x x + k_{y1}(y - D))) + C_2 \exp(\mathrm{i}\gamma_2)\langle x, y|2\rangle \exp(\mathrm{i}(k_x x - k_{y2}(y + D)))\}|^2. \tag{23}$$

   This is calculated at a spot neighborhood. Thus, the information contained at the spot is there to reflect the value given by the mathematical framework unless the detector is lousy; by the structure of this equation, we know then that it makes part of an interference pattern.

   Why does the event appear at that position and not at another one? Such a question is related to the amplifier device not to the quantum mechanics of the probed system. Actually, this is inherent to mixing levels of presentation as discussed earlier, Cf. N. Bohr's postulate supplemented with Eq. (3).
2. When the number of electrons from the source increases, an interference pattern becomes recognizable. This result elicits Eq. (23).
3. We quote Tonomura [12]: "*Even when the electron arrival rate is as low as 10 electrons/s over the entire field of view (so that there is at most only one electron in the apparatus at one time), the accumulation of single electrons still forms the interference pattern*."

   This statement can be seen from the present perspective in a different light. The emergence of an interference pattern is ensured even if you send one-by-one during a period of 1 year or a millennium (all other things been equal) *provided the information revealed by the spot is directly related to the values of* Eq. (23). The distribution when there are few electrons may *seem* quite random but "*the-what-is*" *emerging* there is just the quantum state given as amplitude squared in Eq. (23).

4. For the present view, even if there are two slits there has never been talk about which slit (path) the electron has taken. Quantum mechanics is about quantum states. This means that the electron I-frame would realize only one of the possibilities derived from Eq. (23). It is in this sense that a quantum state is sustained by a material system; sustained but not piloted.

   If you know which slit is used then this would mean that either C_1 or C_2 is zero. In that case, the interference trivially vanishes. The quantum state has changed because the experiment being scrutinized is different compared to the preceding case.
5. Theoretically, there are nodal strips so that no particle spots would be appearing on the screen. In practice, the screen will end up fully covered if you allow the experiment to proceed for a long time. You can discuss this result in the classroom now! In such situation, we would have been doing the theory based on the recording–reading data elicited by the spot counting. The point is that we seek after a quantum-mechanical description of the double-slit diffraction from abstract Hilbert space quantum mechanics projected in configuration space. Spot counting occurs in real space with all experimental errors naturally associated to them. No offense implied!
6. There is never talk about collapse of the wavefunction, quite the contrary. Only a quantum transition is involved; the energy carrier wavefunction where the amplitude affecting the base state $|+\rangle$ is to be imprinted; the Hilbert space is never reduced. With hindsight, the initial state could be restored; in Section 5.5, we discuss about this issue.
7. Performing a phase change so that $(\gamma_2 - \gamma_1) = \pi$ we know already from Eq. (16) that instead of a maximum in the interference pattern at the middle, there must by a nodal region. The experiment was performed by Tonomura and found this good result.

   The energy transfer in our view does not destroy the I-frame quantum state. Only the amplitudes have changed. By disentangling the classical mechanics view of particle from the quantum state sustained by the material system, the "*welcher Weg*" (which-path) problem vanishes.

   Obviously, the I-frame as a material system must have gone through one of the slits, mustn't it? The imprint at the detection screen elicits an energy exchange process.

   But this is not the point. The material system evolves in laboratory space, and the event amplified is, *in itself*, totally irrelevant to quantum mechanics we are probing because it states nothing new; it confirms that quantum state scattering, prepared the way it was, would produce a dispersion of the material system that is tightly associated with a specific interference pattern.

   However, the event is relevant to the experimental work that must be designed so that timing, for example, can be exactly measured. For this particular case, it is the material system that sustains the quantum state.

It is the information carrier as it were; by smashing at the surface makes its presence apparent. The corresponding quantum state exists no more as information is exhausted; by eliciting a location that piece of data can eventually be stored in conjunction with any other datum previously collected.

Before endeavoring the following sections, the reader will find most advantageous to peruse the paper by Karlsson and Brändas presented at the Nobel Symposium in Gimo: *Modern Studies of Basic Quantum Concepts and Phenomena* [13] where most of the experiments discussed in what follows have been examined or reported in the references. Comparisons with the model presented below can hence be performed.

5. QUANTUM STATES FOR QUANTUM MEASUREMENT

We have already hinted the character of a physical quantum state in preceding sections; for example, in Tonomura's experiment. Here, we present analyses of several experimental proposals reported in the literature from the perspective provided by the model underlying the present approach: physical quantum states for quantum measurements. These cases provide severe tests for this new view.

5.1. Scully et al. double-slit setup: basic elements

The reader is referred to Figure 3 in Scully et al. [15]. The issue now is to dissect how the abstract QM approach works.

From that figure, after the first screen (DS-1), the scattered states are collimated by sets of wider slits. The point is that the resulting quantum state has the same nature for both beams; that is, they are prepared in the same manner. After collimation zones, a laser beam is set up perpendicular to the propagation direction from the slits in their way to two cavities; thereon the physical quantum states propagate until interacting further away with the second two-slit screen (DS-2). A recording screen completes the scene.

The key is to calculate the physical quantum states as they reach DS-2. From preceding sections, the theory predicts that if sameness is there, an interference pattern will form and shall be detected.

If the beams come out in different quantum states because of the interaction with each cavity then, depending on the degree of difference, interference pattern may fade away. Before coming to the quantum state generated by the laser, observe the quantum states associated with the collimated beams, $|\Phi\rangle$. They correspond to $|\text{Hole-1}\rangle$ and $|\text{Hole-2}\rangle$ states in their linear superposition given in Eqs. (10 and 11). Since the beams cross a laser beam, we have to introduce an operator action equivalent to the one defined in Eq. (17).

Let x_S indicate location of the first two-slit plane, $|\Phi_{inc}\rangle$ stands for the quantum state impinging at x_S; the interaction with the slits represented by two potential sources generates scattering states. The collimators are sources of containment leading to two identical (beam) states. The interaction with the laser beam leads to the space amplitude (wavefunction) multiplying the I-frame quantum state $\langle x, y, z|(x\rangle x_S)\rangle\,|\Psi\rangle$ in which $\langle x, y, z|(x\,\rangle\, x_S)\rangle$ is defined in Eq. (19) and $|\Psi\rangle$ stands for the internal quantum state sustained by the material system. Labels are added below to identify interactions with the cavities.

Thus, the interactions with double slits, collimators, etc. signal the source of quantum states located inside the setup, but only one material system sustains quantum states: a rubidium atom. The physical quantum states address all possibilities the material system may express. Therefore, the state does not address to the material system as particle so that its whereabouts are not an issue. We summarize the situation by saying that presence of the material system in laboratory space is sufficient yet not its being localized. The concept of presence is required to articulate physical quantum states to the extent they are sustained by material systems.

At the region covered by the laser beam, there is an interaction so that the excited state associated with the internal part of the I-frame system state $|\Psi^*\rangle$ is assumed to have a sufficiently long lifetime. The quantum state prepared by the laser is given by

$$\{C(\Psi^*)|\Psi^*\rangle|0_\omega\rangle + C(\Psi)|\Psi\rangle|1_\omega\rangle\}$$

This is a characteristic entangled state between an EM field and the system to be probed that we write in a simplified manner. The base states are products signaling the possibilities offered by the join system.

The Fence description is completed with the asymptotic states of the EM field $|\mathbf{k}; 1_\omega\rangle$, where the emission source is located at the origin of the $\mathbf{k}$-vector that also identifies a direction $\mathbf{k}/|\mathbf{k}|$ in reciprocal space. Thus, conventionally, $|\Psi\rangle|-\mathbf{k}; 1_\omega\rangle$ signals an EM field in a direction pointing to the I-frame sustaining $|\Psi\rangle$ whereas $|\Psi\rangle|+\mathbf{k}'; 1_\omega\rangle$ stands for one photon emission from the I-frame. These base states supplement a real-space (Fence) description.

The linear superposition given as the scalar product $(|\Psi\rangle|1_\omega\rangle\ |\Psi^*\rangle|0_\omega\rangle)\cdot[C(\Psi)\ C(\Psi^*)]$ represents an entangled state. This form is used to remind that whatever we do with this model, only the amplitudes would change. In an extended base set $(|\Psi\rangle|-\mathbf{k}; 1_\omega\rangle\ |\Psi\rangle|1_\omega\rangle\ |\Psi^*\rangle|0_\omega\rangle\ |\Psi\rangle|+\mathbf{k}'; 1_\omega\rangle)$, a more detailed description becomes possible. In what follows, we discuss situations with the "inner" part of this extended base set, but implicitly, unentanglement/entanglement processes require mechanisms changing the amplitudes.

The amplitude $C(\Psi)$ if different from zero indicates a possibility to engage an interaction with the ground state sustained by the material system that is to be probed; here, one photon could be exchanged. The amplitude $C(\Psi^*)$ if different from zero opens the channel to detect a response from $|\Psi^*\rangle$, that is, a quantum state sustained by the material system; and the energy of the EM field being depleted by the equivalent of one energy quantum. Energy appears "dispersed" so that no exchange with other states is possible. As soon as either $C(\Psi) = 1$ and $C(\Psi^*) = 0$ or vice versa, the possibility opens to sense a full photon exchange through the asymptotic base states. Although the system is trapped in such entangled state, other processes may happen (see below).

Thus, at the entrance of the cavities one has the quantum state $|\mathrm{K}\rangle$:

$$|K\rangle = \langle x, y, z|(x \rangle\, x_{\mathrm{S}})\rangle\{C(\Psi^*)|\Psi^*\rangle|0_\omega\rangle + C(\Psi)|\Psi\rangle|1_\omega\rangle\} = C(\Psi^*)$$
$$\langle x, y, z|(x \rangle\, x_{\mathrm{S}})\rangle|\Psi^*\rangle|0_\omega\rangle + C(\Psi)\langle x, y, z|(x \rangle\, x_{\mathrm{S}})\rangle|\Psi\rangle|1_\omega\rangle. \tag{24}$$

That can be made more explicit because the function $\langle x, y, z|(x\rangle x_{\mathrm{S}})\rangle$ brings information on the channels as linear superposition, given in Eq. (21).

Space information is gathered that will affect the amplitudes of quantum states involving laser excitation.

The base state $|\Psi\rangle|1_\omega\rangle$ stands for the beam's internal quantum state and the laser at frequency ω. The base state $|\Psi^*\rangle|0_\omega\rangle$ represents the electronic excited state with no free electromagnetic energy quantum yet coupled to this "colored" vacuum. The high-energy photon is trapped in the atom as it were, and it will go through the cavity device as long as the entangled state does not spontaneously emit a photon $\hbar\omega$. Such process would destroy the experiment, as we will see below.

Thus, consider $C(\Psi^*) \approx 1$ and $C(\Psi) \approx 0$ in the state vector $[C(\Psi)\, C(\Psi^*)]$. This writing is made for convenience to emphasize that it is the excited state in the cavity which is of our interest. But you cannot erase the base states! Hence, [0 1] refers the internal quantum state while the material system would be present but not localized.

We tinker now with two independent cavities; rearrange the quantum state to make appear the beam labels:

$$|\mathrm{K}\rangle = |\mathrm{Cavity}\rangle = C_1 \exp(\mathrm{i}\gamma_1)\langle x, y|1\rangle \exp(\mathrm{i}(k_{\mathrm{x}}x + k_{\mathrm{y1}}(y - D))\{C(\Psi^*)|\Psi^*\rangle$$
$$|0_\omega\rangle + C(\Psi)|\Psi\rangle|1_\omega\rangle|1_\omega\rangle\} + C_2 \exp(\mathrm{i}\gamma_2)\langle x, y|2\rangle$$
$$\exp(\mathrm{i}(k_{\mathrm{x}}x + k_{\mathrm{y2}}(y + D))\{C(\Psi^*)|\Psi^*\rangle|0_\omega\rangle + C(\Psi)|\Psi\rangle|1_\omega\rangle\}. \tag{25}$$

The material system is chosen so that the excited state shows a lower energy state $|\Psi_{\mathrm{a}}^*\rangle$; the energy gap with respect to $|\Psi^*\rangle$ is negative, and the quantum of energy shows a frequency ω'.

For real space separated the high-quality micromaser cavities, the quantum state along the beam directions can be separately coupled requiring minimal base states written in the following manner:

$$\begin{aligned}
&\text{B-1: } (|\Psi\rangle|1_{\omega}\rangle \quad |\Psi^{*}\rangle|0_{\omega'1}0_{\omega'2}\rangle|0_{\omega}\rangle \quad |\Psi_{\mathrm{a}}^{*}\rangle|1_{\omega'1}0_{\omega'2}\rangle|0_{\omega}\rangle)\\
&\text{B-2: } (|\Psi\rangle|1_{\omega}\rangle \quad |\Psi^{*}\rangle|0_{\omega'1}0_{\omega'2}\rangle|0_{\omega}\rangle \quad |\Psi_{\mathrm{a}}^{*}\rangle|0_{\omega'1}1_{\omega'2}\rangle|0_{\omega}\rangle). \qquad (26)
\end{aligned}$$

At the cavities, the base states read as follows:

$$\begin{aligned}
&\text{Cav-1: } (|\Psi^{*}\rangle|0_{\omega'1}0_{\omega'2}\rangle|0_{\omega}\rangle \quad |\Psi_{\mathrm{a}}^{*}\rangle|1_{\omega'1}0_{\omega'2}\rangle|0_{\omega}\rangle)\\
&\text{Cav-2: } (|\Psi^{*}\rangle|0_{\omega'1}0_{\omega'2}\rangle|0_{\omega}\rangle \quad |\Psi_{\mathrm{a}}^{*}\rangle|0_{\omega'1}1_{\omega'2}\rangle|0_{\omega}\rangle).
\end{aligned}$$

The base state $|\Psi_{\mathrm{a}}^{*}\rangle|1_{\omega'1}0_{\omega'2}\rangle|0_{\omega}\rangle$ corresponds to one photon state at cavity 1 and zero photon state at cavity 2; the energy can be made available in the micromaser photon field; remember that the amplitudes control the processes. The base state $|\Psi^{*}\rangle|0_{\omega'1}0_{\omega'2}\rangle|0_{\omega}\rangle$ corresponds to the internal I-frame excited state system coupled to its electromagnetic vacuum; eventually, it might be coupled to all possible vacua. Both states have the same energy (no jumps then) and, if transition moments are finite, they can be coupled easily by an EM field of frequency in a neighborhood indicated by the labels of $|1_{\omega'1}0_{\omega'2}\rangle$. The corresponding linear superposition (quantum state) is an entangled state.

In order to make contact with Scully et al. article, quantum states are decomposed along beam representations; the base state $|0_{\omega}\rangle$ is not explicitly written (but is always implicit). The quantum state amplitudes take on the form

$$\begin{aligned}
\langle x, y, z|\text{Beam-1}\rangle &= C_1 \exp(\mathrm{i}\gamma_1)\langle x, y|1\rangle \exp(\mathrm{i}(k_{\mathrm{x}}x + k_{\mathrm{y1}}(y - D)))\\
&\times (|\Psi^{*}\rangle|0_{\omega'1}0_{\omega'2}\rangle\ |\Psi_{\mathrm{a}}^{*}\rangle|1_{\omega'1}0_{\omega'2}\rangle) \cdot [C(\Psi^{*}; 0_{\omega'1}0_{\omega'2}) \quad C(\Psi_{\mathrm{a}}^{*}; 1_{\omega'1}0_{\omega'2})]
\end{aligned}$$

and

$$\begin{aligned}
\langle x, y, z|\text{Beam-2}\rangle &= C_2 \exp(\mathrm{i}\gamma_2)\langle x, y|2\rangle \exp(\mathrm{i}(k_{\mathrm{x}}x + k_{\mathrm{y2}}(y + D)))\\
&\times (|\Psi^{*}\rangle|0_{\omega'1}0_{\omega'2}\rangle\ |\Psi_{\mathrm{a}}^{*}\rangle|0_{\omega'1}1_{\omega'2}\rangle) \cdot [C(\Psi^{*}; 0_{\omega'1}0_{\omega'2}) \quad C(\Psi_{\mathrm{a}}^{*}; \mathrm{w}_{\omega'1}1_{\omega'2})]. \qquad (27)
\end{aligned}$$

Observe that if we find physical means to independently modulate $C(\Psi_{\mathrm{a}}^{*}; 1_{\omega'1}0_{\omega'2})$ and $C(\Psi_{\mathrm{a}}^{*}; 0_{\omega'1}1_{\omega'2})$, the local quantum states can be made different. Thus, the quantum states impinging at the second double slit can thereby affect outcomes at the detecting screen. In what follows, we separate the terms just to simplify the writing.

Once the beams are prepared in the way described above, the quantum state is a linear superposition:

$$C_1' \exp(\mathrm{i}\gamma_1)\langle x,y|1\rangle \exp(\mathrm{i}(k_x x + k_{y1}(y-D))) + C_2' \exp(\mathrm{i}\gamma_2)\langle x,y|2\rangle \exp(\mathrm{i}(k_x x + k_{y2}(y+D))). \quad (28)$$

This term multiplies the base state $|\Psi^*\rangle|0_{\omega'1}0_{\omega'2}\rangle$ that carries the information of the state cavities before switching the maser.

Case 1: In Eq. (28), $C_1' = C_1$ and $C_2' = C_2$ and nothing was placed between DS-1 and DS-2 before the recording screen. Then, both beam states are pretty much the same; The conclusion is simple: if this quantum state interacts with the double slit at the right hand side, interference pattern will show up at a recording screen.

Case 2: Coupling to the maser field at frequency ω'. The local base states are given as B-1 and B-2 above Eq. (26). The quantum states are given by the scalar product:

$$|C\rangle \rightarrow (|\Psi_*^*\rangle\,|0_{\omega'1}0_{\omega'2}\rangle\;|\Psi_a^*\rangle|1_{\omega'1}0_{\omega'2}\rangle\;|\Psi_a^*\rangle|0_{\omega'1}1_{\omega'2}\rangle) \times [C(\Psi_*^*;0_{\omega'1}0_{\omega'2}) \quad C(\Psi_a^*;1_{\omega'1}0_{\omega'2}) \quad C(\Psi_a^*;0_{\omega'1}1_{\omega'2})]$$

The linear superposition state with $C(\Psi_a^*;1_{\omega'1}0_{\omega'2}) = 1, C(\Psi_a^*;0_{\omega'1}1_{\omega'2}) = 0$ and $C(\Psi_*^*;0_{\omega'1}0_{\omega'2}) = 0$ defines Beam-1 state where one can detect an ω' photon:

$$\langle x,y,z|\text{Beam-1}\rangle = C_1 \exp(\mathrm{i}\gamma_1)\langle x,y|1\rangle \exp(\mathrm{i}(k_x x + k_{y1}(y-D)) |\Psi_a^*\rangle|1_{\omega'1}0_{\omega'2}\rangle$$

For Beam 2, there is no photon left behind, leading to the amplitudes $C(\Psi_a^*;1_{\omega'1}0_{\omega'2}) = C(\Psi_a^*;0_{\omega'1}1_{\omega'2}) = 0$ and $C(\Psi_*^*;0_{\omega'1}0_{\omega'2}) = 1$:

$$\langle x,y,z|\text{Beam-2}\rangle = C_2 \exp(\mathrm{i}\gamma_2)\langle x,y|2\rangle \exp(\mathrm{i}(k_x x + k_{y2}(y+D))) |\Psi_*^*\rangle|0_{\omega'1}0_{\omega'2}\rangle$$

Beyond the cavity, we have the quantum state:

$$|\text{Case 2}\rangle = \langle x,y,z|\text{Beam-1}\rangle + \langle x,y,z|\text{Beam-2}\rangle = C_1 \exp(\mathrm{i}\gamma_1) \langle x,y|1\rangle \exp(\mathrm{i}(k_x x + k_{y1}(y-D)))|\Psi_a^*\rangle|1_{\omega'1}0_{\omega'2}\rangle + C_2 \exp(\mathrm{i}\gamma_2) \langle x,y|2\rangle \exp(\mathrm{i}(k_x x + k_{y2}(y+D)))|\Psi_*^*\rangle|0_{\omega'1}0_{\omega'2}\rangle$$

It is apparent that the interference pattern will not show up because relevant beam states are different. One can see that the overlaps $\langle 1_1 0_2 | 0_1 0_2 \rangle$ and $\langle \Psi_a^* | \Psi_*^* \rangle$ are both zero. No interference might be expected. This result obtains also by inspecting the incident quantum states that are different, and consequently, one cannot expect interferences. And, whether we know it, the physical quantum state has been formed.

A clear hint follows from the quantum analyses presented so far: the pictures one might obtain are determined by the quantum states impinging at and produced by interaction with DS-2. *There is no observer required*.

The observer we are talking about is the one appearing in the standard QM scheme discussed in Section 2; this is an observer that finally collapses the wavefunction [11]. The physical quantum state discussed here offers a possibility to go beyond passive observation and then using it with varied aims in laboratory devices.

We will come back to this system for further analyses. Now, some important thought experiments are presented for illustrative purposes.

5.2. The Einstein–Podolsky–Rosen thought experiment

This type of experiment [3, 13] involves real-space entangled states. Entangled states belong to Hilbert space, and consequently, a careful definition is required. What entanglement might be and whether one can create entanglement in real space are two key issues to be examined within the quantum state framework. A hint was obtained for the EM field interacting with physical quantum states. Note the contrast between abstract and physical quantum states; the former belongs to the mathematical and the latter are sustained by specific material systems.

For the equivalent to EPR case, two limit situations are taken into account:

1. One-I-frame system: quantum states are sustained by the whole set of interacting material elements. These states are elements of a projected Hilbert space.
2. Two-(or more)-I-frame asymptotic systems: the sum of partial material contents matches material content of the one-I-frame system.

Two (or more) noninteracting quantum states each associated with a corresponding I-frame so that in laboratory space they are located at will in an experiment; these are asymptotic states.

Quantum states for systems' type (1) and (2) are not commensurate. I-frames belong to laboratory space, and consequently, asymptotic states evolve in real space separately, whereas the one-I-frame states evolve in Hilbert space; following the I-frame motion, the internal quantum states are not changed unless real-space interaction sources are allowed for.

Consider a setup where the two-I-frame states are sent in a collision trajectory; remember the I-frame is a classical physics device. The initial state is a direct product of state functions for each I-frame system; at a collision point, they continue to be a simple product and they separate away as a simple product. This product defines a nonentangled state.

The quantum states for the one-I-frame system involve a nonseparable materiality; these states should not include I-frame-related asymptotic states.

At the Fence, let us introduce a model incorporating both types of states that may be used to carry out calculations.

The one- and two-I-frame systems are put together in a box with equal volume. Use base functions constructed with box base states; these latter have only one-I-frame reference, namely, the box size, location, and possibly orientation.

Asymptotic states are simple products labeled with box (n_{k}) and internal (λ_{km}) quantum numbers. For example, $|n_{\mathrm{n}}, \lambda_{\mathrm{n1}}\rangle \otimes |n_{\mathrm{m}}, \lambda_{\mathrm{mk}}\rangle$, etc.

The one-I-frame case has one box label and internal quantum numbers. For example, $|n, \kappa_{\mathrm{nj}}\rangle$, $|m, \kappa_{\mathrm{mj}}\rangle$, . . . etc. The first number is a box state label.

With this trick, one can now handle processes where entanglement can be varied at will. The issue is the representation of quantum states of systems having the same material content although a large number of autonomous subsystems are identifiable at a Fence. This is physics and chemistry unified by quantum physics.

All sorts of asymptotic states together with the one-I-frame system quantum states cover all possibilities; meaning is that all thinkable processes can be described as changes of quantum states using as base states simple products, and I-frame base states provided the total number of material elements are conserved. Basically, a sort of abstract quantum chemistry emerges if base states can be related to those characterizing chemical species.

Consider an entangled base state $|m, \kappa_{\mathrm{n}}\rangle$ and an asymptotic state $|n, \lambda_{\mathrm{na}}\rangle \otimes |n_{\mathrm{m}}, \lambda_{\mathrm{mb}}\rangle$, the quantum state is the linear superposition:

$$(|\mathrm{m}_1, \kappa_{\mathrm{m1}}\rangle|\mathrm{n}, \lambda_{\mathrm{na}}\rangle \otimes |n_{\mathrm{m}}, \lambda_{\mathrm{mb}}\rangle)[C_1\ C_2]$$

The states $[C_1\ C_2]$ define an entangled state with limit point states [1 0] and [0 1]. All these states belong to the same box-Hilbert space. Yet, we keep the information on the I-frame by using labels a and b.

The box-Hilbert space is now rigged with the asymptotic states that can be probed at the laboratory as if they were space separate quantum objects.

A probing process would force a physical transition from box-Hilbert space states to an asymptotic (laboratory) physical space. The transitions from box states to asymptotic or laboratory states are produced by external sources forcing conservation laws as the case might be. If one wants to speak in terms of time evolution, such process cannot be given in terms of standard unitary quantum-mechanical time evolution.

In probing, the state [0 1] correlations to the product $|n_{\rm n}, \lambda_{\rm na}\rangle \otimes |n_{\rm m}, \lambda_{\rm mb}\rangle$ would allow measurements associated with I-frame system sustaining $|n_{\rm m}, \lambda_{\rm mb}\rangle$ the time in laboratory space, this helps introduce a concept of *event*. The probing apparatus defines the location of the event.

Furthermore, if we want to stick to the asymptotic system definition, note that such states do not entangle with each other because they never interact. The entangled base state is already there! The process leading to a change of amplitudes is completely based on quantum mechanics, no superluminal effects.

By counting asymptotic base states, one can find a permutation involving labels a and b, $|n_{\rm n}, \lambda_{\rm nb}\rangle \otimes |n_{\rm m}, \lambda_{\rm ma}\rangle$, or the equivalent writing, $|n_{\rm m}, \lambda_{\rm ma}\rangle \otimes |n_{\rm n}, \lambda_{\rm nb}\rangle$. Thus, the preceding probing would have yielded a response from $|n_{\rm n}, \lambda_{\rm nb}\rangle$.

Arranging the possible responses (keep a and b in order) for our present illustration, the quantum state would read as follows:

$$\left(\frac{1}{\sqrt{2}}\right)\left(|n_{\rm n}, \lambda_{\rm na}\rangle \otimes |n_{\rm m}, \lambda_{\rm mb}\rangle \pm |n_{\rm m}, \lambda_{\rm ma}\rangle \otimes |n_{\rm n}, \lambda_{\rm nb}\rangle\right) \tag{29}$$

This entangled quantum state states us the available possibilities. Probing at b-position will yield a response from either $|n_{\rm m}, \lambda_{\rm mb}\rangle$ or $|n_{\rm n}, \lambda_{\rm nb}\rangle$. The relative intensity responses are equal to $1/2$. Moreover, Eq. (29) imposes correlations at a-position. The probing device will register correlations implied by the quantum state (Cf. Eq. (3)); the probing device for this case cannot impose these correlations.

Examine now correlations including I-frames. Let us designate the momentum associated with I-frame, one by $\mathbf{k}_1$ and other by $\mathbf{k}_2$. The frame state reads $\exp(\mathrm{i}\mathbf{k}_1 \cdot \mathbf{x})\ \phi_1(\mathbf{x}_1)$ and $\exp(\mathrm{i}\mathbf{k}_2 \cdot \mathbf{x})\ \phi_2(\mathbf{x}_2)$.

The simplest procedure is to take the origin of a global I-frame so that $\mathbf{P} = \mathbf{0}$ and linear momentum conservation forces $\mathbf{k}_1 = -\mathbf{k}_2$. At the antipodes, $|\mathbf{k}_1| = |\mathbf{k}_2|$ so that the common I-frame is restricted now. The particle model in this frame becomes strongly correlated. If spin quantum state for I-frame, one corresponds to the linear superposition $(\alpha\ \ \beta)[c_1 c_2]_1$ and the other I-frame system should display the state $(\alpha\ \ \beta)[c_2 - c_1]_2$, namely, an orthogonal quantum state. The quantization of three axes is fixed. Spin and space are correlated in this manner. Now, the label states $(\alpha\ \ \beta)[c_2 - c_1]_1$ and $(\alpha\ \ \beta)[c_1 c_2]_2$ present another set of possibilities. This is because quantum states concern possibilities. All of them must be incorporated in a base state set. At this point, classical and quantum-physical descriptions differ radically. The former case handles objects that are characterized by properties, whereas the latter handle objects that are characterized by quantum states sustained by specific materiality.

The base states necessary to complete a discussion of the EPR experiment can be reduced to three generic ones. A two-label system with total

spin $S = s_1 + s_2$ with values 0 or 1 is quantized along the three directions (arbitrary z-axis): $S_z = s_{z1} + s_{z2}$. Including spin space, functions read as follows:

$$\Psi(S = 0, \mathrm{Ms} = 0) = \langle \mathbf{x}_1, \mathbf{x}_2 | \phi_{\Sigma=0} \rangle (\alpha(1)\beta(2) - \beta(1)\,\alpha(2))/\sqrt{2}$$

$$\Psi(S = 1, \mathrm{Ms} = 0) = \langle \mathbf{x}_1, \mathbf{x}_2 | \phi_{\Sigma=1} \rangle (\alpha(1)\beta(2) + \beta(1)\,\alpha(2))/\sqrt{2}$$

$$\Psi(S = 1, \mathrm{Ms} = 1) = \langle \mathbf{x}_1, \mathbf{x}_2 | \phi_{\Sigma=1} \rangle \alpha(1)\,\alpha(2)$$

$$\Psi(S = 1, \mathrm{Ms} = -1) = \langle \mathbf{x}_1, \mathbf{x}_2 | \phi_{\Sigma=1} \rangle \beta(1)\,\beta(2)$$

Note that the configuration space function $\langle \mathbf{x}_1, \mathbf{x}_2 | \phi_{\Sigma=1} \rangle$ under permutations must be antisymmetric to ensure symmetry.

A model function for the one-I-frame system is formed from products $\phi_1(\mathbf{x}_1)\phi_2(\mathbf{x}_2)$ and $\phi_2(\mathbf{x}_1)\phi_1(\mathbf{x}_2)$ referred to a unique I-frame. The space functions standing for $\langle \mathbf{x}_1, \mathbf{x}_2 | \phi_{\Sigma=0} \rangle$ and $\langle \mathbf{x}_1, \mathbf{x}_2 | \phi_{\Sigma=1} \rangle$ are represented by:

$$\langle \mathbf{x}_1, \mathbf{x}_2 | \phi_{\Sigma=0} \rangle = 1/\sqrt{2}\ (\phi_1(\mathbf{x}_1)\,\phi_2\,(\mathbf{x}_2) + \phi_2(\mathbf{x}_1)\,\phi_1(\mathbf{x}_2))$$

$$\langle \mathbf{x}_1, \mathbf{x}_2 | \phi_{\Sigma=1} \rangle = 1/\sqrt{2}\ (\phi_1(\mathbf{x}_1)\,\phi_2(\mathbf{x}_2) - \phi_2(\mathbf{x}_1)\,\phi_1(\mathbf{x}_2))$$

These functions represent genuine entangled states in configuration space. Now move to a Fence region.

In the limit where asymptotic states $\psi_1(\mathbf{x}_1)\psi_2(\mathbf{x}_2)$ or $\psi_2(\mathbf{x}_1)\psi_1(\mathbf{x}_2)$ can be locally probed, an entangled state is defined by the mappings

$$\langle \mathbf{x}_1, \mathbf{x}_2 | \phi_{\Sigma=0} \rangle \rightarrow \langle \mathbf{x}_1, \mathbf{x}_2 | \psi_{\Sigma=0} \rangle = 1/\sqrt{2}\ (\psi_1(\mathbf{x}_1)\psi_2(\mathbf{x}_2) + \psi_2(\mathbf{x}_1)\psi_1(\mathbf{x}_2))$$

$$\langle \mathbf{x}_1, \mathbf{x}_2 | \phi_{\Sigma=1} \rangle \rightarrow \langle \mathbf{x}_1, \mathbf{x}_2 | \psi_{\Sigma=1} \rangle = 1/\sqrt{2}\ (\psi_1(\mathbf{x}_1)\psi_2(\mathbf{x}_2) - \psi_2(\mathbf{x}_1)\psi_1(\mathbf{x}_2))$$

The condition imposed onto the I-frames must conserve linear momentum thereby implying that a successful probing at a space point directly implies a possible response at the antipode.

Now, introduce the spin to get $\Phi(S = 0, \mathrm{Ms} = 0)$ corresponding to the state $\Psi(S = 0, \mathrm{Ms} = 0)$ where the space function $\langle \mathbf{x}_1, \mathbf{x}_2 | \phi_{\Sigma=0} \rangle$ is replaced by $\langle \mathbf{x}_1, \mathbf{x}_2 | \psi_{\Sigma=0} \rangle$. A similar operation applies to $\Phi(S = 1, \mathrm{Ms} = 0)$, $\Phi(S = 1, \mathrm{Ms} = 1)$, and $\Phi(S = 1, \mathrm{Ms} = -1)$ where the space function $\langle \mathbf{x}_1, \mathbf{x}_2 | \phi_{\Sigma=1} \rangle$ is replaced by $\langle \mathbf{x}_1, \mathbf{x}_2 | \psi_{\Sigma=1} \rangle$.

A probing device designed to detect locally an asymptotic quantum state must correlate to a linear superposition of states with different spin states with $\mathrm{Ms} = 0$. This would stand as a physical process at the Fence.

One obtain states that have the form

$$1/\sqrt{2}\ (\psi_1(\mathbf{x}_1)\psi_2(\mathbf{x}_2)\alpha(1)\beta(2) + \beta(1)\alpha(2)\psi_2(\mathbf{x}_1)\psi_1(\mathbf{x}_2))$$

Thus, there are two possible outcomes: either $\psi_1(\mathbf{x}_1)\psi_2(\mathbf{x}_2)\alpha(1)\beta(2)$ or $\beta(1)\alpha(2)\psi_2(\mathbf{x}_1)\psi_1(\mathbf{x}_2)$, so that at position 1, if spin state is probed and one gets [1 0] (spin α), necessarily, without sending any signal position 2 detects state [0 1], no superluminal signal. There is just a quantum phenomenon. Or if one gets the product form: $\beta(1)\alpha(2)\psi_2(\mathbf{x}_1)\psi_1(\mathbf{x}_2)$, signaling at position 2 one measures spin state for one-I-frame system [1 0] or spin α and necessarily, without sending any signal position 1 detects state [0 1] or spin β. One can generalize the results with the more general spinor representation.

The reality criterion defined by EPR is the following: *If, without in any way disturbing a system, we can predict with certainty (i.e., with probability equal to unity) the value of a physical quantity, then there exists an element of physical reality corresponding to this physical quantity.*

Probing a quantum system implies quantum transitions that may generate one among various alternatives (possibilities). For the present case, when probing the result is, say, $[c_1\ c_2]_1$, one should get $[c_2 - c_1]_2$ when both apparatuses have equal orientation. The *physical quantity* is the entangled quantum state that clearly does not lead to a classical physics property.

The difference with respect to the standard approach lies in the nature of the quantum state. Spin is not taken as a property of a particle. Spin quantum state is sustained by material systems but otherwise a Hilbert space element. A quantum state can be probed with devices located in laboratory (real) space thereby selecting one outcome from among all *possible* events embodied in the quantum state. The presence of the material system is transformed into the localization of the two elements incorporated in the EPR experiment. If you focus on the localization aspect from the beginning, one is bound to miss the quantum-physical edge.

A usual manner to set up EPR paradox is to *consider a pair of spin one-half particles formed somehow in the singlet spin state and moved freely in opposite directions*. This view collides head-on with the quantum state description advanced here. The spin singlet is a one-I-frame state so that no free motion is possible for individual particle-states. The quantum-mechanical entangled state in the box state representation does not have real-space location, the box does; if you like, it is present but not localized. On the other hand, the probing apparatus has a definite space position with respect to the box; actually, it is implicitly included there and can be located through interaction sources. The physical interaction with the material support is exclusive—only one possibility is "materialized" as it were—to predict which one is beyond the capabilities of QM. Yet, it predicts all of them so that relative intensities are predicted as discussed above. The magnetic field and its gradient prompt for a transition of the entangled state to one of the base components with their own I-frames; thus, a kick on the I-frame of this asymptotic state sends that system in a particular direction. The EPR experiment only dissolves into nothing more than a misunderstanding.

The box space used to "dissolve" the I-frames of particle states so that only one-I-frame system obtains and its quantum state embraces all spaces required to actually locate the measuring apparatuses. Interactions between both systems implying energy exchange stop quantum evolution of the probed quantum state by generating another quantum state transporting relevant information to be recorded or translated into reading devices. The probing apparatus prompts for a transition from entangled to asymptotic states that would *remain correlated*. The distance between the asymptotic systems may be as large as one wishes provided these states are shielded. It is constructed to do that job.

5.3. The Wheeler's delayed-choice experiments

During the "thought" experiment era, Wheeler proposed a challenging one named by him as a delayed-choice experiment [18]. Today, the families of experimental setups can be constructed with beam splitters, mirrors, and photodetectors so that the ideas underlying "thought" experiment could be tested. Recently, it was reported as an experimental realization of Wheeler's delayed-choice thought ("gedanken") experiment [19]; there, results' descriptions are made with the help of wave/particle paradigm.

Here, quantum states describing the physical situations are constructed. Only one material system at a time is assumed to be in the apparatus much like Tonomura's experiment.

We first define basic elements of the model to, thereafter, construct basis wavefunctions; finally, a quantized EM-field representation is used to further discuss the experimental results.

1. Beam splitter. This device (BS) is similar to a double-slit arrangement; here, it is the nature of the material located at vertex-1 (v-1), that produces the physical effect, that is, a quantum state $|\Psi\rangle$ impinges at v-1 where a BS is placed; after interaction, the quantum state coming horizontally to v-1 is scattered along two principal base states: $|a\rangle\langle a| + |b\rangle\langle b|$, where the label a indicates direction 1–2 or 3–4 and label b signals either directions 1–3 or 2–4 as the case might be. Colloquially, $|\Psi\rangle$ is a split resulting in a quantum state that is given by a linear superposition:

$$|\Psi\rangle \rightarrow \mathrm{BS} \rightarrow |1\rangle = \langle \mathrm{a}|\Psi\rangle|\mathrm{a}\rangle + \mathrm{i}\langle \mathrm{b}|\Psi\rangle|\mathrm{b}\rangle$$

The scattered state at vertex-1 is labeled as $|1\rangle$. The amplitudes are $\langle \mathrm{a}|\Psi\rangle = 1/\sqrt{2}$ and $\langle \mathrm{b}|\Psi\rangle = 1/\sqrt{2}$. The linear superposition reads $(|\mathrm{a}\rangle|\mathrm{b}\rangle)$ $[1/\sqrt{2}\mathrm{i}/\sqrt{2}]$, and if necessary, a subindex may refer to the vertex added to the column vector amplitudes; the base row vector is always $(|\mathrm{a}\rangle|\mathrm{b}\rangle)$.

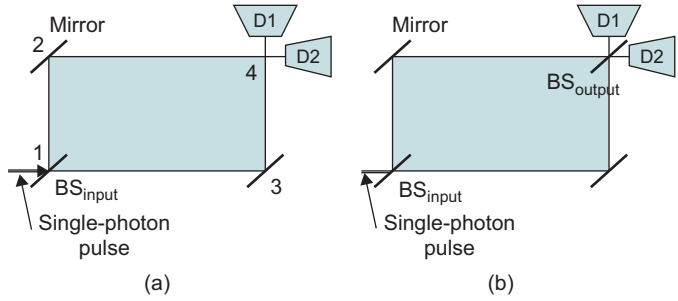

Scheme 1 Mach–Zehnder like interferometer

Decomposing a global quantum state following the channel disposition of the mirrors, one gets Scheme 1a:

Input $|\Psi\rangle \rightarrow$ BS$_{input}$ $\uparrow$ Chanel 1–2 : $[i/\sqrt{2}\ \ 0]$; Chanel 1–3: $[0\ \ 1/\sqrt{2}]$
Input Mirror-2: $[i/\sqrt{2}\ \ 0]_{\uparrow}$ $\rightarrow$ Output Channel 2–4: $[0\ \ -1/\sqrt{2}]_{\rightarrow}$;
Input Mirror-2: $[0\ \ 1/\sqrt{2}]_{\rightarrow}$ $\rightarrow$ Output Channel 3–4: $[1/\sqrt{2}\ \ 0]_{\uparrow}$.
Detector D1 interacts with quantum state $[1/\sqrt{2}\ \ 0]_{\uparrow}$ yielding relative intensity response $|1/\sqrt{2}|^2 = 1/2$.
Detector D2 interacts with quantum state $[0\ \ -1/\sqrt{2}]_{\rightarrow}$ yielding relative intensity response $|-1/\sqrt{2}|^2 = 1/2$.

Quantum mechanics describes propagation of the quantum state that can be locally modulated (mirrors). The detectors, on the other hand, belong to real space where information gathered from them includes supplementary elements corresponding to energy that is exchanged in quanta. The granularity associated with this process does not belong to Hilbert space. Or, in other words, quantum mechanics does not predict the trajectory of energy quanta. The quantum must be present when the experiment proceeds, but its localization is irrelevant to QM.

We examine now the modulation introduced by a beam splitter located at vertex-4 as shown in Scheme 1b. The result is

toward D1: $1/\sqrt{2}[-i/\sqrt{2}\ \ 0]_{\uparrow}$ Channel 2–4: $[0\ \ -1/\sqrt{2}]_{\rightarrow} \rightarrow$ BS$_{output}$
toward D2: $1/\sqrt{2}[0\ \ -1/\sqrt{2}]_{\rightarrow}$
toward D1: $1/\sqrt{2}[i/\sqrt{2}\ \ 0]_{\uparrow}$ Channel 3–4: $[i/\sqrt{2}\ \ 0]_{\uparrow} \rightarrow$ BS$_{output}$
toward D2: $1/\sqrt{2}[0\ \ -1/\sqrt{2}]_{\rightarrow}$
Detector D1: $1/\sqrt{2}[-i/\sqrt{2}\ \ 0] + 1/\sqrt{2}[i/\sqrt{2}\ \ 0] = [(-i/2 + i/2)\ \ 0] = [0\ \ 0]$
Detector D2: $1/\sqrt{2}[0\ \ -1/\sqrt{2}] + 1/\sqrt{2}[0\ \ -1/\sqrt{2}] = [0\ \ -1]$.

The relative intensity concentrates on detector D2.

The analysis displayed above shows that it is the quantum state that is probed at the detectors determining the outcome.

Yet, quantum events do take place at the detectors. No-event is an event. The quantum state relevant under these circumstances is the physical quantum states equivalent to Eq. (19). First use Eq. (18) with state [1 0] indicating one-energy quantum in the system. This statement means everywhere inside the setup. The quantum state impinging at D1 is a direct product [0 0]⊗[1 0], whereas at D2 it reads [0 –1]⊗[1 0]. Using Eq. (3), we see that the root amplitude multiplying the photon transition is zero at D1, is zero always, whereas at D2 the root amplitude is -1 which ensures the possibility that the photon is transferred (emitted) thereby prompting for an event.

It is the quantum state that is probed seems obvious from presentation given, but a phase shift (PS) operation can check it: PS[a b] → [a b exp(iϕ)]. Now,

Channel 2–4: PS[0 $-1/\sqrt{2}]_{\rightarrow}$ → [0 $-1/\sqrt{2}\exp(i\phi)$] → BS_{output}
toward D1: $1/\sqrt{2}[-i/\sqrt{2}\exp(i\phi)\ \ 0]_{\uparrow}$
toward D2: $1/\sqrt{2}[0 - 1/\sqrt{2}\exp(i\phi)]_{\rightarrow}$

Whereas

Channel 3–4: $[i/\sqrt{2}\ \ 0]_{\uparrow}$ → BS_{output}
toward D1: $1/\sqrt{2}[i/\sqrt{2}\ \ 0]_{\uparrow}$
toward D2: $1/\sqrt{2}[0\ \ -1/\sqrt{2}]_{\rightarrow}$.

The quantum state arriving at D1 yields

$$1/\sqrt{2}[-i/\sqrt{2}\ \exp(i\phi)0]_{\uparrow} + 1/\sqrt{2}[i/\sqrt{2}\ \ 0]_{\uparrow} = 1/2[i(1 - \exp(i\phi))0]_{\uparrow}.$$

The quantum state arriving at D2 yields

$$1/\sqrt{2}\,[0\ \ -1/\sqrt{2}\ \exp(i\phi)]_{\rightarrow} + 1/\sqrt{}\,2[0\ \ -1/\sqrt{2}]_{\rightarrow} = 1/2\,[0 - (1 + \exp(i\phi))]_{\rightarrow}.$$

For $\phi = \pi/2$, we have the quantum state at D1 equals to $1/2[(i + 1)\ \ 0]_{\uparrow}$ and at D2 equals to $1/2[0\ \ -(1 + i)]_{\rightarrow}$, and both detector will click with equal relative intensities!

A phase shift is a pure quantum-mechanical modulation that, for the present case, produces an effect at the Fence (laboratory).

The results of this thought experiment and the way it is described in the present approach deny validity (pertinence) to the common statement: *quantum entities can behave like particles or waves depending on how they are observed*.

If the terms, particles or waves, imply classical physics systems, as they do when invoking the principle of complementarity, then the results analyzed here imply the particle-wave duality belonging to a classical view with no place to claim in QM as presented here.

This issue is very important. We will examine this matter a little further.

5.4. Particle picture and delayed-choice experiment

The particle picture has not been retained in this paper. Yet, it is a dominant view. Thus, it seems timely to introduce it through the master presentation made by Wheeler himself.

Referring to the fundamental discussions between Albert Einstein and Nils Bohr, Wheeler writes:

"Of all the idealized experiments taken up by the two friends in their effort to win agreement, none is simpler than the beam splitter." (See Figure 4 from Wheeler's paper [18]). He continues: "With the final half-silvered mirror in place the photoreceptor at the" lower left (D2 for the present case) "click-click as the successive photons arrive but the adjacent counter register nothing;" (this corresponds to our D2 counter). "This is evidence of interference between beams 4a and 4b; or, in photon language, evidence that each arriving light quantum has arrived by both routes," that is, 134 *and* 124. "In such experiments, Einstein originally argued, it is un-reasonable for a single photon to travel simultaneously two routes. Remove the half-silvered mirror," (the one called BS_{output}), as in Scheme 1a, "one will find that the one counter goes off, or the other. Thus the photon has traveled only *one* route. It travels only one route, but it travels both routes; it travels both routes, but it travels only one route." The text continues: *"What a nonsense! How obvious it is that quantum theory is inconsistent!"*

So far goes Einstein's criticism. The answer by Bohr as quoted by Wheeler is interesting: Bohr emphasized that "there is no inconsistency. We are dealing with two different experiments. The one with the half-silvered mirror removed tells which route. The one with the half-silvered mirror in place provides evidence that the photon traveled both routes. But it is impossible to do both experiments at once."

Quantum mechanics is about quantum states and their (parametric) time evolution. They are related to material substrates in real space, no doubt, but as such (quantum states) they belong to Hilbert space. In this latter space, pictorial descriptions originated in our real-world perceptions do not make sense. There are no quantum entities that can behave like particles or waves; see the comments made by P. Knight in [20]. From the perspective displayed in Section 5.3, it is not difficult to see that when real-space and Hilbert space descriptions are not distinguished properly, whenever a particle description is used to examine quantum-mechanical outcomes, weirdness would pop up. It is the way one understands quantum states, that is, at stake. More to the point: it is the classical particle/wave picture that is part of the problem.

But according to the present approach, they behave as quantum states in Hilbert space. These latter can be diffracted and modulated interference patterns. This latter is taken as the signal of wave behavior in the standard textbooks. But, as water waves in a pond designed to mimic a two-slit setup

and electromagnetic waves in similar arrangement produce interference patterns, it does not mean that water waves are equivalent or equal to electromagnetic waves. Quantum states in particular situations do relate to patterns of interference. At *detection*, they exchange energy in quanta through a quantum interaction; this is a fact inferred from Planck's experiments. And as we saw in the two-slit experiments discussed in Section 5.1 as an event realizes at a given spot, it is modulated by the wavefunction there. If anything, the "particle" and "wave" behaviors are "simultaneously" in effect at the point where the click-event emerges they cannot possibly be separated. The complementarity principle applies only to the real concepts of particle and wave. It has no relevance if a full quantum-mechanical description is at work.

5.5. Coherence lost and regained

The relative phases appearing in quantum states can experimentally be manipulated. Brändas pointed out to me that Chapman et al. [16] have shown that coherence can be lost by photon interaction with a quantum state and that coherence could be recovered experimentally.

The quantum state approach used by us leads to similar equations reported there. The chapter is formulated in the particle/wave language that N. Bohr popularized among physicists. This issue is examined again in Section 6.

The flaw in Bohr's view lies in the assumption that the measuring device must be macroscopic and "reality" the one emerging in our daily life, to be communicated with everyday language.

But language grows as new "continents" are discovered and new words and concepts would find their way to the civil society beyond the jargon we employ in scientists' societies.

6. BACK TO QUANTUM STATES FOR QUANTUM PROBING

At a Fence implications derived from quantum state, changes are confronted to representation of time and space including time scales, duration, and location (presence) of laboratory material elements (objects). This is a reality constructed with the help of theoretic concepts; it is not something that you may simply "observe." Xenophanes (ca. 500 BC) already pointed out similar ideas (Wikipedia). The concept of quantum state is central to the quantum-physical view. Basically, there is no need for observers but of experimenters able to change, alter, capture, and interpret signals from the surrounding interfaces. A new dimension incorporates to our view of what is called reality.

Thought and laboratory experiments to be examined later have been extensively described and analyzed in the literature [13]. Basically, a particle/wave picture and Bohr's complementarity principle are the ground

elements that sustain the description of experimental results. A classical physics picture dominates both at a descriptive level and in constructing quantum states. And, consequently, one finds studies in which an origin to quantum-mechanical complementarity is sought by "which way" experiment in atom interferometry. The problem is that a classical picture and an abstract quantum-mechanical one are not commensurate; in this context, the term quantum-mechanical complementarity is contradictory. Whether an alternative can be found is the issue examined below.

6.1. The Scully et al. atom interferometer

The introductory aspects related to these experiments are examined in Section 5.1 where a simplified base state model is presented. Here quantum optical test proposals are discussed. For details, view Figure 5 of Ref. [15]; there, emphasis is provided on the location and construction of quantum states.

The scheme is used to help construct quantum states adapted (relevant) to the new situations. Interaction operators represent slits. The quantum states obtained are those that will interact at the slits located on the right screen. These states are then scattered by the slits and proceed to check the quantum states impinging at the recording screen.

The material system sustaining the quantum states of interest corresponds to an atom showing a long-lived Rydberg state. In our view, it is the entangled state discussed at several places that show a long lifetime before emitting a photon. "Communication" (interactions) between cavities can be allowed; this is done through the electro-optic shutters separating both cavities. Three generic cases are examined: (1) Shutter is closed and no interaction between cavities; (2) Shutter open; (3) Shutter open and a measuring device separates both cavities.

The heuristic analysis in Section 5.1 is completed now.

$|\Phi_{\text{inc}}\rangle = |\text{Ingoing-state}\rangle = |00\rangle$

Channel adapted base states:

$|10\rangle = |\text{Rb-ground-state}\rangle_1 = \phi_1(\mathbf{x})|\text{GS}\rangle = \phi_1(\mathbf{x})|\text{i}\rangle$
$|20\rangle = |\text{Rb-ground-state}\rangle_2 = \phi_2(\mathbf{x})|\text{GS}\rangle = \phi_2(\mathbf{x})|\text{i}\rangle.$

Laser interaction base states (GS = ground state):

$$
\begin{aligned}
&|11\rangle = \phi_1(\mathbf{x})|\text{GS}\rangle|1_\omega\rangle;\\
&|11E\rangle = |\text{GS};1_\omega\rangle_1 = \phi_1(\mathbf{x})|\Psi^*\rangle|0_\omega\rangle\\
&|22\rangle = \phi_2(\mathbf{x})|\text{GS}\rangle|1_\omega\rangle;\\
&|22E\rangle = |\text{GS};1_\omega\rangle_2 = \phi_2(\mathbf{x})|\Psi^*\rangle|0_\omega\rangle.
\end{aligned}
\tag{30}
$$

The model is the simplest one. See Section 5.1 for some variations including entanglement.

Cavity dressed base states:

$$
\begin{aligned}
&|1\rangle = |11E\rangle|0_{\omega'}\rangle_1|0_{\omega'}\rangle_2 = \phi_1(\mathbf{x})|\mathrm{GS};1_\omega\rangle|0_\omega\rangle|0_{\omega'}\rangle_1|0_{\omega'}\rangle_2 = \\
&\quad \phi_1(\mathbf{x})|\mathrm{Rb}63\mathrm{p}_{3/2}\rangle_1 \quad |0_{\omega'}\rangle_1|0_{\omega'}\rangle_2 \quad |0_\omega\rangle = |\Psi_*^*00\rangle_1 = |\mathrm{a}00;E\rangle_1; \\
&|2\rangle = |21E\rangle|0_{\omega'}\rangle_1|0_{\omega'}\rangle_2 = \phi_2(\mathbf{x})|\mathrm{GS};1_\omega\rangle|0_\omega\rangle|0_{\omega'}\rangle_1|0_{\omega'}\rangle_2 = \\
&\quad \phi_2(\mathbf{x})|\mathrm{Rb}63\mathrm{p}_{3/2}\rangle_2 \quad |0_{\omega'}\rangle_1|0_{\omega'}\rangle_2 \quad |0_\omega\rangle = |\Psi_*^*00\rangle_2 = |\mathrm{a}00;E\rangle_2; \\
&|3\rangle = |\Psi_\beta^*10\rangle = \phi_1(\mathbf{x})|\mathrm{Rb}61\mathrm{d}_{5/2}\rangle_1 \quad |1_{\omega'}\rangle_1|0_{\omega'}\rangle_2 \quad |0_\omega\rangle = |\mathrm{b}10\rangle; \\
&|4\rangle = |\Psi_\beta^*;10\rangle = \phi_1(\mathbf{x})|\mathrm{Rb}61\mathrm{d}_{5/2};1_{\omega'}\rangle_1|0_{\omega'}\rangle_1|0_{\omega'}\rangle_2|0_\omega\rangle = |\mathrm{b}10;E\rangle \\
&|5\rangle = |\Psi_{\beta'}^*10\rangle = \phi_1(\mathbf{x})|\mathrm{Rb}61\mathrm{d}_{3/2}\rangle_1|1_{\omega'}\rangle_1|0_{\omega'}\rangle_2 \quad |0_\omega\rangle = |\mathrm{c}10\rangle; \\
&|6\rangle = |\Psi_{\beta'}^*;10\rangle = \phi_1(\mathbf{x})|\mathrm{Rb}61\mathrm{d}_{3/2};1_{\omega'}\rangle_1|0_{\omega'}\rangle_1|0_{\omega'}\rangle_2 \quad |0_\omega\rangle = |\mathrm{c}10;E\rangle \\
&|7\rangle = |\Psi_\beta^*01\rangle = \phi_2(\mathbf{x})|\mathrm{Rb}61\mathrm{d}_{5/2}\rangle_2|1_{\omega'}\rangle_2|0_{\omega'}\rangle_1 \quad |0_\omega\rangle = |\mathrm{b}01\rangle \\
&|8\rangle = |\Psi_\beta^*;01\rangle = \phi_2(\mathbf{x})|\mathrm{Rb}61\mathrm{d}_{5/2};1_{\omega'}\rangle_2|0_{\omega'}\rangle_20_{\omega'}\rangle_1 \quad |0_\omega\rangle = |\mathrm{b}01;E\rangle \\
&|9\rangle = |\Psi_{\beta'}^*01\rangle = \phi_2(\mathbf{x})|\mathrm{Rb}61\mathrm{d}_{3/2}\rangle_2|1_{\omega'}\rangle_2|0_{\omega'}\rangle_1 \quad |0_\omega\rangle = |\mathrm{c}01\rangle \\
&|10\rangle = |\Psi_{\beta'}^*;01\rangle = \phi_2(\mathbf{x})|\mathrm{Rb}61\mathrm{d}_{3/2};1_{\omega'}\rangle_2|0_{\omega'}\rangle_2|0_{\omega'}\rangle_1|0_\omega\rangle = |\mathrm{c}01;E\rangle \qquad (31)
\end{aligned}
$$

The cavity photon entangled with the material system state is written as $|\mathrm{Rb}\ 61\mathrm{d}_{5/2};1_{\omega'}\rangle_{k=1,2}$. Base states $|\mathrm{Rb}\ 63\mathrm{p}_{3/2}\rangle$ and $|\mathrm{Rb}61\mathrm{d}_{5/2}\rangle_1|1_{\omega'}\rangle$ have equal energy; they relate to two different states at lower energy: a λ state. Symbol $|\Psi_*^*00\rangle$ reminds the case.

6.1.1. Quantum states: possible situations

The base set displayed in Eq. (31) represents important cases. Let us select few of them that may be relevant to discuss situations mentioned in Ref. [15].

The laser beam sets up the channel states into a linear superposition that for channel 1 reads as follows:

$$C_1^{11}|11\rangle + C_2^{11}|11E\rangle = C_1^{11}\phi_1(\mathbf{x})|\mathrm{GS}\rangle|1_\omega\rangle + C_2^{11}\phi_1(\mathbf{x})|\mathrm{GS};1_\omega\rangle|0_\omega\rangle$$

A similar relation holds for channel 2 with obvious changes. At the cavity, the active component is related to C_2^{11} because it is the base state $|\mathrm{GS};1_\omega\rangle$ that would correspond in energy to $|\mathrm{Rb}\ 63\mathrm{p}_{3/2}\rangle$ that opens channels to interact with base states $|\mathrm{Rb}\ 61\mathrm{d}_{5/2}\rangle$ (b-state) and $|\mathrm{Rb}\ 61\mathrm{d}_{3/2}\rangle$ (c-state).

The states $C_1^{11} = 0$ and $C_2^{11} = 1$ open couplings to the cavity. Thus, one proceeds to signal this base state as $|\mathrm{Rb}\ 63\mathrm{p}_{3/2}\rangle = |\Psi_*^*00\rangle = |\mathrm{a}00;E\rangle$. The avatars

related to this state are related to channel processes; this is why one label base states with subindexes.

The first result corresponds to a trapping of the entangled state inside the cavity. The lifetime at $|\text{Rb } 63\text{p}_{3/2}\rangle$ is such that it remains with $C_2^{11} = 1$.

With $C_2^{11} = 1$, the base state is left free to act as root for processes connected to ω'-photon emission related to internal base states $|\text{Rb } 61\text{d}_{3/2}$ or $\text{d}_{5/2}\rangle$.

Observe that inside cavities, the base states $|\text{Rb } 61\text{d}_{3/2}$ or $\text{d}_{5/2}; 1_{\omega'}\rangle$ and the level $|\text{Rb } 63\text{p}_{3/2}\rangle|0_{\omega'}\rangle$ have the same energy. Thus, the entangled base states $|\text{b}01; E\rangle$, $|\text{b}10; \text{E}\rangle$, $|\text{c}01; E\rangle$, and $|\text{c}10; E\rangle$ may connect the cavity to external states, for example, $|\text{a}00; E\rangle_1$ and $|\text{a}00; E\rangle_2$.

What is the role of entangled states inside the cavity? Terms, for example, such as those in $|3\rangle$ and $|4\rangle$ appear as linear superpositions (omitting common factors):

$$C_3 \quad |\text{Rb } 61\text{d}_{5/2}\rangle_1 \, |1_{\omega'}\rangle_1 |0_{\omega'}\rangle_2 + C_4 \quad |\text{Rb}61\text{d}_{5/2}; 1_{\omega'}\rangle_1 |0_{\omega'}\rangle_1 |0_{\omega'}\rangle_2$$

Normalization $|C_3|^2 + |C_4|^2 = 1$ leads to assign $C_3 = \cos\alpha$ and $C_4 = \sin\alpha$. Angle α here is a parameter (real number). The system can be prepared in different guises if one can fix the parameter.

If $C_3 = 1$, then $C_4 = 0$; there is some ambiguity. The base state $|\text{Rb } 61\text{d}_{5/2}\rangle_1$ $|1_{\omega'}\rangle_1$ may stand for a photon state that is directed toward the material system; it may also describe a photon state moving away (emission of some sort).

If a quantum state starting from $|\text{Rb}63\text{p}_{3/2}\rangle$, then we take $C_4 = 1$ and $C_3 = 0$. The process described by the arrival state $C_4 = 0$ and $C_3 = 1$ can be seen in a two-fold manner: (1) The ω'-photon is sent away into the cavity by spontaneous emission; (2) The linear superposition becomes periodic in time where the state is an entangled state; the energy $\hbar\omega'$ is no longer available.

Thus, a time-dependent state stands for a system where one cavity photon is no longer available. When state $C_3(\omega'' t) = 1$ where ω'' characterizes a weak interaction one has a possibility to "release" one photon ω' to the cavity; the base state required to complete the description is $|\text{Rb } 61\text{d}_{5/2}\rangle_1 |0_{\omega'}\rangle_1 |0_{\omega'}\rangle_2$. The quantum state takes on the form:

$$\begin{aligned} &C_3\phi_1(\mathbf{x})|\text{Rb}61\text{d}_{5/2}\rangle_1|1_{\omega'}\rangle_1|0_{\omega'}\rangle_2 + C_4\phi_1(\mathbf{x})|\text{Rb}61\text{d}_{5/2}; 1_{\omega'}\rangle_1|0_{\omega'}\rangle_1|0_{\omega'}\rangle_2 \\ &\quad + C_{3'}\Psi_1(\mathbf{x})|\text{Rb}61\text{d}_{5/2}\rangle_1|1_{\omega'}\rangle_1|0_{\omega'}\rangle_2 \end{aligned}$$

The third term corresponds to recoil is associated with spontaneous photon emission in a direction different from $\phi_1(\mathbf{x})$, justifying the change into $\Psi_1(\mathbf{x})$. Such photon state is not correlated to the initial interacting state. The reason is due to the stochastic nature of spontaneous processes. The quantum state amplitudes are $C_3 = C_4 = 0$ and $C_{3'} = 1$. The change is physically irreversible.

6.1.2. Detector function

The incoming states $|\Phi_{inc}\rangle$ are planar wave states sustained by the Rubidium atom. The collimators allow separation in space; base states $|10\rangle$ and $|20\rangle$ propagate along channels 1 and 2; $\phi_1(\mathbf{x})$ and $\phi_2(\mathbf{x})$ are the scattered states at DS-1 and, as the source state is the same and we take identical slit interaction potentials, these functions differ only in space origin. After interaction with the laser beam the base states label from $|1\rangle$ to $|10\rangle$ are sufficient for discussing several possibilities

Case 1: Absence of laser and cavities system

$$\langle \mathbf{x}|1\rangle = \phi_1(\mathbf{x})|\mathrm{GS}\rangle \text{ and } \langle \mathbf{x}|2\rangle = \phi_2(\mathbf{x})|\mathrm{GS}\rangle.$$

After DS-2, the quantum state is the linear superposition:

$$|\Psi\rangle = (1/2)(\phi_1(\mathbf{x}) + \phi_2(\mathbf{x}))|\mathrm{GS}\rangle.$$

The channels are apparent.

Case 2: Absence of cavities system

The quantum state after laser beam interaction is space separated by the collimators:

$$\begin{aligned}\langle \mathbf{x}|1\rangle &= C_1^{11}\phi_1(\mathbf{x})|\mathrm{GS}\rangle|1_\omega\rangle + C_2^{11E}\phi_1(\mathbf{x})|\mathrm{GS};1_\omega\rangle = (C_1^{11}|\mathrm{GS}\rangle|1_\omega\rangle \\ &\quad + C_2^{11E}|\mathrm{GS};1_\omega\rangle)\phi_1(\mathbf{x}) \\ \langle \mathbf{x}|2\rangle &= C_1^{22}\phi_2(\mathbf{x})|\mathrm{GS}\rangle|1_\omega\rangle + C_2^{22E}\phi_2(\mathbf{x})|\mathrm{GS};1_\omega\rangle = (C_1^{22}|\mathrm{GS}\rangle|1_\omega\rangle \\ &\quad + C_2^{22E}|\mathrm{GS};1_\omega\rangle)\,\phi_2(\mathbf{x}).\end{aligned}$$

Symmetry imposes the equalities $C_1^{11} = C_1^{22} = D_1$ and $C_2^{11E} = C_2^{22E} = D_2$. This means that quantum states for both channels are the same.

The linear superposition generated by DS-2 reads as follows:

$$\begin{aligned}|\Psi\rangle &= (\mathrm{D}_1|\mathrm{GS}\rangle|1_\omega\rangle + \mathrm{D}_2|\mathrm{GS};1_\omega\rangle)\phi_1(\mathbf{x}) + (\mathrm{D}_1|\mathrm{GS}\rangle|1_\omega\rangle \\ &\quad + \mathrm{D}_2|\mathrm{GS};1_\omega\rangle)\phi_2(\mathbf{x})) = (\mathrm{D}_1|\mathrm{GS}\rangle|1_\omega\rangle + \mathrm{D}_2|\mathrm{GS};1_\omega\rangle)(\phi_1(\mathbf{x}) + \phi_2(\mathbf{x})).\end{aligned}$$

If sameness criterion fulfils, an interference pattern is expected at recording screen.

Case 3: Include laser and cavities system

The groundwork with bases set has been done above. Here, we leave outside the base states $|0\rangle, |01\rangle$, and $|02\rangle$ appearing in Eq. (31). Now, let us examine some situations present in article by Scully et al., namely, shutters are closed.

States given in terms of linear superpositions cover all available space:

$$|+\rangle = 1/\sqrt{2}|\text{Cav-1}(10)\rangle + 1/\sqrt{2}|\text{Cav-2}(01)\rangle$$
$$|-\rangle = 1/\sqrt{2}|\text{Cav-1}(10)\rangle - 1/\sqrt{2}|\text{Cav-2}(01)\rangle.$$

In terms of these new states, cavity 1 state reads as follows:

$$|\text{Cav-1}\rangle = (1/\sqrt{2})(|+\rangle + |-\rangle)$$
$$|\text{Cav-2}\rangle = (1/\sqrt{2})(|+\rangle - |-\rangle).$$

Cavity states are represented in the base set (Eq. (31)) as:

$$|\text{Cav-1}(10)\rangle = [0_1 \;\; 0_2 \;\; C_3 \;\; C_4 \;\; C_5 \;\; C_6 \;\; 0_7 \;\; 0_8 \;\; 0_9 \;\; 0_{10}]$$
$$|\text{Cav-2}(01)\rangle = [0_1 \;\; 0_2 \;\; 0_3 \;\; 0_4 \;\; 0_5 \;\; 0_6 \;\; C_7 \;\; C_8 \;\; C_9 \;\; C_{10}].$$

In what follows, the base states with configuration $61d_{3/2}$ will be left idle, namely, amplitudes equal to zero: $C_5 = C_6 = C_9 = C_{10} = 0$. This is done to simplify the writing only.

With the laser turned-on, the quantum state at the cavities appears as follows:

$$\begin{aligned}
&1/\sqrt{2}\,\phi_1(\mathbf{x})|\text{Cav-1}(10)\rangle + 1/\sqrt{2}\,\phi_1(\mathbf{x})|\text{Cav-2}(01)\rangle \\
&\quad = (C_3|\text{Rb } 61d_{5/2}\rangle|1_{\omega'}\rangle_1|0_{\omega'}\rangle_2|0_\omega\rangle + C_4|\text{Rb } 61d_{5/2}; 1_{\omega'}\rangle_1|0_{\omega'}\rangle_1|0_{\omega'}\rangle_2|0_\omega\rangle)\phi_1(\mathbf{x}) \\
&\qquad + (C_7|\text{Rb } 61d_{5/2}\rangle|1_{\omega'}\rangle_2|0_{\omega'}\rangle_1|0_\omega\rangle + C_8|\text{Rb } 61d_{5/2}; 1_{\omega'}\rangle_2|0_{\omega'}\rangle_2|0_{\omega'}\rangle_1 \\
&\qquad\quad |0_\omega\rangle)\phi_2(\mathbf{x})
\end{aligned}$$

Reorganizing this equation with $|0_\omega\rangle$ as common factor:

$$\begin{aligned}
&\{C_3|\text{Rb } 61d_{5/2}\rangle|1_{\omega'}\rangle_1|0_{\omega'}\rangle_2\phi_1(\mathbf{x}) + C_7|\text{Rb } 61d_{5/2}\rangle|1_{\omega'}\rangle_2|0_{\omega'}\rangle_1\phi_2(\mathbf{x})\}|0_\omega\rangle \\
&+ \{C_4|\text{Rb } 61d_{5/2}; 1_{\omega'}\rangle_1|0_{\omega'}\rangle_1|0_{\omega'}\rangle_2)\phi_1(\mathbf{x}) \\
&+ C_8|\text{Rb } 61d_{5/2}; 1_{\omega'}\rangle_2|0_{\omega'}\rangle_2|0_{\omega'}\rangle_1)\phi_2(\mathbf{x})\}|0_\omega\rangle.
\end{aligned}$$

The second line corresponds to a nonseparable photon state, whereas the first line would correspond to a direct product state between material system base state and photon fields. It is the sum that describes an entangled state.

The quantum state with $C_4 = C_8 = 0$ and $C_3 = C_7 = 1/\sqrt{2}$ corresponds to Eq. (6) in Ref. [15]. This state misses entanglement. By symmetry, the state should have amplitudes $|C_4| = |C_8| = |C_3| = |C_7| = 1/2$.

If there is a photon in the cavity prior to the passage of the material system, the base set must be modified. Then, that photon state can be

associated with

$$|\text{Rb } 61d_{5/2}; 1_{\omega'}\rangle_1|1_{\omega'}\rangle_1|0_{\omega'}\rangle_1|0_{\omega'}\rangle_2)\,\phi_1(\mathbf{x})|0_\omega\rangle \quad \text{or}$$
$$|\text{Rb } 61d_{5/2}; 1_{\omega'}\rangle_2|1_{\omega'}\rangle_2|0_{\omega'}\rangle_2|0_{\omega'}\rangle_1)\,\phi_2(\mathbf{x})|0_\omega\rangle.$$

If such beam states proceed until the double slit located at the right screen according to this device, they must form a linear superposition

$$C_{4'}|\text{Rb } 61d_{5/2}; 1_{\omega'}\rangle_1|1_{\omega'}\rangle_1|0_{\omega'}\rangle_1|0_{\omega'}\rangle_2)\,\phi_1(\mathbf{x})|0_\omega\rangle \pm$$
$$C_{8'}|\text{Rb } 61d_{5/2}; 1_{\omega'}\rangle_2|1_{\omega'}\rangle_2|0_{\omega'}\rangle_2|0_{\omega'}\rangle_1)\,\phi_2(\mathbf{x})|0_\omega\rangle.$$

At DS-2, the cavity components differ in a phase factor indicating the origin; otherwise, they are not the same thereby closing the possibility for an interference pattern. Actually, one has $\langle 1_{\omega'2}|0_{\omega 2'}\rangle\langle 1_{\omega'1}|0_{\omega 1'}\rangle = 0$.

If there are N-photons at each cavity, the base functions would read as follows:

$$|\text{Rb } 61d_{5/2}; 1_{\omega'}\rangle_1|N+1_{\omega'}\rangle_1|N_{\omega'}\rangle_2)\phi_1(\mathbf{x})|0_\omega\rangle \quad \text{or}$$
$$|\text{Rb } 61d_{5/2}; 1_{\varpi'}\rangle_2|N+1_{\omega'}\rangle_2|N_{\omega'}\rangle_1)\phi_2(\mathbf{x})|0_\omega\rangle.$$

But now, the field quantum states are no longer orthogonal. An interference pattern can hence be detected. This result is quoted in Ref. [15].

Beyond the cavity space, the material system is released through the nonentangled state inside the cavity:

$$|\text{Cav-1(10)}; E\rangle \rightarrow |\text{Cav-1(10)}; \text{Free}\rangle.$$

Namely,

$$|\text{Cav-1(10)}; E\rangle = [0_1\ 0_2\ 0_3\ C_4\ 0_5\ C_6\ 0_7\ 0_8\ 0_9\ 0_{10}] \rightarrow$$
$$|\text{Cav-1(10)}; \text{Free}\rangle = [0_1\ 0_2\ C_3\ 0_4\ C_5\ 0_6\ 0_7\ 0_8\ 0_9\ 0_{10}]$$

and

$$|\text{Cav-2(01)}; E\rangle = [0_1\ 0_2\ 0_3\ 0_4\ 0_5\ 0_6\ 0_7\ C_8\ 0_9\ C_{10}] \rightarrow$$
$$|\text{Cav-2(01)}; \text{Free}\rangle = [0_1\ 0_2\ 0_3\ 0_4\ 0_5\ 0_6\ C_7\ 0_8\ C_9\ 0_{10}].$$

The entangled states are those operational in opening the quantum states where no photon is left at the cavities. In this case, one gets:

$$|\text{Cav-1 Outgoing}\rangle = [0_1\ 1/\sqrt{2}_2\ 0_3\ 0_4\ 0_5\ 0_6\ 0_7\ 0_8\ 0_9\ 0_{10}]$$
$$|\text{Cav-2 Outgoing}\rangle = [0_1\ 1/\sqrt{2}_2\ 0_3\ 0_4\ 0_5\ 0_6\ 0_7\ 0_8\ 0_9\ 0_{10}].$$

The beam quantum states are the same for channels 1 and 2. This is the condition required so that interference fringes will show up. Once the beam states interact at the slits, one will have the scattered state

$$\begin{aligned}|\text{Scatt.State} +\rangle &= |\text{Cav-1 Outgoing}\rangle + |\text{Cav-2 Outgoing}\rangle \\ &= \{C_1 \exp(\mathrm{i}\mathbf{K}.\mathbf{R}_1) + C_2 \exp(\mathrm{i}\mathbf{K}.\mathbf{R}_2)\}|\text{Rb } 63\mathrm{p}_{3/2}\rangle|0_{\omega'}\rangle_1|0_{\omega'}\rangle_2|0_{\omega}\rangle.\end{aligned}$$

Now, one can expect constructive interference.
One can immediately see that

$$\begin{aligned}|\text{Scatt.State} -\rangle &= |\text{Cav-1 Outgoing}\rangle - |\text{Cav-2 Outgoing}\rangle \\ &= \{C_1 \exp(\mathrm{i}\mathbf{K}.\mathbf{R}_1) - C_2 \exp(\mathrm{i}\mathbf{K}.\mathbf{R}_2)\}|\text{Rb } 63\mathrm{p}_{3/2}\rangle|0_{\omega'}\rangle_1|0_{\omega'}\rangle_2|0_{\omega}\rangle\end{aligned}$$

The scheme shows antifringes with a minimum instead of a maximum.

If one asks for the path followed by the system, the answer has the two sides. For the scattered state |Scatt.State⟩, both slits are used with equal weights. For the material system, there cannot be a simple answer: quantum mechanics handle quantum states not the path(s) followed by the material system sustaining the quantum state. But, for sure, the material system must be present at the detecting surface.

Which way does it take the material system through the system? Again, this is not a question that can be answered by abstract QM. Yet, hidden variable model can give an answer, but this is not the issue here.

The above case corresponds to shutters closed; now, we look at *shutters open*.

Thus, the system is described by linear superpositions over the cavities with base states: $|+\rangle$ and $|-\rangle$. However, as we introduce interactions with the cavity coupled to devices that can inform whether a photon is left in one cavity or the other one can first try a simple analysis when one photon is left behind. The statement "photon left behind" is understood as a quantum state, having amplitude one at the base state indicating that such is the case.

For the sake of simplicity, assume that one ω'-photon is left at Cav-1. The symmetry is broken so we can apply a construction using the channel concept. For Cav-1 the quantum state can be constructed with a simplified model for which only $\mathrm{d}_{5/2}$ states are given the possibility to show nonzero amplitudes. The outgoing channel looks like:

$$\begin{aligned}|\text{Cav-1 Outgoing}\rangle &= [0_1\ 0_2\ C_3\ 0_4\ 0_5\ 0_6\ 0_7\ 0_8\ 0_9\ 0_{10}] \\ |\text{Cav-2 Outgoing}\rangle &= [0_1\ 0_2\ 0_3\ 0_4\ 0_5\ 0_6\ C_7\ 0_8\ 0_9\ 0_{10}]\end{aligned}$$

These quantum states are orthogonal. And lack of sameness permits concluding that there will be no interference figure at the measuring surface. That's it. There is no need for an observer to check it; the quantum state suffices. But article by Scully et al. is much more challenging.

6.2. *Welcher Weg* setup

Scully et al. [15] have suggested still one thought setup that taken together with the micromaser *welcher Weg* detector would permit testing some issues in the orthodox quantum measurement model. Here, we construct the quantum states for the cases presented in that paper and discuss some of the measuring alternatives. To this end we use the extended base set presented above.

Case 1: Shutters are closed.

A photon is left behind without specifying in which cavity it is; this ensures presence but not localizability. The quantum state is then a linear superposition of states with one photon free:

$$
\begin{aligned}
|+\rangle &= \left(\frac{1}{\sqrt{2}}\right)(|\text{Cav-1}(10)\rangle + |\text{Cav-2}(01)\rangle) \\
&\rightarrow [0_1\ \ 0_2\ \ C_3\ \ C_4\ \ 0_5\ \ 0_6\ \ C_7\ \ C_8\ \ 0_9\ \ 0_{10}] \\
|-\rangle &= \left(\frac{1}{\sqrt{2}}\right)(|\text{Cav-1}(10)\rangle - |\text{Cav-2}(01)\rangle) \\
&\rightarrow [0_1\ \ 0_2\ \ C_3\ \ C_4\ \ 0_5\ \ 0_6 - C_7 - C_8\ \ 0_9\ \ 0_{10}]
\end{aligned}
$$

A free-photon state possibility obtains when $C_4 = C_8 = 0$ and both cavity states are given as:

$$
\begin{aligned}
|+\rangle+|-\rangle \rightarrow [0_1\ 0_2\ C_3\ C_4\ 0_5\ 0_6\ 0_7\ 0_8\ 0_9\ 0_{10}] &= |\text{cav-1}\rangle|0_{\omega'}\rangle_2\ |0_\omega\rangle \\
&= \{C_3|\text{Rb } 61\text{d}_{5/2}\rangle|1_{\omega'}\rangle_1\}|0_{\omega'}\rangle_2|0_\omega\rangle \\
|+\rangle-|-\rangle \rightarrow [0_1\ 0_2\ 0_3\ 0_4\ 0_5\ 0_6\ C_7\ C_8\ 0_9\ 0_{10}] &= |\text{cav-2}\rangle|0_{\omega'}\rangle_1\ |0_\omega\rangle \\
&= \{C_7|\text{Rb } 61\text{d}_{5/2}\rangle|1_{\omega'}\rangle_2\}|0_{\omega'}\rangle_1|0_\omega\rangle.
\end{aligned}
$$

Both possibilities have equal weights when shutters are closed so that one reconstitute the linear combinations for the $|+\rangle$ and $|-\rangle$ states.

Case 2: Shutters open.

What may happen if the photon left "behind" is detected and absorbed by a detector?

The answer may be constructed as follows. Again, amplitudes $C_4 = C_8 = 0$ and a photon state are left behind and, by symmetry $C_3 = C_7 = 1/\sqrt{2}$:

$$
\begin{aligned}
|3+7\rangle &= [0_1\ \ 0_2\ \ 1/\sqrt{2}_3\ \ 0_4\ \ 0_5\ \ 0_6\ \ 1/\sqrt{2}_7\ \ 0_8\ \ 0_9\ \ 0_{10}] \\
&= 1/\sqrt{2}_3|\text{Rb } 61\text{d}_{5/2}\rangle|1_{\omega'}\rangle_1 + 1/\sqrt{2}_7|\text{Rb } 61\text{d}_{5/2}\rangle|1_{\omega'}\rangle_2 \\
|3-7\rangle &= [0_1\ \ 0_2\ \ 1/\sqrt{2}_3\ \ 0_4\ \ 0_5\ \ 0_6 - 1/\sqrt{2}_7\ \ 0_8\ \ 0_9\ \ 0_{10}] \\
&= 1/\sqrt{2}_3|\text{Rb } 61\text{d}_{5/2}\rangle|1_{\omega'}\rangle_1 - 1/\sqrt{2}_7|\text{Rb } 61\text{d}_{5/2}\rangle|1_{\omega'}\rangle_2.
\end{aligned}
$$

First, there is need for one "free photon" so that we have to produce a transitions between $|3+7\rangle$ and $|3-7\rangle$.

If detection breaks the symmetry, no interference can be expected.

In case of nondetection, the interaction produces either state. Once a given state is produced, both beams have a full degree of sameness. If the state to be sensed corresponds to $|3+7\rangle$, there will be interference, whereas if it is $|3-7\rangle$, there is a minimum in between the shadows of the slits instead of a maximum.

For an experiment where these quantum states are produced with equal weights, no interference will show up. If one could "distillate" the information yielding separate registers so that one could display the separate states, then coherence for each separate state type will be recovered. This situation relates to Chapman's et al. experiment [16].

Now, we come back to article by Scully et al., we quote:

> *"Consider now the arrangement of the atomic beam/micro maser system indicated in", Fig. 3a,.... "imagine that on opening the shutters, light will be allowed to interact with the photoreceptor wall. In this way the radiation, which is left either in the upper or in the lower cavity, depending upon whether the atom traveled along the upper or lower path, will now be absorbed and the "memory of passage" (the welcher Weg information) could be said to be erased."*
> *"Do we now (after erasure) regain interferences fringes? The answer is yes, but how can be that?"*

The answer in terms of internal quantum states is less evident. For, assume the photon left is now absorbed, and then the quantum state of the material support has not been necessarily restituted. This issue is examined now. We need supplementary base states $|\mathrm{Rb}\ 61\mathrm{d}_{5/2}\rangle|0_{\omega'}\rangle_1$ and $|\mathrm{Rb}\ 61\mathrm{d}_{5/2}\rangle|0_{\omega'}\rangle_2$. Now, if memory passage is erased and we get back the linear superpositions $|3+7\rangle$ and $|3-7\rangle$ that are equally possible, then we are back to the situation where either quantum state can be detected. This issue is now examined.

6.3. Quantum eraser

There is something more extraordinary in Ref. [15]. These authors suggested a correlation between the state of detector and the presence of fringes and antifringes.

Let us quote the text from Ref. [15]: "*...a, Quantum eraser configuration in which electro-optic shutters separate microwave photons in two cavities from the thin-film semiconductor (detector wall) which absorbs microwave photons and acts as a photodetector. b, Density of particles on the screen depending upon whether a photocount is observed in the detector wall ('yes') or not ('no'), demonstrating that correlations between event on the screen and the eraser photocount are necessary to retrieve the interference pattern.*"

In other words, the observer seems to be playing an important role. This contradicts all we have said so far. We will discuss this issue now.

Take the case where *a photocount is observed in the detector wall ("yes")*, the quantum state is now of the form $|3-7\rangle$ and associates with a label state $|\lambda=-1\rangle$. Store the quantum state by collecting the position of the impact event; save the data set. If no-photocount is detected, the impact position of datum is stored with label $|\lambda=+1\rangle$, indicating that this event is associated with state $|3+7\rangle$. This process corresponds to "distillation" of quantum states into two exclusive data sets that can now be independently displayed.

The key to the problem is to understand that the correlations of any kind were done at full quantum level once ω'-photon detection took place and nowhere else.

Thus, there is no need to force the statement indicating that "*correlations between event on the screen and the eraser photocount are necessary to retrieve the interference pattern*" because they are not.

All the weirdness laid onto Quantum Mechanics account is actually due to enforcing a classical particle-wave picture.

The analysis within the particle model interpretation is developed by Scully et al. [15]. We suggest the reader to carefully study Ref. [15]. Here, we quote the result most relevant for the present discussion: "*...we find that the interference fringes disappear once we have which-path information, but we conclude that this disappearance originates in correlations between the measuring apparatus and the system being observed. The principle of complementarity is manifest although the position-momentum uncertainty relation plays no role*."

With hindsight gathered above with a filter device labeling state $|3-7\rangle$ with $\lambda=-1$ value so that only events with this detection signature are registered anti-interference will show up. Proceeding in similar way for $\lambda=+1$ for another detecting surface, we get $|3+7\rangle$ as selected state. The results do not depend upon interaction with the detector.

The interpretation of QM formalism in terms of the complementarity principle leads to puzzling situations; the particle-wave view seems to be fundamentally flawed to the extent classical concepts do not belong to an interpretive framework to quantum mechanics.

In QM without particle interpretation, the statement: *interference fringes disappear once we have which-path information* has truth content. The statement: *disappearance originates in correlations between the measuring apparatus and the system being observed*, is not fully granted. From the present stand point, it is false.

For, the total quantum state as seen at the detecting screen if no distillation process applies is a mixture related to the alternatives "eraser photon yes or no."

The fringes or antifringes will appear once a sorting out collects the two classes of quantum states in separate groups. There is no special correlation between the measuring apparatus and *the system being observed* for the simple reason that all results are there but mixed.

6.4. Entanglement issues

The preceding discussions raise, beyond the particular cases, important issues. A few are described now.

Quantum and classic theoretic frameworks relies on coordinate sets, and the origin of which is defined with respect to space-time inertial frame characteristic of special relativity framework. A clear-cut correspondence is never a transparent endeavor; the origin of an I-frame designates a junction point. Care is required to differentiate real space from configuration space situations. Yet quantum interactions between inner and outer states couple both levels as mentioned earlier, for example, EPR entanglement cases.

Quantum entanglement between matter-sustained quantum states and those presenting EM quantum states is one basic ingredient in discussing, for example, Eq. (31) in Scully et al. atom interferometer analysis. Also, in Section 4.2, a quantized EM field was used. Some key issues were not examined there; below focus is on one issue concerning laboratory (real)/Fock space [5] connection.

In laboratory space, energy can and must be traded, measured, and spilled (entropy). In Hilbert/Fock space, energy is used as a label.

Consider the entangled base states: $|E_{\rm k}; 0_\omega\rangle$ and $|E_{\rm k'}; 1_\omega\rangle$ with $E_{\rm k'}\rangle E_{\rm k}$. In laboratory space, uncorrelated direct product states $|E_{\rm k}\rangle \otimes |0_\omega\rangle$ and $|E_{\rm k'}\rangle \otimes |1_\omega\rangle$ can stand as base states for independently prepared EM and material-sustained quantum states, namely, $|\Psi, t'\rangle \otimes |{\rm EM}, t'\rangle$ for times $t'\rangle t_o$. From the infinite possibilities embodied here, one select those that might be relevant for describing a source of an EM system and the location for a given I-frame.

An entangled quantum state is generically designated as $|\Psi; {\rm EM}, t\rangle$. Base states look like $|E_{\rm k}; 0_\omega\rangle$ or $|E_{\rm k'}; 1_\omega\rangle$; here, the EM field and the quantum state bases are not separable. It is a common situation to get an energy shell domain where energy labels add up to a fixed energy value within $\pm\Delta E$. Linear superpositions in an energy shell obtain once time-dependent interaction operators in the combined Hilbert–Fock space are included. Schrödinger's time evolution operates if and only if there is no one spontaneous emission rooted at the entangled state. Such is the hypothesis behind Scully et al. case.

Entangled states through appropriate interactions can be controlled and forced to exchange energy with surroundings. Because a result of such interactions is a new quantum state, time evolution starts up anew.

Experimentally what can be controlled (modify) is information that is being transported by quantum EM systems through phase modulators and/or elastic scattering; for example, see Wheeler's cases discussed earlier. Otherwise, emitters (sources) and receptors (sinks) would act as toll bridge to control exchanges of energy providing an example of Fence processes. As we discussed for Tonomura's experiment, events carry information on a quantum state. Once accidental events are put aside, cumulative information yields a picture as it were of a quantum state.

Let us introduce an energy shell base set and include nonentangled bases to discuss more concrete issues at a Fence:

$$(\ldots |E_{k'}\rangle \otimes |1_\omega\rangle \quad |E_{k'}; 1_\omega\rangle \quad |E_k; 0_\omega\rangle \quad |E_k\rangle \otimes |0_\omega\rangle \ldots)$$

The generic amplitudes are given as

$$[\ldots C_{k'+1\omega}\ C_{k'\cap 1\omega}\ C_{k\cap 0\omega}\ C_{k+0\omega} \ldots].$$

For a quantum state defined by $C_{k'+1\omega} = 1$ with $k' =$ (Ground state) and all other amplitudes zero, one identifies cases of photon states that may or may not interact with the ground state. I-frame localizes the quantum state so that one takes this case to represent an impinging light field:

$$[\ldots 1\ 0\ 0\ 0 \ldots].$$

The entangled state is generically given as linear superpositions:

$$[\ldots 0\ C_{k'\cap 1\omega}\ C_{k\cap 0\omega} 0 \ldots]$$

Among all possible entangled states, one can select two classes of interest for us:

$$[\ldots 0\ 1\ 0\ 0 \ldots] \quad \text{and} \quad [\ldots 0\ 0\ 1\ 0 \ldots]$$

The latter describes entanglement of the zero-point energy state with the "excited" state sustained by a material system; the former corresponds to ground state entanglement with a photon field.

Spontaneous emission relates the quantum states:

$$[\ldots 0\ 1\ 0\ 0 \ldots]\ (\rightarrow)\ [\ldots 0\ 0\ 0\ 1 \ldots]$$

It is linear momentum and direction of emission that cannot be predicted by quantum theory. The massive nature of the I-frame and the high density of states at outgoing EM channel permit understanding why it is possible to calculate all possibilities but not isolated events.

In laboratory space, the state $[\ldots 0\ 0\ 0\ 1 \ldots]$ is localized at the I-frame that would act as the emission source. A detector at a given distance and position may or may not detect the energy equivalent to one quantum, yet a quantum-mechanical interaction is ensured.

The entangled state, viz. $[\ldots 0\ C_{k'\cap 1\omega}\ C_{k\cap 0\omega}\ 0 \ldots]$ can be used through stimulated emission to generate a photon state coherent to an external photon state by using an appropriate cavity. Lasers for instance are based on such processes.

The similar type of entangled state can be a starting point for internal changes leading to different quantum states sustained by the I-frame material; dark states are useful in many respects.

In Chemistry, a covalent bond corresponds to an entangled state sustained by two-electron state. An entangled state $|\Psi; \mathrm{EM}, t\rangle$ given as a linear

superposition including entangled and nonentangled base states is sufficient to theoretically handle chemical process as we have recently shown [21]. Quantum-mechanical frameworks for studying enzyme catalysis become possible [22].

Special theory of relativity introduces a fundamental measure of time through signals propagating at a speed independent from the state of uniform motion of sources and sinks. The signal corresponds to electromagnetic radiation (e.g., light). In vacuum, the speed of light is constant.

A second element comes from electrodynamics involving the product of wavelength and frequency: $\lambda\nu = c$; both factors can be modulated. But once the value of one of them is determined, the other is fixed; their product stands for a universal constant.

The third element originates from quantum physics relating an electromagnetic frequency ν to an energy difference between energy eigenstates, quantum base states (N. Bohr relation); see discussion section and Section 4.2. These elements allow for the introduction of length and time standards.

One of the problems confronting the development of quantum physics relates to a view that theory would describe material (natural) objects: position, speed, and physical properties directly coupled to things in real space. This latter is seldom given a precise definition.

Therefore, historically, an interpretation of the theoretical structure became necessary and influenced by the particle view; in this context, one finds statements of the kind: a material system, say, one electron is in (or occupies) a specific (base) state; linear superpositions are reduced or collapsed whenever a measurement takes place; the statement, Schrödinger cat is either alive or dead or in a linear superposition where the cat is both dead and alive does not make sense; a real object cannot be seen in that manner. For sure, this paradigm must be revised, and if it is to be used at all, it must be done with caution. Philosophy has been one of the domains of the culture in deep crisis all along the twenty century. Wittgenstein, Heidegger, Carnap, and others [23, 24] have severely criticized the philosophies of knowledge that, on the other hand, are usually claimed to be required to understand QM [2, 3, 6, 9]; refer pages 519 onward from Ref. [3]; in particular, criticisms of subject-object philosophy that is a predominant view in our Western societies. This view underlies current interpretations of QM [9, 25]; this chapter represents an effort to move beyond this descriptive level by clearly showing the possibility to extend the concept of quantum state.

7. DISCUSSION

The theoretic model featuring physical quantum states presented here was used to examine several aspects of physical quantum measurements. The physical model replaces ontological (metaphysical) and knowledge-theory

based ideas dominating and prevailing approaches as discussed by Malin [6]. Most, if not all, of putative weirdness imputed to QM can be removed as classical physics pictures of particles and waves are replaced by physical elements belonging to a quantum world, that is, quantum states in Hilbert space. Yet, recording–reading of quantum states relate to events located in laboratory (real) space where energy and linear/angular momentum are conserved quantities; one must extend the scheme to describe laboratory situations. One of the junctions between Hilbert and laboratory space is identified in this work by the old N. Bohr's postulate qualified by the amplitude at the root state: $E_i - E_j$ being a difference of energy eigenvalues in Hilbert space. This is mapped to energy in real space through an electromagnetic radiation ω, namely, $E_i - E_j = \hbar\omega$.

The present approach conflicts with Copenhagen view tenets quoted in Section 3.2. The concept of object is replaced by the elementary constitutive materials, viz. electron and nuclei sustaining quantum states. The parameters defining charge spin and mass enter those differential equations used to calculate model quantum states (time-independent eigenvalue Schrödinger equation or relativistic equations [5]).

Registering on a screen, an individual spot, as seen in Scully et al. model, epitomizes (in the standard approach) an individual measurement (Cf. Ref [11]). If one focuses only on the spots, individual results then look purely random without any possibility of detailed causal explanation [17]. From the perspective developed here, the spots will pattern the quantum state one sets up to measure. Energy in the form of quanta is required to imprint the measuring device. The result is an ordered picture of a quantum state emerging from the spots aggregate in laboratory (real) space. The event also includes information on the probing apparatus with associated noise.

The energy difference implied in Eq. (3) must be traded with an external source. The electromagnetic field must be quantized to serve as a source effective in measuring. This implies participation of at least four composite base states examined in Section 4.2. Temporal trapping of a photon energy that fulfills Bohr's relationship, $\hbar\omega = (\varepsilon_k - \varepsilon_{k'})$, is made through an entangled state (Cf. Section 6.4). The wavefunction is referred to an I-frame that provides real-space localization, and in this sense, this process has a local character. Yet, there is no jump. The equivalent of a spontaneous photon emission is inseparable to the de-excitation leading to the root state involved in the process that in the present case is the ground state sustained by the material system; energy is conserved.

Light, or more generally electromagnetic radiation, travels as a quantum state. It is produced as a quantum state; it can be a scattering state from a source. It is detected by quantum states sustained by material systems. At these two instances, energy is exchanged in quanta according to Planck's law eliciting granularity (clicks). Time spent to travel between a source and detector corresponds to the distance divided by the speed of light. It is a zero rest mass system. Diffraction and interference produced by

interactions (scattering) with material systems express the quantum nature of EM radiation at a laboratory level.

Entanglement is a phenomenon involving quantum states. This is true for material (EPR) systems. It is also true for EM radiation. There are quantum-physical devices that can produce entangled EM quantum states. A two-photon entangled state may or may not show a spherical symmetry; such state correlates responses that may appear at antipodes detectors or, depending on the generating source at definite angles. The detector produces a quantum transition that put amplitudes over asymptotic states. Being a quantum state sustained by a material support, such state can be modulated by external devices such as glass fibers leaving entanglement unaltered thereby protecting the state in a way similar to the collimators in Scully et al. experiment presented above. Because a light quantum state has no space degree of freedom except for detection/emission sources, two-photon entanglement can be detected at any distance one wants to put measuring apparatuses. Anton Zeilinger and his coworkers have demonstrated real space–independent entanglement conducted in various locations, for example, a pair of mountain peaks in the Canary Islands [27].

Problem of borders: this is a most debated issue put up by Arndt et al. in form of a question [26]: "... where exactly is the boundary between the quantum and classical worlds—if, indeed, there is one?" This problem must be discussed with care. A tentative answer to this question would be: there seems to be no absolute boundary. If there were one, this would be located in real space; but consequently noncommensurability prevents such statement to be true.

Sheldon Goldstein [25] writes: "It seems clear that quantum mechanics is fundamentally about atoms and electrons, quarks and strings, and not primarily about those particular macroscopic regularities associated with what we call measurements of the properties of these things."

Classical physics categories are not sufficient to describe phenomena in the realm of quantum physics. Thus, objects wouldn't exist in a superposition of different states; molecules as massive objects do not interfere in a quantum sense. But what about experiments described and discussed by Arndt et al. [26, 28]? We comment the issue below.

Any quantum system can be associated to an I-frame; thereby, internal and "external" (I-frame) quantum states can be determined or at least observed as done in astronomy. Probing (measuring) a quantum system breaks Hilbert space-time evolution thereby preparing a new quantum state. This latter can be used to detect the result due to probing. See Ref. [29] for an illustration. Gravitation is a prototype of classical effects. From neutron interference spectroscopy gravitation effects on quantum states are well documented.

Come back to the model from EPR in Section 5.2 to "quantize" the situation; the inclusion of a sufficiently large Box, with periodic boundary conditions, allows for box-Hilbert space construction. It is sufficient to get

a diffracting grating of dimensions appropriate to the I-frame system to describe interactions leading to the diffracted quantum state. This latter plus the incident quantum state lead to diffraction motifs as discussed here. The quantum behavior is not related to mass or complexity of the material system sustaining the quantum states. The quantum states *sustained* by C_{60} offers a beautiful example [28] of quantum behavior; again, the quantum state is not a real predicate of the material system, yet a presence of the latter is required as extensively examined in this chapter. The concept of being sustained by a material system does not mean that this latter occupies the quantum state. This is a strict requirement.

For the model discussed in the EPR section there are no limits to the quantum world. If limits there are, they are put forward by limitations in our probing/detection apparatuses. In this context, use of language must be careful: separate what belongs to Hilbert and Fock spaces from what belongs to I-frame classical physics states; the concept of Fence was introduced just to remind of such situations. With some minor "language editing" the discussion presented by Zeilinger and coworkers [26] on Talbot–Lau interferometer applications is enlightening.

In "real" life: objects there are; who could deny this matter of fact? But for quantum physics they are either, sources to scattered radiation that bring forth elements required to describe their appearances (or nature), or they act as receptors once the corresponding entangled state evolves; for a given cross section the EM radiation scattered by the surface corresponds to a physical quantum state. The detector is activated by physical quantum states. Because the surface should emit in all accessible directions (if sufficient energy is available), the *same* quantum states can be registered at different points in real space; the observer does not play any special role then. The scattered state is independent from any experiment planned to detect it. The receptor interacts with incident quantum states bringing information about the scattering source.

Yet, the talking in terms of particles and waves goes on unabated [13, 19, 27]. Such is the case for the experimental realization of Wheeler's delayed-choice "gedanken" experiment reported by Jacques et al. [19]. The conclusion we get is exactly the opposite than the one reported by them. What this beautiful experiment shows, according to us, is the incompatibility of classical physics categories concerning objects, photons as particles in this case, and confirming the quantum nature of the EM radiation [30]. A similar conclusion obtains after analyses of the model reported in Ref. [15]. Of course, if one insists in wave/particle duality mantra to describe quantum-physical experiments, one would have to live with QM "weirdness" and hear again Einstein's observations quoted before. We have come to a point in time where we have to move on from the object/subject worldview and start to accept not only the novelty of quantum physics; also that classical descriptions are useful, but not apodictic.

The merger is between Special Theory of Relativity and abstract quantum states through rigged Hilbert spaces; the inertial frame is used to set up an abstract configuration space in laboratory space. At the abstract level, both formalisms are required.

But stakes are much higher. If quantum computers are to be one day constructed [27, 29, 31, 32], a proper understanding of quantum physics, including entangled states [32], is mandatory. Entanglement between objects, be they microscopic or macroscopic, does not make sense: objects are classical entities with properties independent of any measurement, and this is so by definition. However, entanglement between quantum states sustained by macroscopic materials is more natural extension to present quantum views.

Quantum mechanics predicts the quantum state (all possibilities at once) but not individual events. Independent collections of such events do reflect quantum states as extensively discussed in this paper. The quantum state does not represent the material system that as a matter of theoretical fact only sustains it. This result may be difficult to swallow within a probabilistic approach. But this is the way it is in a quantum physics where quantum states for quantum measurements occupy center stage. Individual quantum events elicit targeted quantum states; we have to design the measuring device to determine just the quantum state that has been prepared. Statistical predictions are not compulsorily required; statistics gather a sufficiently large set of events to display the quantum state pattern (e.g., Tonomura's experiment).

An important question is in place before closing this paper: Did something fundamentally new appeared since Gimo' Nobel Symposium?

A tentative answer to this question is affirmative. As noted by Dowling and Milburn [33], we are moving from passive observers to active experimenters: "In the second quantum revolution, we are actively employing quantum mechanics to alter the quantum face of our physical world."

Now, quantum states are sustained by material systems, but the material substrate is not occupying a quantum state. Hence, one can change the quantum states while maintaining invariant the material support: this is just what Chemistry is all about [21, 22]; see also [34] where quantum states for quantum chemistry beyond potential energy surfaces are examined. Time evolution of a quantum state interacting with scattering sources in a quantum manner requires presence but not localization of the material substrate. Such concepts were not yet developed at the time of Gimo's meeting.

Actually, the line of thought retained clearly indicates that objects are no longer considered as constituents of the experiments; quantum states do.

Thus, any quantum system that can be localized would play the role of a measuring device or as a device able to be used and/or integrated with others in more involved circuitry. The concept of quantum states for quantum measurements may help developing a rational quantum-physical framework with no spooky action at a distance, etc. Extensions leading to

descriptions of chemical processes in terms of a rational quantum-physical framework may help in a better understanding of Chemistry and related domains.

ACKNOWLEDGMENTS

The author thanks Erkki Brändas for a number of comments and suggestions that have helped improve this paper. The ideas presented here started from the discussions with Henk Fidder, the author is most indebted to him. The author would specially like to thank Uppsala University and the Department of Physical Chemistry and Analytical Chemistry for all resources provided at his disposal.

REFERENCES

[1] L.E. Ballentine, Quantum Mechanics: A Modern Development, World Scientific, Singapore, 1998.
[2] J. von Neumann, Mathematical Foundations of Quantum Mechanics, Princeton University Press, New Jersey, 1955.
[3] R. Omnès, The Interpretation of Quantum Mechanics, Princeton University Press, New Jersey, 1994.
[4] H. Fidder, O. Tapia, The quantum measurement problem, Int. J. Quantum Chem. 97 (2004) 670–678.
[5] O. Tapia, Quantum Physical Chemistry, 2010; Electronic version: http://www.fki.uu.se/Personal/tapia-orlando/index.shtm.
[6] S. Malin, What are quantum states? Quantum Inf. Proc. 5 (2006) 233.
[7] M. Ozawa, Quantum measuring processes of continuous observables, J. Math. Phys. 25 (1984) 79–87.
[8] W.M. de Muynck, Preparation and measurement: Two independent sources of uncertainty in quantum mechanics, arXiv:quant-ph/9901010v1.
[9] F. Laloë, Do we really understand quantum mechanics? Strange correlations, paradoxes, and theorems, Am. J. Phys. 69 (2001) 655–701.
[10] L.E. Ballentine, The statistical interpretation of quantum mechanics, Rev. Mod. Phys. 42 (1970) 358–381.
[11] E.P. Wigner, The problem of measurement, Am. J. Phys. 31 (1963) 6–15.
[12] A. Tonomura, Recent advances in electron interferometry, Ann. NY. Acad. Sci. 755 (1995) 227–240.
[13] E.B. Karlsson, E. Brändas, Modern studies of basic quantum concepts and phenomena, Phys. Scripta T76 (1998) 7. The papers were published also in book form by World Scientific Publishing Co.Pte.Ltd.
[14] R.P. Feynman, A.R. Hibbs, Quantum Mechanics and Path Integrals, McGraw-Hill, Inc., New York, 1965.
[15] M.O. Scully, B.-G. Englert, H. Walther, Quantum optical tests of complementarity, Nature 351 (1991) 111–116.
[16] M.S. Chapman, T.D. Hammond, A. Lenef, J. Schmiedmayer, R.A. Rubenstein, E. Smith, et al., Photon scattering from atoms in an atom interferometer: Coherence lost and regained, Phys. Rev. Lett. 75 (1995) 3783–3787.

[17] A. Bohr, B.R. Mottelson, O. Ulfbeck, The geometric and atomic world views, PNAS 105 (2008) 17301–17306.
[18] J.A. Wheeler, Law without law, in: J.A. Wheeler, W.H. Zurek, (Eds.), Quantum Theory and Measurement, Princeton University Press, NJ, 1984, p. 182–213.
[19] V. Jacques, E. Wu, F. Grosshans, F. Treussart, Ph. Grangier, A. Aspect, et al., Experimental realization of Wheeler's delayed-choice gedanken experiment, Science 315 (2007) 966–968.
[20] P. Knight, Quantum mechanics: Where the weirdness comes from, Nature 395 (1998) 12–13.
[21] O. Tapia, Quantum linear superposition theory for chemical processes: A generalized electronic diabatic approach, Adv. Quantum Chem. 56 (2009) 31–93.
[22] O. Tapia, Beyond standard quantum chemical semi-classic approaches: Towards a quantum theory of enzyme catalysis, in: P. Paneth, A. Dybala-Defratyka (Eds.), Kinetics and Dynamics, From nano- to bio-scale, Challenges and advances in computational chemistry and physics 12, Springer Science, Dordrecht, 2010, p. 267–298.
[23] M.A. Friedman, Parting of the Ways: Carnap, Cassirer, and Heidegger, Open Court, Chicago, 2000.
[24] A. Shimony, Philosophical and experimental perspectives on Quantum Physics, in: D. Greenberger, W.L. Reiter, A. Zeilinger, Epistemological and Experimental Perspectives on Quantum Physics, Kluwer Academic Publishers, Dordrecht, 1999, p. 1–18.
[25] Sh. Goldstein, Quantum theory without observers-part one, Phys. Today (1998) (March) 42–46; Part two (April) 38–42.
[26] M. Arndt, K. Hornberger, A. Zeilinger, Probing the limits of the quantum world, Phys. World 18 (2005) 35–40.
[27] A. Zeilinger, Dance of the Photons, Farrar, Straus and Giroux, New York, 2010.
[28] M. Arndt, O. Nairz, J. Vos-Andreae, C. Keller, G. van der Zouw, A. Zeilinger, Wave-particle duality of C_{60} molecules, Nature 401 (1999) 680–682.
[29] A.J. Berkeley, H. Xu, R.C. Ramos, M.A. Gubrud, F.W. Strauch, P.R. Johnson, et al., Entangled macroscopic quantum states in two superconducting qbits, Science 300 (2003) 1548–1550.
[30] W.E. Lamb, W.P. Schleich, M.O. Scully, C.H. Townes, Laser physics: Quantum controversy in action, Rev. Mod. Phys. 71 (1999) S263–S273.
[31] Yu.A. Pashkin, T. Yamamoto, O. Ostafiev, Y. Nakamura, D.V. Averin, J.S. Tsai, Quantum oscillations in two coupled charge qubits, Nature 421 (2003) 823–826.
[32] A. Wójcik, Defining entanglement, Science 301 (2003) 1182.
[33] J.P. Dowling, G.J. Milburn, Quantum technology: The second quantum revolution, Phil. Trans. R. Soc. London, A 361 (2003) 1655–1674.
[34] R. Crespo, M.-C. Piqueras, J.M. Aullo, O. Tapia, A theoretical study of semiclassic models: Towards a quantum mechanical representation of chemical processes, Int. J. Quantum Chem. 111 (2011) 263–271.

CHAPTER 3

Molecular Properties through Polarizable Embedding

Jógvan Magnus Haugaard Olsen[a] and **Jacob Kongsted**[a]

Contents

1. Introduction 108
2. Theoretical Basis for Polarizable Embedding 109
   2.1. Polarizable embedding applied to density functional theory 118
   2.2. Polarizable embedding within response theory 118
   2.3. Calculation of nuclear magnetic shielding tensors for embedded molecules 130
3. Results and Discussion 132
   3.1. The accuracy of the embedding potential: A hierarchy of force fields 133
   3.2. Excitation energies 136
   3.3. Nuclear magnetic resonance chemical shifts 137
   3.4. Second hyperpolarizabilities 138
4. Conclusion 140
Acknowledgment 141
References 141

Abstract We review the theory related to the calculation of electric and magnetic molecular properties through polarizable embedding. In particular, we derive the expressions for the response functions up to the level of cubic response within the density functional theory-based polarizable embedding (PE-DFT) formalism. In addition, we discuss some illustrative applications related to the calculation of nuclear magnetic resonance parameters, nonlinear optical properties, and electronic excited states in solution.

[a] Department of Physics and Chemistry, University of Southern Denmark, Odense M, Denmark
E-mail address: kongsted@ifk.sdu.dk (Jacob Kongsted)

Advances in Quantum Chemistry, Volume 61
ISSN 0065-3276, DOI: 10.1016/B978-0-12-386013-2.00003-6

1. INTRODUCTION

Accurate modeling of general molecular properties, for example properties related either to molecular ground or excited states, of large molecules or molecular samples currently represents one of the greatest and most significant challenges to modern quantum chemistry. Direct determination of molecular properties, without relying on any parametrized or fitting procedures, requires the use of quantum mechanics. However, from a chemical point of view, it is well recognized that in many cases, the physical changes, for example a chemical reaction or a physical absorption of light, are well localized within some part of the total molecular system. This fact gives rise to the introduction of molecular subsystems in the sense that one subsystem may be more important to describe accurately than another and specifically that the use of quantum mechanics might only be needed in one or a small number of these subsystems. This is, for example, the case when dealing with a solute–solvent system or in more general terms a molecule subjected to a structured environment. In these cases, the part of the system not directly involved in the electronic processes can be described effectively using, for example, classical mechanics. Even though linear scaling techniques are becoming more advanced and may be used to describe larger and more complex systems, effects due to conformational sampling still persist and may become more important as the size of the molecular system is increased. In fact, in many cases, it is mandatory to include effects of nuclear dynamics in combination with the electronic structure in order to pursue a direct comparison with experimental data.

With the aim of addressing large molecular systems, we review a recently developed focused model based on the combined use of quantum mechanics and molecular mechanics (QM/MM) [1–5]. Our approach uses a fully self-consistent polarizable embedding scheme which we denote the PE model [6, 7]. The PE model is generally compatible with any quantum chemical method, but here we focus on its combination with density functional theory (DFT) and time-dependent density functional theory (TD-DFT). The PE method is based on the use of an electrostatic embedding potential which is modeled by localized multipole moment expansions of the molecules, or more generally the fragments, located in the classically treated part of the system. However, the electrostatic embedding potential only accounts for the permanent charge distribution of the environment, and in order to account for many-body induction effects, that is, the polarization of the environment both internally and by the quantum mechanically treated subsystem, we assign a set of localized anisotropic dipole polarizability tensors at the expansion centers giving rise to an induced charge distribution in the environment. The latter is represented in terms of induced dipoles that are determined based on classical response theoretical methods [8]. The localized multipoles and polarizabilities are determined using quantum mechanical methods. The functional form of the polarizable

embedding potential shows some similarities to that of the EFP method by Gordon et al. [9–11]; however, the strength of the PE scheme is the ability to describe excited states and general molecular properties on the same footing as the ground state. This is achieved through a formulation of the PE model within the context of time-dependent quantum mechanical response theory. The PE-DFT model has been implemented up to and including cubic response [6]. This allows for the evaluation of, for example, vertical electronic excitation energies and the related one-, two-, and three-photon transition moments. Furthermore, electronic second-, third-, and fourth-order ground state molecular properties, such as dynamic (second-hyper)polarizabilities, are available, as are excited state first- and second-order molecular properties. In addition, magnetic properties, such as magnetizabilities, nuclear shielding constants, and spin–spin coupling constants, may also be computed, using gauge invariant atomic orbitals (GIAOs) when needed.

Inclusion of nuclear dynamics is of crucial importance especially for larger molecular samples, for example, solutions. Nuclear dynamics is in the present method accounted for by combining the PE scheme with classical molecular dynamics (MD) simulations. This is done in a sequential manner, that is, we first perform MD simulations, and then using an appropriate number of configurations extracted from the MD simulations, we simulate the electronic structure. Thereby, we neglect the effect of the electronic structure on the configurations, and the accuracy of our approach relies first of all on the use of an accurate classical potential to be used for the MD simulations. Inclusion of explicit polarization into force field methods have in recent years received much attention [12]. The current status is that polarization may contribute significantly and specifically to specific solvation processes. For example, polarization causes a significant increase in the dipole moment of a water molecule in the liquid state and may in addition constitute as much as 50% of the total interaction energy [13]. An important point that is followed within the present PE scheme is to be able to calculate all properties characterizing the intermolecular interactions by quantum mechanical methods.

In the following, we will first present a formal derivation of the general PE equations rooted in intermolecular perturbation theory. Next follows a derivation of the PE scheme within the concepts of time-dependent density functional theory, and finally, we present a few illustrative examples. The PE model has been implemented in the Dalton program package [14].

2. THEORETICAL BASIS FOR POLARIZABLE EMBEDDING

The objective of the PE model is to incorporate the effects from a medium into the electronic density of a central molecular core so as to keep the computational cost low while still retaining good accuracy. This is achieved

through the PE potential operator. We begin by considering a simple supermolecular system which we divide into two fragments A and B. The final equations for the supermolecular system are easily generalized to molecular systems with any number of fragments. Fragment A consists of M_{A} nuclei and fragment B consists of M_{B} nuclei. The derivations are carried out using the second quantization formalism [15]. The total nonrelativistic electronic Hamiltonian for the supermolecular system can be written as

$$\hat{H} = \hat{H}^{\mathrm{A}} + \hat{H}^{\mathrm{B}} + \hat{V}^{\mathrm{AB}}, \tag{1}$$

where $\hat{H}^{\mathrm{A}}$ and $\hat{H}^{\mathrm{B}}$ are the fragment Hamiltonians, which contain terms that are specific to fragment A and B, respectively, and $\hat{V}^{\mathrm{AB}}$ is the Coulomb interaction Hamiltonian, which contains all terms related to the interactions between the two fragments. The fragment Hamiltonians are defined as

$$\hat{H}^{i} = \sum_{pq} h^{i}_{pq} \hat{E}^{i}_{pq} + \frac{1}{2} \sum_{pqrs} g^{i}_{pqrs} \hat{e}^{i}_{pqrs} + V^{i}_{\mathrm{nuc}}, \tag{2}$$

where $i = \mathrm{A}$ or B. Here, h_{pq} is an integral over the kinetic energy and nuclear–electron attraction operators, g_{pqrs} is an integral over the electron–electron repulsion operator, and V_{nuc} is the nuclear–nuclear repulsion energy.

Before we define the interaction Hamiltonian, it is convenient first to define the wavefunction of the supermolecular system. We assume that the fragment wavefunctions in isolated form are known, that is,

$$\hat{H}^{\mathrm{A}}|\mathrm{A}\rangle = E^{\mathrm{A}}|\mathrm{A}\rangle \quad \text{and} \quad \hat{H}^{\mathrm{B}}|\mathrm{B}\rangle = E^{\mathrm{B}}|\mathrm{B}\rangle, \tag{3}$$

and that they are individually normalized

$$\langle \mathrm{A}|\mathrm{A}\rangle = 1 \quad \text{and} \quad \langle \mathrm{B}|\mathrm{B}\rangle = 1. \tag{4}$$

The wavefunctions can be expressed as a wave operator acting on the vacuum state

$$|\mathrm{A}\rangle = \hat{\psi}^{\mathrm{A}}|vac\rangle \quad \text{and} \quad |\mathrm{B}\rangle = \hat{\psi}^{\mathrm{B}}|vac\rangle. \tag{5}$$

The form of the wave operators need not be defined, but, in principle, they can describe any type of wavefunction, for example, Hartree–Fock or coupled-cluster wavefunctions. However, at their core, they always consist of strings of creation operators. We define the supermolecular wavefunction as

$$|\mathrm{AB}\rangle = \hat{\psi}^{\mathrm{A}}\hat{\psi}^{\mathrm{B}}|vac\rangle, \tag{6}$$

which is a simple product between the fragment wavefunctions because we require that the following commutation property is fulfilled

$$[\hat{\psi}^{\mathrm{A}}, \hat{\psi}^{\mathrm{B}}] = 0. \tag{7}$$

This corresponds to the assumption that there is no overlap between the wavefunctions of fragments A and B, thereby neglecting exchange and charge-transfer effects between the fragments. This is, in most cases, a reasonable approximation if the distance between the fragments is large but will introduce increasingly larger errors with shorter distances. The underlying commutation rules that apply to the elementary operators are

$$\left[\hat{a}^{\dagger\mathrm{A}}_{p\sigma}, \hat{a}^{\dagger\mathrm{B}}_{q\tau}\right] = \left[\hat{a}^{\mathrm{A}}_{p\sigma}, \hat{a}^{\mathrm{B}}_{q\tau}\right] = \left[\hat{a}^{\dagger\mathrm{A}}_{p\sigma}, \hat{a}^{\mathrm{B}}_{q\tau}\right] = 0, \tag{8}$$

that is, the elementary operators that belong to different fragments commute. Within each fragment, however, the elementary operators obey the usual anticommutation rules.

We are now ready to define the interaction Hamiltonian as

$$\hat{V}^{\mathrm{AB}} = \sum_{pq\in\mathrm{A}} v^{\mathrm{AB}}_{pq}\hat{E}^{\mathrm{A}}_{pq} + \sum_{rs\in\mathrm{B}} v^{\mathrm{AB}}_{rs}\hat{E}^{\mathrm{B}}_{rs} + \sum_{\substack{pq\in\mathrm{A}\\ rs\in\mathrm{B}}} v^{\mathrm{AB}}_{pq,rs}\hat{E}^{\mathrm{A}}_{pq}\hat{E}^{\mathrm{B}}_{rs} + v^{\mathrm{AB}}_{\mathrm{nuc}}, \tag{9}$$

which contains terms that account for nuclear–electron attraction, electron–electron repulsion, and nuclear–nuclear repulsion between the two fragments. Here, we have used the commutation rule defined in Eq. (8) to simplify the two-electron part of the interaction Hamiltonian. The v^{AB}_{pq} factor is an integral over the nuclear–electron attraction operator where the electrons belong to fragment A and the nuclei to fragment B, and it is defined as

$$v^{\mathrm{AB}}_{pq} = -\sum_{m=1}^{M_{\mathrm{B}}} \int \phi^{\mathrm{A}*}_{p}(\mathbf{r}) \frac{Z^{\mathrm{B}}_{m}}{|\mathbf{r}-\mathbf{R}_{m}|} \phi^{\mathrm{A}}_{q}(\mathbf{r}) \mathrm{d}\mathbf{r} = -\sum_{m=1}^{M_{\mathrm{B}}} \int \frac{\rho^{\mathrm{A}}_{pq}(\mathbf{r}) Z^{\mathrm{B}}_{m}}{|\mathbf{r}-\mathbf{R}_{m}|} \mathrm{d}\mathbf{r}. \tag{10}$$

The above equation implicitly defines our use of ρ^{A}_{pq}. Conversely, v^{AB}_{rs} is an integral over the nuclear–electron attraction operator where the electrons belong to fragment B and the nuclei to fragment A, and it is therefore given by

$$v^{\mathrm{AB}}_{rs} = -\sum_{n=1}^{M_{\mathrm{A}}} \int \phi^{\mathrm{B}*}_{r}(\mathbf{r}) \frac{Z^{\mathrm{A}}_{n}}{|\mathbf{R}_{n}-\mathbf{r}|} \phi^{\mathrm{B}}_{s}(\mathbf{r}) \mathrm{d}\mathbf{r} = -\sum_{n=1}^{M_{\mathrm{A}}} \int \frac{Z^{\mathrm{A}}_{n} \rho^{\mathrm{B}}_{rs}(\mathbf{r})}{|\mathbf{R}_{n}-\mathbf{r}|} \mathrm{d}\mathbf{r}, \tag{11}$$

which again implicitly defines our use of ρ^{B}_{rs}. The $v^{\mathrm{AB}}_{pq,rs}$ integral is over the electron–electron repulsion operator where the electrons always belong to

different fragments, and it is defined as

$$v^{\mathrm{AB}}_{pq,rs} = \iint \phi^{\mathrm{A}*}_p(\mathbf{r})\phi^{\mathrm{B}*}_r(\mathbf{r}')\frac{1}{|\mathbf{r}-\mathbf{r}'|}\phi^{\mathrm{A}}_q(\mathbf{r})\phi^{\mathrm{B}}_s(\mathbf{r}')\mathrm{d}\mathbf{r}\mathrm{d}\mathbf{r}'. \tag{12}$$

However, since we are using a product wavefunction of nonoverlapping fragment wavefunctions, this is a purely Coulombic integral. Therefore, we can immediately rewrite it to

$$v^{\mathrm{AB}}_{pq,rs} = \iint \rho^{\mathrm{A}}_{pq}(\mathbf{r})\frac{1}{|\mathbf{r}-\mathbf{r}'|}\rho^{\mathrm{B}}_{rs}(\mathbf{r}')\mathrm{d}\mathbf{r}\mathrm{d}\mathbf{r}', \tag{13}$$

which describes the purely Coulombic interactions between the electronic densities of fragment A and B. Finally, the $v^{\mathrm{AB}}_{\mathrm{nuc}}$ term is the nuclear–nuclear repulsion energy defined as

$$v^{\mathrm{AB}}_{\mathrm{nuc}} = \sum_{n=1}^{M_{\mathrm{A}}}\sum_{m=1}^{M_{\mathrm{B}}}\frac{Z^{\mathrm{A}}_n Z^{\mathrm{B}}_m}{|\mathbf{R}_n - \mathbf{R}_m|}. \tag{14}$$

We now turn our focus on one of the fragments, which we arbitrarily choose as fragment A, and we want to describe the interaction effects from fragment B on this central core. A Rayleigh–Schrödinger perturbation treatment of the supermolecular system, where the interaction Hamiltonian $\hat{V}^{\mathrm{AB}}$ acts as the perturbation, allows us to derive equations for the main contributions to the interaction energy. The energy up to second order in the perturbation is given by

$$E^{(0)} = \langle \mathrm{AB}|\hat{H}^{\mathrm{A}} + \hat{H}^{\mathrm{B}}|\mathrm{AB}\rangle = \langle \mathrm{A}|\hat{H}^{\mathrm{A}}|\mathrm{A}\rangle + \langle \mathrm{B}|\hat{H}^{\mathrm{B}}|\mathrm{B}\rangle \tag{15}$$

$$E^{(1)} = \langle \mathrm{AB}|\hat{V}^{\mathrm{AB}}|\mathrm{AB}\rangle \tag{16}$$

$$E^{(2)} = -\sum_{\substack{ij,\\ i+j\neq 0}} \frac{\langle \mathrm{AB}|\hat{V}^{\mathrm{AB}}|\mathrm{A}^i\mathrm{B}^j\rangle\langle \mathrm{A}^i\mathrm{B}^j|\hat{V}^{\mathrm{AB}}|\mathrm{AB}\rangle}{\epsilon^{\mathrm{AB}}_{ij} - \epsilon^{\mathrm{AB}}_{00}}, \tag{17}$$

which we will use to obtain approximated energy expressions from which we will ultimately derive an effective operator. Thereby, we incorporate effects that lead to the first- and second-order energies into the electron density of the central core. We are only interested in the first- and second-order energies since the zeroth-order energy is simply a sum of the energies of the isolated fragments.

To proceed, we want to eliminate the wavefunction belonging to fragment B. Our strategy is to recast the interaction Hamiltonian using a Taylor

series expansion of $|\mathbf{r} - \mathbf{r}'|^{-1}$ and $|\mathbf{r} - \mathbf{R}_m|^{-1}$ around an origin $\mathbf{R}_o$ located inside fragment B. Here, $\mathbf{r}'$ and $\mathbf{R}_m$ are electronic and nuclear coordinates, respectively, belonging to fragment B; the point $\mathbf{r}$ is, for now, an arbitrary point outside the charge distribution of fragment B. Later, $\mathbf{r}$ will either refer to an electronic or nuclear coordinate inside the central core system. The expansion of $|\mathbf{r} - \mathbf{r}'|^{-1}$ can be written in closed form using a multi-index notation

$$\frac{1}{|\mathbf{r} - \mathbf{r}'|} = \sum_{|k|=0}^{\infty} \frac{(-1)^{|k|}}{k!} \left(\nabla^k \frac{1}{|\mathbf{r} - \mathbf{R}_o|} \right) (\mathbf{r}' - \mathbf{R}_o)^k \tag{18}$$

where the multi-index $k = (k_x, k_y, k_z)$ is a 3-tuple of nonnegative integers, $|k| = k_x + k_y + k_z$ and ∇^k is defined as the multi-index power of the partial derivative operator

$$\nabla^k = \left(\frac{\partial}{\partial r_x} \right)^{k_x} \left(\frac{\partial}{\partial r_y} \right)^{k_y} \left(\frac{\partial}{\partial r_z} \right)^{k_z}. \tag{19}$$

For each value of $|k|$, the summation in Eq. (18) is over $3^{|k|}$ elements; for example, for $|k| = 1$, the summation is over three elements, namely, $(1, 0, 0)$, $(0, 1, 0)$, and $(0, 0, 1)$, which represent the x, y, and z components, respectively. The multi-index also specifies the Cartesian component, for example, $k = (2, 1, 0)$ is the xxy component. The convergence of the expansion depends on the distance from the origin to $\mathbf{r}$ relative to the extent of the charge distribution of both fragments. At large distances, it usually converges rapidly but worsens as the distance becomes shorter and can even diverge at short distances. Using distributed multipole expansions of the charge distribution improves the convergence; however, at very short distances, the error from the expansion will still be significant.

In Eq. (18), we recognize the first quantization kth-order electronic multipole moment operator $(\mathbf{r}' - \mathbf{R}_o)^k$. An analogous expansion of $|\mathbf{r} - \mathbf{R}_m|^{-1}$ would yield the nuclear multipole moment operator $(\mathbf{R}_m - \mathbf{R}_o)^k$. The higher-order multipole moments generally depend on the choice of origin; however, to simplify the notation, we omit any explicit reference to this dependence. The partial derivatives in Eq. (18) are elements of the so-called interaction tensors defined as

$$T^{(k)}_{AB}(\mathbf{r}) = \nabla^k \frac{1}{|\mathbf{r} - \mathbf{R}_o|}. \tag{20}$$

The multi-index in parentheses, used as superscript on the tensor, is actually the norm $|k|$; however, since it also specifies the rank of the tensor, and therefore we use a special notation.

We can now rewrite the interaction Hamiltonian by replacing all occurrences of $|\mathbf{r} - \mathbf{r}'|^{-1}$ and $|\mathbf{r} - \mathbf{R}_m|^{-1}$ in Eqs. (10, 11, 13, and 14) with the

appropriate Taylor expansion. The interaction Hamiltonian is thereby redefined to

$$\hat{V}^{\mathrm{AB}} = \sum_{|k|=0}^{\infty} \frac{(-1)^{|k|}}{k!} \hat{F}_{\mathrm{A}}^{(k)} \hat{Q}_{\mathrm{B}}^{(k)}, \tag{21}$$

where $\hat{F}_{\mathrm{A}}^{(k)}$ and $\hat{Q}_{\mathrm{B}}^{(k)}$ act on the wavefunctions belonging to fragment A and B, respectively. The $\hat{F}_{\mathrm{A}}^{(k)}$ operator is defined as

$$\hat{F}_{\mathrm{A}}^{(k)} = F_{\mathrm{A,nuc}}^{(k)} + \hat{F}_{\mathrm{A,el}}^{(k)} = \sum_{n=1}^{M_{\mathrm{A}}} Z_n^{\mathrm{A}} T_{\mathrm{AB}}^{(k)}(\mathbf{R}_n) - \sum_{pq \in \mathrm{A}} \left(\int \rho_{pq}^{\mathrm{A}}(\mathbf{r}) T_{\mathrm{AB}}^{(k)}(\mathbf{r}) \mathrm{d}\mathbf{r} \right) \hat{E}_{pq}^{\mathrm{A}}, \tag{22}$$

the expectation value of which gives the electrostatic potential, electric field, and field gradient for $|k| = 0, 1, 2$, respectively. The $\hat{Q}_{\mathrm{B}}^{(k)}$ operator is the multipole moment operator defined as

$$\begin{aligned} \hat{Q}_{\mathrm{B}}^{(k)} = Q_{\mathrm{B,nuc}}^{(k)} + \hat{Q}_{\mathrm{B,el}}^{(k)} = & \sum_{m=1}^{M_{\mathrm{B}}} Z_m^{\mathrm{B}} \left(\mathbf{R}_{\mathrm{m}} - \mathbf{R}_{\mathrm{o}}\right)^k \\ & - \sum_{rs \in \mathrm{B}} \left(\int \rho_{rs}^{\mathrm{B}}(\mathbf{r}') \left(\mathbf{r}' - \mathbf{R}_{\mathrm{o}}\right)^k \mathrm{d}\mathbf{r}' \right) \hat{E}_{rs}^{\mathrm{B}}. \end{aligned} \tag{23}$$

Using the redefined interaction Hamiltonian, the first-order energy (Eq. (16)) yields

$$E_{\mathrm{es}}^{\mathrm{AB}} = \langle \mathrm{AB} | \hat{V}^{\mathrm{AB}} | \mathrm{AB} \rangle = \sum_{|k|=0}^{\infty} \frac{(-1)^{|k|}}{k!} \left(F_{\mathrm{A,nuc}}^{(k)} + \langle \mathrm{A} | \hat{F}_{\mathrm{A,el}}^{(k)} | \mathrm{A} \rangle \right) Q_{\mathrm{B}}^{(k)}, \tag{24}$$

which is the electrostatic interaction energy given in terms of the multipole moments $Q_{\mathrm{B}}^{(k)}$ of fragment B. The definition of the electrostatic energy given in Eq. (24) will be used to construct an effective operator so that this effect is incorporated directly in the electron density of the central core fragment.

The second-order energy (Eq. (17)) needs further breakdown before we can identify the relevant energy contributions we need. First of all, we see that it is expressed as a sum-over-states that includes all terms except when both fragments A and B are in their ground state, that is, $i = 0$ and $j = 0$. It is therefore possible to separate it into three different contributions: two of which only include excited states in one fragment, these are the induction energy terms, and one which includes excited states in both fragments simultaneously, which is the dispersion energy [16]. Although the

dispersion energy can be important, it is neglected in our model since there is no straightforward way of including it in operator form. The induction energy of fragment A can be rewritten in terms of the multipole moments of fragment B using the interaction Hamiltonian as defined in Eqs. (21–23)

$$E_{\mathrm{ind}}^{\mathrm{A}} = -\sum_{i\neq 0} \frac{\langle \mathrm{AB}|\hat{V}^{\mathrm{AB}}|\mathrm{A}^i\mathrm{B}\rangle\langle \mathrm{A}^i\mathrm{B}|\hat{V}^{\mathrm{AB}}|\mathrm{AB}\rangle}{\epsilon_i^{\mathrm{A}} - \epsilon_0^{\mathrm{A}}}. \tag{25}$$

Taking the expectation value with respect to the wavefunction belonging to fragment B yields

$$E_{\mathrm{ind}}^{\mathrm{A}} = -\sum_{|k|=0}^{\infty} \frac{(-1)^{|k|}}{k!} Q_{\mathrm{B}}^{(k)} \sum_{i\neq 0} \frac{\langle \mathrm{A}|\hat{F}_{\mathrm{A}}^{(k)}|\mathrm{A}^i\rangle\langle \mathrm{A}^i|\hat{F}_{\mathrm{A}}^{(k)}|\mathrm{A}\rangle}{\epsilon_i^{\mathrm{A}} - \epsilon_0^{\mathrm{A}}} Q_{\mathrm{B}}^{(k)}, \tag{26}$$

which is the interaction energy due to the polarization of fragment A by the multipole moments of fragment B in its ground state. In our model, this energy contribution is implicitly included via the use of an effective operator that includes the multipole moments of fragment B, thus polarizing the electron density of fragment A. The induction energy of fragment B is defined analogous to the induction energy of fragment A

$$E_{\mathrm{ind}}^{\mathrm{B}} = -\sum_{j\neq 0} \frac{\langle \mathrm{AB}|\hat{V}^{\mathrm{AB}}|\mathrm{AB}^j\rangle\langle \mathrm{AB}^j|\hat{V}^{\mathrm{AB}}|\mathrm{AB}\rangle}{\epsilon_j^{\mathrm{B}} - \epsilon_0^{\mathrm{B}}}, \tag{27}$$

which we can rewrite to

$$E_{\mathrm{ind}}^{\mathrm{B}} = -\sum_{|k|=0}^{\infty} \frac{(-1)^{|k|}}{k!} \langle \mathrm{A}|\hat{F}_{\mathrm{A}}^{(k)}|\mathrm{A}\rangle \sum_{j\neq 0} \frac{\langle \mathrm{B}|\hat{Q}_{\mathrm{B}}^{(k)}|\mathrm{B}^j\rangle\langle \mathrm{B}^j|\hat{Q}_{\mathrm{B}}^{(k)}|\mathrm{B}\rangle}{\epsilon_j^{\mathrm{B}} - \epsilon_0^{\mathrm{B}}} \langle \mathrm{A}|\hat{F}_{\mathrm{A}}^{(k)}|\mathrm{A}\rangle. \tag{28}$$

We recognize the sum-over-states part of the expression as the polarizabilities of fragment B. Note that the zeroth-order term, where $\hat{Q}_{\mathrm{B}}^{(0)} = q_{\mathrm{B}}$, does not contribute due to orthogonality. Truncating the expansion at $|k| = 1$, that is, at the dipole level, and evaluating the expectation values yields

$$E_{\mathrm{ind}}^{\mathrm{B}} = -\frac{1}{2}\left(\mathbf{F}_{\mathrm{nuc}}^{\mathrm{A}} + \mathbf{F}_{\mathrm{el}}^{\mathrm{A}}\right)\boldsymbol{\alpha}^{\mathrm{B}}\left(\mathbf{F}_{\mathrm{nuc}}^{\mathrm{A}} + \mathbf{F}_{\mathrm{el}}^{\mathrm{A}}\right) = -\frac{1}{2}\left(\mathbf{F}_{\mathrm{nuc}}^{\mathrm{A}} + \mathbf{F}_{\mathrm{el}}^{\mathrm{A}}\right)\boldsymbol{\mu}_{\mathrm{ind}}^{\mathrm{B}}(\mathbf{F}_{\mathrm{tot}}), \tag{29}$$

where $\left(\mathbf{F}_{\mathrm{nuc}}^{\mathrm{A}} + \mathbf{F}_{\mathrm{el}}^{\mathrm{A}}\right)$ is the electric field due to the nuclei and electrons, respectively, in fragment A and $\boldsymbol{\mu}_{\mathrm{ind}}^{\mathrm{B}}(\mathbf{F}_{\mathrm{tot}})$ is the dipole moment induced by the total electric field $\mathbf{F}_{\mathrm{tot}}$. In this case, the total electric field stems only from the

nuclei and electrons in fragment A. Generally, however, it is a sum of all electric fields including the field from other induced dipoles. This is a classical energy expression which we use to allow polarization of fragment B by the electrons and nuclei in fragment A. The induction energy is nonadditive due to the mutual polarization and therefore has to be solved for self-consistently.

We now have the energy expression needed to derive a generalized PE potential operator within a given QM formalism. For a system consisting of any number of fragments, where one is chosen as the central core system and the other fragments are represented by a multicenter multipole moment expansion and distributed dipole–dipole polarizability tensors, the relevant energy is given by

$$E_{\text{tot}}^{\text{PE}} = E_{\text{QM}}^{\text{PE}} + E_{\text{es}}^{\text{PE}} + E_{\text{ind}}^{\text{PE}}. \tag{30}$$

The $E_{\text{QM}}^{\text{PE}}$ term is the energy of the isolated core fragment evaluated at a given level of theory, and $E_{\text{es}}^{\text{PE}}$ is the electrostatic interaction energy given by

$$E_{\text{es}}^{\text{PE}} = \sum_{s=1}^{S} \sum_{|k|=0}^{K} \frac{(-1)^{|k|}}{k!} \left(F_{s,\text{nuc}}^{(k)} + \langle 0|\hat{F}_{s,\text{el}}^{(k)}|0\rangle \right) Q_s^{(k)}, \tag{31}$$

where we have introduced the truncation level K and summation over S sites in the surrounding fragments. The nuclear contribution $F_{s,\text{nuc}}^{(k)}$ is defined as

$$F_{s,\text{nuc}}^{(k)} = \sum_{n=1}^{M} Z_n T_{ns}^{(k)}(\mathbf{R}_n), \tag{32}$$

and the electronic contribution is given by the expectation value over the operator $\hat{F}_{s,\text{el}}^{(k)}$, which is defined by

$$\hat{F}_{s,\text{el}}^{(k)} = \sum_{pq} t_{s,pq}^{(k)} \hat{E}_{pq}, \tag{33}$$

where the $t_{s,pq}^{(k)}$ integral is defined as

$$t_{s,pq}^{(k)} = -\int \rho_{pq}(\mathbf{r}) T_s^{(k)}(\mathbf{r}) \mathrm{d}\mathbf{r}. \tag{34}$$

The subindices on the interaction tensors specify which position vectors it contains, for example, $T_{ns}^{(k)} = \nabla^k \frac{1}{|\mathbf{R}_n - \mathbf{R}_s|}$. One index implicitly specifies that the other coordinate is an electron coordinate, for example, $T_s^{(k)} = \nabla^k \frac{1}{|\mathbf{r} - \mathbf{R}_s|}$. The

induction energy $E_{\text{ind}}^{\text{PE}}$ due to the polarization of the surrounding fragments is given by

$$E_{\text{ind}}^{\text{PE}} = -\frac{1}{2}\sum_{s=1}^{S}\left(\mathbf{F}_{\text{nuc}} + \mathbf{F}_{\text{el}} + \mathbf{F}_{\text{mul}}\right)\boldsymbol{\mu}_s^{\text{ind}}(\mathbf{F}_{\text{tot}}), \tag{35}$$

where the additional electric field, $\mathbf{F}_{\text{mul}}$, stems from the multipole moments of all the other fragments and the total electric field $\mathbf{F}_{\text{tot}}$ is a sum of contributions from the electrons and nuclei in the central core and the multipole moments and induced dipoles from all other fragments. An induced dipole moment is given by

$$\boldsymbol{\mu}_s^{\text{ind}}(\mathbf{F}_{\text{tot}}) = \boldsymbol{\alpha}_s\mathbf{F}_{\text{tot}} = \boldsymbol{\alpha}_s\left(\mathbf{F}_{\text{nuc}} + \mathbf{F}_{\text{el}} + \mathbf{F}_{\text{mul}} + \mathbf{F}_{\text{ind}}\right), \tag{36}$$

where the electric field from the other induced dipoles $\mathbf{F}_{\text{ind}}$ is given by

$$\mathbf{F}_{\text{ind}} = \sum_{s'\neq s}^{S}\mathbf{T}_{s'}^{(2)}\boldsymbol{\mu}_{s'}^{\text{ind}}(\mathbf{F}_{\text{tot}}). \tag{37}$$

Inserting Eq. (37) into Eq. (36) and summing over all sites yields a system of coupled equations

$$\sum_{s}^{S}\boldsymbol{\mu}_s^{\text{ind}}(\mathbf{F}_{\text{tot}}) = \sum_{s}^{S}\boldsymbol{\alpha}_s\left(\mathbf{F}_{\text{nem}} + \sum_{s'\neq s}^{S}\mathbf{T}_{s'}^{(2)}\boldsymbol{\mu}_{s'}^{\text{ind}}(\mathbf{F}_{\text{tot}})\right), \tag{38}$$

where the electric field from all sources, except induced dipoles, has been collected in a single term $\mathbf{F}_{\text{nem}} = \mathbf{F}_{\text{nuc}} + \mathbf{F}_{\text{el}} + \mathbf{F}_{\text{mul}}$. The induced dipole moments can be solved for iteratively using the Jacobi method or directly through matrix-vector multiplication using the equation given by

$$\boldsymbol{\mu}^{\text{ind}} = \mathbf{B}\mathbf{F}, \tag{39}$$

where $\mathbf{B}$ is the symmetric $3S \times 3S$-dimensional classical response matrix [8] connecting the electric fields and the set of induced dipoles

$$\boldsymbol{\mu}^{\text{ind}} = \begin{pmatrix}\boldsymbol{\mu}_1^{\text{ind}}\\ \boldsymbol{\mu}_2^{\text{ind}}\\ \vdots\\ \boldsymbol{\mu}_S^{\text{ind}}\end{pmatrix}. \tag{40}$$

The response matrix is defined as

$$\mathbf{B} = \begin{pmatrix} \boldsymbol{\alpha}_1^{-1} & \mathbf{T}_{12}^{(2)} & \cdots & \mathbf{T}_{1S}^{(2)} \\ \mathbf{T}_{21}^{(2)} & \boldsymbol{\alpha}_2^{-1} & \ddots & \vdots \\ \vdots & \ddots & \ddots & \mathbf{T}_{(S-1)S}^{(2)} \\ \mathbf{T}_{S1}^{(2)} & \cdots & \mathbf{T}_{S(S-1)}^{(2)} & \boldsymbol{\alpha}_S^{-1} \end{pmatrix}^{-1}, \tag{41}$$

where the diagonal blocks contain the inverse polarizability tensors and the off-diagonal blocks are rank 2 interaction tensors.

2.1. Polarizable embedding applied to density functional theory

The PE-DFT method is derived by constructing an effective Kohn–Sham (KS) operator, that is,

$$\hat{f}_{\text{eff}} = \hat{f}_{\text{KS}} + \hat{v}_{\text{PE}}, \tag{42}$$

where $\hat{f}_{\text{KS}}$ is the ordinary vacuum KS operator and $\hat{v}_{\text{PE}}$ is the PE potential operator. The contributions to the effective KS operator is determined by minimization of the energy with respect to the electron density. Therefore, we only need to consider terms that depend on the electron density, that is, the electronic parts of the electrostatic interaction energy (Eq. (31)) and the induction energy (Eq. (35)), keeping in mind that the induced dipoles also depend on the density through the electric field. Thus, the PE potential operator is found to be

$$\hat{v}_{\text{PE}} = \sum_{s=1}^{S} \sum_{|k|=0}^{K} \frac{(-1)^{|k|}}{k!} Q_s^{(k)} \hat{F}_{s,\text{el}}^{(k)} - \sum_{s=1}^{S} \boldsymbol{\mu}_s^{\text{ind}}(\mathbf{F}_{\text{tot}}) \hat{\mathbf{F}}_{s,\text{el}}^{(1)}, \tag{43}$$

where the induced dipole moments need to be updated in each self-consistent field (SCF) iteration due to the density dependence, thus leading to a fully self-consistent treatment of the polarization.

2.2. Polarizable embedding within response theory

Here, we provide the theoretical basis for incorporating the PE potential in quantum mechanical response theory, including the derivation of the contributions to the linear, quadratic, and cubic response functions. The derivations follow closely the formulation of linear and quadratic response theory within DFT by Sałek et al. [17] and cubic response within DFT by Jansik et al. [18] Furthermore, the derived equations show some similarities to other response-based environmental methods, for example, the polarizable continuum model [19, 20] (PCM) or the spherical cavity dielectric

continuum approach [21, 22]. This is not surprising since these two methods also explicitly include the polarizable nature of the surrounding. Physically, both the PE and dielectric continuum models are furthermore based on the use of a nonlinear effective Hamiltonian.

We start the derivations by considering the expectation value of a time-independent operator $\hat{A}$ which is expanded in orders of a time-dependent perturbation

$$\langle t|\hat{A}|t\rangle = \langle t|\hat{A}|t\rangle^{(0)} + \langle t|\hat{A}|t\rangle^{(1)} + \langle t|\hat{A}|t\rangle^{(2)} + \langle t|\hat{A}|t\rangle^{(3)} + \cdots . \tag{44}$$

The first term on the right-hand side is the time-independent expectation value, whereas the second, third, and fourth terms describe the linear, quadratic, and cubic response to the perturbation, respectively. The Fourier transformed representations are given by

$$\langle t|\hat{A}|t\rangle^{(1)} = \int \langle\langle \hat{A}; \hat{V}^{\omega_1} \rangle\rangle_{\omega_1} \exp(-i\omega_1 t) \mathrm{d}\omega_1 \tag{45}$$

$$\langle t|\hat{A}|t\rangle^{(2)} = \frac{1}{2} \iint \langle\langle \hat{A}; \hat{V}^{\omega_1}, \hat{V}^{\omega_2} \rangle\rangle_{\omega_1,\omega_2} \exp(-i(\omega_1+\omega_2)t) \mathrm{d}\omega_1 \mathrm{d}\omega_2 \tag{46}$$

$$\begin{aligned}\langle t|\hat{A}|t\rangle^{(3)} = \frac{1}{6} \iiint & \langle\langle \hat{A}; \hat{V}^{\omega_1}, \hat{V}^{\omega_2}, \hat{V}^{\omega_3} \rangle\rangle_{\omega_1,\omega_2,\omega_3} \\ & \times \exp(-i(\omega_1+\omega_2+\omega_3)t) \mathrm{d}\omega_1 \mathrm{d}\omega_2 \mathrm{d}\omega_3,\end{aligned} \tag{47}$$

where $\langle\langle \hat{A}; \hat{V}^{\omega_1} \rangle\rangle_{\omega_1}$, $\langle\langle \hat{A}; \hat{V}^{\omega_1}, \hat{V}^{\omega_2} \rangle\rangle_{\omega_1,\omega_2}$, and $\langle\langle \hat{A}; \hat{V}^{\omega_1}, \hat{V}^{\omega_2}, \hat{V}^{\omega_3} \rangle\rangle_{\omega_1,\omega_2,\omega_3}$ are the linear, quadratic, and cubic response functions, respectively, and the perturbation operator is defined as

$$\hat{V}(t) = \int \hat{V}^{\omega} \exp(-i\omega t) \mathrm{d}\omega. \tag{48}$$

The time development of the molecular orbitals is determined by the time-dependent KS equations

$$\left(\hat{H}(t) + \hat{V}(t)\right)|t\rangle = i\frac{\partial}{\partial t}|t\rangle \tag{49}$$

where $\hat{H}(t)$ is the time-dependent KS Hamiltonian given by

$$\hat{H}(t) = \sum_{pq} f_{pq}(t)\hat{E}_{pq} \tag{50}$$

and $|t\rangle$ is the time-dependent KS determinant. We use an exponential parametrization of the KS determinant

$$|t\rangle = \exp(-\hat{\kappa}(t))|0\rangle \tag{51}$$

where $|0\rangle$ is the unperturbed KS determinant and $\hat{\kappa}(t)$ is the anti-Hermitian time-evolution operator defined as

$$\hat{\kappa}(t) = \sum_{pq} \kappa_{pq}(t)\hat{E}_{pq}, \tag{52}$$

with $\kappa_{pq}(t)$ as the time-dependent variational parameters. Thus, the expectation value over a time-independent operator $\hat{A}$ becomes

$$\langle \hat{A} \rangle = \langle t|\hat{A}|t\rangle = \langle 0| \exp\big(\hat{\kappa}(t)\big)\hat{A} \exp(-\hat{\kappa}(t))|0\rangle \tag{53}$$

which can be expanded using a Baker–Campbell–Hausdorff (BCH) expansion [15]

$$\begin{aligned}\langle \hat{A} \rangle = \langle 0|\hat{A}|0\rangle + \langle 0|[\hat{\kappa}(t), \hat{A}]|0\rangle + \frac{1}{2}\langle 0|[\hat{\kappa}(t), [\hat{\kappa}(t), \hat{A}]]|0\rangle \\ + \frac{1}{6}\langle 0|[\hat{\kappa}(t), [\hat{\kappa}(t), [\hat{\kappa}(t), \hat{A}]]]|0\rangle + \cdots .\end{aligned} \tag{54}$$

The time-evolution operator can be expanded in orders of the perturbation

$$\hat{\kappa}(t) = \hat{\kappa}^{(1)}(t) + \hat{\kappa}^{(2)}(t) + \hat{\kappa}^{(3)}(t) + \cdots \tag{55}$$

with the following representations in frequency space

$$\hat{\kappa}^{(1)}(t) = \int \hat{\kappa}^{\omega_1} \exp(-i\omega_1 t)\mathrm{d}\omega_1 \tag{56}$$

$$\hat{\kappa}^{(2)}(t) = \frac{1}{2}\iint \hat{\kappa}^{\omega_1,\omega_2} \exp(-i(\omega_1 + \omega_2)t)\mathrm{d}\omega_1\mathrm{d}\omega_2 \tag{57}$$

$$\hat{\kappa}^{(3)}(t) = \frac{1}{6}\iiint \hat{\kappa}^{\omega_1,\omega_2,\omega_3} \exp(-i(\omega_1 + \omega_2 + \omega_3)t)\mathrm{d}\omega_1\mathrm{d}\omega_2\mathrm{d}\omega_3. \tag{58}$$

Inserting the expansion of the time-evolution operator (Eq. (55)) into the BCH expansion of the expectation value given in Eq. (54) leads to

$$\begin{aligned}\langle \hat{A} \rangle = \langle 0|\hat{A}|0\rangle + \langle 0|[\hat{\kappa}^{(1)}(t), \hat{A}]|0\rangle + \langle 0|[\hat{\kappa}^{(2)}(t), \hat{A}]|0\rangle + \langle 0|[\hat{\kappa}^{(3)}(t), \hat{A}]|0\rangle \\ + \frac{1}{2}\langle 0|[\hat{\kappa}^{(1)}(t), [\hat{\kappa}^{(1)}(t), \hat{A}]]|0\rangle + \frac{1}{2}\langle 0|[\hat{\kappa}^{(1)}(t), [\hat{\kappa}^{(2)}(t), \hat{A}]]|0\rangle \\ + \frac{1}{2}\langle 0|[\hat{\kappa}^{(2)}(t), [\hat{\kappa}^{(1)}(t), \hat{A}]]|0\rangle + \frac{1}{6}\langle 0|[\hat{\kappa}^{(1)}(t), [\hat{\kappa}^{(1)}(t), [\hat{\kappa}^{(1)}(t), \hat{A}]]]|0\rangle.\end{aligned} \tag{59}$$

From this expression, we can identify terms according to their order in the perturbation as follows:

$$\langle t|\hat{A}|t\rangle^{(1)} = \langle 0|[\hat{\kappa}^{(1)}(t), \hat{A}]|0\rangle \tag{60}$$

$$\langle t|\hat{A}|t\rangle^{(2)} = \langle 0|[\hat{\kappa}^{(2)}(t), \hat{A}]|0\rangle + \frac{1}{2}\langle 0|[\hat{\kappa}^{(1)}(t), [\hat{\kappa}^{(1)}(t), \hat{A}]]|0\rangle \tag{61}$$

$$\begin{aligned}\langle t|\hat{A}|t\rangle^{(3)} = {} & \langle 0|[\hat{\kappa}^{(3)}(t), \hat{A}]|0\rangle + \frac{1}{2}\langle 0|[\hat{\kappa}^{(1)}(t), [\hat{\kappa}^{(2)}(t), \hat{A}]]|0\rangle \\ & + \frac{1}{2}\langle 0|[\hat{\kappa}^{(2)}(t), [\hat{\kappa}^{(1)}(t), \hat{A}]]|0\rangle \\ & + \frac{1}{6}\langle 0|[\hat{\kappa}^{(1)}(t), [\hat{\kappa}^{(1)}(t), [\hat{\kappa}^{(1)}(t), \hat{A}]]]|0\rangle\end{aligned} \tag{62}$$

Comparing Eqs. (60–62) to Eqs. (45–47) shows that the response functions can be obtained by Fourier transformation to the frequency domain. This leads to the following expressions for the response functions up to cubic response

$$\langle\langle \hat{A}; \hat{V}^{\omega_1}\rangle\rangle_{\omega_1} = \langle 0|[\hat{\kappa}^{\omega_1}, \hat{A}]|0\rangle \tag{63}$$

$$\langle\langle \hat{A}; \hat{V}^{\omega_1}, \hat{V}^{\omega_2}\rangle\rangle_{\omega_1,\omega_2} = \langle 0|[\hat{\kappa}^{\omega_1,\omega_2}, \hat{A}]|0\rangle + \hat{P}_{12}\langle 0|[\hat{\kappa}^{\omega_1}, [\hat{\kappa}^{\omega_2}, \hat{A}]]|0\rangle \tag{64}$$

$$\begin{aligned}\langle\langle \hat{A}; \hat{V}^{\omega_1}, \hat{V}^{\omega_2}, \hat{V}^{\omega_3}\rangle\rangle_{\omega_1,\omega_2,\omega_3} = {} & \langle 0|[\hat{\kappa}^{\omega_1,\omega_2,\omega_3}, \hat{A}]|0\rangle \\ & + \frac{3}{2}\hat{P}_{123}\langle 0|[\hat{\kappa}^{\omega_1}, [\hat{\kappa}^{\omega_2,\omega_3}, \hat{A}]]|0\rangle \\ & + \frac{3}{2}\hat{P}_{123}\langle 0|[\hat{\kappa}^{\omega_1,\omega_2}, [\hat{\kappa}^{\omega_3}, \hat{A}]]|0\rangle \\ & + \hat{P}_{123}\langle 0|[\hat{\kappa}^{\omega_1}, [\hat{\kappa}^{\omega_2}, [\hat{\kappa}^{\omega_3}, \hat{A}]]]|0\rangle,\end{aligned} \tag{65}$$

where the symmetrizers $\hat{P}_{12}$ and $\hat{P}_{123}$ have been introduced. The symmetrizers are defined through

$$\hat{P}_{12}A(\omega_1, \omega_2) = \frac{1}{2}\big(A(\omega_1, \omega_2) + A(\omega_2, \omega_1)\big) \tag{66}$$

$$\begin{aligned}\hat{P}_{123}A(\omega_1, \omega_2, \omega_3) = \frac{1}{6}\Big(& A(\omega_1, \omega_2, \omega_3) + A(\omega_1, \omega_3, \omega_2) + A(\omega_2, \omega_1, \omega_3) \\ & + A(\omega_2, \omega_3, \omega_1) + A(\omega_3, \omega_1, \omega_2) + A(\omega_3, \omega_2, \omega_1)\Big),\end{aligned} \tag{67}$$

and they ensure that the response functions satisfy the proper symmetry condition.

The electron density can also be expanded in orders of the perturbation as

$$\rho(\mathbf{r},t) = \sum_n \rho^{(n)}(\mathbf{r},t) = \sum_n \sum_{pq} \phi_p^*(\mathbf{r})\phi_q(\mathbf{r}) D_{pq}^{(n)}, \tag{68}$$

where we can immediately write down the corrections to the density matrix up to third order by using the preceding derivations

$$D_{pq}^{\omega_1} = \langle 0|[\hat{\kappa}^{\omega_1}, \hat{E}_{pq}]|0\rangle \tag{69}$$

$$D_{pq}^{\omega_1,\omega_2} = \langle 0|[\hat{\kappa}^{\omega_1,\omega_2}, \hat{E}_{pq}]|0\rangle + \hat{P}_{12}\langle 0|[\hat{\kappa}^{\omega_1}, [\hat{\kappa}^{\omega_2}, \hat{E}_{pq}]]|0\rangle \tag{70}$$

$$\begin{aligned} D_{pq}^{\omega_1,\omega_2,\omega_3} = {} & \langle 0|[\hat{\kappa}^{\omega_1,\omega_2,\omega_3}, \hat{E}_{pq}]|0\rangle \\ & + \frac{3}{2}\hat{P}_{123}\langle 0|[\hat{\kappa}^{\omega_1}, [\hat{\kappa}^{\omega_2,\omega_3}, \hat{E}_{pq}]]|0\rangle \\ & + \frac{3}{2}\hat{P}_{123}\langle 0|[\hat{\kappa}^{\omega_1,\omega_2}, [\hat{\kappa}^{\omega_3}, \hat{E}_{pq}]]|0\rangle \\ & + \hat{P}_{123}\langle 0|[\hat{\kappa}^{\omega_1}, [\hat{\kappa}^{\omega_2}, [\hat{\kappa}^{\omega_3}, \hat{E}_{pq}]]]|0\rangle. \end{aligned} \tag{71}$$

Finally, we also expand the time-dependent Kohn–Sham Hamiltonian as:

$$\hat{H}(t) = \sum_n \sum_{pq} f_{pq}^{(n)} \hat{E}_{pq} = \sum_n \sum_{pq} \left(\delta_{0n} h_{pq} + j_{pq}^{(n)} + v_{\mathrm{xc},pq}^{(n)} + v_{\mathrm{PE},pq}^{(n)}\right) \hat{E}_{pq}, \tag{72}$$

where h_{pq} is an integral over the kinetic energy and nuclear-attraction operators, $j_{pq}^{(n)}$ is a nth-order Coulomb integral, and $v_{\mathrm{xc},pq}^{(n)}$ is a nth-order integral over the exchange-correlation potential. The final term $v_{\mathrm{PE},pq}^{(n)}$ is a nth-order integral over the PE potential defined as

$$v_{\mathrm{PE},pq}^{(n)} = \delta_{0n} \sum_{s=1}^{S} \sum_{|k|=0}^{K} \frac{(-1)^{|k|}}{k!} Q_s^{(k)} t_{s,pq}^{(k)} - \sum_{s=1}^{S} \boldsymbol{\mu}_s^{\mathrm{ind}}(\mathbf{F}_{\mathrm{tot}}^{(n)}) \mathbf{t}_{s,pq}^{(1)}. \tag{73}$$

For $n > 0$, it is only the induction part of $v_{\mathrm{PE},pq}^{(n)}$ that contributes due to the density dependence in the induced dipoles via the electric fields.

The $\kappa_{pq}(t)$ parameters are obtained through the Ehrenfest theorem which can be written as [23]

$$\langle 0|\left[\hat{\mathbf{q}}, \exp\left(\hat{\kappa}(t)\right)\left(\hat{H}(t) + \hat{V}(t) - i\frac{\mathrm{d}}{\mathrm{d}t}\right)\exp\left(-\hat{\kappa}(t)\right)\right]|0\rangle = 0, \tag{74}$$

where $\hat{\mathbf{q}}$ is a vector collecting all the excitation operators $\hat{E}_{pq}$. Equation (74) is then expanded in a BCH expansion, and the perturbation expansions of the time-evolution operator $\hat{\kappa}(t)$ and the KS Hamiltonian $\hat{H}(t)$ are inserted. Subsequently, terms that are first-, second-, and third-order in the perturbation, respectively, are collected. Thereby, we obtain sets of equations that can be used to determine the variational parameters, thus allowing us to calculate the linear, quadratic, and cubic response functions.

2.2.1. Linear response

Collecting all first-order terms obtained through the BCH expansion of the Ehrenfest theorem given in Eq. (74) leads to a system of differential equations

$$\langle 0|[\hat{\mathbf{q}}, \hat{H}^{(1)} + \hat{V}(t)]|0\rangle + \langle 0|[\hat{\mathbf{q}}, [\hat{\kappa}^{(1)}, \hat{H}^{(0)}]]|0\rangle + i\langle 0|[\hat{\mathbf{q}}, \dot{\hat{\kappa}}^{(1)}]|0\rangle = 0. \tag{75}$$

A Fourier transformation yields a more convenient algebraic equation

$$\langle 0|[\hat{\mathbf{q}}, [\hat{H}^{0}, \hat{\kappa}^{\omega_1}] - \hat{H}^{\omega_1}]|0\rangle - \omega_1 \langle 0|[\hat{\mathbf{q}}, \hat{\kappa}^{\omega_1}]|0\rangle = \langle 0|[\hat{\mathbf{q}}, \hat{V}^{\omega_1}]|0\rangle, \tag{76}$$

which can be written in matrix form as

$$(\mathbf{E} - \omega_1 \mathbf{S})\, \boldsymbol{\kappa}^{\omega_1} = \mathbf{V}^{\omega_1}, \tag{77}$$

where it has been used that $\hat{\kappa}^{\omega_1} = \hat{\mathbf{q}}^{\dagger} \boldsymbol{\kappa}^{\omega_1}$. The $\mathbf{E}$ matrix is defined through

$$\mathbf{E}\boldsymbol{\kappa}^{\omega_1} = -\langle 0|[\hat{\mathbf{q}}, [\hat{\kappa}^{\omega_1}, \hat{H}^{0}] + \hat{H}^{\omega_1}]|0\rangle, \tag{78}$$

the generalized overlap matrix is defined as

$$\mathbf{S} = \langle 0|[\hat{\mathbf{q}}, \hat{\mathbf{q}}^{\dagger}]|0\rangle, \tag{79}$$

and the perturbation vector is given by

$$\mathbf{V}^{\omega_1} = \langle 0|[\hat{\mathbf{q}}, \hat{V}^{\omega_1}]|0\rangle. \tag{80}$$

Having determined the first-order time-evolution parameters through Eq. (77), the linear response function $\langle\langle \hat{A}; \hat{V}^{\omega_1} \rangle\rangle_{\omega_1}$ for the property $\hat{A}$ perturbed by a periodic perturbation $\hat{V}^{\omega_1}$ with associated frequency ω_1 can be calculated as

$$\langle\langle \hat{A}; \hat{V}^{\omega_1} \rangle\rangle_{\omega_1} = \langle 0|[\hat{\kappa}^{\omega_1}, \hat{A}]|0\rangle = -\mathbf{A}^{\dagger} \boldsymbol{\kappa}^{\omega_1}. \tag{81}$$

Explicit contributions from the PE potential only enter the linear response function through the **E** matrix as

$$\mathbf{E}_{\mathrm{PE}}\boldsymbol{\kappa}^{\omega_1} = -\langle 0|[\hat{\mathbf{q}}, [\hat{\kappa}^{\omega_1}, \hat{v}^0_{\mathrm{PE}}] + \hat{v}^{\omega_1}_{\mathrm{PE}}]|0\rangle. \tag{82}$$

We define a new set of operators using one-index transformed integrals [15]

$$\hat{Q}^{\omega_1}_1 = [\hat{\kappa}^{\omega_1}, \hat{v}^0_{\mathrm{PE}}] = \hat{v}^0_{\mathrm{PE}}(\kappa^{\omega_1}) \tag{83}$$

$$\hat{Q}^{\omega_1}_2 = \hat{v}^{\omega_1}_{\mathrm{PE}} = -\sum_{s=1}^{S} \boldsymbol{\mu}^{\mathrm{ind}}_s(\tilde{\mathbf{F}}^{\omega_1})\hat{\mathbf{F}}^{(1)}_{s,\mathrm{el}}, \tag{84}$$

where the induced dipole moments are calculated using the transformed electric field $\tilde{\mathbf{F}}^{\omega_1}$ with elements evaluated according to

$$\tilde{\mathbf{F}}^{\omega_1}_s = \langle 0|[\hat{\kappa}^{\omega_1}, \hat{\mathbf{F}}^{(1)}_{s,\mathrm{el}}]|0\rangle = \langle 0|\hat{\mathbf{F}}^{(1)}_{s,\mathrm{el}}(\kappa^{\omega_1})|0\rangle. \tag{85}$$

Using the newly defined operators leads to a simplified expression for the PE contribution to the linearly transformed **E** matrix given by

$$\mathbf{E}_{\mathrm{PE}}\boldsymbol{\kappa}^{\omega_1} = -\langle 0|[\hat{\mathbf{q}}, \hat{Q}^{\omega_1}_1 + \hat{Q}^{\omega_1}_2]|0\rangle. \tag{86}$$

The $\hat{Q}^{\omega_1}_1$ operator gives the zeroth-order PE contribution to the linear response which corresponds to a static environment which does not respond to the applied perturbation, whereas the $\hat{Q}^{\omega_2}_2$ operator describes the dynamical response of the environment due to the perturbation. Here, it is important to note that this is the fully self-consistent many-body response without approximations, as opposed to other similar implementations [24, 25]. A common approximation corresponds to the use of a block-diagonal classical response matrix (Eq. (41)) in the response calculations, thus neglecting the off-diagonal interaction tensors, whereas we include the full classical response matrix in our model.

2.2.2. Quadratic response

The derivation of quadratic response proceeds analogous to the linear response case. Thus, we collect second-order terms from the BCH expansion of the Ehrenfest theorem as given in Eq. (74) and Fourier transform the resulting expression. In matrix form, this leads to

$$(\mathbf{E} - (\omega_1 + \omega_2)\mathbf{S})\boldsymbol{\kappa}^{\omega_1,\omega_2} = \mathbf{V}^{\omega_1,\omega_2}, \tag{87}$$

where the **E** matrix is defined through

$$\mathbf{E}\boldsymbol{\kappa}^{\omega_1,\omega_2} = \langle 0|[\hat{\mathbf{q}}, [\hat{H}^0, \hat{\kappa}^{\omega_1,\omega_2}] - {}^2\hat{H}^{\omega_1,\omega_2}]|0\rangle, \tag{88}$$

the **S** matrix is again the general overlap matrix, and the second-order perturbation vector $\mathbf{V}^{\omega_1,\omega_2}$ is defined as

$$\mathbf{V}^{\omega_1,\omega_2} = \hat{P}_{12}\Big(\langle 0|[\hat{\mathbf{q}},[\hat{\kappa}^{\omega_1},[\hat{\kappa}^{\omega_2},\hat{H}^0]] + 2[\hat{\kappa}^{\omega_1},\hat{H}^{\omega_2}+\hat{V}^{\omega_2}] + \omega_2[\hat{\mathbf{q}},[\hat{\kappa}^{\omega_1},\hat{\kappa}^{\omega_2}]] + {}^1\hat{H}^{\omega_1,\omega_2}]|0\rangle\Big). \tag{89}$$

We have used that the second-order perturbed density matrix elements (see Eq. (70)) can be separated into components due to first- and second-order parameters, respectively,

$$D_{pq}^{\omega_1,\omega_2} = {}^1D_{pq}^{\omega_1,\omega_2} + {}^2D_{pq}^{\omega_1,\omega_2}, \tag{90}$$

where

$${}^1D_{pq}^{\omega_1,\omega_2} = \hat{P}_{12}\langle 0|[\hat{\kappa}^{\omega_1},[\hat{\kappa}^{\omega_2},\hat{E}_{pq}]]|0\rangle \tag{91}$$

$${}^2D_{pq}^{\omega_1,\omega_2} = \langle 0|[\hat{\kappa}^{\omega_1,\omega_2},\hat{E}_{pq}]|0\rangle. \tag{92}$$

The separation of the density matrix elements allows the corresponding separation of the second-order Hamiltonian

$$\hat{H}^{\omega_1,\omega_2} = {}^1\hat{H}^{\omega_1,\omega_2} + {}^2\hat{H}^{\omega_1,\omega_2}, \tag{93}$$

where ${}^1\hat{H}^{\omega_1,\omega_2}$ depends on first-order parameters and ${}^2\hat{H}^{\omega_1,\omega_2}$ depends on second-order parameters. Instead of solving Eq. (87) for the second-order time-evolution parameters, we can solve the adjoint second-order linear response equation

$$\boldsymbol{\kappa}^{\mathbf{A}^\dagger}\big(\mathbf{E} - (\omega_1+\omega_2)\mathbf{S}\big) = \mathbf{A}^\dagger. \tag{94}$$

The first-order parameters are determined by solving two first-order linear response equations

$$\big(\mathbf{E} - \omega_i\mathbf{S}\big)\boldsymbol{\kappa}^{\omega_i} = \mathbf{V}^{\omega_i}, \tag{95}$$

where $i = 1$ or 2. The quadratic response function $\langle\langle \hat{A};\hat{V}^{\omega_1},\hat{V}^{\omega_2}\rangle\rangle_{\omega_1,\omega_2}$ for the property $\hat{A}$ perturbed by two periodic perturbations $\hat{V}^{\omega_1}$ and $\hat{V}^{\omega_2}$ with associated frequencies ω_1 and ω_2, respectively, is given by

$$\langle\langle \hat{A};\hat{V}^{\omega_1},\hat{V}^{\omega_2}\rangle\rangle_{\omega_1,\omega_2} = \langle 0|[\hat{\kappa}^{\omega_1,\omega_2},\hat{A}]|0\rangle + \hat{P}_{12}\langle 0|[\hat{\kappa}^{\omega_1},[\hat{\kappa}^{\omega_2},\hat{A}]]|0\rangle. \tag{96}$$

The explicit PE contributions to the quadratic response function enter the **E** matrix (Eq. (88)) and the $\mathbf{V}^{\omega_1,\omega_2}$ vector (Eq. (89)). Contributions that appear

in the **E** matrix are analogous to the linear response case, that is,

$$\mathbf{E}_{\mathrm{PE}}\boldsymbol{\kappa}^{\omega_1,\omega_2} = -\langle 0|[\hat{\mathbf{q}}, \hat{Q}_1^{\omega_1,\omega_2} + \hat{Q}_2^{\omega_1,\omega_2}]|0\rangle, \tag{97}$$

where

$$\hat{Q}_1^{\omega_1,\omega_2} = [\hat{\kappa}^{\omega_1,\omega_2}, \hat{v}_{\mathrm{PE}}^0] = \hat{v}_{\mathrm{PE}}^0(\kappa^{\omega_1,\omega_2}) \tag{98}$$

$$\hat{Q}_2^{\omega_1,\omega_2} = {}^2\hat{v}_{\mathrm{PE}}^{\omega_1,\omega_2} = -\sum_{s=1}^{S} \boldsymbol{\mu}_s^{\mathrm{ind}}({}^2\tilde{\mathbf{F}}^{\omega_1,\omega_2})\hat{\mathbf{F}}_{s,\mathrm{el}}^{(1)}. \tag{99}$$

The induced dipoles in $\hat{Q}_2^{\omega_1,\omega_2}$ are calculated using the transformed electric field with elements given by

$${}^2\tilde{\mathbf{F}}_s^{\omega_1,\omega_2} = \langle 0|[\hat{\kappa}^{\omega_1,\omega_2}, \hat{\mathbf{F}}_{s,\mathrm{el}}^{(1)}]|0\rangle = \langle 0|\hat{\mathbf{F}}_{s,\mathrm{el}}^{(1)}(\kappa^{\omega_1,\omega_2})|0\rangle. \tag{100}$$

The contributions to the perturbation vector are

$$\mathbf{V}_{\mathrm{PE}}^{\omega_1,\omega_2} = \langle 0|[\hat{\mathbf{q}}, \hat{Q}_3^{\omega_1,\omega_2} + \hat{Q}_4^{\omega_1,\omega_2} + \hat{Q}_5^{\omega_1,\omega_2}]|0\rangle, \tag{101}$$

where we have used new operators defined by

$$\hat{Q}_3^{\omega_1,\omega_2} = \hat{P}_{12}[\hat{\kappa}^{\omega_1}, [\hat{\kappa}^{\omega_2}, \hat{v}_{\mathrm{PE}}^0]] = \hat{P}_{12}\hat{v}_{\mathrm{PE}}^0(\kappa^{\omega_2}, \kappa^{\omega_1}) \tag{102}$$

$$\begin{aligned}\hat{Q}_4^{\omega_1,\omega_2} &= 2\hat{P}_{12}[\hat{\kappa}^{\omega_1}, \hat{v}_{\mathrm{PE}}^{\omega_2}] \\ &= -2\hat{P}_{12}\sum_{s=1}^{S} \boldsymbol{\mu}_s^{\mathrm{ind}}(\tilde{\mathbf{F}}^{\omega_2})[\hat{\kappa}^{\omega_1}, \hat{\mathbf{F}}_{s,\mathrm{el}}^{(1)}] \\ &= -2\hat{P}_{12}\sum_{s=1}^{S} \boldsymbol{\mu}_s^{\mathrm{ind}}(\tilde{\mathbf{F}}^{\omega_2})\hat{\mathbf{F}}_{s,\mathrm{el}}^{(1)}(\kappa^{\omega_1})\end{aligned} \tag{103}$$

$$\begin{aligned}\hat{Q}_5^{\omega_1,\omega_2} &= \hat{P}_{12}\,{}^1\hat{v}_{\mathrm{PE}}^{\omega_1,\omega_2} \\ &= -\hat{P}_{12}\sum_{s=1}^{S} \boldsymbol{\mu}_s^{\mathrm{ind}}({}^1\tilde{\mathbf{F}}^{\omega_1,\omega_2})\hat{\mathbf{F}}_{s,\mathrm{el}}^{(1)}.\end{aligned} \tag{104}$$

The perturbed electric field $\tilde{\mathbf{F}}^{\omega_2}$ is defined analogous to Eq. (85), and ${}^1\tilde{\mathbf{F}}^{\omega_1,\omega_2}$ is defined through

$${}^1\tilde{\mathbf{F}}_s^{\omega_1,\omega_2} = \langle 0|[\hat{\kappa}^{\omega_1}, [\hat{\kappa}^{\omega_2}, \hat{\mathbf{F}}_{s,\mathrm{el}}^{(1)}]]|0\rangle = \hat{\mathbf{F}}_{s,\mathrm{el}}^{(1)}(\kappa^{\omega_2}, \kappa^{\omega_1}). \tag{105}$$

The zeroth-order terms, that is, $\hat{Q}_1^{\omega_1,\omega_2}$ and $\hat{Q}_3^{\omega_1,\omega_2}$, give the contributions to the response function that arise from a static environment analogous to the linear response case. All the other contributions, that is, $\hat{Q}_2^{\omega_1,\omega_2}$, $\hat{Q}_4^{\omega_1,\omega_2}$, and $\hat{Q}_5^{\omega_1,\omega_2}$, account for the dynamical response of the environment due to the periodic perturbations.

2.2.3. Cubic response

The derivation of cubic response is analogous to what we have seen so far. We use the BCH expansion of the Ehrenfest theorem but now collect terms that are third order in the perturbation. The resulting matrix equation is

$$\big(\mathbf{E} - (\omega_1 + \omega_2 + \omega_3)\mathbf{S}\big)\boldsymbol{\kappa}^{\omega_1,\omega_2,\omega_3} = \mathbf{V}^{\omega_1,\omega_2,\omega_3}, \tag{106}$$

where $\mathbf{S}$ is the general overlap matrix, the $\mathbf{E}$ matrix is defined through

$$\mathbf{E}\boldsymbol{\kappa}^{\omega_1,\omega_2,\omega_3} = \langle 0|[\hat{\mathbf{q}}, [\hat{H}^0, \hat{\kappa}^{\omega_1,\omega_2,\omega_3}] - {}^2\hat{H}^{\omega_1,\omega_2,\omega_3}]|0\rangle, \tag{107}$$

and the third-order perturbation vector is given by

$$\begin{aligned}
\mathbf{V}^{\omega_1,\omega_2,\omega_3} = \hat{P}_{123}\langle 0|[\hat{\mathbf{q}}, [\hat{\kappa}^{\omega_1}, [\hat{\kappa}^{\omega_2}, [\hat{\kappa}^{\omega_3}, \hat{H}^0]]] + \frac{3}{2}[\hat{\kappa}^{\omega_1}, [\hat{\kappa}^{\omega_2,\omega_3}, \hat{H}^0]] \\
+ \frac{3}{2}[\hat{\kappa}^{\omega_1,\omega_2}, [\hat{\kappa}^{\omega_3}, \hat{H}^0]] + 3[\hat{\kappa}^{\omega_1}, [\hat{\kappa}^{\omega_2}, \hat{H}^{\omega_3} + \hat{V}^{\omega_3}]] \\
+ 3[\hat{\kappa}^{\omega_1}, \hat{H}^{\omega_2,\omega_3}] + 3[\hat{\kappa}^{\omega_1,\omega_2}, \hat{H}^{\omega_3} + \hat{V}^{\omega_3}] \\
+ \omega_3[\hat{\kappa}^{\omega_1}, [\hat{\kappa}^{\omega_2}, \hat{\kappa}^{\omega_3}]] + \frac{3}{2}(\omega_2 + \omega_3)[\hat{\kappa}^{\omega_1}, \hat{\kappa}^{\omega_2,\omega_3}] \\
+ \frac{3}{2}\omega_3[\hat{\kappa}^{\omega_1,\omega_2}, \hat{\kappa}^{\omega_3}] + {}^1\hat{H}^{\omega_1,\omega_2,\omega_3}]|0\rangle.
\end{aligned} \tag{108}$$

Here, we have also separated the perturbed density matrix into terms that depend on first- and second-order, and third-order parameters, respectively, as

$$D_{pq}^{\omega_1,\omega_2,\omega_3} = {}^1D_{pq}^{\omega_1,\omega_2,\omega_3} + {}^2D_{pq}^{\omega_1,\omega_2,\omega_3} \tag{109}$$

where

$$\begin{aligned}
{}^1D_{pq}^{\omega_1,\omega_2,\omega_3} = \hat{P}_{123}\langle 0|\tfrac{3}{2}[\hat{\kappa}^{\omega_1}, [\hat{\kappa}^{\omega_2,\omega_3}, \hat{E}_{pq}]] + \tfrac{3}{2}[\hat{\kappa}^{\omega_1,\omega_2}, [\hat{\kappa}^{\omega_3}, \hat{E}_{pq}]] \\
+ [\hat{\kappa}^{\omega_1}, [\hat{\kappa}^{\omega_2}, [\hat{\kappa}^{\omega_3}, \hat{E}_{pq}]]]|0\rangle
\end{aligned} \tag{110}$$

$${}^2D_{pq}^{\omega_1,\omega_2,\omega_3} = \langle 0|[\hat{\kappa}^{\omega_1,\omega_2,\omega_3}, \hat{E}_{pq}]|0\rangle. \tag{111}$$

Thus allowing us to write the third-order Hamiltonian as

$$\hat{H}^{\omega_1,\omega_2,\omega_3} = {}^1\hat{H}^{\omega_1,\omega_2,\omega_3} + {}^2\hat{H}^{\omega_1,\omega_2,\omega_3} \tag{112}$$

where ${}^1\hat{H}^{\omega_1,\omega_2,\omega_3}$ depends on first- and second-order parameters and ${}^2\hat{H}^{\omega_1,\omega_2,\omega_3}$ only depends on third-order parameters. The first- and second-order variational parameters are determined by solving three first-order linear response equations

$$\big(\mathbf{E} - \omega_i \mathbf{S}\big)\boldsymbol{\kappa}^{\omega_i} = \mathbf{V}^{\omega_i}, \tag{113}$$

where $i = 1$, 2, or 3, and three second-order linear response equations

$$\big(\mathbf{E} - (\omega_i + \omega_j)\mathbf{S}\big)\boldsymbol{\kappa}^{\omega_i,\omega_j} = \mathbf{V}^{\omega_i,\omega_j} \tag{114}$$

where $j > i$ and $i, j = 1$, 2, or 3, or the adjoints (Eq. (94)) of them. The third-order parameters are determined by the adjoint third-order linear response equation

$$\boldsymbol{\kappa}^{\mathbf{A}^\dagger}\big(\mathbf{E} - (\omega_1 + \omega_2 + \omega_3)\mathbf{S}\big) = \mathbf{A}^\dagger. \tag{115}$$

The cubic response function $\langle\langle \hat{A}; \hat{V}^{\omega_1}, \hat{V}^{\omega_2}, \hat{V}^{\omega_3} \rangle\rangle_{\omega_1,\omega_2,\omega_3}$ for the property $\hat{A}$ perturbed by the periodic perturbations $\hat{V}^{\omega_1}$, $\hat{V}^{\omega_2}$, and $\hat{V}^{\omega_3}$ with associated frequencies ω_1, ω_2, and ω_3, respectively, is given by

$$\begin{aligned}
\langle\langle \hat{A}; \hat{V}^{\omega_1}, \hat{V}^{\omega_2}, \hat{V}^{\omega_3} \rangle\rangle_{\omega_1,\omega_2,\omega_3} = {} & \langle 0|[\hat{\kappa}^{\omega_1,\omega_2,\omega_3}, \hat{A}]|0\rangle \\
& + \frac{3}{2}\hat{P}_{123}\langle 0|[\hat{\kappa}^{\omega_1}, [\hat{\kappa}^{\omega_2,\omega_3}, \hat{A}]]|0\rangle \\
& + \frac{3}{2}\hat{P}_{123}\langle 0|[\hat{\kappa}^{\omega_1,\omega_2}, [\hat{\kappa}^{\omega_3}, \hat{A}]]|0\rangle \\
& + \hat{P}_{123}\langle 0|[\hat{\kappa}^{\omega_1}, [\hat{\kappa}^{\omega_2}, [\hat{\kappa}^{\omega_3}, \hat{A}]]]|0\rangle.
\end{aligned} \tag{116}$$

We will now detail the explicit contributions that are due to the PE potential to the cubic response function, which enter through the $\mathbf{E}$ matrix and the $\mathbf{V}^{\omega_1,\omega_2,\omega_3}$ vector. The contributions to the $\mathbf{E}$ matrix are defined through

$$\mathbf{E}_{\mathrm{PE}}\boldsymbol{\kappa}^{\omega_1,\omega_2,\omega_3} = -\langle 0|[\hat{\mathbf{q}}, \hat{Q}_1^{\omega_1,\omega_2,\omega_3} + \hat{Q}_2^{\omega_1,\omega_2,\omega_3}|0\rangle, \tag{117}$$

where the $\hat{Q}_1^{\omega_1,\omega_2,\omega_3}$ operator contains the zeroth-order PE potential operator and is defined as

$$\hat{Q}_1^{\omega_1,\omega_2,\omega_3} = [\hat{\kappa}^{\omega_1,\omega_2,\omega_3}, \hat{v}^0_{\mathrm{PE}}] = \hat{v}^0_{\mathrm{PE}}(\boldsymbol{\kappa}^{\omega_1,\omega_2,\omega_3}), \tag{118}$$

and the $\hat{Q}_2^{\omega_1,\omega_2,\omega_3}$ operator contains the part of the third-order PE potential operator that only depends on the third-order parameters and is defined as

$$\hat{Q}_2^{\omega_1,\omega_2,\omega_3} = {}^2\hat{v}_{\mathrm{PE}}^{\omega_1,\omega_2,\omega_3} = -\sum_{s=1}^{S} \boldsymbol{\mu}_s^{\mathrm{ind}}({}^2\tilde{\mathbf{F}}^{\omega_1,\omega_2,\omega_3})\hat{\mathbf{F}}_{s,\mathrm{el}}^{(1)}. \tag{119}$$

The induced dipoles in $\hat{Q}_2^{\omega_1,\omega_2,\omega_3}$ depend on the transformed electric field ${}^2\tilde{\mathbf{F}}^{\omega_1,\omega_2,\omega_3}$ that is given through

$${}^2\tilde{\mathbf{F}}_s^{\omega_1,\omega_2,\omega_3} = \langle 0|[\hat{\kappa}^{\omega_1,\omega_2,\omega_3}, \hat{\mathbf{F}}_{s,\mathrm{el}}^{(1)}]|0\rangle = \langle 0|\hat{\mathbf{F}}_{s,\mathrm{el}}^{(1)}(\boldsymbol{\kappa}^{\omega_1,\omega_2,\omega_3})|0\rangle. \tag{120}$$

The contributions to the perturbation vector are defined as

$$\begin{aligned}\mathbf{V}_{\mathrm{PE}}^{\omega_1,\omega_2,\omega_3} = \langle 0|[\hat{\mathbf{q}}, \hat{Q}_3^{\omega_1,\omega_2,\omega_3} + \hat{Q}_4^{\omega_1,\omega_2,\omega_3} + \hat{Q}_5^{\omega_1,\omega_2,\omega_3} + \hat{Q}_6^{\omega_1,\omega_2,\omega_3} \\ + \hat{Q}_7^{\omega_1,\omega_2,\omega_3} + \hat{Q}_8^{\omega_1,\omega_2,\omega_3} + \hat{Q}_9^{\omega_1,\omega_2,\omega_3}]|0\rangle,\end{aligned} \tag{121}$$

where we again define new operators. Here, the $\hat{Q}_3^{\omega_1,\omega_2,\omega_3}$, $\hat{Q}_4^{\omega_1,\omega_2,\omega_3}$, and $\hat{Q}_5^{\omega_1,\omega_2,\omega_3}$ operators contain the zeroth-order PE potential operator and are defined as

$$\hat{Q}_3^{\omega_1,\omega_2,\omega_3} = \hat{P}_{123}[\hat{\kappa}^{\omega_1}, [\hat{\kappa}^{\omega_2}, [\hat{\kappa}^{\omega_3}, \hat{v}_{\mathrm{PE}}^0]]] = \hat{P}_{123}\hat{v}_{\mathrm{PE}}^0(\boldsymbol{\kappa}^{\omega_3}, \boldsymbol{\kappa}^{\omega_2}, \boldsymbol{\kappa}^{\omega_1}) \tag{122}$$

$$\hat{Q}_4^{\omega_1,\omega_2,\omega_3} = \frac{3}{2}\hat{P}_{123}[\hat{\kappa}^{\omega_1}, [\hat{\kappa}^{\omega_2,\omega_3}, \hat{v}_{\mathrm{PE}}^0]] = \frac{3}{2}\hat{P}_{123}\hat{v}_{\mathrm{PE}}^0(\boldsymbol{\kappa}^{\omega_2,\omega_3}, \boldsymbol{\kappa}^{\omega_1}) \tag{123}$$

$$\hat{Q}_5^{\omega_1,\omega_2,\omega_3} = \frac{3}{2}\hat{P}_{123}[\hat{\kappa}^{\omega_1,\omega_2}, [\hat{\kappa}^{\omega_3}, \hat{v}_{\mathrm{PE}}^0]] = \frac{3}{2}\hat{P}_{123}\hat{v}_{\mathrm{PE}}^0(\boldsymbol{\kappa}^{\omega_3}, \boldsymbol{\kappa}^{\omega_1,\omega_2}), \tag{124}$$

whereas the $\hat{Q}_6^{\omega_1,\omega_2,\omega_3}$ and $\hat{Q}_7^{\omega_1,\omega_2,\omega_3}$ operators contain first-order PE potential operators and are defined as

$$\begin{aligned}\hat{Q}_6^{\omega_1,\omega_2,\omega_3} &= 3\hat{P}_{123}[\hat{\kappa}^{\omega_1}, [\hat{\kappa}^{\omega_2}, \hat{v}_{\mathrm{PE}}^{\omega_3}]] \\ &= -3\hat{P}_{123}\sum_{s=1}^{S} \boldsymbol{\mu}_s^{\mathrm{ind}}(\tilde{\mathbf{F}}^{\omega_3})\hat{\mathbf{F}}_{s,\mathrm{el}}^{(1)}(\boldsymbol{\kappa}^{\omega_2}, \boldsymbol{\kappa}^{\omega_1}),\end{aligned} \tag{125}$$

$$\hat{Q}_7^{\omega_1,\omega_2,\omega_3} = 3\hat{P}_{123}[\hat{\kappa}^{\omega_1,\omega_2}, \hat{v}_{\mathrm{PE}}^{\omega_3}] = -3\hat{P}_{123}\sum_{s=1}^{S} \boldsymbol{\mu}_s^{\mathrm{ind}}(\tilde{\mathbf{F}}^{\omega_3})\hat{\mathbf{F}}_{s,\mathrm{el}}^{(1)}(\boldsymbol{\kappa}^{\omega_1,\omega_2}). \tag{126}$$

The transformed electric field $\tilde{\mathbf{F}}^{\omega_3}$ is defined through

$$\tilde{\mathbf{F}}_s^{\omega_3} = \langle 0|[\hat{\kappa}^{\omega_3}, \hat{\mathbf{F}}_{s,\mathrm{el}}^{(1)}]|0\rangle = \langle 0|\hat{\mathbf{F}}_{s,\mathrm{el}}^{(1)}(\boldsymbol{\kappa}^{\omega_3})|0\rangle. \tag{127}$$

The $\hat{Q}_8^{\omega_1,\omega_2,\omega_3}$ operator contains a second-order PE potential operator and is defined as

$$\hat{Q}_8^{\omega_1,\omega_2,\omega_3} = 3\hat{P}_{123}[\hat{\kappa}^{\omega_1}, \hat{v}_{\mathrm{PE}}^{\omega_2,\omega_3}] = -3\hat{P}_{123}\sum_{s=1}^{S} \boldsymbol{\mu}_s^{\mathrm{ind}}(\tilde{\mathbf{F}}^{\omega_2,\omega_3})\hat{\mathbf{F}}_{s,\mathrm{el}}^{(1)}(\boldsymbol{\kappa}^{\omega_1}), \tag{128}$$

where the induced dipoles depend on the electric field from the second-order electron density (Eq. (90)). The transformed electric field $\tilde{\mathbf{F}}^{\omega_2,\omega_3}$ is therefore given through

$$\begin{aligned}\tilde{\mathbf{F}}_s^{\omega_2,\omega_3} &= \langle 0|[\hat{\kappa}^{\omega_2,\omega_3}, \hat{\mathbf{F}}_{s,\mathrm{el}}^{(1)}] + \hat{P}_{23}[\hat{\kappa}^{\omega_2}, [\hat{\kappa}^{\omega_3}, \hat{\mathbf{F}}_{s,\mathrm{el}}^{(1)}]]|0\rangle \\ &= \langle 0|\hat{\mathbf{F}}_{s,\mathrm{el}}^{(1)}(\boldsymbol{\kappa}^{\omega_2,\omega_3}) + \hat{P}_{23}\hat{\mathbf{F}}_{s,\mathrm{el}}^{(1)}(\boldsymbol{\kappa}^{\omega_3}, \boldsymbol{\kappa}^{\omega_2})|0\rangle. \end{aligned} \tag{129}$$

Finally, the $\hat{Q}_9^{\omega_1,\omega_2,\omega_3}$ operator, which contains the part of the third-order PE potential operator and depends on lower order variational parameters, is defined as

$$\hat{Q}_9^{\omega_1,\omega_2,\omega_3} = \hat{P}_{123}\,{}^1\hat{v}_{\mathrm{PE}}^{\omega_1,\omega_2,\omega_3} = -\hat{P}_{123}\sum_{s=1}^{S} \boldsymbol{\mu}_s^{\mathrm{ind}}({}^1\tilde{\mathbf{F}}^{\omega_1,\omega_2,\omega_3})\hat{\mathbf{F}}_{s,\mathrm{el}}^{(1)}. \tag{130}$$

Here, the induced dipoles depend on the electric field from the part of the third-order electron density which depends on lower order parameters (Eq. (110)). The transformed electric field ${}^1\tilde{\mathbf{F}}^{\omega_1,\omega_2,\omega_3}$ is, thus, defined through

$$\begin{aligned}{}^1\tilde{\mathbf{F}}_s^{\omega_1,\omega_2,\omega_3} &= \langle 0|\frac{3}{2}[\hat{\kappa}^{\omega_1}, [\hat{\kappa}^{\omega_2,\omega_3}, \hat{\mathbf{F}}_{s,\mathrm{el}}^{(1)}]] + \frac{3}{2}[\hat{\kappa}^{\omega_1,\omega_2}, [\hat{\kappa}^{\omega_3}, \hat{\mathbf{F}}_{s,\mathrm{el}}^{(1)}]] \\ &\quad + [\hat{\kappa}^{\omega_1}, [\hat{\kappa}^{\omega_2}, [\hat{\kappa}^{\omega_3}, \hat{\mathbf{F}}_{s,\mathrm{el}}^{(1)}]]]|0\rangle \\ &= \langle 0|\frac{3}{2}\hat{\mathbf{F}}_{s,\mathrm{el}}^{(1)}(\boldsymbol{\kappa}^{\omega_2,\omega_3}, \boldsymbol{\kappa}^{\omega_1}) + \frac{3}{2}\hat{\mathbf{F}}_{s,\mathrm{el}}^{(1)}(\boldsymbol{\kappa}^{\omega_3}, \boldsymbol{\kappa}^{\omega_1,\omega_2}) \\ &\quad + \hat{\mathbf{F}}_{s,\mathrm{el}}^{(1)}(\boldsymbol{\kappa}^{\omega_3}, \boldsymbol{\kappa}^{\omega_2}, \boldsymbol{\kappa}^{\omega_1})|0\rangle. \end{aligned} \tag{131}$$

Considerations regarding the effect that the operators have, with respect to the response in the environment, are analogous to the linear and quadratic response, that is, zeroth-order terms correspond to a static environment, whereas higher-order terms account for dynamic response in the environment.

2.3. Calculation of nuclear magnetic shielding tensors for embedded molecules

Nuclear magnetic resonance (NMR) is one of the most important site-specific and sensitive probes for electronic environments and hence for molecular

structure determination. In this section, we will briefly outline the theory related to the calculation of NMR shielding constants within the polarizable embedding approach. The nuclear magnetic shielding tensor $\boldsymbol{\sigma}^N$ for nucleus N is defined as the second-order response of the electronic energy to an external magnetic induction ($\mathbf{B}$) and a nuclear magnetic moment ($\mathbf{m}_N$). In the atomic orbital (AO) basis, the expression becomes (see e.g., the discussion in Refs. [26, 27])

$$\begin{aligned}\sigma_{ij}^N &= 1 + \left[\frac{\mathrm{d}^2 E}{\mathrm{d}B_i \mathrm{d}m_{N_j}}\right]_{B=m_{N_j}=0} \\ &= 1 + \sum_{\mu\nu} D_{\mu\nu} \frac{\partial^2 h_{\mu\nu}}{\partial B_i \partial m_{N_j}} + \sum_{\mu\nu} \frac{\partial D_{\mu\nu}}{\partial B_i} \frac{\partial h_{\mu\nu}}{\partial m_{N_j}},\end{aligned} \tag{132}$$

where $D_{\mu\nu}$ is an element of the density matrix in the AO basis and $h_{\mu\nu}$ is a matrix element of the effective one-electron Hamiltonian. In our implementation of the nuclear magnetic shielding tensors, the second term in Eq. (132) (the paramagnetic contribution) is determined by solving a set of PE-DFT response equations [23, 24, 28] for the three components of the magnetic induction. In order to ensure origin-independent results for the nuclear magnetic shielding constants, we use gauge-including atomic orbitals (GIAOs) [29–32]—that is, the AO basis functions depend explicitly on the magnetic induction through

$$\chi_\mu(\mathbf{B}) = \exp\left(\frac{-i}{2}(\mathbf{B} \times \mathbf{R}_\mu) \cdot \mathbf{r}\right) \chi_\mu(0), \tag{133}$$

where $\mathbf{R}_\mu$ is the vector giving the position of the nucleus to which the field-dependent basis function is attached relative to the global gauge origin, and $\chi_\mu(0)$ indicates a conventional AO basis function not depending on $\mathbf{B}$. Equation (132) applies both to the case of a molecule in vacuum and within an environment. The (polarizable) environment contributes both through the density matrix, which is obtained self-consistently including the perturbation from the surroundings, *and* through the derivative of the density matrix (or the response vectors in our context) with respect to the magnetic induction, that is, both terms in Eq. (132) contain the effect of the environment [33].

The first derivative of the density matrix with respect to the magnetic induction is obtained by solving the coupled-perturbed Kohn–Sham (CPKS) equations to which the first derivative of the effective Kohn–Sham operator with respect to the magnetic induction contributes. We refer to Ref. [34] for a discussion of this and related issues regarding the calculation of nuclear magnetic shielding constants using HF or DFT methods. In our context, we need to solve the response equations corresponding to the perturbation from

the magnetic induction. Due to the use of GIAOs, specific corrections arising from the effective operator describing the environment effects will appear. In the following, we will focus on these contributions [35].

In the field-dependent AO basis, an element of the PE potential operator becomes

$$v_{\mathrm{PE},\mu\nu} = \sum_{s=1}^{S}\sum_{|k|=0}^{K}\frac{(-1)^{|k|}}{k!}Q_s^{(k)}t_{s,\mu\nu}^{(k)} - \sum_{s=1}^{S}\boldsymbol{\mu}_s^{\mathrm{ind}}(\mathbf{F}_{\mathrm{tot}})\mathbf{t}_{s,\mu\nu}^{(1)}, \tag{134}$$

where the integrals are taken over the interaction tensors used in all cases of the field-dependent AOs. The first derivative of the PE potential operator with respect to the magnetic induction may be written in the same form as $\hat{v}_{\mathrm{PE}}$ but with modified integrals [35]

$$\frac{dv_{\mathrm{PE},\mu\nu}}{dB_i} = \sum_{s=1}^{S}\sum_{|k|=0}^{K}\frac{(-1)^{|k|}}{k!}Q_s^{(k)}t_{s,\mu\nu,B_i}^{(k)} - \sum_{s=1}^{S}\boldsymbol{\mu}_s^{\mathrm{ind}}(\mathbf{F}_{\mathrm{tot}})\mathbf{t}_{s,\mu\nu,B_i}^{(1)}. \tag{135}$$

In Eq. (135), $t_{s,\mu\nu,B_i}^{(k)}$ is defined as

$$t_{s,\mu\nu,B_i}^{(k)} = \langle\chi_\mu^{B_i}|T_s^{(k)}(\mathbf{r})|\chi_\nu\rangle + \langle\chi_\mu|T_s^{(k)}(\mathbf{r})|\chi_\nu^{B_i}\rangle, \tag{136}$$

where the superscript on the atomic orbitals indicates differentiation of the relevant quantity. Such integrals may be evaluated, following the notation introduced in Refs. [28, 36], by use of the general expression for the first derivative of an arbitrary nondifferential operator (I) that does not depend on the magnetic induction

$$(I_{\mu\nu,\mathbf{B}})_{\mathbf{B}=0} = \frac{i}{2}Q_{MN}\langle\chi_\mu|\mathbf{r}I|\chi_\nu\rangle, \tag{137}$$

where we have located χ_μ at $\mathbf{R}_M$ and χ_ν at $\mathbf{R}_N$, and where Q_{MN} is defined as

$$Q_{MN} = \begin{pmatrix} 0 & -Z_{MN} & Y_{MN} \\ Z_{MN} & 0 & -X_{MN} \\ -Y_{MN} & X_{MN} & 0 \end{pmatrix}. \tag{138}$$

Finally, combining Eqs. (135 and 137) enables us to derive an equation for calculating the required derivatives of the environmental contributions because of the use of GIAOs.

3. RESULTS AND DISCUSSION

In the following, we will review a few selected applications related to the PE-DFT approach. Here, the focus will be on solute–solvent systems, although

the PE scheme is generally applicable to any confined molecular system such as for example photoactive proteins [7]. We will begin by discussing the general accuracy of the embedding potential.

3.1. The accuracy of the embedding potential: A hierarchy of force fields

To model the effects of the solvent molecules in a solute–solvent system, we use PE potentials based on a hierarchy of force fields as defined by the LoProp approach [37], which is a scheme for calculating localized multipoles and polarizabilities. The derived force fields are based on B3LYP/aug-cc-pVTZ and have been obtained from the Molcas program [38]. The force fields are classified as MXPY where X denotes the highest order of the multipole moments and Y indicates whether it includes isotropic ($Y = 1$) or anisotropic ($Y = 2$) polarizabilities. These parameters are attributed to the atomic sites of the solvent molecules, which, in the present context, will be water. In addition to the MXPY force fields, we also define a force field denoted M2P2BM, which includes multipoles up to quadrupoles and anisotropic polarizabilities assigned to both atomic sites and bond midpoints. The above discussed force fields all include polarization effects explicitly. However, to compare with force fields where polarization is included implicitly, a series of force fields using the PCM model [19], which we denote MXPCM, is also derived and discussed. In this case, the induction effects are incorporated implicitly into the multipole moments. Finally, we have, for comparison, also included results based on the use of the conventional Ahlström [39] force field (a simplified polarizable force field) and the standard nonpolarizable TIP3P force field due to Jorgensen [40].

The quality of the force fields is assessed by comparing the molecular electrostatic potentials, in the vicinity of the molecule, based on the force field and quantum chemical reference calculations. The electrostatic potential is the most suitable observable for such a comparison since it enters directly in the PE potential operator. To probe the electrostatic potential, a grid was constructed around the water molecule, see Ref. [6] for details concerning the construction of this grid. The electrostatic potential, due to the multipoles, at the ath grid point was calculated according to

$$\varphi_a = \sum_{s=1}^{S} \sum_{|k|=0}^{K} \frac{(-1)^{|k|}}{k!} T_{as}^{(k)} Q_s^{(k)}, \tag{139}$$

where the summation is over all multipole expansion centers in the molecule and all multipoles. The QM electrostatic potential at the ath grid point is the expectation value of the $|\mathbf{r}_a - \mathbf{r}|^{-1}$ operator plus the nuclear contribution. The B3LYP exchange-correlation functional and the aug-cc-pVTZ basis set, that is, the same method used to derive the LoProp force fields, were used to evaluate the QM reference electrostatic potential. The analysis is then performed

in terms of the root mean square deviation (RMSD)

$$\mathrm{RMSD} = \sqrt{\frac{1}{N}\sum_{a}\left(\varphi_a - \varphi_a^{\mathrm{QM}}\right)^2}, \tag{140}$$

where N is the number of the grid points. Following similar strategies, it is possible to probe the quality of the polarizabilities. However, for the polarizabilities, it is necessary to apply an external homogeneous electric field in the calculation of the electrostatic potential. This field will give rise to induced dipoles, which in turn creates an electrostatic potential around the molecule. Two calculations are then performed at the B3LYP/aug-cc-pVTZ level: one with and another without the external electric field. The QM reference is then obtained by subtracting the electrostatic potential in vacuum from that in the external field at every grid point.

In Figure 3.1, we present the RMSD obtained by a comparison between the molecular electrostatic potential due to multipole moments taken from the considered force fields and the quantum mechanically computed potential for different distances from the molecular van der Waals surface. From Figure 3.1, it is clearly demonstrated that the multipole expansion is appropriate at large distances from the molecule and that higher order multipoles are mandatory to consider when the molecular potential close to the

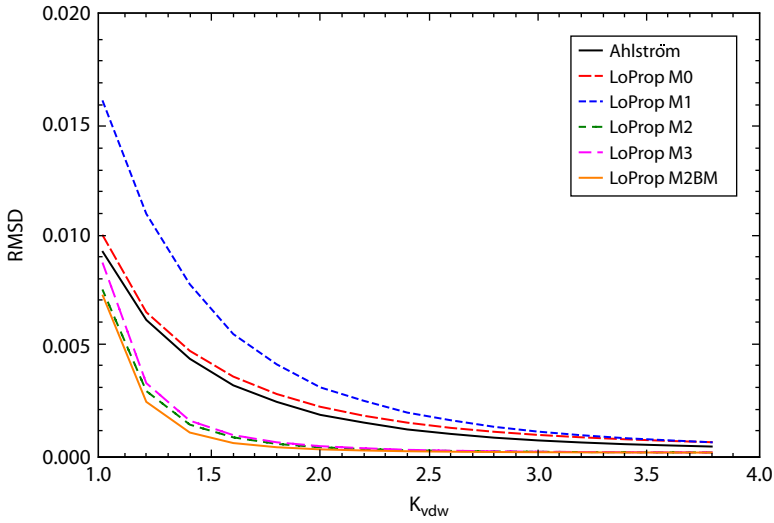

Figure 3.1 The RMSD of the molecular electrostatic potential due to the multipoles of a water molecule as a function of the distance from the molecular van der Waals surface. The distance from the surface is given as the factor scaling the van der Waals radii. The RMSD is in a.u. Results from Ref. [6].

molecule is probed. Quadrupole moments have a very pronounced effect and improve the molecular electrostatic potential considerably, as it was also found in Ref. [41]. On the other hand, the octopole moments contribute little to the accuracy of the electrostatic potential. The atomic point charges in the Ahlström force field are constructed so as to implicitly include higher order multipoles. However, it is evident from Figure 3.1 that the improvement is negligible compared with the M0 force field and cannot match the performance of the M2 force field. We see that the LoProp force field that includes multipoles at bond midpoints (M2BM) offers minor improvement as well. We also inspected the M3BM force field, and additional octopoles placed at bond midpoints were found to provide virtually no improvement.

Similarly, in Figure 3.2, we compare the induced changes in the electrostatic potentials due to an external electric field. From this we observe that the distributed isotropic polarizabilities in the LoProp force field lead to a more accurate account of the polarization of the electrostatic potential as compared to the single molecular isotropic polarizability assigned to the oxygen site of the water molecule in the Ahlström force field. Further improvement, though not that pronounced, is achieved by using the anisotropic polarizabilities. However, a larger difference in other molecules with a higher degree of anisotropy than the water molecule could be expected. We note that the RMSD in the case of induced dipoles is smaller by at least an order of magnitude than that due to the multipoles. This indicates

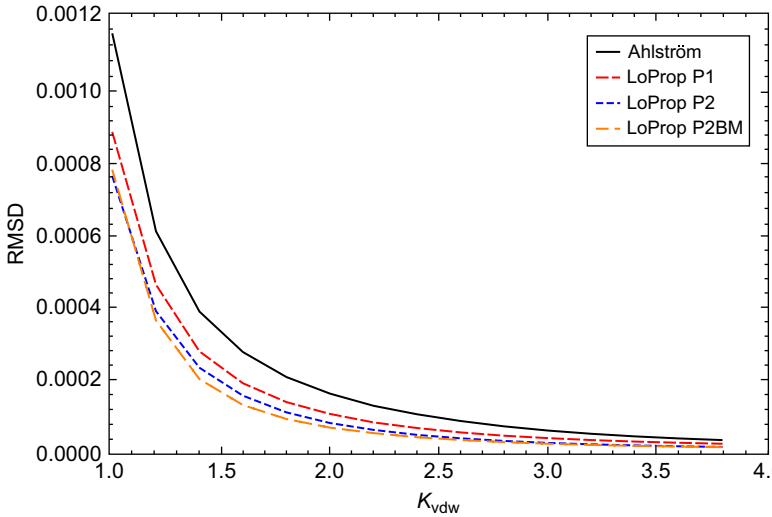

Figure 3.2 The RMSD of the molecular electrostatic potential due to the induced dipole moments of a water molecule as a function of the distance from the molecular van der Waals surface. The distance from the surface is given as the factor scaling the van der Waals radii. The RMSD is in a.u. Results from Ref. [6].

that the specific description of the polarization is not as important as an accurate account of the electrostatics.

3.2. Excitation energies

In this section, we examine the effects from a water solvent on the excitation energies of the solute molecule, acetone, using the PE-DFT method in combination with the embedding potentials assessed in Section 3.1 More specifically, we investigate the behavior of the solvent-induced shifts of the excitation energies as we vary the complexity of the force field used in the PE-DFT calculations. The QM region is restricted to contain only the solute molecule, and we thereby only include electrostatic and induction effects in the calculated shifts. The PE-DFT results for the shift of the excitation energies in acetone are the statistical averages over 120 molecular configurations extracted from a molecular dynamics simulation [6]. A spherical cutoff radius equal to 12 Å based on the distance between the center of masses of the solute and solvent molecules was used for every configuration. The calculations are furthermore based on the use of the CAM-B3LYP hybrid exchange-correlation functional [42] in combination with the aug-cc-pVDZ basis set.

The calculated solvent shifts are shown in Figure 3.3 together with the experimental solvent shift [43]. The first columns, that is, M0, M1, M2 M3 show the trends of the shifts with increasing order of the multipole expansion. These force fields do not model solvent polarization and are only used to investigate the effects of the higher order multipoles on the

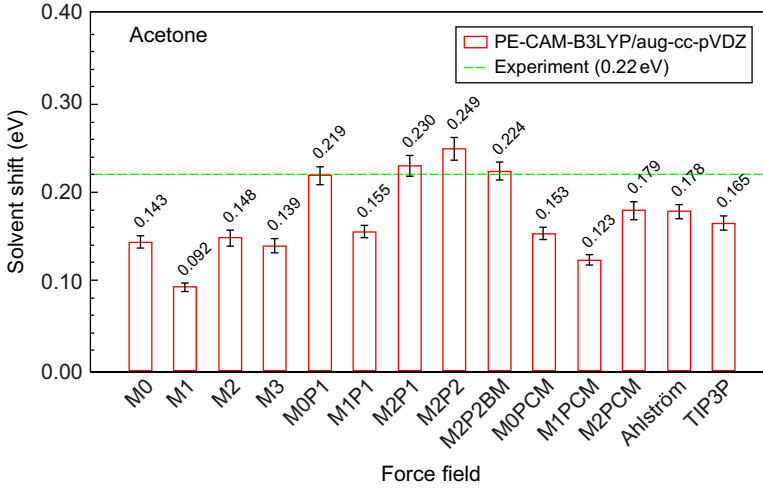

Figure 3.3 The gas-to-aqueous solvent shift of the lowest $n \rightarrow \pi^*$ excitation energy in acetone. Results from Ref. [6].

excitation energies. In all cases, we observe a large effect from both the dipole and quadrupole moments. On the other hand, the inclusion of octopoles leads to very small changes, indicating that we are converged at the quadrupole level with respect to the order of the permanent multipole moments. Thereby, we find a clear correlation between the trends here and the behavior of the force fields in terms of how well they reproduce the QM electrostatic potential. Note that the shifts at the M0 and M2 and M3 levels in general are very similar due to the fact that the effects from the dipole and quadrupole moments tend to cancel each other. Introducing distributed isotropic polarizabilities in addition to the permanent multipoles, that is, M0P1, M1P1 and M2P1, leads to an increase of the solvent shifts. Comparing the shifts calculated at the M2P1 level to the M2 level shows that the solvent shifts are increased from about 50% in the case of $n \rightarrow \pi^*$ transitions in acetone. This clearly shows that induction effects have a significant impact on the solvent shifts and therefore must be taken into account. The use of distributed anisotropic polarizabilities, that is, the M2P2 force field, only gives small improvements as compared to the distributed isotropic polarizabilities. This can probably be explained by the rather small degree of anisotropy of the water molecule. Using the most sophisticated LoProp force field, M2P2BM, decreases the solvent shifts by a small amount as compared to the M2P2 force field. This indicates that the M2P2 force field has a tendency to overestimate the induction effects, at least in the present case. It is interesting to note that the M0P1 force field performs rather well compared with the full M2P2BM force field. Therefore, we find that an acceptable approximation would be to use the M0P1 force field that captures the main parts of the electrostatics and induction effects due to a water solvent on the vertical excitation energies.

Recognizing that it is necessary to include the induction effects, a natural question is whether an explicit inclusion of polarization is needed or if it is sufficient to have implicit polarization by using enhanced permanent multipoles as obtained in the MXPCM force fields. Using the M0PCM, M1PCM, and M2PCM force fields, we obtained larger solvent shifts as compared to the M0, M1, and M2 force fields. Still, these MXPCM-based solvent shifts are not as accurate as in the case where explicit polarization has been taken into account, which clearly illustrates the importance of explicit polarization effects.

3.3. Nuclear magnetic resonance chemical shifts

As a further example on the use of the PE scheme, we discuss the calculation of NMR shielding constants for molecules in solution. More specifically, we will focus on the case of pyridine in water solution [44]. The NMR calculations presented here are based on the use of the PBE0 functional combined with the 6-311++G(2d,2p) basis set. The PE-DFT results for the NMR

Table 3.1 The statistically averaged ^{15}N NMR isotropic shielding constants of pyridine in aqueous solution, σ^N, (in ppm) and corresponding solvent shifts, $\Delta\sigma^N$. Experimental data is taken from Ref. [46]. Results from Ref. [44]

QM part	σ^N	$\Delta\sigma^N$
NC_5H_5	-62.0 ± 0.3	28.9 ± 0.3
$NC_5H_5 + 1\ H_2O$	-64.7 ± 0.6	26.2 ± 0.6
$NC_5H_5 + 2\ H_2O$	-65.9 ± 0.6	25.0 ± 0.6
exp.		29.7

shielding constants of pyridine are the statistical averages over 200 molecular configurations extracted from a molecular dynamics simulation [44]. The NMR results will be restricted to the use of the Ahlström water potential. Below, we will address the issue of hydrogen bonding between pyridine and water and investigate the effect of this on the NMR shielding constant of the nitrogen nucleus in pyridine. Our interest is in the gas-to-aqueous solution shifts of the ^{15}N NMR isotropic shielding constants denoted by $\Delta\sigma^N$.

The computed gas-to-aqueous solution shifts of the ^{15}N NMR isotropic shielding constant of pyridine are collected in Table 3.1. We begin by considering the pyridine molecule at the selected PBE0/6-311++G(2d,2p) level and all water molecules treated classically using the Ahlström force field. The obtained solvent shift in σ^N of 28.9 $\pm$ 0.3 ppm is in fairly good agreement with the experimental result of 29.7 ppm. As discussed in the previous sections, the Ahlström water potential is not completely converged with respect to the electrostatic potential. Furthermore, it is well known that nonelectrostatic solute–solvent effects may have a nonnegligible effect on NMR shielding tensors. Therefore, we include in the QM region one or two explicit water molecules selected from the molecular dynamics simulation. For these extended PE-DFT calculations, we observe a decrease in the predicted result from the solvent shift of the ^{15}N NMR isotropic shielding constant of 2.7 ppm when one water molecule is included in the QM region and a further 1.2 ppm when two water molecules are treated by quantum mechanics. Overall, it is seen that inclusion of explicit water molecules at the QM level leads to slightly underestimated results for the predicted solvent shifts. The reason for this decreased agreement between experiment and theory is most likely to be found in the neglect of rovibrational averaging on $\Delta\sigma^N$, something which has previously been proved to be important in some cases [45].

3.4. Second hyperpolarizabilities

As a final example of the applicability of the PE-DFT method, we consider in this section calculations related to a higher order response property, namely,

the second hyperpolarizability. The calculation of accurate nonlinear optical (NLO) properties of molecules in the condensed phase is a challenging task for theorists. The importance of models capable of predicting molecular NLO properties may be attributed to the potential design of new materials geared toward application in optical devices. Microscopically, the relevant optical properties are, to lowest orders, the first and second frequency-dependent hyperpolarizabilities. Accurate calculations of these hyperpolarizabilities have, for atoms and small molecules in the gas phase, become feasible using either finite field (FF) techniques or the theory of response functions. The latter approach, which will be used here, offers some advantages: (1) it is numerically stable, (2) it requires fewer calculations to be performed by the user and, (3) it is general in the sense that all frequency combinations of the properties may be addressed, that is, third harmonic generation (THG) second hyperpolarizabilities may be calculated, which is not possible using an approach based on the FF scheme.

Table 3.2 contains results of the rotationally averaged static second hyperpolarizability, $\gamma_{||}$, of a methanol molecule in liquid methanol. The calculations are based on the use of the CAM-B3LYP hybrid exchange-correlation functional in combination with the very flexible d-aug-cc-pVTZ basis set and the M2P2BM water potential. Generally, calculations of hyperpolarizabilities require the use of basis sets with very diffuse basis functions that reflect the choice of this specific basis set. The results are furthermore based on averaging of 100 snapshots extracted from a 4-ns long molecular dynamics simulation. From the results in Table 3.2, we observe a significant dependence on the force field used in the PE calculations. Clearly, the results based on the M0 potential lead to underestimated results for the second hyperpolarizability. In accordance with the results previously discussed for the electronic excitation energies, we observe a convergence in the solvent electrostatic potential at the level of quadrupoles, that is, inclusion of octopoles lead to changes that are almost within the statistical uncertainty

Table 3.2 Statistically averaged static mean second hyperpolarizabilities of methanol in methanol solution. Results are in a.u.

Force field	$\gamma_{\|\|}$
M0	3724 ± 46
M1	4541 ± 55
M2	4374 ± 74
M3	4494 ± 72
M2P1	5028 ± 109
M2P2	4902 ± 112
M2P2BM	4967 ± 97

Table 3.3 Statistically averaged static and dynamic third harmonic generation mean second hyperpolarizabilities of methanol in vacuum or in methanol solution. Results are in a.u. and are based on the use of the M2P2BM water potential

$\gamma_{\|\|}(-3\omega;\omega,\omega,\omega)$	$\omega = 0.0000$	$\omega = 0.0239$	$\omega = 0.0656$
Vacuum	3853	4151	7573
Methanol solution	4970 ± 54	5400 ± 62	11001 ± 223

of the averaged property. Explicit inclusion of polarization effects is seen to enhance this fourth-order property markedly. On the other hand, the different descriptions of the polarizability, that is, isotropic or anisotropic, lead to deviations that again are within the statistical error.

The dispersion related to the second hyperpolarizability of methanol is shown in Table 3.3 where we have included, in addition to the rotationally averaged static second hyperpolarizability, results related to the THG at two different frequencies. As opposed to the results in Table 3.2, we have, for the results presented in Table 3.3, used 400 snapshots. This has been done in order to reduce the statistical error. From this table, we observe that in the low frequency limit, the dispersion is similar in both gas phase and in solution, whereas an enhanced dispersion is observed in the higher frequency region for methanol in solution as compared to methanol in the gas phase. This increase in dispersion also results in an increase in the statistical error related to the second hyperpolarizability, that is, because of local anisotropies in the environment, each methanol molecule possesses a slightly different dispersion in the second hyperpolarizability, leading to an increase in the statistical error. As seen from the results in Table 3.3, the solvent shift, that is, the difference between the second hyperpolarizability in solution and in gas phase, is always positive; again, we observe that the solvent shift is similar for the lower frequencies, whereas it increases for frequencies lying in the higher frequency regime. Thus, a frequency-dependent solvent shift may only be estimated from its static limit, but for high-level results, the frequency dependence of the solvent shift needs to be included explicitly.

4. CONCLUSION

We have presented a general review of polarizable embedding within quantum chemistry. Special attention has been given to the theoretical background of polarizable embedding and its extension to the calculation of general molecular properties within the framework of time-dependent density functional theory. In addition, we have presented a few selected applications limited to the use of polarizable embedding for the description of solute molecular properties. Current investigations based on the use

of polarizable embedding are in the direction of applications for biological relevant molecules such as photoactive proteins and rational approaches to the design of general materials.

ACKNOWLEDGMENT

The authors thank the Danish Center for Scientific Computing for computational resources. J.K. thanks the Danish Natural Science Research Council/The Danish Councils for Independent Research and the Lundbeck Foundation for financial support.

REFERENCES

[1] A. Warshel, M. Levitt, Theoretical studies of enzymic reactions: Dielectric, electrostatic and steric stabilization of the carbonium ion in the reaction of lysozyme, J. Mol. Biol. 103 (1976) 227.
[2] U.C. Singh, P.A. Kollman, A combined ab initio quantum mechanical and molecular mechanical method for carrying out simulations on complex molecular systems: Applications to the ch3cl + cl- exchange reaction and gas phase protonation of polyethers, J. Comput. Chem. 7 (1986) 718.
[3] M.J. Field, P.A. Bash, M. Karplus, A combined quantum mechanical and molecular mechanical potential for molecular dynamics simulations, J. Comput. Chem. 11 (1990) 700.
[4] J. Gao, X. Xia, A priori evaluation of aqueous polarization effects through monte carlo qm-mm simulations, Science 258 (1992) 631.
[5] H. Lin, D.G. Truhlar, Qm/mm: What have we learned, where are we, and where do we go from here? Theor. Chem. Acc. 117 (2007) 185.
[6] J.M. Olsen, K. Aidas, J. Kongsted, Excited states in Solution through Polarizable Embedding, J. Chem. Theory Comput. 6 (2010) 3721.
[7] T. Rocha-Rinza, K. Sneskov, O. Christiansen, U. Ryde, J. Kongsted, Unraveling the similarity of the photoabsorption of deprotonated p-coumaric acid in the gas phase and within the photoactive yellow protein, Phys. Chem. Chem. Phys. 13 (2011) 1585.
[8] J. Applequist, J.R. Carl, K.-K. Fung, Atom dipole interaction model for molecular polarizability, application to polyatomic molecules and determination of atom polarizabilities, J. Am. Chem. Soc. 94 (1972) 2952.
[9] P.N. Day, J.H. Jensen, M.S. Gordon, S.P. Webb, W.J. Stevens, M. Krauss, D. Garmer, H. Basch, D. Cohen, An effective fragment method for modeling solvent effects in quantum mechanical calculations, J. Chem. Phys. 105 (1996) 1968.
[10] M.S. Gordon, M.A. Freitag, P. Bandyopadhyay, J.H. Jensen, V. Kairys, W.J. Stevens, The effective fragment potential method: A QM-based MM approach to modeling environmental effects in chemistry, J. Phys. Chem. A 105 (2001) 293.
[11] M.S. Gordon, L.V. Slipchenko, H. Li, J.H. Jensen, The effective fragment potential: A general method for predicting intermolecular interactions, Ann. Rep. Comput. Chem. 3 (2007) 177.
[12] W.L. Jorgensen, Special issue on polarization, J. Chem. Theory Comput. 3 (2007) 1877.
[13] H. Yu, W.F. van Gunsteren, Accounting for polarization in molecular simulation, Comput. Phys. Commun. 172 (2005) 69.
[14] DALTON, A molecular electronic structure program, Release 2.0, 2005. See http://www.kjemi.uio.no/software/dalton/dalton.html

[15] T. Helgaker, P. Jørgensen, J. Olsen, Molecular Electronic-Structure Theory, Wiley, Chichester, England, 2000.
[16] A.J. Stone, The Theory of Intermolecular Forces, Oxford University Press Inc, New York, 1996.
[17] P. Sałek, O. Vahtras, T. Helgaker, H. Ågren, Density-functional theory of linear and nonlinear time-dependent molecular properties, J. Chem. Phys. 117 (2002) 9630.
[18] B. Jansik, P. Salek, D. Jonsson, O. Vahtras, H. Ågren, Cubic response functions in time-dependent density functional theory, J. Chem. Phys. 122 (2005) 054107.
[19] J. Tomasi, B. Mennucci, R. Cammi, Quantum mechanical continuum solvation models, Chem. Rev. 105 (2005) 2999.
[20] R. Cammi, L. Frediani, B. Mennucci, K. Ruud, Multiconfigurational self-consistent field linear response for the polarizable continuum model: Theory and application to ground and excited-state polarizabilities of para-nitroaniline in solution, J. Chem. Phys. 119 (2003) 5818.
[21] K.V. Mikkelsen, P. Jorgensen, H.J.Aa. Jensen, A multiconfigurational self-consistent reaction field response method, J. Chem. Phys. 100 (1994) 6597.
[22] K.O. Sylvester-Hvid, K.V. Mikkelsen, D. Jonsson, P. Norman, H. Ågren, Nonlinear optical response of molecules in a nonequilibrium solvation model, J. Chem. Phys. 109 (1998) 5576.
[23] J. Olsen, P. Jørgensen, Linear and nonlinear response functions for an exact state and for an mcscf state, J. Chem. Phys. 82 (1985) 3235.
[24] C.B. Nielsen, O. Christiansen, K.V. Mikkelsen, J. Kongsted, Density functional self-consistent quantum mechanics/molecular mechanics theory for linear and nonlinear molecular properties: Applications to solvated water and formaldehyde, J. Chem. Phys. 126 (2007) 154112.
[25] S. Yoo, F. Zahariev, S. Sok, M.S. Gordon, Solvent effects on optical properties of molecules: A combined time-dependent density functional theory/effective fragment potential approach, J. Chem. Phys. 129 (2008) 144112.
[26] J. Gauss, Effects of electron correlation in the calculation of nuclear magnetic resonance chemical shifts, J. Chem. Phys. 99 (1993) 3629.
[27] T. Helgaker, M. Jaszunski, K. Ruud, Ab initio methods for the calculation of nmr shielding and indirect spin-spin coupling constants, Chem. Rev. 99 (1999) 293.
[28] K. Ruud, T. Helgaker, R. Kobayashi, P. Jørgensen, K. Bak, H. Jensen, Multiconfigurational self-consistent field calculations of nuclear shieldings using london atomic orbitals, J. Chem. Phys. 100 (1994) 8178.
[29] F. London, Théorie quantique des courants interatomiques dans les combinaisons aromatiques, J. Phys. Radium 8 (1937) 397.
[30] H. Hameka, Theory of magnetic properties of molecules with particular emphasis on the hydrogen molecule, Rev. Mod. Phys. 34 (1962) 87.
[31] R. Ditchfield, A gauge-invariant lcao method for n.m.r. chemical shifts, Mol. Phys. 27 (1974) 789.
[32] K. Wolinski, J. Hinton, P. Pulay, Efficient implementation of the gauge-independent atomic orbital method for nmr chemical shift calculations, J. Am. Chem. Soc. 112 (1990) 8251.
[33] Q. Cui, M. Karplus, Molecular properties from combined qm/mm methods. 2. Chemical shifts in large molecules, J. Phys. Chem. B 104 (2000) 3721.
[34] J.R. Cheeseman, G.W. Trucks, T.A. Keith, M.J. Frisch, A comparison of models for calculating nuclear magnetic resonance shielding tensors, J. Chem. Phys. 104 (1996) 5497.
[35] J. Kongsted, C.B. Nielsen, K.V. Mikkelsen, O. Christiansen, K. Ruud, Nuclear magnetic shielding constants of liquid water: Insights from hybrid quantum mechanics/molecular mechanics models, J. Chem. Phys. 126 (2007) 034510.
[36] T. Helgaker, P. Jørgensen, An electronic hamiltonian for origin independent calculations of magnetic properties, J. Chem. Phys. 95 (1991) 2595.
[37] L. Gagliardi, R. Lindh, G. Karlström, Local properties of quantum chemical systems: The loprop approach, J. Chem. Phys. 121 (2004) 4494.

[38] G. Karlström, R. Lindh, P.-Å. Malmqvist, B.O. Roos, U. Ryde, V. Veryazov, P.-O. Widmark, M. Cossi, B. Schimmelpfennig, P. Neograd y, L. Seijo, Molcas: A program package for computational chemistry, Comp. Mat. Sci. 28 (2003) 222.
[39] P. Ahlström, A. Wallqvist, S. Engström, B. Jönsson, A molecular dynamics study of polarizable water, Mol. Phys. 68 (1989) 563.
[40] W.L. Jorgensen, Quantum and statistical mechanical studies of liquids. 10. Transferable intermolecular potential functions for water, alcohols, and ethers, application to liquid water, J. Am. Chem. Soc. 103 (1981) 335.
[41] P. Söderhjelm, J.W. Krogh, G. Karlström, U. Ryde, R. Lindh, Accuracy of distributed multipoles and polarizabilities: Comparison between the loprop and mpprop models, J. Comput. Chem. 28 (2007) 1083.
[42] T. Yanai, D.P. Tew, N.C. Handy, A new hybrid exchangecorrelation functional using the coulomb-attenuating method (cam-b3lyp), Chem. Phys. Lett. 393 (2004) 51.
[43] I. Renge, Solvent dependence of n-pi* absorption in acetone, J. Phys. Chem. A 113 (2009) 10678.
[44] K. Aidas, K.V. Mikkelsen, J. Kongsted, Modelling spectroscopic properties of large molecular systems, the combined density functional theory/molecular mechanics approach, J. Chem. Meth. Sci. Eng. 7 (2007) 135.
[45] J. Kongsted, K. Ruud, Solvent effects on zero-point vibrational corrections to optical rotations and nuclear magnetic resonance shielding constants, Chem. Phys. Lett. 451 (2008) 226.
[46] M. Witanowski, L. Stefaniak, G.A. Webb, Annual Reports on NMR Spectroscopy, Vol. 25, Academic Press: London, 1993.

CHAPTER 4

Parametric Analysis of Time Signals and Spectra from Perspectives of Quantum Physics and Chemistry

Dževad Belkić[a]

Contents

1. Introduction 147
2. Time-Dependent Quantum-Mechanical Spectral Analysis 149
3. Time-Independent Quantum-Mechanical Spectral Analysis 154
4. Equivalence of Autocorrelation Functions and Time Signals 157
5. The Lanczos Algorithm for State Vectors 162
   5.1. Jacobi matrix 163
   5.2. Jacobi eigenvalue problem 164
6. The Lanczos Orthogonal Polynomials 169
   6.1. Three-term recursion 169
   6.2. The Jacobi state vectors without diagonalization of the Jacobi matrix 171
   6.3. The Jacobi matrix and the Lanczos polynomial matrix within the same system of linear equations 173
7. Recursions for Derivatives of the Lanczos Polynomials 175
8. Secular Equation and the Characteristic Polynomial 176
9. Power Series Representations for Two Lanczos Polynomials 178
10. Rooting High-Degree Polynomials 180
    10.1. Improved Newton–Raphson algorithm with approximate allowance of higher order derivatives 180
    10.2. Diagonalization of the Hessenberg or companion matrix 182
11. The Lanczos Vector Space 183
    11.1. The space structure via the scalar product as the generalized Stieltjes integral 183
    11.2. The passage from the Stieltjes to the Cauchy integral via the Dirac-Lebesgue measure for discretization of inner products 183

[a] Nobel Medical Institute, Karolinska Institute, Department of Oncology and Pathology, Stockholm, Sweden

Advances in Quantum Chemistry, Volume 61
ISSN 0065-3276, DOI: 10.1016/B978-0-12-386013-2.00004-8

12. Completeness of the Lanczos Polynomials 185
13. Dual Lanczos Representation via State Vectors and Secular Polynomials 189
13.1. Matrix elements of the evolution operator in terms of the Lanczos states 189
13.2. Matrix elements of the evolution operator in terms of the Lanczos polynomials 189
14. Closed Expression for the Krylov–Schrödinger Overlap Determinant 190
15. Explicit Solution of the Lanczos Algorithm 190
16. Explicit Lanczos Wave Packet Propagation 192
17. Mapping from Monomials u^n to the Lanzos Polynomials $Q_n(u)$ 193
18. Mapping from the Krylov–Schrödinger to the Lanczos States 195
19. The Padé–Lanczos Approximant 197
20. Inversion of the Krylov–Schrödinger General Matrix 200
21. The Lanczos Continued Fractions 203
22. Equations for Eigenvalues via Continued Fractions 205
23. Explicit Padé Approximant: A Closed, General Expression 206
24. Analytical Expressions for the General Continued Fraction Coefficients 208
25. Eigenvalues without Eigenproblems or Characteristic Equations 209
26. Analytical Expressions for the General Lanczos Coupling Constants 212
27. Contracted Continued Fractions 214
28. Recursive Solutions of Tridiagonal Inhomogeneous Systems of Linear Equations 215
28.1. Gaussian elimination method 215
28.2. The power moment problem 217
28.3. The problem of spectral analysis 218
29. Padé-Based Exactness and Mathematical Modelings 222
29.1. Recapitulations on exact quantification in MRS by the FPT 222
29.2. Padé approximant for cell surviving fractions in radiobiological modelings 225
30. Illustrations 226
30.1. Magnetic resonance spectroscopy 226
30.2. Cell surviving fractions after irradiation: Padé-linear quadratic (PLQ) model 254
31. Conclusions 256
Acknowledgments 258
References 258

Abstract This work is on signal processing from the perspective of quantum physics and chemistry. The major computational algorithms of linear algebra used in these two disciplines are theoretically analyzed. The results of concrete numerical computations are presented for one of the most versatile strategies called the fast Padé transform (FPT). For concreteness, the specific illustrations are given for magnetic resonance spectroscopy, in which the so-called quantification problem is of paramount importance. However, this

method is applicable to many other problems in sciences and technologies, whenever the theoretically generated or experimentally measured data need to be analyzed and interpreted through signal processing. The FPT is a high-resolution parametric spectral analyzer, which can unambiguously and exactly reconstruct the entire quantitative information from every single genuine molecule in the examined matter. Among other physical quantities, this method can provide the abundance or concentrations of all the physical constituents from the investigated substance. The FPT is a rich mathematical construct with the unique polynomial quotient P_K/Q_K that performs optimal synthesis or decomposition of complicated lineshapes in the given energy or frequency spectra. The denoising Froissart filter for exact signal-noise separation by pole-zero cancellations is an integral part of this multifaceted and comprehensive theory of resonant scattering and spectroscopy.

Quantification of time signals and frequency spectra is mathematically equivalent to the harmonic inversion problem. Here, the time signal points or autocorrelation functions are given, and the task is to reconstruct the unknown input components comprised of harmonic variables in terms of the fundamental complex-valued frequencies and the corresponding amplitudes. This is also known as the problem of spectral analysis in the mathematical literature. Such inverse problems are mathematically ill-conditioned and ill-posed in the sense that even the slightest perturbations in the input data could yield widely different components of the total shape spectra. In practice, this means that nearly the same (in the least-square sense) overall envelope could be obtained with entirely different component spectra for each constituent resonance. This ambiguity, which is typically encountered in all the available fitting algorithms, is also characterized by missing the genuine and producing false peaks. In contrast to such unacceptable features and insurmountable difficulties of the fitting techniques, the main characteristics of the FPT are reviewed as they can be applied to solving the harmonic inverse problem exactly by retrieving the true number of resonances with all their spectral parameters and by unequivocally separating the physical (genuine) from unphysical (noisy, spurious) content of the analyzed time signal.

1. INTRODUCTION

We study the quantification problem for general time signals and their spectra. The specific illustrations are given for data from nuclear magnetic resonance spectroscopy (MRS) [1–9]. The quantification (or harmonic inversion) problem entails using the encoded time signals to reconstruct the true number of resonances, as well as all the constituent physical transients (harmonics), together with the pairs of spectral parameters that are complex-valued frequencies and the corresponding amplitudes [2]. Moreover, every time signal has a structure that is quantifiable by a relatively limited number of parameters. In practice, neither this structure nor the related parameters of the studied time signals are known prior to signal processing. The task of spectral synthesis is to reconstruct these unknown quantities from the given

time signal, and this is achieved by performing spectral decomposition. To this end, a number of methods are available [10–21]. We presently achieve this goal by using the nonlinear parametric signal processor called the fast Padé transform (FPT) [22–34]. For a given Maclaurin series, a frequency spectrum in the FPT is defined by the unique ratio of two polynomials P_K/Q_K, where K is the total number of resonances (genuine plus spurious). The fast Fourier transform (FFT), with its spectrum given by a single Riemann polynomial R_N, where N is the total signal length, cannot solve this quantification problem. This occurs because the FFT ignores the structure of the investigated time signal. There are two kinds of spectral shapes in signal processing. These are the component shape spectra for each separate resonance and the total shape spectrum as the sum of all the separate component shape spectra, resulting from interference patterns of all the individual resonances. The FFT, as a linear nonparametric processor, can give only the envelope or total shape spectra [2]. In contrast, the FPT as a nonlinear parametric estimator, can generate the component and the total shape spectra [2]. This occurs because prior to constructing any spectrum, the FPT can retrieve the peak positions, widths, heights, and phases of individual physical resonances.

The main distinction between these two kinds of processors is in the type of information extracted from the input time signal. Nonparametric processors can generate only qualitative information, which is used to plot graphs of spectral shapes. However, the quantitative data of critical importance are provided by parametric estimators through unfolding the hidden spectral structure of the envelope. The quantitative features of resonances (peak position, width, height, and phase) reconstructed by the FPT are needed to estimate molecular concentrations. To re-emphasize, with the FPT, these key resonance parameters are retrieved first. Then, the spectra can be constructed in any mode if desired. This is a completely different methodology from fitting estimators that require the envelope spectrum from the FFT before attempting to quantify the encoded time signals. These two distinct approaches, the FFT followed by ambiguous fittings versus unambiguous and self-contained estimation by the FPT are anticipated to give substantially different results, especially with respect to closely overlapping resonances that are often of critical importance in applications across interdisciplinary fields.

The FPT converges when all the reconstructed genuine frequencies and amplitudes become stable. This point of stabilization is a veritable signature of recovery of the exact number K_{G} of genuine resonances ($K_{\mathrm{G}} < K$). With any further increase of the partial signal toward the full signal length, that is, beyond the point at which full convergence was first reached, all the genuine frequencies and amplitudes remain constant and so do the ensuing spectra via the saturation $P_K/Q_K = P_{K_{\mathrm{G}}+K_{\mathrm{F}}}/Q_{K_{\mathrm{G}}+K_{\mathrm{F}}} = P_{K_{\mathrm{G}}}/Q_{K_{\mathrm{G}}}$, where K_{F} is the number of Froissart or spurious resonances. Protection against contamination by some K_{F} noisy or noise-like resonances is provided within the FPT itself, since each pole in the spectrum P_K/Q_K due to spurious resonances

stemming from the characteristic equation of the denominator polynomial, $Q_K = 0$, coincides with the corresponding zero of the numerator polynomial, $P_K = 0$. This leads to pole-zero cancellation in the Padé polynomial quotient of the FPT. Such a feature can be used to differentiate between spurious and genuine content of the signal. Since the unphysical poles and zeros always appear as pairs in the FPT, they are viewed as doublets. These are called Froissart doublets after Froissart who, through numerical experiments, discovered this extremely useful phenomenon that is unique to the Padé methodology [35, 36].

The present study illustrates the use of the fast Padé transform in the theory of resonances. We show how the FPT obtains the numerically exact solution of a highly challenging harmonic inversion problem with 25 tightly packed resonances, some of which are practically degenerate. Each resonance is characterized by four real parameters describing the spectral position, height, width, and phase. Therefore, the present model signal possesses 100 real-valued spectral parameters. All these parameters are entered with accuracy that is deemed sufficient for realistic applications. Once the time signal is constructed as a linear combination of 25 damped complex harmonics and digitized, the input data for solving the quantification problem consists merely of the numerical values of the signal points. The task is to retrieve all the 100 input spectral parameters with their given accuracy together with the exact number K_G of genuine resonances. This would expose the fast Padé transform to the most stringent testing for stability and robustness against perturbations due to the unavoidable computational round-off errors. Spectral analyzers that do not pass such a demanding and fully controlled testing cannot be considered reliable when dealing with the corresponding experimentally measured time signals.

2. TIME-DEPENDENT QUANTUM-MECHANICAL SPECTRAL ANALYSIS

The nonstationary quantum-mechanical spectral analysis uses the time-dependent Schrödinger equation [2]:

$$i\frac{\partial}{\partial t}|\Phi(t)) = \widehat{\Omega}|\Phi(t)), \tag{1}$$

with the boundary condition $|\Phi(0)) = |\Phi_0)$, where $|\Phi_0)$ is the known initial state vector of the investigated system whose dynamics are governed by total "Hamiltonian" $\widehat{\Omega}$. In order to include resonances associated with complex-valued frequencies, the "Hamiltonian" is hereafter conceived as a non-Hermitian linear operator. In particular, non-Hermiticity of $\widehat{\Omega}$ implies that the scalar product is defined as the symmetric inner product $(\chi|\psi) = (\psi|\chi)$. No conjugation via the star superscript is placed onto either of the two state

vectors $(\chi|$ or $|\psi)$. To symbolically indicate this special feature of the symmetry of the scalar product, soft round brackets $|\psi)$ and $(\chi|$ are used in place of the usual Dirac "bra-ket" notation $\langle\chi|$ and $|\psi\rangle$ with $\langle\chi|\psi\rangle = \langle\psi^*|\chi^*\rangle$ and $\langle\chi^*|\psi\rangle = (\chi|\psi)$. An abstract formulation of quantum mechanics and its deterministic postulate imply that if the wave packet $|\Phi(0))$ of any generic system under study is well prepared/controlled at the initial time $t = 0$ and if its further development is propagated by the given dynamics/interactions, then the state $|\Phi(t))$ will be known exactly at any later instant t [2]. In the Schrödinger picture of quantum mechanics, operators are stationary and wave functions are time dependent. For a stationary dynamical operator $\widehat{\Omega}$, which describes a conservative physical system, Eq. (1) possesses the solution of the following type:

$$|\Phi(t)) = \widehat{\mathrm{U}}(t)|\Phi_0), \quad |\Phi_0) \equiv |\Phi(0)), \tag{2}$$

where the beginning of counting the time is chosen to be zero according to the mentioned initial condition to Eq. (1). Here, $\widehat{\mathrm{U}}(t)$ is the dynamical evolution/relaxation linear operator of the system:

$$\widehat{\mathrm{U}}(t) = \mathrm{e}^{-i\widehat{\Omega}t}. \tag{3}$$

In Eq. (2), $|\Phi_0)$ represents the initial unnormalized state of the studied system at the time $t = 0$:

$$||\Phi_0||^2 \equiv (\Phi_0|\Phi_0) = C_0 = c_0 \neq 0, \tag{4}$$

where the constant c_0 is not necessarily unity, but it could be a complex number. The spectral representation of the operator $\widehat{\mathrm{U}}(t)$ follows from using the well-known property:

$$f(\widehat{\Omega}) = \sum_{k=1}^{K} f(\omega_k)\widehat{\pi}_k, \quad \widehat{\pi}_k = |\Upsilon_k)(\Upsilon_k|, \quad 1 \leq k \leq K. \tag{5}$$

Here, $f(\widehat{\Omega})$ is any operator analytic function, $\widehat{\pi}_k$ is the projection operator, and $|\Upsilon_k)$ is the complete eigenfunction of the studied system obeying the stationary Schrödinger equation:

$$\widehat{\Omega}|\Upsilon_k) = \omega_k|\Upsilon_k), \tag{6}$$

or more generally,

$$f(\widehat{\Omega})|\Upsilon_k) = f(\omega_k)|\Upsilon_k). \tag{7}$$

The main postulate of quantum mechanics is that the whole information of a general system under study is contained in the total wave functions $\{|\Upsilon_k)\}$. This is known as completeness of the quantum-mechanical description. Such a circumstance is coherent with Eq. (6) since $\widehat{\Omega}$ is assumed to carry the whole information of the investigated system. This is formally expressed through the closure relation for the exact orthonormalized basis $\{|\Upsilon_k)\}$:

$$\sum_{k=1}^{K} \widehat{\pi}_k = \widehat{1}, \quad (\Upsilon_{k'}|\Upsilon_k) = c_0 \delta_{k,k'}. \tag{8}$$

Here, the rank K is an arbitrary positive integer that can be finite or infinite, in which case Eq. (8) represents local or global closure relation, respectively. Setting now $f(\widehat{\Omega}) = e^{-i\widehat{\Omega}t}$ in Eq. (5) gives the sought spectral representation of the evolution operator:

$$\widehat{U}(t) = \sum_{k=1}^{K} e^{-i\omega_k t}\widehat{\pi}_k, \quad \mathrm{Im}(\omega_k) < 0. \tag{9}$$

The state $|\Phi(t))$ at the instant t is obtained by propagating the initial well-prepared wave packet $|\Phi_0)$ from $t = 0$ to t via $\widehat{U}(t)$. Given $|\Phi_0)$ at $t = 0$, there will be a nonzero probability amplitude to find the system in the state $|\Phi(t))$ at the later time $t > 0$ if the two wave packets have a nonvanishing overlap. This overlap is found quantum mechanically by projecting $|\Phi(t))$ onto $(\Phi_0|$ by their scalar product:

$$C(t) = (\Phi_0|\Phi(t)) = (\Phi_0|\widehat{U}(t)|\Phi_0), \tag{10}$$

where Eq. (2) is used. The quantity $C(t)$ is called the autocorrelation function since it measures the degree of correlations between the states $|\Phi(t = 0))$ and $|\Phi(t \neq 0))$ under the influence of the dynamical operator $\widehat{\Omega}$. It is the presence of the operator $\widehat{\Omega}$ that makes $|\Phi(t))$ differ from $|\Phi_0)$, as is obvious from Eq. (2). By switching the dynamics off ($\widehat{\Omega} = \widehat{0}$), the system would be allowed to remain indefinitely in the initial state so that $C(t) = (\Phi_0|\Phi_0) = c_0 \neq 0$ as in Eq. (4) at any time t. The initial state $|\Phi_0)$ is assumed to be a nonzero state vector $|\Phi_0) \neq |0)$, as is customary in quantum mechanics. Propagating the initial "zero vector" $|\Phi_0) = |0)$ from $t = 0$ and onward would inevitably lead to the trivial Schrödinger state $|\Phi(t)) = |0)$ at any later time $t \neq 0$, and therefore, this possibility is excluded as uninteresting. At two times t' and t, where $t' < t$, the state vector $|\Phi(t'))$ can be viewed as a delayed "copy" of $|\Phi(t))$. Thus, the overlap between the states $|\Phi(t))$ and $|\Phi(t'))$ for $t' < t$, as per the inner product $(\Phi(t')|\Phi(t))$, represents a measure of correlation between the state and its delayed copy. One such example is taking the time t' all

the way back to the initial moment $t' = 0$. This yields the autocorrelation function $C(t) = (\Phi(0)|\Phi(t))$. At large times t, the autocorrelation function $C(t)$ could be numerically unreliable due to instabilities that stem from considerable oscillations of the overlap $(\Phi_0|\Phi(t))$ as t increases. This could cause a heavy corruption of the quantity $C(t)$ with computational noise, for example, round-off errors that lead to ill-conditioning.

Quantum-mechanical spectral analysis can advantageously to use the formalism of the Green function $\mathcal{G}(\omega)$, which is a matrix element of a resolvent operator $\widehat{\mathrm{G}}(\omega)$:

$$\mathcal{G}(\omega) \equiv (\Phi_0|\widehat{\mathrm{G}}(\omega)|\Phi_0), \tag{11}$$

$$\widehat{\mathrm{G}}(\omega) = \left[(\omega + i\eta)\widehat{1} - \widehat{\Omega}\right]^{-1}. \tag{12}$$

The Green function (11) exhibits singularities (poles, cuts, etc.) because of the presence of the resolvent operator (12). It is often claimed in the literature that $C(t)$ is free from such singularities. This is untrue. The reason being that the severe oscillations of $C(t)$ for large t act as disguised singularities entirely similar to those encountered more transparently in $\mathcal{G}(\omega)$. This is obvious that both functions $C(t)$ and $\mathcal{G}(\omega)$ are built from the same "Hamiltonian" $\widehat{\Omega}$, whose spectrum contains the mentioned singularities. Moreover, the limits $t \longrightarrow \pm\infty$ in $C(t)$ are strictly equivalent to $\eta \longrightarrow 0^{\mp}$ in $\widehat{\mathrm{G}}(\omega)$ in accordance with the so-called Abel limit from the formal scattering theory [2]. As a matter of fact, if one does not encounter instabilities in $C(t)$ in producing a spectrum, this could only mean that the asymptotic region $t \longrightarrow \pm\infty$ has not been approximately reached, with the consequence that some of the long-lived transients did not have sufficient time to decay. In scattering theory, all the transients should decay in order to detect the asymptotically free states of the system.

The term "transient" usually refers to a time-developing phenomenon that dies out after a sufficiently long time lag has elapsed, $t \longrightarrow \infty$ [37]. Such are the envelopes of, for example, experimentally encoded time signals as a linear combination of damped exponentials $\{\exp(-i\omega_k t)\}$ with constant amplitudes in which all complex frequencies $\{\omega_k\}$ must have the negative imaginary parts $\mathrm{Im}(\omega_k) < 0$. Strictly speaking, these are stable transients. A more general meaning of the term transient in sequence-to-sequence transformations has been encountered in quantum-mechanical signal processing [2]. There, the term unstable or secular transients has been used following Shanks [37] whenever referring to, for example, a time signal $c(t)$ in which one or more fundamental frequencies ω_k are exponentially diverging $(\mathrm{Im}(\omega_k) > 0)$. Any finite or infinite sum of harmonics $\{\exp(-i\omega_k t)\}$ would diverge if at least one of the complex fundamental frequencies is secular $\mathrm{Im}(\omega_k) > 0$. In such a case, this whole mentioned sum of exponentials $\{\exp(-i\omega_k t)\}$ in the signal $c(t)$ would cease to have any direct physical meaning, since $c(t) \longrightarrow \infty$ as $t \longrightarrow \infty$. This situation will remain incurable as long

as one keeps adding up directly the partial sums of the time signal as a linear combination of exponentials $\{\exp(-i\omega_k t)\}$. However, such a divergent set of partial sums could still be computed with a finite result $|c(t)| < \infty$ by certain sequence-to-sequence nonlinear transformations that are capable of converting divergent into convergent sequences through the concept of the anti-limit [37]. One such transformation is the Padé approximant (PA) [2], which can also accelerate convergence of slowly converging multidimensional sequences and/or series. Moreover, the PA can induce/force convergence into divergent series by means of the Cauchy analytic continuation.

One of the ways to achieve a mapping from the time domain to the frequency range is the exact Fourier integrals (not to be confused with the Fourier transforms):

$$\mathcal{F}(\omega) = \frac{1}{2\pi}\int_0^\infty \mathrm{d}t\, \mathrm{e}^{i\omega t} C(t), \quad C(t) = \int_0^\infty \mathrm{d}\omega\, \mathrm{e}^{-i\omega t}\mathcal{F}(\omega). \tag{13}$$

Both $\mathcal{F}(\omega)$ and $C(t)$ contain the same operator $\widehat{\Omega}$, which is the source of the complete information about the system. This feature, together with the unitarity and linearity of the standard Fourier operator, guarantees that the information is preserved when passing from the time to the frequency domain. Inserting Eq. (9) into Eq. (10) yields the following result:

$$C(t) = \sum_{k=1}^{K} d_k \mathrm{e}^{-i\omega_k t}, \tag{14}$$

$$d_k = (\Phi_0|\Upsilon_k)^2. \tag{15}$$

By definition (15), the residue d_k is a measure of the extent of the squared projection of the state $|\Upsilon_k)$ onto $(\Phi_0|$. Thus, the amplitudes $\{d_k\}$ are the weights that carry information about the strength of the contributions of individual normal- and natural-mode frequencies $\{\omega_k\}$ to $C(t)$ in Eq. (14). The magnitudes $\{|d_k|\}$ are the intensities of the nonorthogonal "harmonics" $\{\exp(-i\omega_k t)\}$ as the principal components that constitute the autocorrelation function $C(t)$. Moreover, $\phi_k = \mathrm{Arg}(d_k)$ is the phase of $C(t)$. Substituting $C(t)$ from Eq. (14) into Eq. (13) and carrying out the time integral exactly gives a theoretically generated complex spectrum $\mathcal{F}(\omega)$ as:

$$\mathcal{F}(\omega) = -i\sum_{k=1}^{K} \frac{d_k}{\omega - \omega_k}, \tag{16}$$

provided that $\mathrm{Im}(\omega_k) < 0$. The result (16) for $i\mathcal{F}(\omega)$ agrees fully with the Green function $\mathcal{G}(\omega)$ from Eq. (11), as it should. The real quantities, for example, the magnitude $|\mathcal{F}(\omega)|$, power $|\mathcal{F}(\omega)|^2$, absorption, and dispersion spectra

can all be obtained directly from $\mathcal{F}(\omega)$. Under ideal conditions of absence of noise and with no initial time delay, the absorption and dispersion spectra are given by $\mathrm{Re}\{\mathcal{F}(\omega)\}$ and $\mathrm{Im}\{\mathcal{F}(\omega)\}$, respectively. Of course, in practice, these conditions are not fulfilled, and the absorption and dispersion spectra differ from $\mathrm{Re}\{\mathcal{F}(\omega)\}$ and $\mathrm{Im}\{\mathcal{F}(\omega)\}$, respectively. In such cases, certain alternative definitions of the absorption and dispersion spectra, the so-called ersatz spectra, could be used [38, 39]. The resonance parameters from (16) are the position, width, height, and phase of the kth peak deduced from $\mathrm{Re}(\omega_k)$, $\mathrm{Im}(\omega_k)$, $|d_k|$, $\mathrm{Arg}(\omega_k)$, respectively.

3. TIME-INDEPENDENT QUANTUM-MECHANICAL SPECTRAL ANALYSIS

Since the exponentially damped signal (41) is obtained from the matrix element $(\Phi_0|\widehat{\mathrm{U}}|\Phi_0)$, as is clear from Eq. (37), the spectral parameters $\{\omega_k, d_k\}$ of $\{c_n\}$ can be obtained without any fitting by, for example, diagonalizing the evolution operator $\widehat{\mathrm{U}}$ from Eq. (7) or more generally:

$$\widehat{\mathrm{U}}^s|\Upsilon_k) = u_k^s|\Upsilon_k). \tag{17}$$

The eigenvalue problem (17) of the sth power of the evolution operator $\widehat{\mathrm{U}}$ is obtained from Eq. (38) for $f(\widehat{\mathrm{U}}) = \widehat{\mathrm{U}}^s$. In diagonalizations, one does not necessarily need the explicit knowledge of the operator $\widehat{\mathrm{U}}$ itself, but only its matrix elements $(\xi_m|\widehat{\mathrm{U}}|\xi_n)$ are requested. Here, $\{|\xi_n)\}$ is a suitably selected complete set of the expansion functions $\{|\xi_n)\}$ that form a basis, which does not need to be orthonormalized. For example, the collection of the Schrödinger state vectors $\{|\Phi_n)\}_{n=0}^{M-1}$ represents one such basis. The two different states $|\Phi_n)$ and $|\Phi_m)$ are not mutually orthogonal, so that their overlap is generally nonzero:

$$\mathrm{S}_{n,m} \equiv \mathrm{S}_{nm} = (\Phi_m|\Phi_n) \neq c_0\delta_{n,m}. \tag{18}$$

Inserting $|\Phi_n)$ and $(\Phi_m|$ into (18) and using the symmetry of the scalar product, we have:

$$\mathrm{S}_{n,m} = c_{n+m}. \tag{19}$$

In general, we have $c_{n+m} \neq \delta_{n,m}$ so that indeed the states $|\Phi_n)$ and $|\Phi_m)$ are nonorthogonal for $n \neq m$, as stated in Eq. (18). Given N signal points $\{c_n\}$, the sum of the maximal values of indices n and m in Eq. (19) is $n_{\max} + m_{\max} = 2M - 2$. Thus, the upper limit M of the available Schrödinger states $\{|\Phi_n)\}$ will satisfy the relation:

$$2M - 1 = N. \tag{20}$$

Therefore, the overlap matrix $\mathbf{S}$ of the dimension $M \times M$ is given by:

$$\mathbf{S} = \{\mathrm{S}_{n,m}\} \equiv \{\mathrm{S}_{nm}\} = \{c_{n+m}\}_{n,m=0}^{M-1}. \tag{21}$$

The nonorthogonality of the basis $\{|\Phi_n)\}$ implies that the decomposition of the unity operator will not be as simple as in Eq. (8), since the inverse matrix $\mathbf{S}^{-1}$ must be involved via:

$$\widehat{1} = \sum_{k=1}^{K} \sum_{k'=1}^{K} |\Phi_k) \mathrm{S}_{kk'}^{-1} (\Phi_{k'}|. \tag{22}$$

We assume that the Schrödinger basis $\{|\Phi_n)\}$ is locally complete, and this would permit a development of the eigenfunction $|\Upsilon_k)$ of $\widehat{\mathrm{U}}$ from Eq. (17) as follows:

$$|\Upsilon_k) = \sum_{n=0}^{M-1} \mathrm{A}_{n,k} |\Phi_n), \tag{23}$$

where M is given in (20). The expansion coefficients $\{\mathrm{A}_{n,k}\}$ from Eq. (23) are the elements of the column matrix $\mathbf{A}_k = \{\mathrm{A}_{n,k}\} \equiv \{\mathrm{A}_{nk}\}$. Here, the subscript k in the column vector $\mathbf{A}_k$ should not be interpreted as the dimension but as the counting, that is, the running index. We insert this state vector into Eq. (17), which is afterward projected onto the state $(\Phi_m|$ to yield:

$$\sum_{n=0}^{M-1} \mathrm{U}_{n,m}^{(s)} \mathrm{A}_{n,k} = u_k^s \sum_{n=0}^{M-1} \mathrm{S}_{n,m} \mathrm{A}_{n,k}. \tag{24}$$

The matrix element $\mathrm{U}_{n,m}^{(s)}$ is associated with the evolution operator raised to the power s such that:

$$\mathrm{U}_{n,m}^{(s)} \equiv \mathrm{U}_{nm}^{(s)} = (\Phi_m | \widehat{\mathrm{U}}^s | \Phi_n), \tag{25}$$

where $\mathrm{U}_{n,m}^{(0)} \equiv \mathrm{S}_{n,m}$ and $\mathrm{U}_{n,m}^{(1)} \equiv \mathrm{U}_{n,m}$. Then, the system of linear equations (24) can be compactly written in its corresponding matrix representation:

$$\mathbf{U}^{(p)} \mathbf{A}_k = u_k^s \mathbf{S} \mathbf{A}_k, \quad \mathbf{U}^{(s)} = \{\mathrm{U}_{n,m}^{(s)}\}_{n,m=0}^{M-1}. \tag{26}$$

The expansion column matrix $\mathbf{A}_k$ from Eq. (26) is the eigenvector of $\mathbf{U}^{(s)}$, and the elements $\{\mathrm{S}_{nm}\}$ of the overlap matrix $\mathbf{S}$ are given in Eq. (19). The obtained expression (26) is not an ordinary but a generalized eigenvalue problem involving the overlap matrix $\mathbf{S}$ due to the mentioned lack of orthogonality

of the Schrödinger basis functions $|\Phi_m)$ and $|\Phi_n)$ for $n \neq m$. As a direct consequence of this latter fact, instead of Eq. (17), one solves a more difficult, generalized eigenvalue problem involving the overlap matrix $\mathbf{S}$, which is a bottleneck of every nonorthogonal basis. In fact, in such a case, one solves two eigenvalue problems in succession since diagonalization of $\mathbf{S}$ precedes that of $\mathbf{U}$. Each of these two diagonalizations customarily leads to spurious eigenvalues. This problem could be considerably mitigated if an orthogonal basis set is used from the onset, which deals only with ordinary eigenvalue problems in which the matrix $\mathbf{S}$ is not present. Such a basis has been thoroughly analyzed in Ref. [2] using the Lanczos recursive algorithm of wave packet propagations. In the Schrödinger basis $\{|\Phi_n)\}$, the elements of matrix $\mathbf{U}$ are calculated as:

$$\mathrm{U}_{n,m}^{(s)} = c_{n+m+s}, \tag{27}$$

where Eqs. (36), (40) and (43) are used. Hence, the matrix element of the sth power of the evolution operator $\widehat{\mathrm{U}}$ taken over two general Schrödinger states $|\Phi_n)$ and $(\Phi_m|$ is reduced to only one single value of the autocorrelation function or the time signal $c_{n+m+s} = C_{n+m+s}$. Obviously, this result also includes the overlap matrix $\mathbf{S}$ that is obtained for $s = 0$ as a special case of $\mathbf{U}^{(s)}$. Similarly, the evolution matrix $\mathbf{U} = \mathbf{U}^{(1)}$ is obtained for $s = 1$, and it reads as:

$$\mathbf{U} = \{\mathrm{U}_{n,m}\} \equiv \{\mathrm{U}_{nm}\} = \{c_{n+m+1}\}_{n,m=0}^{M-1}. \tag{28}$$

Once the whole set $\{u_k, \mathrm{A}_{n,k}\}$ is obtained by solving the generalized eigenvalue problem (26), the eigenfrequencies are deduced from the relation

$$\omega_k = i\tau^{-1} \ln(u_k), \tag{29}$$

where the principal branch should be taken from the multivalued complex logarithm. Hereafter, we shall adhere to the standard convention according to which the correct branch of a multivalued function $f(z)$ is obtained by selecting the least value of the argument $\mathrm{Arg}(f(z)) = \tan^{-1}([\mathrm{Im}\{f(z)\}]/[\mathrm{Re}\{f(z)\}])$. The residues $\{d_k\}$ associated with the eigenfrequencies $\{\omega_k\}$ are calculated by inserting the expansion (23) for $|\Upsilon_k)$ into Eq. (15) and using Eq. (40), as well as Eq. (43) with the result:

$$d_k = \left(\sum_{n=0}^{M-1} c_n \mathrm{A}_{n,k} \right)^2. \tag{30}$$

The above procedure constitutes a computational tool for obtaining the spectrum of the evolution matrix $\mathbf{U}_M = \{c_{n+m+1}\}_{n,m=0}^{M-1}$ through diagonalization in the Schrödinger basis $\{|\Phi_n)\}$. This procedure works optimally if the signal

length N is not too long, say $N \leq N_{\text{cut}} \approx 300$, in which case the problem of ill-conditioning in solving the generalized eigenvalue problem (26) can be under control [38–42]. Using the sequence $\{|\Phi_n)\}$ as a basis set makes the data matrix **U** full since these Schrödinger states are delocalized. The term "delocalized" means that the set $\{|\Phi_n)\}$ is totally independent of the selected frequency window $[\omega_{\min}, \omega_{\max}]$ from which the eigenvalues $\{u_k\}$ are supposed to be extracted. The basis set $\{|\Phi_n)\}$ is not practical for large N for which the so-called dimensionality reduction of the original problem is needed, as can be accomplished in either the time [43] or the frequency domain [40].

4. EQUIVALENCE OF AUTOCORRELATION FUNCTIONS AND TIME SIGNALS

In practice, one equidistantly discretizes (digitizes) the continuous (analog) time variable t as $t = t_n = n\Delta t \equiv n\tau (n = 0, 1, 2, \ldots, N-1)$, where the nonnegative integer n counts the time. The quantity τ is the time increment (the time lag) or the sampling time, which is also called the dwell time $\tau = T/N$ in ion cyclotron resonance mass spectroscopy (ICRMS) [44]. Hereafter, we shall write:

$$C_n \equiv C(n\tau), \quad |\Phi_n) \equiv |\Phi(n\tau)), \tag{31}$$

for the discrete counterparts of $C(t)$ and $|\Phi(t)$, respectively. In practice, T is finite, which implies that the time Fourier integrals from Eq. (13) should have the upper limits equal to T with $T < \infty$. In such a case, the Fourier integral $F(\omega)$ of the autocorrelation function $C(t)$ is introduced as:

$$F(\omega) = \frac{1}{T} \int_0^T \mathrm{d}t\, C(t)\, \mathrm{e}^{i\omega t}. \tag{32}$$

This expression can be discretized if the integral in Eq. (32) is represented by its Riemann sum F_k, which can subsequently be evaluated, for example, at the Fourier grid $\omega = \widetilde{\omega}_k$:

$$F_k = \frac{1}{N} \sum_{n=0}^{N-1} C_n\, \mathrm{e}^{in\widetilde{\omega}_k \tau} = \frac{1}{N} \sum_{n=0}^{N-1} C_n \mathrm{e}^{2i\pi nk/N}, \quad \widetilde{\omega}_k \equiv \frac{2\pi k}{T} = \frac{2\pi k}{N\tau}, \tag{33}$$

where $0 \leq k \leq N-1$ and $F_k \equiv F(\widetilde{\omega}_k)$. This is the complex form of the discrete Fourier transform (DFT) [45], which is defined only at the Fourier frequencies $\omega = \widetilde{\omega}_k$. If we multiply (33) by $(1/N)\exp(-im\widetilde{\omega}_k\tau)$ and sum the result over k from 0 to $N-1$, we shall retrieve all the elements from the original set

$\{C_n\}$ through the inverse discrete Fourier transform (IDFT):

$$C_n = \sum_{k=0}^{N-1} F_k \, \mathrm{e}^{-in\widetilde{\omega}_k\tau} = \sum_{k=0}^{N-1} F_k \mathrm{e}^{-2i\pi nk/N}, \quad 0 \le n \le N-1, \tag{34}$$

where the orthogonalization property of the harmonic basis set functions $\{|\exp(-i\widetilde{\omega}_k\tau))\}_{k=0}^{N-1}$ is used:

$$\frac{1}{N}\sum_{k=0}^{N-1} \mathrm{e}^{2i\pi(n-m)k/N} = \delta_{n,m}, \tag{35}$$

with $\delta_{n,m}$ being the usual Kronecker $\delta-$symbol: $\delta_{n,m}=1$ for $n=m$ and $\delta_{n,m}=0$ for $n \neq m$. The Fourier frequencies $\{\widetilde{\omega}_k\}$ from Eq. (33) are purely real so that the exponentials in Eq. (34) are unattenuated. Unlike Eq. (14), where the elements ω_k from the set $\{\omega_k\}$ are the unknown peak parameters, the frequencies $\widetilde{\omega}_k$ from Eq. (33) are fixed in advance, and this latter feature leads to linearity of both DFT and IDFT. In Eqs. (33) and (34), one encounters three sequences $\{C_n, F_k, |\exp(-i\widetilde{\omega}_k\tau))\}_{n,k=0}^{N-1}$, each of which is of length N. A direct computation by means of the DFT would require N^2 multiplications that are drastically reduced to only $N\log_2 N$ multiplications in the FFT [45].

Due to the exponential nature of the evolution operator (3), construction of its discrete counterpart $\widehat{\mathrm{U}}(t)=\widehat{\mathrm{U}}(t_n)=\widehat{\mathrm{U}}(n\tau)$ at the time $t=t_n \equiv n\tau$ is done simply through raising the ansatz $\widehat{\mathrm{U}} \equiv \widehat{\mathrm{U}}(\tau)$ to the nth power:

$$\widehat{\mathrm{U}}(n\tau)=\widehat{\mathrm{U}}^n, \quad \widehat{\mathrm{U}} \equiv \widehat{\mathrm{U}}(\tau)=\mathrm{e}^{-i\widehat{\Omega}\tau} \quad \Longrightarrow \quad |\Phi_n)=\widehat{\mathrm{U}}^n|\Phi_0). \tag{36}$$

The set $\{|\Phi_n)\}$ represents the Schrödinger basis that could be used for diagonalization of the evolution/relaxation matrix $\mathbf{U}$. In quantum chemistry, linear programming, and the engineering literature, the set $\{|\Phi_n)\}$ is called the Krylov basis. In quantum-mechanical signal processing, the term Schrödinger basis is more transparent since it points directly at the quantum-mechanical origin of the state functions $\{|\Phi_n)\}$ that do stem from the Schrödinger equation (1). The discrete/digital counterpart of Eq. (9) can be written as:

$$\widehat{\mathrm{U}}^n = \sum_{k=1}^{K} \mathrm{e}^{-in\omega_k\tau}\widehat{\pi}_k, \quad \mathrm{Im}(\omega_k) < 0. \tag{37}$$

For any operator analytic function $f(\widehat{\mathrm{U}})$, the eigenproblem is defined as in Eq. (6) via:

$$\widehat{\mathrm{U}}|\Upsilon_k) = u_k|\Upsilon_k), \quad u_k = \mathrm{e}^{-i\omega_k\tau}, \quad f(\widehat{\mathrm{U}})|\Upsilon_k) = f(u_k)|\Upsilon_k). \tag{38}$$

Usage of Eqs. (10), (14) and (36) gives the discrete autocorrelation function:

$$C_n = (\Phi_0|\Phi_n) = (\Phi_0|\widehat{\mathrm{U}}^n|\Phi_0), \tag{39}$$

$$C_n = \sum_{k=1}^{K} d_k u_k^n. \tag{40}$$

The same result (40) for C_n can be obtained by inserting Eq. (37) for $\widehat{\mathrm{U}}^n$ into Eq. (39). The decomposition (40) of the autocorrelation functions $\{C_n\}$ into the sum of K products, that is, transients $\{d_k u_k^n\}$ of a geometric progression type, constitutes the harmonic inversion. The set of at least $2K$ points $\{C_n\}$ is given in advance, whereas the unknown pair of $2K$ parameters $\{u_k, d_k\}_{k=1}^{K}$ represent the solution of the problem. The representation (40) of each element C_n of the given set $\{C_n\}$ with the task of finding the unknown pairs $\{\omega_k, d_k\}$ and the order K is hereafter called the "harmonic inversion problem" (HIP). A large fraction of experimentally encoded time signals $c(t)$ in many fields yields spectra that are well approximated by sums of damped exponentials:

$$c(t) = \sum_{k=1}^{K} d_k \mathrm{e}^{-i\omega_k t}. \tag{41}$$

In other words, such signals are just like the autocorrelation functions (14). This means that in the time domain, each signal point $c_n \equiv c(n\tau)$ from the experimentally recorded sequence $\{c_n\}$ is built from a linear combination of discrete attenuated exponentials:

$$c_n = \sum_{k=1}^{K} d_k \mathrm{e}^{-in\omega_k \tau} = \sum_{k=1}^{K} d_k u_k^n, \tag{42}$$

precisely as in Eq. (40) provided that the amplitudes $\{d_k\}$ are identified via the prescription $d_k = (\Phi_0|\Upsilon_k)^2$ from Eq. (15). Hence, such experimentally measured signals are mathematically equivalent to the autocorrelation functions in both the digital and analog representations:

$$c_n = C_n, \quad c(t) = C(t). \tag{43}$$

In this work, we will most frequently use the symbols $c_n \equiv c(n\tau)$ when referring to both the time signals and the autocorrelation functions $C_n \equiv C(n\tau)$. The set $\{\exp(-i\omega_k t)\}$ is exceedingly nonorthogonal, and this property causes numerical difficulties in all methods for nonlinear fittings of experimental time signals $\{c_n\}$ to the form (42) as discussed in Ref. [46]. If instead of the matrix element $(\Phi_0|\widehat{\mathrm{U}}^s|\Phi_0)$, we consider a more general scalar product

involving two different Schrödinger states $(\Phi_m|\widehat{\mathrm{U}}^s|\Phi_n)$, then Eq. (43) together with the symmetry of the inner product would immediately lead to:

$$\mathrm{U}^{(s)}_{n,m} \equiv (\Phi_m|\widehat{\mathrm{U}}^s|\Phi_n) = \mathrm{C}_{n+m+s} = c_{n+m+s}, \quad \mathrm{S}_{n,m} = c_{n+m}. \tag{44}$$

These signal points $\{c_{n+m+s}\}$ can be used to set up the following matrix,

$$\mathbf{H}_n(c_s) = \mathbf{U}^{(s)}_n = \begin{pmatrix} c_s & c_{s+1} & c_{s+2} & \cdots & c_{s+n-1} \\ c_{s+1} & c_{s+2} & c_{s+3} & \cdots & c_{s+n} \\ c_{s+2} & c_{s+3} & c_{s+4} & \cdots & c_{s+n+1} \\ \vdots & \vdots & \vdots & \vdots & \vdots \\ c_{s+n-1} & c_{s+n} & c_{s+n+1} & \cdots & c_{s+2n-2} \end{pmatrix}, \tag{45}$$

and its determinant,

$$\mathrm{H}_n(c_s) = \det \mathbf{H}_n(c_s) = \begin{vmatrix} c_s & c_{s+1} & c_{s+2} & \cdots & c_{s+n-1} \\ c_{s+1} & c_{s+2} & c_{s+3} & \cdots & c_{s+n} \\ c_{s+2} & c_{s+3} & c_{s+4} & \cdots & c_{s+n+1} \\ \vdots & \vdots & \vdots & \vdots & \vdots \\ c_{s+n-1} & c_{s+n} & c_{s+n+1} & \cdots & c_{s+2n-2} \end{vmatrix}, \tag{46}$$

where $\mathbf{U}^{(s)}_n = \{\mathrm{U}^{(s)}_{i,j}\}^{n-1}_{i,j=0}$. The "argument" c_s in the small parenthesis in $\mathbf{H}_n(c_s)$ denotes the leading element from the first row and first column in the matrix (45). The matrix $\mathbf{H}_n(c_s)$ is called the Hankel matrix. In signal processing, the experimentally measured signal points are the input data to a theoretical analysis, and as such, matrix (45) is named the data matrix. The determinant $\mathrm{H}_n(c_s)$ from (46), which is associated with matrix $\mathbf{H}_n(c_s)$, is called the Hankel determinant. Returning to Eq. (42), we set the time t to zero, that is, $n = 0$, and derive the sum rule for the residues:

$$\sum_{k=1}^{K} d_k = c_0 \neq 0, \tag{47}$$

where the closure (8) is used. Here, the first recorded signal point c_0 is related to the norm of the initial state $|\Phi_0)$ according to Eq. (4).

In addition to Eq. (11), it is also useful to introduce the Green function $\widehat{\mathrm{R}}(u)$ as the matrix elements of an alternative resolvent operator associated with $\widehat{\mathrm{U}}$:

$$\widehat{\mathrm{R}}(u) = \left(\widehat{1}u - \widehat{\mathrm{U}}\right)^{-1}, \quad u = \mathrm{e}^{-i\omega\tau}. \tag{48}$$

The exact quantum-mechanical spectrum of the operator $\widehat{\mathrm{R}}(u)$ is defined through the following Green function:

$$\mathcal{R}(u) = \left(\Phi_0|\widehat{\mathrm{R}}(u)|\Phi_0\right). \tag{49}$$

Using the projection operator $\widehat{\pi}_k$ from Eq. (8), we obtain the exact spectral representation of the Green operator and the Green function:

$$\widehat{\mathrm{R}}(u) = \sum_{k=1}^{K} \frac{\widehat{\pi}_k}{u - u_k}, \tag{50}$$

$$\mathcal{R}(u) = \sum_{k=1}^{K} \frac{d_k}{u - u_k}, \tag{51}$$

which is recognized as the PA in its paradiagonal form. When the binomial series expansion is used for Eq. (50) and the result inserted into Eq. (49) with the subsequent usage of Eqs. (42) and (36), the following Maclaurin series is obtained for the exact spectrum:

$$\mathcal{R}(u) = \sum_{n=0}^{\infty} c_n u^{-n-1}. \tag{52}$$

In the exact spectrum (52), an infinite set $\{c_n\}_{n=0}^{\infty}$ is needed. However, any set of experimentally measured time signal points $\{c_n\}_{n=0}^{N-1}$ or theoretically generated autocorrelation functions $\{C_n\}_{n=0}^{N-1}$ is of a finite length $N < \infty$. In such cases, for example, the FFT can only produce either a band-limited spectrum or a periodically repetitive spectrum after exhausting all the available signal points. The former case assumes that the c_n's represent a function of compact support with $c_n = 0$ for $n \geq N$, whereas the latter case supposes that the c_n's are periodic with period N so that $c_{n+N} = c_n$ for $n \geq N$. Both assumptions are arbitrary. Parametric methods can go beyond the FFT since they do not make such assumptions. Instead, they draw inferences about the unknown exact spectrum built from an infinite set $\{c_n\}$ while dealing only with a finite number of the available c_n's. This leads to a resolution that can be better than the Rayleigh limit $2\pi/(N\tau)$ fixed by the FFT. For instance, the PA for stationary signals can generate any number of the c_n's for $n \geq N$ from the given finite set $\{c_n\}_{n=0}^{N-1}$. This is equally true for the ARMA method that combines the autoregressive (AR) estimator and the moving average (MA) model. The ARMA is known as the method of choice in mathematical statistics, speech processing, and in other fields. The PA and ARMA are mathematically equivalent but may differ in computational implementations [2].

5. THE LANCZOS ALGORITHM FOR STATE VECTORS

The Lanczos algorithm [2] is one of the most widely used eigenvalue solvers for large matrices. This recursive method is usually formulated with the dynamic operator $\widehat{\Omega}$, but we shall presently use the evolution operator $\widehat{\mathrm{U}}(\tau)$. We shall study a general system and focus our attention on the resolvent operator $\widehat{\mathrm{R}}(u)$. This is the Green resolvent from (48), which is associated with the evolution operator $\widehat{\mathrm{U}}(\tau)$ from Eq. (36). The corresponding Green function $\mathcal{R}(u)$ is given in Eq. (49). We shall now perform a parallel study of the spectra of the operators $\widehat{\mathrm{U}}(\tau)$ and $\widehat{\mathrm{R}}(u)$. One of the possibilities for obtaining the spectrum of the evolution operator $\widehat{\mathrm{U}}(\tau)$ is to diagonalize directly the original eigenvalue problem (38) in a conveniently chosen complete orthonormal basis. Such a basis can be constructed from, for example, the Lanczos states $\{|\psi_n)\}$ that are associated with matrix $\mathbf{U}=\{\mathrm{U}_{n,m}\}$. The Lanczos states $\{|\psi_n)\}$ are presently generated from the recursion [47, 48]:

$$\beta_{n+1}|\psi_{n+1}) = \left\{\widehat{\mathrm{U}}(\tau) - \alpha_n\widehat{1}\right\}|\psi_n) - \beta_n|\psi_{n-1}), \quad n>0, \quad |\psi_0) = |\Phi_0), \tag{53}$$

$$\alpha_n = \frac{(\psi_n|\widehat{\mathrm{U}}(\tau)|\psi_n)}{(\psi_n|\psi_n)}, \quad \beta_n = \frac{(\psi_{n-1}|\widehat{\mathrm{U}}(\tau)|\psi_n)}{(\psi_{n-1}|\psi_{n-1})}, \quad \beta_0 = 0. \tag{54}$$

The sum $\alpha_n|\psi_n) + \beta_n|\psi_{n-1})$ appearing on the rhs of (53) represents the two orthogonalizing terms that are subtracted from $\widehat{\mathrm{U}}(\tau)|\psi_n)$ to discard certain pathways from the intermediate state $|\psi_n)$, such as the return to $|\Phi_0)$. In applications, the Lanczos algorithm is customarily introduced with the matrix $\mathbf{U}(\tau)$ instead of the operator $\widehat{\mathrm{U}}(\tau)$ with the appropriate replacement of the wave function by the corresponding column state vector. In such cases, the matrix-vector multiplication is carried out at each iteration, and this is the most computer time-consuming part of the matrix version of the Lanczos algorithm. Of course, there is a flexibility in the Lanczos algorithm, which permits the recursion to be carried out with tensors, matrices, operators, or scalars [2]. In Section 15, we shall show that the operator version (53) can be used to establish the analytical Lanczos algorithm with an arbitrary state $|\psi_n)$ in an explicit form. The recurrence (53) is symmetric in the sense that the component $|\psi_{n+1})$ in $\widehat{\mathrm{U}}(\tau)|\psi_n)$ is the same as the constituent $|\psi_n)$ in $\widehat{\mathrm{U}}(\tau)|\psi_{n+1})$. Here, the general element $\mathrm{U}_{n,m}$ of the evolution matrix $\mathbf{U}(\tau)$ is a complex symmetric matrix with the elements:

$$\mathrm{U}^{(s)}_{n,m} = (\psi_m|\widehat{\mathrm{U}}^s(\tau)\psi_n) = (\psi_n|\widehat{\mathrm{U}}^s(\tau)|\psi_m) = \mathrm{U}^{(s)}_{m,n}. \tag{55}$$

Of course, the matrix elements in the basis set of the Lanczos $\{|\psi_n)\}$ and Schrödinger $\{|\Phi_n)\}$ states are different, but for simplicity, we shall use the same formal label $\mathrm{U}^{(s)}_{n,m}$ in both Eqs. (44) and (55). Multiplying Eq. (53)

throughout by the term $\beta_1\beta_2\cdots\beta_n$ leads to the following results:

$$|\tilde{\psi}_{n+1}) = \left\{\widehat{\mathrm{U}}(\tau) - \alpha_n\right\}|\tilde{\psi}_n) - \beta_n^2|\tilde{\psi}_{n-1}), \tag{56}$$

$$|\tilde{\psi}_n) \equiv \bar{\beta}_n|\psi_n), \quad \bar{\beta}_n = \prod_{m=1}^{n}\beta_m \neq 0, \quad n \geq 1, \quad |\tilde{\psi}_0) = |\Phi_0). \tag{57}$$

The alternative recursion (57) involves the monic Lanczos states $\{|\tilde{\psi}_n)\}$. Here, the term "monic" serves to indicate that for any given integer n, the highest state $|\Phi_n)$ in the finite sum, which defines the vector $|\tilde{\psi}_n)$, always has an overall multiplying coefficient equal to unity similarly to a monic polynomial [2]. The Lanczos states $\{|\tilde{\psi}_n)\}$ are orthogonal, but unnormalized, as opposed to orthonormalized Lanczos states $\{|\psi_n)\}$. By construction, both sequences $\{|\psi_n)\}$ and $\{|\tilde{\psi}_n)\}$ lead to certain linear combinations of powers of the operator $\widehat{\mathrm{U}}(\tau)$ acting on the initial state $|\Phi_0)$. Therefore, due to the relation $|\Phi_n) = \widehat{\mathrm{U}}^n(\tau)|\Phi_0)$ from Eq. (36), the vectors $\{|\psi_n)\}$ and $\{|\tilde{\psi}_n)\}$ are certain sums of Schrödinger states $\{|\Phi_n)\}$.

5.1. Jacobi matrix

Once the set $\{\alpha_n, \beta_n\}$ is generated, the matrix $\mathbf{U} = \{\mathrm{U}_{n,m}\}$ becomes automatically available. This is seen by projecting (53) onto the state $(\psi_m|$ and using Eq. (55) for $s = 1$ to obtain $\mathrm{U}_{n,m} = c_0(\alpha_n\delta_{n,m} + \beta_{n+1}\delta_{n+1,m} + \beta_n\delta_{n-1,m})$. Or by writing $\delta_{n-1,m}$ equivalently as $\delta_{n,m+1}$, we have [47, 48]:

$$\mathrm{U}_{n,m} = c_0(\alpha_n\delta_{n,m} + \beta_m\delta_{n+1,m} + \beta_n\delta_{n,m+1}) \equiv c_0\mathrm{J}_{n,m}. \tag{58}$$

Here, the elements $\mathrm{U}_{n,m}$ are alternatively denoted by $c_0\mathrm{J}_{n,m}$ to indicate that the matrix $\mathbf{U}$ in the basis $\{|\psi_n)\}$ is a tridiagonal matrix, which is equivalently called the Jacobi matrix or $\mathbf{J}$-matrix and denoted by $\mathbf{J} = \{\mathrm{J}_{n,m}\}$. Hence, in the Lanczos basis, the evolution matrix $\mathbf{U}$ automatically acquires its tridiagonal (codiagonal) form of the type of a $\mathbf{J}$-matrix in a finite dimension, say $M \times M$ such that $\mathbf{U}_M = \mathrm{trid}_M[\beta, \alpha, \beta] \equiv c_0\mathbf{J}_M$. This is due to the definition of the basis $\{|\psi_n)\}$ in which the above matrix element $\mathrm{U}_{n,m}$ is equal to 0 for $|m - n| > 1$ and otherwise $(\psi_m|\psi_m) = (\psi_0|\psi_0) = (\Phi_0|\Phi_0) = c_0 \neq 0$ for any nonnegative integer m. Thus, in general, the orthogonality relation for the basis $\{|\psi_n)\}$ is given by [47, 48]:

$$(\psi_m|\psi_n) = c_0\delta_{n,m}, \tag{59}$$

as the explicit calculations of the first few overlaps of Lanczos states (53) indeed confirm. According to Eq. (59), both the denominators $(\psi_n|\psi_n)$ and $(\psi_{n-1}|\psi_{n-1})$ in the expression (54) for $\{\alpha_n, \beta_n\}$ are equal to $c_0 \neq 0$. It then

follows from the above statements that the matrix $\mathbf{U}_M$ is 0 everywhere except on the diagonal and the two codiagonals that are the subdiagonal and the superdiagonal whose elements reside immediately at the two opposite sides of the main diagonal [45]:

$$\mathbf{U}_M = c_0 \mathbf{J}_M, \quad \mathbf{J}_M = \begin{pmatrix} \alpha_0 & \beta_1 & 0 & 0 & \cdots & \cdots & 0 \\ \beta_1 & \alpha_1 & \beta_2 & 0 & \cdots & \cdots & 0 \\ 0 & \beta_2 & \alpha_2 & \beta_3 & \cdots & \cdots & 0 \\ 0 & 0 & \beta_3 & \alpha_3 & \cdots & \cdots & 0 \\ \vdots & \vdots & \vdots & \ddots & \ddots & \ddots & \vdots \\ 0 & 0 & 0 & \cdots & \beta_{M-2} & \alpha_{M-2} & \beta_{M-1} \\ 0 & 0 & 0 & \cdots & 0 & \beta_{M-1} & \alpha_{M-1} \end{pmatrix}. \tag{60}$$

This is a band-structured matrix or a band matrix which is in this particular tridiagonal form also called the Jacobi matrix. Projecting both sides of Eq. (53) onto $\beta_{n+1}(\psi_{n+1}|$ and using Eq. (59), we find:

$$\beta_{n+1}^2 = \frac{\|\{\widehat{\mathrm{U}}(\tau) - \alpha_n \widehat{1}\}|\psi_n) - \beta_n|\psi_{n-1})\|^2}{c_0} \neq 0. \tag{61}$$

This is an alternative definition of the Lanczos parameter β_n that is equivalent to Eq. (54). The expression (61) shows that β_{n+1}^2 is proportional to the squared norm of the state $\{\widehat{\mathrm{U}}(\tau) - \alpha_n \widehat{1}\}|\psi_n) - \beta_n|\psi_{n-1})$. Note that the Lanczos algorithm is closely related to the so-called reduced partitioning procedure [16, 19].

5.2. Jacobi eigenvalue problem

Returning to Eq. (60), it should be noted that there are many good programs available in the literature for finding eigenvalues and eigenvectors of the Jacobi matrix $\mathbf{J}$. Among these, we recommend the routines COMQR and F02AMF from the computation libraries EISPACK [49] and NAG [50] libraries (see also [51]). Of course, the matrix (60) in the studied model is an approximation to the exact evolution matrix $\mathbf{U}_N$. In principle, we should use a different label, say $\mathbf{U}_M^a = c_0 \mathbf{J}_M$, in Eq. (60) to distinguish this approximation from the exact matrix $\mathbf{U}_N$. Instead, to avoid clutter, it will be understood hereafter that the notation $\mathbf{U}_M = \{\mathrm{U}_{n,m}\}_{n,m=0}^{M-1}$ refers to the approximation $\mathbf{U}_M^a$ which is $c_0 \mathbf{J}_M = \{c_0 \mathrm{J}_{n,m}\}_{n,m=0}^{M-1}$ from Eq. (60). Moreover, the important thing to observe is that the approximation (60) to the exact evolution operator covers only a part of the generally infinite-dimensional vector space $\mathcal{H}$ for the general system under study. The relevant Lanczos subspace $\mathcal{L}_M = \mathrm{span}\{|\psi_0), |\psi_1), |\psi_2), \ldots, |\psi_{M-1})\} \subset \mathcal{H}$ is spanned by the

above-constructed set $\{|\psi_n)\}$ $(1 \le n \le M)$. Suppose that we wish to obtain the K eigenvalues $\{u_k\}_{k=1}^{K}$ of the evolution matrix $\mathbf{U}_N$. Despite the inherent limitations of the above model, by choosing M to be sufficiently large, the $\mathbf{J}$-matrix (60) will still be able to extract good approximate eigenvalues $\{u_k^M\}$ to the exact set $\{u_k\}$. This is the so-called Lanczos phenomenon, which states that the exact $\mathbf{U}$-matrix and its approximation $c_0\mathbf{J}$ from Eq. (60) share a common set of eigenvalues, provided that M is large enough [52]. In practice, M is usually chosen to be greater than K to assure that all the relevant eigenvalues are indeed extracted from the selected interval. The relation $M > K$ implies a local overcompleteness of the basis $\{|\psi_n)\}_{n=0}^{M-1}$, and this leads to the appearance of the so-called singular eigenvalues. Overcompleteness means that the number of equations is larger than the number of unknown quantities $(M > K)$. This mathematical ill-conditioning of the problem is usually tackled by several standard procedures, for example, the Cholesky or the Householder decomposition, the singular value decomposition (SVD), or the so-called QZ algorithm [45, 49–51]. This is reminiscent of a situation encountered in solving the harmonic inversion problem through nonlinear fitting, in which the lack of knowledge of K is handled by guessing an integer M that could lead to underfitting $(M < K)$ or overfitting $(M > K)$. Underfitting leaves some $K - M$ physical (genuine) resonances undetected. Overfitting yields some $M - K$ unphysical (spurious) resonances. Both situations are unacceptable from theoretical and practical standpoints. This highlights the necessity for having a method of known validity to determine the exact number K of resonances directly from the raw data that are available as the experimentally measured time signals $\{c_n\}$. By contrast, in the FPT, the true number K of resonances is determined without any ambiguity from the uniqueness of the Padé polynomial quotient for a given series of the input signal points $\{c_n\}$ [47, 53].

In the Lanczos algorithm, a sufficiently large number M is not necessary only for obtaining accurate eigenvalues but also for arriving at good eigenvectors if they are needed in the analysis. For a large enough M, the basis $\{|\psi_n)\}_{n=0}^{M-1}$ will be capable of approximately spanning the vector space of the exact wave functions $\{|\Upsilon_k)\}$ in the chosen frequency range. This circumstance permits arriving at an accurate approximation $|\Upsilon_k^M)$ to the exact state vector $|\Upsilon_k)$ by forming a linear combination of M functions $\{|\psi_n)\}$ [47, 48]:

$$|\Upsilon_k^M) = \sum_{n=0}^{M-1} Q_{n,k}|\psi_n). \tag{62}$$

The unknown expansion coefficients $\{Q_{n,k}\}$ from (62) are the elements of the column matrix $\mathbf{Q}_k = \{Q_{n,k}\}$ with $Q_{n,k} \equiv Q_n(u_k)$. We insert (62) into the eigenvalue problem (38), then project the result onto the state vector $(\psi_m|$, and

finally use the orthogonality condition (59) to write:

$$\sum_{n=0}^{M-1} Q_{n,k}(\psi_m|\widehat{\mathrm{U}}(\tau)|\psi_n) = u_k \sum_{n=0}^{M-1} Q_{n,k}(\psi_m|\psi_n) = c_0 u_k \sum_{n=0}^{M-1} Q_{n,k}\delta_{n,m} = c_0 u_k Q_{m,k}. \quad (63)$$

From here, with the help of Eq. (60), the eigenvalue problem for the **J**-matrix is deduced in the form of a finite system of linear equations,

$$\sum_{n=0}^{M-1} \mathrm{J}_{n,m} Q_{n,k} = u_k Q_{m,k}, \quad (64)$$

or in the equivalent matrix form

$$\mathbf{J}_M \mathbf{Q}_k = u_k \mathbf{Q}_k. \quad (65)$$

The eigenvector $\mathbf{Q}_k$ corresponds to the eigenvalue u_k in a finite chain model of the length M. As opposed to the Schrödinger states $\{|\Phi_n)\}$, the Lanczos basis $\{|\psi_n)\}$ produces the matrix elements $\{\mathrm{U}_{n,m}\}$ as a nonlinear combination of c_n due to the presence of the normalization factor β_{n+1} of the state ψ_{n+1} in the recursion (53). The constant coefficients α_n and β_n are the coupling constants or the recurrence (or chain) parameters of the Lanczos states $\{|\psi_n)\}$. The Lanczos algorithm (53) generates a wave packet propagation leading directly to tridiagonalization of the evolution matrix $\mathbf{U}(\tau)$. In this method, $|\psi_{n+1})$ is automatically normalized to $c_0 \neq 0$ and orthogonalized to $|\psi_n)$ and $|\psi_{n-1})$. However, by construction of the chain, it follows that $|\psi_{n+1})$ is also orthogonal to all the remaining previous elements $|\psi_{n-2}), \ldots, |\psi_0)$ so that

$$\widehat{1} = \sum_{k=1}^{K} |\psi_k)(\psi_k|. \quad (66)$$

The Lanczos algorithm (53) is a low-storage method as opposed to the corresponding Gram–Schmidt orthogonalization (GSO), which uses all states at each stage of the computation. Otherwise, the final explicit results are rigorously the same in the GSO and the Lanczos orthogonalizations. Physically, the state $|\psi_n)$ is essentially the nth environment of $|\psi_0)$. But the coupling of $|\psi_n)$ with its surroundings is assumed significant only with the two nearest neighbors (environments) or "orbitals" $|\psi_{n+1})$ and $|\psi_{n-1})$. A useful consequence of this in practice is that the $(n+1)$st iteration in Eq. (53) yielding the state $\beta_{n+1}|\psi_{n+1})$ needs to store only the two preceding states $|\psi_{n-1})$ and $|\psi_n)$ since all other vectors can safely be overwritten. This extreme storage economy is the key to the success of the scheme (53) relative to, for example, the GSO, which requires a copy of the surrounding orbitals for each newly

generated state vector.[1] Hence, the recursion (53), which is also known as the nearest neighbor approximation, the chain model, the tight binding model, or the localized orbital model, is one of the ways to create a local representation of the "Hamiltonian" $\widehat{\Omega}$, which can be Hermitian or complex symmetric operator or the like. This model fulfills the plausible physical demand that the local density of states is predominantly determined by the local orbital itself, whereas the progressively more remote orbitals play a less important role. This is because the stronger effect on the state of interest is naturally expected to come from the nearest readily accessible orbitals without traversing many intermediate states that could act as barriers or obstacles to the passage. Thus, the chain model with its Lanczos state recursion is a mathematical prescription for the physical concept of a local environment. Clearly, each successive orbital in the chain of orbitals will progressively cluster in the periphery of the environment of the initial orbital $|\psi_0) = |\Phi_0)$. The measure of the effect of this environment onto the investigated state of the system is given by the coupling parameters $\{\alpha_n, \beta_n\}$ of the recurrence (53). It is then clear that the chain model, in fact, describes the overall evolution of the system from the given initial state $|\Phi_0)$. The Lanczos algorithm converts the original, completely filled evolution matrix $\mathbf{U}_N$ into its Jacobi counterpart, a sparse matrix $c_0\mathbf{J}_M$ of a considerably reduced dimension $M \ll N$. Strictly speaking, the respective dimensions of the original evolution matrix and its Jacobi counterpart are the same. In other words, tridiagonalization itself does not literally reduce the dimension of the original large problem, but it makes the underlying Jacobi matrix sparse. However, the coupling parameters $\{\alpha_n, \beta_n\}$ that determine the elements of the obtained **J**-matrix are of decreasing importance with increased dimension M. This is, in turn, equivalent to an effective dimensionality reduction $M \ll N$ of the original problem of a large size N. As a result of the Lanczos conversion $\mathbf{U}_N \longrightarrow \mathbf{U}_M$, the transformed evolution matrix $\mathbf{U}_M = c_0\mathbf{J}_M$ is capable of governing the motion of the studied system among its states in the vector space $\mathcal{L}_M \subset \mathcal{H}$ of a significantly reduced dimension relative to that for the original matrix $\mathbf{U}_N$. We may say that the Lanczos state localization is economical because it introduces only those intermediate states of $\widehat{\Omega}$ or $\widehat{\mathrm{U}}(\tau)$, which are coupled to the initial state $|\Phi_0)$. By construction, the chain $\{|\psi_n)\}$ contains progressively less important environments of the initial state $|\Phi_0)$, and this is adequate since the essential physics is often ingrained in only the first few neighboring states of $|\Phi_0)$. This is also economical as it actually implies that the full transformation leading to a long chain $\{|\psi_n)\}$ is not necessary. Such a circumstance is reminiscent of the situation encountered in the time domain, where the envelope of the signal

[1]The majority of the elements of a large **J**-matrix are zero. For example, some 99.9% zeros can be found in a $10^4 \times 10^4$ matrix **J** from (60) of a typical size encountered in many problems in solid-state physics to which the chain model has been extensively applied in the past [48].

$c(t)$ decays exponentially as t increases. Moreover, not only that the signal $\{c_n\}$ possesses larger intensities $|d_k|$ at earlier time in the recording but also it exhibits more rapid changes in oscillations. At long times, the intensities $\{d_k\}$ decrease to the level in which the signal becomes heavily corrupted with background noise. Thus, it is advantageous to complete the experimental encoding of the time signal reasonably quickly by avoiding the excessively long tail of $c(t)$ since with a large acquisition time T, one will inevitably measure mainly noise in the asymptotic region of the variable t [2]. This is at variance with the request of the Fourier-based spectroscopy, which demands a large T, since the resolution of the FFT is pre-assigned as $2\pi/T$.

The quest for the locality of operators $\widehat{\Omega}$ or $\widehat{\mathrm{U}}$ is natural in view of the fact that, in practice, one rarely needs the whole informational content of the Green resolvent $\widehat{\mathrm{R}}(u)$ but only a pre-assigned matrix element [47]. An important example of the need for such local information is the Green function $\mathcal{R}(u)$ from (49). Physically, $\mathcal{R}(u)$ describes the effect of the rest of the system onto its one selected part. Therefore, it is plausible that the examined local orbital itself should play the major role and that the successively more distant neighbors are expected to exhibit lesser effects. The Lanczos algorithm of nearest neighbors achieves this hierarchy of environments, whose relative influence to the local density of states is explicitly weighted and displayed. Each element of the set $\{|\psi_n)\}$ has the symmetry of $|\psi_0)$ as a result of the repeated action of $\widehat{\Omega}$ or $\widehat{\mathrm{U}}$ onto the initial state $|\psi_0) = |\Phi_0)$. If the set $\{|\psi_n)\}$ is required to contain functions of different symmetry, it will be necessary to consider different initial orbitals. The chain (53) does not contain those orbitals $|\psi_n)$ that are uncoupled to $|\psi_0)$ indicating the zero survival probability $(\psi_n|\psi_0) = 0$ of the state vector $|\psi_n)$ for $n \neq 0$ as in (59). Any matrix can be transformed into its corresponding Jacobi matrix. It is then clear that the chain model is equivalent to expressing the matrix $\mathbf{U}$ as the corresponding Jacobi matrix or tridiagonal matrix $c_0\mathbf{J}$ [47, 48]. An original problem under study might be of a high dimension N, that is, of a large number of degrees of freedom that could be strongly coupled to each other, leading to serious storage and computer time-consuming problems. In such cases, the standard diagonalization of the associated dynamic matrix $\mathbf{U}_N$ would require N^2 registers. This constraint can be dramatically relaxed to the amount of stores of only $2N$ if $\mathbf{U}_N$ possesses a local representation stored in a compact form (60), which emerges from the recursion (53).

Suppose that $\widehat{\Omega} = \widehat{\mathrm{H}}$, where $\widehat{\mathrm{H}}$ is a Hermitian Hamiltonian of the studied system. Let the set $\{|\psi_n)\}$ be generated from (53) with $\widehat{\mathrm{U}}(\tau)$ replaced by $\widehat{\mathrm{H}}$. In such cases, the coupling parameters $\{\alpha_n, \beta_n\}$ would have a direct physical meaning and interpretation. An example of a physical system, which is itself a realization of the chain model, is the one-dimensional ion crystallization of multiple-charged ions in a storage ring with electron cooling. Such a special crystallization of ions in storage rings has recently been achieved experimentally [54]. A multielectron ionic system of this type,

which represents a one-dimensional chain of clustered ions, could be treated within the frozen-core approximation, in which only one electron is active, whereas the other electrons have a passive role consisting of screening the nuclear charge. The Hamiltonian of this one-electron model in the case of a semi-infinite strip $(-\infty, n)$ could be readily set up and spectrally analyzed in the chain model. In the simplifying circumstance of a one-dimensional chain of hydrogen-like ions, the chain model would allow the electron to hop from one orbital (e.g., an s-orbital with zero value of the angular momentum) to another orbital of a neighboring ion. Here, all the recurrence parameters $\{\alpha_n\}$ are the same constant, equal to a given s-orbital energy, whereas the couplings $\{\beta_n\}$ are the "hopping" elements from one ion to the next. According to Eq. (61), the parameter β_{n+1} is proportional to the norm of the state $|\psi_{n+1}) = [\{\widehat{\mathrm{H}} - \alpha_n \widehat{1}\}|\psi_n) - \beta_n|\psi_{n-1})]/\beta_{n+1}$ for $\widehat{\Omega} = \widehat{\mathrm{H}}$. Therefore, the Lanczos coupling constants β_{n+1} and β_{n-1} can be considered a measure of the strength of the interaction between the states $|\psi_n)$ and $|\psi_{n\pm1})$. Similarly, α_n is the self-energy of the orbital $|\psi_n)$. The state vector $|\psi_n)$ can be viewed as a linear combination of the wave functions $\widehat{\mathrm{H}}^n|\psi_0)$, and this itself might be considered as the sum of all the pathways consisting of n steps, starting from the initial configuration $|\psi_0) = |\Phi_0)$. Here, the term "step" means a hop from one orbital to another, connected by the nonzero hopping matrix element of $\widehat{\mathrm{H}}$ with the assumption that the steps between the nearest neighbors are the most important.

6. THE LANCZOS ORTHOGONAL POLYNOMIALS

6.1. Three-term recursion

The Lanczos algorithm of tridiagonalization is the key step for converting the original (presumably large) matrix $\mathbf{U}_N$ into its corresponding sparse $\mathbf{J}$-matrix $c_0\mathbf{J}_M$ as given in Eq. (60) [48]. The kth eigenstate of the $\mathbf{J}$-matrix is given by the vector $\mathbf{Q}_k$, which corresponds to the eigenvalue u_k. By definition, the quantities $\{\mathbf{Q}_k\}$ are the column vectors $\mathbf{Q}_k = \{Q_{n,k}\}$ whose elements $Q_{n,k}$ are the expansion coefficients of the unnormalized total eigenstate $|\Upsilon_k^\infty)$ developed in the complete Lanczos set $\{|\psi_n)\}$ of the most general infinite chain model:

$$|\Upsilon_k^\infty) = \sum_{n=0}^{\infty} Q_{n,k}|\psi_n), \quad Q_n(u_k) \equiv Q_{n,k}, \tag{67}$$

which is an extension of Eq. (62) to the infinite chain ($M = \infty$). This is an unnormalized state vector. Its norm is obtained by using the orthogonalization from Eq. (8) yielding:

$$\|\Upsilon_k^\infty\|^2 = (\Upsilon_k^\infty|\Upsilon_k^\infty) = c_0 \sum_{n=0}^{\infty} Q_{n,k}^2. \tag{68}$$

The normalized total wave function $|\Upsilon_k^+)$ is determined by:

$$|\Upsilon_k^+) = \|\Upsilon_k^\infty\|^{-1}|\Upsilon_k^\infty) = \left[c_0 \sum_{n=0}^{\infty} Q_{n,k}^2\right]^{-1/2} |\Upsilon_k^\infty), \tag{69}$$

where $|\Upsilon_k^\infty)$ is taken from Eq. (67). Substituting the state vector (67) into Eq. (38), which is then multiplied by $(\psi_m|$ from the left, the eigenvalue problem of the infinite-dimensional Jacobi matrix is obtained using Eq. (59) in the form given either by an infinite system of linear equations:

$$\sum_{n=0}^{\infty} \mathrm{J}_{n,m} Q_{n,k} = u_k Q_{m,k}, \tag{70}$$

or via the corresponding matrix equation:

$$\mathbf{J}_\infty \mathbf{Q}_k = u_k \mathbf{Q}_k. \tag{71}$$

This is an ordinary eigenvalue problem in which the tridiagonal Jacobi matrix $\mathbf{J}_\infty$ is given in Eq. (60) with $M = \infty$. The residues $\{d_k\}$ are defined by Eq. (15), where $|\Upsilon_k)$ is the exact complete state vector normalized to $c_0 \neq 0$. The same type of definition for d_k is valid for an approximation such as Eq. (67), provided that normalization is properly included according to Eq. (69):

$$d_k = (\Phi_0|\Upsilon_k^+)^2. \tag{72}$$

Inserting Eq. (67) into Eq. (69) and then substituting the obtained result into Eq. (72) yields:

$$d_k^\infty = \frac{c_0 Q_{0,k}^2}{\sum\limits_{n=0}^{\infty} Q_{n,k}^2}, \tag{73}$$

where the superscript ∞ in the residue d_k^∞ is introduced to point at the infinite chain ($M = \infty$). Comparing Eqs. (68 and 73) gives the following:

$$d_k^\infty = \frac{c_0^2 Q_{0,k}^2}{\|\Upsilon_k^\infty\|^2}. \tag{74}$$

Note that we do not need to solve Eq. (71) to obtain the wave function $|\Upsilon_k^\infty)$ from Eq. (67). This is because the whole sequence $\{Q_{n,k}\}$ can also be generated recursively using the already obtained sets $\{\alpha_n, \beta_n\}$ and $\{u_k\}$. To this end, we substitute Eq. (67) into the time-independent Schrödinger equation (38) and

exploit the linearity of $\widehat{\mathrm{U}}(\tau)$ to write as follows:

$$\widehat{\mathrm{U}}(\tau)\sum_{n=0}^{\infty} Q_{n,k}|\psi_n) = u_k \sum_{n=0}^{\infty} Q_{n,k}|\psi_n). \tag{75}$$

Eliminating the term $\widehat{\mathrm{U}}(\tau)|\psi_n)$ from the lhs of Eq. (75) by the recursion (53), we obtain:

$$\sum_{n=0}^{\infty} Q_{n,k}\{\alpha_n|\psi_n) + \beta_{n+1}|\psi_{n+1}) + \beta_n|\psi_{n-1})\} = u_k \sum_{n=0}^{\infty} Q_{n,k}|\psi_n). \tag{76}$$

From here, the sought recursion for $\{Q_{n,k}\}$ can immediately be extracted if the whole inner part of the sum on the lhs of Eq. (76) could also be reduced to the nth state $|\psi_n)$ just as in $u_k \sum_{n=0}^{\infty} Q_{n,k}|\psi_n)$ on the rhs of the same equation. Then, a comparison of the multipliers of the same vector $|\psi_n)$ would give the sought result. This is indeed possible by the index changes $n \pm 1 \longrightarrow n'$ in the two terms containing $|\psi_{n\pm1})$ on the lhs of Eq. (76), so that:

$$\sum_{n=0}^{\infty} v_n^{(k)}|\psi_n) \equiv \sum_{n=0}^{\infty}\{(\alpha_n - u_k)Q_n(u_k) + \beta_{n+1}Q_{n+1}(u_k) + \beta_n Q_{n-1}(u_k)\}|\psi_n) = |0), \tag{77}$$

where the relation $\beta_0 = 0$ from Eq. (54) is used along with the defining initialization $Q_{-1}(u_k) \equiv 0$. In Eq. (77), the symbol $|0)$ denotes the zero state vector, as before. Since the set $\{|\psi_n)\}$ is a basis, its elements $|\psi_n)$ are linearly independent. This implies that Eq. (77) can be satisfied only if all the auxiliary coefficients $\{v_n^{(k)}\}$ multiplying the nth term $|\psi_n)$ are equal to zero. This yields the Lanczos recursion for the state vectors $\mathbf{Q}_k = \{Q_n(u_k)\}$ corresponding to the eigenvalues $\{u_k\}$:

$$\beta_{n+1}Q_{n+1}(u_k) = (u_k - \alpha_n)Q_n(u_k) - \beta_n Q_{n-1}(u_k), \tag{78}$$

$$Q_{-1}(u_k) = 0, \quad Q_0(u_k) = 1. \tag{79}$$

6.2. The Jacobi state vectors without diagonalization of the Jacobi matrix

This recurrence relation and the available triple set $\{\alpha_n, \beta_n; u_k\}$ are sufficient to completely determine the state vector $\mathbf{Q}_k$ without any diagonalization of the associated Jacobi matrix $\mathbf{U} = c_0\mathbf{J}$, which is given in Eq. (60). Of course, diagonalization of $\mathbf{J}$ might be used to obtain the eigenvalues $\{u_k\}$, but this is not the only approach at our disposal. Alternatively, the same set $\{u_k\}$ is also obtainable by rooting the characteristic polynomial or eigenpolynomial from

a secular equation,[2] which is entirely equivalent to the eigenvalue problem (38) [47]. Moreover, this characteristic polynomial is, in fact, proportional to $Q_K(u)$. Hence, the eigenvalue set $\{u_k\}_{k=1}^K$ coincides with the roots of the following characteristic equation:

$$Q_K(u_k) = 0, \quad 1 \le k \le K. \tag{80}$$

Returning to Eqs. (68) and (73), we combine $Q_0(u_k) = 1$ from Eq. (78) to obtain the following expression for the residue d_k:

$$d_k^\infty = \frac{c_0}{\sum_{n=0}^{\infty} Q_{n,k}^2} \quad \Longrightarrow \quad d_k^\infty = \frac{c_0^2}{\|\Upsilon_k^\infty\|^2}. \tag{81}$$

The Green operator $\widehat{\mathrm{G}}(\omega)$ from Eq. (12) can provide information about the studied physical system at any frequency ω and not just at ω_k that belongs to $|\Upsilon_k)$, as opposed to the Schrödinger eigenvalue problem (6). This is an apparent paradox, since the same operator $\widehat{\Omega}$ constitutes the only source of information in both the Green and the Schrödinger formalisms. Indeed, the Green function is known to be a powerful tool that can analytically continue the Schrödinger spectrum $\{\omega_k\}$ to encompass any value of ω. But the same ought to be also true for the stationary Schrödinger state vector, which one should be able to compute numerically at any ω, in addition to the eigenvalues ω_k, as permitted by the argument of analytical continuation [37, 55]. This follows from the fact that once the Green function is available at a fixed frequency ω, one can compute the corresponding state vector at the same ω by certain well-known integral transforms. Alternatively, we can show that Eq. (78) is valid at an arbitrary value of $u = \exp(-i\omega\tau)$ and not just at $u_k = \exp(-i\omega_k\tau)$ if we have a straightforward definition of the stationary Schrödinger state $|\Upsilon^\infty(u))$ for a given u [48]. Fixing $u = u_k$ here would retrieve the eigenstate (67) corresponding to the eigenvalue u_k. Similar to the pure eigenvector (67), the state $|\Upsilon^\infty(u))$ at any u can also be conceived as a linear combination of the Lanczos basis states:

$$|\Upsilon^\infty(u)) = \sum_{n=0}^{\infty} Q_n(u)|\psi_n). \tag{82}$$

The quantity $|\Upsilon^\infty(u))$ will describe an extended spectrum of $\widehat{\mathrm{U}}(\tau)$, beyond the Schrödinger eigenvalue set $\{u_k\}$, if the image $\widehat{\mathrm{U}}(\tau)|\Upsilon^\infty(u))$ of the operator

[2]The optimal method for finding all the roots of a given polynomial is to use the corresponding Hessenberg matrix to solve its well-conditioned eigenvalue problem [45, 47]. By contrast, any direct rooting of polynomials is known to be an ill-conditioned procedure, as discussed in Section 10.

$\widehat{\mathrm{U}}(\tau)$ is proportional to the same vector $|\Upsilon^{\infty}(u))$, for example,

$$\widehat{\mathrm{U}}(\tau)|\Upsilon^{\infty}(u)) = u|\Upsilon^{\infty}(u)), \tag{83}$$

which is true. This is nothing but rephrasing that the stationary Schrödinger equation at any u, and the Schrödinger eigenvalue problem (38) follows at once by the specification to the ridge $u = u_k$, as pointed out earlier in Refs. [47, 48]. Likewise, evaluating $|\Upsilon^{\infty}(u))$ at the eigenvalue $u = u_k$ leads to $|\Upsilon_k^{\infty}) \equiv |\Upsilon^{\infty}(u_k))$, where $|\Upsilon_k^{\infty})$ is the eigenvector as in Eq. (67). Adopting the infinite chain model and proceeding exactly along the lines (75) and (77) by using u in lieu of u_k, we obtain the Lanczos recursive algorithm for $Q_n(u)$:

$$\beta_{n+1}Q_{n+1}(u) = (u - \alpha_n)Q_n(u) - \beta_n Q_{n-1}(u), \tag{84}$$

$$Q_{-1}(u) = 0, \quad Q_0(u) = 1. \tag{85}$$

We see that the expansion coefficients in Eq. (82) are polynomials of degree n in the complex variable u. The same polynomials $Q_n(u_k) = Q_{n,k}$ evaluated at $u = u_k$ are also present in Eq. (67). Having obtained the whole set $\{Q_n(u)\}$ from the recursion (84), the usage of Eq. (82) would give the sought state vector $|\Upsilon^{\infty}(u))$ at any u. This is a simple computational tool, which resolves the above paradox, making the stationary Schrödinger equation (83) also formally usable at any u, as is the case with the corresponding Green function from Eq. (49) [47, 48].

6.3. The Jacobi matrix and the Lanczos polynomial matrix within the same system of linear equations

It is possible to interconnect the matrices $\mathbf{J}$ and $\mathbf{Q}_k$ through a compact matrix equation [48]. This follows from the tridiagonal structure of the matrix in Eq. (60), which allows one to deduce Eq. (78) directly from the product $\mathbf{JQ}_k$ at the set of the eigenvalues $\{u_k\}$. By the same reasoning, this conclusion can also be extended to encompass Eq. (84) at values of u other than u_k. Thus, the polynomials $\{Q_v(u)\}$ satisfy the matrix equation:

$$\begin{pmatrix} u-\alpha_0 & -\beta_1 & 0 & 0 & \cdots & 0 \\ -\beta_1 & u-\alpha_1 & -\beta_2 & 0 & \cdots & 0 \\ 0 & -\beta_2 & u-\alpha_2 & -\beta_3 & \cdots & 0 \\ \vdots & \vdots & \ddots & \ddots & \ddots & \vdots \\ 0 & 0 & 0 & -\beta_{n-1} & u-\alpha_{n-1} & -\beta_n \\ 0 & 0 & 0 & \cdots & -\beta_n & u-\alpha_n \end{pmatrix} \begin{pmatrix} Q_0(u) \\ Q_1(u) \\ Q_2(u) \\ \vdots \\ Q_{n-1}(u) \\ Q_n(u) \end{pmatrix} = \begin{pmatrix} 0 \\ 0 \\ 0 \\ \vdots \\ 0 \\ \beta_{n+1}Q_{n+1}(u) \end{pmatrix}, \tag{86}$$

where a finite sequence of $n+1$ polynomials $\{Q_v\}_{v=0}^{n}$ is considered. Obtaining the results of the indicated multiplication on the lhs of Eq. (86) and

comparing them with the elements of the column matrix from the rhs of the same equation, we readily arrive at Eq. (84).

The recursion (84) can be extended to operators and matrices. This is done by using the Cayley–Hamilton theorem [2], which states that for a given analytic scalar function $f(u)$, the expression for its operator counterpart $f(\widehat{\mathrm{U}})$ is obtained via replacement of u by $\widehat{\mathrm{U}}$ as in Eq. (6). In this way, we can introduce the Lanczos operator and matrix polynomials defined by the following recursions:

$$\beta_{n+1}Q_{n+1}(\widehat{\mathrm{U}}) = (\widehat{\mathrm{U}} - \alpha_n\widehat{1})Q_n(\widehat{\mathrm{U}}) - \beta_n Q_{n-1}(\widehat{\mathrm{U}}), \tag{87}$$

$$Q_{-1}(\widehat{\mathrm{U}}) = 0, \quad Q_0(\widehat{\mathrm{U}}) = \widehat{1}, \tag{88}$$

$$\beta_{n+1}Q_{n+1}(\mathbf{U}) = (\mathbf{U} - \alpha_n\mathbf{1})Q_n(\mathbf{U}) - \beta_n Q_{n-1}(\mathbf{U}), \tag{89}$$

$$Q_{-1}(\mathbf{U}) = 0, \quad Q_0(\mathbf{U}) = \mathbf{1}, \tag{90}$$

where $\mathbf{0}$ and $\mathbf{1}$ are the zero and unit matrices of the same dimension as $\mathbf{U}$. The eigenstates $\{Q_n(u_k)\}$ of the $\mathbf{J}$-matrix from Eq. (60) are the regular solutions of the three-term contiguous recurrence (78). This recurrence is a difference equation, which is a discrete counterpart of the corresponding second-order differential equation. Given the recursions (53) for $|\psi_n)$ and (89) for $Q_n(\widehat{\mathrm{U}})$, we can observe inductively that the following relationship is valid:

$$|\psi_n) = Q_n(\widehat{\mathrm{U}})|\psi_0), \tag{91}$$

where $\widehat{\mathrm{U}} \equiv \widehat{\mathrm{U}}(\tau)$ and $|\psi_0) = |\Phi_0)$. This equation defines the Lanczos polynomial propagation of the initial wave packet $|\Phi_0)$. Within second-order differential equations satisfied by the classical orthogonal polynomials [45], we always introduce a pair of solutions, one regular and the other irregular, called the polynomials of the first and the second kind, respectively. Using the analogy between differential and difference equations, we can identify the solution $Q_n(u)$ of the difference equation (84) as the Lanczos polynomial of the first kind. Similarly, the same equation has another solution, which is the Lanczos polynomial of the second kind $P_n(u)$. In other words, $P_n(u)$ satisfies the same recurrence (84), so that [47, 48]:

$$\beta_{n+1}P_{n+1}(u) = (u - \alpha_n)P_n(u) - \beta_n P_{n-1}(u), \tag{92}$$

$$P_0(u) = 0, \quad P_1(u) = 1. \tag{93}$$

Note that the initial conditions for $P_n(u)$ are different from those for $Q_n(u)$, as seen in Eqs. (84) and (92). In particular, the initialization to the recurrence (92) scales the degree of the polynomial $P_n(u)$ downward by 1. This implies that $P_n(u)$ is a polynomial of degree $n-1$ as opposed to $Q_n(u)$, which is the nth degree polynomial. Thus, the polynomial $P_n(u)$ has $n-1$ zeros and that is by one fewer than in the case of $Q_n(u)$.

7. RECURSIONS FOR DERIVATIVES OF THE LANCZOS POLYNOMIALS

Once the polynomial set $\{Q_n(u)\}$ becomes available from Eq. (84), the same type of recursion can automatically be derived for general derivatives $\{(\mathrm{d}/\mathrm{d}u)^m Q_n(u)\}$. This is greatly simplified by the following relation:

$$\left(\frac{\mathrm{d}}{\mathrm{d}u}\right)^m [uQ_n(u)] = uQ_{n,m}(u) + mQ_{n,m-1}(u), \tag{94}$$

$$Q_{n,m}(u) = \left(\frac{\mathrm{d}}{\mathrm{d}u}\right)^m Q_n(u), \quad Q_{n,0}(u) = Q_n(u), \tag{95}$$

$$Q_{n,m}(0) = \left[\left(\frac{\mathrm{d}}{\mathrm{d}u}\right)^m Q_n(u)\right]_{u=0}. \tag{96}$$

The expression (94) can easily be established in an inductive manner, as pointed out in Ref. [56]. Hereafter, we use the notation $Q_{n,s}(u)$ for the sth derivative of $Q_n(u)$ with respect to u instead of the more standard notation $Q_n^{(s)}(u)$. The reason for this is that the notation $Q_n^{(s)}(u)$ is customarily employed in the theory and applications of the so-called delayed orthogonal polynomials constructed from power moments, autocorrection functions, or signal points $\{\mu_{n+s}\} = \{C_{n+s}\} = \{c_{n+s}\}$, where the first $s < N$ points $\{\mu_r\} = \{C_r\} = \{c_r\}$ $(0 \le r \le s-1)$ are either skipped or simply missing from the full set of N elements. Delayed time signals $\{c_{n+s}\}$ are thoroughly studied in Refs. [2, 25]. If the expression (84) is differentiated m times and Eq. (94) is used, the following recursion is obtained inductively for the derivatives $\{Q_{n,m}(u)\}$ [47]:

$$\beta_{n+1}Q_{n+1,m}(u) = (u-\alpha_n)Q_{n,m}(u) - \beta_n Q_{n-1,m}(u) + mQ_{n,m-1}(u), \tag{97}$$

$$Q_{-1,m}(u) = 0, \quad Q_{0,0}(u) = Q_0(u) = 1. \tag{98}$$

This is a fast and accurate way of computing derivatives $\{Q_{n,m}(u)\}$ of any order $m > 0$. Similarly, the availability of the polynomials $\{P_n(u)\}$ from Eq. (92) enables the derivation of a recursive way of computing derivatives $\{P_{n,m}(u)\}$ via the analogy with Eq. (97):

$$\beta_{n+1}P_{n+1,m}(u) = (u-\alpha_n)P_{n,m}(u) - \beta_n P_{n-1,m}(u) + mP_{n,m-1}(u), \tag{99}$$

$$P_{0,m}(u) = 0, \quad P_{1,0}(u) = P_1(u) = 1, \tag{100}$$

$$P_{n,m}(u) = \left(\frac{\mathrm{d}}{\mathrm{d}u}\right)^m P_n(u), \quad P_{n,0}(u) = P_n(u), \tag{101}$$

$$P_{n,m}(0) = \left[\left(\frac{\mathrm{d}}{\mathrm{d}u}\right)^m P_n(u)\right]_{u=0}. \tag{102}$$

8. SECULAR EQUATION AND THE CHARACTERISTIC POLYNOMIAL

The eigenequation (71) can formally be rewritten as a problem of finding zeros of the matrix equation $(u\mathbf{1}-\mathbf{U})\mathbf{Q}_k=\mathbf{0}$. This matrix equation can operationally be solved by conversion to its corresponding scalar counterpart, that is, a determinantal equation known as the secular equation [2]:

$$\det[u\mathbf{1}-\mathbf{U}]=0. \tag{103}$$

The roots $\{u_k\}_{k=1}^{K}$ of Eq. (103) coincide with the eigenvalues of matrix $\mathbf{U}$. On the other hand, the function $\det[u\mathbf{1}-\mathbf{U}]$ is proportional to its Kth degree characteristic polynomial, which is equal to $Q_K(u)$ up to an overall multiplicative constant of the normalization type:

$$Q_K(u)=\frac{\det[u\mathbf{1}-\mathbf{U}]}{\bar{\beta}_K}, \tag{104}$$

where $\bar{\beta}_K$ is defined by Eq. (57). The K zeros $\{u_k\}_{k=1}^{K}$ of the characteristic polynomial $Q_K(u)$ coincide with the K eigenvalues of the $\mathbf{U}$-matrix (60) for $M=K$. Let us now link the secular equation with the Lanczos recursion. To this end, we insert Eq. (82) into Eq. (83) and then multiply the results from the left by $(\psi_m|$ to obtain the following system of linear equations:

$$\sum_{n=0}^{\infty}\mathrm{U}_{n,m}Q_n(u)=uQ_m(u). \tag{105}$$

The tridiagonal structure (58) of the elements $\mathrm{U}_{n,m}$ implies that the matrix form of Eq. (105) coincides with Eq. (86) if the matrix of the infinite dimension in Eq. (105) is appropriately truncated. Then, let the determinant of the tridiagonal matrix $\mathrm{trid}_{n+1}[\beta,\alpha-u,\beta]$ for a finite chain be denoted by $\tilde{Q}_{n+1}(u)$:

$$\tilde{Q}_{n+1}(u)=\begin{vmatrix} u-\alpha_0 & -\beta_1 & 0 & 0 & \cdots & 0\\ -\beta_1 & u-\alpha_1 & -\beta_2 & 0 & \cdots & 0\\ 0 & -\beta_2 & u-\alpha_2 & -\beta_3 & \cdots & 0\\ \vdots & \vdots & \vdots & \vdots & \ddots & \vdots\\ 0 & 0 & 0 & -\beta_{n-1} & u-\alpha_{n-1} & -\beta_n\\ 0 & 0 & 0 & \cdots & -\beta_n & u-\alpha_n \end{vmatrix}. \tag{106}$$

Usually, one solves (105) by first finding the zero of the determinant:

$$\tilde{Q}_K(u_k)=0 \quad\Longrightarrow\quad \omega_k=i\tau^{-1}\ln(u_k), \tag{107}$$

and then one searches for the eigenvectors [48]. Let us assume that the determinants $\tilde{Q}_{n-1}(u)$ and $\tilde{Q}_n(u)$ are known, and we wish to obtain $\tilde{Q}_{n+1}(u)$. For this purpose, we use the fact that the determinant in Eq. (106) is sparse and has only two nonzero elements in the last $(n+1)$st row, such as $-\beta_n$ and $u-\alpha_n$. This means that the Cauchy expansion theorem for determinants used to develop $\tilde{Q}_{n+1}$ in the elements of the $(n+1)$st row will yield the sum of only two determinants that are themselves the Lanczos polynomials:

$$\tilde{Q}_{n+1}(u) = (u-\alpha_n)\tilde{Q}_n(u) - \beta_n^2\tilde{Q}_{n-1}(u)\,, \tag{108}$$

$$\tilde{Q}_{-1}(u) = 0, \quad \tilde{Q}_0(u) = 1. \tag{109}$$

This recursion coincides with the definition of the Askey–Wilson polynomials [2]:

$$X_{n+1}(z) - (z-a_n)X_n(z) + b_n^2 X_{n-1}(z) = 0. \tag{110}$$

Multiplying both sides of Eq. (84) by the term $\beta_1\beta_2\cdots\beta_n$ and proceeding the same way as in deriving the recursion (57) for the state vectors $\{|\psi_n)\}$, we get the following:

$$\begin{aligned}&[(\beta_1\beta_2\cdots\beta_{n-1}\beta_n\beta_{n+1})Q_{n+1}(u)]\\ &\quad = (u-\alpha_n)[(\beta_1\beta_2\cdots\beta_{n-1}\beta_n)Q_n(u)] - \beta_n^2[(\beta_1\beta_2\cdots\beta_{n-1})Q_{n-1}(u)],\end{aligned}$$

and this will be reduced to Eq. (108) if we define

$$\tilde{Q}_n(u) \equiv \bar{\beta}_n Q_n(u), \tag{111}$$

where $\bar{\beta}_n = \beta_1\beta_2\cdots\beta_n \neq 0$, as in Eq. (57). Therefore, the determinant $\tilde{Q}_n(u)$ is also a polynomial of degree n in variable u. Recalling Eq. (67), we see that every total eigenstate $|\Upsilon_k^\infty)$ is proportional to the sum of the products of the determinant $Q_{n,k} = Q_n(u_k)$ and the Lanczos vector $|\psi_n)$. Taking into account Eqs. (107) and (111), the K eigenvalues $\{u_k\}$ of the chain of K states can equivalently be conceived as the roots of the polynomial $Q_K(u)$ of the Kth degree:

$$Q_K(u_k) = 0, \quad Q_K(u) = \frac{1}{\beta_K}[(u-\alpha_{K-1})Q_{K-1}(u) - \beta_{K-1}^2 Q_{K-2}(u)], \tag{112}$$

as in Eq. (80). This is also clear from Eq. (86) that links the matrix $\mathbf{J}_n$ with the polynomials $\{Q_n(u)\}$. The eigenvalue problem (71) will coincide exactly with Eq. (86) at $u = u_k$ and $n = K-1$ if $Q_K(u_k) = 0$, in which case the rhs of Eq. (86) is the column zero vector. Hence, the eigenvalues $\{u_k\}$ can be

found either by diagonalizing the **J**-matrix from Eq. (60), through solving the ordinary eigenvalue problem (71) with a truncation of n, or equivalently by searching for the zeros of the polynomial $Q_K(u)$, that is, finding the roots in Eq. (112). If Eq. (71) is used to obtain u_k, one would not know in advance whether the **J**-matrix (60) possesses degenerate eigenvalues $u_{k'} = u_k$ $(k' \neq k)$. However, such information can be deduced from the fact that all the eigenvalues $\{u_k\}$ from Eq. (71) are also the roots of the characteristic polynomial $Q_K(u)$. To show this, let us assume that there is, for example, one such degenerate eigenvalue. This means that the rank of the **J**-matrix $\mathrm{trid}_K[\beta, \alpha, \beta]$ of the type (60) for the specified dimension $M = K$ will automatically be reduced from K to $K-1$. Consequently, every Kth minor of $\det[u\mathbf{1} - \mathbf{U}]$, where $\mathbf{U} = c_0\mathbf{J}_K$ according to Eq. (60), will be zero, and therefore, $\tilde{Q}_{K-1}(u_k) = 0$. This also implies $Q_{K-1}(u_k) = 0$ due to Eq. (111) since $\bar{\beta}_{K-1} \neq 0$ according to Eq. (57). However, if $u = u_k$ is a root, then the secular equation would imply that $Q_K(u_k) = 0$. Therefore, using Eq. (78) we also have $Q_{K+1}(u_k) = 0$. In such cases, the recurrence (78) would mean that every element $Q_{K-m}(u)$ of the set $\{Q_{K-m}\}_{m=0}^{K}$ is zero, and therefore, $Q_0(u) = 0$ [48]. This contradicts the initialization $Q_0(u) = 1$ from Eq. (78). Hence, all the eigenvalues $\{u_k\}$ of the **J**-matrix (60) are nondegenerate ($u_{k'} \neq u_k$ for $k' \neq k$), and by implication,

$$Q_{K-1}(u_k) \neq 0. \tag{113}$$

Another line of reasoning proving Eq. (113) is as follows. Suppose that all the roots $\{u_k\}_{k=1}^{K}$ are nondegenerate, $u_{k'} \neq u_k (k' \neq k)$. This assumption is equivalent to saying that the polynomial $Q_K(u)$ has no multiple roots. In such cases, the following factorization is possible, $Q_K(u) = q_{K,0}(u - u_1)(u - u_2)\cdots(u - u_k)\cdots(u - u_K)$, where $q_{K,0}$ is the coefficient multiplying the highest power u^K in the power series representation of $Q_K(u)$. If the opposite were true, that is, if $Q_{K-1}(u_k) = 0$, then the polynomials $Q_{K-1}(u)$ and $Q_K(u)$ would have a common factor, say $(u - u_{k'})$. However, this means that the same common divisor $(u - u_{k'})$ will also be contained in $Q_{K-2}(u)$ and in $Q_{K-3}(u)$, all the way down to $Q_0(u)$ since K is any nonnegative integer. Hence, $Q_0(u) = q_{K,0}(u - u_{k'})$, which is a contradiction with $Q_0(u) = 1$ from Eq. (84). Therefore, nondegeneracy of the roots $\{u_k\}_{k=1}^{K}$ of the polynomial $Q_K(u)$ implies $Q_{K-1}(u_k) \neq 0$, as stated in Eq. (113). Conversely, the structure of the recursion (84), with its initial conditions, implies that all the roots $\{u_k\}_{k=1}^{K}$ originating from $Q_K(u_k) = 0$ are nondegenerate [47, 48].

9. POWER SERIES REPRESENTATIONS FOR TWO LANCZOS POLYNOMIALS

For many purposes, it is important to have the explicit representations of both polynomials $P_n(u)$ and $Q_n(u)$ as the finite linear combinations of the

powers of u, such as

$$P_n(u) = \sum_{r=0}^{n-1} p_{n,n-r} u^r, \quad Q_n(u) = \sum_{r=0}^{n} q_{n,n-r} u^r, \tag{114}$$

where the constants $\{p_{n,n-r}, q_{n,n-r}\}$ are the expansion coefficients. We recall that the polynomials $P_n(u)$ and $Q_n(u)$ are of degree $n-1$ and n, respectively. Obviously, with a change of the dummy index $r \longrightarrow n-r$ in Eq. (114), we could equivalently write $Q_n(u) = \sum_{r=0}^{n} q_{n,r} u^{n-r}$. Inserting Eq. (114) into Eq. (92) and then equating the multipliers of like powers of u, we obtain the following recursion [2]:

$$\beta_{n+1} p_{n+1,n+1-r} = p_{n,n+1-r} - \alpha_n p_{n,n-r} - \beta_n p_{n-1,n-1-r}, \tag{115}$$

$$p_{n,-1} = 0, \quad p_{n,m} = 0, \quad m > n, \quad p_{0,0} = 0, \quad p_{1,1} = 1. \tag{116}$$

Repeating the same procedure with Eqs. (84) and (114) will produce the recursive relation [2]:

$$\beta_{n+1} q_{n+1,n+1-r} = q_{n,n+1-r} - \alpha_n q_{n,n-r} - \beta_n q_{n-1,n-1-r}, \tag{117}$$

$$q_{n,-1} = 0, \quad q_{n,m} = 0, \quad m > n, \quad q_{0,0} = 1. \tag{118}$$

It then follows that the Lanczos expansion coefficients form a lower triangular matrix $\mathbf{q} = \{q_{i,j}\}$ with zero elements above the main diagonal [45]:

$$\mathbf{q} = \begin{pmatrix} q_{0,0} & 0 & 0 & 0 & 0 & \cdots & 0 \\ q_{1,0} & q_{1,1} & 0 & 0 & 0 & \cdots & 0 \\ q_{2,0} & q_{2,1} & q_{2,2} & 0 & 0 & \cdots & 0 \\ q_{3,0} & q_{3,1} & q_{3,2} & q_{3,3} & 0 & \cdots & 0 \\ \vdots & \vdots & \vdots & \vdots & \vdots & \ddots & \vdots \\ q_{n,0} & q_{n,1} & q_{n,2} & q_{n,3} & q_{n,4} & \cdots & q_{n,n} \end{pmatrix}. \tag{119}$$

The two leading coefficients $p_{K,1}$ and $q_{K,0}$ in the polynomials $P_K(u)$ and $Q_K(u)$ are, respectively,

$$p_{K,1} = \frac{\beta_1}{\bar{\beta}_K} = \frac{1}{\prod_{m=2}^{K} \beta_m}, \quad q_{K,0} = \frac{1}{\bar{\beta}_K} = \frac{1}{\prod_{m=1}^{K} \beta_m}, \tag{120}$$

where $\bar{\beta}_K$ is from Eq. (57). The expansion coefficients $\{q_{n,n-r}\}$ are the prediction coefficients of the LP method [38]. The ratio of the coefficients $p_{K,1}$ and $q_{K,0}$

from Eq. (120) is reduced to the parameter β_1 according to the following:

$$\frac{p_{K,1}}{q_{K,0}} = \beta_1. \tag{121}$$

An alternative way of computing the coefficients $\{p_{n,n-r}\}$ and $\{q_{n,n-r}\}$ comes from observing that the two power series representations in Eq. (114) are the truncated Maclaurin expansions. Thus,

$$p_{n,n-r} = \frac{1}{r!} P_{n,r}(0), \quad q_{n,n-r} = \frac{1}{r!} Q_{n,r}(0), \tag{122}$$

where the derivatives $Q_{n,r}(u)$ and $P_{n,r}(u)$ are defined in Eqs. (95) and (101), respectively. The two polynomials from Eq. (114) can now be written as:

$$P_n(u) = \sum_{r=0}^{n-1} \frac{1}{r!} P_{n,r}(0) u^r, \quad Q_n(u) = \sum_{r=0}^{n} \frac{1}{r!} Q_{n,r}(0) u^r, \tag{123}$$

where $P_0(u) \equiv 0$ as in (92).

10. ROOTING HIGH-DEGREE POLYNOMIALS

10.1. Improved Newton–Raphson algorithm with approximate allowance of higher order derivatives

The Lanczos polynomial of the first kind $Q_K(u)$ with its K zeros $\{u_k\}_{k=1}^K$ can be expressed as:

$$Q_K(u) = \frac{1}{\bar{\beta}_K} \prod_{k=1}^{K} (u - u_k), \tag{124}$$

where $1/\bar{\beta}_K = q_{K,0}$ from Eq. (120) is the leading coefficient in the power series representation (114) of the polynomial $Q_K(u)$. One of the ways to find the zeros $\{u_k\}$ of the polynomial $Q_K(u)$ is to use the Newton–Raphson algorithm [45]. This is a nonlinear iterative method that, as such, needs the starting values $\{u_{k,0}\}$ that can be chosen, for example, randomly on the unit circle but never on the real axis [2]. In other words, the initial guess should be a complex number $\mathrm{Im}(u_{k,0}) \neq 0$. Then, the successively better approximations $\{u_{k,n+1}\}(n = 0, 1, 2, \ldots)$ for the kth root of the equation $Q_K(u_k) = 0$ are

constructed from the iteration formula:

$$u_{k,n+1} = u_{k,n} - v_k, \quad v_k = \frac{Q_K(u_{k,n})}{Q'_K(u_{k,n})} \quad (n = 0, 1, 2, \ldots), \tag{125}$$

where the first derivative $Q'_K(u)$ is computed exactly from Eq. (97) for $m = 1$ at $u = u_{k,n}$:

$$\beta_K Q'_K(u) = (u - \alpha_{K-1}) Q'_{K-1}(u) - \beta_{K-1} Q'_{K-2}(u) + Q_{K-1}(u), \tag{126}$$

$$Q'_m(u) = 0, \quad Q_0(u) = 1, \tag{127}$$

where $m = -1$ and $m = 0$. Given a prescribed accuracy threshold $\xi > 0$, the value $u_{k,n}$, as the approximation of the kth root at the nth iteration, will be satisfactory if either $Q_K(u_{k,n}) \approx 0$ or $|u_{k,n+1} - u_{k,n}| < \xi$. If neither of the two latter conditions is fulfilled after, for example, some 100 iterations or so, the process is considered diverging from the exact root u_k. In such cases, a new initial value for $u_{k,0}$ is selected, and the procedure is repeated [2]. When convergence is reached at a given iteration $n = m$, the sought root u_k is set to be $u_k \equiv u_{k,m}$. The Newton–Raphson method has a quadratic convergence rate, as can be seen from the development of the rhs of Eq. (125) in a power series in terms of $u_k^{(n)} - u_k$ [2, 45]:

$$u_k^{(n+1)} - u_k^{(n)} = a_{2,k}[u_k^{(n)} - u_k]^2 + a_{3,k}[u_k^{(n)} - u_k]^3 + \cdots + a_{m,k}[u_k^{(n)} - u_k]^m + \cdots, \tag{128}$$

where the expansion coefficients $\{a_{m,k}\}$ depend only on the root u_k. Due to the absence of the linear term $a_{1,k}[u_k^{(n)} - u_k]$ on the rhs of Eq. (128), it is clear that from a certain point on, the error $u_k^{(n+1)} - u_k^{(n)}$ will be of the order of the magnitude of the square of the preceding error $u_k^{(n)} - u_k^{(n-1)}$. Once this step has been reached, every further iteration will approximately double the number of correct decimal places relative to the previously achieved approximation. Hence, the name "quadratic convergence" [2, 45]. To mimic the higher order derivatives that are absent from Eq. (125), we found in practice that the following modification of the Newton–Raphson algorithm is very useful for obtaining complex roots of any function, including our characteristic equation $Q_K(u_k) = 0$ [53]:

$$u_{k,n+1} = u_{k,n} - v_k \left\{ \frac{Q_K(u_{k,n} - v_k) - Q_K(u_{k,n})}{2Q_K(u_{k,n} - v_k) - Q_K(u_{k,n})} \right\}, \tag{129}$$

which differs from Eq. (125) by the presence of the rational function in the curly brackets multiplying the Newton quotient $v_k = Q_K(u_{k,n})/Q'_K(u_{k,n})$.

In practice, we observed that the method in Eq. (129) converges quickly and consistently to at least eight decimal places in less than 10 iterations [53].

10.2. Diagonalization of the Hessenberg or companion matrix

In general, rooting a higher degree polynomial, say $K \geq 100$, is known to be an ill-conditioned nonlinear problem. Therefore, for high degrees K, it is better to solve Eq. (80) by more robust methods of linear algebra. One such method is diagonalization of the corresponding $K \times K$ square Hessenberg matrix (also known as the companion matrix) denoted by $\tilde{\mathbf{H}}$, which is defined by [45]:

$$\tilde{\mathbf{H}} = \begin{pmatrix} -\frac{q_{K,1}}{q_{K,0}} & -\frac{q_{K,2}}{q_{K,0}} & \cdots & -\frac{q_{K,K-1}}{q_{K,0}} & -\frac{q_{K,K}}{q_{K,0}} \\ 1 & 0 & \cdots & 0 & 0 \\ 0 & 1 & \cdots & 0 & 0 \\ \vdots & \vdots & \vdots & \vdots & \vdots \\ 0 & 0 & \cdots & 1 & 0 \end{pmatrix}, \tag{130}$$

$$Q_K(u) = \frac{\det[u\mathbf{1} - \tilde{\mathbf{H}}]}{\bar{\beta}_K}. \tag{131}$$

Note that Eq. (131) is equivalent to Eq. (104) on account of Eq. (120). When all the roots $\{u_k\}_{k=1}^K$ are found, a simple analytical expression for $Q'_K(u_k)$ can also be obtained. Using Eq. (124), we obtain the following:

$$Q'_K(u) = \frac{1}{\bar{\beta}_K} \sum_{k''=1}^{K} \left\{ \prod_{k'=1(k' \neq k'')}^{K} (u - u_{k'}) \right\}. \tag{132}$$

Here, exactly at $u = u_k$, the whole product in the curly brackets vanishes due to the presence of the factor $(u - u_k)|_{u \to u_k}$, so that [2]:

$$Q'_K(u_k) = \frac{1}{\bar{\beta}_K} \prod_{k'=1(k' \neq k)}^{K} (u_k - u_{k'}), \tag{133}$$

$$Q'_K(u_k) \neq 0, \quad u_{k'} \neq u_k, \quad k' \neq k. \tag{134}$$

Due to its remarkable sparseness, the matrix $\tilde{\mathbf{H}}$ from Eq. (130) is easy to diagonalize even for higher dimensions. In this way, we have explicitly obtained very accurate eigenvalues $\{u_k\}_{k=1}^K$ for $K \sim 1000$ [38, 39] via the NAG library [50]. However, the same library fails when we used its corresponding routine in an attempt to directly root polynomials of much lower degrees, $K \geq 120$.

11. THE LANCZOS VECTOR SPACE

11.1. The space structure via the scalar product as the generalized Stieltjes integral

In Section 5, we have introduced the finite-dimensional Lanczos subspace $\mathcal{L}_M \subset \mathcal{H}$ spanned by the Lanczos state vectors $\{|\psi_n)\}_{n=0}^{M-1}$ via:

$$\mathcal{L}_M = \text{span}\{|\psi_0), |\psi_1), |\psi_2), \ldots, |\psi_{M-1})\}. \tag{135}$$

The Lanczos vector space $\mathcal{L}_M$ can be defined through its basis and the appropriate scalar product. A finite sequence of the Lanczos orthogonal polynomials of the first kind is complete, as will be shown in Section 12, and therefore, the set $\{Q_n(u)\}$ with K elements represents a basis. Thus, the polynomial set $\{Q_n(u)\}_{n=0}^{K}$ will be our fixed choice for the basis in $\mathcal{L}_K$. Of particular importance is the set $\mathcal{K}$ of the zeros $\{u_k\}_{k=1}^{K}$ of the Kth degree characteristic polynomial $Q_K(u)$:

$$\mathcal{K} \equiv \{u_k\}_{k=1}^{K}, \quad Q_K(u_k) = 0. \tag{136}$$

These zeros $\{u_k\}$ of $Q_K(u)$ coincide with the eigenvalues of both the evolution matrix $\mathbf{U}$ and the corresponding Hessenberg matrix $\tilde{\mathbf{H}}$ from Eqs. (131) and (130), respectively. The zeros of $Q_K(u)$ are called eigenzeros. The structure of $\mathcal{L}_M$ is determined by its scalar product for analytic functions of complex variable z or u. For any two regular functions $f(u)$ and $g(u)$ from $\mathcal{L}_M$, the scalar product in $\mathcal{L}_M$ is defined by the generalized Stieltjes integral:

$$(f(u)|g(u)) = (g(u)|f(u)) = \frac{1}{2\pi i} \oint_C f(z)g(z)\mathrm{d}\sigma_0(z); \quad f, g \in \mathcal{L}_M, \tag{137}$$

which is symmetric, that is, without conjugation of the soft "bra" vector $(f(u)|$. Here, $\mathrm{d}\sigma_0(z)$ is a general, complex valued Lebesgue measure and the closed contour C encircles counterclockwise the eigenvalue set $\mathcal{K}$. Since the polynomials $\{Q_n(u)\}$ have no multiple zeros, all the spectral representations of functions in $\mathcal{L}_M$ will exhibit only simple poles.

11.2. The passage from the Stieltjes to the Cauchy integral via the Dirac-Lebesgue measure for discretization of inner products

Hereafter, the generalized Lebesgue measure $\sigma_0(z)$ from Eq. (137) is specified as:

$$\sigma_0(z) = \sum_{k=1}^{K} d_k \vartheta(z - u_k), \quad \vartheta(z - u_k) = \begin{cases} 1 & z \in \mathcal{K} \\ 0 & z \notin \mathcal{K} \end{cases} \tag{138}$$

where d_k is the residue (15) and $\vartheta(z-u_k)$ is the generalized real-valued Heaviside function of the complex argument $z-u_k$, which is a generalization of the real case (138). Using the formula for the derivative $\mathrm{d}\vartheta(z)/\mathrm{d}z=\delta(z)$, where $\delta(z)$ is the complex-valued Dirac function, we have the following expression for the measure in $\mathcal{L}_M$:

$$\mathrm{d}\sigma_0(z)=\rho_0(z)\mathrm{d}z, \quad \rho_0(z)=\sum_{k=1}^{K} d_k\delta(z-u_k). \tag{139}$$

The generalized Dirac function of a complex variable from Eq. (139) belongs to the class of the so-called ultra distributions [2]. In the present context, $\delta(z-u_k)$ has the same operational property as the usual Dirac function with a real argument, except that the contour integrals are involved, viz:

$$\oint_C \mathrm{d}z f(z)\delta(z-u_k)=f(u_k), \tag{140}$$

where the function $f(z)$ of complex variable z is analytic throughout the same contour C as in Eq. (137). More generally, if $f(z)$ is regular within and on the contour C and $g(z)$ has K simple zeros $\{v_k\}_{k=1}^{K}$ within C, we can apply the Cauchy residue theorem to write:

$$\oint_C \mathrm{d}z f(z)\delta(g(z))=\sum_{k=1}^{K}\frac{f(v_k)}{g'(v_k)}, \tag{141}$$

where $g'(z)=(\mathrm{d}/\mathrm{d}z)g(z)$ and $g(v_k)=0$ $(1\le k\le K)$. The weight function $\rho_0(z)$ from Eq. (139) is reminiscent of the so-called "complex impulse train function" in signal processing [2]. If one formally sets the eigenvalues $\{\omega_k\}$ of the operator $\widehat{\Omega}$ to be equal to the Fourier grid points $\{\tilde{\omega}_k\}$, one would equate the residues $\{d_k\}$ with the complex Fourier amplitude $\{F_k\}$. Both $\{\tilde{\omega}_k\}$ and $\{F_k\}$ are given in Eq. (33). In such cases, the special impulse train function $\sum_k F_k\delta(\omega-\tilde{\omega}_k)$ would represent the Fourier stick spectrum with jumps or heights $|F_k|$ at the grid points $\omega=\tilde{\omega}_k$ and would otherwise be zero elsewhere. In Eq. (139), the quantities $\{|d_k|\}$ also have the meaning of heights or jumps in the spectrum (51) constructed from the peak parameters $\{u_k, d_k\}$. The discrete counterpart of the symmetric inner product (137) for the pair $\{f(u), g(u)\}\in\mathcal{L}_M$ is given by:

$$(f(u)|g(u))=(g(u)|f(u))=\sum_{k=1}^{K} d_k f(u_k)g(u_k), \tag{142}$$

where the residue $d_k=(\Phi_0|\Upsilon_k)^2$ from the definition (15) is a complex-valued weight function.

12. COMPLETENESS OF THE LANCZOS POLYNOMIALS

In practice, the complete state vector $|\Upsilon_k^{\infty})$ is computed from the infinite sum over n in Eq. (67) by monitoring convergence of the corresponding sequence of partial sums $\sum_{n=0}^{M-1} Q_{n,k}|\psi_n)$ with the progressively increasing integer M. For a fixed large integer M, the total state vector (82) is approximated by its finite chain counterpart $|\Upsilon^{\infty}(u)) \approx |\Upsilon^{M}(u))$:

$$|\Upsilon^{M}(u)) = \sum_{n=0}^{M-1} Q_n(u)|\psi_n). \tag{143}$$

At the eigenvalues $u = u_k$, we have the wave function $|\Upsilon_k^M)$ whose corresponding residue d_k^M is an approximation to d_k^{∞} from Eq. (81) such that $d_k^{\infty} \approx d_k^M$ for large M, where:

$$d_k^M = \frac{c_0}{\sum\limits_{n=0}^{M} Q_{n,k}^2}. \tag{144}$$

The numerator of the quotient in this equation is the norm of the state vector $|\Upsilon_k^M)$, and therefore,

$$\|\Upsilon_k^M\|^2 = (\Upsilon_k^M|\Upsilon_k^M) = c_0 \sum_{n=0}^{M-1} Q_{n,k}^2 \quad \Longrightarrow \quad d_k^M = \frac{c_0^2}{\|\Upsilon_k^M\|^2}. \tag{145}$$

The finite sum in the denominator of Eq. (144) can be evaluated analytically for any finite integer M. Moreover, we shall show that a more general expression of the type $\sum_{n=0}^{M-1} P_n(u)Q_n(u')$ can be derived algebraically in a closed form. In this regard, we first write the two recursions (84) and (92) at two arbitrary values of the variables u and u' as:

$$\beta_n P_n(u) = (u - \alpha_{n-1})P_{n-1}(u) - \beta_{n-1}P_{n-2}(u), \tag{146}$$

$$P_0(u) = 0, \quad P_1(u) = 1, \tag{147}$$

$$\beta_n Q_n(u') = (u' - \alpha_{n-1})Q_{n-1}(u') - \beta_{n-1}Q_{n-2}(u'), \tag{148}$$

$$Q_{-1}(u') = 0, \quad Q_0(u') = 1. \tag{149}$$

Multiplying Eqs. (146 and 148) by $Q_{n-1}(u')$ and $P_{n-1}(u)$, respectively, and subtracting the results from each other, we obtain:

$$\begin{aligned} P_{n-1}(u)Q_{n-1}(u') = \beta_n \frac{P_n(u)Q_{n-1}(u') - P_{n-1}(u)Q_n(u')}{u - u'}, \\ - \beta_{n-1} \frac{P_{n-1}(u)Q_{n-2}(u') - P_{n-2}(u)Q_{n-1}(u')}{u - u'}. \end{aligned} \tag{150}$$

Summing up over n will give:

$$\sum_{n=0}^{M-1} P_n(u)Q_n(u') = \beta_M \frac{P_M(u)Q_{M-1}(u') - P_{M-1}(u)Q_M(u')}{u-u'}. \tag{151}$$

This is called the extended Christoffel–Darboux formula for the sum of the products of the Lanczos polynomials of the first and second kind, $Q_n(u)$ and $P_n(u)$, respectively. Of course, the sum in Eq. (151) could start from $n=1$ due to $P_0(u)=0$, but this is not done to allow the possibility to replace $P_n(u)$ by $Q_n(u)$ in the sequel. When P_n is used instead of Q_n, the result (151) is reduced to:

$$\sum_{n=0}^{M-1} Q_n(u)Q_n(u') = \beta_M \frac{Q_M(u)Q_{M-1}(u') - Q_{M-1}(u)Q_M(u')}{u-u'}. \tag{152}$$

This is the original Christoffel–Darboux formula that includes only the polynomials of the first kind [47, 48]. The formula (151) with mixed polynomials P_n and Q_m has no meaning at $u'=u$. However, this is not so in the case of Eq. (152), which is well defined in the limit $u \longrightarrow u'$. The indeterminate expression $0/0$ is regularized by the l'Hôpital rule which gives:

$$\sum_{n=0}^{M-1} Q_n^2(u) = \beta_M [Q'_M(u)Q_{M-1}(u) - Q'_{M-1}(u)Q_M(u)], \tag{153}$$

where $Q'_n(u) = \mathrm{d}Q_n(u)/\mathrm{d}u$. Setting here $u=u_k$ and inserting the resulting expression for the term $\sum_{n=0}^{M-1} Q_n^2(u_k)$ into Eq. (144) for the residue d_k^M in the case of the finite chain of any fixed length M, we have:

$$d_k^M = \frac{c_0}{\beta_M} \frac{1}{Q'_M(u_k)Q_{M-1}(u_k) - Q'_{M-1}(u_k)Q_M(u_k)}. \tag{154}$$

Let us now set $M=K$, where K is the number of the roots $\{u_k\}_{k=1}^K$ of $Q_K(u)$. In such a case, taking u as the eigenvalue u_k and using $Q_K(u_k)=0$ from Eq. (112), we simplify Eq. (153) as:

$$\sum_{n=0}^{K-1} Q_n^2(u_k) = \beta_K Q'_K(u_k)Q_{K-1}(u_k). \tag{155}$$

This reduces (154) to the Christoffel formula for the Gauss numerical integration/quadrature [45]:

$$d_k = \frac{c_0}{\beta_K} \frac{1}{Q'_K(u_k)Q_{K-1}(u_k)}, \quad d_k \equiv d_k^K, \tag{156}$$

where $Q_{K-1}(u_k) \neq 0$, as per Eq. (113). If the norm of the state vector $|\Upsilon_k^K)$:

$$\|\Upsilon_k\|^2 = (\Upsilon_k|\Upsilon_k) = c_0 \sum_{n=0}^{K-1} Q_{n,k}^2, \quad |\Upsilon_k) \equiv |\Upsilon_k^K), \tag{157}$$

is substituted into Eqs. (155) and (156), then:

$$d_k = \frac{c_0^2}{\|\Upsilon_k\|^2}. \tag{158}$$

At $u = u_k$, we abbreviate $|\Upsilon_k) \equiv |\Upsilon_k^K)$ and write the expansion (143) for $M = K$ as:

$$|\Upsilon_k) = \sum_{n=0}^{K-1} Q_{n,k}|\psi_n). \tag{159}$$

The result (156) should be contrasted to the usual applications of the Lanczos algorithm, in which the residue d_k is computed numerically from the defining relation $d_k = (\Phi_0|\Upsilon_k^+)^2$ as in Eq. (72) via squaring the overlap between the initial state $|\Phi_0)$ and an approximate total wave function $|\Upsilon_k^+)$. Taking u and u' as the eigenvalues $u = u_k$ and $u' = u_{k'}$, the results (152) and (153) become:

$$\sum_{n=0}^{K-1} Q_n(u_k)Q_n(u_{k'}) = \beta_K \frac{Q_K(u_k)Q_{K-1}(u_{k'}) - Q_{K-1}(u_k)Q_K(u_{k'})}{u_k - u_{k'}}, \tag{160}$$

$$\sum_{n=0}^{K-1} Q_n^2(u_k) = \beta_K [Q_K'(u_k)Q_{K-1}(u_k) - Q_{K-1}'(u_k)Q_K(u_k)]. \tag{161}$$

The use of the characteristic equation $Q_K(u_k) = 0 = Q_K(u_{k'})$ in Eqs. (160) and (161) will give:

$$\begin{aligned} &\sum_{n=0}^{K-1} Q_n(u_k)Q_n(u_{k'}) = 0, \quad k' \neq k, \\ &\sum_{n=0}^{K-1} Q_n^2(u_k) = \beta_K Q_K'(u_k)Q_{K-1}(u_k), \quad k' = k. \end{aligned} \tag{162}$$

With the help of the Kronecker δ-symbol $\delta_{k,k'}$, the two separate results from Eq. (162) for $k' \neq k$ and $k' = k$ can be combined into a single equation as:

$$\sum_{n=0}^{K-1} Q_n(u_k)Q_n(u_{k'}) = c_0 \frac{\delta_{k,k'}}{d_k}. \tag{163}$$

In Eq. (162), the result (156) is used to identify the residue d_k. Note that the upper limit $K-1$ in Eq. (163) could be replaced by K on account of the characteristic equation $Q_K(u_k)=0$. The expression (163) represents the local completeness relation or closure for the Lanczos polynomial $\{Q_n(u_k)\}$.

Next, we are interested in considering the weighted products $d_k Q_n(u_k) Q_m(u_k)$ summed over all the eigenvalues $\{u_k\}_{k=1}^K$ for two arbitrary degrees n and m:

$$I_{n,m} \equiv \sum_{k=1}^{K} d_k Q_n(u_k) Q_m(u_k). \tag{164}$$

Here, the sum over k can be carried out with the following result

$$I_{n,m} = c_0 \delta_{n,m}. \tag{165}$$

Using Eq. (142), we see that the integral $I_{n,m}$ coincides with the scalar product $(Q_m(u)|Q_n(u))$:

$$(Q_m(u)|Q_n(u)) = \sum_{k=1}^{K} d_k Q_n(u_k) Q_m(u_k) = c_0 \delta_{n,m}. \tag{166}$$

This is the orthogonality relation of the two Lanczos polynomials $Q_n(u)$ and $Q_m(u)$ with the weight function, which is the residue d_k [48]. We recall that the sequence $\{Q_{n,k}\} \equiv \{Q_n(u_k)\}$ coincides with the set of eigenvectors of the Jacobi matrix (60).

Given the inner product (142), the two polynomials $Q_n(u)$ and $Q_m(u)$ from the set $\{Q_v(u)\}$ are said to be orthogonal to each other with respect to the complex weight d_k. Since the set $\{Q_n(u)\}$ is complete, every function $f(u) \in \mathcal{L}_M$ can be expanded in a series in terms of $\{Q_n(u)\}$:

$$f(u) = \sum_{n=0}^{\infty} \gamma_n Q_n(u), \tag{167}$$

where the expansion coefficients $\{\gamma_n\}$ is given by

$$\gamma_n = \frac{(f(u)|Q_n(u))}{c_0}. \tag{168}$$

Thus, we have proven that the eigenvectors $\mathbf{Q}_k = \{Q_{n,k}\}$ of the **J**-matrix (60) form an orthonormal complete set of vectors and hence represent a basis set. We emphasize that orthonormality is a matter of convenience, but completeness is essential both in theory and in practice [57].

13. DUAL LANCZOS REPRESENTATION VIA STATE VECTORS AND SECULAR POLYNOMIALS

13.1. Matrix elements of the evolution operator in terms of the Lanczos states

Besides the signal points $\{c_n\}$, the key ingredients of spectral analysis are the Lanczos coupling constants $\{\alpha_n, \beta_n\}$. They are defined in terms of the elements of the basis set $\{|\psi_n)\}$ of the Lanczos state vectors, as stated in Eq. (54). The common matrix element from Eq. (54) is of the following type:

$$\mathrm{L}_{n,m}^{(s)} \equiv (\psi_m|\widehat{\mathrm{U}}^s|\psi_n), \tag{169}$$

where the evolution operator $\widehat{\mathrm{U}}$ is raised to power s which can be any integer.

13.2. Matrix elements of the evolution operator in terms of the Lanczos polynomials

We can eliminate $\widehat{\mathrm{U}}^s(\tau)$ from Eq. (169) by using the closure (8) for the normalized full state vectors $\{|\Upsilon_k)/\|\Upsilon_k\|\}$ together with the eigenproblem $\widehat{\mathrm{U}}^s|\Upsilon_k) = u_k^s|\Upsilon_k)$ that comes from Eq. (38):

$$\mathrm{L}_{n,m}^{(s)} = \frac{1}{c_0^2}\sum_{k=1}^{K} d_k u_k^s (\psi_m|\Upsilon_k)(\Upsilon_k|\psi_n), \tag{170}$$

where Eq. (158) is utilized. Inserting the expansion (159) into Eq. (170) and using Eq. (59) will give:

$$\mathrm{L}_{n,m}^{(s)} \equiv (\psi_m|\widehat{\mathrm{U}}^s|\psi_n) = (Q_m(u)|u^s|Q_n(u)), \tag{171}$$

where the definition (142) of the scalar product in the Lanczos space $\mathcal{L}_K$ is used. With the result (171) at hand, the couplings $\{\alpha_n, \beta_n\}$ from Eq. (54) can be equivalently written as:

$$\alpha_n = \frac{(Q_n(u)|u|Q_n(u))}{(Q_n(u)|Q_n(u))}, \quad \beta_n = \frac{(Q_{n-1}(u)|u|Q_n(u))}{(Q_{n-1}(u)|Q_{n-1}(u))}. \tag{172}$$

The significance of this finding is in establishing the Lanczos dual representation $\{|\psi_n), Q_n(u)\}$ that enables the following equivalent definitions:

$$\begin{aligned} \alpha_n &= \frac{(\psi_n|\widehat{\mathrm{U}}|\psi_n)}{(\psi_n|\psi_n)} = \frac{(Q_n(u)|u|Q_n(u))}{(Q_n(u)|Q_n(u))}, \\ \beta_n &= \frac{(\psi_{n-1}|\widehat{\mathrm{U}}|\psi_n)}{(\psi_{n-1}|\psi_{n-1})} = \frac{(Q_{n-1}(u)|u|Q_n(u))}{(Q_{n-1}(u)|Q_{n-1}(u))}. \end{aligned} \tag{173}$$

This duality enables switching from the work with the Lanczos state vectors $\{|\psi_n)\}$ to the analysis with the Lanczos polynomials $\{Q_n(u)\}$. A change from one representation to the other is readily accomplished along the lines indicated in this section, together with the basic relations from Sections 11 and 12, in particular, the definition (142) of the inner product in the Lanczos space $\mathcal{L}_K$, the completeness (163) and orthogonality (166) of the polynomial basis $\{Q_{n,k}\}$.

14. CLOSED EXPRESSION FOR THE KRYLOV–SCHRÖDINGER OVERLAP DETERMINANT

We carried out an explicit calculation of the first few determinants $\{\det \mathbf{S}_n\} = \{\mathrm{H}_n(c_0)\}$ from (46) and deduced the most general result for any n as follows:

$$\mathrm{H}_n(c_0) \equiv \det \mathbf{S}_n = c_0^n \beta_1^{2n-2} \beta_2^{2n-4} \beta_3^{2n-6} \cdots \beta_{n-1}^2 = c_0^n \prod_{m=1}^{n-1} \beta_m^{2n-2m}, \tag{174}$$

$$= \frac{c_0^n}{q_{1,0}^2 q_{2,0}^2 q_{3,0}^2 \cdots q_{n-1,0}^2} = \frac{c_0^n}{\prod_{m=1}^{n-1} q_{m,0}^2}. \tag{175}$$

This finding, which was mentioned in Section 4, exhibits a remarkably regular factorability of the general result for $\mathrm{H}_n(c_0)$ as a direct consequence of a judicious combination of symmetry of the Hankel determinant (46) and the Lanczos orthogonal polynomials. Thus, given either the set $\{\beta_\nu\}$ or $\{q_{\nu,0}\}$, the Hankel determinant $\mathrm{H}_n(c_0)$ or equivalently the overlap determinant $\det \mathbf{S}_n$ in the Schrödinger or Krylov basis $\{|\Phi_n)\}$ can be constructed at once from Eq. (175). This is very useful in practical computations.

15. EXPLICIT SOLUTION OF THE LANCZOS ALGORITHM

Inspecting the explicit expressions for the first few Lanczos polynomials, we deduced the following expression for the general degree n:

$$\tilde{Q}_n(u) = \frac{(-1)^n}{c_0^n \prod_{m=1}^{n} \beta_m^{2n-2m}} \begin{vmatrix} 1 & u & u^2 & \cdots & u^n \\ c_0 & c_1 & c_2 & \cdots & c_n \\ c_1 & c_2 & c_3 & \cdots & c_{n+1} \\ c_2 & c_3 & c_4 & \cdots & c_{n+2} \\ \vdots & \vdots & \vdots & \ddots & \vdots \\ c_{n-1} & c_n & c_{n+1} & \cdots & c_{2n-1} \end{vmatrix}, \tag{176}$$

where $\tilde{Q}_n(u) = \bar{\beta}_n Q_n(u)$, as in (111). The part $\prod_{m=1}^{n} \beta_m^{2n-2m}$ of the multiplying coefficient in (176) can equivalently be written as $\prod_{m=1}^{n} q_{m,0}^2$, via $\prod_{m=1}^{n} \beta_m^{2n-2m} = \prod_{m=1}^{n} q_{m,0}^2$, which was also used in (175). The result (176) represents the explicit orthonormalization of the polynomial sequence $\{Q_n(u)\}$. This is the explicit Lanczos algorithm, as opposed to the recursive relation (84). The expressions (53), (84), and (92) relate to the implicit Lanczos algorithms since the solution to the problem is not immediately available, but it is attainable through recursions. Extending the Cayley–Hamilton theorem to encompass determinants with a mixed structure of scalars and operators/matrices as elements, we can immediately generalize (176) to $\tilde{Q}_n(\widehat{\mathbf{U}})$ or $\tilde{Q}_n(\mathbf{U})$ through the replacement of the 1st raw $\{1 \; u \; u^2 \; \dots \; u^n\}$ in $\tilde{Q}_n(u)$ by $\{\hat{1} \; \hat{\mathbf{U}} \; \hat{\mathbf{U}}^2 \; \dots \; \hat{\mathbf{U}}^n\}$ or $\{\mathbf{1} \; \mathbf{U} \; \mathbf{U}^2 \; \cdots \; \mathbf{U}^n\}$, respectively, for instance:

$$\tilde{Q}_n(\widehat{\mathbf{U}}) = \frac{(-1)^n}{c_0^n \prod_{m=1}^{n} \beta_m^{2n-2m}} \begin{vmatrix} \hat{1} & \widehat{\mathbf{U}} & \widehat{\mathbf{U}}^2 & \cdots & \widehat{\mathbf{U}}^n \\ c_0 & c_1 & c_2 & \cdots & c_n \\ c_1 & c_2 & c_3 & \cdots & c_{n+1} \\ c_2 & c_3 & c_4 & \cdots & c_{n+2} \\ \vdots & \vdots & \vdots & \ddots & \vdots \\ c_{n-1} & c_n & c_{n+1} & \cdots & c_{2n-1} \end{vmatrix}. \tag{177}$$

Further, regarding $\{|\psi_n)\}$, it is also possible to have the explicit Lanczos algorithm by deriving the expression that holds the whole result with no recourse to recurrence relations. For example, applying the explicit Lanczos polynomial operator $Q_n(\widehat{\mathbf{U}})$ from Eq. (177) to $|\psi_0) = |\Phi_0)$ will generate the wave packet $|\psi_n)$ according to $|\psi_n) = Q_n(\widehat{\mathbf{U}})|\psi_0)$ as in Eq. (91). Therefore, the final result is the following expression for the explicit Lanczos states $\{|\psi_n)\}$:

$$|\tilde{\psi}_n) = \frac{(-1)^n}{c_0^n \prod_{m=1}^{n} \beta_m^{2n-2m}} \begin{vmatrix} |\Phi_0) & |\Phi_1) & |\Phi_2) & \cdots & |\Phi_n) \\ c_0 & c_1 & c_2 & \cdots & c_n \\ c_1 & c_2 & c_3 & \cdots & c_{n+1} \\ c_2 & c_3 & c_4 & \cdots & c_{n+2} \\ \vdots & \vdots & \vdots & \ddots & \vdots \\ c_{n-1} & c_n & c_{n+1} & \cdots & c_{2n-1} \end{vmatrix}, \tag{178}$$

where $|\tilde{\psi}_n) = \bar{\beta}_n |\psi_n)$, as in Eq. (57). This expression for the explicit Lanczos orthogonalization of the Schrödinger state vectors $\{|\Phi_n)\}$ coincides with the result obtained by the Gram–Schmidt orthogonalization [2, 53]. Using Eq. (178), it is readily shown that:

$$(\Phi_0|\psi_n) = 0, \tag{179}$$

where $n \geq 1$, in agreement with the orthogonality condition (59) recalling that $|\Phi_0) = |\psi_0)$.

16. EXPLICIT LANCZOS WAVE PACKET PROPAGATION

Given the initial state $|\Phi_0)$ of a system at time $t = 0$, the Schrödinger state $|\Phi_n)$ at a later time $n\tau$ is obtained by propagation via the evolution operator $\widehat{\mathrm{U}}(\tau)$, such that $|\Phi_n) = \widehat{\mathrm{U}}^n(\tau)|\Phi_0)$, as in Eq. (36). To get the spectrum of $\widehat{\mathrm{U}}(\tau)$, diagonalization techniques could be used with the Schrödinger basis set $\{|\Phi_n)\}$. Such a basis is delocalized, causing matrices to be full, and this enhances the ill-conditioning of the problem. One of the ways to counteract this is to switch to a localized basis set given by the Fourier sum of $\{|\Phi_n)\}$ as done, for example, in the filter diagonalization (FD) method [40, 42]. The result of this change of the basis is a modification of the Schrödinger matrix $\mathbf{U}$, which then becomes diagonally dominated and hence of significantly reduced ill-conditioning [42, 47]. Another way to obtain sparse diagonalizing matrices is provided by switching from $\{|\Phi_n)\}$ to the Lanczos basis set $\{|\psi_n)\}$ in which the vectors $\{|\psi_n)\}$ are implicitly generated via the recursion (53). The resulting evolution matrix $\mathbf{U}(\tau)$ is tridiagonal, as in (60). We see from the definition (53) that each state vector $|\psi_n)$ is a result of repeated applications of $\widehat{\mathrm{U}}(\tau)$ onto the initial wave packet $|\psi_0) = |\Phi_0)$. This is expected to yield an expression in which the general vector $|\psi_n)$ is given by a linear combination of Schrödinger states $|\Phi_n) = \widehat{\mathrm{U}}^n(\tau)|\Phi_0)$. Such a feature can be well analyzed within, for example, the concept of a polynomial Lanczos propagation of wave packets $\{|\psi_n)\}$ from the initial state vector $|\psi_0) = |\Phi_0)$ via, $|\psi_n) = Q_n(\widehat{\mathrm{U}})|\psi_0)$, as in Eq. (91). This equation defines the Lanczos polynomial propagation of the initial wave packet $|\Phi_0)$. Here, $Q_n(\widehat{\mathrm{U}})$ is the Lanczos operator polynomial defined by the recursion (89) that results from applying the Cayley–Hamilton theorem to Eq. (84). Of course, the same theorem can also be applied to power series representation (114) giving:

$$Q_n(\widehat{\mathrm{U}}) = \sum_{r=0}^{n} q_{n,n-r}\widehat{\mathrm{U}}^r, \tag{180}$$

where the coefficients $\{q_{n,n-r}\}$ are given recursively in Eq. (117). Inserting the finite sum (180) into Eq. (91) and using Eq. (36), we derive immediately the following result:

$$|\psi_n) = \sum_{r=0}^{n} q_{n,n-r}|\Phi_r). \tag{181}$$

Hence, as expected, the general Lanczos state $|\psi_n)$ is indeed a linear combination of the Schrödinger states $\{|\Phi_r)\}$. The availability of the explicit formula (181) for any state vector $|\psi_n)$ also permits deriving the explicit expressions for the coupling constants $\{\alpha_n, \beta_n\}$. Thus, inserting Eq. (181) into Eq. (54), we have:

$$\alpha_n = \frac{1}{c_0} \sum_{r=0}^{n} \sum_{r'=0}^{n} q_{n,n-r} q_{n,n-r'} c_{r+r'+1},$$
$$\beta_n = \frac{1}{c_0} \sum_{r=0}^{n} \sum_{r'=0}^{n-1} q_{n,n-r} q_{n-1,n-r'-1} c_{r+r'+1}. \tag{182}$$

This can be considerably simplified according to:

$$\alpha_n = \frac{1}{c_0} \sum_{m=0}^{2n} a_{n,m} c_{m+1}, \quad \beta_n = \frac{1}{c_0} \sum_{m=0}^{2n-1} b_{n,m} c_{m+1},$$
$$a_{n,m} = \sum_{r=r_1^a}^{r_2} q_{n,n-r} q_{n,n-m+r}, \quad b_{n,m} = \sum_{r=r_1^b}^{r_2} q_{n,n-r} q_{n-1,n-1-m+r},$$
$$r_1^a = \max\{0, m-n\}, \quad r_1^b = \max\{0, m-n+1\}, \quad r_2 = \min\{n, m\}. \tag{183}$$

We have checked through the several first terms that these formulae yield the correct results for the Lanczos parameters α_n and β_n.

17. MAPPING FROM MONOMIALS u^n TO THE LANZOS POLYNOMIALS $Q_n(u)$

The orthogonal characteristic polynomials or eigenpolynomials $\{Q_n(u)\}$ play one of the central roles in spectral analysis since they form a basis due to the completeness relation (163). They can be computed either via the Lanczos recursion (84) or from the power series representation (114). The latter method generates the expansion coefficients $\{q_{n,n-r}\}$ through the recursion (117). Alternatively, these coefficients can be deduced from the Lanczos recursion (97) for the rth derivative $Q_{n,r}(0)$ since we have $q_{n,n-r} = (1/r!)Q_{n,r}(0)$ as in Eq. (122). The polynomial set $\{Q_n(u)\}$ is the basis comprised of scalar functions in the Lanczos vector space $\mathcal{L}$ from Eq. (135). In Eq. (135), the definition (142) of the inner product implies that the polynomials $Q_n(u)$ and $Q_m(u)$ are orthogonal to each other (for $n \neq m$) with respect to the complex weight function d_k, as per (166). The completeness (163) of the set $\{Q_n(u)\}$ enables expansion of every function $f(u) \in \mathcal{L}$ in a series in terms of the

polynomials $\{Q_n(u)\}$, as shown in Eq. (167). Doing this with the monomial $f(u) = u^m$ yields:

$$u^m = \sum_{r=0}^{m} \mu_{r,m} Q_r(u), \tag{184}$$

where

$$\mu_{r,m} = \frac{(u^m | Q_r(u))}{c_0}. \tag{185}$$

The expansion coefficients $\{\mu_{r,m}\}$ are called the modified moments [58]. They have the following property [2]:

$$\mu_{n,m} = 0 \quad (m = 0, 1, 2, \ldots, n-1). \tag{186}$$

In other words, the modified moments fill in an upper triangular matrix $\boldsymbol{\mu} = \{\mu_{i,j}\}$ in which all the elements below the main diagonal are equal to zero [45]:

$$\boldsymbol{\mu} = \begin{pmatrix} \mu_{0,0} & \mu_{0,1} & \mu_{0,2} & \mu_{0,3} & \mu_{0,4} & \cdots & \mu_{0,n} \\ 0 & \mu_{1,1} & \mu_{1,2} & \mu_{1,3} & \mu_{1,4} & \cdots & \mu_{1,n} \\ 0 & 0 & \mu_{2,2} & \mu_{2,3} & \mu_{2,4} & \cdots & \mu_{2,n} \\ 0 & 0 & 0 & \mu_{3,3} & \mu_{3,4} & \cdots & \mu_{3,n} \\ \vdots & \vdots & \vdots & \vdots & \vdots & \ddots & \vdots \\ 0 & 0 & 0 & 0 & 0 & \cdots & \mu_{n,n} \end{pmatrix}. \tag{187}$$

The scalar product of u^n with u^m read as:

$$(u^m | u^n) = c_{n+m}. \tag{188}$$

We can calculate the same scalar product $(u^m | u^n)$ by using (184) for both u^m and u^n so that:

$$(u^m | u^n) = c_0 \sum_{r=0}^{n} \mu_{r,n} \mu_{r,m}. \tag{189}$$

On comparing Eqs. (188) and (189), we deduce:

$$\sum_{r=0}^{n} \mu_{r,n} \mu_{r,m} = \frac{c_{n+m}}{c_0}. \tag{190}$$

Combining Eqs. (114) and (188) leads to the following:

$$\mu_{n,m} = \frac{1}{c_0} \sum_{r=0}^{n} c_{m+r} q_{n,n-r}. \tag{191}$$

Furthermore, using Eq. (191), the following system of linear equations for the coefficients $\{q_{n,n-r}\}$ of the polynomial $Q_n(u)$ is obtained, as typical for the PA:

$$\sum_{r=0}^{n} c_{m+r} q_{n,n-r} = 0 \quad (m = 0, 1, 2, \ldots, n-1). \tag{192}$$

This demonstrates the equivalence between the harmonic inversion and the moment problem [2].

18. MAPPING FROM THE KRYLOV–SCHRÖDINGER TO THE LANCZOS STATES

In Eq. (181), we give the mapping $|\psi_n) = \sum_{r=0}^{n} q_{n,n-r} |\Phi_r)$ between the two different representations $\{|\psi_n)\}$ and $\{|\Phi_n)\}$. Here, the expansion coefficients $\{q_{n,n-r}\}$ play the role of the elements of the direct transformation $|\psi_n) \longrightarrow |\Phi_n)$ between the Lanczos and the Schrödinger states. The result (181) shows that each Lanczos state $|\psi_n)$ is a linear combination of n Schrödinger states $\{|\Phi_m)\} (0 \le m \le n)$. To proceed further in this direction, we need the inverse transformation $|\Phi_n) \longrightarrow |\psi_n)$. This could be obtained using Eq. (36) as the definition of the Schrödinger state $|\Phi_n) = \widehat{\mathrm{U}}^n(\tau)|\Phi_0)$, if we have $\widehat{\mathrm{U}}^n$ as a linear combination of the polynomials $\{Q_r(\widehat{\mathrm{U}})\}$, such that the ansatz $Q_r(\widehat{\mathrm{U}})|\Phi_0)$ could be used to identify the Lanczos state $|\psi_r)$ via Eq. (91). The mapping $\widehat{\mathrm{U}}^n \longrightarrow Q_n(\widehat{\mathrm{U}})$ can be obtained as the operator counterpart of Eq. (184) by resorting to the Cayley–Hamilton theorem [2]:

$$\widehat{\mathrm{U}}^n = \sum_{r=0}^{n} \mu_{r,n} Q_r(\widehat{\mathrm{U}}). \tag{193}$$

Substituting this expression into $|\Phi_n) = \widehat{\mathrm{U}}^n(\tau)|\Phi_0)$ from Eq. (36), we have:

$$|\Phi_n) = \sum_{r=0}^{n} \mu_{r,n} |\psi_r). \tag{194}$$

Hence, the inverse mapping $|\Phi_n) \longrightarrow |\psi_n)$ between the Schrödinger and Lanczos states is carried out by means of the matrix $\boldsymbol{\mu}$ of modified moments

$\{\mu_{i,j}\}$ [58]. The inner product between two Schrödinger states $(\Phi_m|$ and $|\Phi_n)$ from Eq. (194) is given by:

$$(\Phi_m|\Phi_n) = c_0 \sum_{r=0}^{n} \mu_{r,n}\mu_{r,m}. \tag{195}$$

According to Eq. (44), we have $(\Phi_m|\Phi_n) = c_{n+m}$, which is the general element $S_{n,m}$ of the Schrödinger overlap matrix $\mathbf{S} = \{S_{n,m}\} = \{c_{n+m}\}$ and therefore:

$$\sum_{r=0}^{n} \mu_{r,n}\mu_{r,m} = \frac{c_{n+m}}{c_0} = \frac{S_{n,m}}{c_0}, \tag{196}$$

as in Eq. (190). Our formula (196) can also be verified in the opposite direction by using Eq. (185) for both $\mu_{r,m}$ and $\mu_{r,n}$ together with Eqs. (142) and (163). In this checking of Eq. (196), we used the completeness relation (163) in the form $\sum_{r=0}^{n} Q_r(u_k)Q_r(u_{k'}) = c_0\delta_{k,k'}/d_k$ with the underlying characteristic equation that is here defined by $Q_n(u_k) = 0$. The final result (196) is, of course, independent of the eigenvalues $\{u_k\}$. This, in turn, proves the correctness of the inverse transformation (194) between the Schrödinger and Lanczos states. Similarly, it can be verified that a direct transformation (181) between the Lanczos and Schrödinger states can reconstruct the orthonormalization condition so that:

$$(\psi_m|\psi_n) = c_0\delta_{n,m}, \tag{197}$$

as in Eq. (59) for the Lanczos states. This establishes the correctness of Eq. (181). Moreover, in a mixed scalar product between Lanczos and Schrödinger states, we project $|\psi_n)$ onto $(\Phi_m|$ and use Eqs. (59) and (194) to deduce:

$$(\Phi_m|\psi_n) = \sum_{r=0}^{m} \mu_{r,m}(\psi_r|\psi_n) = \sum_{r=0}^{m} \mu_{r,m}\{c_0\delta_{r,n}\} = c_0\mu_{n,m},$$

$$\therefore \quad \frac{(\Phi_m|\psi_n)}{c_0} = \mu_{n,m}. \tag{198}$$

Thus, the scalar product $(\Phi_m|\psi_n)/c_0$ between the Schrödinger $(\Phi_m|$ and Lanczos $|\psi_n)$ states is equal to the modified moment $\mu_{n,m}$, which is equivalently defined by Eq. (185). Using the property (186) of $\mu_{n,m}$ for $(m < n)$, it follows:

$$(\Phi_m|\psi_n) = 0 \quad (m = 0, 1, 2, \ldots, n-1). \tag{199}$$

Hence, every Lanczos state $|\psi_n)$ is orthogonal to each Schrödinger state $(\Phi_m|$ for $0 \le m \le n-1$ and this generalizes $(\Phi_0|\psi_n) = 0$ from Eq. (179). Similarly,

inserting Eq. (181) into $(\Phi_m|\psi_n)$, we obtain:

$$(\Phi_m|\psi_n) = \sum_{r=0}^{n} q_{n,n-r}(\Phi_m|\Phi_r) = \sum_{r=0}^{n} q_{n,n-r}c_{m+r},$$

$$\therefore \quad (\Phi_m|\psi_n) = \sum_{r=0}^{n} c_{m+r}q_{n,n-r}. \tag{200}$$

A comparison between Eqs. (198) and (200) yields the following expression:

$$\mu_{n,m} = \frac{1}{c_0}\sum_{r=0}^{n} c_{m+r}q_{n,n-r} \quad \text{(QED)}, \tag{201}$$

which confirms the previously obtained formula (191).

19. THE PADÉ–LANCZOS APPROXIMANT

Given the eigenvalue set $\mathcal{K}$ from Eq. (136), the polynomial $Q_K(u)$ can be expressed through a product of the type $Q_K(u) = q_{K,0}(u-u_1)(u-u_2)\cdots(u-u_K)$, as in Eq. (124), where $q_{K,0} = 1/\bar{\beta}_K$ is the leading coefficient (120) in the power series representation (114) of the polynomial $Q_K(u)$. On the other hand, the Lanczos orthogonal polynomial of the second kind $P_n(u)$ from Eq. (114) has one zero less than the corresponding polynomial of the first kind $Q_n(u)$ since the degrees of the polynomials $P_n(u)$ and $Q_n(u)$ are $n-1$ and n, respectively. This suggests that there ought to be a linear transformation, say $\mathcal{T}$, which is capable of deducing the polynomial $P_K(u)$ from a function containing the quotient $\propto Q_K(z)/(u-z)$. The contour integral in Eq. (137) is well suited for such a task of the operator $\mathcal{T}$. Clearly, this is contingent on a judicious modification of the function $Q_K(z)/(u-z)$ to meet the requirement of a regular behavior throughout the complex z-plane bounded by the contour C, which encompasses the eigenset $\mathcal{K}$. Such an adjustment is possible through a replacement of the ansatz $Q_K(z)/(u-z)$ by the following first-order finite difference:

$$g(u,z) = \frac{Q_K(u) - Q_K(z)}{u-z}, \quad P_K(u) = \mathcal{T}g(u,z), \tag{202}$$

so that the polynomial $P_K(u)$ should be deducible from the linear mapping $P_K(u) = \mathcal{T}g(u,z)$. This is indeed possible by selecting the operator $\mathcal{T}$ to be proportional to the contour integral from Eq. (137). Such a choice leads naturally to the following integral representation for the Lanczos polynomial of

the second kind $P_n(u)$:

$$P_n(u) = \frac{\beta_1}{c_0}\frac{1}{2\pi i}\oint_C \mathrm{d}\sigma_0(z)\frac{Q_n(u)-Q_n(z)}{u-z}, \tag{203}$$

where C is the contour from Eq. (137). This is easily transformed to the following expression:

$$\frac{c_0}{\beta_1}\frac{P_K(u)}{Q_K(u)} = \sum_{k=1}^{K}\frac{d_k}{u-u_k}, \tag{204}$$

where the residue $d_k = (\Phi_0|\Upsilon_k)^2$ is from Eq. (15). The rhs of Eq. (204) is equal to the spectral representation of the Kth rank approximation to the total Green function $\mathcal{R}(u)$ from Eq. (51). The representation $(c_0/\beta_1)P_K(u)/Q_K(u)$ from Eq. (204) for the Green function $\mathcal{R}(u)$ will be called the Padé–Lanczos approximant (PLA) of the order $(K-1,K)$ and, as such, will be denoted by $\mathcal{R}^{\mathrm{PLA}}_{K,K}(u) \equiv \mathcal{R}^{\mathrm{PLA}}_{K}(u)$ [47, 48]:

$$\mathcal{R}(u) \approx \mathcal{R}^{\mathrm{PLA}}_{K}(u), \quad \mathcal{R}^{\mathrm{PLA}}_{K}(u) \equiv \frac{c_0}{\beta_1}\frac{P_K(u)}{Q_K(u)}. \tag{205}$$

The Lanczos algorithm and the Padé approximant have also been combined in other research fields, for example, in computational and applied mathematics [2], as well as in engineering via circuit theory [59]. The authors of Refs. [59, 60] from 1995, being apparently unaware of the earlier work [48] from 1972, rederived through a different procedure the Padé–Lanczos approximant and called it the Padé via Lanczos (PVL) method.

The numerator $P_K(u)$ and denominator $Q_K(u)$ polynomials from Eq. (205) are of degree $K-1$ and K, respectively, so that the ensuing PLA belongs to the "subdiagonal" case of the general order Padé approximant [2, 61]. The PLA can also be introduced by starting from inversion of the matrix $(\Phi_0|\{u\mathbf{1}-\mathbf{U}\}^{-1}|\Phi_0)$, as will be analyzed in Section 20. In either case, the name Padé–Lanczos approximant and the associated acronym PLA is used to emphasize that the PA via the representation $(c_0/\beta_1)P_K(u)/Q_K(u)$ for the Green function $\mathcal{R}(u)$ from Eq. (49), is generated by the Lanczos algorithms for the numerator and denominator polynomials $P_K(u)$ and $Q_K(u)$, respectively. In addition to the subdiagonal PLA, we can also introduce the general PLA as a ratio of two Lanczos polynomials of degrees $L-1$ and K as follows:

$$\mathcal{R}^{\mathrm{PLA}}_{L,K}(u) \equiv \frac{c_0}{\beta_1}\frac{P_L(u)}{Q_K(u)}, \tag{206}$$

where $K \geq L$. If $L=K$, we have the subdiagonal PLA, whereas the case $L=K+m$, where m is a positive integer ($m \geq 2$), represents the mth "paradiagonal" PLA. The pure diagonal PLA corresponds to $L-1=K$. We saw

in Section 6 that the polynomials $P_K(u)$ and $Q_K(u)$ are generated individually in the course of producing the Lanczos states $\{|\psi_n)\}$ in K iterations. Such a computation depends on the availability of the coupling parameters $\{\alpha_n, \beta_n\}$ that are generated within the recursion for the state vectors $\{|\psi_n)\}$. However, this is not how the Lanczos polynomials should be constructed in practice. It would be advantageous to dissociate completely the recursions for $\{P_n(u), Q_n(u)\}$ from the Lanczos algorithm for $\{|\psi_n)\}$. To this end, one needs an autonomous strategy for computations of the constants $\{\alpha_n, \beta_n\}$. Such are the powerful Chebyshev, Gragg, and Wheeler algorithms linked to the nearest neighbor method in Refs. [2, 47]. Generation of the constants $\{\alpha_n, \beta_n\}$ is of paramount importance since these parameters contain the whole information about the studied system. This is the case because the Green function, density of states, evolution matrix, autocorrelation function, etc. can all be expressed solely in terms of the couplings $\{\alpha_n, \beta_n\}$. In this way, one can bypass altogether any reliance of the polynomials $\{P_n(u), Q_n(u)\}$ on the Lanczos recursion for the state vectors $\{|\psi_n)\}$.

The spectral representation of $\mathcal{R}_K^{\mathrm{PLA}}(u)$ from Eq. (205) is given by the Heaviside partial fractions [2]:

$$\mathcal{R}_K^{\mathrm{PLA}}(u) = \frac{c_0}{\beta_1}\frac{P_K(u)}{Q_K(u)} = \sum_{k=1}^{K}\frac{d_k}{u-u_k}. \tag{207}$$

This expression for $\mathcal{R}_K^{\mathrm{PLA}}(u)$ represents a meromorphic function since its poles are the only singularities encountered. Therefore, the zeros of $P_K(u)$ and $Q_K(u)$ are the zeros and poles of $\mathcal{R}_K^{\mathrm{PLA}}(u)$, respectively. There are K poles $\{u_k\}_{k=1}^K$ of $\mathcal{R}_K^{\mathrm{PLA}}(u)$ since $Q_K(u)$ is a polynomial of the Kth degree. The Heaviside partial fraction (207) includes only the first-order poles $\{u_k\}$ since the polynomials $P_K(u)$ and $Q_K(u)$ have no multiple zeros as shown in Section 8. The definition (205) of the PLA obeys the main property of the general PA, according to which the Maclaurin expansions of the Green functions $\mathcal{R}(u)$ and $\mathcal{R}_K^{\mathrm{PLA}}(u)$ in powers of the variable u agree with each other, exactly term by term, including the power $2K-1$:

$$\mathcal{R}(u) - \frac{c_0}{\beta_1}\frac{P_K(u)}{Q_K(u)} = \mathcal{O}(u^{2K}), \quad u \to 0. \tag{208}$$

Here, as usual, the remainder symbol $\mathcal{O}(u^{2K})$ represents a Maclaurin series in powers of u such that the starting term is u^{2K}.

The above derivation shows that the definition of the residue $d_k = (\Phi_0|\Upsilon_k)^2$ from the general expression (15) is transferred as intact to the spectral representation (207) in the PLA. Therefore, such an introduction of the PLA falls precisely within the so-called state expansion methods in signal processing [2, 47]. This establishes the PLA as a complete eigenvalue solver since the computed Lanczos pair $\{|\psi_n), Q_n(u)\}$, as well as the zeros of the

characteristic polynomial $Q_K(u)$, also provide the whole eigenset $\{u_k, |\Upsilon_k)\}$ according to (67). However, although the residues $\{d_k\}$ in other state expansion methods, for example, FD [40, 42] or decimated signal diagonalization (DSD) [38, 39] necessitate explicit computations to obtain some approximations of the full exact eigenstate vector $|\Upsilon_k)$, the PLA possesses an alternative procedure. This procedure does not require any knowledge about the state vector $|\Upsilon_k)$. It is an explicit expression for d_k as the Cauchy residue of the quotient $P_K(u)/Q_K(u)$:

$$d_k = \frac{c_0}{\beta_1} \lim_{u \to u_k} (u - u_k) \frac{P_K(u)}{Q_K(u)} = \frac{c_0}{\beta_1} \frac{P_K(u_k)}{Q'_K(u_k)}, \tag{209}$$

with the result,

$$\mathcal{R}_K^{\mathrm{PLA}}(u) = \sum_{k=1}^{K} \left\{ \frac{c_0}{\beta_1} \frac{P_K(u_k)}{Q'_K(u_k)} \right\} \frac{1}{u - u_k}. \tag{210}$$

20. INVERSION OF THE KRYLOV–SCHRÖDINGER GENERAL MATRIX

Once the Lanczos coupling constants $\{\alpha_n, \beta_n\}$ have been computed, we could construct the Green function $\mathcal{R}(u) = c_0(\Phi_0|\{u\mathbf{1} - \mathbf{U}\}^{-1}|\Phi_0)$, which is defined in Eq. (49). If in the formula (49) for $\mathcal{R}(u)$, we use the Lanczos representation for the matrix $u\mathbf{1} - \mathbf{U}$ based on Eq. (60) within the infinite chain model, we shall have:

$$\mathcal{R}(u) = c_0 \begin{pmatrix} u - \alpha_0 & -\beta_1 & 0 & \cdots & \cdots & 0 & \cdots \\ -\beta_1 & u - \alpha_1 & -\beta_2 & \cdots & \cdots & 0 & \cdots \\ 0 & -\beta_2 & u - \alpha_2 & \cdots & \cdots & 0 & \cdots \\ \vdots & \vdots & \vdots & \ddots & \ddots & \vdots & \vdots \\ 0 & 0 & 0 & -\beta_{n-1} & u - \alpha_{n-1} & -\beta_n & \cdots \\ 0 & 0 & 0 & 0 & -\beta_n & u - \alpha_n & \cdots \\ \vdots & \vdots & \vdots & \vdots & \vdots & \vdots & \vdots \end{pmatrix}^{-1}_{00}, \tag{211}$$

where the symbol $(\cdots)^{-1}_{00}$ denotes $(\cdots)^{-1}_{00} \equiv (\Phi_0|(\cdots)^{-1}|\Phi_0)$ and $(\cdots)^{-1} \equiv (u\mathbf{1} - \mathbf{U})^{-1}$. However, by definition, the matrix element (211) of the inverse matrix $(u\mathbf{1} - \mathbf{U})^{-1}$ is given by the ratio of the corresponding determinant $\det[u\mathbf{1} - \mathbf{U}]$ and the associated main cofactor. Therefore,

$$\mathcal{R}(u) = c_0 \frac{D_1(u)}{D_0(u)}. \tag{212}$$

Here, $D_0(u)$ is the determinant of the matrix $u\mathbf{1}-\mathbf{U}$ for the infinite chain model ($M=\infty$):

$$D_0(u)=\begin{vmatrix} u-\alpha_0 & -\beta_1 & 0 & \cdots & \cdots & 0 & \cdots \\ -\beta_1 & u-\alpha_1 & -\beta_2 & \cdots & \cdots & 0 & \cdots \\ 0 & -\beta_2 & u-\alpha_2 & \cdots & \cdots & 0 & \cdots \\ \vdots & \vdots & \vdots & \ddots & \ddots & \vdots & \vdots \\ 0 & 0 & 0 & -\beta_{n-1} & u-\alpha_{n-1} & -\beta_n & \cdots \\ 0 & 0 & 0 & 0 & -\beta_n & u-\alpha_n & \cdots \\ \vdots & \vdots & \vdots & \vdots & \vdots & \vdots & \vdots \end{vmatrix}, \quad (213)$$

and $D_1(u)$ is the corresponding main cofactor of $D_0(u)$ at the position $u-\alpha_0$. In other words, $D_1(u)$ is obtained by removing the first row and the first column from $D_0(u)$:

$$D_1(u)\equiv\begin{vmatrix} u-\alpha_1 & -\beta_2 & 0 & \cdots & \cdots & 0 & \cdots \\ -\beta_2 & u-\alpha_2 & -\beta_3 & \cdots & \cdots & 0 & \cdots \\ 0 & -\beta_3 & u-\alpha_3 & \cdots & \cdots & 0 & \cdots \\ \vdots & \vdots & \vdots & \ddots & \ddots & \vdots & \vdots \\ 0 & 0 & \cdots & -\beta_{n-1} & u-\alpha_{n-1} & -\beta_n & \cdots \\ 0 & 0 & \cdots & 0 & -\beta_n & u-\alpha_n & \cdots \\ \vdots & \vdots & \vdots & \vdots & \vdots & \vdots & \vdots \end{vmatrix}. \quad (214)$$

The results of truncation of the infinite-order determinants $D_0(u)$ and $D_1(u)$ at $n=K$ will be denoted by $D_{0,K}(u)$ and $D_{1,K}(u)$, respectively, such that $D_{0,K}(u)=\tilde{Q}_K(u)$ according to (106):

$$D_{0,K}(u)\equiv\begin{vmatrix} u-\alpha_0 & -\beta_1 & 0 & \cdots & \cdots & 0 \\ -\beta_1 & u-\alpha_1 & -\beta_2 & \cdots & \cdots & 0 \\ 0 & -\beta_2 & u-\alpha_2 & \cdots & \cdots & 0 \\ \vdots & \vdots & \vdots & \ddots & \ddots & \vdots \\ 0 & 0 & 0 & -\beta_{K-2} & u-\alpha_{K-2} & -\beta_{K-1} \\ 0 & 0 & 0 & 0 & -\beta_{K-1} & u-\alpha_{K-1} \end{vmatrix}, \quad (215)$$

$$D_{1,K}(u)\equiv\begin{vmatrix} u-\alpha_1 & -\beta_2 & 0 & \cdots & \cdots & 0 \\ -\beta_2 & u-\alpha_2 & -\beta_3 & \cdots & \cdots & 0 \\ 0 & -\beta_3 & u-\alpha_3 & \cdots & \cdots & 0 \\ \vdots & \vdots & \vdots & \ddots & \ddots & \vdots \\ 0 & 0 & \cdots & -\beta_{K-2} & u-\alpha_{K-2} & -\beta_{K-1} \\ 0 & 0 & \cdots & 0 & -\beta_{K-1} & u-\alpha_{K-1} \end{vmatrix}. \quad (216)$$

The ensuing Green function $c_0 D_{1,K}(u)/D_{0,K}(u)$ is an approximation to $\mathcal{R}(u)$ from (212):

$$\mathcal{R}(u) \approx \mathcal{R}_K(u), \quad \mathcal{R}_K(u) \equiv c_0 \frac{D_{1,K}(u)}{D_{0,K}(u)}. \tag{217}$$

The determinant $D_0(u)$ can be computed iteratively by expressing it in terms of its subdeterminants $D_1(u)$ and $D_2(u)$ via the usage of the Cauchy expansion for determinants, as we have done in Refs. [2, 47]. The determinant $D_2(u)$ is obtained by deleting the first two rows and the first two columns from $D_0(u)$. Thus, in a complete analogy with Eq. (108), we have:

$$D_0(u) = (u - \alpha_0) D_1(u) - \beta_1^2 D_2(u). \tag{218}$$

In order to continue this iterative process further by descending to lower ranks, we denote by $D_n(u)$ the determinant that is obtained by deleting the first n rows and columns from $D_0(u)$. Then by working inductively with the help of the Cauchy expansion for determinants, we obtain the generalization of Eq. (218) as:

$$D_{n-1}(u) = (u - \alpha_{n-1}) D_n(u) - \beta_n^2 D_{n+1}(u), \tag{219}$$

with the initializations $D_{-1}(u) = 0$ and $D_0(u) = 1$. This three-term contiguous relation for $D_n(u)$ falls precisely into the category of the Askey–Wilson polynomials [2], just like the oppositely recurring counterpart of (108). When the Askey–Wilson polynomials are divided by the constant $\bar{\beta}_n$ from Eq. (57), the Lanczos polynomials $\{Q_n(u)\}$ are obtained as in Eq. (111). In particular,

$$D_{0,K}(u) = (\beta_1 \beta_2 \beta_3 \cdots \beta_K) Q_K(u) = \tilde{Q}_K(u), \tag{220}$$

$$D_{1,K}(u) = (\beta_2 \beta_3 \cdots \beta_K) P_K(u) = \tilde{P}_K(u). \tag{221}$$

Here, $\tilde{P}_K(u)$ is the minor of the determinant (106) at the position $u - \alpha_0$ for $n = K - 1$, obtained by deleting the first column and the first row from Eq. (106). Thus, $\tilde{P}_K(u) = D_{1,K}(u)$ as per Eq. (216),

$$c_0 \frac{D_{1,K}(u)}{D_{0,K}(u)} = c_0 \frac{\tilde{P}_K(u)}{\tilde{Q}_K(u)} = c_0 \frac{(\beta_2 \beta_3 \cdots \beta_K) P_K(u)}{(\beta_1 \beta_2 \beta_3 \cdots \beta_K) Q_K(u)} = \frac{c_0}{\beta_1} \frac{P_K(u)}{Q_K(u)}, \tag{222}$$

where $Q_K(u)$ and $P_K(u)$ are the Lanczos polynomials (84) and (92) of degrees K and $K - 1$, respectively. Therefore, truncation of the infinite-order determinants $D_0(u)$ and $D_1(u)$ at the finite order $n = K - 1$ leads to the following

approximation for the quotient $\mathcal{R}(u)$ from Eq. (217):

$$\mathcal{R}_K(u) = \frac{c_0}{\beta_1}\frac{P_K(u)}{Q_K(u)} = \mathcal{R}_K^{\mathrm{PLA}}(u), \tag{223}$$

in agreement with the previously established expression (205) for the resolvent $\mathcal{R}_K^{\mathrm{PLA}}(u)$ in the PLA. The result $\mathcal{R}_K^{\mathrm{PLA}}(u)$ from Eq. (223) is the PLA of the order $(K-1, K)$ for the exact expression for $\mathcal{R}(u)$ from Eq. (212). The above derivation demonstrates that the explicit and exact inversion of scaled evolution matrix $u\mathbf{1} - \mathbf{U}$ is possible for any finite rank, and the analytical result is precisely the Padé–Lanczos approximant. It should be recalled that in the literature, the algorithm of the Lanczos continued fractions for iterative computation of the diagonal or off-diagonal Green functions is also known as the recursion method [48] or equivalently the recursive residue generation method (RRGM) [62]–[64].

21. THE LANCZOS CONTINUED FRACTIONS

A general continued fraction (CF) [2, 65] is another way of writing the PA as a staircase with descending quotients. There are several equivalent symbolic notations in use for a given CF and two of them are given by:

$$\cfrac{A_1}{B_1 + \cfrac{A_2}{B_2 + \cfrac{A_3}{B_3 + \ddots}}} \equiv \frac{A_1}{B_1}\boldsymbol{+}\frac{A_2}{B_2}\boldsymbol{+}\frac{A_3}{B_3}\boldsymbol{+}\cdots \tag{224}$$

The lhs of Eq. (224) is a natural way of writing the staircase-shaped continued fraction, but for frequent usage, the rhs of the same equation is more economical as it takes less space. It should be observed that the plus signs in boldface on the rhs of Eq. (224) are lowered to remind us of a "step-down" process in forming the CF. In other words, the rhs of Eq. (224) could also be equivalently written using the ordinary plus signs as $A_1/(B_1 + A_2/(B_2 + A_3/(B_3 + \cdots)))$ [47, 48]. In this section, we shall connect the PLA to the CF by returning to the recursion (219) for the Lanczos determinants $\{D_n(u)\}$ [2, 48, 65]. Letting $n \longrightarrow n+1$ and dividing both sides of Eq. (219) by $D_n(u)$ will yield [2, 48]:

$$\frac{D_n(u)}{D_{n+1}(u)} = u - \alpha_n - \beta_{n+1}^2 \frac{D_{n+2}(u)}{D_{n+1}(u)}. \tag{225}$$

Denoting the ratio $D_{n+1}(u)/D_n(u)$ by $\Gamma_n(u)$,

$$\Gamma_n(u) = \frac{D_{n+1}(u)}{D_n(u)}\,. \tag{226}$$

We can rewrite Eq. (225) in the following form:

$$\Gamma_n(u) = \frac{1}{u - \alpha_n - \beta_{n+1}^2 \Gamma_{n+1}(u)}. \tag{227}$$

In order to obtain the Nth order approximation to $\mathcal{R}(u)$, we use the backward recurrence (227) with the initialization $\Gamma_{N+1}(u) = 0$ and subsequently descend all the way down to $n = 0$. The final result is $\Gamma_0 = D_1(u)/D_0(u)$. Then, using $\mathcal{R}(u) = c_0 D_1(u)/D_0(u)$ from Eq. (212), we obtain:

$$\mathcal{R}(u) = c_0 \Gamma_0(u), \tag{228}$$

so that with the help of Eqs. (226) and (227), we arrive at:

$$\mathcal{R}(u) = \mathcal{R}^{\mathrm{LCF}}(u), \tag{229}$$

$$\mathcal{R}^{\mathrm{LCF}}(u) = \frac{c_0}{u - \alpha_0} \underset{-}{} \frac{\beta_1^2}{u - \alpha_1} \underset{-}{} \frac{\beta_2^2}{u - \alpha_2} \underset{-}{} \frac{\beta_3^2}{u - \alpha_3} \underset{-}{} \cdots. \tag{230}$$

This procedure of obtaining the Green function $\mathcal{R}(u)$ is called hereafter the method of the Lanczos continued fractions (LCF) in the symbolic notation from the rhs of Eq. (224). Then, we say that the quantity $\mathcal{R}^{\mathrm{LCF}}(u)$ is the infinite-order LCF for the exact Green function $\mathcal{R}(u)$ from Eq. (49). A truncation at the nth term in Eq. (230) leads to the approximation:

$$\mathcal{R}^{\mathrm{LCF}}(u) \approx \mathcal{R}_n^{\mathrm{LCF}}(u). \tag{231}$$

Here, $\mathcal{R}_n^{\mathrm{LCF}}(u)$ is the LCF of the nth order:

$$\mathcal{R}_n^{\mathrm{LCF}}(u) = \left\{\mathcal{R}^{\mathrm{LCF}}(u)\right\}_{\beta_n = 0} \quad (n = 1, 2, 3, \ldots), \tag{232}$$

$$\mathcal{R}_n^{\mathrm{LCF}}(u) = \frac{c_0}{u - \alpha_0} \underset{-}{} \frac{\beta_1^2}{u - \alpha_1} \underset{-}{} \frac{\beta_2^2}{u - \alpha_2} \underset{-}{} \frac{\beta_3^2}{u - \alpha_3} \underset{-}{} \cdots \underset{-}{} \frac{\beta_{n-1}^2}{u - \alpha_{n-1}}. \tag{233}$$

No matrix inversion is encountered in Eq. (230). Stated equivalently, the matrix $u\mathbf{1} - \mathbf{U}$ associated with the resolvent operator $\widehat{\mathrm{R}}(u)$ from Eq. (48) is inverted iteratively through its corresponding LCF. The LCF as a versatile convergence accelerator can yield the frequency spectrum (230) with

a reduced number of terms $\{\alpha_n, \beta_n\}$. The meaning of the nearest neighbor approximation within the LCF is that the coefficients $\{\alpha_n, \beta_n\}$ become increasingly less significant for determination of the Green function $\mathcal{R}(u)$ as one progresses further down the continued fraction in Eq. (230). Explicit calculations of the first few terms easily reveal a general pattern from which it follows:

$$\mathcal{R}_n^{\mathrm{LCF}}(u) = \mathcal{R}_n^{\mathrm{PLA}}(u), \tag{234}$$

where the term $\mathcal{R}_n^{\mathrm{PLA}}(u)$ is given in Eq. (205) for $K = n$ as the quotient of the two Lanczos polynomials $P_n(u)$ and $Q_n(u)$, that is, $\mathcal{R}_n^{\mathrm{PLA}}(u) = (c_0/\beta_1)P_n(u)/Q_n(u)$. Then, according to Eq. (234), the nth-order Lanczos continued fraction, which is derived from the expression (211) for the exact Green function $\mathcal{R}(u)$ from Eq. (49), is mathematically equivalent to the Padé–Lanczos approximant.

22. EQUATIONS FOR EIGENVALUES VIA CONTINUED FRACTIONS

If the set of the couplings $\{\alpha_n, \beta_n\}$ is precomputed, it is clear from the preceding section that the LCF is technically more efficient than the PLA. This is because the PLA still needs to generate the Lanczos polynomials $\{P_K(u), Q_K(u)\}$ to arrive at Eq. (205), whereas LCF does not. The LCF is an accurate, robust, and fast processor for computation of shape spectra with an easy way of programming implementations in practice. For parametric estimations of spectra, there are two options. We can search for the poles in Eq. (230) from the inherent polynomial equation after the LCF is reduced to its polynomial quotient, which is precisely the PLA. In such a case, the efficiency of the LCF is the same as that of the PLA. However, the poles in Eq. (230) can be obtained without reducing $\mathcal{R}_n^{\mathrm{LCF}}(u)$ to the polynomial quotient. Since $\bar{\beta}_K \neq 0$, as per Eq. (61), we can rewrite the characteristic equation (112) as $\tilde{Q}_K(u) = 0$. This can be stated as the tridiagonal secular equation:

$$\tilde{Q}_K(u) \equiv \begin{vmatrix} u-\alpha_0 & -\beta_1 & 0 & \cdots & \cdots & 0 \\ -\beta_1 & u-\alpha_1 & -\beta_2 & \cdots & \cdots & 0 \\ 0 & -\beta_2 & u-\alpha_2 & \cdots & \cdots & 0 \\ \vdots & \vdots & \vdots & \ddots & \ddots & \vdots \\ 0 & 0 & 0 & -\beta_{K-2} & u-\alpha_{K-2} & -\beta_{K-1} \\ 0 & 0 & 0 & 0 & -\beta_{K-1} & u-\alpha_{K-1} \end{vmatrix} = 0. \tag{235}$$

Expanding the determinantal equation (235) by the Cauchy rule, we readily obtain the following continued fraction:

$$u=\alpha_0-\frac{\beta_1^2}{u-\alpha_1}\underline{-}\frac{\beta_2^2}{u-\alpha_2}\underline{-}\frac{\beta_3^2}{u-\alpha_3}\underline{-}\cdots\underline{-}\frac{\beta_{K-1}^2}{u-\alpha_{K-1}}. \tag{236}$$

The solutions $\{u_k\}_{k=1}^K$ of this equation are the eigenvalues of $\mathbf{U}(\tau)$. Clearly, Eq. (236) is a transcendental equation. This is because the kth solution $u=u_k$ is given only implicitly since u appears in the continued fraction from the rhs of Eq. (236), and the unknown u is also present on the lhs of the same equation. The modified Newton–Raphson iterative method used in Eq. (129) can be employed to solve $\tilde{F}(u)=0$ for $u=u_k$, where $\tilde{F}(u)$ is the difference between the lhs and rhs of Eq. (236). Many quantum-mechanical eigenvalue problems can be reduced to diagonalization of triangular matrices. Alternatively, the eigensolutions can be obtained using the corresponding secular determinantal equations similar to Eq. (235) but with the real variable ω instead of the complex exponential $u=\exp(-i\omega\tau)$. A good example for this is the extraction of extremely accurate eigenvalues (also called the "characteristic numbers") of the Mathieu function.

23. EXPLICIT PADÉ APPROXIMANT: A CLOSED, GENERAL EXPRESSION

In the preceding section, the continued fractions were introduced in an indirect way into the spectral analysis. Alternatively, they are analyzed in this section in a direct manner. By definition, the infinite-order CF to the series (52) is given by:

$$\mathcal{R}^{\mathrm{CF}}(u)=\frac{a_1}{u}\underline{-}\frac{a_2}{1}\underline{-}\frac{a_3}{u}\underline{-}\frac{a_4}{1}\underline{-}\frac{a_5}{u}\underline{-}\frac{a_6}{1}\underline{-}\frac{a_7}{u}\underline{-}\cdots. \tag{237}$$

The unknown set $\{a_n\}$ is determined from the condition of equality between the expansion coefficients of the series of the rhs of Eq. (237) developed in powers of u^{-1} and the signal points $\{c_n\}$ from Eq. (52), which we rewrite as the following ordinary summation:

$$\mathcal{R}(u)=\frac{c_0}{u}+\frac{c_1}{u^2}+\frac{c_2}{u^3}+\frac{c_3}{u^4}+\frac{c_4}{u^5}+\frac{c_5}{u^6}+\frac{c_6}{u^7}+\cdots. \tag{238}$$

In practice, the rhs of Eq. (237) cannot be used to the infinite order, and therefore, a truncation is required. The infinite order CF, that is, $\mathcal{R}^{\mathrm{CF}}(u)$, which is truncated at the finite order n, is called the nth-order CF approximant $\mathcal{R}_n^{\mathrm{CF}}(u)$,

where n is a positive integer ($n = 1, 2, 3, \ldots$). This truncation is done by setting all the higher order coefficients $\{a_{m \geq n+1}\}$ to zero from the onset:

$$\mathcal{R}_n^{\mathrm{CF}}(u) \equiv \{\mathcal{R}^{\mathrm{CF}}(u)\}_{a_m = 0, m \geq n+1} \quad (n = 1, 2, 3, \ldots). \tag{239}$$

The first few even-order CF approximants $\{\mathcal{R}_{2n}^{\mathrm{CF}}(u)\}$ can be easily extracted. This permits deduction of the general expression for the even- and odd-order continued fractions:

$$\mathcal{R}_{2n}^{\mathrm{CF}}(u) = a_1 \frac{\tilde{P}_n^{\mathrm{CF}}(u)}{\tilde{Q}_n^{\mathrm{CF}}(u)}. \tag{240}$$

$$\mathcal{R}_{2n-1}^{\mathrm{CF}}(u) \equiv \{\mathcal{R}_{2n}^{\mathrm{CF}}(u)\}_{a_{2n} = 0} \quad (n = 1, 2, 3, \ldots). \tag{241}$$

The polynomials $\tilde{P}_n^{\mathrm{CF}}(u)$ and $\tilde{Q}_n^{\mathrm{CF}}(u)$ from Eq. (240) are given by their general power series representations as:

$$\tilde{P}_n^{\mathrm{CF}}(u) = \sum_{r=0}^{n-1} \tilde{p}_{n,n-r} u^r, \quad \tilde{Q}_n^{\mathrm{CF}}(u) = \sum_{r=0}^{n} \tilde{q}_{n,n-r} u^r. \tag{242}$$

The general expansion coefficients $\tilde{p}_{n,n-r}$ and $\tilde{q}_{n,n-r}$ of the polynomials $\tilde{P}_n^{\mathrm{CF}}(u)$ and $\tilde{Q}_n^{\mathrm{CF}}(u)$ are:

$$\tilde{p}_{n,m} = (-1)^{m-1} \underbrace{\sum_{r_1=3}^{2(n-m+2)} a_{r_1} \sum_{r_2=r_1+2}^{2(n-m+3)} a_{r_2} \cdots \sum_{r_{m-1}=r_{m-2}+2}^{2n} a_{r_{m-1}}}_{m-1 \text{ summations}}, \tag{243}$$

$$\tilde{q}_{n,m} = (-1)^{m} \underbrace{\sum_{r_1=2}^{2(n-m+1)} a_{r_1} \sum_{r_2=r_1+2}^{2(n-m+2)} a_{r_2} \sum_{r_3=r_2+2}^{2(n-m+3)} a_{r_3} \cdots \sum_{r_m=r_{m-1}+2}^{2n} a_{r_m}}_{m \text{ summations}}, \tag{244}$$

where $n \geq m$. The explicit results (243) and (244) have originally been derived in Ref. [47]. They express both $\tilde{p}_{n,n-r}$ and $\tilde{q}_{n,n-r}$ as the compact analytical formulae for arbitrary values of nonnegative integers $\{n, r\}$. Our closed analytical expressions (243) and (244) contain only the continued fraction coefficients $\{a_n\}$. Therefore, in order to design a purely algebraic analytical method, the remaining central problem is to obtain a general analytical formula for any CF coefficient a_n in the case of an arbitrary positive integer n. This problem will be tackled and solved in the next section. Note that the forms of the general coefficients from the rhs of Eqs. (243) and (244) are such that they could be efficiently computed using a recursive algorithm from Ref. [2].

24. ANALYTICAL EXPRESSIONS FOR THE GENERAL CONTINUED FRACTION COEFFICIENTS

Here, we shall focus on the exact general analytical expression for all the expansion coefficients a_n in the CF from Eq. (237). For this purpose, one can use the theorem of uniqueness of two power series expansions for the same function. The rhs of Eqs. (52) and (237) shows two different representations of the same Green function (49). Therefore, if we develop the nth-order CF, $\mathcal{R}_n^{\rm CF}(u)$, from Eq. (237) in powers of u^{-1}, the ensuing mth ($m \leq n$) expansion coefficient must be identical to the coefficients $\{c_n\}$ from the series (52). The series expansion of the rhs of Eq. (237) in terms of powers of u^{-1} can be obtained by first expressing $\mathcal{R}_n^{\rm CF}(u)$ as the associated PA, that is, $a_1\tilde{P}_n^{\rm CF}(u)/\tilde{Q}_n^{\rm CF}(u)$. This can be followed by the inversion of the denominator polynomial $\tilde{Q}_n^{\rm CF}(u)$ to obtain a series in u^{-1}. Such a series can then be multiplied by the numerator polynomial $\tilde{P}_n^{\rm CF}(u)$, and the result would be a new series. Finally, the first n terms of this latter series can be equated to the first n time signal points from Eq. (52), according to the uniqueness expansion theorem for the function (49). This method provides the transformation between the general autocorrelation functions $\{C_n\} = \{c_n\}$ and the coefficients $\{a_n\}$ of the continued fractions (237). Such a uniquely defined transformation has been obtained for the first time by Belkić [47] in an explicit analytical form for any value of the nonnegative integer n ($n = 0, 1, 2, 3, \ldots$). We have already derived the explicit expressions for the polynomials $\tilde{P}_n^{\rm CF}(u)$ and $\tilde{Q}_n^{\rm CF}(u)$ with the most general expansion coefficients (243) and (244). Therefore, the polynomial $\tilde{Q}_n^{\rm CF}(u)$ can be explicitly inverted. Then, it would be tempting to multiply $\tilde{P}_n^{\rm CF}(u)$ by $[\tilde{Q}_n^{\rm CF}(u)]^{-1}$ and arrive directly at the nth expansion coefficient of $\mathcal{R}_n^{\rm CF}(u)$ developed as a series in powers of u^{-1}. However, it is less cumbersome to carry out separate, explicit calculations for $1 \leq n \leq 7$, as we did [47]. The obtained results provided a clear way to deduce the general CF coefficient a_n for any integer $n \geq 1$ as the following compact expression:

$$a_{n+1} = \frac{c_n - \sigma_n \pi_{n-1} - \lambda_n \pi_{n-4}}{\pi_n}, \tag{245}$$

$$c_n = \pi_{n+1} + \sigma_n \pi_{n-1} + \lambda_n \pi_{n-4}, \tag{246}$$

with

$$\pi_n = \prod_{i=1}^{n} a_i, \quad \sigma_n = \left(\sum_{j=2}^{n} a_j \right)^2,$$

$$\lambda_n = \sum_{j=\left[\frac{n-1}{2}\right]}^{n-3} a_j \xi_j^2, \quad \xi_j = \sum_{k=2}^{j+1} a_k \sum_{\ell=2}^{k+1} a_\ell, \tag{247}$$

where

$$\pi_n \equiv 0 \quad (n \leq 0), \quad \sigma_n \equiv 0 \quad (n \leq 3). \tag{248}$$

If the time signal points $\{c_n\}$ or autocorrelation functions $\{C_n\}$ are given, the analytical formula (246) yields the whole set of the expansion coefficients $\{a_n\}$ of the continued fractions $\mathcal{R}^{\mathrm{CF}}(u)$ from Eq. (245) of the Green function $\mathcal{R}(u)$ from Eq. (238). Conversely, if the coefficients $\{a_n\}$ are given, the closed expression (245) supplies the entire set $\{c_n\}$. We see from Eq. (245) that each a_{n+1} is given in terms of one fixed c_n and the string $\{a_m\}$ $(1 \leq m \leq n)$. These earlier coefficients $\{a_m\}$ $(1 \leq m \leq n)$ can be eliminated altogether from any a_n so that:

$$a_{2n} = \frac{\mathrm{H}_n(c_1)}{\mathrm{H}_{n-1}(c_1)} \frac{\mathrm{H}_{n-1}(c_0)}{\mathrm{H}_n(c_0)}, \tag{249}$$

$$a_{2n+1} = \frac{\mathrm{H}_{n+1}(c_0)}{\mathrm{H}_n(c_0)} \frac{\mathrm{H}_{n-1}(c_1)}{\mathrm{H}_n(c_1)}. \tag{250}$$

Using Eq. (45), which states that the $n \times n$ Hankel matrix $\mathbf{H}_n(c_s)$ is equal to the matrix $\mathbf{U}_n^{(s)}$ of the evolution operator $\widehat{\mathrm{U}}$ raised to the power s, namely $\widehat{\mathrm{U}}^s$, we can write equivalently:

$$a_{2n} = \frac{\det \mathbf{U}_n}{\det \mathbf{U}_{n-1}} \frac{\det \mathbf{S}_{n-1}}{\det \mathbf{S}_n}, \tag{251}$$

$$a_{2n+1} = \frac{\det \mathbf{S}_{n+1}}{\det \mathbf{S}_n} \frac{\det \mathbf{U}_{n-1}}{\det \mathbf{U}_n}. \tag{252}$$

Here, we used the relationships $\mathbf{U}^{(0)} \equiv \mathbf{S}$ and $\mathbf{U}^{(1)} \equiv \mathbf{U}$, where $\mathbf{U}$ is the evolution or relaxation matrix and $\mathbf{S}$ is the Schrödinger or the Krylov overlap matrix.

25. EIGENVALUES WITHOUT EIGENPROBLEMS OR CHARACTERISTIC EQUATIONS

In this section, we shall show how the eigenvalues $\{u_k\}$ $(1 \leq k \leq K)$ can be obtained without actually solving the eigenproblem $\widehat{\mathrm{U}}|\Upsilon_k) = u_k|\Upsilon_k)$ or the characteristic equation $Q_K(u) = 0$. Instead of these two latter classical procedures for arriving at the required eigenset $\{u_k\}$, we shall use the Shanks transform [37] and the Rutishauser [66, 67] quotient difference algorithm, the QD. The form of the Shanks transform that will be used here is $e_m(c_n) = \mathrm{H}_{m+1}(c_n)/\mathrm{H}_m(\Delta^2 c_n)$, which for the time signal points c_n from Eq. (42)

can be rewritten as:

$$e_k(c_n) = \frac{1}{\mathrm{W}_k^2} \frac{\mathrm{H}_{k+1}(c_n)}{\mathrm{H}_k(c_n)}, \tag{253}$$

where $\mathrm{W}_k = \prod_{j=1}^{k}(u_j - 1) \neq 0$. Moreover, we have:

$$\frac{\mathrm{H}_{k+1}(c_n)}{\mathrm{H}_k(c_n)} = \mathrm{R}_k^2 d_{k+1} u_{k+1}^n, \quad \mathrm{R}_k = \frac{\mathrm{V}_{k+1}}{\mathrm{V}_k}, \tag{254}$$

where V_k is the Vandermonde determinant [45], which is equal to the product of all the differences $(u_j - u_{j'}) \neq 0$ with $j > j'$:

$$\mathrm{V}_k \equiv \begin{vmatrix} 1 & 1 & \cdots & 1 \\ u_1 & u_2 & \cdots & u_k \\ u_1^2 & u_2^2 & \cdots & u_k^2 \\ \vdots & \vdots & \ddots & \vdots \\ u_1^{k-1} & u_2^{k-1} & \cdots & u_k^{k-1} \end{vmatrix} = \prod_{j=1}^{k} \prod_{j'=1(j>j')}^{k} (u_j - u_{j'}). \tag{255}$$

This determinant is nonsingular. This is due to the inequality $V_k \neq 0$ that holds true because the roots $\{u_j\}$ are never equal to $u_{j'}$ for $j' \neq j$. The quotient $\mathrm{V}_{k+1}/\mathrm{V}_k$ is computed via the Vandermonde determinant with the following:

$$\mathrm{R}_k = \prod_{j=1}^{k} (u_{k+1} - u_j). \tag{256}$$

Thus, the Shanks transform becomes:

$$e_k(c_n) = \rho_k^2 d_{k+1} u_{k+1}^n, \quad \rho_k = \frac{\mathrm{R}_k}{\mathrm{W}_k}. \tag{257}$$

From here it follows, $e_{k-1}(c_{n+1})/e_{k-1}(c_n) = u_k$, so that,

$$u_k = \lim_{n\to\infty} \frac{e_{k-1}(c_{n+1})}{e_{k-1}(c_n)}. \tag{258}$$

The limit $n \to \infty$ is taken on the rhs of this equation since the lhs of the same equation is independent of n. The relation (258) can equivalently be written as:

$$u_k = \lim_{n\to\infty} \frac{\varepsilon_{2k-2}^{(n+1)}}{\varepsilon_{2k-2}^{(n)}}, \tag{259}$$

where $\varepsilon_m(c_n) \equiv \varepsilon_n^{(m)}$ is a quantity that connects the four adjacent elements of the Padé table by the Wynn $\varepsilon-$ recursion [68]:

$$\varepsilon_n^{(m+1)} = \varepsilon_{n+1}^{(m-1)} + \frac{1}{\varepsilon_{n+1}^{(m)} - \varepsilon_n^{(m)}}, \tag{260}$$

$$\varepsilon_n^{(m)} \equiv \varepsilon_m(c_n), \quad \varepsilon_n^{(-1)} = 0, \quad \varepsilon_n^{(0)} = c_n. \tag{261}$$

According to Eq. (253), the transform $e_k(c_n)$ is proportional to the quotient $\mathrm{H}_{k+1}(c_n)/\mathrm{H}_k(c_n)$. Moreover, the constant of proportionality $1/\mathrm{W}_k^2$ is independent on n. Since u_k is obtained from the ratio $e_{k-1}(c_{n+1})/e_{k-1}(c_n)$, the constant $1/\mathrm{W}_k^2$ can be ignored altogether. Therefore, for computation of u_k, it is natural to use only the ratio $\mathrm{H}_k(c_n)/\mathrm{H}_{k-1}(c_n)$ that will be denoted as $\mathrm{H}_k^{(n)}$:

$$\mathrm{H}_k^{(n)} \equiv \frac{\mathrm{H}_k(c_n)}{\mathrm{H}_{k-1}(c_n)}. \tag{262}$$

Employing Eq. (254), we can rewrite Eq. (262) via:

$$\mathrm{H}_k^{(n)} = \mathrm{R}_{k-1}^2 d_k u_k^n. \tag{263}$$

Hence, regarding u_k, we need the quotient $\mathrm{H}_k^{(n+1)}/\mathrm{H}_k^{(n)}$, as in $e_{k-1}(c_{n+1})/e_{k-1}(c_n)$ via Eq. (258). It is convenient to label the quotient $\mathrm{H}_k^{(n+1)}/\mathrm{H}_k^{(n)}$ by $q_k^{(n)}$:

$$q_k^{(n)} \equiv \frac{\mathrm{H}_k^{(n+1)}}{\mathrm{H}_k^{(n)}}. \tag{264}$$

Thus, combining Eqs. (263) and (264), we arrive at $q_k^{(n)} = u_k$, so that:

$$u_k = \lim_{n\to\infty} q_k^{(n)}. \tag{265}$$

In this way, the eigenvalue u_k is obtained directly from the quotient $q_k^{(n)} = \mathrm{H}_k^{(n+1)}/\mathrm{H}_k^{(n)}$ in the limit $n \to \infty$ via Eq. (265). Using Eqs. (262) and (264), we can calculate $q_k^{(n)}$ explicitly as:

$$q_k^{(n)} = \frac{\mathrm{H}_{k-1}(c_n)\mathrm{H}_k(c_{n+1})}{\mathrm{H}_{k-1}(c_{n+1})\mathrm{H}_k(c_n)}. \tag{266}$$

It is also important to introduce another determinantal ratio obtained from Eq. (262) by the simultaneous changes $\mathrm{H}_k^{(n+1)} \to \mathrm{H}_{k+1}^{(n)}$ in the numerator and $\mathrm{H}_k^{(n)} \to \mathrm{H}_k^{(n+1)}$ in the denominator. The new quotient $\mathrm{H}_{k+1}^{(n)}/\mathrm{H}_k^{(n+1)}$ will be

denoted by $e_k^{(n)}$:

$$e_k^{(n)} \equiv \frac{\mathrm{H}_{k+1}^{(n)}}{\mathrm{H}_k^{(n+1)}}. \tag{267}$$

Inserting Eq. (263) into Eq. (267) gives:

$$e_k^{(n)} = \left(\frac{\mathrm{R}_k}{\mathrm{R}_{k-1}}\right)^2 \frac{d_{k+1}}{d_k u_k} \left(\frac{u_{k+1}}{u_k}\right)^n. \tag{268}$$

If the eigenvalues $\{u_k\}$ are ordered according to

$$0 < |u_1| < |u_2| < \cdots < |u_{k-1}| < |u_k| < |u_{k+1}| < \cdots < |u_K| < 1, \tag{269}$$

then it follows from Eq. (268) that:

$$\lim_{n\to\infty} e_k^{(n)} = 0. \tag{270}$$

Thus, the determinantal quotient $e_k^{(n)} = \mathrm{H}_{k+1}^{(n)}/\mathrm{H}_k^{(n+1)}$ tends to zero when $n \to \infty$ provided that the eigenvalues are ordered as in Eq. (269). Similarly to Eq. (266), we can use Eq. (262) to calculate $e_k^{(n)}$ explicitly viz:

$$e_k^{(n)} = \frac{\mathrm{H}_{k-1}(c_{n+1})\mathrm{H}_{k+1}(c_n)}{\mathrm{H}_k(c_n)\mathrm{H}_k(c_{n+1})}. \tag{271}$$

The vectors $\{q_k^{(n)}, e_k^{(n)}\}$ in their respective forms (266) and (271) are recognized to be the same as the corresponding ones from the QD algorithm [66].

The derivation from this section shows that the Shanks transform, the Wynn ε-algorithm, and Rutishauser QD algorithm can all give the eigenvalues $\{u_k\}$ $(1 \le k \le K)$ without resorting to the more conventional procedures, for example, the eigenproblem $\widehat{\mathrm{U}}|\Upsilon_k) = u_k|\Upsilon_k)$ or the characteristic equation $Q_K(u) = 0$. Of course, in practice, the vectors $e_k(c_n)$, $\varepsilon_k(c_n)$, $q_k^{(n)}$, and $e_k^{(n)}$ needed for obtaining the eigenvalues $\{u_k\}$ are not computed via the Hankel determinants at all, but through their respective recursions. Usually, the Shanks and the Rutishauser algorithms are presented and analyzed separately in the literature. However, in this section, we show how the need for the introduction of the two vectors $q_k^{(n)}$ and $e_k^{(n)}$ from the QD algorithm can be naturally motivated within the analysis of the Shanks transform.

26. ANALYTICAL EXPRESSIONS FOR THE GENERAL LANCZOS COUPLING CONSTANTS

Written in the Padé form (240), the function $\mathcal{R}_{2n}^{\mathrm{CF}}(u)$ ought to be identical to the corresponding result $\mathcal{R}_n^{\mathrm{PLA}}(u)$ from the PLA due to the uniqueness of

the Padé approximant proven in Ref. [2]. More specifically, both expressions $\mathcal{R}_{2n}^{\mathrm{CF}}(u)$ and $\mathcal{R}_{n}^{\mathrm{PLA}}(u)$ must represent the same Padé approximants to the same series (52) for $\mathcal{R}(u)$. Therefore, we must have:

$$\mathcal{R}_{2n}^{\mathrm{CF}}(u) = \mathcal{R}_{n}^{\mathrm{PLA}}(u), \tag{272}$$

where $\mathcal{R}_{n}^{\mathrm{PLA}}(u)$ is given in (205) for $K=n$ as the quotient of the two Lanczos polynomials $P_n(u)$ and $Q_n(u)$, that is, $\mathcal{R}_{n}^{\mathrm{PLA}}(u) = (c_0/\beta_1)P_n(u)/Q_n(u)$. We use Eq. (205) to multiply and divide $\mathcal{R}_{n}^{\mathrm{PLA}}(u)$ by $\{\beta_2\beta_3\cdots\beta_n\}$ via $\mathcal{R}_{n}^{\mathrm{PLA}}(u) = c_0[(\beta_2\beta_3\cdots\beta_n)P_n(u)]/[(\beta_1\beta_2\beta_3\cdots\beta_n)]Q_n(u)$ so that:

$$\mathcal{R}_{n}^{\mathrm{PLA}}(u) = c_0\frac{\tilde{P}_n(u)}{\tilde{Q}_n(u)}, \tag{273}$$

$$\tilde{P}_n(u) = \{\beta_2\beta_3\cdots\beta_n\}P_n(u) = \tilde{P}_n^{\mathrm{CF}}(u), \tag{274}$$

$$\tilde{Q}_n(u) = \{\beta_1\beta_2\beta_3\cdots\beta_n\}Q_n(u) = \tilde{Q}_n^{\mathrm{CF}}(u), \tag{275}$$

where $a_1 = c_0$. Letting $n+1 \longrightarrow n$ in Eq. (106), $\tilde{Q}_n(u)$ from the PLA becomes $\tilde{Q}_n(u) = D_{0,n}$, where $D_{0,n}$ is from Eq. (215) for $K=n$. In Eq. (275), the uniqueness of the PA yields the equalities, $\tilde{P}_n(u) = \tilde{P}_n^{\mathrm{CF}}(u)$ and $\tilde{Q}_n(u) = \tilde{Q}_n^{\mathrm{CF}}(u)$. Thus, using Eq. (275) and the expansions for $\{P_n(u),\ Q_n(u)\}$ and $\{\tilde{P}_n^{\mathrm{CF}}(u),\ \tilde{Q}_n^{\mathrm{CF}}(u)\}$ from Eqs. (114) and (242), respectively, we obtain the following:

$$\tilde{p}_{n,n-r} = \frac{\bar{\beta}_n}{\beta_1}p_{n,n-r}, \quad \tilde{q}_n = \bar{\beta}_n q_{n,n-r}, \tag{276}$$

where $\bar{\beta}_n$ is from Eq. (57). The expansion coefficients $q_{n,n-r}$ are given in terms of the Lanczos coupling constants $\{\alpha_n, \beta_n\}$, whereas the parameters $\{a_n\}$ of the continued fractions determine the coefficients $\tilde{q}_{n,n-r}$, as in Eq. (244). Therefore, the relationship (276) between $q_{n,n-r}$ and $\tilde{q}_{n,n-r}$ could be exploited to establish the relationship between the sets $\{\alpha_n, \beta_n\}$ and $\{a_n\}$. With this goal, we consider the first few coefficients $\{q_{n,n-r}\}$ and $\{\tilde{q}_{n,n-r}\}$ from which we deduce the following:

$$\alpha_n = a_{2n+1} + a_{2n+2}, \quad \beta_n^2 = a_{2n}a_{2n+1} \quad (n \geq 1), \tag{277}$$

with $\alpha_0 = a_2$ and $\beta_0 = 0$. These are the sought general analytical expressions for any Lanczos coupling parameters $\{\alpha_n, \beta_n\}$ in terms of the continued fraction coefficients $\{a_n\}$, whose entire set is available from the single closed formula (245). Inserting the expressions for a_{2n} and a_{2n+1} from Eq. (250) into Eq. (277), we can write the following explicit analytical formulae for any

Lanczos coupling parameters $\{\alpha_n, \beta_n\}$:

$$\alpha_n = \frac{\mathrm{H}_{n+1}(c_0)}{\mathrm{H}_n(c_0)} \frac{\mathrm{H}_{n-1}(c_1)}{\mathrm{H}_n(c_1)} + \frac{\mathrm{H}_{n+1}(c_1)}{\mathrm{H}_n(c_1)} \frac{\mathrm{H}_n(c_0)}{\mathrm{H}_{n+1}(c_0)}, \tag{278}$$

$$\beta_n^2 = \frac{\mathrm{H}_{n-1}(c_0)\mathrm{H}_{n+1}(c_0)}{[\mathrm{H}_n(c_0)]^2}. \tag{279}$$

Here, β_n^2 is given exclusively in terms of the determinant of the Schrödinger overlap matrix $\mathrm{H}_m(c_0) = \det \mathbf{S}_m$. Recursive numerical computations of the Hankel determinants $\mathrm{H}_m(c_0)$ and $\mathrm{H}_m(c_1)$ from Eq. (278) can be carried out by, for example, Gordon's [69] product-difference (PD) algorithm that is accurate, efficient, and robust with only $\sim n^2$ multiplications relative to some formidable $n!$ multiplications in the Cramer rule via direct evaluations. Moreover, the same PD recursion can also be used for the CF coefficients $\{a_n\}$ [53].

27. CONTRACTED CONTINUED FRACTIONS

Employing the relationships from (277), we can rewrite the Lanczos continued fraction (230) as:

$$\mathcal{R}^{\mathrm{LCF}}(u) = \frac{a_1}{u - a_2} - \frac{a_2 a_3}{u - (a_3 + a_4)} - \frac{a_4 a_5}{u - (a_5 + a_6)} - \frac{a_6 a_7}{u - (a_7 + a_8)} - \ldots. \tag{280}$$

A truncation of this expression at the order n will give the nth-order LCF approximant:

$$\mathcal{R}_n^{\mathrm{LCF}}(u) = \{\mathcal{R}^{\mathrm{LCF}}(u)\}_{a_m = 0, m \geq 2n+1} \quad (n = 1, 2, 3, \ldots). \tag{281}$$

For an arbitrary positive integer n, the following equivalence exists:

$$\mathcal{R}_n^{\mathrm{LCF}}(u) = \mathcal{R}_{2n}^{\mathrm{CF}}(u) \quad (n = 1, 2, 3, \ldots). \tag{282}$$

This implies, according to $\mathcal{R}_n^{\mathrm{LCF}}(u) = \mathcal{R}_n^{\mathrm{PLA}}(u)$ from Eq. (234), that we have, in general,

$$\mathcal{R}_n^{\mathrm{PLA}}(u) = \mathcal{R}_{2n}^{\mathrm{CF}}(u) \quad (n = 1, 2, 3, \ldots). \tag{283}$$

Let us recall the definition of the contracted continued fraction (CCF). A general CF, say $\tilde{C}(z)$, whose approximants coincide with a subset of the approximants of another continued fraction $C(z)$ is called a contraction of

$C(z)$ [65]. The result (282) shows that the approximant $\mathcal{R}_n^{\mathrm{LCF}}(u)$ of order n of the Lanczos continued fraction $\mathcal{R}^{\mathrm{LCF}}(u)$ is equal exactly to the approximant $\mathcal{R}_{2n}^{\mathrm{CF}}(u)$ of order $2n$ of the continued fraction $\mathcal{R}^{\mathrm{CF}}(u)$ from Eq. (237) of the series (52). Thus, $\mathcal{R}^{\mathrm{CCF}}(u)$ is a contraction of $\mathcal{R}^{\mathrm{CF}}(u)$. Therefore, the PLA is equal to the LCF and the CCF.

28. RECURSIVE SOLUTIONS OF TRIDIAGONAL INHOMOGENEOUS SYSTEMS OF LINEAR EQUATIONS

Here, we shall develop a recurrence algorithm for solving a general tridiagonal inhomogeneous system of n linear equations. This will be illustrated for two important classes of problems, such as the power moment problem and spectral analysis, as frequently encountered in physics and chemistry, as well as in linear algebra.

28.1. Gaussian elimination method

Consider the following system of inhomogeneous equations in the general case [2]:

$$
\begin{aligned}
&B_1x_1 + C_1x_2 + 0 + 0 + 0 + \cdots + 0 + 0 + 0 + 0 = D_1\\
&A_2x_1 + B_2x_2 + C_2x_3 + 0 + \cdots + 0 + 0 + 0 + 0 = D_2\\
&0 + A_3x_2 + B_3x_3 + C_3x_4 + 0 + \cdots + 0 + 0 + 0 + 0 = D_3\\
&\qquad\qquad\qquad\qquad\vdots\\
&0 + 0 + 0 + 0 + 0 + \cdots + A_{n-2}x_{n-3} + B_{n-2}x_{n-2} + C_{n-2}x_{n-1} + 0 = D_{n-2}\\
&0 + 0 + 0 + 0 + 0 + \cdots + 0 + A_{n-1}x_{n-2} + B_{n-1}x_{n-1} + C_{n-1}x_n = D_{n-1}\\
&0 + 0 + 0 + 0 + 0 + \cdots + 0 + 0 + A_nx_{n-1} + B_nx_n = D_n,
\end{aligned}
\tag{284}
$$

where A_r, B_r, C_r, and D_r are the known constants. The equivalent matrix form of (284) reads as:

$$
\begin{pmatrix}
B_1 & C_1 & 0 & 0 & 0 & \cdots & 0 & 0 & 0\\
A_2 & B_2 & C_3 & 0 & 0 & \cdots & 0 & 0 & 0\\
0 & A_3 & B_3 & C_3 & 0 & \cdots & 0 & 0 & 0\\
\vdots & \vdots & \vdots & \vdots & \vdots & \ddots & \vdots & \vdots & \vdots\\
0 & 0 & 0 & 0 & 0 & \cdots & A_{n-1} & B_{n-1} & C_{n-1}\\
0 & 0 & 0 & 0 & 0 & \cdots & 0 & A_n & B_n
\end{pmatrix}
\begin{pmatrix} x_1\\ x_2\\ x_3\\ \vdots\\ x_{n-1}\\ x_n \end{pmatrix}
=
\begin{pmatrix} D_1\\ D_2\\ D_3\\ \vdots\\ D_{n-1}\\ D_n \end{pmatrix},
\tag{285}
$$

or in the abbreviated form:

$$\mathbf{E}\mathbf{x} = \mathbf{D}, \tag{286}$$

where $\mathbf{E} = \{E_{r,s}\}$ is the $n \times n$ matrix with the elements $E_{r,s} = A_r\delta_{r,s+1} + B_s\delta_{r,s} + C_r\delta_{r+1,s}$ and $\delta_{n,m}$ is the Kronecker δ-symbol. In Eq. (284), $\mathbf{x} = \{x_r\}$ is an unknown column vector, whereas $\mathbf{D} = \{D_r\}$ is an inhomogeneous column vector with the given elements D_r $(1 \leq r \leq n)$.

We solve the system (284) by the Gaussian elimination method. To this end, we multiply the last line $A_n x_{n-1} + B_n x_n = D_n$ in Eq. (284) by C_{n-1} and write:

$$C_{n-1}x_n = \frac{C_{n-1}D_n}{B_n} - \frac{A_n C_{n-1}}{B_n}x_{n-1}. \tag{287}$$

Similarly, when the first to the last line in Eq. (284), that is, $A_{n-1}x_{n-2} + B_{n-1}x_{n-1} + C_{n-1}x_n = D_{n-1}$, is multiplied by C_{n-2}, we get:

$$C_{n-2}x_{n-1} = C_{n-2}\frac{D_{n-1} - \dfrac{C_{n-1}D_n}{B_n}}{B_{n-1} - \dfrac{C_{n-1}A_n}{B_n}} - \frac{A_{n-1}C_{n-2}}{B_{n-1} - \dfrac{C_{n-1}A_n}{B_n}}x_{n-2}. \tag{288}$$

Here, we also used the last line in Eq. (284). Similarly, we multiply the second to the last line in Eq. (284), that is, $A_{n-2}x_{n-3} + B_{n-2}x_{n-2} + C_{n-2}x_{n-1} = D_{n-2}$, by C_{n-3} and obtain:

$$C_{n-3}x_{n-2} = C_{n-3}\frac{D_{n-2} - C_{n-2}\dfrac{D_{n-1} - \dfrac{C_{n-1}D_n}{B_n}}{B_{n-1} - \dfrac{C_{n-1}A_n}{B_n}}}{B_{n-2} - \dfrac{A_{n-1}C_{n-2}}{B_{n-1} - \dfrac{C_{n-1}A_n}{B_n}}} - \frac{A_{n-2}C_{n-3}}{B_{n-2} - \dfrac{A_{n-1}C_{n-2}}{B_{n-1} - \dfrac{C_{n-1}A_n}{B_n}}}x_{n-3}. \tag{289}$$

From the particular expressions (287)–(289), we can immediately write down the general recursion for the solution x_r of the system (284). With this aim, let us introduce the two auxiliary vectors V_n and W_n as follows:

$$\left.\begin{aligned} V_n &= \frac{C_n}{B_n - A_n V_{n-1}}, \quad V_0 = 0 \\ W_n &= \frac{D_n - A_n W_{n-1}}{B_n - A_n V_{n-1}}, \quad W_0 = 0 \end{aligned}\right\}. \tag{290}$$

Then, the general element x_r of the column vector $\mathbf{x}=\{x_r\}$ from Eq. (284) or Eq. (285) is given by the following simple recursion:

$$\left.\begin{aligned} x_n &= W_n \\ x_m &= W_{m-1} - V_{m-1}x_{m+1}, \quad (1 \le m < n) \end{aligned}\right\}, \tag{291}$$

where n is the number of equations in Eq. (284). The relationship in Eq. (291) recurs downward from the maximal value n of the subscript to the minimum which is 1.

28.2. The power moment problem

In the power moment problem [69], there is only one nonzero element of the inhomogeneous column vector $\mathbf{D}=\{D_r\}$ from Eq. (284), that is, $D_n \propto \delta_{n,1}$, where $\delta_{n,m}$ is the Kronecker δ-symbol. Thus,

$$B_n=\xi_n, \quad A_n=-\zeta_n^{1/2}, \quad C_n=-\zeta_{n+1}^{1/2}, \quad D_n=-\zeta_1\delta_{n,1}, \tag{292}$$

$$\begin{aligned}
&\xi_1x_1-\zeta_2^{1/2}x_2+0\cdot x_3+0\cdot x_4+0\cdot x_5+\cdots+0=-\zeta_1\\
&-\zeta_2^{1/2}x_1+\xi_2x_2-\zeta_3^{1/2}x_3+0\cdot x_4+0\cdot x_5+\cdots+0=0\\
&0\cdot x_1-\zeta_3^{1/2}x_2+\xi_3x_3-\zeta_4^{1/2}x_4+0\cdot x_5+\cdots+0=0\\
&\qquad\qquad\vdots\\
&0+0+0+0+0+\cdots+0-\zeta_{n-1}^{1/2}x_{n-2}+\xi_nx_{n-1}-\zeta_n^{1/2}x_n=0\\
&0+0+0+0+0+\cdots+0-\zeta_n^{1/2}x_{n-1}+\xi_nx_n=0,
\end{aligned} \tag{293}$$

or in the matrix representation:

$$\begin{pmatrix}
\xi_1 & -\zeta_2^{1/2} & 0 & 0 & 0 & \cdots & 0 & 0 & 0\\
-\zeta_2^{1/2} & \xi_2 & -\zeta_3^{1/2} & 0 & 0 & \cdots & 0 & 0 & 0\\
0 & -\zeta_3^{1/2} & \xi_3 & -\zeta_4^{1/2} & 0 & \cdots & 0 & 0 & 0\\
\vdots & \vdots & \vdots & \vdots & \vdots & \ddots & \vdots & \vdots & \vdots\\
0 & 0 & 0 & 0 & 0 & \cdots & -\zeta_{n-1}^{1/2} & \xi_n & -\zeta_n^{1/2}\\
0 & 0 & 0 & 0 & 0 & \cdots & 0 & -\zeta_n^{1/2} & \xi_n
\end{pmatrix}
\begin{pmatrix} x_1\\ x_2\\ x_3\\ \vdots\\ x_{n-1}\\ x_n \end{pmatrix}$$

$$= -\begin{pmatrix} \zeta_1\\ 0\\ 0\\ \vdots\\ 0\\ 0 \end{pmatrix}. \tag{294}$$

It then follows from Eq. (288) that:

$$-\zeta_n^{1/2}x_n = -\frac{\zeta_n}{\xi_n}x_{n-1}, \quad -\zeta_n^{1/2}x_{n-1} = -\frac{\zeta_{n-1}}{\xi_{n-1}-\dfrac{\zeta_n}{\xi_n}}x_{n-2}, \tag{295}$$

$$-\zeta_{n-2}^{1/2}x_{n-2} = -\frac{\zeta_{n-2}}{\xi_{n-2}-\dfrac{\zeta_{n-1}}{\xi_{n-1}-\dfrac{\zeta_n}{\xi_n}}}x_{n-3}. \tag{296}$$

The recursions (295) and (296) permit extension to the general result for x_2 in n steps:

$$\zeta_2^{1/2}x_2 = \left(\frac{\zeta_2}{\xi_2}-\frac{\zeta_3}{\xi_3}-\frac{\zeta_4}{\xi_4}-\frac{\zeta_5}{\xi_5}-\cdots-\frac{\zeta_{n-1}}{\xi_{n-1}}-\frac{\zeta_n}{\xi_n}\right)x_1. \tag{297}$$

By reference to the first equation of the system (293), we can eliminate x_2 from Eq. (297) so that

$$\zeta_1 = -\left(\xi_1-\frac{\zeta_2}{\xi_2}-\frac{\zeta_3}{\xi_3}-\frac{\zeta_4}{\xi_4}-\frac{\zeta_5}{\xi_5}-\cdots-\frac{\zeta_{n-1}}{\xi_{n-1}}-\frac{\zeta_n}{\xi_n}\right)x_1. \tag{298}$$

Thus, the solution for the first element x_1 of the column vector $\mathbf{x}=\{x_n\}$ $(n=1,2,\dots)$ is

$$x_1 = -\frac{\zeta_1}{\xi_1}-\frac{\zeta_2}{\xi_2}-\frac{\zeta_3}{\xi_3}-\frac{\zeta_4}{\xi_4}-\frac{\zeta_5}{\xi_5}-\cdots-\frac{\zeta_{n-1}}{\xi_{n-1}}-\frac{\zeta_n}{\xi_n}. \tag{299}$$

The solution (299) is the continued fraction of the order n. The system (293) is encountered in statistical mechanics [69] when applying the method of power moments to obtain a sequence of approximations to the partition function $Q(\beta)$ defined as the Stieltjes integral $\int_0^\infty \exp(-\beta E)\mathrm{d}\varphi(E)$, where β is a parameter proportional to the reciprocal temperature of the investigated system, $\mathrm{d}\varphi(E)$ is a density of states, and $\varphi(E)$ is a positive, nondecreasing function of energy E.

28.3. The problem of spectral analysis

The second example from the general system (284) is of direct relevance to the Lanczos continued fraction (LCF). The Lanczos inhomogeneous tridiagonal system of linear equations can be identified from Eq. (284) by specifying $D_n \propto \delta_{n,1}$ and:

$$B_n = u-\alpha_{n-1}, \quad A_n = -\beta_{n-1}, \quad C_n = -\beta_n, \quad D_n = c_0\delta_{n,1}, \tag{300}$$

where α_n and β_n are Lanczos parameters Eq. (54) and Eq. (173). The system Eq. (284) now reads as:

$$\begin{aligned}
&(u-\alpha_0)x_1-\beta_1x_2+0+0+0+\cdots+0+0+0+0=c_0\\
&-\beta_1x_1+(u-\alpha_1)x_2-\beta_2x_3+0+0+\cdots+0+0+0+0=0\\
&0-\beta_2x_2+(u-\alpha_2)x_3-\beta_3x_4+0+\cdots+0+0+0+0=0\\
&\qquad\qquad\vdots\\
&0+0+0+0+0+\cdots+0-\beta_{n-2}x_{n-2}+(u-\alpha_{n-2})x_{n-1}-\beta_{n-1}x_n=0\\
&0+0+0+0+0+\cdots+0+0-\beta_{n-1}x_{n-1}+(u-\alpha_{n-1})x_n=0
\end{aligned} \tag{301}$$

or in the associated matrix form:

$$\begin{pmatrix}
u-\alpha_0 & -\beta_1 & 0 & 0 & 0 & \cdots & 0 & 0 & 0\\
-\beta_1 & u-\alpha_1 & -\beta_2 & 0 & 0 & \cdots & 0 & 0 & 0\\
0 & -\beta_2 & u-\alpha_2 & -\beta_3 & 0 & \cdots & 0 & 0 & 0\\
\vdots & \vdots & \vdots & \vdots & \vdots & \ddots & \vdots & \vdots & \vdots\\
0 & 0 & 0 & 0 & 0 & \cdots & -\beta_{n-2} & u-\alpha_{n-2} & -\beta_{n-1}\\
0 & 0 & 0 & 0 & 0 & \cdots & 0 & -\beta_{n-1} & u-\alpha_{n-1}
\end{pmatrix}
\begin{pmatrix} x_1\\ x_2\\ x_3\\ \vdots\\ x_{n-1}\\ x_n \end{pmatrix}$$

$$= \begin{pmatrix} c_0\\ 0\\ 0\\ \vdots\\ 0\\ 0 \end{pmatrix}. \tag{302}$$

In this case by using Eqs. (287–289), we obtain:

$$-\beta_{n-1}x_n = -\frac{\beta_{n-1}^2}{u-\alpha_{n-1}}x_{n-1} \tag{303}$$

$$-\beta_{n-2}x_{n-1} = -\frac{\beta_{n-2}^2}{u-\alpha_{n-2}-\dfrac{\beta_{n-1}^2}{u-\alpha_{n-1}}}x_{n-2} \tag{304}$$

$$-\beta_{n-3}x_{n-2} = -\frac{\beta_{n-3}^2}{u-\alpha_{n-3}-\dfrac{\beta_{n-2}^2}{u-\alpha_{n-2}-\dfrac{\beta_{n-1}^2}{u-\alpha_{n-1}}}}x_{n-3}. \tag{305}$$

By continuing this recursion further for the next $n-2$ steps, we get

$$\beta_1 x_2 = \left(\frac{\beta_1^2}{u-\alpha_1} \underset{-}{} \frac{\beta_2^2}{u-\alpha_2} \underset{-}{} \frac{\beta_3^2}{u-\alpha_3} \underset{-}{} \cdots \underset{-}{} \frac{\beta_{n-1}^2}{u-\alpha_{n-1}} \right) x_1, \tag{306}$$

where the symbolic notation for the continued fractions is used. We can eliminate x_2 from Eq. (306), and this yields the solution for x_1:

$$x_1 = \frac{c_0}{u-\alpha_0} \underset{-}{} \frac{\beta_1^2}{u-\alpha_1} \underset{-}{} \frac{\beta_2^2}{u-\alpha_2} \underset{-}{} \frac{\beta_3^2}{u-\alpha_3} \underset{-}{} \cdots \underset{-}{} \frac{\beta_{n-1}^2}{u-\alpha_{n-1}}. \tag{307}$$

Hence, the first component x_1 of the n-dimensional column vector $\mathbf{x} = \{x_r\}$ $(1 \le r \le n)$ from Eq. (301) coincides with the Lanczos continued fraction $\mathcal{R}_n^{\mathrm{LCF}}(u)$ to the Green function $\mathcal{R}(u)$ from Eq. (12):

$$\begin{aligned} \mathcal{R}_n^{\mathrm{LCF}}(u) &= x_1 \\ &= \frac{c_0}{u-\alpha_0} \underset{-}{} \frac{\beta_1^2}{u-\alpha_1} \underset{-}{} \frac{\beta_2^2}{u-\alpha_2} \underset{-}{} \frac{\beta_3^2}{u-\alpha_3} \underset{-}{} \cdots \underset{-}{} \frac{\beta_{n-1}^2}{u-\alpha_{n-1}}. \end{aligned} \tag{308}$$

A recursive algorithm for $\mathcal{R}_n^{\mathrm{CF}}(u)$ is available from Eq. (291) as

$$\left. \begin{aligned} \Gamma_m = \frac{1}{u-\alpha_m-\beta_{m+1}^2\Gamma_{m+1}} \quad , \quad \Gamma_{N+1} = 0 \\ \therefore \quad \mathcal{R}_N^{\mathrm{LCF}}(u) = c_0\Gamma_0 \end{aligned} \right\}, \tag{309}$$

where $\Gamma_m \equiv \Gamma_m(u)$, in agreement with Eq. (227). Obviously, the relation Eq. (309) can be expressed through continued fractions from which we have:

$$\mathcal{R}_{e,n}^{\mathrm{CCF}}(u) = \mathcal{R}_{2n}^{\mathrm{CF}}(u) = \mathcal{R}_{e,n}^{\mathrm{LCF}}(u) \quad (n = 1, 2, 3, \ldots). \tag{310}$$

Thus, the LCF of the nth order, $\mathcal{R}_n^{\mathrm{LCF}}(u)$, is the same as $\mathcal{R}_{2n}^{\mathrm{CF}}(u)$, which is an even-order general continued fraction, the CF, obtained from Eq. (239) when the suffix n is taken to be $2n$. In other words, $\mathcal{R}_n^{\mathrm{LCF}}(u)$ is the contracted continued fraction (CCF) relative to $\mathcal{R}_n^{\mathrm{CF}}(u)$, as pointed out in Section 27. To emphasize that we are dealing here with the even part of $\mathcal{R}_n^{\mathrm{CF}}(u)$, we added the subscript "e" (for even) in Eq. (310). The relationship Eq. (308) indicates that the same result for the Lanczos continued fraction $\mathcal{R}_n^{\mathrm{LCF}}(u)$ can also be obtained by finding the first element x_1 of the system Eq. (285) of linear equations. The major practical significance of this equivalence is in the fact that systems of linear equations represent the most robust section of linear algebra packages [48–51]. Even such powerful algorithms are unnecessary

for a special class of inhomogeneous linear systems with tridiagonal structure Eq. (284), since the solution $\{x_r\}$ can be obtained with the help of a remarkably simple recursion Eq. (291).

There is more to the presented strategy than the equivalence Eq. (308). To illuminate an additional advantage of the presented formalism, we shall analyze its application to the quantification problem (harmonic inversion) with the goal of determining the key spectral parameters $\{u_k, d_k\}$. To this end, we rewrite the matrix equation (302) as follows:

$$(u\mathbf{1} - \mathbf{J}) \cdot \mathbf{x} = c_0 \mathbf{e}_1, \tag{311}$$

where $\mathbf{x} = \{x_r\}$ is an unknown column vector, $\mathbf{1}$ is the unit $n \times n$ matrix, $\mathbf{e}_1 = \{1_r\}$ is the unit column vector $1_r = \delta_{r,1}$, and $\mathbf{J} \equiv \mathbf{J}_n = \{\mathrm{J}_{i,j}\}$ is the symmetric tridiagonal Jacobi evolution $n \times n$ matrix in the Lanczos representation from Eq. (60) for $M = n$, that is, $\mathbf{J}_M = \mathbf{J}_n \equiv \mathbf{J}$. The matrix element $\mathrm{J}_{i,j}$ is given by $\mathrm{J}_{i,j} = \alpha_i \delta_{i,j} + \beta_j \delta_{i+1,j} + \beta_i \delta_{i,j+1}$, as in Eq. (58). The matrix equation (311) can formally be solved by writing:

$$\mathbf{x} = c_0 (u\mathbf{1} - \mathbf{J})^{-1} \mathbf{e}_1, \tag{312}$$

assuming that the inverse of $u\mathbf{1} - \mathbf{J}$ exists. As before, we only need the first element x_1 from Eq. (60) to obtain $\mathcal{R}_n^{\mathrm{LCF}}(u)$ as per Eq. (308). We can obtain x_1 by diagonalizing the matrix $\mathbf{J}$ on a basis belonging to a vector space with the symmetric scalar product. This amounts to transforming our system to another basis in which the matrix $\mathbf{J}$ is diagonal, with the eigenvalues $\{u_j\}$ given by:

$$u_j = (\mathbf{T}^{-1} \mathbf{J} \mathbf{T})_{jj}, \tag{313}$$

where $\mathbf{T} = \{\mathrm{T}_{ij}\}$ is the transformation unitary matrix. In the new basis, the vector $\mathbf{x}$ becomes:

$$\mathbf{x} = c_0 \mathbf{T}\mathbf{T}^{-1} (u\mathbf{1} - \mathbf{J})^{-1} \mathbf{T}\mathbf{T}^{-1} \mathbf{e}_1. \tag{314}$$

From here, the first element x_1 is at once extracted as [69]:

$$x_1 = \sum_{j=1}^{n} \frac{d_j}{u - u_j}, \tag{315}$$

$$d_j = c_0 \mathrm{T}_{1j}^2. \tag{316}$$

We recall that the Lanczos continued fraction is equivalent to the Padé–Lanczos approximant, which is defined in Eq. (207) through its polynomial quotient or equivalently via the sum of the Heaviside partial

fractions. The form (315) also coincides with the Heaviside partial fractions (207) of $\mathcal{R}_n^{\mathrm{LCF}}(u)$, as expected due to the equivalence (308). Hence, with the spectral pairs $\{u_j, d_j\}$ found via Eqs. (313 and 316), the formalism from this section based on Ref. [69] solves fully the spectral problem of quantification or the harmonic inversion nonlinear problem by using purely linear algebra for which the most stable algorithms are available [45, 49–51].

29. PADÉ-BASED EXACTNESS AND MATHEMATICAL MODELINGS

Here, we shall carry out a succinct, preparatory analysis needed for the next section which deals with the two important applications of the Padé methodologies in oncology: magnetic resonance spectroscopy for diagnostics and biological modeling of cell surviving fractions for dose planning systems in radiotherapy.

29.1. Recapitulations on exact quantification in MRS by the FPT

For a given time signal $\{c_n\}$ $(0 \le n \le N-1)$, the exact spectrum $F(z)$ of a finite rank N is the truncated Maclaurin expansion:

$$F(z) = \frac{1}{N}\sum_{n=0}^{N-1} c_n z^{-n}; \quad z = \mathrm{e}^{i\omega\tau}, \quad \mathrm{Re}(\omega) > 0. \tag{317}$$

Here, z is a complex harmonic variable, τ is the sampling time, whereas ω ($\omega = 2\pi\nu$) and ν are the complex angular and linear frequency, respectively. The sum in Eq. (317) is also known as the finite-rank Green function. In the current and the next section, the fast Padé transform for $F(z)$ is represented by the two equivalent variants, FPT$^{(\pm)}$, via $F(z) \approx G^{\pm}(z^{\pm 1})$, with $G^{\pm}(z^{\pm 1})$ being the unique polynomial quotients in their respective variables $z^{\pm 1}$:

$$G^{\pm}(z^{\pm 1}) \equiv \frac{P_K^{\pm}(z^{\pm 1})}{Q_K^{\pm}(z^{\pm 1})} = \frac{\sum_{r=r^{\pm}}^{K} p_r^{\pm} z^{\pm r}}{\sum_{s=0}^{K} q_s^{\pm} z^{\pm s}} = b_0^{\pm} + \sum_{k=1}^{K} \frac{d_k^{\pm} z^{\pm 1}}{z^{\pm 1} - z_{k,Q}^{\pm}} = \frac{p_K^{\pm}}{q_K^{\pm}} \prod_{k=1}^{K} \frac{(z^{\pm 1} - z_{k,P}^{\pm})}{(z^{\pm 1} - z_{k,Q}^{\pm})}, \tag{318}$$

where $\{z_{k,P}^{\pm}, z_{k,Q}^{\pm}\}$ are the fundamental harmonics given by the solutions of the characteristic equations $P_K^{\pm}(z_{k,P}^{\pm}) = 0, Q_K^{\pm}(z_{k,Q}^{\pm}) = 0$. Further, $\{p_r^{\pm}, q_s^{\pm}\}$ $(r^{+} = 1, r^{-} = 0)$ are the expansion coefficients and $b_0^{\pm} = p_0^{\pm}/q_0^{\pm}$ with $b_0^{+} = 0$ due to $p_0^{+} = 0$. Quantities, $d_k^{\pm}$ are the fundamental amplitudes (the Cauchy residues of $G^{\pm}$) $d_k^{\pm} = \{P_K^{\pm}(z^{\pm 1})/[(\mathrm{d}/\mathrm{d}z^{\pm 1})Q_K^{\pm}(z^{\pm 1})]\}_{z^{\pm 1} = z_{k,Q}^{\pm}} = (p_K^{\pm}/q_K^{\pm}) \prod_{k'=1}^{K}(z^{\pm 1} - z_{k',Q}^{\pm})/\{[(z^{\pm 1} - z_{k',Q}^{\pm})]_{k' \ne k}\}$. The second subscripts P and Q in the fundamental harmonics are introduced as a reminder that $z_{k,P}^{\pm}$ and $z_{k,Q}^{\pm}$ satisfy the secular equations for the $P_K^{\pm}(z^{\pm 1})$ and $Q_K^{\pm}(z^{\pm 1})$ polynomials, respectively. This distinction is needed especially when dealing with Froissart doublets. The

polynomial expansion coefficients $\{p_r^{\pm}, q_s^{\pm}\}$ are determined from the definition of the FPT$^{(+)}$ and FPT$^{(-)}$ through the asymptotes for $z \to 0$ and $z \to \infty$ via $F(z) - G^{\pm}(z^{\pm 1}) = \mathcal{O}^{\pm}(z^{\pm(2K+1)})$, where $\mathcal{O}^{\pm}(z^{\pm(2K+1)})$ symbolizes the residual series (errors) that begin with powers $z^{\pm(2K+1)}$. These definitions yield the systems of linear equations for the coefficients $\{p_r^{\pm}\}$ and $\{q_s^{\pm}\}$ of $P_K^{\pm}(z^{\pm 1})$ and $Q_K^{\pm}(z^{\pm 1})$ as $\sum_{s=1}^{K} q_s^{+} c_{m+1} = -c_m$, $p_\ell^{+} = \sum_{r=0}^{K-\ell} c_r q_{r+\ell}^{+}$ $(0 \le m \le L, 1 \le \ell \le K)$ for the FPT$^{(+)}$ and $\sum_{s=1}^{K} q_s^{-} c_{K+m-s} = -c_{K+m}$, $p_\ell^{-} = \sum_{r=0}^{\ell} c_r q_{\ell-r}^{-}$ $(1 \le m \le L, 0 \le \ell \le K)$ for the FPT$^{(-)}$. There are two systems of these equations in each variant of the FPT, but only those for the coefficients $\{q_s^{\pm}\}$ need to be explicitly solved. This is because when the sets $\{q_s^{\pm}\}$ become available, the equations for $\{p_r^{\pm}\}$ are automatically the analytical expressions with all the known quantities and, thus, no system for the coefficients of the polynomials $P_K^{\pm}(z^{\pm 1})$ should be solved. The convergence regions in $G^{\pm}(z^{\pm 1})$ from Eq. (318) for the FPT$^{(+)}$ and the FPT$^{(-)}$ are inside ($|z| < 1$) and outside ($|z| > 1$) the unit circle, respectively.

Once the polynomials $P_K^{\pm}$ and $Q_K^{\pm}$ are uniquely extracted from the given FID using Eq. (318), the FPT$^{(\pm)}$ can yield the complex mode spectra $P_K^{\pm}/Q_K^{\pm}$ whose variables $z^{\pm 1}$ are defined at an arbitrary frequency ω. This is advantageous relative to the FFT, whose spectra $F_k \equiv F(\mathrm{e}^{-2\pi i k/N})$ are limited to the Fourier grid $\{2\pi k/(N\tau)\}$ $(0 \le k \le N-1)$ with no interpolation or extrapolation features based upon the studied FID. The difference $2\pi/(N\tau)$ between any two equidistant Fourier grid points represents the resolution in the FFT, which is predetermined by the total acquisition time, $T = N/\tau$. To resolve any two closely spaced resonances, the FFT requires long T, due to the lack of extrapolation features in the FFT. However, at long T physical harmonics from a time signal decay practically to zero (due to the exponential damping for complex fundamental frequencies), so that noise becomes dominant. Such difficulties are absent from the FPT due to the extrapolation and interpolation characteristics of the rational functions from Eq. (318).

Overall, the FFT can estimate merely the total lineshapes of the spectral peaks, but not their parameters. By definition, nonparametric estimators, such as the FFT, cannot solve autonomously the quantification problem. To this end, postprocessing is needed via fitting, numerical quadratures for peak areas, etc. By contrast, the FPT can obtain the spectral lineshapes and the peak parameters on the same footing. Such a key advantage is due to both nonparametric and parametric signal processing in the FPT. As a nonparametric analyzer, the FPT yields the total shape spectra by computing the quotients $P_K^{\pm}/Q_K^{\pm}$ at the selected frequencies ω from any desired range and spacing without the need to perform quantification at all. When applied as a parametric estimator, the FPT solves the quantification problem explicitly and exactly by computing the spectral parameters (positions, widths, heights, and phases) from the reconstructed fundamental harmonics $z_{k,Q}^{\pm}$ and amplitudes $d_k^{\pm}$ for every physical resonance. This is accomplished by rooting the denominator polynomials $Q_K^{\pm}$ to obtain the fundamental

frequencies $\{\omega_k^{\pm}\} \equiv \{\omega_{k,Q}^{\pm}\}$ and using the quoted analytical formulae for the Cauchy residues of $P_K^{\pm}/Q_K^{\pm}$ to compute the amplitudes $\{d_k^{\pm}\}$.

A critically important feature of the FPT is its ability to reconstruct exactly the total true number of physical harmonics in the given FID. Each FID is a sum of damped complex exponentials with stationary and nonstationary (polynomial type) amplitudes, associated with nondegenerate (Lorentzian) and degenerate (non-Lorentzian) spectra. This type of FID is ubiquitous across interdisciplinary research fields, including MRS. In practice, determination of the exact number of resonances can be accomplished via Froissart doublets (pole-zero cancellations). The total number of genuine resonances is given by the degree K of the denominator polynomials $Q_K^{\pm}$. The only known information about this degree K is that it must obey the inequality $2K \leq N$. Algebraically, the $2K$ unknown spectral parameters (frequencies and amplitudes) require at least $2K$ signal points from the whole set of N available FID entries. To unambiguously determine K, one computes a short sequence of the FPTs by varying the degree K' of the polynomials in the Padé spectra $\{P_{K'}^{\pm}/Q_{K'}^{\pm}\}$ until all the results stabilize/saturate. When this happens, say at some $K' = K''$, we are sure that the true number K is obtained as $K = K''$. If we keep increasing the running order K' of the FPT beyond the stabilized value K, we would always obtain the same results for $K' = K + m$ and for K using any positive integer m as $P_{K+m}^{\pm}(z^{\pm 1})/Q_{K+m}^{\pm}(z^{\pm 1}) = P_K^{\pm}(z^{\pm 1})/Q_K^{\pm}(z^{\pm 1})$ $(m = 1, 2, ...)$. The mechanism by which this is achieved (the maintenance of the overall stability, including the constancy of the value of the true number of resonances) is provided by the pole-zero cancellation. By not knowing the exact number K in advance, we would keep increasing the order $K' = K + m$, and this would lead to extra roots from $P_{K+m}^{\pm}$ and $Q_{K+m}^{\pm}$. All the roots of $P_{K+m}^{\pm}$ and $Q_{K+m}^{\pm}$ are the respective zeros and poles in the spectra $P_{K+m}^{\pm}/Q_{K+m}^{\pm}$ because these latter rational polynomials are meromorphic functions. Such extra zeros and poles are spurious, as they cannot be found in the input FID, which is built from K true harmonics alone. The unequivocal signatures of spurious poles and zeros are their coincidences $z_{k,Q}^{\pm} = z_{k,P}^{\pm}$. Moreover, spurious amplitudes are zero-valued $d_k^{\pm} = 0$ at $z_{k,Q}^{\pm} = z_{k,P}^{\pm}$, as per the stated formulae for the Cauchy residues that are the differences between poles and zeros. Therefore, in the spectra $P_{K+m}^{\pm}/Q_{K+m}^{\pm}$ for $m > 1$, all spurious poles and zeros, found beyond the stabilized number K of resonances, will automatically cancel each other because of the special form of the Padé spectrum given by the polynomial quotients. Hence stability of the Padé spectra via the said relation $P_{K+m}^{\pm}/Q_{K+m}^{\pm} = P_K^{\pm}/Q_K^{\pm}$ $(m = 1, 2, ...)$. Such a stabilization condition is the signature of the determination of the exact total number K of resonances. This stability stems primarily from the constancy of the fundamental spectral parameters that are reconstructed exactly from the FID by the FPT$^{(\pm)}$. Both the pole-zero cancellations leading to the true K and the exact reconstruction of all the fundamental frequencies as well as the amplitudes are illustrated in the next section.

29.2. Padé approximant for cell surviving fractions in radiobiological modelings

Theoretical descriptions for cell survival upon irradiation are of critical importance for accuracy in dose planning systems for cancer therapy by particle and ray beams. The simplest theory is obtained by adapting the radioactive decay law without cell repair, as done in the linear (L) model for the cell surviving fraction, $S_F^{(L)}(D) = e^{-\alpha D}$, where D is the absorbed dose. Here, the sensitivity parameter $\alpha > 0$ describes the direct cell kill per gray (Gy). The resulting dose–effect curve is linear via a straight line in a semilogarithmic plot for $S_F^{(L)}(D)$. However, the corresponding experimental data show deviations via a shoulder at intermediate doses. This is due to the lack of cell repair in the L model. The situation is partially remedied via the replacement of αD in the L model by the biological effect $E(D) = \alpha D + \beta D^2$. Parameter $\beta > 0$ multiplying the quadratic (D^2) term approximately describes the cell repair per Gy^2. Substitution of $E(D)$ for αD in the L model gives the linear-quadratic (LQ) model, $S_F^{(LQ)}(D) = e^{-\alpha D - \beta D^2}$. Here, the linear $e^{-\alpha D}$ and quadratic $e^{-\beta D^2}$ terms dominate at low and high doses, respectively. Often, the LQ model compares reasonably well with measurements at low and intermediate doses. However, at high doses, experimental data behave like $S_F(D) \sim e^{-D/D_0}$, as opposed to the corresponding Gaussian asymptote $S_F^{(LQ)}(D) \sim e^{-\beta D^2}$ of the LQ model. Dose D_0, as the reciprocal of the final slope, represents the dose at which the surviving fraction e^{-D/D_0} drops by a factor of $1/e \approx 1.27183 \approx 0.3679$, or by 36.79%. Thus, D_0 can be taken as one of the input data to theoretical modelings, since it can be easily and accurately determined even by hand from the final portion of any experimentally measured survival curve $S_F(D)$ plotted on a semilogarithmic graph. To amend the LQ model, we have introduced the Padé Linear Quadratic (PLQ) model, which automatically provides a missing smooth transition from the quadratic (D^2) to the linear (D) term at large doses. This is done by conceiving the LQ-based effect $\alpha D + \beta D^2$ merely as the first two expansion terms of a series. Such a series could be modeled by its Padé approximant, or PA, as a ratio of two polynomials. In so doing, the PLQ is constrained to simultaneously satisfy two conditions: (i) preservation of the formal expression for the LQ-based effect $\alpha D + \beta D^2$, which now appears as the numerator of the PA, and (ii) improvement of the incorrect high-dose limit of the LQ model by the denominator $1 + \gamma D\,(\gamma > 0)$ of the Padé-based biological effect via $E_P(D) = (\alpha D + \beta D^2)/(1 + \gamma D)$. This yields the PLQ model:

$$S_F^{(PLQ)}(D) = e^{-\frac{\alpha D + \beta D^2}{1 + \gamma D}}. \tag{319}$$

We use the same labels α and β in $S_F^{(LQ)}(D)$ and $S_F^{(PLQ)}(D)$, but the numerical values of these parameters differ in the two theories. There is one extra parameter (γ) in the PLQ relative to the LQ model. However, γ need not

be an independent parameter. It could be constrained to the form $\gamma = \beta D_0$, where D_0 is the required final slope, which can be taken from the input data, as explained. In this way, the PLQ model possesses only two free parameters α and β, as in the LQ model. The initial and final slopes in the PLQ model are given by α and β/γ. Hence, at high doses, the PLQ possesses the exponential fall-off $S_{\rm F}^{(\rm PLQ)}(D) \approx {\rm e}^{-\beta D/\gamma} = {\rm e}^{-D/D_0}$, as in measurements. In the LQ model, the initial slope is α, but the high-dose limit of $S_{\rm F}^{(\rm LQ)}(D)$ continues to bend following a Gaussian curve with no final slope. The PLQ model can also be derived from the Michaelis–Menten enzyme kinetics for lesion recovery through saturable repair. This is seen in the Padé-based biological effect $\mathrm{E_P}(D) = [1 + (\beta/\alpha)D][\alpha D/(1 + \gamma D)]$, where $1 + (\beta/\alpha)D$ describes precipitation of the average specific energy around sublesions and $\alpha D/(1 + \gamma D)$ is the Michaelis–Menten rate for conversion of sublesions to repaired lesions. In this latter term, as the number of sublesions αD increases, the average repair rate $\alpha/(1 + \gamma D)$ per repairable lesion decreases, due to both an overload and a limited amount of enzymes. As a result, $\alpha D/(1 + \gamma D)$ tends to a constant, $\alpha/\gamma = (1/D_0)(\alpha/\beta)$, at large doses. Thus, saturation of the enzymes complex repair system is correctly described by the PLQ model. Detailed comparisons with many experimental data systematically reveal a clear out-performance of the LQ by the PLQ model, as will also be shown in the next section.

30. ILLUSTRATIONS

30.1. Magnetic resonance spectroscopy

We use Eq. (42) to generate a noise-free complex-valued synthesized time signal $\{c_n\}(0 \le n \le N - 1)$ or equivalently the free induction decay (FID) curve. The chosen signal length N is 1024, and the bandwidth is set to be 1000 Hz. This yields the sampling rate $\tau = 1$ ms and the total duration time of the signal $T = N\tau = 1.024$ s. Table 4.1 gives the input data for the quantification problem to be solved in the present work. These data are the complex fundamental frequencies and the corresponding amplitudes from the noise-free model signal (42) whose associated spectrum is comprised of a total of 25 resonances, some of which are individual although tightly packed peaks, whereas others are closely overlapped or nearly degenerate. The numerical values of the spectral parameters were chosen to correspond to the typical frequencies and amplitudes found in proton MR time signals encoded in vivo from a healthy human brain at 1.5T [71]. The columns in Table 4.1 of the input fundamental transients are headed by labels n_k°, Re(ν_k) (ppm), Im(ν_k) (ppm), $|d_k|$ (au), and M_k, which represent the running number, real and imaginary frequencies (both in parts per million, ppm), absolute values of amplitudes (in arbitrary units, au), and the molecular (metabolite) assignments, respectively. The phases of all the amplitudes are set to be equal to zero.

On inspection of the values of all the other fundamental parameters for the synthesized time signal from Table 4.1, it can be seen that the corresponding

Table 4.1 Four-digit numerical values for all the input spectral parameters: the real $\mathrm{Re}(\nu_k)$ and imaginary $\mathrm{Im}(\nu_k)$ parts of the complex frequencies ν_k, and the absolute values $|d_k|$ of the complex amplitudes d_k of 25 damped complex exponentials from the synthesized time signal Eq. (42) similar to a short echo time ($\sim$20 ms) encoded FID via MRS at the magnetic field strength $B_0 = 1.5\mathrm{T}$ from a healthy human brain [71]. Every phase $\{\phi_k\}$ of the amplitudes is set to zero (0.000), for example, each d_k is chosen as purely real, $d_k = |d_k| \exp(i\phi_k) = |d_k|$. The letter M_k denotes the kth metabolite

INPUT DATA for ALL SPECTRAL PARAMETERS of a SYNTHESIZED TIME SIGNAL or FID				
no	$\mathrm{Re}(\nu_k)$ (ppm)	$\mathrm{Im}(\nu_k)$ (ppm)	$\lvert d_k\rvert$ (au)	M_k
1	0.985	0.180	0.122	Lip
2	1.112	0.257	0.161	Lip
3	1.548	0.172	0.135	Lip
4	1.689	0.118	0.034	Lip
5	1.959	0.062	0.056	Gaba
6	2.065	0.031	0.171	NAA
7	2.145	0.050	0.116	NAAG
8	2.261	0.062	0.092	Gaba
9	2.411	0.062	0.085	Glu
10	2.519	0.036	0.037	Gln
11	2.675	0.033	0.008	Asp
12	2.676	0.062	0.063	NAA
13	2.855	0.016	0.005	Asp
14	3.009	0.064	0.065	Cr
15	3.067	0.036	0.101	PCr
16	3.239	0.050	0.096	Cho
17	3.301	0.064	0.065	PCho
18	3.481	0.031	0.011	Tau
19	3.584	0.028	0.036	m-Ins
20	3.694	0.036	0.041	Glu
21	3.803	0.024	0.031	Gln
22	3.944	0.042	0.068	Cr
23	3.965	0.062	0.013	PCr
24	4.271	0.055	0.016	PCho
25	4.680	0.108	0.057	Water

exact absorption spectrum, defined as the real part of the associated complex-valued spectrum, possesses a variety of structures, including isolated, overlapped, tightly overlapped, and nearly degenerate resonances. The exact absorption component shape spectra for the clinically most informative

frequencies (0–5 ppm) will have isolated, but closely-lying resonances that are associated with the following 10 peaks: $n_k^\circ = 8, 9, 10, 13, 18, 19, 20, 21, 24, 25$ located at chemical shifts 2.261 ppm, 2.411 ppm, 2.519 ppm, 2.855 ppm, 3.481 ppm, 3.584 ppm, 3.694 ppm, 3.803 ppm, 4.271 ppm, 4.680 ppm, respectively. In addition, overlapped resonances will appear corresponding to the following 11 peaks: $n_k^\circ = 1, 2$ (0.985 ppm, 1.112 ppm), $n_k^\circ = 3, 4$ (1.548 ppm, 1.689 ppm), $n_k^\circ = 5, 6, 7$ (1.959 ppm, 2.065 ppm, 2.145 ppm), $n_k^\circ = 14, 15$ (3.009 ppm, 3.067 ppm), and $n_k^\circ = 16, 17$ (3.239 ppm, 3.301 ppm). The very closely overlapped resonances will appear as the following two peaks: $n_k^\circ = 22, 23$ (3.944 ppm, 3.965 ppm). These latter resonances are separated from each other by 0.021 ppm. Finally, there will be almost degenerate resonances that are comprised of two peaks $n_k^\circ = 11, 12$ (2.675 ppm, 2.676 ppm) separated by a mere 0.001 ppm. In the absorption total shape spectrum, these two nearly coincident peaks will be completely unresolved and will appear as a single resonance. It is expected that in the $n_k^\circ = 11$ and 12 peaks of near degeneracy all the conventional fitting techniques would fail to detect the smaller peak ($n_k^\circ = 11$). In fact, there would be no justifiable reason to initialize fitting two peaks for a resonance that appears to be a single structure. Even if a fitting procedure were to begin with the two preassigned modeling resonances, disregarding the appearance of a bell-shaped single peak, there would be no justifiable reason for not choosing even a larger number, for example, three, four, or more small peaks below the dominant resonance $n_k^\circ = 12$.

We shall also carry out spectral analysis using a noise-corrupted time signal. The specifics of the present model for the noise run are as follows. We add random numbers $\{r_n\}$ to the mentioned noiseless time signal $\{c_n\}$ to generate the noisy input data $\{c_n + r_n\}$ $(0 \le n \le N-1)$. More precisely, this additive noise r_n is a set $\{r_n\}$ $(0 \le n \le N-1)$ of N random Gauss-distributed zero mean numbers (orthogonal in the real and imaginary parts) with the standard deviation $\sigma = \lambda \times \text{RMS}$. Here, λ is the selected noise level and the acronym RMS stands for root mean square (or equivalently the quadratic mean) of the noiseless time signal. For the given noiseless set $\{|c_n|\}$ generated with the spectral parameters from Table 1, RMS is defined by the arithmetic mean (average) value, $\text{RMS} = \left(\sum_{n=0}^{N} |c_n|^2/N\right)^{1/2}$. According to our noise model, adding λ% noise $\{r_n\}$ to noiseless data $\{c_n\}$ of $\text{RMS}_{\text{noise-free}}$ would produce noisy data $\{c_n + r_n\}$ whose $\text{RMS}_{\text{noise-corrupted}}$ is λ% of $\text{RMS}_{\text{noise-free}}$ so that $\text{RMS}_{\text{noise-corrupted}} = \lambda\, \text{RMS}_{\text{noise-free}}$. Here, λ is a fixed number expressed in percent. For example, adding 10% noise would yield a new RMS (noisy), which is 10% of the old RMS (noiseless), $\sigma = 0.01\, \text{RMS}_{\text{noise-free}}$. In the present computations, we shall fix the noise level λ to be a constant number equal to 0.00289 so that $\sigma = 0.00289\, \text{RMS}$ in which, as stated, $\text{RMS} \equiv \text{RMS}_{\text{noise-free}}$. The value 0.00289 in the standard deviation σ of noise is chosen to approximately match 1.5% of the height of the weakest resonance ($n_k^\circ = 13$) in the spectrum. Such a noise level is sufficient to illustrate the main principles

of Froissart doublets. However, the Padé-based processing can successfully handle spectra and images with much higher noise levels in simulated and encoded data as shown in Refs. [28, 29], but this is not presently displayed within Froissart doublets due to clutter of an exceedingly large number of spurious resonances. Crucially, however, for quantitative inspection by the FPT, the tabular output list is of primary significance. Thus, a possible clutter on graphs with reduced visibility is of no relevance to the usefulness of the concept of Froissart doublets.

We shall begin with the analysis for the noise-free FID. Table 4.2 presents the detailed convergence rates of the numerical values of the complex frequencies and amplitudes for the reconstructed resonances by the FPT$^{(-)}$ using six partial signal lengths ($N/32 = 32$, $N/16 = 64$, $N/8 = 128$, $N/4 = 256$, $N/2 = 512$), as well as the full FID ($N = 1024$). In panels (i), (ii), and (iii) of Table 4.2, the spectral parameters of the detected 10, 14, and 20 resonances are shown at $N/32 = 32, N/16 = 64$, and $N/8 = 128$, respectively. Clearly, these latter findings are approximate values for the corresponding exact input data for the parameters. This occurs because the number of signal points ($N/M \leq 128$) is not sufficient. In contrast, panels (iv), (v), and (vi) of Table 4.2 display the spectral parameters found at $N/4 = 256, N/2 = 512$, and $N = 1024$, respectively. These latter results should be compared with the corresponding input data from Table 4.1. It, thereby, can be seen that from, for example, panel (iv) of Table 4.2 for a quarter ($N/4 = 256$) of the full signal length N that the FPT$^{(-)}$ has retrieved the entire set of 25 resonances with all their exact values for all the spectral parameters. Furthermore, it is remarkable that these reconstructed spectral parameters remain totally unchanged, even after attaining full convergence, when further signal points are included beyond $N/4$. This is shown on panels (v) and (vi) for $N/2 = 512$ and $N = 1024$, respectively. This unique feature of the Padé polynomial quotient, for example, P_K^-/Q_K^- and so on, is related to pole-zero cancellations or Froissart doublets. A veritable signature of reconstruction of the true number K of resonances is provided by the attained convergence of the spectral parameters. If one continues to increase K in the ratio P_K^-/Q_K^- even after convergence has been achieved, the converged results for the Padé quotient in the FPT$^{(-)}$ will not change because the new poles from Q_{K+m}^- will be exactly the same as the new zeros of P_{K+m}^-. In such cases, pole-zero cancellation occurs in the Padé quotient yielding $P_{K+m}^-/Q_{K+m}^- = P_K^-/Q_K^-$, where m is any positive integer. We have verified that this holds true in the present computation, as seen on panels (iv)–(vi) of Table 4.2. Synergistically, the same computation demonstrates that all the amplitudes $\{d_k^-\}$ associated with the poles from the Froissart doublets are identical to zero. Theoretically, the strict algebraic condition $2K = N$ implies that only 100 FID points should be sufficient for the FPT$^{(-)}$ to exactly reconstruct all the 25 unknown complex frequencies and 25 complex amplitudes. However, panel (iv) of Table 4.2 reveals that full convergence is attained

Table 4.2 Convergence of the spectral parameters in the FPT$^{(-)}$ for signal lengths N/M ($N = 1024, M = 1$–32)

CONVERGENCE of SPECTRAL PARAMETERS in FPT$^{(-)}$; FID LENGTH: N/M, $N = 1024$, $M = 1$–32

(i) $N/32 = 32$ (15 Missing Peaks)				(ii) $N/16 = 64$ (11 Missing Peaks)			
n_k^o	Re(ν_k^-) (ppm)	Im(ν_k^-) (ppm)	$\lvert d_k^-\rvert$ (au)	n_k^o	Re(ν_k^-) (ppm)	Im(ν_k^-) (ppm)	$\lvert d_k^-\rvert$ (au)
1	1.010	0.206	0.223	1	0.989	0.180	0.130
–	–	–	–	2	1.121	0.241	0.148
3	1.517	0.420	0.254	3	1.562	0.206	0.195
4	1.643	0.097	0.038	–	–	–	–
–	–	–	–	5	2.030	0.012	0.026
6	2.064	0.069	0.339	6	2.055	0.071	0.376
–	–	–	–	–	–	–	–
–	–	–	–	–	–	–	–
–	–	–	–	9	2.473	0.193	0.313
–	–	–	–	10	2.590	0.054	0.062
–	–	–	–	–	–	–	–
12	2.637	0.274	0.421	–	–	–	–
–	–	–	–	–	–	–	–
–	–	–	–	–	–	–	–
15	3.055	0.139	0.417	15	3.057	0.051	0.160
–	–	–	–	16	3.237	0.071	0.177
17	3.376	0.038	0.018	–	–	–	–
–	–	–	–	–	–	–	–
–	–	–	–	19	3.565	0.045	0.035
–	–	–	–	–	–	–	–
–	–	–	–	21	3.776	0.068	0.075
–	–	–	–	22	3.941	0.048	0.087
23	3.968	0.114	0.222	–	–	–	–
24	4.093	0.083	0.080	24	4.269	0.054	0.016
25	4.681	0.106	0.056	25	4.680	0.108	0.057

(iii) $N/8 = 128$ (5 Missing Peaks)				(iv) $N/4 = 256$ (Converged)			
n_k^o	Re(ν_k^-) (ppm)	Im(ν_k^-) (ppm)	$\lvert d_k^-\rvert$ (au)	n_k^o	Re(ν_k^-) (ppm)	Im(ν_k^-) (ppm)	$\lvert d_k^-\rvert$ (au)
1	0.985	0.180	0.122	1	0.985	0.180	0.122
2	1.112	0.256	0.160	2	1.112	0.257	0.161
3	1.545	0.169	0.123	3	1.548	0.172	0.135
4	1.704	0.134	0.051	4	1.689	0.118	0.034
5	2.012	0.072	0.331	5	1.959	0.062	0.056
6	2.045	0.042	0.331	6	2.065	0.031	0.171
7	2.157	0.037	0.041	7	2.145	0.050	0.116
–	–	–	–	8	2.261	0.062	0.092
9	2.351	0.015	0.008	9	2.411	0.062	0.085
10	2.507	0.129	0.196	10	2.519	0.036	0.037
–	–	–	–	11	2.675	0.033	0.008
12	2.655	0.048	0.059	12	2.676	0.062	0.063
13	2.809	0.018	0.001	13	2.855	0.016	0.005
–	–	–	–	14	3.009	0.064	0.065
15	3.072	0.053	0.183	15	3.067	0.036	0.101
16	3.231	0.078	0.207	16	3.239	0.050	0.096
17	3.367	0.035	0.011	17	3.301	0.064	0.065
–	–	–	–	18	3.481	0.031	0.011
19	3.588	0.022	0.025	19	3.584	0.028	0.036
20	3.699	0.041	0.047	20	3.694	0.036	0.041
21	3.803	0.027	0.036	21	3.803	0.024	0.031
22	3.944	0.046	0.084	22	3.944	0.042	0.068
–	–	–	–	23	3.965	0.062	0.013
24	4.271	0.055	0.016	24	4.271	0.055	0.016
25	4.680	0.108	0.057	25	4.680	0.108	0.057

(*Continued*)

Table 4.2 (Continued)

(v) $N/2 = 512$ (Converged)				(vi) $N = 1024$ (Converged)			
n_k^o	$\mathrm{Re}(\nu_k^-)$ (ppm)	$\mathrm{Im}(\nu_k^-)$ (ppm)	$\lvert d_k^- \rvert$ (au)	n_k^o	$\mathrm{Re}(\nu_k^-)$ (ppm)	$\mathrm{Im}(\nu_k^-)$ (ppm)	$\lvert d_k^- \rvert$ (au)
1	0.985	0.180	0.122	1	0.985	0.180	0.122
2	1.112	0.257	0.161	2	1.112	0.257	0.161
3	1.548	0.172	0.135	3	1.548	0.172	0.135
4	1.689	0.118	0.034	4	1.689	0.118	0.034
5	1.959	0.062	0.056	5	1.959	0.062	0.056
6	2.065	0.031	0.171	6	2.065	0.031	0.171
7	2.145	0.050	0.116	7	2.145	0.050	0.116
8	2.261	0.062	0.092	8	2.261	0.062	0.092
9	2.411	0.062	0.085	9	2.411	0.062	0.085
10	2.519	0.036	0.037	10	2.519	0.036	0.037
11	2.675	0.033	0.008	11	2.675	0.033	0.008
12	2.676	0.062	0.063	12	2.676	0.062	0.063
13	2.855	0.016	0.005	13	2.855	0.016	0.005
14	3.009	0.064	0.065	14	3.009	0.064	0.065
15	3.067	0.036	0.101	15	3.067	0.036	0.101
16	3.239	0.050	0.096	16	3.239	0.050	0.096
17	3.301	0.064	0.065	17	3.301	0.064	0.065
18	3.481	0.031	0.011	18	3.481	0.031	0.011
19	3.584	0.028	0.036	19	3.584	0.028	0.036
20	3.694	0.036	0.041	20	3.694	0.036	0.041
21	3.803	0.024	0.031	21	3.803	0.024	0.031
22	3.944	0.042	0.068	22	3.944	0.042	0.068
23	3.965	0.062	0.013	23	3.965	0.062	0.013
24	4.271	0.055	0.016	24	4.271	0.055	0.016
25	4.680	0.108	0.057	25	4.680	0.108	0.057

with the first 256 time signal points. This occurs because the FPT$^{(-)}$ produces genuine and spurious resonances. In other words, in the polynomial quotient P_K^-/Q_K^-, spurious poles and spurious zeros from the denominator and the numerator, respectively, exist in pairs as Froissart doublets. Therefore, they cancel each other. Thus, each addition of more time signal points yields new Froissart doublets. However, another process takes place at the same time, namely stabilization of the values of the reconstructed physical spectral parameters. Ultimately, saturation occurs when the total number of genuine resonances stop fluctuating. At that point, all the spectral parameters become constant for varying partial signal length. This process of stabilization illustrates how the FPT$^{(-)}$ determines, with certainty, the true total number K of genuine resonances. For the time signal that is currently under study, this stabilization actually takes place by using less than a quarter $N/4 = 256$ of the full FID.

Table 4.3 for the reconstructed spectral parameters from the FPT$^{(+)}$ (left column) and FPT$^{(-)}$ (right column) focuses on a narrow convergence range with three partial signal lengths $N_P = 180, 220, 260$. This is suggested by Table 4.2 in which all the parameters are found to have converged in the interval $[N/8, N/4] = [128, 256]$. Before full convergence, at the lowest partial signal length considered in Table 4.3 ($N_P = 180$) on panels (i) and (iv), peak $n_k^\circ = 11$

Table 4.3 Convergence of the spectral parameters in the FPT$^{(+)}$ and FPT$^{(-)}$ near full convergence for signal lengths $N_P = 180, 220, 260$

FAST PADE TRANSFORM: INSIDE and OUTSIDE the UNIT CIRCLE, FPT$^{(+)}$ and FPT$^{(-)}$; $N_P = 180, 220, 260$

(i) $N_P = 180$ (1 Missing Peak)				(ii) $N_P = 220$ (No Missing Peaks)			
n_k^o	Re(ν_k^+) (ppm)	Im(ν_k^+) (ppm)	$\lvert d_k^+\rvert$ (au)	n_k^o	Re(ν_k^+) (ppm)	Im(ν_k^+) (ppm)	$\lvert d_k^+\rvert$ (au)
1	0.985	0.180	0.122	1	0.985	0.180	0.122
2	1.112	0.257	0.161	2	1.112	0.257	0.161
3	1.548	0.172	0.135	3	1.548	0.172	0.135
4	1.689	0.118	0.034	4	1.689	0.118	0.034
5	1.959	0.062	0.056	5	1.959	0.062	0.056
6	2.065	0.031	0.171	6	2.065	0.031	0.171
7	2.145	0.050	0.115	7	2.145	0.050	0.116
8	2.261	0.062	0.094	8	2.261	0.062	0.092
9	2.411	0.063	0.089	9	2.411	0.062	0.085
10	2.518	0.036	0.037	10	2.519	0.036	0.037
–	–	–	–	11	2.675	0.031	0.006
12	2.675	0.054	0.066	12	2.676	0.061	0.064
13	2.855	0.014	0.004	13	2.855	0.016	0.005
14	3.013	0.054	0.058	14	3.009	0.064	0.065
15	3.065	0.037	0.113	15	3.067	0.036	0.101
16	3.242	0.053	0.120	16	3.239	0.050	0.096
17	3.301	0.052	0.045	17	3.301	0.064	0.065
18	3.482	0.027	0.009	18	3.481	0.031	0.011
19	3.585	0.028	0.036	19	3.584	0.028	0.036
20	3.694	0.036	0.042	20	3.694	0.036	0.041
21	3.803	0.024	0.031	21	3.803	0.024	0.031
22	3.945	0.042	0.072	22	3.944	0.042	0.068
23	3.970	0.057	0.010	23	3.965	0.062	0.013
24	4.271	0.055	0.016	24	4.271	0.055	0.016
25	4.680	0.108	0.057	25	4.680	0.108	0.057

(iii) $N_P = 260$ (Converged)				(iv) $N_P = 180$ (1 Missing Peak)			
n_k^o	Re(ν_k^+) (ppm)	Im(ν_k^+) (ppm)	$\lvert d_k^+\rvert$ (au)	n_k^o	Re(ν_k^-) (ppm)	Im(ν_k^-) (ppm)	$\lvert d_k^-\rvert$ (au)
1	0.985	0.180	0.122	1	0.985	0.180	0.122
2	1.112	0.257	0.161	2	1.112	0.257	0.161
3	1.548	0.172	0.135	3	1.548	0.172	0.135
4	1.689	0.118	0.034	4	1.689	0.118	0.034
5	1.959	0.062	0.056	5	1.959	0.062	0.056
6	2.065	0.031	0.171	6	2.065	0.031	0.171
7	2.145	0.050	0.116	7	2.145	0.050	0.115
8	2.261	0.062	0.092	8	2.261	0.062	0.094
9	2.411	0.062	0.085	9	2.411	0.063	0.088
10	2.519	0.036	0.037	10	2.518	0.036	0.037
11	2.675	0.033	0.008	–	–	–	–
12	2.676	0.062	0.063	12	2.675	0.054	0.066
13	2.855	0.016	0.005	13	2.855	0.015	0.004
14	3.009	0.064	0.065	14	3.011	0.059	0.059
15	3.067	0.036	0.101	15	3.066	0.037	0.108
16	3.239	0.050	0.096	16	3.240	0.051	0.103

(*Continued*)

Table 4.3 (Continued)

FAST PADE TRANSFORM: INSIDE and OUTSIDE the UNIT CIRCLE, $FPT^{(+)}$ and $FPT^{(-)}$; $N_P = 180, 220, 260$

(iii) $N_P = 260$ (Converged)				(iv) $N_P = 180$ (1 Missing Peak)			
n_k^o	$\mathrm{Re}(\nu_k^+)$ (ppm)	$\mathrm{Im}(\nu_k^+)$ (ppm)	$\lvert d_k^+ \rvert$ (au)	n_k^o	$\mathrm{Re}(\nu_k^-)$ (ppm)	$\mathrm{Im}(\nu_k^-)$ (ppm)	$\lvert d_k^- \rvert$ (au)
17	3.301	0.064	0.065	17	3.299	0.061	0.062
18	3.481	0.031	0.011	18	3.480	0.030	0.011
19	3.584	0.028	0.036	19	3.584	0.028	0.035
20	3.694	0.036	0.041	20	3.694	0.036	0.041
21	3.803	0.024	0.031	21	3.803	0.024	0.031
22	3.944	0.042	0.068	22	3.944	0.042	0.067
23	3.965	0.062	0.013	23	3.964	0.061	0.014
24	4.271	0.055	0.016	24	4.271	0.055	0.016
25	4.680	0.108	0.057	25	4.680	0.108	0.057
(v) $N_P = 220$ (Converged)				(vi) $N_P = 260$ (Converged)			
n_k^o	$\mathrm{Re}(\nu_k^-)$ (ppm)	$\mathrm{Im}(\nu_k^-)$ (ppm)	$\lvert d_k^- \rvert$ (au)	n_k^o	$\mathrm{Re}(\nu_k^-)$ (ppm)	$\mathrm{Im}(\nu_k^-)$ (ppm)	$\lvert d_k^- \rvert$ (au)
1	0.985	0.180	0.122	1	0.985	0.180	0.122
2	1.112	0.257	0.161	2	1.112	0.257	0.161
3	1.548	0.172	0.135	3	1.548	0.172	0.135
4	1.689	0.118	0.034	4	1.689	0.118	0.034
5	1.959	0.062	0.056	5	1.959	0.062	0.056
6	2.065	0.031	0.171	6	2.065	0.031	0.171
7	2.145	0.050	0.116	7	2.145	0.050	0.116
8	2.261	0.062	0.092	8	2.261	0.062	0.092
9	2.411	0.062	0.085	9	2.411	0.062	0.085
10	2.519	0.036	0.037	10	2.519	0.036	0.037
11	2.675	0.033	0.008	11	2.675	0.033	0.008
12	2.676	0.062	0.063	12	2.676	0.062	0.063
13	2.855	0.016	0.005	13	2.855	0.016	0.005
14	3.009	0.064	0.065	14	3.009	0.064	0.065
15	3.067	0.036	0.101	15	3.067	0.036	0.101
16	3.239	0.050	0.096	16	3.239	0.050	0.096
17	3.301	0.064	0.065	17	3.301	0.064	0.065
18	3.481	0.031	0.011	18	3.481	0.031	0.011
19	3.584	0.028	0.036	19	3.584	0.028	0.036
20	3.694	0.036	0.041	20	3.694	0.036	0.041
21	3.803	0.024	0.031	21	3.803	0.024	0.031
22	3.944	0.042	0.068	22	3.944	0.042	0.068
23	3.965	0.062	0.013	23	3.965	0.062	0.013
24	4.271	0.055	0.016	24	4.271	0.055	0.016
25	4.680	0.108	0.057	25	4.680	0.108	0.057

is not detected in the $FPT^{(\pm)}$. However, full convergence of the entire set of unknowns in both versions of the FPT is reached at $N_P = 260$ on panels (iii) and (vi). Moreover, it is seen on panel (v) that the $FPT^{(-)}$ converged even at $N_P = 220$. Convergence of the $FPT^{(\pm)}$ is verified to be maintained at $N_P > 260$ as also implied by Table 4.2.

Figure 4.1 illustrates the reason for which mathematical methods are absolutely indispensable in MRS and many other fields that rely on signal processing. The top panel (i) in this figure depicts the time signal from the input data that are reminiscent of those encoded via MRS. The shown free induction decay curve is heavily packed with exponentially decaying oscillations and no other discernable structure appears. Specifically, it is impossible to decipher any physically meaningful information by inspecting an FID directly in the measured time domain. However, from such a time signal, one can compute an MR spectrum that exhibits the definite advantage of displaying a relatively small number of distinct characteristics that are amenable to further analyses and interpretations for practical purposes. A typical total shape spectrum of this type is shown in the middle panel (ii) in Figure 4.1 in the absorption mode. This is obtained by a simple and powerful mathematical transformation of the original time signal into its dual or complementary representation in the frequency domain. The advantage of this passage to the frequency representation is manifested in the emergence of a number of clearly discernable features through the appearance of peaks and valleys. Nevertheless, the total shape spectrum is merely an envelope that, at best, could provide only qualitative information about the overall contribution from the sum of all the constituent resonances but not the individual components themselves. These are seen on panel (iii) in Figure 4.1 as reconstructed by the $\mathrm{FPT}^{(-)}$. Thus, despite being more revealing than the time signal, the spectral envelope from panel (ii) is still only qualitative and inconclusive and, as such, often of limited practical usefulness. Yet, the FFT, as the most frequently used signal processor in many interdisciplinary applications, including ICRMS, NMR, and MRS, is restricted to computations of total shape spectra alone. Overall, the absorption total shape spectra cannot directly provide the information about any feature of resonances, such as the most important abundance or concentrations of the underlying molecules of the examined substance. Indirect information is often surmised from these spectral Fourier-type envelopes by attempting to fit a subjectively preassigned number of resonances hidden beneath each peak structure. The most serious of the drawbacks of such an approach is nonuniqueness, which stems from the fact that virtually any chosen number of components could equally well produce an acceptable error in the conventional least-square adjustments to the given spectral envelope. Hence, for practical purposes, it would be more advantageous to have an alternative mathematical transformation, which would use only the original, unedited, raw time signal to first obtain the unique spectral parameters of each peak (position, width, height, phase) and then to generate the component and total shape spectra in any of the selected modes (absorption, dispersion, magnitude, power). Nevertheless, such spectra with curves, although convenient, are only for visual inspection. As emphasized, the most important are the numerical values of the retrieved spectral parameters and especially molecular concentrations. The reason for

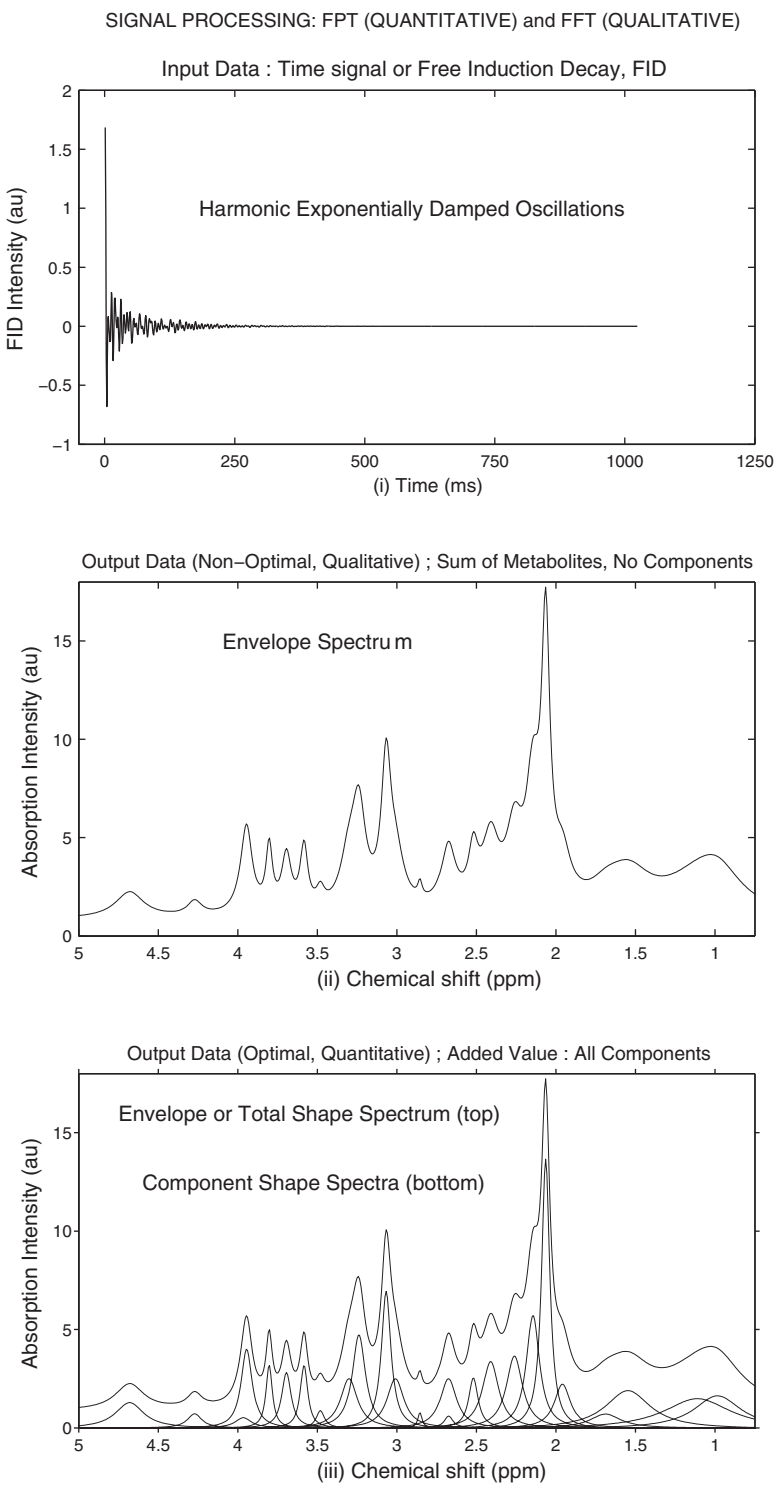

Figure 4.1 (Continued)

Figure 4.1 Time and frequency domain data in signal processing in the noiseless case using the fast Fourier transform (FFT) and fast Padé transform (FPT). Top panel (i): the input FID (to avoid clutter, only the real part of the time signal is shown). Middle panel (ii): absorption total shape spectrum (FFT). Bottom panel (iii): absorption component (lower curves; FPT) and total (upper curve; FPT) shape spectra. Panels (ii) and (iii) are generated using both the real and imaginary parts of the FID.

this is that when analyzing experimentally measured FIDs, it is only with these numbers from tables (rather than with envelopes from graphs) that the adequate quantitative assessment could be made as to which molecule do and which do not have their normal concentrations. Here the word "normal" in the case of the scanned human organ by means of MRS relates to a healthy tissue. To achieve this goal, the mentioned advanced mathematical methods must unambiguously separate the physical from nonphysical (noise, noise-like) contents in the input time-domain data to reconstruct exactly the true number of individual resonances and finally to deduce the concentrations of every physical molecule. The signal processor capable of fulfilling all these most stringent physical for versatile practical applications, including MRS in medical diagnostics, is the fast Padé transform. The FPT yields the unique component shape spectra as on panel (iii) in Figure 4.1. Such component spectra are used to subsequently generate the associated exact envelope. This is opposed to all fitting routines that start from the Fourier envelope spectrum and try to guess the component spectra.

Figure 4.2 shows, on panels (i) and (ii), the real $\mathrm{Re}(c_n)$ and imaginary $\mathrm{Im}(c_n)$ part of the synthesized FID. Panel (iii) in this figure displays the initial convergence regions of the $\mathrm{FPT}^{(+)}$ and $\mathrm{FPT}^{(-)}$ located inside and outside the unit circle $|z| < 1$ and $|z| > 1$ in the complex planes of the harmonic variables z and z^{-1}, respectively. Since the Padé spectra are rational functions given by the quotients of two polynomials, the Cauchy analytical continuation principle lifts the restrictions of the initial convergence regions. Namely, the Cauchy principle extends the initial convergence region from $|z| < 1$ to $|z| > 1$ for the $\mathrm{FPT}^{(+)}$ and similarly from $|z| > 1$ to $|z| < 1$ for the $\mathrm{FPT}^{(-)}$. Thus, both the $\mathrm{FPT}^{(+)}$ and the $\mathrm{FPT}^{(-)}$ continue to be computable throughout the complex frequency plane without encountering any divergent regions. An exception is the set of the fundamental frequencies of the examined FID, which are simultaneously the singular points (poles) of the system's response function. The small dots seen on panel (iii) depict both the exact input harmonic variables $z_k^{\pm 1} = \exp(\pm i\omega_k \tau)$ and the corresponding Padé counterparts $z_k^{\pm} = \exp(\pm i\omega_k^{\pm}\tau)$ reconstructed with $N/4 = 256$, where $\omega_k = 2\pi\nu_k$ and $\omega_k^{\pm} = 2\pi\nu_k^{\pm}$. On panel (iii), the locations of the 1st and the 25th damped harmonics for lipid and water are denoted by Lip and H_2O, respectively. These represent the two endpoints of the complex harmonic variable interval within which all the 25 studied resonances reside. To avoid clutter, numbers for the remaining 23 resonances on both sides of the circumference $|z| = 1$ are

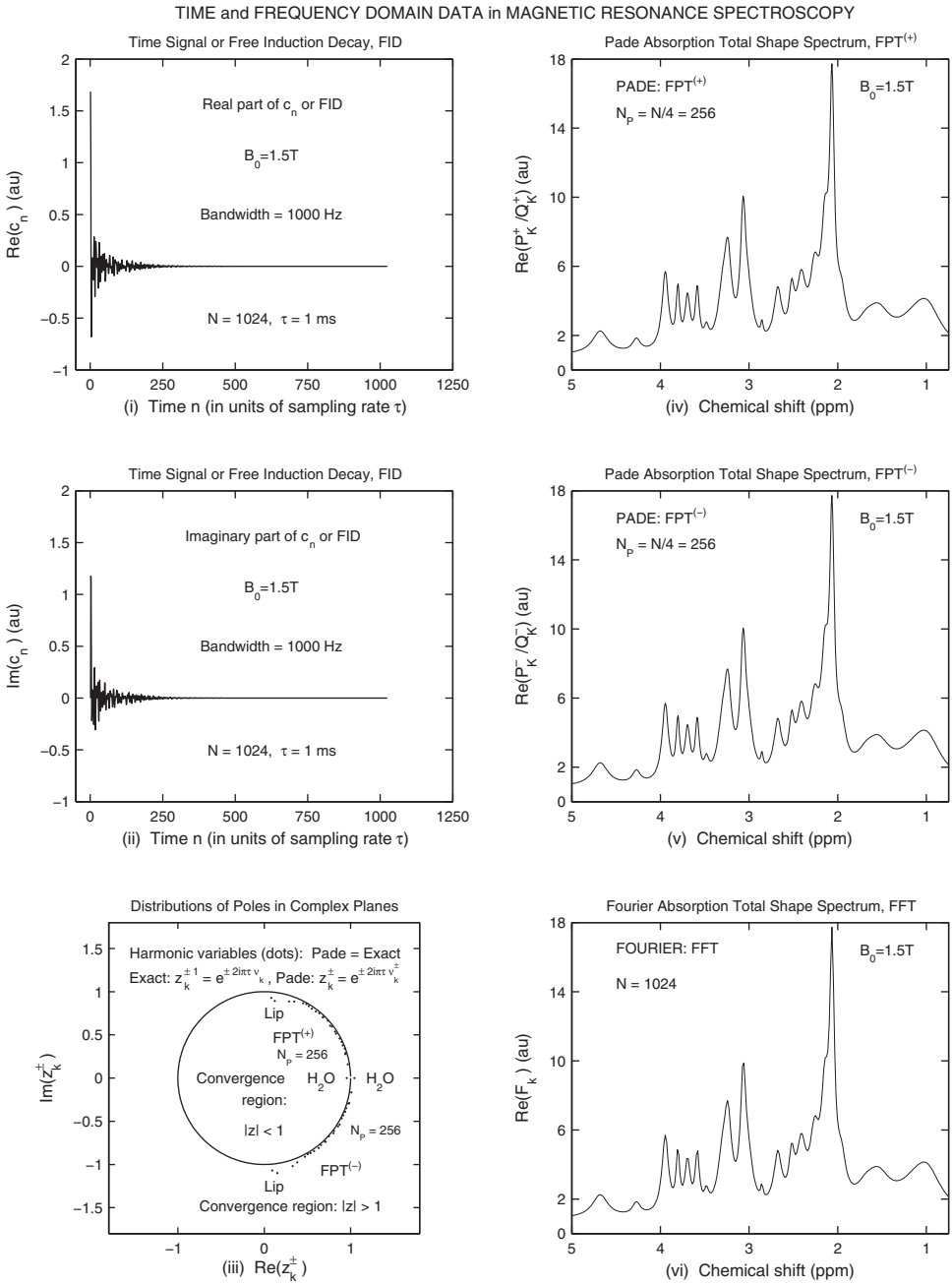

Figure 4.2 Time signal (panels (i), (ii)) and the corresponding absorption total shape spectra (envelope) in the $FPT^{(\pm)}$ (panels (iv), (v)) and FFT (panel (vi)). The initial convergence regions in the $FPT^{(+)}$ and $FPT^{(-)}$, inside and outside the unit circle, respectively, are shown on panel (iii).

not written on panel (iii). These numbers will be shown in Figure 4.6 and 4.7, whereas the corresponding acronyms for the metabolites shall be depicted in Figure 4.5. Panels (iv) and (v) in Figure 4.2 display the two Padé absorption total shape spectra from the Heaviside partial fractions of the $\mathrm{FPT}^{(+)}$ and $\mathrm{FPT}^{(-)}$, respectively, computed using a quarter signal length ($N/4=256$). These results are identical to those obtained with $N/2=512$ and $N=1024$. Panel (vi) in Figure 4.2 presents the Fourier absorption total shape spectrum evaluated via the FFT using the full FID with $N=1024$. A comparison of panels (iv)–(vi) in Figure 4.2 reveals that zero-valued spectra are obtained from the difference between any two selected pairs of these spectra.

In Figure 4.3, we present the absorption total shape spectra computed by the FFT (left column) and $\mathrm{FPT}^{(-)}$ (right column) at three partial signal lengths. On panels (i) and (iv) in Figure 4.3, the most dramatic difference between the FFT and $\mathrm{FPT}^{(-)}$ is seen at the shortest signal length ($N/8=128$). Here, the FFT presents little meaningful spectroscopic information. In contrast, with the $\mathrm{FPT}^{(-)}$, at $N/8=128$, several major peaks are clearly delineated, such as NAA, Cre, Cho, etc. On panel (ii) at $N/4=256$, the FFT has still not predicted the correct height of even the largest resonance (NAA) around 2 ppm, and simultaneously, a number of other peaks are unresolved. On the other hand, with the $\mathrm{FPT}^{(-)}$ shown on panel (v) at $N/4=256$, full convergence of the total shape spectrum is reached. At half signal length $N/2=512$ (not shown), the height of the NAA peak in the FFT is still too short, thus causing the lack of convergence for the whole Fourier spectrum. However, on panel (vi) at $N/2=512$, the $\mathrm{FPT}^{(-)}$ maintains its complete convergence by pole-zero cancellations. Overall, it is seen from Figure 4.3 that the $\mathrm{FPT}^{(-)}$ converges faster than the FFT as the partial signal length is gradually augmented. Moreover, the $\mathrm{FPT}^{(-)}$ produces no Gibbs ringing in the process of converging in a steady fashion as a function of the increased partial signal length, N_{P}. This is in sharp contrast to other existing parametric estimators that are usually unstable as a function of N_{P}, typically undergoing wide oscillations with unacceptable results before eventually converging if they do at all.

At this point, it is instructive to juxtapose to Figure 4.3, a similar Fourier and Padé convergence patterns from Figure 4.4 for a time signal of the total length $N=2048$ and bandwidth $=6001.5$ Hz encoded through MRS at 4T in Ref. [72]. Panel (i) at $N/16=128$ in Figure 4.4 for the FFT shows merely some broad bumps throughout the spectrum. Although the situation is improved on panels (ii) and (iii) at $N/4=512$ and $N/2=1024$, the FFT is still unable to yield the correct ratio of the important peak heights for Cre and Cho. In particular, by exhausting even one half of the full signal length, the Fourier spectrum from panel (iii) has not reached convergence. In contradistinction, the Padé spectrum computed by the $\mathrm{FPT}^{(-)}$ variant at $N/2=1024$ has fully converged on panel (vi). Even at shorter signal lengths $N/16=128$ and $N/4=512$ from panels (iv) and (v), the Padé spectra exhibit good resolution for a number of the dominant peaks. Thus, the $\mathrm{FPT}^{(-)}$ predicts nearly 90% of

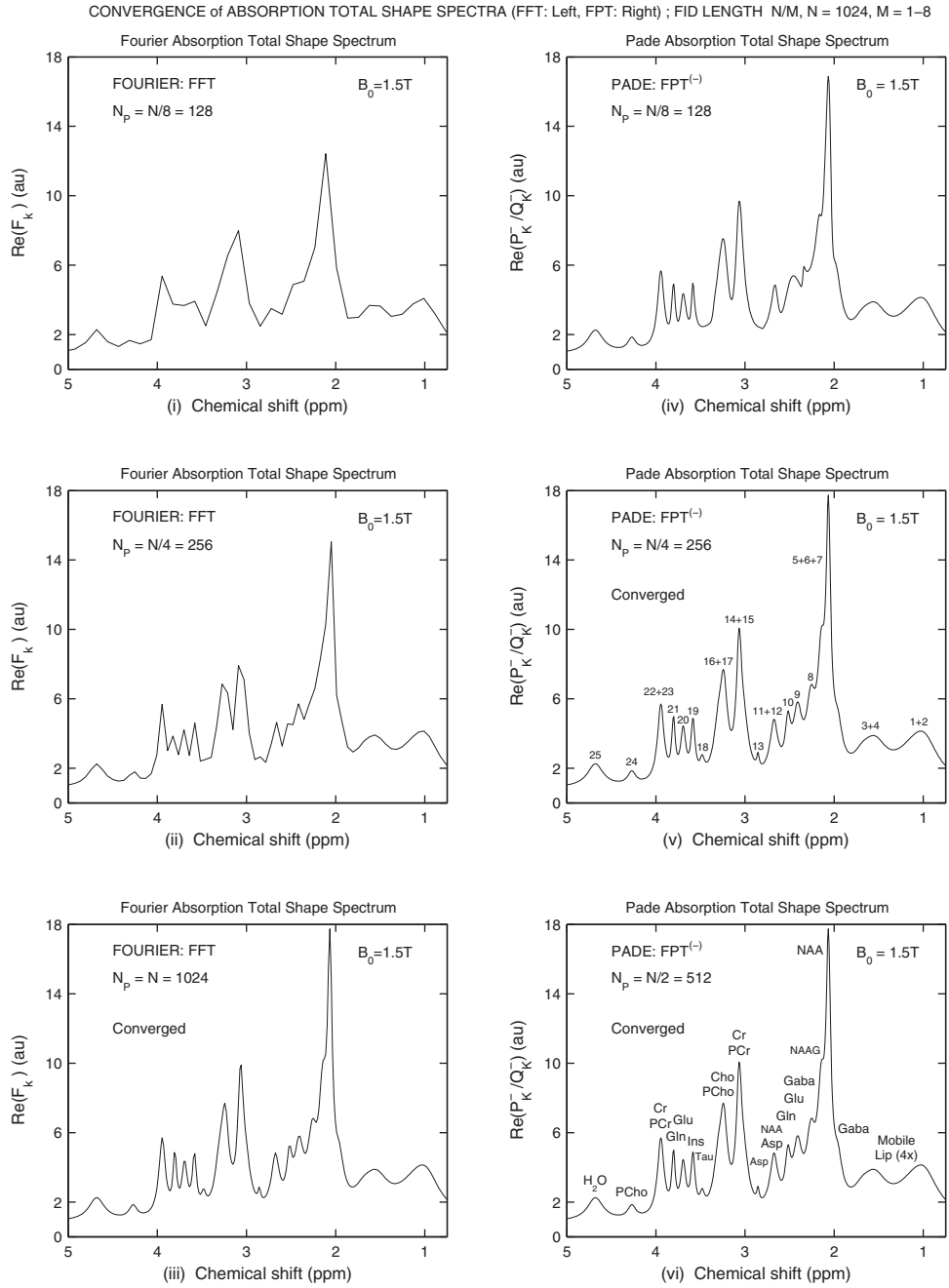

Figure 4.3 Convergence rate as a function of the partial signal length N_P at the fixed bandwidth, 1000 Hz. Fourier (FFT, left panel) and Padé ($FPT^{(-)}$, right panel) absorption total shape spectra computed using the time signal from Figure 4.2 at different partial signal lengths, as well as at the whole FID ($N = 1024$).

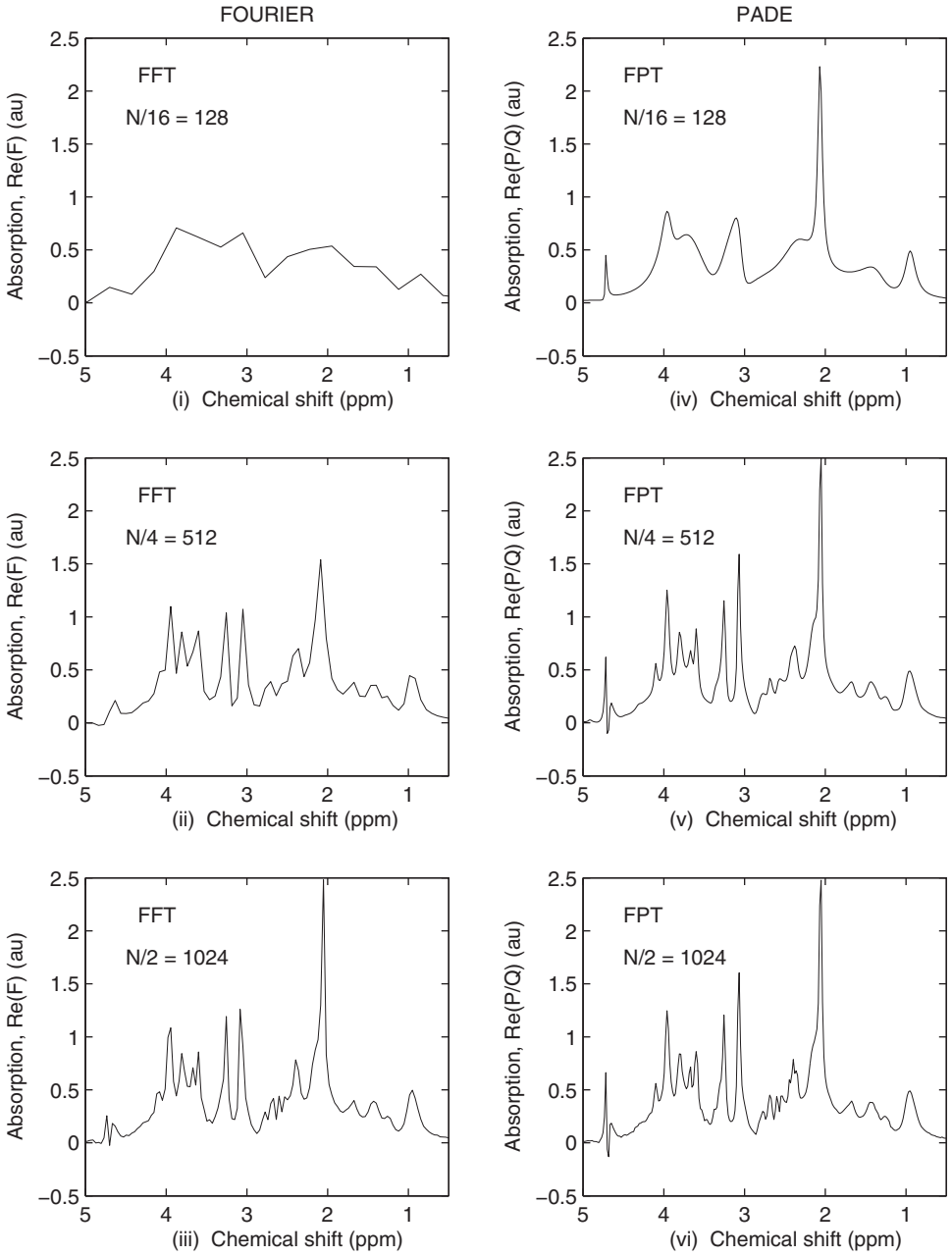

Figure 4.4 Fourier (FFT, left column) and Padé (FPT$^{(-)}$, right column) absorption total shape spectra computed using the time signal (divided by 10^4) at the partial signal lengths $N/16 = 128, N/4 = 512$, and $N/2 = 1024$ on the top, middle, and bottom panels, respectively, where the full signal length is $N = 2048$, as experimentally measured in Ref. [72] at 4T from brain occipital gray matter of a healthy volunteer.

the height of the NAA peak around 2.0 ppm at $N/16 = 128$ on panel (iv), as opposed to a practically structureless FFT spectrum from panel (i). This comparative analyses of Figures 4.3 and 4.4 establish that a faster convergence rates of the FPT$^{(-)}$ relative to the FFT found for a synthesized FID is also confirmed with an experimentally measured time signal [72]. To this end, the FPT$^{(-)}$ needs only either a quarter (Figure 4.3) or one half (Figure 4.4) of the full signal length. With such an achievement, the FPT$^{(-)}$ effectively improves the signal-to-noise (SNR) ratio of the generated spectrum since the unused second half of the FID is mainly noise. This is advantageous relative to the FFT, which converges only when using the full length $N = 1024$ or $N = 2048$ for the synthesized or encoded FID.

Returning to the synthesized FID, Figure 4.5 compares the results of reconstructions by the FPT$^{(+)}$ and FPT$^{(-)}$ (left and right columns). The pertinent details with regard to panels (i) and (iv), as well as (ii) and (v) of Figure 4.5 have already been presented in Figure 4.2. Nevertheless, further important information is presented on panels (ii) and (v) in Figure 4.5 for the absorption total shape spectra by displaying the usual acronyms that locate the positions of the major MR-detectable metabolites associated with resonances stemming from FIDs encoded via MRS from a healthy human brain. Here, the same abbreviations for several resonances (Cho, Glu, NAA) are seen at more than one chemical shift. This is a consequence of the so-called J-coupling [1]. On panels (iii) and (vi) in Figure 4.5, the absorption component shape spectra are presented for each individual resonance. The sums of all of such component shape spectra yield the associated total shape spectra from panels (ii) and (v) in Figure 4.5. Once again, it is seen on panels (iii) and (vi) in Figure 4.5 that only a quarter $N/4 = 256$ of the full FID is necessary for both the FPT$^{(+)}$ and FPT$^{(-)}$ to fully resolve all the individual resonances, including the peaks that are isolated ($n_k^\circ = 8, 9, 10, 13, 18, 19, 20, 21, 24, 25$), overlapped ($n_k^\circ = 1, 2; n_k^\circ = 3, 4; n_k^\circ = 5, 6, 7; n_k^\circ = 14, 15; n_k^\circ = 16, 17$), tightly overlapped ($n_k^\circ = 22, 23$), as well as nearly degenerate ($n_k^\circ = 11, 12$). Furthermore, panels (iii) and (vi) of this figure show that the component shape spectra coincide in the FPT$^{(+)}$ and FPT$^{(-)}$ as in Figure 4.2. Such an equivalence of these two variants is due to the uniqueness of reconstructions in the fast Padé transform. This is in sharp contrast to the nonuniqueness of all fitting techniques.

Figure 4.6 reveals further insights into the exact quantification within the FPT$^{(+)}$. As was previously the case in Figures 4.2 and 4.5, all the obtained results are for $N/4 = 256$. The absorption total shape spectrum is shown on panel (iv) in Figure 4.6, in which the individual numbers of resonances are located near the related peaks. Thus, each well-resolved isolated resonance is marked by the corresponding separate number, for example, $n_k^\circ = 8, 9$, etc. Similarly, the overlapped, tightly overlapped, and nearly degenerate resonances are labeled as the sum of the pertinent peak numbers, for example, $n_k^\circ = 1 + 2$ or $n_k^\circ = 5 + 6 + 7$, etc. On panel (v) in Figure 4.6, the absorption component shape spectra of the constituent resonances $n_k^\circ = 1 - 25$ are

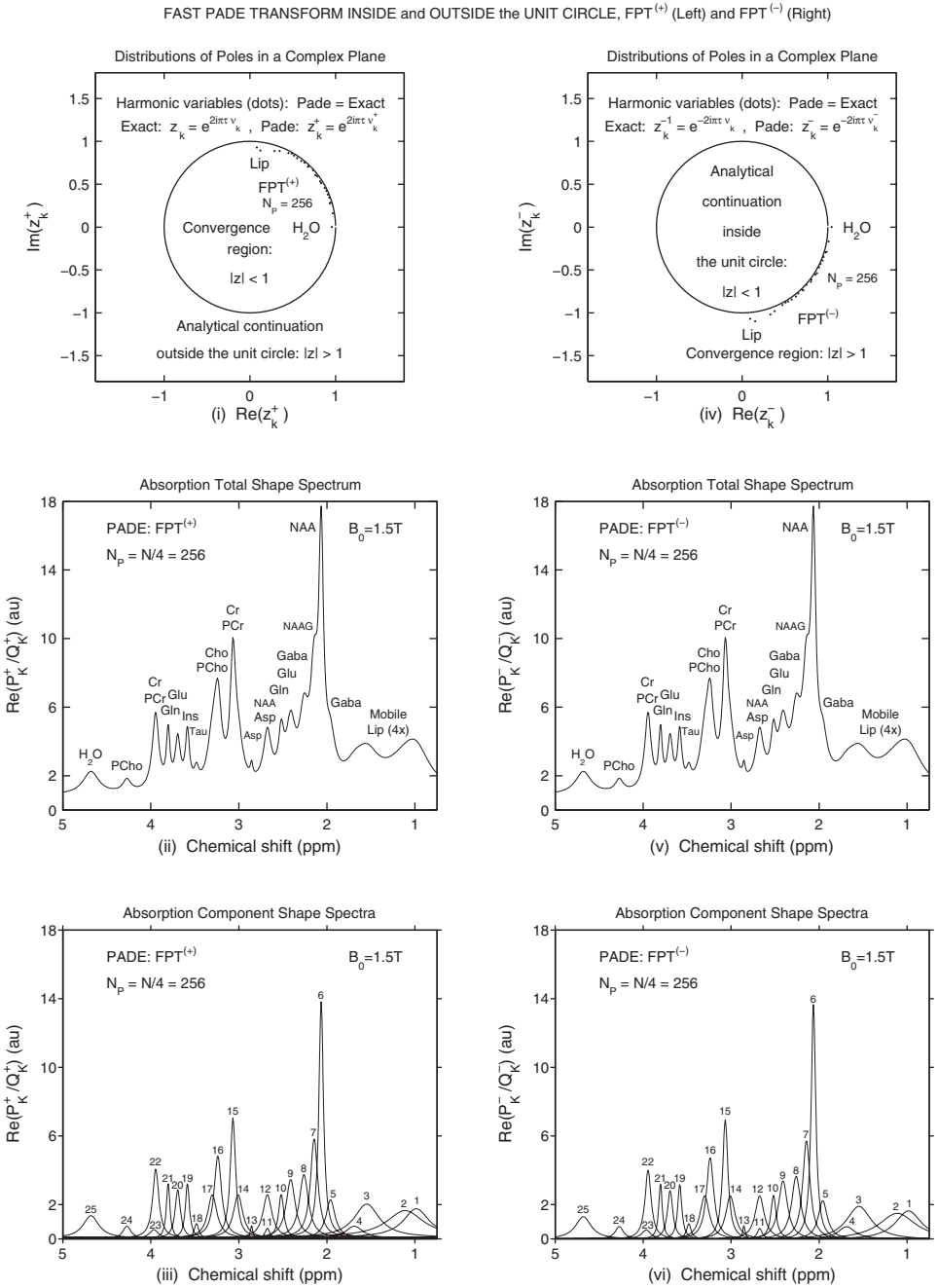

Figure 4.5 The initial convergence regions (panels (i), (iv)), absorption total shape spectra (panels (ii), (v)), and absorption component shape spectra (panels (iii), (vi)) in the $FPT^{(+)}$ (left column) and $FPT^{(-)}$ (right column). The middle panels display the usual abbreviations for the main MR-detectable metabolites in the healthy human brain, whereas the bottom panels give the corresponding numbers of these metabolites (see Table 4.1).

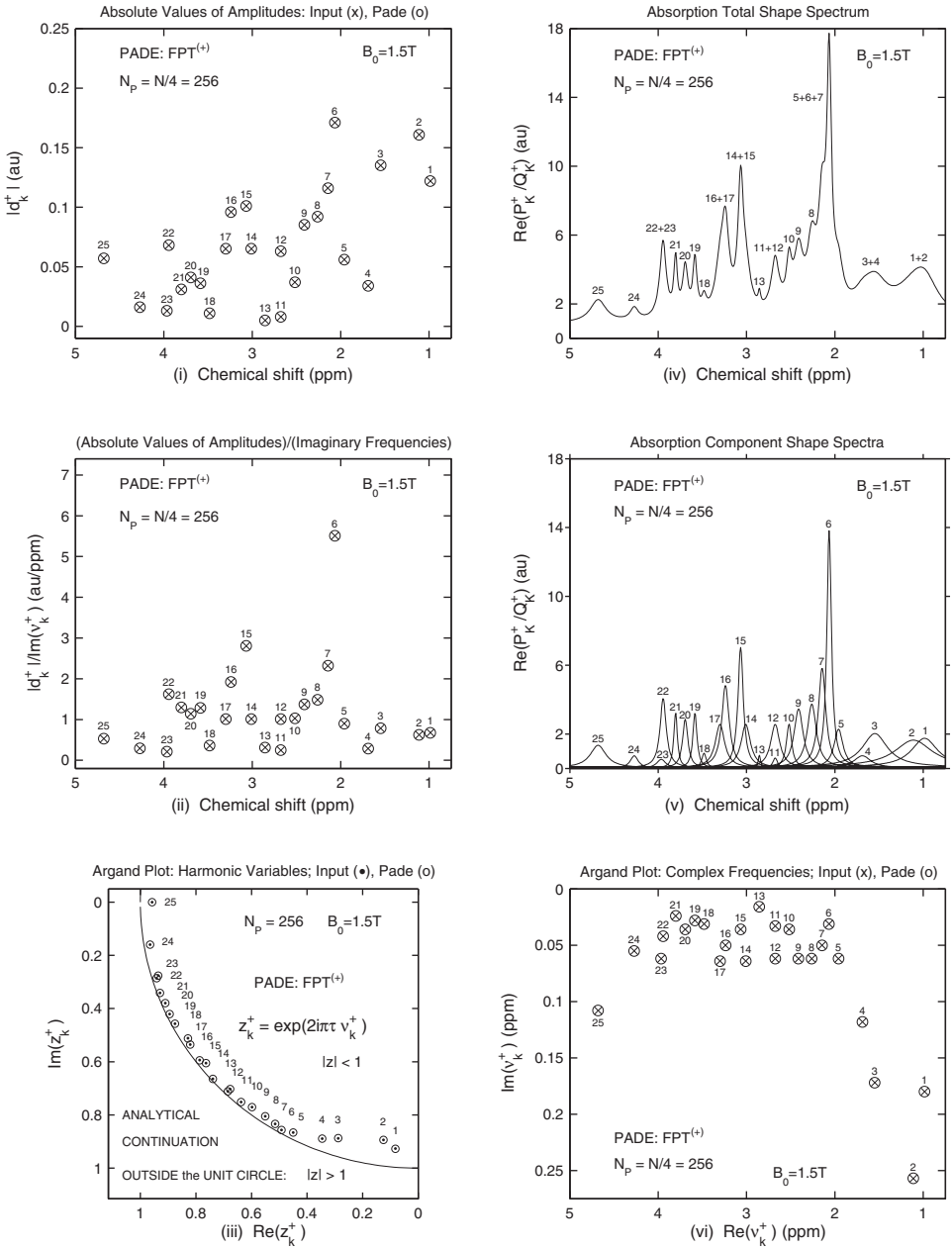

Figure 4.6 Configurations of the reconstructed spectral parameters in the FPT$^{(+)}$. Panel (i): the absolute values $|d_k^+|$ of the amplitudes d_k^+ at the corresponding chemical shifts, $\mathrm{Re}(\nu_k^+)$. Panel (ii): the ratios $|d_k^+|/\mathrm{Im}(\nu_k^+)$ that are proportional to the peak heights. Panel (iii): distributions of poles via the harmonic variable z_k^+ in the complex z^+-plane. Panel (vi): distributions of the fundamental complex frequencies ν_k^+ in the complex ν^+-plane.

shown, and all the individual numbers are indicated for an easier comparison with panel (iv) on the same figure. Thereby, the hidden structures are well delineated in these component shape spectra. These hidden resonances are are overlapped ($n_k^\circ = 1+2, 3+4, 5+6+7, 14+15, 16+17$), tightly overlapped ($n_k^\circ = 22+23$), and nearly degenerate ($n_k^\circ = 11+12$). As seen on panel (v), most resonances, for example, $n_k^\circ = 5-24$ are rather narrow as implied by the relatively small values of $\mathrm{Im}(\nu_k^+)$. Thus, these imaginary frequencies are quite close to the real axis. As a result, these resonances are seen on panel (vi) in a group in the middle part of this subplot. In contrast, panel (vi) in Figure 4.6 shows wider resonances, for example, $n_k^\circ = 1-4$ and $n_k^\circ = 25$ with larger values of $\mathrm{Im}(\nu_k^+)$. Thus, such imaginary frequencies are deeper in the complex plane, and these resonances are quite distant from the real axis, as observed on the far left and the far right parts of panel (vi). Besides panel (vi) in Figure 4.6, graphic presentations of the reconstructed and the input data for the spectral parameters are also presented on panels (i)–(iii). Panel (i) in Figure 4.6 depicts the distribution of the absolute values of the amplitudes at different chemical shifts. It follows from panel (i) that the quantities $|d_k^+|$ do not represent the heights of the absorption peaks from panels (iv) and (v). Instead, the absorption peak heights are directly proportional to the quotient $|d_k^+|/\mathrm{Im}(\nu_k^+)$, as it should be with any Lorentzian. Thus, in Figure 4.6, panel (ii) displays the distribution of these latter quotients of the absolute values of the amplitudes and the imaginary frequencies. It can be observed from panel (ii) that all the 25 ratios $|d_k^+|/\mathrm{Im}(\nu_k^+)$ are, in fact, proportional to the heights of the corresponding peaks in the absorption component shape spectra from panel (v) in Figure 4.6. Panel (iii) from Figure 4.6 shows, in the complex z^+-plane, the distribution of the Padé poles using the complex harmonic variable z_k^+. This is the zoomed version of panels (iii) or (i) from Figures 4.2 or 4.5, respectively. The difference is in displaying only the first quadrant in Figure 4.6 since the rest of the complex z^+-plane does not contain any genuine resonance. Note that on panel (vi), both $\mathrm{Re}(\nu_k^+)$ and $\mathrm{Im}(\nu_k^+)$ are shown in descending order when proceeding from left to right on the abscissa or from bottom to top on the ordinate in Figure 4.6. This convenient layout reveals that all the Padé poles $n_k^\circ = 1-25$ are aligned from right to left regarding the abscissa. The same poles $n_k^\circ = 1-25$ are also packed together near the circumference ($|z| = 1$) of the unit circle in such a way that they follow each other according to their consecutive numbers from inside the unit circle by being aligned upward with respect to the ordinate, as per panel (iii). Panel (iii) in Figure 4.6 shows that the poles contained in the harmonic variable z_k^+ in the polar coordinates are less scattered from each other relative to the associated distributions of the complex frequencies from panel (vi) in the rectangle Descartes coordinates. The reason for this is in the exponential function of the complex frequency, which is plotted on panel (iii), whereas the frequency itself is shown on panel (vi) in Figure 4.6. It is seen on panel (iii) in this figure that all the genuine poles retrieved by the FPT$^{(+)}$ are

found inside the unit circle ($|z| < 1$), as expected. Note that narrow resonances $n_k^\circ = 5 - 24$ are shown to be near the circumference ($|z| = 1$) of the unit circle. On the other hand, the wide resonances seen on panel (iii) in Figure 4.6, such as $n_k^\circ = 1 - 4$ and $n_k^\circ = 25$, lie further from the borderline $|z| = 1$.

Figure 4.7 is similar to Figure 4.6 in many ways. The difference is that Figure 4.7 displays the results of the FPT$^{(-)}$. The interpretation of the results from the FPT$^{(+)}$ as presented on panels (i), (ii), and (iv)–(vi) in Figure 4.6 holds as well with respect to the corresponding findings from the FPT$^{(-)}$ shown on panels (i), (ii), and (iv)–(vi) in Figure 4.7. This observation emerges from the fact that the FPT$^{(+)}$ and FPT$^{(-)}$ generate indistinguishable spectral parameters for the same number of signal points, $N/4 = 256$. However, panel (iii) differs for Figures 4.6 and 4.7 since the information presented in these plots relates to the two complementary regions of the initial convergence, inside and outside the unit circle, for the FPT$^{(+)}$ and FPT$^{(-)}$, respectively. In order to match the configuration from panel (iii) in Figure 4.6, the Padé poles contained in the harmonic variable z_k^- as displayed in the complex z^-–plane on panel (iii) in Figure 4.7 are plotted with the values of $\mathrm{Im}(z_k^-)$ in ascending order when going from bottom to top of the ordinate. This is in contrast to the ordering of $\mathrm{Im}(z_k^+)$ on panel (iii) in Figure 4.6 as anticipated because $\mathrm{Im}(z_k^+) > 0$ and $\mathrm{Im}(z_k^-) < 0$. Thus, in reconstructions by the FPT$^{(+)}$ and FPT$^{(-)}$, the harmonic variables z_k^+ and z_k^- are located in the first and the fourth quadrant of the complex z^+- and z^-–planes, respectively. This is apparent on panel (iii) of Figure 4.2 or on panels (i) and (iv) in Figure 4.5. Furthermore, on panel (iii) in Figure 4.7, all the resonances reconstructed by the FPT$^{(-)}$ are observed to lie outside the unit circle ($|z| > 1$), as expected. A careful inspection reveals that the kth heights $|d_k^\pm|/\mathrm{Im}(\nu_k^\pm)$ shown on panels (ii) in Figures 4.6 and 4.7 do not fully match the corresponding tops of the kth peaks in the component shape spectra $d_k^\pm z^{\pm 1}/(z - z_k^\pm)$ from panel (v). This is explained by the fact that the heights $|d_k^\pm|/\mathrm{Im}(\nu_k^\pm)$ are due to the lineshapes $d_k^\pm/(\omega - \omega_k^\pm)$ rather than to the presently adopted spectra $d_k^\pm z^{\pm 1}/(z - z_k^\pm)$. The former and the latter lineshapes are given in terms of the angular frequencies $\{\omega, \omega_k^\pm\}$ and harmonic variables $\{z^{\pm 1}, z_k^{\pm 1}\}$, respectively, where $z^{\pm 1} = \exp(\pm i\omega\tau)$ and $z_k^{\pm 1} = \exp(\pm i\omega_k\tau)$.

In Figure 4.8, we display the absorption component shape spectra (left column) and total shape spectra (right column) from the FPT$^{(-)}$ computed near full convergence at three partial signal lengths $N_\mathrm{P} = 180, 220, 260$. The three panels on the right column for the total shape spectra have all reached full convergence. However, on the left column for the corresponding component shape spectra, full convergence is achieved only at $N_\mathrm{P} = 220, 260$. On panel (i) for the component shape spectra at $N_\mathrm{P} = 180$, peak $n_k^\circ = 11$ is absent, and peak $n_k^\circ = 12$ is overestimated. Furthermore, the area of the 12th peak is overestimated by the amount of the area of the absent 11th peak. As a consequence of this latter compensation, the total shape spectrum has not reflected that either shortcoming had occurred. Namely,

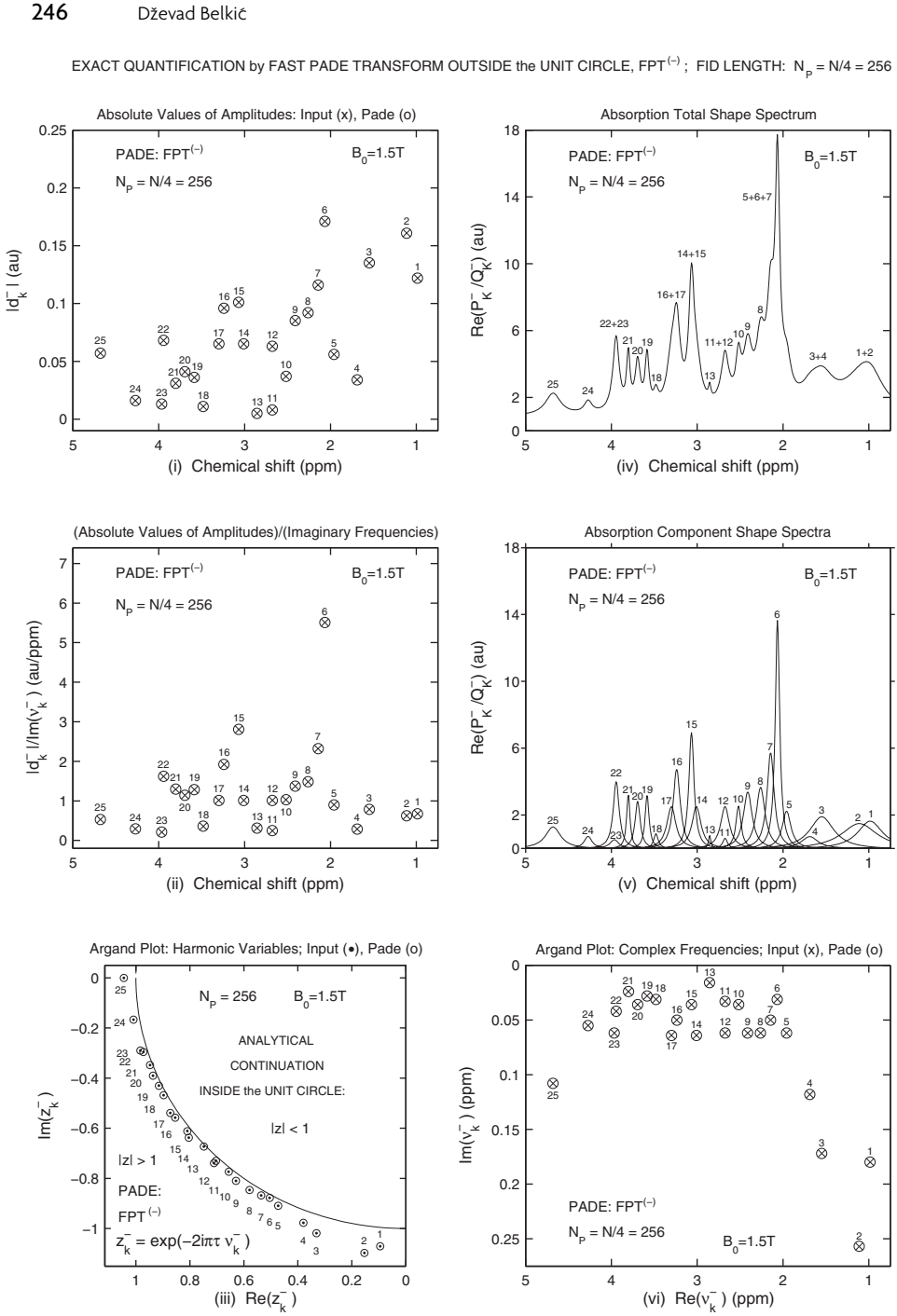

Figure 4.7 (Continued)

Figure 4.7 Configurations of the reconstructed spectral parameters in the FPT$^{(-)}$. Panel (i): the absolute values $|d_k^-|$ of the amplitudes d_k^- at the corresponding chemical shifts, $\mathrm{Re}(\nu_k^-)$. Panel (ii): the ratios $|d_k^-|/\mathrm{Im}(\nu_k^-)$ that are proportional to the peak heights. Panel (iii): distributions of poles via the harmonic variable z_k^- in the complex z^-−plane. Panel (vi): distributions of the fundamental complex frequencies ν_k^- in the complex ν^-−plane.

the total shape spectrum on panel (iv) for $N_\mathrm{P} = 180$ reached complete convergence even though peak $n_k^\circ = 11$ was missing and peak $n_k^\circ = 12$ was overestimated. We verified that this full convergence is also conformed by the corresponding zero-valued spectra for the residual $\mathrm{Re}(P_K^-/Q_K^-)[N] - \mathrm{Re}(P_K^-/Q_K^-)[N_P]$ $(N = 1024, N_\mathrm{P} = 180, 220, 260)$.

The left column in Figure 4.9 shows again the Padé absorption component and total shape spectra but this time superimposed on top of each other at $N_P = 180, 220, 260$. This is particularly illuminating on the right column in Figure 4.9 with the corresponding three consecutive difference spectra on panels (iv): $\mathrm{Re}(P_K^-/Q_K^-)[220] - \mathrm{Re}(P_K^-/Q_K^-)[180]$, (v): $\mathrm{Re}(P_K^-/Q_K^-)[260] - \mathrm{Re}(P_K^-/Q_K^-)[220]$, and (vi): $\mathrm{Re}(P_K^-/Q_K^-)[260] - \mathrm{Re}(P_K^-/Q_K^-)[180]$. These three consecutive difference spectra, built from the corresponding total shape spectra, are seen as identical on panels (iv), (v), and (vi) in Figure 4.9, despite the lack of convergence of the component shape spectrum from panel (i) in the same figure. Hence, we can conclude that while obtaining the residual or error spectra at the level of background noise may be a necessary condition, this is not sufficient for judging the reliability of estimation in practice. Therefore, it is recommended to pass beyond the point where full convergence of the total shape spectra has been reached for the first time (in this case above $N_\mathrm{P} = 180$) in order to verify that anomalies as seen on panels (i) and (iv) of Figure 4.9 do not occur in the final results. Such final results obtained for $N_\mathrm{P} = 220$ and 260 are displayed on panels (ii) and (iii) in Figure 4.8 for the components, as well as panels (v) and (vi) for the envelopes. Clearly, for consistency, monitoring the stability of the component spectra should be done together with the inspection of the constancy of the reconstructed genuine spectral parameters.

Signal-noise separation (SNS) by Froissart doublets within the FPT$^{(+)}$ and FPT$^{(-)}$ is illustrated in Figures 4.10 and 4.11 for the noise-free and noise-corrupted time signals, respectively. Only a small number of all the obtained Froissart doublets appears in the shown frequency window in Figure 4.10. The selected subinterval 0–6 ppm is important because all the MR-detectable brain metabolites lie within this chemical shift domain of the full Nyquist range. Froissart doublets as spurious resonances are detected by the confluence of poles and zeros in the list of the Padé-reconstructed spectral parameters.

It is seen on panel (i) in Figures 4.10 and 4.11 that the FPT$^{(+)}$ disentangles the physical from unphysical resonances by the opposite signs of their imaginary frequencies. In other words, the FPT$^{(+)}$ provides the exact separation of the genuine from any spurious contents of the investigated noise-free and

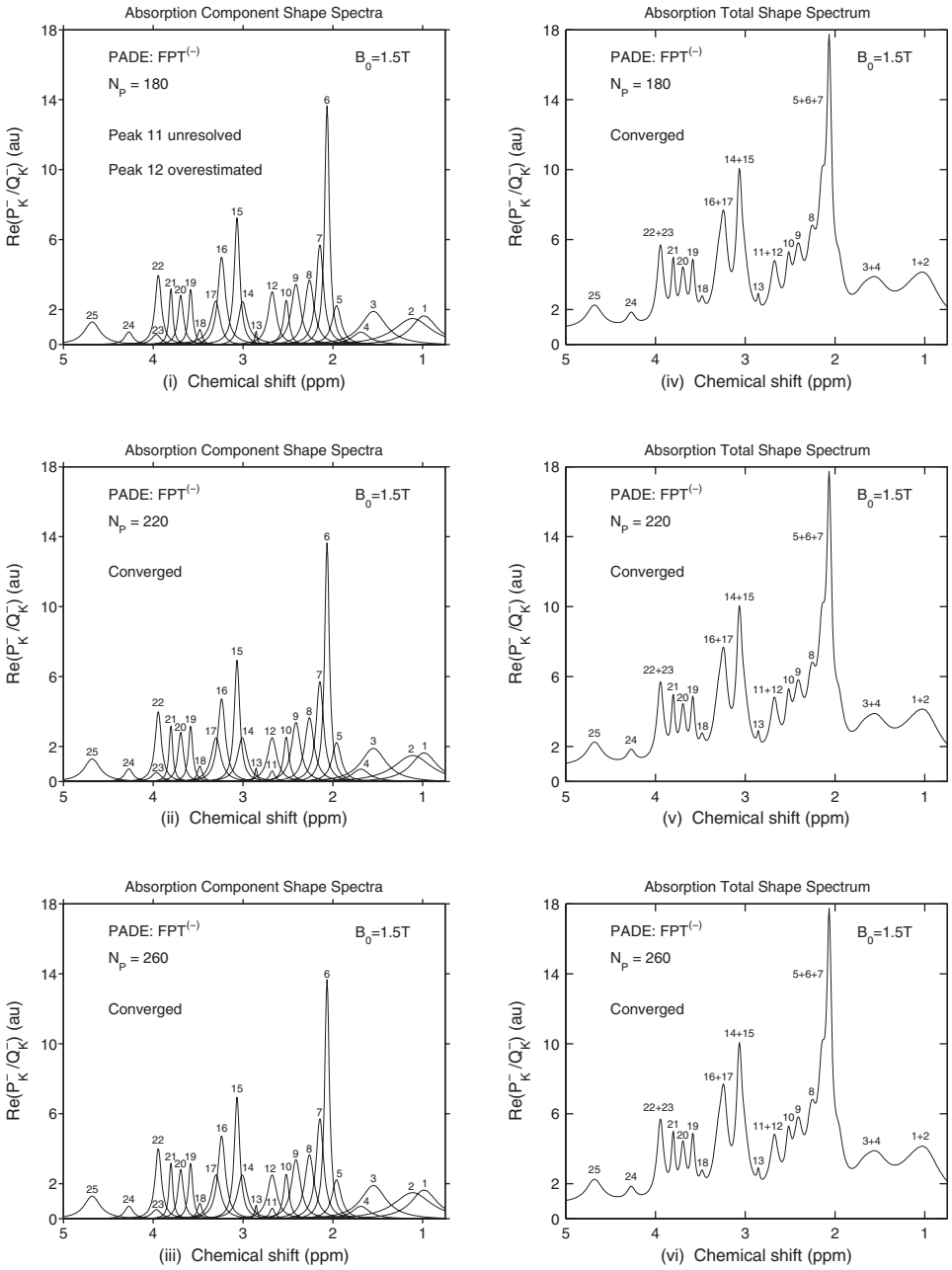

Figure 4.8 Absorption component shape spectra (left) and absorption total shape spectra (right) from the FPT$^{(-)}$ near full convergence for signal lengths $N_P = 180, 220, 260$. On panel (iv) for $N_P = 180$, the total shape spectrum reached full convergence, despite the fact that on panel (i) for the corresponding component shape spectra, the 11th peak is missing and the 12th peak is overestimated.

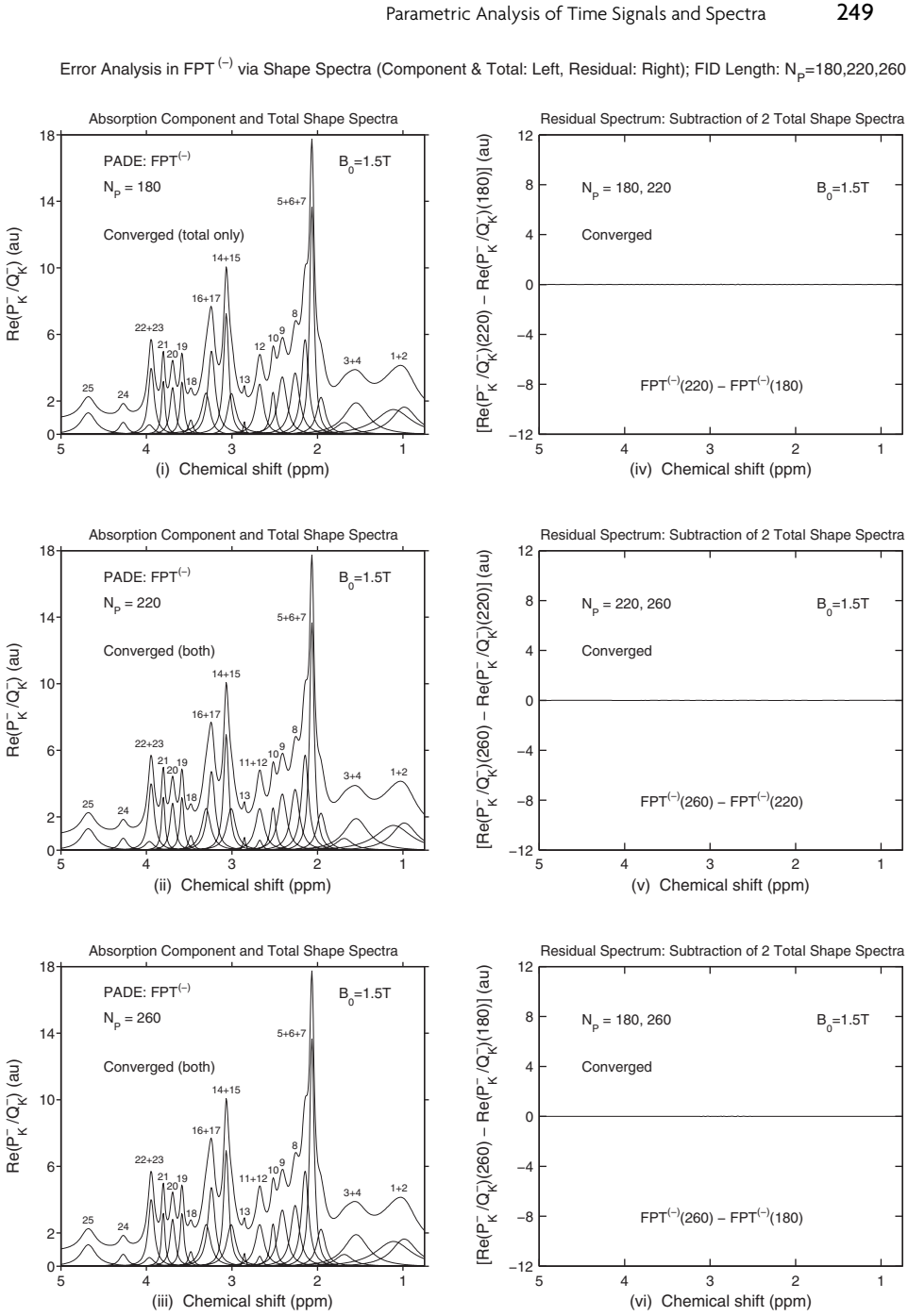

Figure 4.9 (Continued)

Figure 4.9 Residual or error spectra and the reconstruction quality. Left: absorption total shape spectra superimposed on top of the corresponding component shape spectra in the FPT$^{(-)}$ near full convergence for signal lengths $N_P = 180, 220, 260$. Right: Consecutive difference spectra for absorption total shape spectra in the FPT$^{(-)}$ with signal lengths $N_P = 180, 220, 260$. All the residual or error spectra on the right column are equal to zero indicating full convergence of the absorption total shape spectra at all the three partial lengths $N_P = 180, 220, 260$. However, not all the absorption component spectra on panel (i) converged since here, at $N_P = 180$, the 11th peak is not yet reconstructed.

noise-corrupted time signals. By contrast, in the FPT$^{(-)}$ depicted on panel (ii) in Figures 4.10 and 4.11, genuine and spurious resonances are mixed together since they all have the same positive sign of their imaginary frequencies. Nevertheless, the emergence of Froissart doublets also remains evidently clear in the FPT$^{(-)}$ via coincidence of poles and zeros, with the ensuing unambiguous identification of spurious resonances. Precisely due to pole-zero coincidences, each Froissart doublet has zero-valued amplitudes as seen on panel (iii) in Figures 4.10 and 4.11. This result, as another signature of Froissart doublets, represents a further check of consistency and fidelity of separation of genuine from spurious resonances, and this is the basis of the concept of SNS.

The only difference between Froissart doublets for the noise-free $\{c_n\}$ and noise-corrupted $\{c_n + r_n\}$ time signals from Figures 4.10 and 4.11, respectively, is that the latter are more irregularly distributed than the former. This is expected due to the presence of the random perturbation $\{r_n\}$ in the noise-corrupted time signal. However, this difference is irrelevant since the only concern to SNS is that noise-like or noisy information is readily identifiable by pole-zero coincidences. Note that the full auxiliary lines on each subplot in Figures 4.10 and 4.11 are drawn merely to transparently delineate the areas with Froissart doublets.

Once the Froissart doublets are identified and discarded from the whole set of the results, only the reconstructed parameters of the genuine resonances will remain in the output data. Crucially, however, the latter set of Padé-retrieved spectral parameters also contains the exact number K_G of genuine resonances as the difference between the total number K of all the found resonances and the number K_F of Froissart doublets, $K_G = K - K_F$. In Figures 4.10 and 4.11, we used a quarter of the full signal length $N_P = N/4 = 1024/4 = 256$, which corresponds to the Padé polynomial degree $K = 128$ in spectra $P_K^{\pm}/Q_K^{\pm}$. In the whole Nyquist range, the FPT$^{(+)}$ and FPT$^{(-)}$ find 103 Froissart doublets, $K_F = 103$ (all not shown). Therefore, the number K_G of genuine resonances reconstructed by the FPT$^{(+)}$ and FPT$^{(-)}$ is given by $K_G = 128 - 103 = 25$, in exact agreement with the corresponding value of the input data. Overall, Froissart doublets simultaneously achieve three important goals: (1) noise reduction, (2) dimensionality reduction, and (3) stability enhancement. Stability against perturbations of the physical time

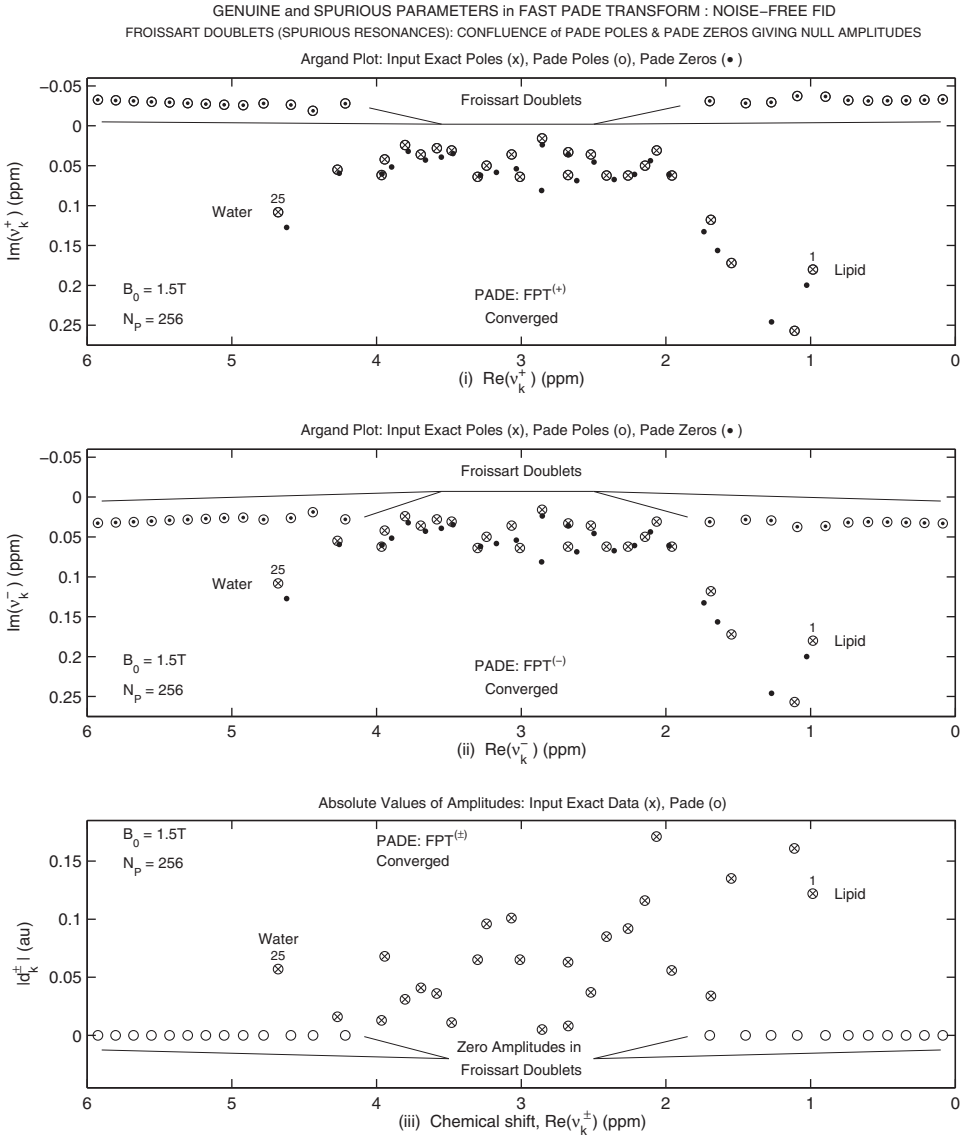

Figure 4.10 A subset of the whole set of Froissart doublets in the FPT$^{(\pm)}$ at a quarter $N/4 = 256$ of the full length ($N = 1024$) of a noise-free time signal. On panel (i), the FPT$^{(+)}$ achieves a total separation of genuine from spurious resonances that are mixed together in the FPT$^{(-)}$ on panel (ii). Panel (iii) shows genuine and spurious amplitudes in the FPT$^{(\pm)}$. The reconstructed converged amplitudes are identical in the FPT$^{(+)}$ and the FPT$^{(-)}$. All the spurious amplitudes are zero-valued.

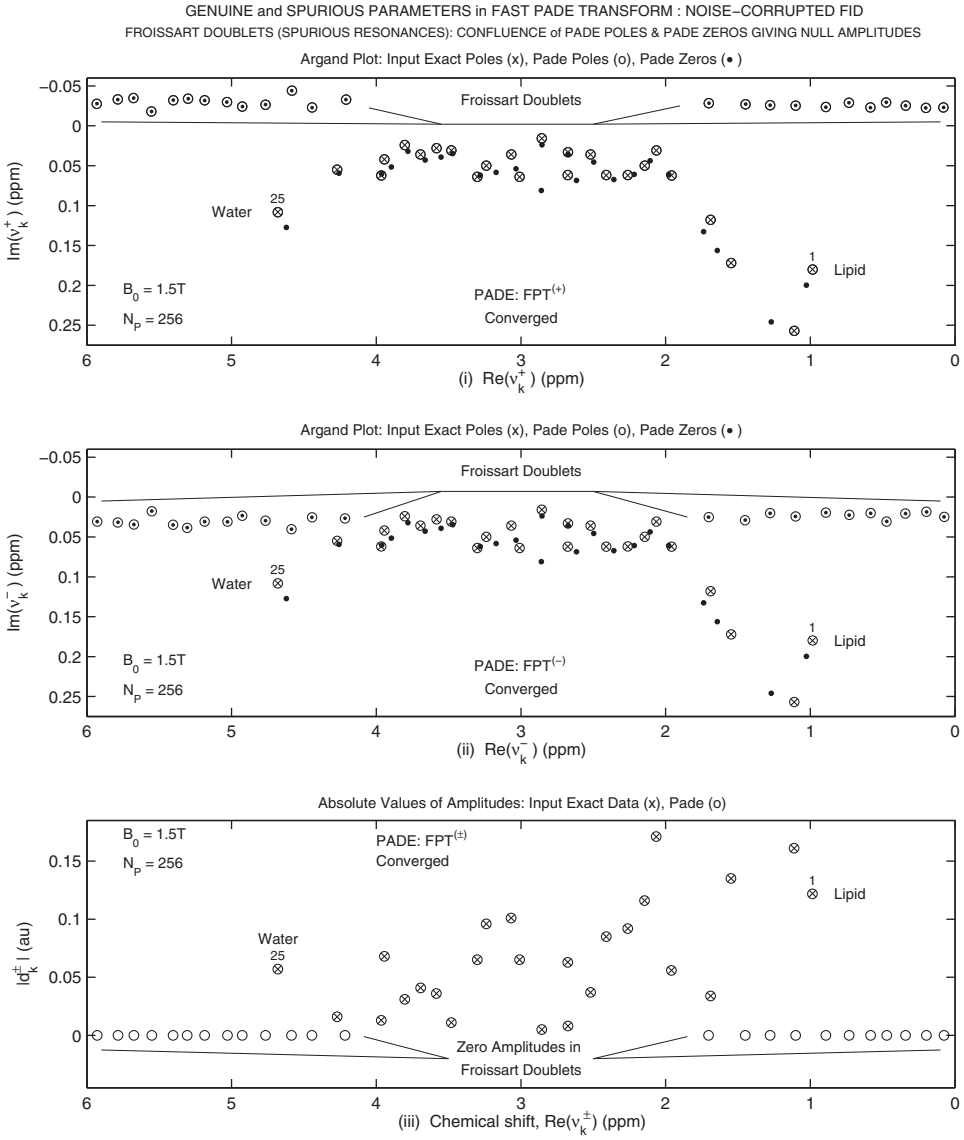

Figure 4.11 A subset of the whole set of Froissart doublets in the $\mathrm{FPT}^{(\pm)}$ at a quarter $N/4 = 256$ of the full length ($N = 1024$) of a noise-corrupted time signal. On panel (i), the $\mathrm{FPT}^{(+)}$ achieves a total separation of genuine from spurious resonances that are mixed together in the $\mathrm{FPT}^{(-)}$ on panel (ii). Panel (iii) shows genuine and spurious amplitudes in the $\mathrm{FPT}^{(\pm)}$. The reconstructed converged amplitudes are identical in the $\mathrm{FPT}^{(+)}$ and $\mathrm{FPT}^{(-)}$. All the spurious amplitudes are zero-valued.

signal under study is critical to the reliability of spectral analysis. The main contributor to instability of systems is its spurious content. Being inherently unstable and incoherent, spuriousness is unambiguously identified by the twofold signature of Froissart doublets (pole-zero coincidences and zero-valued amplitudes) and as such discarded from the output data in the FPT. Only the genuine information that is stable and coherent remains.

Small amplitudes are the cause for great instability of spurious resonances such as Froissart doublets. This is in sharp contrast to the stability of genuine resonances. Such a diametrically opposite behavior of physical and unphysical resonances greatly facilitates the task of distinguishing one from the other. In practical computations, this is easily accomplished by merely monitoring the Padé table when passing from one Padé approximant $P_K^{\pm}(z^{\pm 1})/Q_K^{\pm}(z^{\pm 1})$ to $P_{K+m}^{\pm}(z^{\pm 1})/Q_{K+m}^{\pm}(z^{\pm 1})$ $(m = 1, 2, 3, ...)$. When the order K of the FPT changes, we observe that the parameters of some resonances are robustly stable, whereas the others exhibit great instability. Then the former resonances are identified as genuine and the latter as spurious. In practice, the first feature that is easily spotted in a long output table of spectral parameters from the FPT are literally hundreds of zeros or near-zeros in the column of the reconstructed amplitudes at certain frequencies. These will represent spurious, noise, or noise-related resonances that, in turn, can confidently be dropped from the Padé output list only if the corresponding pole-zero coincidences are observed at the same frequencies. Very feeble resonances cannot be discarded merely on the basis of smallness of their peak heights. For example, in medical diagnostics via MRS, certain true metabolites of diagnostic relevance could well have weak concentrations in the scanned tissue. Only in the case of a correlation between almost zero intensities and pole-zero near-confluences, we could identify/discard spurious resonances with fidelity.

There are many different procedures in various processors for attempting to improve SNR. One of them also exists in the forward and root-reflected backward linear predictor (FB-LP) [10]. Here, the unphysical poles yielding diverging harmonics from the backward recursion are superficially forced to lie inside the unit circle via the so-called root reflection. In addition, in order to partially improve SNR, averaging is performed for the predictions from the forward and root-reflected backward recursions. However, noticeable instabilities exist when attempting to distinguish signal from noise on the basis of near-equalities between poles generated by the forward and root-reflected backward LP expansion coefficients of the characteristic polynomial Q [11]. Such an obstacle is only partially mitigated by the said averaging technique from [10]. Nevertheless, both the nonaveraged [11] and the averaged [10] versions of this method exhibit a common drawback of potentially missing weak genuine components when comparing the poles from the forward and root-reflected backward LP recursions. This is opposed to the robust signal-noise separation in the fast Padé transform via the FPT$^{(\pm)}$, which exploits its additional degree of freedom via the numerator

polynomial P. The latter is absent from all the variants of the LP model, as well as from the autoregressive processor. It is precisely this extra flexibility in the FPT, which sets the stage for the emergence of pole-zero confluences with the resulting null amplitudes that subsequently enable the Froissart strategy to naturally filter out all redundancies via spurious or unphysical resonances from the reconstructed data.

30.2. Cell surviving fractions after irradiation: Padé-linear quadratic (PLQ) model

Finally, we shall illustrate the remaining application of the Padé approximant from Section 29 dealing with cell surviving fractions $S_{\rm F}(D)$ after irradiation through the absorbed dose D. To this end, Figure 4.12 is presented to compare experimental data with the LQ and PLQ models. Shown are the curves of cell surviving fractions $S_{\rm F}(D)$ and reactivity $R(D) \equiv -(1/D)\ln(S_{\rm F})$ on the top and bottom panels, respectively. It is seen that the PLQ model compares more favorably than the LQ model relative to the displayed experimental data. The top panel indicates that the LQ model is relatively satisfactory for $S_{\rm F}(D)$ up to about 6 Gy. Thereafter, $S_{\rm F}^{(\rm LQ)}(D)$ decreases too fast due to the dominance of the Gaussian $\mathrm{e}^{-\beta D^2}$ over the exponential $\mathrm{e}^{-\alpha D}$ at larger values of D. By contrast, $S_{\rm F}^{(\rm PLQ)}(D)$ is in a good agreement with measurement at all doses. In particular, at larger D, it can be seen from the top panel that the PLQ model exhibits a smooth transition to the high-dose asymptote $S_{\rm F}^{(\rm PLQ)}(D) \sim \mathrm{e}^{-D/D_0}$ similarly to the experimental data. As mentioned in Section 29, for the present illustration, we constrained the 3rd adjustable parameter γ to the relationship $\gamma = \beta D_0$. Here, D_0 is the reciprocal of the final slope, considered as the input data, which is taken from the semilogarithmic graph of the measured cell survival curve $S_{\rm F}(D)$. With this constraint, which is not mandatory, the PLQ model possesses only two unknown parameters (α, β), as does the LQ model. However, the reconstructed numerical values of α and β are different in these two models, as can most clearly be seen from the bottom panel of Figure 4.12. Here, the curves for $R(D)$ in the LQ and PLQ models have two different interception points with the ordinate. Therefore, the numerical values for the initial slope α are unequal in these two methods. We have $R^{(\rm LQ)}(D) = \alpha + \beta D$ and $R^{(\rm PLQ)}(D) = (\alpha + \beta D)/(1 + \gamma D)$, where α is the interception of the reactivity line with the ordinate at $D = 0$. Reactivity is seen on the bottom panel in Figure 4.12 to be a straight line and a rectangular parabola in the LQ and PLQ model, respectively. This so-called Fe (full-effect) plot (reactivity versus dose) is instructive, since any departure of experimental data from a straight line indicates the inadequacy of the LQ model, as evident from the bottom panel of Figure 4.12. At high doses, $R^{(\rm LQ)}(D)$ increases indefinitely, and this is at variance with the measured values that tend to a constant, which for large D is also predicted by the PLQ model $R^{(\rm PLQ)}(D) \longrightarrow \beta/\gamma = 1/D_0$. This high-dose saturation effect in the reactivity is a direct consequence of the limited amount of the enzymes that are available for repair of radiation-damaged

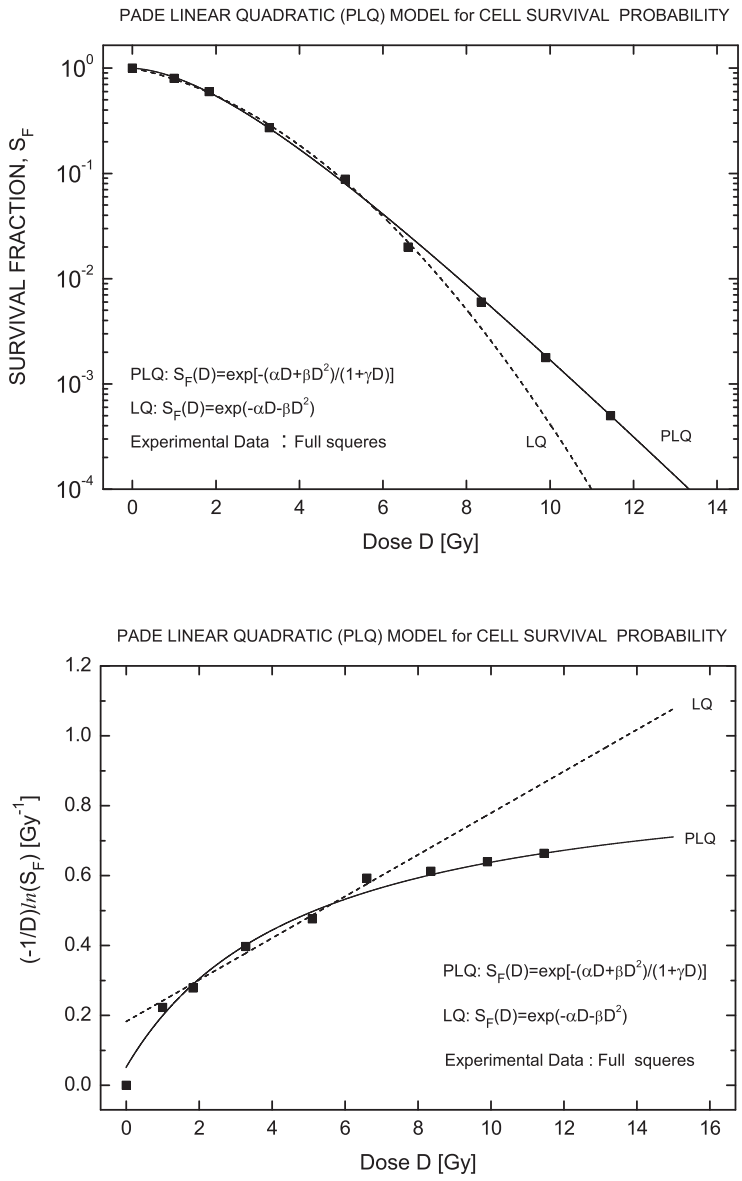

Figure 4.12 Cell survival fractions $S_F(D)$ as a function of absorbed radiation dose D in Gy (top panel). The bottom panel is the so-called reactivity $R(D)$ given by product of the reciprocal dose D^{-1} and the negative natural logarithm of $S_F(D)$, as the ordinate versus D as the abscissa. Experiment (symbols): the mean clonogenic surviving fractions $S_F(D)$ (top panel) and $R(D) \equiv -(1/D)\ln(S_F)$ (bottom panel) for the Chinese hamster cells grown in culture and irradiated by 50 kV X-ray [73]. Theories: solid curve – PLQ (Padé Linear Quadratic) model and dotted curve – LQ model (the straight line $\alpha + \beta D$ on the bottom panel).

cells. For sufficiently large D, the number of lesions is accumulated to such an extent that the enzyme molecules become effectively incapable of repair after which point every radiation damage is essentially lethal. This saturation of the enzyme repair system is the signature for the switch from the cell repair to the cell kill mechanism. It is possible to make another improvement of the dose–effect relation by redefining D. Repair will modify D, and this can be described by introducing a biological dose $D_{\rm B}$ defined as $D_{\rm B}P(0) = D$. Here, $P(0)$ is the repair-based Poisson probability $P(0) = {\rm e}^{-\mu D_{\rm B}}$ (μ is a constant in units ${\rm Gy}^{-1}$) for the number of cells that experience no events during a repair time τ (and thus are certain to survive) when they are expected to receive the dose $D_{\rm B}$. Thus, for the given dose D, the repair-modified dose $D_{\rm B}$ is defined by the real-valued solution of the implicit transcendental equation $D_{\rm B}{\rm e}^{-\mu D_{\rm B}} = D$. To solve this equation, we expand ${\rm e}^{-\mu D_{\rm B}}$ in powers of $D_{\rm B}$. The obtained series is inverted to express $D_{\rm B}$ as an expansion in powers of D. The final result is $D_{\rm B} = (1/\mu)\sum_{k=1}^{\infty}(k^{k-1}/k!)(\mu D)^k \equiv (1/\mu)T(\mu D)$, where T is the Euler tree function, which is related to the Lambert W function by $T(y) = -W(-y)$. This yields the biological effect ${\rm E_B} \equiv \alpha D_{\rm B}$ to all orders as ${\rm E_B} = \alpha D + \beta D^2 + (3/2)(\beta^2/\alpha)D^3 + (8/3)(\beta^3/\alpha^2)D^4 + (125/24)(\beta^4/\alpha^3)D^5 + \cdots = (\alpha^2/\beta)\sum_{k=1}^{\infty}(k^{k-1}/k!)(\beta D/\alpha)^k$ where $\beta = \mu\alpha$. The corresponding cell surviving fraction is $S_{\rm F}^{\rm (B)}(D) \equiv {\rm e}^{-{\rm E_B}} = \exp\left(-[\alpha^2/\beta]\sum_{k=1}^{\infty}[k^{k-1}/k!][\beta D/\alpha]^k\right)$ or $S_{\rm F}^{\rm (B)}(D) = \exp(-\alpha D - \beta D^2 - [3/2][\beta^2/\alpha]D^3 - [8/3][\beta^3/\alpha^2]D^4 - [125/24][\beta^4/\alpha^3]D^5 - \cdots)$. Thus, $S_{\rm F}^{\rm (LQ)}(D)$ is a low-dose limit of $S_{\rm F}^{\rm (B)}(D)$ obtained if only the first two leading terms $\alpha D + \beta D^2$ are kept. The test ratio implies that the series from ${\rm E_B}$ or $S_{\rm F}^{\rm (B)}(D)$ converges for $D \leq (\alpha/\beta)P_0$, where $P_0 = 1/e \approx 1/2.7183 \approx 0.3679$ is the probability at $D = D_0$ for which the repair-free cell surviving fraction ${\rm e}^{-D/D_0}$ drops by a factor of $\sim 1/e$ or by $\sim 36.79\%$. However, besides the above series the definitions $W(x)e^{W(x)} \equiv x$ and $T(x){\rm e}^{-T(x)} \equiv x$ permit several alternative representations for $W, T, {\rm E_B}$ and $S_{\rm F}^{\rm (B)}(D)$, including certain Padé-type approximations [74]. A further analysis of $S_{\rm F}^{\rm (B)}(D)$ will be reported shortly.

31. CONCLUSIONS

The Padé approximant (PA), as a ratio of two polynomials, is the most known rational function. In physics, this polynomial quotient represents the finite rank representation of the Green function or the energy spectrum of a general system. Energy or frequency spectra of a generic system are completely described by the fundamental sets of all the physical poles and zeros. Such key characteristics are directly ingrained in the very form of the PA because its numerator and denominator polynomial give rise to the system zeros and poles, respectively. In spectral analysis and signal processing, the PA is equivalently called the fast Padé transform (FPT). This was done to highlight the fact that the direct and inverse transformations within the FPT from the time to the frequency domain and *vice versa* are possible with no loss

of information. More specifically, from the analytically available expansion coefficients of the continued fraction that are implicit in the FPT, the original noise-free and/or noise-corrupted time signal points can be retrieved exactly. This feature in itself is the key to the definition of a *transform* from the time to the frequency domain and *vice versa*. The most often employed qualitative method for this type of transformation has been the fast Fourier transform (FFT), which is commercially built into spectrometers for physics and chemistry, as well as in scanners for medicine.

The FFT provides only an overall total shape spectrum in the frequency domain, which represents an envelope of all concentrations of molecules in the structural studies of matter. However, the goal is precisely to extract the information that is underneath this envelope, namely the component spectrum for each molecule. Since this is impossible within the Fourier analysis, the customary procedure has been to resort to fitting the total shape spectrum from the FFT by adjusting the entire envelope to a subjectively preselected number of components. The number of molecules and their abundance or concentrations are assessed in postprocessing the given FFT spectrum via least-square fitting. The major drawback of this usual procedure in signal processing is the lack of uniqueness since any number of preassigned peaks can be fitted to a given envelope within a prescribed accuracy. This procedure has not met with success in the interdisciplinary applications, including medical diagnostics, because some physical molecules can be missed and unphysical ones falsely predicted. Moreover, due to its linearity, the FFT imparts noise as unaltered from the time domain to the frequency domain. The FFT has no possibility of separating noise from the true signal. Each molecule has one or more resonant frequencies. Besides concentrations, the task is also to reconstruct these frequencies, known as chemical shifts. The FFT cannot retrieve them since this method deals with the preassigned Fourier grid frequencies as a function of the total acquisition time. This is the main reason for which postprocessing the envelopes from the FFT is used by fitting to surmise the underlying components.

On the other hand, the FPT simultaneously circumvents all these drawbacks of the FFT. As a nonlinear transform, the FPT effectively suppresses noise from the analyzed time signals. Most importantly, the FPT avoids postprocessing altogether via fitting or any other subjective adjustments. This is accomplished by a direct quantification of the time signal through spectral analysis, which provides the unique, exact solution for the inverse harmonic problem. This solution contains four spectral parameters (two complex frequencies and two complex amplitudes) for each resonance or peak in the associated frequency spectrum. From such spectral parameters, the molecular concentrations are unequivocally extracted, thus bypassing the ubiquitous ambiguities from fittings (underfitting associated with missing genuine molecules and overfitting corresponding to finding unphysical resonances). Moreover, the FPT succeeds in solving the most difficult

problem in spectral analysis of time signals corrupted with noise by providing the exact separation of signal from noise. Identification of noise and noise-like information is achieved in the FPT through the appearance of Froissart doublets where poles and zeros coincide in the analyzed spectrum. As a double signature for signal-noise separation, the FPT detects zero or near-zero amplitudes of Froissart doublets. In this way, genuine and spurious resonances are unmistakably disentangled within the FPT.

The expounded features of the FPT have been confirmed in practice for both theoretically generated and experimentally measured time signals. In the present work, we report a part of this achievement as supporting evidence for the most accurate reconstructions that are robust even against computational round-off-errors. For concreteness, the concept of the versatile and powerful Padé methodology and illustrations are presented specifically for time signals encountered the field of nuclear magnetic resonance spectroscopy with clinical applications. However, there is no limitation whatsoever for wide applications of the FPT to any other field dealing with time signals and spectra. Whenever the fast Fourier transform and the accompanying fitting are employed with all their ensuing ambiguities as obvious drawbacks, the fast Padé transform comes to the rescue carrying out spectral analysis of proven validity for reconstructing the hidden information from the studied substance through unequivocal extraction of spectral parameters of all the genuine resonances, including their true number.

ACKNOWLEDGMENTS

This work was supported by the Swedish Cancer Society Research Fund (Cancerfonden), King Gustav the Fifth Jubilee Foundation, and Karolinska Institute Research Fund.

REFERENCES

[1] H. Günther, NMR Spectroscopy, John Willey & Sons, Chichester, 2001.
[2] Dž. Belkić, Quantum-Mechanical Signal Processing and Spectral Analysis, Institute of Physics Publishing, Bristol, 2005.
[3] K. Belkić, Molecular Imaging through Magnetic Resonance for Clinical Oncology, Cambridge International Science Publishing, Cambridge, 2003.
[4] Dž. Belkić, K. Belkić, Signal Processing in Magnetic Resonance Spectroscopy with Biomedical Applications, Taylor & Francis, London, 2010.
[5] E.R. Danielsen, B. Ross, Magnetic Resonance Spectroscopy Diagnosis of Neurological Diseases, Marcel Dekker, New York, 1999.
[6] R.A. de Graff, In Vivo NMR Spectroscopy: Principles and Techniques, John Willey & Sons, Sussex, 2010.
[7] K. Wütrich, NMR in Structural Biology, World Scientific, Singapore, 1995.
[8] M.A. Johnson, K. Jaudzems, K. Wüthrich, J. Mol. Biol. 402 (2010) 619.
[9] C.E. Mountford, S. Doran, C.L. Lean, P. Russell, Chem. Rev. 104 (2004) 3667.

[10] G. Zhu, A. Bax, J. Magn. Reson. 100 (1992) 202.
[11] M.A. Delsuc, F. Ni, G.C. Levy, J. Magn. Reson. 73 (1987) 548.
[12] Ó. Alejos, C. de Francisco, P. Hernández, J.M. Muñoz, Comput. Mater. Sci. 7 (1997) 351.
[13] Ó. Alejos, C. de Francisco, J.M. Muñoz, P. Hernández-Gómez, C. Torres, J. Comp. Meth. Sci. Eng. 1 (2001) 213.
[14] R. Chen, G. Ma, H. Guo, Chem. Phys. Lett. 320 (2000) 567.
[15] H. Guo, J. Comp. Meth. Sci. Eng. 1 (2001) 251.
[16] E.J. Brändas, R.J. Bartlett, Chem. Phys. Lett. 8 (1971) 153.
[17] T.V. Levitina, E.J. Brändas, J. Comp. Meth. Sci. Eng. 1 (2001) 287.
[18] T.V. Levitina, E.J. Brändas, Comput. Chem. 825 (2001) 55.
[19] E.J. Brändas, Mol. Phys. 103 (2005) 2073.
[20] T. Taswell, J. Comput. Appl. Math. 121 (2000) 179.
[21] T. Taswell, J. Comp. Meth. Sci. Eng. 1 (2001) 315.
[22] Dž. Belkić, Nucl. Instr. Meth. Phys. Res. A 525 (2004) 366.
[23] Dž. Belkić, Adv. Quantum Chem. 51 (2006) 157.
[24] Dž. Belkić, Nucl. Instr. Meth. Phys. Res. A 580 (2007) 1034.
[25] Dž. Belkić, Adv. Quantum Chem. 56 (2009) 95.
[26] K. Belkić, Nucl. Instr. Meth. Phys. Res. A 525 (2004) 313.
[27] K. Belkić, Nucl. Instr. Meth. Phys. Res. A 580 (2007) 874.
[28] Dž. Belkić, K. Belkić, Phys. Med. Biol. 51 (2005) 4385.
[29] Dž. Belkić, K. Belkić, Phys. Med. Biol. 51 (2006) 1049.
[30] Dž. Belkić, K. Belkić, J. Math. Chem. 42 (2007) 1.
[31] Dž. Belkić, K. Belkić, J. Math. Chem. 43 (2008) 395.
[32] Dž. Belkić, K. Belkić, J. Math. Chem. 44 (2008) 887.
[33] Dž. Belkić, K. Belkić, J. Math. Chem. 45 (2009) 790.
[34] Dž. Belkić, K. Belkić, J. Math. Chem. 45 (2009) 819.
[35] M. Froissart, Centre Nacional de la Récherche Scientifique, Recherche Cooperative sur Programme N° 25, Strasbourg, J. Carmona, M. Froissart, D.W. Robinson, D. Ruelle (Eds) 9 (1989) 1.
[36] J. Gilevicz, M. Pindor, J. Comput. Appl. Math. 87 (1997) 199.
[37] D. Shanks, J. Math. Phys. 34 (1955) 1.
[38] Dž. Belkić, P.A. Dando, J. Main, H.S. Taylor, J. Chem. Phys. 133 (2000) 6542.
[39] J. Main, P.A. Dando, Dž. Belkić, H.S. Taylor, J. Phys. A: Math. Gen. 33 (2000) 1247.
[40] M.R. Wall, D. Neuhauser, J. Chem. Phys. 102 (1995) 8011.
[41] V.A. Mandelshtam, H.S. Taylor, J. Chem. Phys. 107 (1997) 6756.
[42] V.A. Mandelstham, Progr. Nucl. Magn. Reson. Spectrosc. 38 (1999) 159.
[43] Dž. Belkić, P.A. Dando, H.S. Taylor, J. Main, Chem. Phys. Lett. 315 (1999) 135.
[44] Dž. Belkić, P.A. Dando, J. Main, H.S. Taylor, S.-K. Shin, J. Phys. Chem. A 104 (2000) 11677.
[45] W.H. Press, S.A. Teukolsky, W.T. Vetterling, B.P. Flannery, Numerical Recipes, Cambridge University Press, Cambridge, 1992.
[46] A.A. Istratov, O.F. Vivenko, Rev. Sci. Instr. 70 (1999) 1233.
[47] Dž. Belkić, J. Comp. Meth. Sci. Eng. 3 (2003) 109.
[48] R. Haydock, V. Heine, P.J. Kelly, J. Phys. C 5 (1972) 2845.
[49] B.T. Smith, J.M. Boyle, J.J. Dongarra, B.S. Garbow, V.C. Klema, C.B. Moler, Matrix Eigensystem Routines - EISPACK Guide, Lectures Notes in Computer Science, Springer-Verlag, New York, 1976.
[50] NAG Fortran Library, NAG: Numerical Algorithms Group, 256 Banbury Road, Oxford OX2 7DE, UK, http://www.nag.co.uk/numeric/fl/FLdescription.asp, 2011.
[51] IMSL Fortran Library – Version 6.0 (2007), IMSL Math. Library User's Manuel, International Mathematical Statistical Library, IMSL Inc.: 2500 City West Boulevard, Houston TX 77042, USA.
[52] J.K. Cullum, R.A. Willoughby, Lanczos Algorithm for Large Symmetric Eigenvalue Computations, Birkhäuser, Boston, 1985.

[53] Dž. Belkić, J. Comp. Meth. Sci. Eng. 3 (2003) 563.
[54] M. Steck, K. Beckert, H. Eickloff, B. Franzke, F. Nolden, H. Reich, et al., Phys. Rev. Lett. 77 (1996) 3803.
[55] Dž. Belkić, Nucl. Instr. Meth. Phys. Res. A 525 (2004) 372.
[56] B.I. Schneider, Phys. Rev. A 55 (1997) 3417.
[57] Dž. Belkić, Principles of Quantum Scattering Theory, The Institute of Physics Publishing, Bristol, 2004.
[58] J.C. Wheeler, Rocky Mt. J. Math. 4 (1974) 287.
[59] P. Feldman, R.F. Freund, IEEE Trans. Comput. Aided Des. Integr. Circuits Syst. 14 (1995) 639.
[60] R.F. Freund, P. Feldman, IEEE Trans. Circuits Syst. Anal. Digit. Sign. Process. 43 (1996) 577.
[61] G.A. Baker, J.L. Gammel, The Padé Approximant in Theoretical Physics, Academic Press, New York, 1970.
[62] A. Nauts, R.E. Wyatt, Phys. Rev. Lett. 51 (1983) 2238.
[63] H.O. Karlsson, O. Goscinski, J. Phys. B 25 (1992) 5015.
[64] H.O. Karlsson, O. Goscinski, J. Phys. B 27 (1994) 1061.
[65] H.S. Wall, Analytic Theory of Continued Fractions, D. Van Nostrand Inc, New York, 1948.
[66] H. Rutishauser, Der Quotienten Differenzen Algorithmus, Birkhäuser, Basel & Stuttgart, 1957.
[67] P. Henrici, Proc. Symp. Appl. Math. 15 (1963) 159.
[68] P. Wynn, Math. Tabl. Aids. Comp. 10 (1956) 91.
[69] R.G. Gordon, J. Math. Phys. 2 (1968) 655.
[70] J. Geronimus, Annais de Faculdade de Sciências do Porto 16 (1929) 23.
[71] J. Frahm, H. Bruhn, M.L. Gyngell, K.D. Merboldt, W. Hänicke, R. Sauter, Magn. Reson. Med. 9 (1989) 79.
[72] I. Tkáč, P. Andersen, G. Adriany, H. Merkle, K. Uğurbil, R. Gruetter, Magn. Reson. Med. 46 (2001) 451.
[73] M. Elkind, H. Sutton, Nature 184 (1959) 1293.
[74] Dž. Belkić, J. Math. Chem. 49 (2011) 1618.

CHAPTER 5

Quantum Correlation Effects in Electron Dynamics in Molecular Wires and Solar Cells: The Nonequilibrium Green's Function Approach

Grigory Kolesov and **Yuri Dahnovsky**[a]

Contents

1. Introduction 262
2. Nonequilibrium Green's Function Formalism 264
   2.1. Keldysh contour 264
   2.2. Nonequilibrium Green's functions 267
   2.3. Some useful relations 268
   2.4. The Kadanoff-Baym equations 270
3. Transport in Tunneling Junctions 272
   3.1. Keldysh functions for noninteracting bridge electrons: the diagrammatic approach 274
   3.2. Uncorrelated electrons in tunneling junctions 274
   3.3. Renormalized zeroth Green's functions 277
   3.4. Nonequilibrium Green's functions for interacting bridge electrons 280
   3.5. Noncrossing approximation 283
   3.6. Electron propagator in the noncrossing approximation 284
   3.7. Molecular wire numerical calculations 287
   3.8. Molecular transistors 292
4. Photocurrent in Quantum Dot–Sensitized Solar Cells 299
   4.1. Hamiltonian 300

[a] Department of Physics and Astronomy, University of Wyoming, Laramie, WY, USA.

This article is dedicated to Yngve Öhrn for his contribution to electron propagator methods and their implementation for quantum chemical calculations.

Advances in Quantum Chemistry, Volume 61
ISSN 0065-3276, DOI: 10.1016/B978-0-12-386013-2.00005-X

4.2. Photoelectric current 302
4.3. Uncorrelated electrons in a quantum dot 303
4.4. Correlated QD electrons 306
4.5. Electron–phonon interaction in the semiconductor 307
5. Conclusions 309
Acknowledgments 310
References 310

Abstract In the development of different quantum chemical computational methods the main attention is paid to solving stationary many-body Schrödinger equations. Recent developments in chemistry, physics, energy physics, and materials science have brought forth a new class of problems where the evolution of a system is considered. As in the stationary case correlation effects are also important in the correct description of time-dependent problems. The most rigorous approach to describe system evolution is based on nonequilibrium Green's functions (or Keldysh functions). In chapter 2 we provide a general description of some important properties of nonequilibrium Green's functions. In particular we introduce nonequilibrium Green's functions on a Keldysh contour, describe the projection technique, and derive Kadanoff-Baym equations. The application of nonequilibrium Green's functions to tunneling junctions is given in chapter 3. In this chapter the equation for electric current is presented and Dyson equations for different nonequilibrium Green's functions are derived. As the implementation of the proposed methods, the particular numerical calculations of electric current in molecular diodes and transistors are discussed. We also describe the application of Keldysh functions to the calculations of photoelectric current in quantum dot sensitized solar cells. The general equation for photocurrent is expressed in terms of nonequilibrium Green's functions, which can be found from the proper Dyson equations. These equations contain arbitrary time-dependent electric field in the dipole approximation. The importance of the application of nonequilibrium Green's functions to various time-dependent problems is emphasized in conclusions.

1. INTRODUCTION

One-electron picture of molecular electronic structure provides electronic wavefunction, electronic levels, and ionization potentials. The one-electron model gives a concept of chemical bonding and stimulates experimental tests and predictions. In this picture, orbital energies are equal to ionization potentials and electron affinities. The most systematic approach to calculate these quantities is based on the Hartree–Fock molecular orbital theory that includes many of necessary criteria but very often fails in qualitative and quantitative descriptions of experimental observations.

Following the advances of the many-body theory started in physics in fifties and sixties of the twentieth century [1–8], many researchers in theoretical chemistry employed the ideas developed in physics and extended them to systems with a finite number of electrons [9–21]. Different software packages were developed soon [22] and applied to calculations of ionization potentials and electron affinities of various chemical systems [23–29]. The calculations appeared to be efficient, and the results were amazingly accurate.

The proliferation of experimental techniques in molecular electronics [30, 31] requires the further development of sophisticated computational methods to perform predictive calculations of conduction properties. The success of the electron propagator methodology applied to molecules provides a hope that this method will be also successful in systems combined from finite and infinite electron subsystems. In tunneling junctions, the molecular bridge electrons interact with electrons from the leads, and therefore the electronic levels of the molecular subsystem are modified by this interaction. Even if this interaction is small, there is finite dissipation resulting in the broadening of molecular levels. However, in the case of an isolated molecule, the imaginary part of the molecular Green's functions is infinitesimally small. The most systematic approach is to use many-body theory with a diagrammatic expansion with respect to the perturbation. In a many-electron system, this perturbation is usually the Coulomb interaction. In tunneling junctions, an interaction picture is different; there are two interactions: (1) the interaction between the lead electrons and the electrons in the bridge and (2) the Coulomb interaction within the bridge. The interaction between the bridge and lead electrons makes this problem substantially more complicated than molecular electronic structure calculations because of nonequilibrium conditions determined by the difference in chemical potentials of the leads. In this case, the nonequilibrium Green's function method has to be applied to find electric current in molecular devices.

Another important application of nonequilibrium electron propagator method is in quantum dot–sensitized solar cells. Indeed, to be competitive with conventional energy sources, substantial improvements in the performance and manufacturing cost of solar cells are needed to realize a system cost well below \$0.50/Wp. A critical aspect in reducing the module cost for next-generation systems is improvement of the solar cell efficiencies beyond the Shockley–Queisser limit for a single junction cell (∼32%). This limit is a consequence of the fact that photons below the bandgap of the absorber are not collected, whereas each absorbed photon above contributes only the energy of the electron–hole pair at the bandgap, independent of the photon energy; the excess energy of photoexcited carriers is lost in a short timescale through energy relaxation processes such as phonon emission. Kolondinski et al. [33] proposed a way around this limit through the generation of

multiple electron–hole pairs from a single photon through the creation of secondary carriers using band-to-band impact ionization. Because this process competes with phonon losses, the dynamics of carrier relaxation are of crucial importance in realizing quantum efficiencies much greater than unity. Particularly promising are quantum dot and nanocrystalline materials [32, 34–39] where the reduced dimensionality of the system suppresses the dominant optical phonon relaxation mechanisms. Indeed, the promising results on a two-electron transfer in sensitized QD solar cells have been recently obtained in the study by the group of Parkinson, in which the value of the photocurrent was increased by a factor of two if the frequency of light was greater than a 2.8 times the gap energy value [32]. In such systems, electron transfers from an excitonic QD state to a semiconductor. The estimated radius of the exciton is greater than a size of a quantum dot, and therefore the QD electron subsystem is highly correlated. It is correlated not only by e–e interactions but also by interactions with vibrations both in a QD and a semiconductor. In addition, the electron transfer in such systems is mainly nonequilibrium because of continuos light irradiation. Consequently, novel methods that include e–e and e–ph correlations in strong nonequilibrium environment have to be developed.

For such nonequilibrium processes, the direct mapping of the electron propagator methods to calculations of electric current becomes inapplicable because of the time-dependent nature of electric current in both phenomena. A time-dependent problem requires the further development of the theory of Green's functions to electron dynamics in which e–e correlation effects are taken into account. Such methodology already exists in physics in which many-body ideas have been developed for time-dependent problems. This theory is based on nonequilibrium Green's or Keldysh functions [2, 5, 6, 40–46].

In this work, we present a brief introduction to the nonequilibrium Green's function method and discuss two important examples in which nonequilibrium Green's functions can be employed: (1) electric current calculations in molecular tunneling devices and (2) in quantum dot–sensitized solar cells.

2. NONEQUILIBRIUM GREEN'S FUNCTION FORMALISM

2.1. Keldysh contour

In this section, we introduce the Keldysh formalism that allows for calculations of different quantum correlation functions necessary for various time-dependent problems. In our description, we follow the reviews of Danielewitcz [42] and van Leeuwen and Dahlen [46, 47]. We embark our discussion on the description of evolution of a system that is originally in statistical equilibrium. We are interested in an expectation value of an operator

$\hat{O}$ in a grand canonical ensemble at temperature T:

$$\langle \hat{O} \rangle = Tr\{\hat{\rho}\hat{O}\}, \tag{1}$$

where we denote

$$\hat{\rho} = \frac{e^{-\beta(\hat{H}-\mu\hat{N})}}{Tre^{-\beta(\hat{H}-\mu\hat{N})}}. \tag{2}$$

Initially, at $t < 0$, the isolated system is described by the Hamiltonian $\hat{H}_0$ that does not depend on time. Thus, any expectation value averaged with the density matrix $\hat{\rho}_0$ is time-independent. At $t > 0$, the system is disturbed by an external time-dependent field. Then, the evolution of the expectation value of operator $\hat{O}$ can be presented as follows:

$$\langle \hat{O} \rangle = Tr\{\hat{\rho}_0 \hat{O}_H(t)\} = Tr\{\hat{\rho}_0 \hat{U}(0,t)\hat{O}_I\hat{U}(t,0)\}, \tag{3}$$

where the operator in the Heisenberg representation is $\hat{O}_H(t) = \hat{U}(0,t)$ $\hat{O}\hat{U}(t,0)$. The evolution operator is determined from the following equations:

$$\begin{aligned} i\frac{d\hat{U}(t,t')}{dt} &= \hat{H}_I^i(t)\hat{U}(t,t'), \\ i\frac{d\hat{U}(t,t')}{dt'} &= -\hat{H}_I^i(t)\hat{U}(t,t')\hat{H}(t) \end{aligned} \tag{4}$$

with the initial conditions $\hat{U}(t,t') = 1$. $\hat{H}_I^i(t)$ is the interaction representation of the operator $\hat{H}^i$ defined as follows:

$$\hat{O}_I(t) = \exp\left[i\hat{H}_0(t-t_0)\right]\hat{O}\exp\left[-i\hat{H}_0(t-t_0)\right] \tag{5}$$

The solutions of Eq. (4) are

$$\begin{aligned} \hat{U}(t,t') &= \hat{T}\exp\left[-i\int_{t'}^{t} d\tau \hat{H}_I^i(\tau)\right] \quad t > t', \\ \hat{U}(t,t') &= \hat{\tilde{T}}\exp\left[i\int_{t}^{t'} d\tau \hat{H}_I^i(\tau)\right] \quad t < t'. \end{aligned} \tag{6}$$

The operator $\hat{T}$ rearranges the operators in the chronological order, whereas the operator $\hat{\tilde{T}}$ is the antichronological operator. In addition, the evolution operator satisfies the identity

$$\hat{U}(t,t_1)\hat{U}(t_1,t') = \hat{U}(t,t'). \tag{7}$$

An operator in the Heisenberg representation can be expressed in the interaction representation as follows:

$$\hat{O}_H(t) = \hat{U}(t_0,t)\hat{O}_I(t)\hat{U}(t,t'_0). \tag{8}$$

Assuming that in the density matrix, $\hat{\rho}_0$, $\hat{H}_0$, and $\hat{N}$ (a number of particle operator) commute, then $\hat{\rho}_0$ can be rewritten in terms of the evolution operator $\hat{U}$ with the complex time argument:

$$\hat{\rho}_0 = \frac{\exp\left[\beta\mu\hat{N}\right]\hat{U}(-i\beta,0)}{Tr\left\{\exp\left[\beta\mu\hat{N}\right]\hat{U}(-i\beta,0)\right\}}. \tag{9}$$

Inserting this expression in Eq. (3), we obtain

$$\langle\hat{O}\rangle = \frac{Tr\left\{\exp\left[\beta\mu\hat{N}\right]\hat{U}(-i\beta,0)\hat{U}(0,t)\hat{O}_I(t)\hat{U}(t,0)\right\}}{Tr\left\{\exp\left[\beta\mu\hat{N}\right]\hat{U}(-i\beta,0)\right\}}. \tag{10}$$

If we look at the time arguments in the evolution operator $\hat{U}$ from right to left, we see that the contour begins from $0 \to t \to 0 \to -i\beta$. Such a contour is called a Keldysh contour, γ, [40] and is shown in Figure 5.1. The group property (7) is also applicable to complex arguments on the contour. Using this property, we can present Eq. (10) in the following way:

$$\langle\hat{O}\rangle = \frac{Tr\left\{\exp\left[\beta\mu\hat{N}\right]\hat{T}_c\left\{\exp\left[-i\int_c dz'\hat{H}_I(z')\right]\hat{O}_I(z)\right\}\right\}}{Tr\left\{\exp\left[\beta\mu\hat{N}\right]\hat{T}_c\exp\left[-i\int_c dz'\hat{H}_I(z')\right]\right\}}. \tag{11}$$

The ordering operator $\hat{T}_c$ places the operators in the Taylor expansion of the T_c exponent to the left with a later-in-time variable on the contour γ. The operators are taken in the interaction representation on the Keldysh contour.

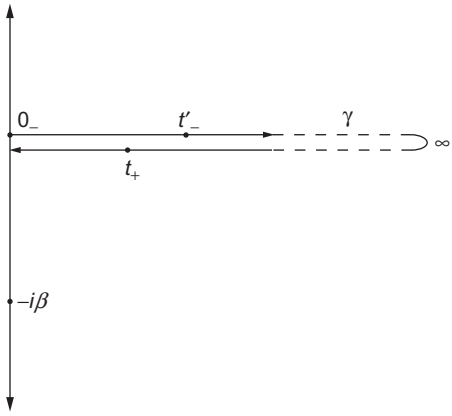

Figure 5.1 The Keldysh contour in the complex plane with t' on the forward branch and t on the backward branch. The contour begins at $t = 0$ on the upper branch and ends at $t = -i\beta$ on the vertical branch. Here "$-$" denotes the forward branch, whereas "$+$" represents the backward branch.

2.2. Nonequilibrium Green's functions

Before defining nonequilibrium Green's functions, we introduce field operators (e.g., a fermion field) $\hat{\psi}^{\dagger}(\mathbf{r})$ and $\hat{\psi}(\mathbf{r})$ satisfying the following anticommutator relation $\left\{\hat{\psi}(\mathbf{r}), \hat{\psi}^{\dagger}(\mathbf{r}')\right\} = \delta(\mathbf{r} - \mathbf{r}')$. The Green's function on a Keldysh contour is defined as

$$G(\mathbf{r}z, \mathbf{r}'z') = \langle \mathbf{r}|\mathbf{G}(z, z')|\mathbf{r}'\rangle = -i\langle \hat{T}_c \hat{\psi}_H(\mathbf{r}, z)\hat{\psi}_H^{\dagger}(\mathbf{r}'z')\rangle, \tag{12}$$

where the field operators are taken in the Heisenberg representation. The Green's function operator (12) can be rewritten as follows:

$$\mathbf{G}(z, z') = \theta(z, z')\mathbf{G}^{>}(z, z') + \theta(z', z)\mathbf{G}^{<}(z, z'). \tag{13}$$

The function $\theta(z, z')$ is equal to 1 if z is later than z' on the contour γ and 0 otherwise. The "lesser" and "greater" Green's functions are defined as

$$-iG^{<}(\mathbf{r}z, \mathbf{r}'z') = \langle \hat{\psi}_H^{\dagger}(\mathbf{r}'z')\hat{\psi}_H(\mathbf{r}, z)\rangle, \tag{14}$$

$$iG^{>}(\mathbf{r}z, \mathbf{r}'z') = \langle \hat{\psi}_H(\mathbf{r}, z)\hat{\psi}_H^{\dagger}(\mathbf{r}'z')\rangle \tag{15}$$

Some interesting properties of nonequilibrium Green's functions can be proved. If we choose $z = 0_-$ (here "$-$" corresponds to time on the upper

branch of γ and "+" to the lower one), which is the earliest time on the Keldysh contour, then [47]

$$\begin{aligned}\mathbf{G}(0_-, z') &= -e^{\beta\mu}\mathbf{G}(-i\beta, z'),\\ \mathbf{G}(z, 0_-) &= \mathbf{G}(z, -i\beta).\end{aligned} \tag{16}$$

These two identities are called Kubo-Martin-Schwinger boundary conditions [47]. From the commutation relation, it follows that

$$i\left(G^{>} - G^{<}\right)(\mathbf{r}z, \mathbf{r}'z) = \delta(\mathbf{r} - \mathbf{r}'). \tag{17}$$

In addition, the following symmetry relation is true on the real axis:

$$\left[\mathbf{G}^{\lessgtr}(t', t)\right]^{\dagger} = -\mathbf{G}^{\lessgtr}(t, t'). \tag{18}$$

These equations are important for solving Kadanoff–Baym equations.

2.3. Some useful relations

Green's function belongs to a larger class of functions of two time-contour variables that includes a divergent term as well:

$$k(z, z') = \delta(z, z')k^{\delta}(z, z') + \theta(z, z')k^{>}(z, z') + \theta(z', z)k^{<}(z, z'). \tag{19}$$

Here a δ-function on a Keldysh contour is defined as

$$\delta(z, z') = \frac{\mathrm{d}\theta(z, z')}{\mathrm{d}z}.$$

As follows from Eq. (12), the Green's function does not have a singular part, but a self-energy operator, Σ, does have it [42]

$$\Sigma(z, z') = \delta(z, z')\Sigma^{\delta}(z, z') + \theta(z, z')\Sigma^{>}(z, z') + \theta(z', z)\Sigma^{<}(z, z'). \tag{20}$$

The Keldysh function space is rather complicated because it has two real-time branches and one imaginary branch. Multiplication rules for operators with time arguments from different branches were proved by Langreth [41] and Wagner [48–50].

Consider the following integral on the Keldysh contour:

$$c(z,z') = \int_{\gamma} \mathrm{d}z_1 a(z,z_1) b(z_1,z'). \tag{21}$$

All three functions belong to the Keldysh space. For any function in the Keldysh space, we define the greater and the lesser functions on the real-time axis as

$$k^{>}(t,t') \equiv k(t_+,t_-) \qquad k^{<}(t,t') \equiv k(t_-,t_+). \tag{22}$$

To account quantum correlations of the function between real and imaginary times on the Keldysh contour, we additionally introduce the following correlation functions:

$$k^{\rceil}(t,\tau) \equiv k(t_\pm,\tau) \qquad k^{\lceil}(\tau,t) \equiv k(\tau,t_\pm). \tag{23}$$

The evaluation of the integral (21) is described in Ref. [47] and results in the following relations (we follow the notation of Ref. [47]):

$$c^{>} = a^{>} \cdot b^{A} + a^{R} \cdot b^{>} + a^{\rceil} \star b^{\lceil} \tag{24}$$

$$c^{<} = a^{<} \cdot b^{A} + a^{R} \cdot b^{<} + a^{\rceil} \star b^{\lceil}, \tag{25}$$

where the following definitions have been introduced:

$$f \cdot g \equiv \int_0^{\infty} \mathrm{d}t_1 f(t_1) g(t_1) \tag{26}$$

$$f \star g \equiv \int_0^{-i\beta} \mathrm{d}\tau_1 f(\tau_1) g(\tau_1). \tag{27}$$

In Eq. (24), we have defined the retarded and advanced functions as

$$k^{R}(t,\tau) \equiv \delta(t,t') k^{\delta} + \theta(t-t') \left[k^{>}(t,t') - k^{<}(t,t') \right], \tag{28}$$

$$k^{A}(t,\tau) \equiv \delta(t,t') k^{\delta} - \theta(t'-t) \left[k^{>}(t,t') - k^{<}(t,t') \right]. \tag{29}$$

It can be also proved that [47]

$$c^R = a^R \cdot b^R, \tag{30}$$

$$c^A = a^A \cdot b^A. \tag{31}$$

The function with time arguments on both real and imaginary time branches of the Keldysh contour can be presented in the following manner:

$$c^\rceil = a^R \cdot b^\rceil + a^\rceil \star b^M, \tag{32}$$

where

$$b^M(\tau, \tau') \equiv b(z = \tau, z' = \tau'). \tag{33}$$

For the Matsubara component, the following relations holds true:

$$c^M = a^M \star a^M. \tag{34}$$

There is another class of identities different from the relations considered earlier. These identities are the products of the functions:

$$c(z, z') = a(z, z')b(z', z). \tag{35}$$

For $z \neq z'$, the following identities are valid:

$$c^> = a^> b^<, \quad c^< = a^< b^>, \quad c^\rceil = a^\rceil b^\lceil, \quad c^\lceil = a^\lceil b^\rceil, \quad c^M = a^M b^M. \tag{36}$$

For retarded and advanced functions in the Keldysh space, we can write

$$\begin{aligned} c^R &= a^R b^< + a^< b^A = a^R b^> + a^> b^A, \\ c^A &= a^A b^< + a^< b^R = a^A b^> + a^> b^R \end{aligned} \tag{37}$$

All these identities are useful in the evaluation of integrals in diagrammatic expansions with respect to interaction and also in the derivation of equations of motion.

2.4. The Kadanoff-Baym equations

For a perturbation, expansion for Green's functions can be described in the same manner as for ordinary Green's function [1, 3, 4, 6–8]. The only

difference is in considering Green's functions and self-energies in a Keldysh space, with the rules discussed in the previous subsections. Besides a diagrammatic expansion, there is an alternative approach based on equation of motion where Green's function of the first order is expressed in terms of Green's function of the second order, the Green's function of the second order is expressed in terms of Green's function of the third order, and so on. The excellent presentations of this approach is given in Ref. [7]. Kadanoff and Baym applied the equation of motion approach to nonequilibrium Green's functions [5]. They derived the following equations:

$$\left(i\frac{\partial}{\partial z}-\hat{\mathbf{H}}_0\right)\mathbf{G}(z,z')=\hat{\mathbf{1}}\delta(z,z')+\int_\gamma dz_1\Sigma(z,z_1)\mathbf{G}(z_1,z'), \tag{38}$$

$$\mathbf{G}(z,z')\left(i\frac{\partial}{\partial z'}-\hat{\mathbf{H}}_0\right)=\hat{\mathbf{1}}\delta(z,z')+\int_\gamma dz_1\mathbf{G}(z,z_1)\Sigma(z_1,z'). \tag{39}$$

The external potential is included in these equations. The self-energy is defined as a function or operator in the Keldysh space according to Eq. (20). Σ obeys the Kubo-Martin-Schwinger boundary conditions (16). The $\binom{<}{>}$-projections of the Kadanoff–Baym equations can written as

$$\left(i\frac{\partial}{\partial t}-\hat{\mathbf{H}}_0\right)\mathbf{G}^{\lessgtr}(t,t')=\Sigma^R\cdot\mathbf{G}^{\lessgtr}+\Sigma^{\lessgtr}\cdot\mathbf{G}^A+\Sigma^{\rceil}\star\mathbf{G}^{\lceil}, \tag{40}$$

$$\mathbf{G}^{\lessgtr}(t,t')\left(i\frac{\partial}{\partial t'}-\hat{\mathbf{H}}_0\right)=\mathbf{G}^{\lessgtr}\cdot\Sigma^A+\mathbf{G}^R\cdot\Sigma^{\lessgtr}+\mathbf{G}^{\rceil}\star\Sigma^{\lceil}. \tag{41}$$

The retarded and advanced projections can be easily found as

$$\left(i\frac{\partial}{\partial t}-\hat{\mathbf{H}}_0\right)\mathbf{G}^{R}_{A}(t,t')=\hat{\mathbf{1}}\delta(t,t')+\Sigma^{R}_{A}\cdot\mathbf{G}^{R}_{A}, \tag{42}$$

$$\mathbf{G}^{R}_{A}(t,t')\left(i\frac{\partial}{\partial t'}-\hat{\mathbf{H}}_0\right)=\hat{\mathbf{1}}\delta(t,t')+\mathbf{G}^{R}_{A}\cdot\Sigma^{R}_{A}. \tag{43}$$

The $(\rceil,\lceil)$-projections obey the following equations:

$$\left(i\frac{\partial}{\partial t}-\hat{\mathbf{H}}_0\right)\mathbf{G}^{\rceil}(t,\tau)=\Sigma^R\cdot\mathbf{G}^{\rceil}+\Sigma^{\rceil}\cdot\mathbf{G}^M, \tag{44}$$

$$\left(i\frac{\partial}{\partial t}-\hat{\mathbf{H}}_0\right)\mathbf{G}^{\lceil}(t,\tau)=\Sigma^{\lceil}\cdot\mathbf{G}^A+\Sigma^M\cdot\mathbf{G}^{\lceil}. \tag{45}$$

Finally, the equation for the Matsubara Green's functions determines from the following equation:

$$\left(\frac{\partial}{\partial\tau} - \hat{\mathbf{H}}_0\right)\mathbf{G}^M(\tau,\tau') = \hat{\mathbf{1}}\delta(\tau,\tau') + \Sigma^M \cdot \mathbf{G}^M. \tag{46}$$

The Kadanov–Baym Eqs. (40), (44), and (46) determine the evolution of a quantum system in the most general way.

3. TRANSPORT IN TUNNELING JUNCTIONS

Here we embark on the application of nonequilibrium Green's functions in chemistry to molecular electronics. This problem is not traditional in chemistry because it includes a single molecule placed between two semi-infinite metal electrodes. A typical molecular device (a molecular wire) is depicted in Figure 5.2. Besides its fundamental importance, molecular electronics is a field in which progress depends on improved techniques for design and optimization of conducting structures at the atomic level [51]. The ability to perform predictive calculations on the conduction properties of large molecules could facilitate efforts to understand and manipulate the mechanisms that are responsible for electron transport. Given the diversity of structures, which may serve as wires, an unbiased theoretical approach based on *ab initio* methodology and not parametrized for a certain class of molecules is likely to have advantages in the interpretation of conduction measurements and in the stimulation of chemical synthesis. Although correlated *ab initio* propagator methods have been successful in computing spectra of large, isolated species [9–21], it is likely that an extension of

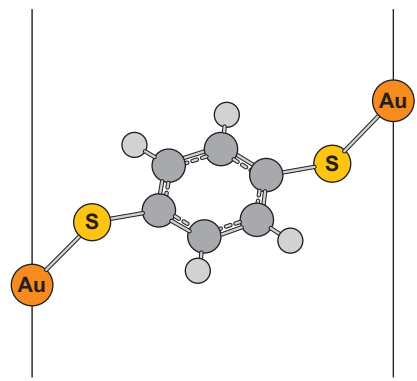

Figure 5.2 Dithiol molecule placed between to gold electrodes.

these capabilities to the determination of nonequilibrium electronic properties would have considerable value, in cost and time, for those who would construct and characterize molecular wires. Among these methods, electron propagator techniques are known for their efficient generation of correlated electron binding energies and Dyson orbitals, which are needed in the leading theories of electron transport. Because molecular electron propagators that are expressed in a finite basis set have no imaginary parts, they exhibit no dissipation [11]. Interaction of the bridge with the leads produces dissipation that appears as the imaginary part of a nonequilibrium Keldysh function. In tunneling junctions, the molecular bridge electrons interact with electrons from the leads, and therefore the electronic levels of the molecular subsystem are modified by this interaction. The most systematic approach in many-body theory is a diagrammatic expansion with respect to the perturbation. In a many-electron system, this perturbation is usually the Coulomb interaction. In the case of tunneling junctions, there are two interactions: (1) the interaction between the lead electrons and the electrons in the bridge and (2) the Coulomb interaction within the bridge (in this work, we consider that the lead electrons are noninteracting). Hence, we consider these two interactions as perturbations. For noninteracting lead electrons, the expression for electric current was obtained in Refs. [45, 52, 53].

$$J = \frac{ie}{2\hbar}\int \frac{\mathrm{d}\omega}{2\pi} Tr\{(\Gamma^L - \Gamma^R)\mathbf{G}^< + (f_L - f_R)(\mathbf{G}^r - \mathbf{G}^a)\}. \tag{47}$$

Here $\Gamma^{L,R}_{n_1,n_2}(\omega)$ are line-broadening matrices defined as follows:

$$\Gamma^{L,R}_{n_1,n_2}(\omega) = \pi \sum_k \left[V_{L,R}(k,n_1)V^*_{L,R}(k,n_2) + c.c.\right]\delta\left(\omega - \varepsilon^{L,R}_k\right). \tag{48}$$

In Eq. (47), $\mathbf{G}^<$, $\mathbf{G}^r$, and $\mathbf{G}^a$ are nonequilibrium Green's functions of the bridge where the interaction between the bridge and leads' electrons is included in the Green's functions. f_L and f_R are fermi functions of the left and right leads, respectively. $V_{L,R}(k,n_1)$ is the matrix element of the interaction between the electrons of the left (right) lead and the bridge electrons. To determine the electric current, it is necessary to find Keldysh functions of the bridge molecule. These Green's functions are modified by the interactions with the leads electrons.

To find nonequilibrium bridge Green's functions, we develop a diagrammatic technique with respect to Coulomb interaction in the bridge. Below, we follow the presentation given in Ref. [54] in which we derive the Dyson equations for bridge Keldysh functions that are modified by the tunneling interactions. Then, we show that Dyson equations for bridge *nonequilibrium* Green's functions have the same topological structure as Dyson equations for *equilibrium* Green's functions (with no interaction with the leads). In these

equations, the zeroth Green's functions are modified by the interaction with the lead electrons.

3.1. Keldysh functions for noninteracting bridge electrons: the diagrammatic approach

The Hamiltonian that describes a tunnel junction is given by the following expression:

$$\hat{H} = \hat{H}_L + \hat{H}_R + \hat{H}_M + \sum_{k,n} \left\{ \left[V_L(k,n) c_k^\dagger d_n + h.c. \right] + \left[V_R(k,n) b_k^\dagger d_n + h.c. \right] \right\}, \quad (49)$$

where only in the bridge Hamiltonian, $\hat{H}_M$, we have included Coulomb interaction between the electrons:

$$\begin{aligned} \hat{H}_L &= \sum_k \varepsilon_k^L c_k^\dagger c_k, \\ \hat{H}_R &= \sum_k \varepsilon_k^R b_k^\dagger b_k, \\ \hat{H}_M &= \sum_n \varepsilon_n d_k^\dagger d_n + \frac{1}{2} \sum_{n_1,n_2,n_3,n_4} V^{(0)}_{n_1,n_2,n_4,n_3} d_{n_1}^\dagger d_{n_2}^\dagger d_{n_3} d_{n_4}. \end{aligned} \quad (50)$$

Here $c_k, c_k^\dagger$ are annihilation and creation fermi operators for the left lead electrons, $b_k, b_k^\dagger$ are the same but for the right lead electrons, and $d_n, d_n^\dagger$ are creation and annihilation operators for the bridge electrons. In Eq. (49), $V_{L,R}(k,n)$ denotes the tunneling matrix element between the the kth electronic state of the left (or right) lead and the nth bridge electronic state. In Eq. (50), $V^{(0)}_{n_1,n_2,n_4,n_3}$ is a Coulomb integral in the bridge. ε_k^L, ε_k^R, and ε_n stand for the single-electron orbital electronic energies in the left lead, the right lead, and the bridge, respectively.

3.2. Uncorrelated electrons in tunneling junctions

To understand the diagrammatic approach, which is introduced below, we first determine the nonequilibrium Green's functions for uncorrelated electrons in the leads and the bridge on a Keldysh contour employing a diagrammatic expansion rather than the equation of motion [45, 52, 53]. For such a system, the Hamiltonian is given by:

$$\hat{H}_0 = \sum_k \varepsilon_k^L c_k^\dagger c_k + \sum_k \varepsilon_k^R b_k^\dagger b_k + \sum_n \varepsilon_n d_k^\dagger d_n. \quad (51)$$

In this subsection, we calculate the Keldysh functions for the electrons in the bridge. Nonequilibrium Green's functions between the bridge, and left lead, and left-lead-bridge electrons are defined in the following way:

$$i\tilde{G}_{nm}(t-t') =< \tilde{T}d_n(t)d_m^{\dagger}(t') >, \tag{52}$$

$$ig^{L}_{kk'}(t-t') =< \tilde{T}c_k(t)c_{k'}^{\dagger}(t') >, \tag{53}$$

$$ig^{R}_{kk'}(t-t') =< \tilde{T}b_k(t)b_{k'}^{\dagger}(t') >, \tag{54}$$

$$i\tilde{G}_{nk}(t-t') =< \tilde{T}d_n(t)c_k^{\dagger}(t') >. \tag{55}$$

The Keldysh functions for the right electrode should be defined in the same manner. In Eqs. (52)–(55), we use time ordering $\tilde{T}$ on a Keldysh contour [6, 40, 42, 45–47].

In the interaction representation, the bridge Keldysh functions are presented as follows:

$$i\tilde{G}^{(0)}_{nm}(t-t') =< \tilde{T}\tilde{d}_n(t)\tilde{d}_m^{\dagger}(t')\hat{S}_c >, \tag{56}$$

where S_c is a scattering matrix [1, 4–8, 45] with the time ordering on the Keldysh contour γ defined in section 2:

$$\hat{S}_c = \tilde{T}exp\left(-i\int_c \mathrm{d}t_1\hat{H}_{int}(t_1)\right) = \sum_{l=0}^{\infty}\frac{(-i)^l}{l!}\int_c \mathrm{d}t_1\ldots\int_c \mathrm{d}t_l\tilde{T}\hat{H}_{int}(t_1)\ldots\hat{H}_{int}(t_l). \tag{57}$$

Here the operators for $\hat{H}_{int}(t)$ are taken in the interaction representation:

$$\begin{aligned}\tilde{d}_n(t) &= e^{i\hat{H}_0 t}d_n e^{-i\hat{H}_0 t},\\ \tilde{c}_k(t) &= e^{i\hat{H}_0 t}c_k e^{-i\hat{H}_0 t},\\ \tilde{b}_k(t) &= e^{i\hat{H}_0 t}b_k e^{-i\hat{H}_0 t}.\end{aligned} \tag{58}$$

In Eq. (57), $\hat{H}_{int}$ in the interaction representation is defined as the interaction between the lead and bridge electrons:

$$\hat{H}_{int}(t) = \sum_{k,n}\left\{\left[V_L(k,n)\tilde{c}_k^{\dagger}(t)\tilde{d}_n(t) + h.c.\right] + \left[V_R(k,n)\tilde{b}_k^{\dagger}(t)\tilde{d}_n(t) + h.c.\right]\right\} \tag{59}$$

For simplicity, we consider only a left lead. The generalization to two leads is straightforward. Since the interaction has an odd number of each operators c and d (see Eq. (59)) and the Taylor expansion in the S-matrix in Eq. (57)

contains only even terms, the nonequilibrium bridge Green's function yields:

$$i\tilde{G}^{(0)}_{nm}(t-t') = < \tilde{T}\tilde{d}_n(t)\tilde{d}^{\dagger}_m(t')\hat{S}_c >= \sum_{l=0}^{\infty}\frac{(-1)^l}{(2l)!}\sum_{k_1,n_1}\dots\sum_{k_{2l},n_{2l}}\int_c \mathrm{d}t_1\dots\int_c \mathrm{d}t_{2l}$$
$$\times <\tilde{T}\tilde{d}_n(t)\tilde{d}^{\dagger}_m(t')\left[V_L(k_1,n_1)\tilde{c}^{\dagger}_{k_1}(t_1)\tilde{d}_{n_1}(t_1)+h.c.\right]\dots$$
$$\times\left[V_L(k_{2l},n_{2l})\tilde{c}^{\dagger}_{k_{2l}}(t_{2l})\tilde{d}_{n_{2l}}(t_{2l})+h.c.\right]>. \tag{60}$$

It is apparent that different types of electrons should be averaged separately. According to Wick's theorem [1, 4, 6–8], the averages of the multiple products of the operators in Eq. (60) can be decoupled into the product of Green's functions (paired operators). To find a Dyson equation, we regroup the infinite sums in the following manner:

$$i\tilde{G}^{(0)}_{nm}(t-t') = \sum_{l=0}^{\infty}\frac{(-1)^l}{(2l)!}\sum_{k_{21-1},n_{21-1}}\sum_{k_{2l},n_{2l}}\int_c \mathrm{d}t_{21-1}\int_c \mathrm{d}t_{2l} < \tilde{T}\tilde{d}_n(t)\tilde{d}^{\dagger}_{n_{2l}}(t_{2l}) >$$
$$\times\left[V_L(k_{2l},n_{2l})V^{*}_L(k_{2l-1},n_{2l-1}) < \tilde{T}\tilde{c}_{k_{2l}}(t_{2l})\tilde{c}^{\dagger}_{k_{2l-1}}(t_{2l-1}) >\right][...], \tag{61}$$

where the rest of the series is presented in the brackets. Due to the symmetry of the integrand in the T-exponent series, t_{2l} and t_{2l-1} can be chosen $2l(2l-1)/2$ times. Therefore, the expression in the brackets is in fact the exact Green's function for the bridge electrons, $i\tilde{G}^{(0)}_{n_2m}(t_2-t')$. Thus, one obtains the following Dyson equation for the bridge Keldysh function:

$$\tilde{G}^{(0)}_{nm}(t-t') = G^{(0)}_{nm}(t-t') + \sum_{n_1,n_2}\int_c \mathrm{d}t_1\int_c \mathrm{d}t_2 G^{(0)}_{nn_1}(t-t_1)\Sigma^{(0)}_{n_1n_2}(t_1-t_2)\tilde{G}^{(0)}_{n_2m}(t_2-t'), \tag{62}$$

where the self-energy matrix is defined in the following manner:

$$\Sigma^{(0)}_{n_1,n_2}(t_1-t_2) = \sum_{k_1,k_2}\left\{\left[V_L(k_1,n_1)g^{L}_{k_1k_2}(t_1-t_2)V^{*}_L(n_2,k_2)\right]\right.$$
$$\left.+\left[V_R(k_1,n_1)g^{R}_{k_1k_2}(t_1-t_2)V^{*}_R(n_2,k_2)\right]\right\}. \tag{63}$$

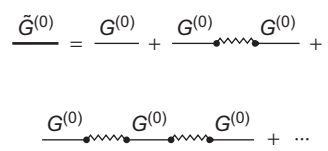

Figure 5.3 Diagrammatic representation of Dyson equation (62). A solid line denotes the zeroth bridge Keldysh function, a wedged line stands for a linear combination of the zeroth lead Keldysh functions determined by Eq. (63), and a dot represents a tunneling transition.

In Eq. (63), the generalization to two leads has been made. Here the left and right lead Keldysh functions are defined by Eqs. (53) and (54). The Dyson equation (62) is diagrammatically presented for noninteracting electrons in Figure 5.3. In this figure, a solid line represents the zeroth bridge Keldysh function, $G^{(0)r}(t-t')$, and a wedged line defines a linear combination of zeroth lead Keldysh functions determined by Eqs. (53) and (54): $\sum_{k_1,k_2} V_L(k_1,n_1) g^L_{k_1k_2}(t_1-t_2) V^*_L(n_2,k_2)$. The dot is interaction, V, that has been included into the definition of a wedged line. The graph describes a perturbation series with respect to $|V|^2$.

3.3. Renormalized zeroth Green's functions

The nonequilibrium zeroth Green's functions are determined by the Dyson equations (62) and (63) on the Keldysh contour. The standard way to solve these equations is to perform a Fourier transform and then solve the algebraic matrix equations for the Green's functions. For the Keldysh functions, this procedure cannot be implemented in a straightforward way because of two time branches. Thus, we should find the Fourier transform for each Keldysh function after applying the Langreth's mapping procedure described in Section 2 [41, 45]. In particular for $\tilde{G}^{(0)<}_{nm}(t-t')$, the Dyson equation is given by

$$\tilde{G}^{(0)<}_{nm}(t-t') = G^{(0)<}_{nm}(t-t') + \sum_{n_1,n_2} \int_{t_0}^{t} \mathrm{d}t_1 \int_{t_0}^{t} \mathrm{d}t_2 G^{(0)r}_{nn_1}(t-t_1) \Sigma^{(0)<}_{n_1n_2}(t_1-t_2) \tilde{G}^{(0)a}_{n_2m}(t_2-t')$$
$$+ \sum_{n_1,n_2} \int_{t_0}^{t} \mathrm{d}t_1 \int_{t_0}^{t} \mathrm{d}t_2 G^{(0)<}_{nn_1}(t-t_1) \Sigma^{(0)a}_{n_1n_2}(t_1-t_2) \tilde{G}^{(0)a}_{n_2m}(t_2-t')$$
$$+ \sum_{n_1,n_2} \int_{t_0}^{t} \mathrm{d}t_1 \int_{t_0}^{t} \mathrm{d}t_2 G^{(0)r}_{nn_1}(t-t_1) \Sigma^{(0)r}_{n_1n_2}(t_1-t_2) \tilde{G}^{(0)<}_{n_2m}(t_2-t'). \qquad (64)$$

For $\tilde{G}^{(0)a}_{nm}(t-t')$, we obtain the following Dyson equation:

$$\tilde{G}^{(0)a}_{nm}(t-t') = G^{(0)a}_{nm}(t-t') + \sum_{n_1,n_2}\int_{t_0}^{t} \mathrm{d}t_1 \int_{t_0}^{t} \mathrm{d}t_2 \tilde{G}^{(0)a}_{nn_1}(t-t_1)\Sigma^{(0)a}_{n_1n_2}(t_1-t_2)G^{(0)a}_{n_2m}(t_2-t'). \tag{65}$$

Thus, the Fourier transform of Eqs. (64) and (65) in a matrix form (here we omit n, m for simplicity) yields, respectively:

$$\begin{aligned}\tilde{G}^{(0)<}(\omega) = {} & G^{(0)<}(\omega) + G^{(0)<}(\omega)\Sigma^{(0)<}(\omega)\tilde{G}^{(0)a}(\omega) \\ & + G^{(0)<}(\omega)\Sigma^{(0)a}(\omega)\tilde{G}^{(0)a}(\omega) + G^{(0)r}(\omega)\Sigma^{(0)r}(\omega)\tilde{G}^{(0)<}(\omega),\end{aligned} \tag{66}$$

and

$$\tilde{G}^{(0)a}(\omega) = G^{(0)a}(\omega) + \tilde{G}^{(0)a}(\omega)\Sigma^{(0)a}(\omega)G^{(0)a}(\omega). \tag{67}$$

From the second equation, we find that

$$\tilde{G}^{(0)<}(\omega) = G^{(0)a}(\omega)\left[\hat{1} - \Sigma^{(0)a}(\omega)G^{(0)a}(\omega)\right]^{-1}. \tag{68}$$

Using this equation, we obtain the matrix solution of Eq. (66)

$$\begin{aligned}\tilde{G}^{(0)<}(\omega) = {} & \left[\hat{1} - G^{(0)r}(\omega)\Sigma^{(0)r}(\omega)\right]^{-1}\left[G^{(0)<}(\omega) + G^{(0)r}(\omega)\Sigma^{(0)<}(\omega)G^{(0)a}(\omega)\right] \\ & \times \left[\hat{1} - \Sigma^{(0)a}(\omega)G^{(0)a}(\omega)\right]^{-1}\end{aligned} \tag{69}$$

To solve Eqs. (68) and (69), we should find $\Sigma^{(0)<}(\omega)$, $\Sigma^{(0)a}(\omega)$, and $\Sigma^{(0)r}(\omega)$ from Eq. (63). Thus,

$$\begin{aligned}\Sigma^{<}_{n_1,n_2}(t_1-t_2) = \sum_{k_1,k_2}\Big\{ & \left[V_L(k_1,n_1)g^{L<}_{k_1k_2}(t_1-t_2)V^*_L(n_2,k_2)\right] \\ & + \left[V_R(k_1,n_1)g^{R<}_{k_1k_2}(t_1-t_2)V^*_R(n_2,k_2)\right]\Big\}.\end{aligned} \tag{70}$$

For noninteracting electrons, $g^{L,R<}_{k_1k_2}(\omega)$ is known [6]

$$g^{L,R<}_{k_1k_2}(\omega) = 2i\pi f_{L,R}(\omega)\delta_{k_1k_2}\delta\left(\omega - \varepsilon^{L,R}_{k_1}\right), \tag{71}$$

where

$$g^{L,R<}_{k_1k_2}(\omega) = \int_{-\infty}^{\infty} \mathrm{d}t\, e^{i\omega t} g^{L,R<}_{k_1k_2}(t) \tag{72}$$

is a Fourier transform of the Green's function. In the noninteracting electron gas approximation:

$$\Sigma^{<}_{n_1,n_2}(\omega) = i\left[f_L(\omega)\Gamma^{L}_{n_1,n_2}(\omega) + f_R(\omega)\Gamma^{R}_{n_1,n_2}(\omega)\right]. \tag{73}$$

Here $\Gamma^{L,R}_{n_1,n_2}(\omega)$ are line-broadening matrices defined as follows:

$$\Gamma^{L,R}_{n_1,n_2}(\omega) = 2\pi \sum_{k} \left[V_{L,R}(k,n_1)V^{*}_{L,R}(n_2,k)\right]\delta\left(\omega - \varepsilon^{L,R}_{k}\right). \tag{74}$$

In this definition, Γ is always positive.

To find $\Sigma^{(0)a}(\omega)$, and $\Sigma^{(0)r}(\omega)$, we employ Eq. (63) where

$$\begin{aligned}\Sigma^{(0)a}_{n_1,n_2}(t_1 - t_2) = \sum_{k_1,k_2} \Big\{ &\left[V_L(k_1,n_1) g^{La}_{k_1k_2}(t_1 - t_2) V^{*}_{L}(n_2,k_2)\right] \\ &+ \left[V_R(k_1,n_1) g^{Ra}_{k_1k_2}(t_1 - t_2) V^{*}_{R}(n_2,k_2)\right]\Big\}. \end{aligned} \tag{75}$$

The retarded Green's function can be easily found from the following relation:

$$\tilde{G}^{r}(\omega) = \left[\tilde{G}^{a}(\omega)\right]^{\dagger}. \tag{76}$$

In the case of noninteracting electrons

$$g^{L,R\,r,a}_{k_1k_2}(\omega) = \frac{\delta_{k_1k_2}}{\omega - \varepsilon^{L,R}_{k} \pm i\delta} \qquad (\delta \to +0). \tag{77}$$

Consequently,

$$\Sigma^{a}_{n_1,n_2}(\omega) = \sum_{k} \left\{ \left[\frac{V_L(k,n_1)V^{*}_{L}(n_2,k)}{\omega - \varepsilon^{L}_{k} - i\delta}\right] + \left[\frac{V_R(k,n_1)V^{*}_{R}(n_2,k)}{\omega - \varepsilon^{R}_{k} - i\delta}\right]\right\}. \tag{78}$$

Equations (73) and (78) coincide with the similar equations obtained by Meir and Wingreen in Refs. [45, 52, 53] by making use of the equation of motion approach.

Now that the self-energy operators are known, the zeroth Keldysh functions can be easily obtained from Eqs. (68) and (69):

$$\tilde{G}^{(0)<}_{nm}(\omega) = i\sum_{l_1 l_2}\left(f_L(\omega)\Gamma^L_{l_1 l_2} + f_R(\omega)\Gamma^R_{l_1 l_2}\right)\frac{(\omega-\varepsilon_m+i\delta)(\omega-\varepsilon_n+i\delta)}{(\omega-\varepsilon_{l_1}-i\delta)(\omega-\varepsilon_{l_2}-i\delta)} \times\left(\omega-\tilde{\varepsilon}_{ml_1}(\omega)+i\frac{\Gamma_{ml_1}(\omega)}{2}\right)^{-1}\left(\omega-\tilde{\varepsilon}_{l_2 n}(\omega)-i\frac{\Gamma_{l_2 n}(\omega)}{2}\right)^{-1}, \quad (79)$$

and

$$\tilde{G}^{(0)r,a}_{nm}(\omega) = \frac{\omega-\varepsilon_m\pm i\delta}{\omega-\varepsilon_n\pm i\delta}\left(\omega-\tilde{\varepsilon}_{mn}(\omega)\pm i\frac{\Gamma_{mn}}{2}\right)^{-1} \quad (80)$$

In Eqs. (79) and (80), we have assumed that V is finite introducing the following definitions:

$$\tilde{\varepsilon}_{mn} \equiv \varepsilon_m + P\sum_k \frac{V^L_{mk}V^{L*}_{kn}}{\omega-\varepsilon^L_k} + P\sum_k \frac{V^R_{mk}V^{R*}_{kn}}{\omega-\varepsilon^R_k},$$
$$\Gamma_{mn}(\omega) = \Gamma^L_{mm}(\omega) + \Gamma^R_{mm}(\omega). \quad (81)$$

The presented derivation of Eqs. (33) and (34) is exact.

In the next section, we show that the Green's functions (79) and (80) become the zeroth Green's functions in diagrammatic expansion if the Coulomb interaction is considered between the bridge electrons.

3.4. Nonequilibrium Green's functions for interacting bridge electrons

In this subsection, we include electron–electron interaction in the bridge Hamiltonian. Thus, the bridge Hamiltonian yields:

$$\hat{H}_M = \sum_n \varepsilon_n d^\dagger_k d_n + \frac{1}{2}\sum_{n_1,n_2,n_3,n_4} V^{(c)}_{n_1,n_2,n_4,n_3} d^\dagger_{n_1} d^\dagger_{n_2} d_{n_3} d_{n_4}, \quad (82)$$

where $V^{(c)}_{n_1,n_2,n_4,n_3}$ represents a four-center Coulomb integral. For simplicity, we assume that there is only one (left) electrode. The generalization to two electrodes will be done at the end. As in the case of noninteracting electrons, we present Keldysh functions described in the same manner as in Eq. (56):

$$iG_{nm}(t-t') = <\tilde{T}\tilde{d}_n(t)\tilde{d}^\dagger_m(t')\hat{S}_C> . \quad (83)$$

Here S_c is a scattering matrix given by Eq. (57). All the operators are taken in the interaction representation described by Eq. (58). The interaction hamiltonian includes now both tunneling and Coulomb terms:

$$\hat{H}_{int}(t) = \sum_{k,n} \left[V_L(k,n)\tilde{c}_k^\dagger(t)\tilde{d}_n(t) + h.c. \right] + \frac{1}{2} \sum_{n_1,n_2,n_3,n_4} V^{(c)}_{n_1,n_2,n_4,n_3} \tilde{d}^\dagger_{n_1} \tilde{d}^\dagger_{n_2} \tilde{d}_{n_3} \tilde{d}_{n_4}. \quad (84)$$

Thus, a diagrammatic expansion in the interaction representation can be presented as follows:

$$\begin{aligned} i\tilde{G}^{(0)}_{nm}(t-t') =& < \tilde{T}\tilde{d}_n(t)\tilde{d}^\dagger_m(t')\hat{S}_C > = \sum_{l=0}^{\infty} \frac{(-1)^i}{(l)!} \int_c dt_1 \ldots \int_c dt_l < \tilde{T}\tilde{d}_n(t)\tilde{d}^\dagger_m(t') \\ & \times \left[\sum_{k_1,n_1} V_L(k_1,n_1)\tilde{c}^\dagger_{k_1}(t_1)\tilde{d}_{n_1}(t_1) + h.c. \right. \\ & \left. + \frac{1}{2} \sum_{n_1,n_2,n_3,n_4} V^{(c)}_{n_1,n_2,n_4,n_3} d^\dagger_{n_1}(t_1) d^\dagger_{n_2}(t_1) d_{n_3}(t_1) d_{n_4}(t_1) \right] \\ & \ldots \left[\sum_{k_l,n_l} V_L(k_l,n_l)\tilde{c}^\dagger_{k_l}(t_l)\tilde{d}_{n_l}(t_l) + h.c. \right. \\ & \left. + \frac{1}{2} \sum_{n_1,n_2,n_3,n_4} V^{(c)}_{n_1,n_2,n_4,n_3} d^\dagger_{n_1}(t_l) d^\dagger_{n_2}(t_l) d_{n_3}(t_l) d_{n_4}(t_l) \right] >. \end{aligned} \quad (85)$$

In Eq. (85) all terms, even and odd, are included in the expansion. As a particular case, we consider a first-order Hartree-Fock exchange diagram that is depicted in Figure (5.4a). The exchange diagram (a) is given by the following equation:

$$\begin{aligned} G^{(1)}_{kl}(t-t') &= (-i)^3 \sum_{n_1 n_2 n_3 n_4} V_{n_1 n_2 n_3 n_4} \int_c dt_1 \tilde{G}_{kn_1}(t-t_1)^{(0)} \tilde{G}^{(0)}_{n_3 n_2}(t_1 - t_1^+) \tilde{G}^{(0)}_{n_4 l}(t_1 - t') \\ &= (-i)^3 \sum_n V_{knnl} \int_c dt_1 \tilde{G}_{kk}(t-t_1)^{(0)} \tilde{G}^{(0)}_{nn}(t_1 - t_1^+) \tilde{G}^{(0)}_{ll}(t_1 - t'). \end{aligned} \quad (86)$$

If we turn the interaction with the leads on as shown in Figure 5.4b, the tunneling self-energy terms can be inserted into a zeroth Green's function by breaking the solid line. In the same manner, all orders of V^2 can be included in the zeroth Green's function as depicted in Figure 5.4c. According to Eq. (62), such insertions are the renormalized zeroth Green's functions

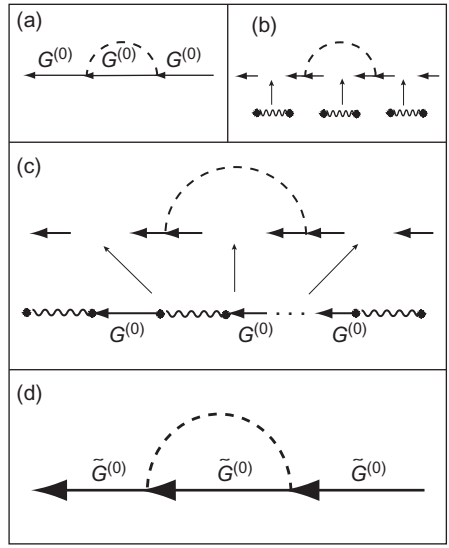

Figure 5.4 Diagrammatic representation of the first-order Hartree–Fock exchange diagram: (a) no interaction with the leads is included, (b) the interaction with the leads is considered in the second order with respect to V^2 for each $G^{(0)}$, (c) the interaction with the lead electrons is considered in all orders to V^2, and (d) the diagram (c) is presented according to Dyson equation (62) where the zeroth Green's functions, $G^{(0)}$, have been substituted by the renormalized zeroth Green's functions, $\tilde{G}^{(0)}$.

shown in Figure 5.4d. Thus, for any order diagram, the lead–bridge interaction retains the topological structure of a graph in the same manner as for noninteracting case where the ordinary zeroth Green's functions are substituted by the renormalized zeroth Green's functions described by Eqs. (79) and (80). The rigorous proof of this is almost the same as for noninteracting electrons presented in Section 3.3 and is based on the essential property of a T-product, $\tilde{T}A(t_1)A(t_2) = \tilde{T}A(t_2)A(t_1)$ independent of the order of operators. Indeed, by grouping the operators $\tilde{T}\tilde{d}(t_1)\tilde{d}(t_2)$ in the product (85), the order of the time sequence becomes irrelevant. This feature is crucial to break up a zeroth-order line and substitute it by a renormalized zero-order Keldysh function. Hence the Dyson equation for nonequilibrium Green's function yields

$$G(t-t') = \tilde{G}^{(0)}(t-t') + \int_c \mathrm{d}t_1 \int_c \mathrm{d}t_2 \tilde{G}^{(0)}(t-t_1)\Sigma(t_1-t_2)G(t_2-t'), \qquad (87)$$

where self-energy operator $\Sigma(t)$ includes all possible diagrams with respect to the Coulomb interaction taken with the renormalized zeroth Keldysh

functions. The approach presented above is valid if the Coulomb interaction is considered between the bridge electrons, while lead electrons are still noninteracting. For the calculation of nonequlibrium Green's functions, such a change is essential because now the zeroth Green's functions have finite imaginary parts as described by Eqs. (79) and (80). Thus, various schemes for calculations of Green's functions have to be modified. As an example of such modification the random phase approximation (RPA) in the bridge molecule was considered in Ref. [54].

3.5. Noncrossing approximation

In this subsection, we describe a method where the electron propagator machinery developed for quantum chemical calculations of single molecules is applied [9–21]. We use a so-called *noncrossing approximation* where a self-energy for interacting bridge electrons is divided into two independent parts [55–57]:

$$\Sigma(\omega) = \Sigma^{(1)}(\omega) + \Sigma^{(2)}(\omega). \tag{88}$$

In Eq. (88), (a) interaction with the electrons inside a molecular bridge with the self-energy $\Sigma^{(1)}$ is the self-energy of bridge electrons and $\Sigma^{(2)}$ is the self-energy for the electrons interacting with the left and right lead electrons. In this approximation, electric current can be expressed in the following way [55]:

$$J = \frac{e}{\hbar}\int \frac{d\omega}{2\pi}(f_L(\omega) - f_R(\omega))Tr\{\Gamma^R \mathbf{G}^r \Gamma^L \mathbf{G}^a\}. \tag{89}$$

In this description [45],

$$\Sigma^<(\omega) = i\left[\Gamma^L(\omega)f_L(\omega) + \Gamma^R(\omega)f_R(\omega)\right], \tag{90}$$

where $f_L(\omega)$ and $f_R(\omega)$ are the fermi functions of the left and right electrodes, respectively. For different electrodes, these functions can have different chemical potentials. The right fermi function also contains a voltage. In the derivation of Eq. (89), we have used the following relation for Keldysh functions [45]:

$$\mathbf{G}^< = \mathbf{G}^r \Sigma^< \mathbf{G}^a. \tag{91}$$

where Γ is assumed to be known [55]:

$$\hat{\Gamma}(\omega) = \frac{1}{2}\left[\hat{\Gamma}^L(\omega) + \hat{\Gamma}^R(\omega)\right]. \tag{92}$$

The retarded and advanced Green functions can be expressed in terms of the electron propagator matrix that is supposed to be known from numerical calculations [55, 56]. Usually, it can be found, for example, from GAUSSIAN program [22] whose output provides all necessary information for the electron propagator, $\hat{\tilde{G}}$ [55, 56]:

$$\hat{G}^r = [\hat{I} + i\hat{\tilde{G}}\hat{\Gamma}]^{-1}\hat{\tilde{G}},$$
$$\hat{G}^a = [\hat{G}^r]^\dagger = \hat{\tilde{G}}[\hat{I} - i\hat{\tilde{G}}\hat{\Gamma}]^{-1}. \tag{93}$$

As discussed in Ref. [55], a $\hat{\Gamma}$ matrix can be of an arbitrary dimension depending upon the number of contact orbitals for the left and right electrodes. If, for instance, the number of terminal orbitals for the left lead is l and for the right lead is r, then the dimension of $\hat{\Gamma}$ is

$$n = l + r.$$

In Ref. [55], we discussed the simplest case where $n = 1 + 1 = 2$, that is, only one orbital from each side is transport active. In general, it might not be the case where several orbitals from the left- and right-hand sides can be active in charge transport [56]. An analysis requires that "the denominators" with matrices in Eq. (93) are presented in terms of matrices in numerators and ω-dependent functions in denominators. Such a representation allows for a simple integration of the integral (89) in a complex half plane with poles that are the roots for a secular equation for the matrices in the denominators for the retarded and advanced Green function matrices (93) [58]. The final expression will be given in terms of the poles, the pole strengths, atomic terminal coefficients, and $\hat{\Gamma}$ matrix elements that can be found from numerical calculations.

3.6. Electron propagator in the noncrossing approximation

To find retarded and advanced Green function matrices, it is necessary to determine an electron propagator matrix, $\hat{\tilde{G}}$, which may be written in terms of its Lehmann representation [1, 7]

$$\hat{\tilde{G}}(\omega) = \sum_l \frac{a_l}{\omega^+ - \varepsilon_l}|l\rangle\langle l|, \tag{94}$$

where a_l and ε_l are called Dyson pole strengths and Dyson poles in which electron and hole states are included. Usually, these poles represent molecular ionization energies (for $\varepsilon_l < 0$) and electron affinities (for $\varepsilon_l > 0$).

The basis set is chosen such that around the lth Dyson pole, the electron propagator matrix is diagonal. Consequently, the eigenstate $|l\rangle$ can be presented as a linear expansion over atomic orbitals with coefficients $c_k(l)$ that depend on the number of the Dyson pole, l, and the number of the atomic orbital, k, so that

$$|l\rangle = \sum_k c_k(l)|k\rangle_{at}. \tag{95}$$

Coefficients, $c_k(l)$, pole strengths, a_l, and poles, ε_l, usually are reported as output in *ab initio* electron propagator calculations on molecules.

Matrix elements of the electron propagator over atomic orbitals that connect the bridge molecule with the left and right electrodes will be needed below. Specific choices of atomic orbitals will depend on the system under study. The number of orbitals participating in such connections determines the rank of the electron propagator matrix. For example, if one atomic orbital, $|k_L\rangle_{at}$, connects the bridge with the left electrode and one atomic orbital, $|k_R\rangle_{at}$, connects the bridge with the right electrode, the rank of the electron propagator matrix will be two. The blocks of the electron propagator matrix read

$$\begin{aligned}
\hat{\hat{G}}_{LL} &= \sum_l \frac{a_l}{\omega^+ - \varepsilon_l} |\langle l|k_L\rangle_{at}|^2, \\
\hat{\hat{G}}_{RR} &= \sum_l \frac{a_l}{\omega^+ - \varepsilon_l} |\langle l|k_R\rangle_{at}|^2, \\
\hat{\hat{G}}_{LR} &= \sum_l \frac{a_l}{\omega^+ - \varepsilon_l} \langle l|k_L\rangle_{at}\ \langle l|k_R\rangle_{at},
\end{aligned} \tag{96}$$

where the lth pole's matrix element is defined as

$$\langle l|k_L\rangle_{at} = \sum_k c_{kl} S_{kk_L} \tag{97}$$

and S_{kk_L} is an overlap matrix element. As soon as the retarded and advanced Green function matrices are known and the trace in Eq. (89) is taken, the integration over ω should be performed. This integral can be evaluated in a lower, complex-ω half plane. Equation (93) indicates that the integrand contains complex poles that are determined by matrices.

To find the integral (89) for electrical current, it is necessary to present the integrand where all the matrices are in a numerator and ordinary poles are in a denominator. There is a special procedure that allows for such a representation. A suitable mathematical theory is described by Gantmakher

in his book [58]. The matrix part of the integrand of Eq. (89) is the following product of four matrices:

$$\hat{\Gamma}^R \hat{G}^r \hat{\Gamma}^L \hat{G}^a. \tag{98}$$

In this product, only the terminal projection of $\hat{G}^r(\omega)$ is needed. For example, if the left terminal has l and the right terminal has r orbitals connecting the bridge with the electrodes, $\hat{G}^r(\omega)$ has the rank $n = l + r$. Consequently, the electron propagator will have the same rank:

$$\hat{\tilde{G}}(\omega) = \sum_k \frac{\hat{A}_l}{\omega - \varepsilon_k}. \tag{99}$$

In the integration for the current expression of Eq. (89) in the complex lower half plane, only the area around the poles where $\omega \simeq \varepsilon_k$ contributes significantly to $\hat{G}^r(\omega)$.

The matrices $\hat{\Gamma}^{L,R}$ in Eq. (100) have a block-diagonal structure in the left and the right corners of the matrix $n \times n$, respectively. Apparently, $\hat{\Gamma}^L \neq \hat{\Gamma}^R$ even if all the $\gamma_i(k)$s are equal to each other [56]:

$$\hat{\Gamma}^L = \begin{pmatrix} \gamma_1^L(k) & \dots & 0 \\ \vdots & \vdots & \vdots \\ 0 & \dots & \gamma_l^L(k) \\ 0 & \dots & 0 \\ \vdots & \vdots & \vdots \\ 0 & \dots & 0 \end{pmatrix}$$

$$\hat{\Gamma}^R = \begin{pmatrix} 0 & \dots & 0 & \dots & 0 \\ \vdots & \vdots & \vdots & \vdots & \vdots \\ 0 & \dots & \gamma_{l+1}^R(k) & \dots & 0 \\ \vdots & \vdots & \vdots & \vdots & \vdots \\ 0 & \dots & \dots & \dots & \gamma_n^R(k) \end{pmatrix}. \tag{100}$$

The final expression for electric current yields [56]

$$J = \frac{e}{\hbar} \sum_k \frac{\tilde{\gamma}_L(k)\tilde{\gamma}_R(k)a_k[f_L(\varepsilon_k) - f_R(\varepsilon_k)]}{|\tilde{\gamma}_L(k) + \tilde{\gamma}_R(k)|}, \tag{101}$$

where a_k is a polestrength of the kth Dyson pole. We have also introduced the following definition of the left- and right-renormalized dissipation

coefficients:

$$\tilde{\gamma}^{L}(k) = \sum_{i=1}^{l} c_i(k)\gamma_i(k)^{L},$$
$$\tilde{\gamma}^{R}(k) = \sum_{i=1+1}^{n} c_i(k)\gamma_i^{R}(k). \tag{102}$$

The diagonal matrix elements in Eq. (102) are positive and given by [55, 56]

$$\begin{aligned} c_1 &= \langle 1|k\rangle^2, \\ c_2 &= \langle 2|k\rangle^2 \\ &\vdots \end{aligned} \tag{103}$$

The coefficients in Eq. (103) are determined by Eq. (97).

The proposed formalism does not contain any self-consistent procedure that implies a single quasiparticle approximation. The derived expression for electric current (101) is presented in terms of the parameters that are a standard output in numerical calculations, that is, Dyson poles, Dyson polestrengths, coefficients for terminal atomic orbitals, and overlap integrals. All the parameters depend on applied voltage that should be introduced into a microscopic Hamiltonian of the bridge. This research deals with the most general case in which the bridge is connected to the left lead by l and to the right lead by r atomic orbitals. The rigorous definition of contact (terminal) orbitals has been given by Eq. (103). To find the integral of the current with the integrand where the "poles" are represented by matrices (see Eq. (89)), we have employed a procedure proposed by Gantmakher [58] that transforms the "matrix poles" into ordinary complex poles. Such a mathematical technique significantly facilitates the calculation of the electrical current (89).

3.7. Molecular wire numerical calculations

In this subsection, we apply the theory developed in subsections 3.1–3.6 to particular calculations. Electron binding energies, molecular and atomic orbitals, ionization potentials, electron affinities, etc. play a crucial role in determining the suitability of a molecule to be a proper candidate for a device with desired properties. These parameters should be accurately determined by reliable methods. There are several computational schemes that are based on a tight binding approximation (uncorrelated electrons) [59–63], density function theory [64–72], a many-body electron scattering approach [73–75], and an *ab initio* electron propagator approach [55–57, 76]. The expression for electric current (see Refs. [55, 56]) has been derived in terms of outputs from a standard commercial software package,

Gaussian-03 [22], and then this expression was used for numerical calculations for current–voltage characteristics of a molecular wire with a 1,4-benzenedithiol (BDT) molecular bridge [76]. A BDT molecular bridge was intensively studied by different experimental groups [30, 31] from which monotonic current–voltage characteristics were obtained. In addition, this molecule as a molecular bridge was computationally studied by employing DFT (see the discussion in Reference [66]) from which the discrepancy of the factor of 50 with the experimental data [31] was found. Other DFT-based electronic structure calculations differ in details; nevertheless, most of the calculations provide similar results (see the discussion in review [77]). Such a substantial discrepancy between the theory and experiment has motivated our investigation to use alternative *ab initio* electron structure computational schemes, in particular electron propagator methods [55, 56, 76]. These techniques rigorously include electron correlations providing accurate ionization potentials and electron affinities. The poles can be found as outputs of numerical calculations within the Gaussian software [22]. It is important to note that the electron correlation approach to tunneling in molecular junctions provides a different physical picture than the DFT approach. The lead electrons tunnel to bridge ionization levels rather than to excited states of a neutral molecule. Such a picture is natural in order for the bridge to remain a neutral molecule during a transport process.

Next we present numerical calculations described in Ref. [78]. Our investigation included only a single *d* gold atomic orbital [55] and was focused on a planar conformation that forced the C-S-Au angle to be 180°; however, the experimental geometry of the attachment is unknown. Indeed, it is more natural for a 1,4-benzenedithiol (BDT) bridge molecule to be attached with 109° tetrahedral angle as in a gas phase [79]. Forcing this angle to be 180° causes the sulfur p-orbitals to overlap with benzene π-orbitals, destroying the aromaticity of the ring. Such a configuration is energetically unfavorable. Thus, additional investigation of electric current through a BDT molecule with different attachment conformations and the inclusion of all gold atomic orbitals is necessary. Moreover, we provide some unusual fermi energy dependencies of electric current with a strong negative differential resistance at low voltages that could be useful to design new electronic devices.

In an initial step, a full geometry optimization is performed on the *Au-BDT-Au* molecule to obtain the most energetically favorable starting conformation. Three spatial conformations are considered for the computation of the current as shown in Figure 5.5. These conformations are selected to represent a variety of experimental conditions.

For three different configurations, A_0, A_1, and A_2, the current–voltage characteristics are shown in Figures 5.6, 5.7, and 5.8 at $\varepsilon_f = -1.10$ eV, $\varepsilon_f = -1.30$ eV, and $\varepsilon_f = -1.35$ eV, respectively.

We have studied different configurations with various fermi energies and concluded that configuration A_2 with $\varepsilon_f = -1.35$ eV explains the experimental dependences [31] in the best way. Indeed, configuration A_1 exhibits a

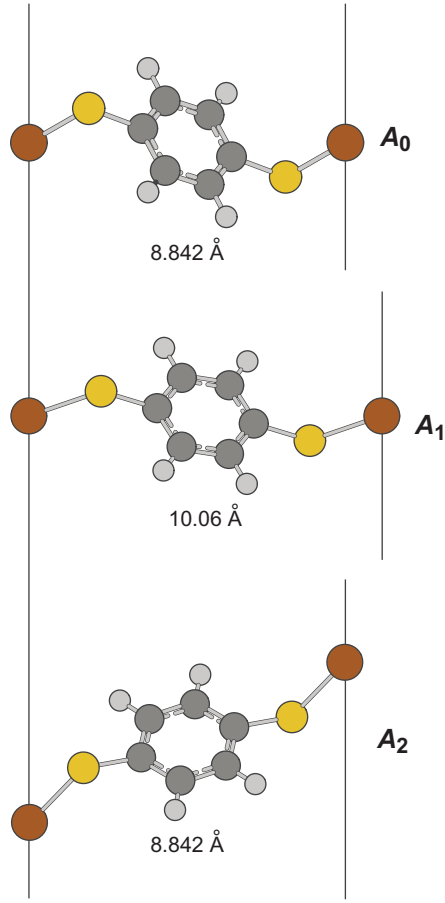

Figure 5.5 A_0 represents the gas-phase conformation with the optimized Au–Au distance of 8.842 Å. A_1 depicts the molecule with the stretched Au–Au distance of 10.061 Å along the *y*-axis. A_2 shows the molecule with the stretched Au–Au distance of 10.061 Å placed between electrodes that are separated by 8.824 Å.

small Coulomb blockade effect, whereas configuration A_0 reveals a smaller peak (a negative differential resistance) in the current–voltage characteristics at lower voltages. Our calculations show that the main contribution to the current for these fermi energies is because of the overlap between gold d and sulphur p orbitals in molecular Dyson orbital 40.

3.7.1. Negative differential resistance

The current–voltage characteristic is given in Figure 5.9. The detailed analyses reveal that at $\varepsilon_f = 0.4$ eV, the main contribution to the conductivity at

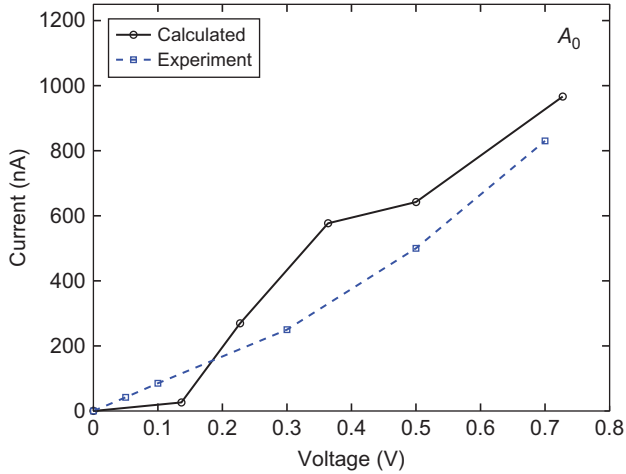

Figure 5.6 Current versus voltage at $\varepsilon_f = -1.10$ eV for configuration A_0.

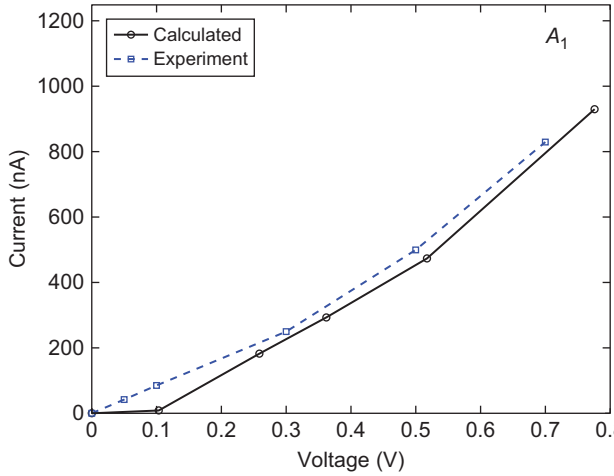

Figure 5.7 Current versus voltage at $\varepsilon_f = -1.30$ eV for configuration A_1.

voltages above 1 eV is because of Dyson orbital 40, whereas the conductivity at lower voltages is determined by Dyson orbital 42. It is important to understand a quantum mechanical origin of such a peak-wise behavior versus applied voltage. In general, a current–voltage behavior depends on three different factors according to Eqs. (101), (102), and (103): (1) the difference between the fermi functions, $f_L(\varepsilon_l) - f_R(\varepsilon_l)$, (2) coefficients $d_k(V)$, and (3) overlap integrals $S_{ik}^{L,R}(V)$. The difference between the fermi functions

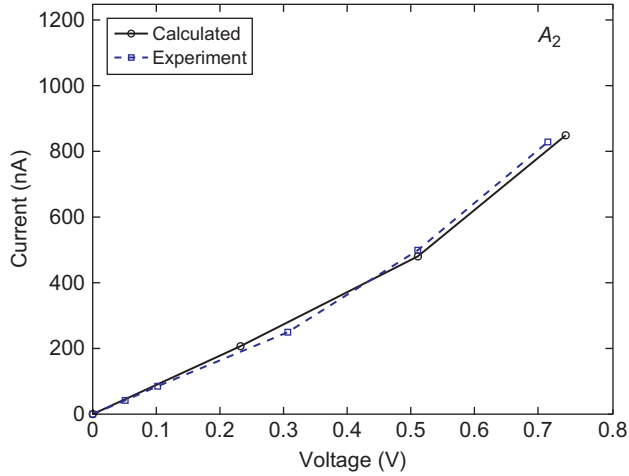

Figure 5.8 Current versus voltage at $\varepsilon_f = -1.35$ eV for configuration A_2.

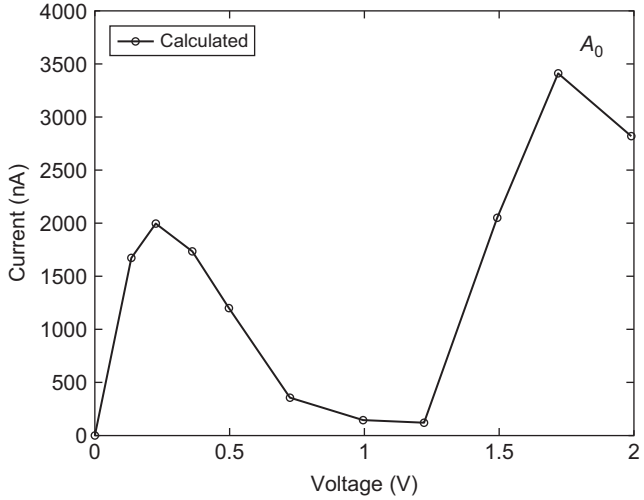

Figure 5.9 Current–voltage characteristics at $\varepsilon_f = 0.40$ eV for configuration A_0.

selects the range of Dyson poles and Dyson orbitals participating in the conductivity; the coefficients $d_k(V)$ determine the weight of a kth bridge atomic orbital in a molecular Dyson orbital; whereas the overlap integrals reflect the strength of the interaction between the ith gold orbital and the kth bridge atomic orbital (e.g., a sulfur orbital). The signs of $d_k(V)$ and $S_{ik}^{L,R}(V)$ can be positive or negative, resulting in strong quantum interference between the electrons described by different bridge and gold atomic orbitals,

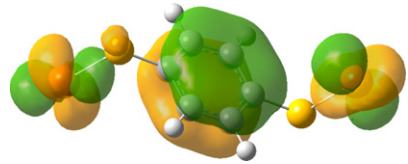

Figure 5.10 Molecular Dyson orbital 42 at $V = 0.227$ V.

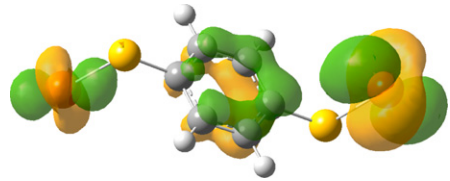

Figure 5.11 Molecular Dyson orbital 42 at $V = 0.727$ V.

whereas the contributions due to the gold terminal orbitals, c_i^2, are summed independently.

The peak in current–voltage characteristics shown in Figure 5.9, can be explained from a quantum chemical point of view. Figure 5.10 depicts Dyson molecular orbital 42 in which one finds the strong overlap between the aromatic π-molecular orbital of the benzene ring and the $6d_{yz}$ gold atomic orbital at the peak value, $V = 0.227$ V. As discussed earlier, the current vanishes at $V = 0.727$ V. The corresponding molecular orbital picture is shown in Figure 5.11 where the aromaticity of the benzene π molecular orbital is destroyed resulting in the weak overlap with the gold atomic orbitals of the left electrode. Consequently, the current sharply drops. Since the electron propagator methods employ optimized conformations and include electron correlations in the most accurate manner, they provide a promising computational approach for the explanation of experimental data and the prediction of novel important properties in molecular tunneling junctions.

3.8. Molecular transistors

In this subsection, we apply the electron propagator methodology to molecular transistors. Building a single-molecule field-effect transistor can be considered an important step toward the ultimate goal for molecular electronics. There have been experimental [80–83, 85] and theoretical studies [84, 86–89] in three-terminal molecular devices (transistors) with large and small gate modulation in the current. Field-effect transistor type behavior has been demonstrated in different systems such as carbon nanotubes [91, 93] and molecular wires with strong Coulomb blockade [94], and Kondo effects [95–98]. To explain these strong electron correlation effects,

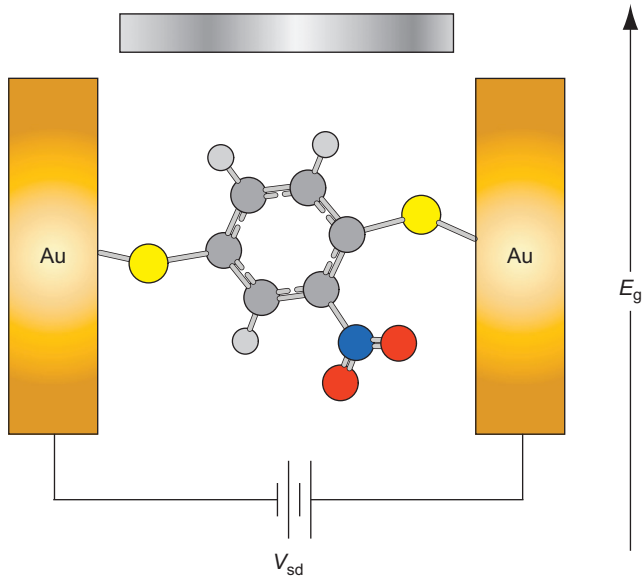

Figure 5.12 The coordinate system used to compute the gate voltage characteristics of the 2-nitro-1,4-benzenedithiol (nitro-BDT) molecular wire. The Au–Au distance is 10.061Å, and the Au–Au axis makes an angle of $\theta = 16.3^\circ$ with the *y*-axis.

reliable computational schemes are necessary. However, it was experimentally [80–83, 85] and theoretically [84, 86–90] proved that a 1,4-benzenedithiol (BDT)-type molecular transistor does not show any significant dependence on a gate electric field. We schematically demonstrate a transistor setup in Figure 5.12. In Ref. [90], we study the effect of electron correlations in molecular transistors with molecular bridges based on 1,4-benzenedithiol (BDT) and 2-nitro-1,4-benzenedithiol (nitro-BDT) by using ab initio electron propagator calculations. We find that there is no gate field effect for the BDT-based transistor in accordance with the experimental data (see Figure 5.13). After verifying the computational method on the BDT molecule, we consider a transistor with a nitro-BDT molecular bridge. From the electron propagator calculations, we predict strong negative differential resistance at small positive and negative values of source–drain voltages [90]. The quantum chemical calculations provide a deep insight into the mechanism of the origin of the peak and the minimum in the current versus applied voltage. As shown in Figure 5.13, both *MO 48* and *Mo 49* equally contribute to the current at the peak ($V_{sd} = 0.3$ eV). The overlaps between sulfur and gold orbitals on the left become much smaller at $V_{sd} = 0.5$ eV than at the peak value for *MO 48*. While the voltage has little effect on the overlap values for *MO 49*, this orbital does not contribute to the current due to the vanishing difference

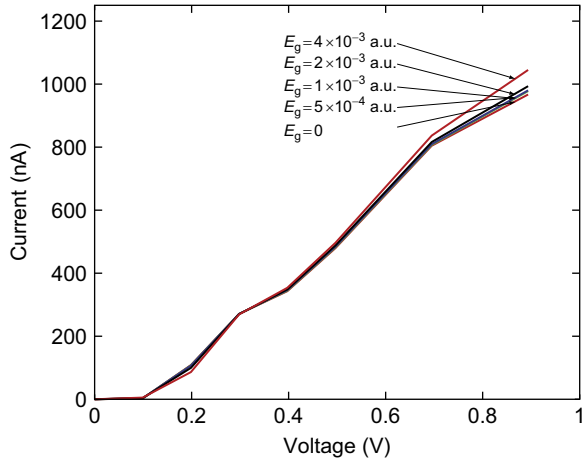

Figure 5.13 Current versus voltage curves at different gate voltages ($\varepsilon_f = -1.35$ eV) for the *Au-BDT-Au* molecular wire. 1 a.u. = 5.142 × 10^{11} V m^{-1}. Thus, 0.0020 a.u. = 1.0 V/10 Å.

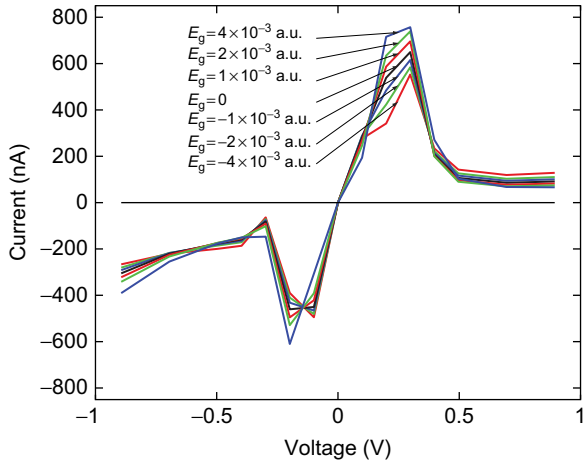

Figure 5.14 Current versus voltage curves at different gate voltages ($\varepsilon_f = -1.35$ eV) for the *Au-nitro-BDT-Au* molecular wire. 1 a.u. = 5.142 × 10^{11} V m^{-1}. Thus, 0.0020 a.u. = 1.0 V/10 Å.

between the fermi functions. This difference indicates that both left and right lead electronic states are occupied, and therefore the electron cannot tunnel due to the Pauli principle. As shown in Figures 5.13 and 5.14, the dependences of I–V curves on the gate voltage are weak. As mentioned earlier, 1,4-benzenedithiol (BDT)-type molecular transistor does not show any significant dependence on a gate electric field. In Figures 5.15 and 5.16 we present a molecular orbital picture of the two main orbitals that contribute to

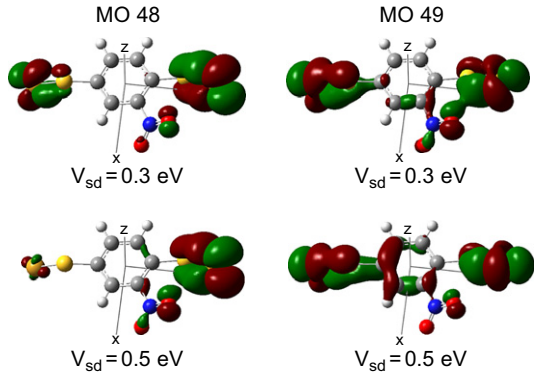

Figure 5.15 *Au-nitro-BDT-Au* molecular orbitals as a function of source–drain voltage ($\varepsilon_f = -1.35$ eV). Orbital 48 is shown in the left column, orbital 49 in the right column.

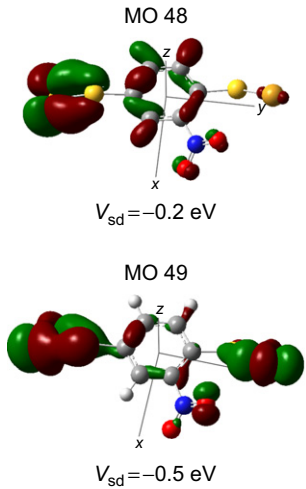

Figure 5.16 *Au-nitro-BDT-Au* molecular orbitals as a function of source–drain voltage ($\varepsilon_f = -1.35$ eV).

the current, i.e. MO 48 and Mo 49. Additionally, we have also analyzed the contribution due to different terms in Eq. (102), such as a Fermi function difference for the left and right electrodes in the expression for the current. The overlaps of the sulfur p-orbitals with the gold d-orbitals at the left and right electrodes are well pronounced. At the plateau value of the peaks with $V_{sd} = 0.5$ eV, the contribution from these orbitals is, however, different. The overlaps between sulfur and gold orbitals on the left side of the bridge become much smaller than at the peak value for MO 48. While the voltage

has very little affect the overlap values for MO 49, this orbital does not contribute to the current because it is switched off by the difference between the Fermi functions. This difference almost vanishes indicating that both left and right lead states are occupied, and therefore, there is no place for the electron to go on. The experimental conditions, however, do not reflect the whole range of possibilities. In order to improve the performance of a BDT-based transistor, we propose a new architecture where the electric field is normal to a benzene ring plane [92] as shown in Figure 5.17. It was found that the BDT-based transistor exhibits strong negative differential resistance at different values of the gate field [92]. The peak in the I–V curves is more pronounced for the higher values of E_g as shown in Figure 5.18. The higher the gate field, the narrower the peak. We found that at $E_g = 4 \cdot 10^{-3}$ a.u, the peak/valley ratio is about 20. The explanation of a such strong peak behavior is presented in terms of the overlap of different molecular orbitals participating in the conduction (see Figure 5.19). For the BDT molecular device, the disappearance of the peak is due to the dramatic drop in γ^R at $V_{sd} = 0.9$ eV because of the complicated interference of different atomic orbitals in molecular orbital No. 40 (HOMO-15).

For a molecular transistor based on an asymmetric nitro-BDT molecular bridge, we have also found a strong nonlinear behavior in the I–V characteristics. Since the molecule is asymmetric, we have studied the current for

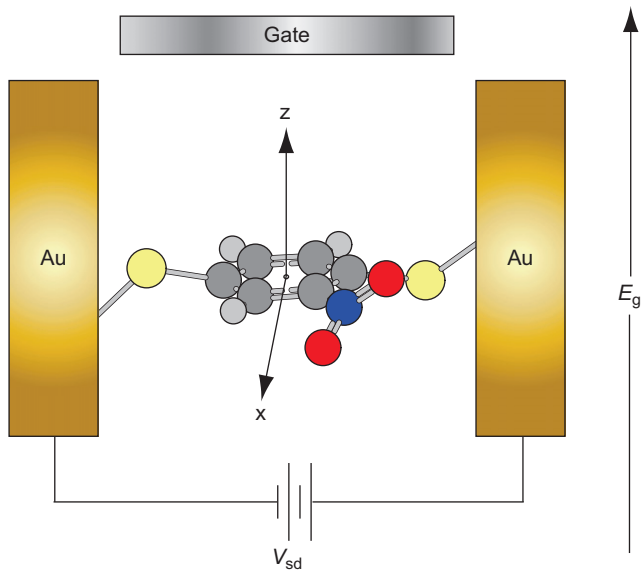

Figure 5.17 Schematic architecture of a molecular transistor based on a nitro-BDT type molecular bridge. The electric field is directed perpendicular to the plane of the benzene ring.

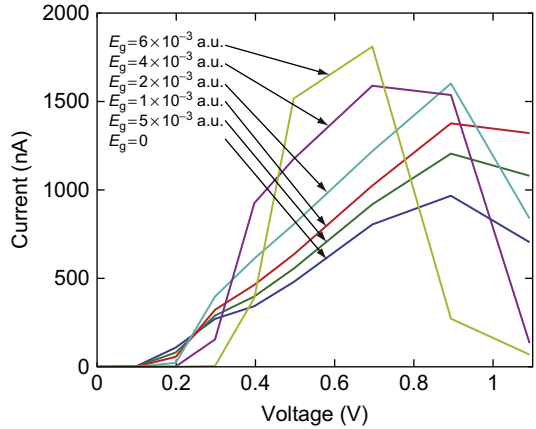

Figure 5.18 Current versus voltage curves at different gate voltages ($\varepsilon_f = -1.35$ eV) for the *Au-BDT-Au* molecular wire. 1 a.u. = 5.142 × 10^{11} V m^{-1}. Thus, 0.0020 a.u. = 1.0 V/10 Å.

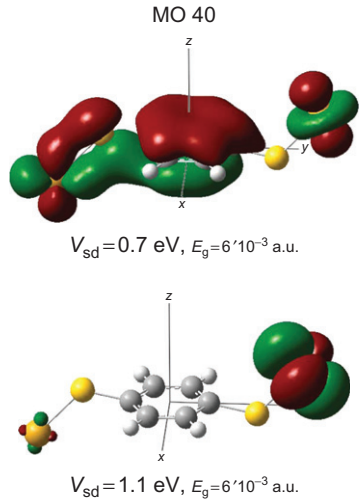

Figure 5.19 Molecular orbital picture of *Au-BDT-Au* as a function of source–drain voltage ($\varepsilon_f = -1.35$ eV).

positive and negative values of V_{sd} and E_g. The complex behavior of the current on V_{sd} and E_g is shown in Figure 5.20. For applications, we have found a strong negative differential resistance at low voltage, $V_{sd} = 0.1$ eV. The explanation of peak/valley behavior is given in terms of a molecular orbital picture (see Figure 5.21). In this case, the origin of the drop is rather different.

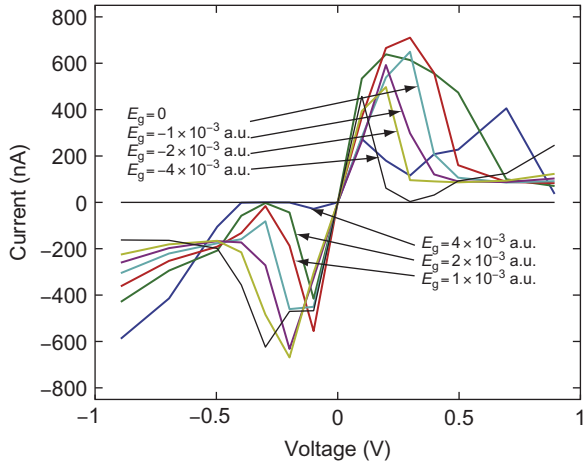

Figure 5.20 Current versus voltage curves at different gate fields ($\varepsilon_f = -1.35$ eV) for the *Au-nitro-BDT-Au* molecular wire.

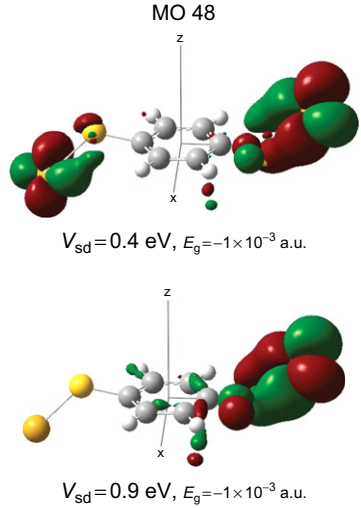

Figure 5.21 Molecular orbital picture for the *Au-nitro-BDT-Au* molecular wire at the peak ($V_{sd} = 0.4$ eV) and valley ($V_{sd} = 0.9$ eV) values of the source–drain voltage.

As shown in Table 5.1, for $V < 0.2$ eV, MO 49 contributes the most, whereas at $V = 0.3$ eV, MO 48 (HOMO-18) and 49 (HOMO-17) make nearly equal contributions. Then, molecular orbital 49 is switched off at $V = 0.4$ eV due to the fermi function difference resulting in the dramatic drop in the current [92].

Table 5.1 Line width functions, fermi terms and current for the *Au-nitro-BDT-Au* molecular wire. $\vec{E}_z = -0.0010$ a.u.

V_{sd}	MO	$\gamma^L(l)$	$\gamma^R(l)$	$f_L(\varepsilon_l) - f_R(\varepsilon_l)$	$J(nA)$
0.0	48	0.006463	0.000774	0.0000	0.0
	49	0.005993	0.007339	0.0000	0.0
0.1	48	0.006556	0.000878	0.0000	0.0
	49	0.006665	0.006483	0.4601	368.0
0.2	48	0.006711	0.001193	0.0100	2.5
	49	0.007316	0.005550	0.8633	663.2
0.3	48	0.007026	0.002448	0.7347	324.7
	49	0.007693	0.004043	0.5979	385.7
0.4	48	0.002761	0.006815	0.9397	449.4
	49	0.006430	0.005717	0.1475	108.7
0.5	48	0.000705	0.007545	0.9413	147.7
	49	0.008815	0.004994	0.0164	12.8
0.7	48	0.000408	0.007365	0.9364	88.1
	49	0.009161	0.004427	0.0001	0.1
0.9	48	0.000396	0.007115	0.9058	82.7
	49	0.009065	0.004255	0.0000	0.0

The applications of nonequilibrium Green's functions to the calculations of different molecular devices show the importance of electron correlation effects. The electron propagator method is able to explain experimental data and predict new electronic devices.

4. PHOTOCURRENT IN QUANTUM DOT–SENSITIZED SOLAR CELLS

Our interest in quantum dot–sensitized solar cells (QDSSC) is motivated by recent experiments in the Parkinson group (UW), where a two-electron transfer from excitonic states of a QD to a semiconductor was observed [32]. The main goal of this section is to understand a fundamental mechanism of electron transfer in solar cells. An electron transfer scheme in a QDSSC is illustrated in Figure 5.22. As discussed in introduction, quantum correlations play a crucial role in electron transfer. Thus, we briefly describe the theory [99] in which different correlation mechanisms such as e–ph and e–e interactions in a QD and e–ph interactions in a SM are considered. A time-dependent electric field of an arbitrary shape interacting with QD electrons is described in a dipole approximation. The interaction between a SM and a QD is presented in terms of the tunneling Hamiltonian, that is, in

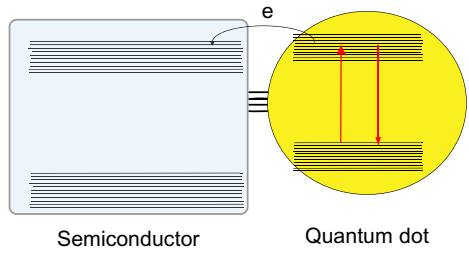

Figure 5.22 Schematic illustration of electron transfer in a QDSSC.

the same manner as in the case of tunneling junctions [45, 52, 53, 55, 56]. For this system, we derive an expression for photoelectric current where light is considered to be of an arbitrary intensity, shape, and frequency. The photocurrent is expressed in terms of QD and SM nonequilibrium quantum correlation functions (Keldysh functions) [5, 6, 40–43, 45].

The description of the photocurrent that we propose to use for this approach is similar to the theoretical scheme applied to tunneling junctions [54] that has been presented in Section 3. The origin of electric current in QDSSCs is due to a time-dependent electric field rather than a chemical potential difference in the leads. Thus, we modify the theory used in tunneling junctions [54] by including a time-dependent electric field interacting with the QD electrons. The proposed scheme is rather general because it is designed to describe various correlation effects such as multiexciton generation and recombination, electron–phonon relaxation in a semiconductor and a QD, and hot-carrier transfer.

4.1. Hamiltonian

The Hamiltonian that describes a QD–SM solar cell is given by the following expression:

$$\hat{H} = \hat{H}_{SM} + \hat{H}_{QD} + \hat{H}_{SM-QD} + \hat{H}_{QD-light}. \tag{104}$$

1. For the correct description of electron transfer processes (forward and backward electron transfers) and also relaxation from conduction to valence bands in a semiconductor, we include e-ph interaction into a semiconductor Hamiltonian:

$$\hat{H}_{SM} = \sum_{k,\lambda} \varepsilon^{s}_{k,\lambda} c^{\dagger}_{k,\lambda} c_{k,\lambda} + \sum_{q} \omega^{s}_{q} b^{\dagger}_{q} b_{q} + \sum_{q,k,\lambda} M^{\lambda}_{q} \hat{A}_{q} c^{\dagger}_{k+q,\lambda} c_{k,\lambda}. \tag{105}$$

Here $c_{k,\lambda}, c^{\dagger}_{k,\lambda}$ and $b_q, b^{\dagger}_q$ are annihilation and creation fermi operators for the semiconductor electrons and phonons, respectively. $\varepsilon^{s}_{k,\lambda}$ is the energy of noninteracting electrons. M^{λ}_{q} is a semiconductor electron–phonon constant, and ω^{s}_{q} is a phonon frequency (the index s indicates that a phonon belongs to a semiconductor). A phonon amplitude is defined in a standard way [6]:

$$A_q \equiv b_{q,s} + b^{\dagger}_{q,s}, \tag{106}$$

2. A QD Hamiltonian includes both Coulomb and electron–phonon interactions. Apparently, the phonon modes (denoted as QD) in the quantum dot are different from the semiconductor ones. The electron–phonon interaction determines relaxation processes in quantum dot (hot electrons or excitons). Thus, the QD Hamiltonian yields

$$\hat{H}_{QD} = \sum_{n} \varepsilon^{QD}_{n} d^{\dagger}_{k} d_n + \frac{1}{2} \sum_{n_1,n_2,n_3,n_4} V^{(0)}_{n_1,n_2,n_4,n_3} d^{\dagger}_{n_1} d^{\dagger}_{n_2} d_{n_3} d_{n_4} + \sum_{q} \omega^{QD}_{i} a^{\dagger}_{i} a_i + \sum_{i,n} M_{i,n} d^{\dagger}_{n} d_n (a^{\dagger}_{i} + a_i). \tag{107}$$

Here $d_n, d^{\dagger}_{n}$ and $a_i, a^{\dagger}_{i}$ are annihilation and creation operators for the QD electrons and phonons, respectively. As in case (1), M^{λ}_{q} is a semiconductor electron–phonon constant and ω^{QD}_{i} is a phonon frequency. ε^{QD}_{n} is the energy of noninteracting electrons and $V^{(0)}_{n_1,n_2,n_4,n_3}$ is a Coulomb integral.

3. The interaction between the quantum dot and semiconductor is considered in the tunneling approximation introduced by Bardeen [6]:

$$\hat{H}_{SM-QD} = \sum_{k,\lambda;n} \left[V(k,\lambda;n) c^{\dagger}_{k,\lambda} d_n + h.c. \right], \tag{108}$$

where $V(k,\lambda;n)$ denotes the tunneling matrix element between the (k,λ) semiconductor and nth QD electronic states.

4. The interaction between QD electrons and light is considered in the dipole approximation:

$$\hat{H}_{QD-light} = -\mathbf{E}(t) \cdot \sum_{n \neq m} \mathbf{p}_{nm}\, d^{\dagger}_{n} d_m, \tag{109}$$

where

$$\mathbf{p}_{nm} \equiv e \int d^3 r \psi^{\dagger}_{n}(\mathbf{r}) \mathbf{r} \psi^{\dagger}_{m}(\mathbf{r}). \tag{110}$$

is the dipole matrix element between the n and m electronic states ($n \neq m$). The electric field, $\mathbf{E}(t)$ can have an arbitrary shape.

4.2. Photoelectric current

Photoelectric current is defined as a charge flux in the semiconductor channel

$$J(t) = -e\left\langle \frac{\mathrm{d}\hat{N}_{SM}(t)}{\mathrm{d}t} \right\rangle, \tag{111}$$

where the operator of the number of electrons is given by the following expression:

$$\hat{N}_{SM} \equiv \sum_{k,\lambda} c^{\dagger}_{k,\lambda} c_{k,\lambda}. \tag{112}$$

In Eq. (111), the average is taken over QD and SM electronic and vibrational states. Then, making use of the Heisenberg equation, we obtain the following expression for the photocurrent [45, 52]:

$$J = \frac{2e}{\hbar} \Re \left\{ \sum_{k,\lambda,n} V(k,\lambda;n) G^{<}_{k,\lambda;n}(t,t) \right\}, \tag{113}$$

where the mixed lesser Green's function is defined in the following way [45, 52]:

$$G^{<}_{k,\lambda;n}(t,t') \equiv i\langle c^{\dagger}_{k,\lambda}(t) d_n(t') \tag{114}$$

The next step, as described in Refs. [45, 52] for tunneling junctions, is to employ the equation of motion approach. This procedure is not applicable for a solar cell problem because the existence of SM electron–phonon interaction. To find the mixed lesser Green's functions (114), we employ a diagrammatic expansion with respect to all types of interactions: e–e in Eq. (107) in the QD, e–ph interactions in both QD (see Eq. (107)) and semiconductor (see Eq. (105)), the tunneling term described by Eq. (108), and the interaction with light (see Eq. (109)). A similar diagrammatic expansion was introduced in a tunneling junction problem in Ref. [54]. Hence, we choose the following terms for the noninteracting Hamiltonian:

$$\hat{H}_0 = \hat{H}^0_{SM} + \hat{H}^0_{QD}, \tag{115}$$

where $\hat{H}^0_{SM}$ and $\hat{H}^0_{QD}$ are defined as follows:

$$\hat{H}^0_{SM} = \sum_{k,\lambda} \varepsilon^s_{k,\lambda} c^\dagger_{k,\lambda} c_{k,\lambda} + \sum_q \omega^s_q b^\dagger_q b_q,$$
$$\hat{H}^0_{QD} = \sum_n \varepsilon^{QD}_n d^\dagger_k d_n + \sum_q \omega^{QD}_i a^\dagger_i a_i. \tag{116}$$

The interaction term is taken in the form:

$$\hat{H}^{int} = \hat{H}^{int}_{SM} + \hat{H}^{int}_{QD} + \hat{H}_{SM-QD}, \tag{117}$$

where

$$\hat{H}^{int}_{SM} = \sum_{q,k,\lambda} M^\lambda_q \hat{A}_q c^\dagger_{k+q,\lambda} c_{k,\lambda},$$
$$\hat{H}^{int}_{QD} = \frac{1}{2} \sum_{n_1,n_2,n_3,n_4} V^{(0)}_{n_1,n_2,n_4,n_3} d^\dagger_{n_1} d^\dagger_{n_2} d_{n_3} d_{n_4} + \sum_{i,n} M_{i,n} d^\dagger_n d_n (a^\dagger_i + a_i) - \mathbf{E}(t) \cdot \sum_{n \neq m} \mathbf{p}_{nm}\, d^\dagger_n d_m,$$
$$\hat{H}_{SM-QD} = \sum_{k,\lambda,n} \left[V(k,\lambda;n) c^\dagger_{k,\lambda} d_n + V(k,\lambda;n)^* d^\dagger_n c_{k,\lambda} \right]. \tag{118}$$

For simplicity, the *QD* and *SM* indices in the e–ph constants have been omitted in Eq. (118); however, the frequencies and e–ph constants are obviously different in the both subsystems. In the proposed description, we assume that equilibrium Green's functions of the semiconductor and the quantum dot are known. However, to find QD equilibrium Green's function in a time-dependent field is not an easy task because it is not even clear whether Dyson equations for SM and QD Keldysh functions *exist* for different types of fermions interacting with each other. This problem is rather complicated even for molecular wires [54]. Thus, we expect this problem to be even more complicated for solar cell systems where the interaction with light makes the problem essentially time dependent. In this section, we prove that Dyson equations for nonequilibrium Green's functions do exist. In our description, we adopt a graduate approach to the problem introducing different approximations step by step. As the first and the easiest step, we consider only uncorrelated electrons.

4.3. Uncorrelated electrons in a quantum dot

To understand the diagrammatic approach which is introduced below, we first determine nonequilibrium Green's functions for uncorrelated electrons in a semiconductor and a quantum dot using a diagrammatic expansion on

a Keldysh contour rather than the equation of motion method employed in the tunneling junction problem [45, 52, 53]. Thus, the goal is to calculate the mixed Keldysh functions for Eq. (114). Nonequilibrium Green's functions for the quantum dot and semiconductor have been defined by Eqs. (52)–(55). The mixed Keldysh functions has been presented by Eq. (56) in the interaction representation. $\hat{H}_{int}$ is defined as the interaction between the SM and QD electrons and the interaction of the QD electrons with light in the interaction representation:

$$\hat{H}_{int}(t) = \sum_{k,n} \left[V(k,n)\tilde{c}_k^\dagger(t)\tilde{d}_n(t) + h.c. \right] - \mathbf{E}(t) \cdot \sum_{n \neq m} \mathbf{p}_{nm}\, \tilde{d}_n^\dagger \tilde{d}_m. \tag{119}$$

The detailed diagrammatic analysis results in the following Dyson integral equation for the mixed Keldysh function on the Keldysh contour [99]:

$$\tilde{G}_{kn}^{(0)}(t-t') = \sum_{k_1,n_1} \int_c dt_1 V^*(k_1,n_1)\tilde{G}_{n_1 n}^{(p)}(t,t_1) g_{k_1,k}^{(0)}(t_1-t'). \tag{120}$$

In the same way, we obtain the integral Dyson equation for the QD Keldysh functions (52):

$$\tilde{G}_{nm}^{(p)}(t,t') = G_{nm}^{(0)}(t-t') + \sum_{n_1,n_2} \int_c \mathrm{d}t_1 \int_c \mathrm{d}t_2 G_{nn_1}^{(0)}(t-t_1)\Sigma_{n_1 n_2}^{(0)}(t_1-t_2)\tilde{G}_{n_2 m}^{(p)}(t_2,t'), \tag{121}$$

where the self-energy matrix is defined as follows:

$$\Sigma_{n_1,n_2}^{(0)}(t_1,t_2) = \sum_{k_1,k_2} \left[V(k_1,n_1) g_{k_1 k_2}^{(0)}(t_1-t_2) V^*(n_2,k_2) \right] - \mathbf{E}(t_1)\cdot \mathbf{p}_{n_1 n_2}\delta(t_1-t_2) \tag{122}$$

In Eq. (122), the QD and SM zeroth Keldysh functions are noninteracting fermion Green's functions [6]. The expression for nonequilibrium Green's function for noninteracting electron can be found in Ref. [6]. The Dyson equation (121) for noninteracting electrons is diagrammatically shown in Figure 5.23. In this Figure, the solid line represents the zeroth QD Keldysh function, $G^{(p)r}(t-t')$, the wavy line defines a linear combination of zeroth SM Keldysh functions determined by Eq. (122), and the dashed-dot line stands for the interaction of the QD electrons with light. The solid dot denotes the tunneling interaction, V. The graph describes a perturbation series with respect to $|V|^2$. In Figure 5.24, we graphically define different types of interactions that are used in this section.

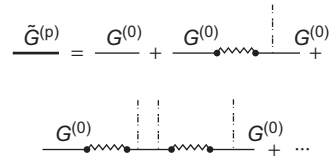

Figure 5.23 Diagrammatic representation of Dyson Eq. (121). The solid line denotes the zeroth QD Keldysh function, the wavy line stands for a linear combination of the zeroth SM Keldysh functions determined by Eq. (122), the dashed-dot line denotes the interaction with the electric field, and the dot represents the tunneling transition

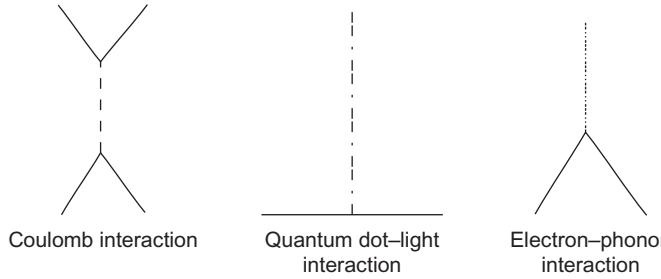

Figure 5.24 Diagrammatic representation of different interactions: the dashed line stands for the Coulomb, the dashed-single-dot line for quantum dot–light, and the dashed-double-dot line for electron–phonon interactions.

Finally, we find the expression for photocurrent in the semiconductor. From Eq. (120), we take a projection of the mixed Keldysh function on the Keldysh contour to $G^{<}_{kn}$ in accordance with the Langreth' procedure [41, 45]:

$$\tilde{G}^{(0)<}_{kn}(t,t') = \sum_{k_1,n_1} \int_c \mathrm{d}t_1 V^*(k_1,n_1) \Big[\tilde{G}^{(p)r}_{n_1 n}(t,t_1) g^{(0)<}_{k,k_1}(t_1 - t') + \tilde{G}^{(p)<}_{n_1 n}(t,t_1) g^{(0)a}_{k,k_1}(t_1 - t') \Big]. \tag{123}$$

Then we substitute $\tilde{G}^{(0)<}_{kn}(t,t_1)$ from Eq. (123) into the expression (113) for photoelectric current. Thus, the following expression for the current can be obtained:

$$J = \frac{2e}{\hbar} \Re \int \mathrm{d}t_1 \left\{ \sum_{k_1,k_2,n,m} V(k_1,n) V^*(k_2,m) \Big[\tilde{G}^{(p)r}_{nm}(t,t_1) g^{(0)<}_{k_1,k_2}(t_1 - t) + \tilde{G}^{(p)<}_{nm}(t,t_1) g^{(0)a}_{k_1,k_2}(t_1 - t) \Big] \right\}, \tag{124}$$

where $g^{(0)a,r,<}_{k_1,k_2}(t_1 - t)$ are the SM zeroth Keldysh functions for noninteracting electrons [6] and the nonequilibrium QD Green's functions can be found from Eqs. (121) and (122). This expression is different from a similar expression for electric current in tunneling junctions [45, 52, 53]. In Eq. (124), the QD Green's functions contain a time-dependent electric field rather than a right electrode.

4.4. Correlated QD electrons

In this subsection, we include electron–electron and electron–phonon interactions into the QD Hamiltonian. Thus, the QD Hamiltonian yields

$$\hat{H}_{QD} = \sum_n \varepsilon^{QD}_n d^\dagger_k d_n + \frac{1}{2} \sum_{n_1,n_2,n_3,n_4} V^{(0)}_{n_1,n_2,n_4,n_3} d^\dagger_{n_1} d^\dagger_{n_2} d_{n_3} d_{n_4} + \sum_q \omega^{QD}_i a^\dagger_i a_i + \sum_{i,n} M_{i,n} d^\dagger_n d_n (a^\dagger_i + a_i) - \mathbf{E}(t) \cdot \sum_{n \neq m} \mathbf{p}_{nm} d^\dagger_n d_m. \quad (125)$$

where $V^{(c)}_{n_1,n_2,n_4,n_3}$ represents a Coulomb four center integral. As in the case of noninteracting electrons, we define Keldysh functions in the same manner as in Eq. (56). All the operators are taken in the interaction representation described by Eq. (58). The interaction Hamiltonian includes the tunneling, Coulomb, electron–phonon, and electron–photon (light) terms:

$$\hat{H}_{int}(t) = \sum_{k,n} \left[V(k,n) \tilde{c}^\dagger_k(t) \tilde{d}_n(t) + h.c. \right] + \frac{1}{2} \sum_{n_1,n_2,n_3,n_4} V^{(c)}_{n_1,n_2,n_4,n_3} \tilde{d}^\dagger_{n_1} \tilde{d}^\dagger_{n_2} \tilde{d}_{n_3} \tilde{d}_{n_4} + \sum_{i,n} M_{i,n} d^\dagger_n d_n (a^\dagger_i + a_i) - \mathbf{E}(t) \cdot \sum_{n \neq m} \mathbf{p}_{nm} d^\dagger_n d_m \quad (126)$$

The derivation on a Dyson equation on the Keldysh contour is similar to the derivation presented in Section 4 [54]. The difference is in the interactions. In the present derivation, we also include the interaction with irradiation. For any order diagram with respect to the Coulomb interaction, the semiconductor–quantum dot and quantum dot–light interactions retains the topological structure of a graph in the same manner as for noninteracting case where the ordinary zeroth Green's functions are substituted by the renormalized zeroth Green's functions described by Eqs. (121) and (122).

We also consider the QD electron–phonon interaction into the calculations. As discussed earlier, the zeroth Green's functions should be substituted by $G^{(p)}$ from Eqs. (121) and (122). The electron–phonon interaction introduces additional vertices where the zeroth Green's functions are changed by the renormalized ones as shown in Figure 5.25. Hence, the Dyson equation for

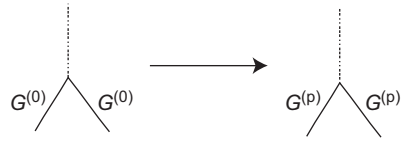

Figure 5.25 Electron–phonon vertices in a quantum dot where the zeroth electron Green's functions are exchanged by the renormalized ones from Eqs. (121) and (122).

the nonequilibrium QD Green's function yields

$$G(t,t') = \tilde{G}^{(p)}(t,t') + \int_c \mathrm{d}t_1 \int_c \mathrm{d}t_2 \tilde{G}^{(p)}(t,t_2)\Sigma(t_1,t_2)G(t,t'), \tag{127}$$

where self-energy operator $\Sigma(t)$ includes all possible diagrams with respect to the Coulomb and e–ph interactions taken with the renormalized zeroth Keldysh functions. This equation is exact. The approach presented above is valid if the Coulomb electron–phonon interactions are considered only for the QD electrons, while the semiconductor electrons are still nonintersecting.

Finally, the photoelectric current can be found from Eq. (124) where the QD Green's functions are now the solution of different Dyson equations (127):

$$J = \frac{2e}{\hbar}\Re \int \mathrm{d}t_1 \left\{ \sum_{k_1,k_2,n,m} V(k_1,n)V^*(k_2,m) \left[\tilde{G}^r_{nm}(t,t_1) g^{(0)<}_{k_1,k_2}(t_1-t) + \tilde{G}^<_{nm}(t,t_1) g^{(0)a}_{k_1,k_2}(t_1-t) \right] \right\}, \tag{128}$$

This equation is valid for a *cw* electric field.

4.5. Electron–phonon interaction in the semiconductor

Electron–phonon interaction in a semiconductor is the main factor for relaxation of a transferred electron. There are two different relaxation processes that decrease the efficiency of light conversion in a solar system: (1) relaxation of an electron from a semiconductor conduction band to a valence band and (2) a backward electron transfer reaction. The forward and backward electron transfer processes have been already included in the tunneling interaction, $\hat{H}_{SM-QD}$, described by Eq. (108). However, the effect of SM e–ph interaction is important for the correct description of electron transfer in the SM–QD solar cell system. In the previous section, we have gradually considered different types of interactions in the quantum dot and obtained the exact expression for the photocurrent (128) where the exact nonequilibrium QD Green's functions determined from Eq. (127) have been used. However, in

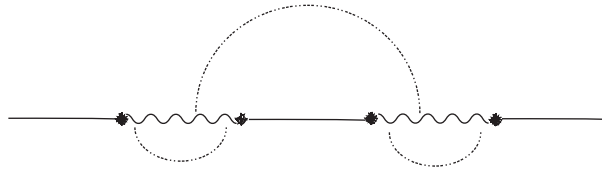

Figure 5.26 Diagrammatic representation of the SM e–ph interaction in the QD Green's function expansion. There are two types of diagrams: the phonon Green's function connects two SM Green's functions separated by the QD Green's function (the diagram above the time line), and the phonon Green's function is located within the same semiconductor electron Green's function (two dashed lines below the time line).

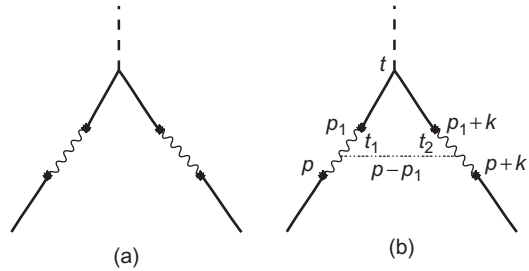

Figure 5.27 (a) Vertex with no semiconductor electron–phonon correction and (b) the vertex with the second-order electron–phonon correction.

the expression (128), we have employed the *zeroth* SM Keldysh functions. The interaction of the semiconductor electrons with phonons can substantially change the expression for the current. Indeed, as shown in Figure 5.26, the crossings between two different semiconductor electron Green's functions separated by the QD Green's functions make the procedure of the insertion of the tunneling interaction and the interaction of the QD electrons with light inapplicable any longer. Thus, we are not able to derive Dyson equations in this case. The similar problem exists for tunneling junctions where e–e correlation effects in the leads have been disregarded [54]. By making use of the Migdal's theorem [100], it can be shown that crossing diagrams can be safely neglected for wide-gap semiconductors [99]. The comparison of two types diagrams considering zeroth- and first-order corrections due to the e–ph interaction for the vertex shown in Figure 5.27. The ratio between diagrams (a) and (b) can be evaluated [99, 101] and appears to be small with respect to the parameter

$$I^{(2)} \sim \frac{\omega_D}{\varepsilon_F} \sim \left(\frac{m}{M}\right)^{\frac{1}{2}} \ll 1, \tag{129}$$

Thus, according to the Migdal's theorem, we can safely neglect the vertices of type (*b*) (see Figure 5.27) in the diagrammatic expansion for the QD Green's functions. Consequently, the rules applied to the derivation of the QD Green's functions remain the same, and the procedure described in the derivation of Eq. (128), see also Figure 5.4, remains unchanged with the one important difference where the *exact* SM electron Green's function modified by the electron–phonon interaction substitutes the zeroth (without e–ph interaction) SM electron Green's function. The final expression for the photoelectric current now is given by the following expression:

$$J = \frac{2e}{\hbar}\Re\int \mathrm{d}t_1 \left\{ \sum_{k_1,k_2,n,m} V(k_1,n)V^*(k_2,m)\left[\tilde{G}^r_{nm}(t,t_1)g^<_{k_1,k_2}(t_1-t) + \tilde{G}^<_{nm}(t,t_1)g^a_{k_1,k_2}(t_1-t)\right]\right\}. \tag{130}$$

This equation looks similar to Eq. (128). However, there is the essential difference between these two equations. In Eq. (130), we employ the exact semiconductor Green's functions modified by the e–ph interaction. These Green's functions appear in the expressions for the QD Keldysh functions and for the photocurrent. The dependence of the current on a light frequency determines a photocurrent spectrum in a solar cell.

The Migdal's theorem is valid for wide-gap semiconductors where the fermi energy is approximately equal to a half of the gap. Semiconductors used in solar cells are usually wide-gap semiconductors. For example, the gap for a TiO_2 is 3.2 eV, whereas a typical Debye frequency is about 0.1 eV. Thus, the expression for the photocurrent (130) holds true.

5. CONCLUSIONS

The proliferation of novel experimental techniques in Physics, Chemistry, and Materials Science requires new computational approaches in order to explain new experimental data and predict novel materials with desired properties. The latter being important for practical applications contains combinations of a single molecule and infinite subsystems of atoms (metal electrode) or a large cluster (a quantum dot) and a semiconductor surface. Besides the large sizes of these systems, there is a *second* complication related to nonequilibrium conditions and time-dependent interactions. In the case of molecular devices, an applied voltage creates a nonequilibrium charge flow (electric current). For QD sensitized solar cells, continuous irradiation results in photocurrent in a charge separation. The *third* important complication is due to strong correlation effects such as electron–electron and electron–phonon correlations. Hence, a problem of correlated electron

dynamics becomes even more complex than for electronic structure calculations.

For correct description of various nonequilibrium properties of the systems mentioned earlier, we adopt the approach that was already used in Quantum Chemistry in 70s and 80s by different research groups [9–21]. This approach is based on *ab initio* calculations of one-particle Green's functions or electron propagators. The electron propagator methods are very attractive because of clear and successive approximations employed in calculations. Calculations without any adjustable parameters are straightforward and provide reliable results. If it turns out that calculations based on these approximations do not fit experimental data, there is a straightforward way to improve them by adding more diagrams. In this work, we have adopted this approach and extended it to the description of various nonequilibrium processes. The proposed methodology is based on nonequilibrium Green's functions or Keldysh functions. These functions are useful for the correct description of correlated electron dynamics in molecular tunneling devices and quantum dot–sensitized solar cells where oversimplified uncorrelated rate equation approach fails. The exact equations for electric current (Section 3) and photocurrent (Section 4) calculations have been presented in terms of Keldysh functions with their brief description given in Section 2. The problem becomes more complicated if one considers exciton or multiple exciton generation. For proper descriptions of these quasiparticles, one should take into account second-order Green's functions for a single exciton or higher order Green's functions for multiple excitons. The latter approach requires new computational schemes.

It becomes more and more obvious that a further development of nonequilibrium electron propagator methodology is necessary to describe various dynamic processes in Chemistry, Physics, and Materials Science.

ACKNOWLEDGMENTS

This work was supported by a grant (DE-SC0004981) from the Department of Energy to the University of Wyoming and by the University of Wyoming School of Energy Resources through its Graduate Assistantship program.

REFERENCES

[1] A.A. Abrikosov, L.G. Gorkov, I.E. Dzyaloshinski, Methods of Quantum Field Theory in Statistical Physics, Dover, New York, 1963.
[2] D.N. Zubarev, Double-time Green Functions in statistical physics, Sov. Phys. Usp. 3 (1960) 320.
[3] P. Noziéres, Theory of Interacting Fermi Systems, Benjamin, New York, 1964.

[4] A.L. Fetter, J.D. Walecka, Quantum Theory of Many-Particle Systems, McGraw-Hill, New York, 1971.
[5] L.P. Kadanof, G. Baym, Quantum Statistical Mechanics, W. A. Benjamin, Inc, New York, 1962.
[6] G.D. Mahan, Many-Particle Physics, Kluwer, New York, 2000.
[7] A.B. Migdal, Theory of Finite Fermi-Systems and Properties of Atomic Nuclei, Nauka, Moscow, 1983 (in Russian).
[8] J.W. Negele, H. Orland, Quantum Many-Particle Systems, Addison-Wesley, New York, 1988.
[9] J. Linderberg, Y. Öhrn, Propagators in Quantum Chemistry, second ed., Wiley Interscience, Hoboken, NJ, 2004.
[10] W. von Niessen, J. Schirmer, L.S. Cederbaum, Computational methods for the one-particle Green's function, Comput. Phys. Rep. 1 (1984) 57.
[11] G. Csanak, H.S. Taylor, R. Yaris, in: D.R. Bates, I. Esterman (Eds.), Green's Function Technique in Atomic and Molecular Physics: in Advances in Atomic, Molecular Physics, and Optical Physics, Advances in Atomic and Molecular Physics, Vol. 7, Academic, New York, 1971, p. 287.
[12] Y. Öhrn, G. Born, in: P. O. Löwdin (Ed.), Electron propagator theory and calculations, Advances in Quantum Chemistry, Vol. 13, Academic Press, New York, 1981, p. 1.
[13] M.F. Herman, K.F. Freed, D.L. Yeager, in: I. Prigogine, S.A. Rice (Eds.), Theoretical Studies of the Equations of Motion - Green's Function Methods for the Evaluation of Atomic and Molecular Ionization Potentials, Electron Affmities, and Excitation Energies, Advances in Chemical Physics, Vol. 48, Wiley, New York, 1981, p. 1.
[14] P. Jørgensen , J. Simons, Second Quantization-Based Methods in Quantum Chemistry, Academic Press, New York, 1981.
[15] L.S. Cederbaum, W. Domke, in: I. Prigogine, S.A. Rice (Eds.), Theoretical Aspects of ionization potentials and photoelectron spectroscopy: A Green's function approach, Advances in Chemical Physics, Vol. 36, Wiley, New York, 1977, p. 205.
[16] D.J. Rowe, Equations-of-motion method and the extended shell model, Rev. Mod. Phys. 40 (1968) 153.
[17] T. Shibuya, V. McKoy, Higher Random-Phase Approximation as an Approximation to the Equations of Motion, Phys. Rev. A 2 (1970) 2208.
[18] J. Simons, W.D. Smith, Theory of electron affinities of small molecules, J. Chem. Phys. 58 (1973) 4899.
[19] G.D. Purvis, Y. Öhrn, A comment on a theory of electron affinities, Chem. Phys. Lett. 33 (1975) 396.
[20] P. Jørgensen, J. Simons, A complete treatment of the electron propagator through third order, J. Chem. Phys. 63 (1975) 5320.
[21] J.V. Ortiz, in: J.R. Sabin, S.B. Trickey (Eds.), Toward an exact one-electron picture of chemical binding, Advances in Quantum Chemistry, Vol. 35, Academic Press, New York, 1999, p. 33.
[22] M.J. Frisch, G.W. Trucks, H.B. Schlegel, G.E. Scuseria, M.A. Robb, J.R. Cheeseman, et al., Gaussian 03, Revision B.03, Gaussian, Inc., Pittsburgh PA, 2003.
[23] A. Guevara-Garca, A. Martinez, J.V. Ortiz, Structures with Al-H Bonds Represented in the Photoelectron Spectrum of $Al_3O_4H_2$, J. Chem. Phys. 124 (2006) 214304.
[24] J.V. Ortiz, Book review, Propagators in Quantum Chemistry, Int. J. Quantum Chem. 100 (2004) 59.
[25] O. Dolgounitcheva, V.G. Zakrzewski, J.V. Ortiz, Electron Propagator Calculations Show that Alkyl Substituents Alter Porphyrin Ionization Energies, J. Am. Chem. Soc. 127 (2005) 8240.
[26] X. Li, A.E. Kuznetsov, H.-F. Zhang, A.I. Boldyrev, L.-S. Wang, Observation of All-Metal Aromatic Systems, Science 291 (2001) 859.

[27] A.N. Alexandrova, A.I. Boldyrev, H.-J. Zhai, L.S. Wang, All-boron aromatic clusters as potential new inorganic ligands and building blocks in chemistry, Coord. Chem. Rev. 250 (2006) 2811.
[28] A.I. Boldyrev, L.S. Wang, All-Metal Aromaticity and Antiaromaticity, Chem. Rev. 105 (2005) 3716.
[29] A.E. Kuznetsov, K.A. Birch, A.I. Boldyrev, X. Li, H.-J. Zhai, L.S. Wang, All-Metal Antiaromatic Molecule: Rectangular Al4 4- in the Li3Al4 - Anion, Science 300 (2003) 622.
[30] M.A. Reed, C. Zhou, C.J. Muller, T.P. Burgin, J.M. Tour, Conductance of a Molecular Junction Science 278 (1997) 252.
[31] X. Xiao, B. Xu,N.J. Tao, Measurement of single molecule conductance: Benzenedithiol and benzenedimethanethiol, Nano Lett. 4 (2004) 267.
[32] J.B. Sambur, T. Novet, B.A. Parkinson, Multiple exciton collection in a sensitized photovoltaic system, Science 330 (2010) 63.
[33] S. Kolodinski, J. Werner, T. Wittchen, H. Queisser, Quantum efficiencies exceeding unity due to impact ionization in silicon solar cells, Appl. Phys. Lett. 63 (1993) 2405.
[34] R. Schaller, V. Klimov, High efficiency carrier multiplication in PbSe nanocrystals: Implications for solar energy conversion, Phys. Rev. Lett. 92 (2004) 186601.
[35] M.T. Spitler, B.A. Parkinson, Dye sensitization of single crystal semiconductor electrodes, Acc. Chem. Res. 42 (2009) 2017–2029.
[36] A.L. Efros, V.A. Kharchenko, M. Rosen, Breaking the phonon bottleneck in nanometer quantum dots: Role of Auger-like processes, Solid State Commun. 93 (1995) 281.
[37] A.L. Efros, M. Rosen, The electron structure of semiconductor nanocrystals, Ann. Rev. Mater. Sci. 30 (2000) 475.
[38] A. Shabaev, A.L. Efros, A. Nozik, J. Multiexciton, Generation by a single photon in nanocrystals, Nano Lett. 6 (2006) 28562863.
[39] V.L. Rupasov, V.I. Klimov, Carrier multiplication in semiconductor nanocrystals via intraband optical transitions involving virtual biexciton states, Phys. Rev. B 76 (2007) 125321.
[40] L.V. Keldysh, Nonequilibrium Green's functions, Zh. Exp. Teor. Fiz. 47 (1964) 115 [Sov. Phys. JETP 20 (1965) 1018].
[41] D.C. Langreth, in: J.T. Devreese, V.E. van Doren (Eds.), Linear and nonlinear response theory with applications, Linear and Nonlinear Electron Transport in Solids, Plenum Press, New York, 1975, p. 3.
[42] P. Danielewicz, Quantum theory of nonequilibrium processes, Ann. Phys. 152 (1984) 239.
[43] M. Bonitz, R. Nareyka, D. Semkat, (Eds.), Progress in Nonequilibrium Green's Functions, World Scientific, Singapore, 2000.
[44] M. Bonitz, D. Semkat, (Eds.), Progress in Nonequilibrium Green's Functions, World Scientific, Singapore, 2003.
[45] H. Haug, A.-P. Jauho, Progress in Nonequilibrium Green's Functions, Springer, New York, 1996.
[46] R. van Leeuwen, N.E. Dahlen, An Introduction to Nonequilibrium Green Functions, http://molsim.chem.uva.nl/han/2004/NGF.pdf (2005).
[47] R. van Leeuwan, N.E. Dahlen, G. Stefanucci, C.O. Almbadh, Lecture and Notes in Physics, Vol. 706, Springer, Berlin, 2006, p. 33.
[48] M. Wagner, Expansions of nonequilibrium Green's functions, Phys. Rev. B 44 (1991) 6104.
[49] M. Wagner, Nonadiabatic transport in finite systems. I. Formal theory, Phys. Rev. B 45 (1992) 11595.
[50] M. Wagner, Nonadiabatic transport in finite systems. II. Magnetotransport in a quasi-one-dimensional channel, Phys. Rev. B 45 (1992) 11606.
[51] A. Nitzan, M. Ratner, Electron transport in molecular wire junctions, Science 300 (2003) 1384.

[52] A.-P. Jauho, N.S. Wingreen, Y. Meir, Time-Dependent Transport in Interacting and Noninteracting Resonant Tunneling Systems, Phys. Rev. B 50 (1994) 5528–5544.
[53] Y. Meir, N.S. Wingreen, Landauer Formula for the Current through an Interacting Electron Region, Phys. Rev. Lett. 68 (16) (1992) 2512–2515.
[54] Yu. Dahnovsky, Electron-electron correlations in molecular tunnel junctions: A diagrammatic approach, Phys. Rev. B 80 (2009) 165305.
[55] Yu. Dahnovsky, V.G. Zakrzewski, A. Kletsov, J.V. Ortiz, Ab Initio electron propagator theory of molecular wires: I. Formalism, J. Chem. Phys. 123 (2005) 184711.
[56] Yu. Dahnovsky, J.V. Ortiz, J. Chem. Ab initio electron propagator theory of molecular wires: II. Multiorbital terminal description, Phys. 124 (2006) 144114.
[57] O. Dolgounitcheva, V.G. Zakrzewski, A. Kletsov, M.R. Sterling , Yu. Dahnovsky, J.V. Ortiz, Correlated, Ab Initio Calculations in the Study of Molecular Wires, Int. J. Quant. Chem. 106 (2006) 3387.
[58] F.R. Gantmakher, The Theory of Matrices, Chelsea Publishing Company, New York, 1959, (or more recent edition (in Russian) (Nauka, Moscow, 1988)).
[59] J.M. Seminario, J.M. Derosa, Molecular Gain in a Thiotolane System, J. Am. Chem. Soc. 123 (2001) 12418.
[60] C. Joachim, J.F. Vinuesa, Length dependence of the electronic transparence (conductance) of a molecular wire, Europhys. Lett. 33 (1996) 635.
[61] M. Magoga, C. Joachim, Conductance and transparence of long molecular wires, Phys. Rev. B 56 (1997) 4722.
[62] A. Tikhonov, R.D. Coalson, Yu. Dahnovsky, Calculating electron transport in a tight binding model of a field-driven molecular wire: Floquet theory approach, J. Chem. Phys. 116 (2002) 10909.
[63] A. Tikhonov, R.D. Coalson, Yu. Dahnovsky, Calculating electron current in a tight-binding model of a field-driven molecular wire: Application to xylyl-dithiol, J. Chem. Phys. 117 (2002) 567.
[64] N.D. Lang, Ph. Avouris, Carbon-Atom Wires: Charge-Transfer Doping, Voltage Drop, and the Effect of Distortions, Phys. Rev. Lett. 84 (2000) 358.
[65] M. DiVentra, S.T. Pantelides, N.D. Lang, First-Principles Calculation of Transport Properties of a Molecular Device, Phys. Rev. Lett. 84 (2000) 979.
[66] J. Tomfohr, O.F. Sankey, Theoretical analysis of electron transport through organic molecules, J. Chem. Phys. 120 (2004) 1542.
[67] D.S. Kosov, Lagrange multiplier based transport theory for quantum wires, J. Chem. Phys. 120 (2004) 7165.
[68] D.S. Kosov, Kohn–Sham equations for nanowires with direct current, J. Chem. Phys. 119 (2003) 1.
[69] F. Evers, F. Weigend, M. Koentopp, Conductance of molecular wires and transport calculations based on density-functional theory, Phys. Rev. B 69 (2004) 235411.
[70] M. Koentopp, K. Burke, F. Evers, Zero-bias molecular electronics: Exchange-correlation corrections to Landauer's formula, Phys. Rev. B 73 (2006) 121403(R).
[71] A. Arnold, F. Weigend, F. Evers, Quantum chemistry calculations for molecules coupled to reservoirs: Formalism, implementation, and application to benzenedithiol, J. Chem. Phys. 126 (2007) 17410.
[72] P. Schmitteckert, F. Evers, Exact Ground State Density-Functional Theory for Impurity Models Coupled to External Reservoirs and Transport Calculations, Phys. Rev. Lett. 100 (2008) 08640.
[73] M.A. Kozhushner, V.S. Polyanskii, I.I. Oleynik, Tunneling and resonant conductance in one-dimensional molecular structures, Chem. Phys. 319 (2005) 368.
[74] M.A. Kozhushner, V.S. Polyanskii, I.I. Oleynik, Bound states of tunneling electrons in molecular chains, Phys. Rev. B 74 (2006) 165103.

[75] I.I. Oleynik, M.A. Kozhushner, V.S. Polyanskii, L. Yu, Rectification mechanism in diblock oligomer molecular diodes, Phys. Rev. Lett. 96 (2006) 096803.
[76] M.R. Sterling, O. Dolgunitcheva, V.G. Zakrzewski, Yu. Dahnovsky, J.V. Ortiz, Correlated, ab initio electron propagators in the study of molecular wires: Application to a single molecular bridge placed between two model leads, Intern. J. Quant. Chem. 107 (2007) 3228.
[77] S.M. Linsay, M.A. Ratner, Recent progress in the measurement and modeling of transport in molecular junctions, Adv. Mater. 19 (2007) 23.
[78] W.D. Wheeler, Yu. Dahnovsky, Quantum interference in molecular wires: Electron propagator calculations, J. Phys. Chem. C 112 (2008) 13769–13774.
[79] D. Krger, H. Fuchs, R. Rousseau, D. Marx, M. Parrinello, Interaction of short-chain alkane thiols and thiolates with small gold clusters: Adsorption structures and energetics, J. Chem. Phys. 115 (2001) 4776.
[80] B. Xu, X. Xiao, X. Yang, L. Zang, N. Tao, J. Am. Chem. Soc. 127 (2005) 2386.
[81] X. Li, B. Xu, X. Xiao, X. Yang, L. Zang, N. Tao, Large Gate Current Modulation in a Room Temperature Single Molecule Transistor, Faraday Discuss. 131 (2006) 111.
[82] K. Xiao, Y. Liu, T. Qi, W. Zhang, F. Wang, J. Gao, et al., A Highly ⊓-Stacked Organic Semiconductor for Field-Effect Transistors Based on Linearly Condensed Pentathienoacene J. Am. Chem. Soc. 127 (2005) 1381.
[83] J.-O. Lee, G. Lientsching, F. Wiertz, M. Struijk, R.A.J. Janssen, R. Egberink, et al., Absence of Strong Gate Effects in Electrical Measurements on Phenylene-Based Conjugated Molecules, Nano Lett. 3 (2003) 113.
[84] E.G. Emberly, G. Kirczenow, Multiterminal molecular wire systems: A self-consistent theory and computer simulations of charging and transport, Phys. Rev. B 62 (2000) 10451.
[85] E.S. Soldatov, V.V. Khanin, A.S. Trifonov, S.P. Gubin, V.V. Kolosov, D.E. Presnov, et al., arXiv: cond-mat/9610155v2.
[86] G. Begemann, D. Darau, A. Donarini, M. Grifoni, Symmetry fingerprints of a benzene single-electron transistor: Interplay between Coulomb interaction and orbital symmetry, Phys. Rev. B 77 (2008) 201406.
[87] F. Jiang, Y.X. Zhou, H. Chen, R. Note, H. Mizuseki, Y. Kawazoe, aXiv: cond-matt/0605156v1 (2006).
[88] A. Gosh, T. Rakshit, S. Datta, arXiv: cond-matt/0212166v2 (2004).
[89] S.N. Rashkeev, M. Di Ventra, S.T. Pantelides, Transport in molecular transistors: Symmetry effects and nonlinearities, Phys. Rev. B 66 (2002) 033301.
[90] W.D. Wheeler, Yu. Dahnovsky, Molecular transistors based on BDT-type molecular bridges, J Chem. Phys. C 112 (2008) 13769.
[91] S.J. Tans, A.R. Verschueren, C. Dekker, Room-temperature transistor based on a single carbon nanotube, Nature 393 (1998) 49.
[92] W.D. Wheeler, Yu. Dahnovsky, Molecular transistors with perpendicular gate field architecture: A strong gate field effect, J. Phys. Chem. C 113 (2009) 13774.
[93] P.C. Collins, M.S. Arnold, P. Avouris, Engineering Carbon Nanotubes and Nanotube Circuits Using Electrical Breakdown, Science 292 (2001) 706.
[94] Y. Cui, C. Lieber, Functional Nanoscale Electronic Devices Assembled Using Silicon Nanowire Building Blocks, Science 291 (2001) 851.
[95] H. Park, J. Park, A.K.L. Lim, E.H. Anderson, A.P. Avisatos, P.L. McEuen, Nanomechanical oscillations in a single-C60 transistor, Nature 407 (2000) 57.
[96] J. Park, A.N. Pasupathy, J.L. Goldsmith, C. Chang, Y. Yaish, J.R. Petta, et al., Coulomb blockade and the Kondo effect in single-atom transistors, Nature 417 (2002) 722.
[97] W.J. Liang, M. Shores, M. Bockrath, J.R. Long, H. Park, Kondo resonance in a single-molecule transistor, Nature 417 (2002) 725.

[98] S. Kubatkin, A. Danilov, M. Hjort, J. Cornil, J.-L. Bredas, N. Stuhr-Hansen, et al., Single-electron transistor of a single organic molecule with access to several redox states, Nature 425 (2003) 698.
[99] Yu. Dahnovsky, Quantum correlated electron dynamics in a quantum-dot sensitized solar cell: The Keldysh function approach, Phys. Rev. B (2011) (accepted).
[100] A.B. Migdal, Interaction between electrons and lattice vibrations in a normal metal, Sov. Phys. JETP 7 (1958) 996.
[101] M.B. Sadovskii, Diagrammatics, World Scientific, Singapore, 2006.

CHAPTER 6

Electron Impact Inner-Shell Ionization of Atoms

A. K. Fazlul Haque[a], **M. Alfaz Uddin**[a], **M. Shahjahan**[a], **M. Rashid Talukder**[b], **Arun K. Basak**[a], and **Bidhan C. Saha**[c]

Contents

1. Introduction 318
2. Outline of the Models 322
   2.1. MBELL model 322
   2.2. Outline of the XCVTS model 324
   2.3. GKLV model 326
   2.4. Outline of the MUIBED Model 328
3. Experimental Data Sources 330
4. Discussion and Conclusions 330
Acknowledgments 375
References 376

Abstract Electron impact inner-shell ionization cross-section (EIICS) calculations of neutral atoms with atomic numbers $Z = 6$–92 for K-shell, $Z = 18$–92 for L-shell, and $Z = 79$–92 for M-shell have been reviewed. In this work, the evaluations of the EIICS are discussed using our recently propounded easy-to-use models that are found adequately successful in describing the experimental cross sections. The selection of the range of atomic number Z for different inner-shells was guided by the availability of the EIICS data either from experiments or from rigorous quantal calculations. Details of the models have been

[a] Department of Physics, [b]Department of Applied Physics and Electronic Engineering, University of Rajshahi, Rajshahi, Bangladesh
[c] Department of Physics, Florida A & M University, Tallahassee, Florida, USA.
E-mail address: bidhan.saha@famu.edu

Advances in Quantum Chemistry, Volume 61
ISSN 0065-3276, DOI: 10.1016/B978-0-12-386013-2.00006-1

presented and their findings are compared with the experimental and other theoretical results. Our models describe the experimental results nicely for K-, L-, and M-shell ionization for $Z \leq 92$ in the energy range $E \leq 2$ GeV.

1. INTRODUCTION

The interaction of an incident charged particle with a neutral target atom may give rise to elastic and various inelastic processes. Among them, the ionization process plays a pivotal role for the understanding of collision dynamics in general. The knowledge of ionization cross sections is also very essential in numerous applied fields such as plasma physics, astrophysics, laser physics, semiconductor etching, radiation science, and so on. Moreover, these cross sections are needed in the quantitative elemental analyses using three types of material characterizations, for example, electron probe microanalysis, Auger electron spectroscopy, and electron energy loss spectroscopy. Thus, EI ionization of atomic targets enjoys the heart of many applications in diverse fields.

Modeling applications depend heavily on the vast amount of sufficiently accurate EI ionization cross sections (EIICS) data for a wide range of atomic species and incident energies, as opposed to a few simple atomic targets restricted to limited discrete incident energies, suitable for the measurement of EIICS data through experiments. The acute dearth of EIICS data calls for their theoretical determination. In this review, the experimental data are labeled by EIICS to distinguish from the theoretical ionization data, which are calculated by adopting single one-step collision mechanism. The theoretical results are referred to as EI single ionization cross sections (EISICS). Applications of various quantum mechanical treatments, such as Born approximations (BA) [1–10], T-matrix [11] and R-matrix [12], and the convergent close-coupling method [13, 14], have been developed for accurate EISICS for few selective systems, especially for the e^-–H system [13–18]. These arduous calculations are not very friendly for a speedy generation of the EISICS data for applications. Moreover, in their numerical pursuits, their involvements with various approximations considerably dampened their suitability in terms of energy domain and species. It thus underscores the need for the development of analytical empirical and semiempirical models for rapid generation of EISICS data.

In literature, there are few good reviews on the EISICS calculations [19, 20], using the simple-to-use models with limited reliability at higher energies, where relativistic energies become important and hence their use remains questionable. The models, which have enjoyed wide applications, are the semiclassical models of Thomson [21], Gryzinski [22], and Kolbenstvedt [23] and the empirical formula of Lotz [24] and Bernshtam et al. [25]. The model of Deutsch and Märk (DM) [26] combines the binary-encounter approximation of Gryzinski with the dipole interaction of the Born–Bethe theory [27]. Both the nonrelativistic [26] and relativistic DM [28] models do not satisfy

the asymptotic Bethe condition [27]. To meet this condition, Deutsch et al. revised the DM model by replacing the Gryzinski-type energy dependence with a scaled $\ln(U)/U$, where U denotes the reduced incident energy, leading to what is referred to as revised DM (RDM) model [29]. However, the RDM model fails to describe the K-shell EIICS for C and heavier atoms. Haque et al. [30] remedied those by infusing in the RDM model a Gryzinski-type relativistic factor G_R (Eq. 3 in Ref. [30]) and an appropriate ionic correction factor F_{ion} (Eq. 5 in Ref. [30]). The resulting model has been coined as the modified RDM (MRDM) in Ref. [30]. The expression for the K-shell ionization EISICS in MRDM as a function of U (after combining Eqs. (1, 2, and 6) in Ref. [30]) is given by

$$\sigma_{\mathrm{MRDM}}(U) = \pi r_K^2 g_K N_K G_K F_{\mathrm{ion}} \left[\frac{\ln(c_K U)}{U}\right]\left[\frac{A_1 - A_2}{1 + (U/A_3)^p} + A_2\right], \tag{1}$$

where r_K refers to the radius of maximum radial density, N_K is the number of electrons in the K-shell, g_K is the weighting factor [29], and A_1, A_2, A_3, p, and c_K are the fitting parameters of this model. The MRDM model attained a profound success in describing the K-shell EIICS data of targets with atomic number $Z = 1$–92 for incident energies up to 2 GeV. The Eq. (5) of Ref. [30] has two inadvertent mistakes. The corrected F_{ion}, should read as

$$F_{\mathrm{ion}} = 1 + 6.75\left(\frac{q}{UZ^{1.5}}\right)^{0.85}, \tag{2}$$

and the value of "$g_K = 70$" must be replaced by "$E_K g_K = 70$" for all atoms including H.

The binary-encounter-dipole (BED) model of Kim and Rudd [31] couples the modified form of Mott cross section [32] with the Born–Bethe theory [27]. BED requires the differential continuum oscillator strength (DOS) $\frac{df}{dw}$, which is rather difficult to obtain. The simplest approximate version of BED is the binary-encounter-Bethe (BEB) [31] model, which does not need the knowledge of DOS for calculating the EISICS.

Bell et al. [33] proposed an analytical formula, widely known in the literature as the *Belfast ionization* (BELI) formula [34] that contains the dipole interaction term for the electron-impact ionization of atoms and ions. It has been applied to light atomic and ionic targets with species-dependent parameters. Godunov and Ivanov [34] applied the BELI formula to the EI ionization of Ne^{q+} ions. Here also no generality as to parameters of the formula was provided regarding the species-dependent parameters. Moreover, the BELI formula does not make any allowance for relativistic effects. Haque et al. [35–38] have proposed a modification of this BELI model for evaluating the EI K-, L-, and M-shell ionization cross sections of atoms. The relativistic and ionic effects are also incorporated in their modified BELI (MBELL) [35–38] model in addition to generalizing the species-independent

parameters in terms of the orbital quantum numbers (nl). For relativistic corrections, a Gryzinski-type relativistic factor [22] has been introduced. The ionic correction (see Eq. (7)) depends on the effective charge, q, as seen by the incident electron while ionizing an atom and the time of interaction, dictated by the incident energy.

According to Godunov and Ivanov [34], a better fit to the experimental EIICS data can be achieved using a nonlinear term instead of a polynomial expansion for the cross section in BELI [33] or MBELL [35, 38] models. This has been implemented successfully by Patoary et al. [39] for K-shell ionization in their DMEMP model, incorporating the orbit-radial aspect of DM, dipole interaction term of BELI and the nonlinear feature, where the polynomial expansion is replaced by a single exponential term. It is important to note that the Eq. (6) of [39] for K-shell ionization cross section, σ_{DMEMP} (E) should read as

$$\sigma_{\mathrm{DMEMP}} = \pi r_K^2 N_K g_K F_{\mathrm{ion}} G_{\mathrm{R}}\left(U_K\right)/(Z^{\lambda} U_K)\left[A \ln\left(\frac{E}{I_K}\right) \times \exp\left\{\sum_{i=1}^{2} B_i \left(1 - \left(\frac{I_K}{E}\right)\right)\right\}\right] \tag{3}$$

Here E, I_K, and $U_K = E/I_K$ denote, respectively, the incident energy, ionization potential for the K-shell electron, and the corresponding reduced energy. A, B's, and λ are the required fitting parameters. Talukder et al. [40] have infused the *nonlinearity* of these parameters just by replacing the series of Eq. (3) with a single orbital-dependent parameter depending only on the reduced energy. For both the open and closed shell targets with atomic numbers $1 \leq Z \leq 92$, they have obtained reliable ionization cross sections easily for energies up to about 10 keV.

Vriens [41] modified the classical binary encounter (BEA) model of Gryzinski [22] by including both the exchange and the interference effects because of the exchange and direct terms. Roy and Rai [42, 43] extended this model to the ionization of atoms using the Hartree–Fock velocity distribution of the target electron and also expressed the Vriens model in a useful dimensionless form. Uddin et al. [44, 45] have applied this dimensionless Vriens model to the H and He isoelectronic series with some simple modifications, considering the increasing ionic effect [35] among the members of the series. Potoary et al. [46] have used the dimensionless form of the BEA model after incorporating relativistic correction factor with immense success for the K-shell ionization to atomic targets in the range $2 \leq Z \leq 92$ up to the incident energy of 1 GeV.

Recently, Campos et al. [47] have proposed an analytical model (henceforth referred to as CVTS) to describe the K- and L-shell ionization of neutral atoms over a wide range of atomic numbers $4 \leq Z \leq 79$ at reduced energies $U \leq 10$. The application of the CVTS model relies on two parameters,

which are monotonically decreasing functions of the atomic number Z. These parameters are determined by fitting the experimental absolute EIICS data of the K- and L-shell, with the calculated distorted-wave Born approximation (DWBA) EISICS. The simple structure of the CVTS [35] reduces computing time considerably for obtaining the EISICS results with an accuracy of DWBA. The success of this model provides impetus for a further extension of its applicability to larger domains of both Z and U by incorporating the appropriate ionic and relativistic correction factors. In the process, Haque et al. [48] infused in the CVTS model a Gryzinski-type relativistic factor [22] and an ionic factor [35] not only to provide its completeness but also to render its wide applicability with sufficient accuracy. The values of the parameters needed for this modified model are determined by the best fits to the available K-, L-, and M-shell experimental ionization cross-section data. The model is referred to as the XCVTS [48] model.

Kolbenstvedt [23], in his attempt to find a suitable method for calculating K-shell EISICS, proposed a model (KLV) by combining both the distant and close contributions to the collision cross sections. According to the model, the contribution of σ_{ph} from distant collisions is because of an exchange of virtual photons between the incident and target electrons leading to ionization by the photoelectric effect. The cross section σ_M from close encounters is contributed from the Møller interaction [49] incorporated in the impulse approximation. The model has been applied successfully to the description of K-shell ionization of silver and tin at incident energies much higher than the K-shell ionization potential. It, however, overestimates the cross sections from the threshold to peak region of the cross section and underestimates them at ultrahigh energies, although doing well in the moderately high energies. In the modified KLV (MKLV) [50] and the generalized MKLV (GKLV) [51] models, Uddin et al. [50] and Haque et al. [51] have demonstrated successfully how to fit the data over the entire energy domain from low to relativistic energies. It was shown that the contribution of the σ_{ph} part, which dominates the ionization cross section near threshold, is very large in comparison with the contribution of σ_{M} in the low-energy region and is responsible for generating abnormally high cross sections in that region. Therefore, Haque et al. [50, 51] modified the behavior of the σ_{ph} part at the low-energy region first by modifying the energy denominator (as shown in Eqs. (15 and 17)) of the first factor in its expression involving the effective charge as discussed earlier in Ref. [52] and then multiplying with an energy-dependent factor. To account for the proper relativistic contribution to the cross section, they also incorporated another multiplying factor to the total Kolbenstvedt cross section—a sum of σ_{ph} and σ_M. In treating the K-shell ionization problems, the MKLV model [50] has shown considerable success, but the GKLV model [51] with only two orbital-dependent fitting parameters produced very encouraging results for the K-, L-, and M-shell ionization of atoms even at relativistic energy domain.

Huo [53] has derived an improved version of the binary-encounter dipole (iBED) model. Its simplified form, siBED model, contains a two-parameter Born term instead of the Bethe part of the BED model [31]. Uddin et al. [54] have introduced both the ionic and relativistic corrections in this model to generate the modified siBED (MRIBED) model. The MRIBED model has been successfully applied to the *K*-shell ionization [54, 55] of atoms with atomic numbers $Z = 1$–50, and EI ionization (EII) of He- [56] and Be-isoelectronic sequences [57] for incident energies extended to relativistic domain. However, at ultrarelativistic energies, it underestimates substantially the EIICS data. In view of the parent siBED model [53] having a sound physical basis and its modified versions [54–57] showing remarkable successes in the aforementioned cases, Patoary et al. [58] have recently extended the MRIBED model to ultrahigh energies with the following steps:

1. The removal of the relativistic corrections, implemented kinematically on the parent siBED model [53] to yield the MRIBED model [54] but retaining the ionic correction incorporated in the latter. The model with only the ionic correction has been termed as the QIBED model in Ref. [55].
2. The implementation of the generalization procedure, which treats the ionization of both filled and unfilled configurations of the *K*-shell [54], to the QIBED model.
3. The incorporation of relativistic correction factors, similar to Gryzinski's relativistic factor [22], on the QIBED model. The resulting model, referred to as MUIBED in Ref. [58], has been successfully tested with various experimental EIICS data for *K*-, *L*-, and *M*-shell ionization of atoms.

2. OUTLINE OF THE MODELS

2.1. MBELL model

The total cross section of electron impact single ionization, according to Haque et al. [35–37], contributed from different ionized *nl*-orbits is given by

$$\sigma_{\mathrm{MBELL}}(E) = \sum_{nl} N_{nl} F_{\mathrm{ion}} G_{\mathrm{R}} \sigma_{\mathrm{BELL}}(E), \tag{4}$$

where N_{nl} is the number of electrons in the ionized *nl*-orbit and $\sigma_{\mathrm{BELI}}(E)$ having the form [33]:

$$\sigma_{\mathrm{BELI}} = \frac{1}{I_{nl}E}\left[A \ln\left(\frac{E}{I_{nl}}\right) + \sum_{k=1}^{7} B_k \left(1 - \frac{I_{nl}}{E}\right)^K\right]. \tag{5}$$

Here, E is the energy of the incident electron and I_{nl} is the ionization potential of the *nl*-orbit. A and B_k are the so-called fitting BELL parameters. G_{R} is

the Gryzinski's relativistic factor [22] defined in terms of the reduced energy $U = E/I_{nl}$ as

$$G_{\mathrm{R}} = \left(\frac{1+2J}{U+2J}\right)\left(\frac{U+J}{1+J}\right)^2 \times \left(\frac{(1+U)(U+2J)(1+J)^2}{J^2(1+2J)+U(U+2J)(1+J)^2}\right)^{1.5}, \quad (6)$$

where $J = m_{\mathrm{e}}c^2/I_{nl}$ with m_{e} as the electron rest mass and c as the speed of light in vacuum. F_{ion} is the ionic correction factor involving the ionic parameters m and λ having the form

$$F_{\mathrm{ion}} = 1 + m\left(\frac{q}{ZU}\right)^{\lambda}. \quad (7)$$

In Eq. (7), $q = Z - N_{\mathrm{U}}$, with N_{U} representing the total number of electrons from the interior 1*s*-orbit up to the relevant *nl*-orbit, is the effective charge of the target as seen by the incident electron. The form of the ionic factor is such as to take care of its effects in two counts:

1. The enhancement of cross sections because of the greater overlap of the charge clouds of the incident and target electrons.
2. The decrease of the enhancement with the increase of the incident energy as the incident electron can spend less time in the vicinity of the atomic field.

For an ionized orbital *nl*, the Bell parameters A and B_k with $k = 1$–7, shown in Eq. (5) above, are obtained by fitting the EIICS data of atomic targets having their outermost orbit with the configuration *nl*. Following the prescription of Ref. [37], the ionic parameters m and λ are then extracted from the experimental data of the ionic targets. Having obtained the values of m and λ for a particular l, these parameters are then used for all orbits with the same l and different n. This means that the ionic parameters for the 1*s*, 2*s*, and 3*s* orbits are the same and likewise, those for the 2*p* and 3*p* are identical. The detailed procedure is outlined in Ref. [37]. The parameters are optimized by minimizing the chi-square, defined as

$$\chi^2 = \frac{1}{N_{\mathrm{p}}}\sum_{i=1}^{N_{\mathrm{p}}}\left[\frac{\sigma_{\mathrm{cal}}(U_i) - \sigma_{\mathrm{exp}}(U_i)}{\sigma_{\mathrm{exp}}(U_i)}\right]^2. \quad (8)$$

Here N_{p} is the number of data points. $\sigma_{\mathrm{cal}}(U_i)$ and $\sigma_{\mathrm{exp}}(U_i)$ refer, respectively, to the calculated and experimental cross sections at the reduced energy point U_i for a particular ionizing orbit. The optimization procedure (in both local and global modes) has been repeated over a number of targets for the same ionizing orbit until the parameter values converge over fitting the experimental data sets. To derive the parameters, the data are chosen with the following criteria: (1) the systematic error associated with the

experimental data collection is less than 20% and (2) in the case of multiple data sets for a given target, the data sets do not differ by more than 12% within error-bars. The optimized values of the parameters of the MBELL model are listed in Table 6.1.

2.2. Outline of the XCVTS model

In finding an analytical expression to simulate the distorted-wave Born approximation (DWBA)-generated EISICS data of the *K*- and *L*-shell ionization of atoms, Campos et al. [47] in their CVTS model have adopted the Bethe's asymptotic condition in a parameterized form to fit low-energy data. Their resultant expression is given by

$$\sigma_{\mathrm{CVTS}}(U) = \frac{A_\xi(Z)}{B_\xi(Z) + U} \ln(U). \tag{9}$$

Here $A_\xi(Z)$ and $B_\xi(Z)$ represent the two Z-dependent parameters of the model and ξ ($\cong nl$) denotes a particular subshell in which ionization takes place. The two parameters, $A_\xi(Z)$ and $B_\xi(Z)$, are obtained by fitting the calculated DWBA results. Equation (9) has been found to describe well the EIICS data for the reduced incident energies $U \leq 10$ but does not provide satisfactory results at high- and ultrarelativistic energies.

In extending the CVTS model to relativistic energies, Haque et al. [48] incorporated in their XCVTS model a Gryzniski-type [22] relativistic factor $R(U)$ given by

$$R(U) = \left(\frac{1+2J}{U+2J}\right)\left(\frac{U+J}{1+J}\right)^{\delta_1} \times \left(\frac{(1+U)(U+2J)(1+J)^2}{J^2(1+2J)+U(U+2J)(1+J)^2}\right)^{1.5} \times \left(1.0 - \frac{\delta_2 U^{\delta_3}}{J^2}\right), \tag{10}$$

and an ionic factor of the type [35–37]:

$$F_{\mathrm{ion}} = 1 + \varsigma\left(\frac{q}{U}\right)^{\eta}. \tag{11}$$

In Eq. (10), $J = m_e c^2/I$, as before, with I denoting the ionization potential concerned. The parameters δ_1, δ_2, and δ_3 are determined from the *K*-shell ionization data [48]. The last factor on the right side is introduced, following Casnati et al. [59] and Hombourger [60], to mitigate the divergence of EISICS at the ultrarelativistic energy region. In Eq. (11), $q = Z - N_{\mathrm{U}}$, is the effective charge with N_{U} representing the total number of electrons from the innermost 1*s*-orbit to the relevant ionizing subshell ξ of the target. The parameters ζ and η for the relevant ionized shell are obtained by fitting the experimental data.

Table 6.1 The BELL parameters A and B's, and the ionic parameters m and λ for the $1s$, $2s$, $2p$, $3s$, $3p$, and $3d$ orbits. The parameters are in the unit of 10^{-13} eV$^2 \cdot$ cm^2

		Parameter values									
Shell	Orbit	A	B_1	B_2	B_3	B_4	B_5	B_6	B_7	m	λ
K	$1s$	+0.525	−0.510	+0.2000	+0.050	−0.025	−0.100	0.0	0.0	+3.0	+1.270
L	$2s$	+0.530	−0.410	+0.1500	+0.150	−0.200	−0.150	0.0	0.0	+3.0	+1.270
	$2p$	+0.600	−0.400	−0.7100	+0.655	+0.425	−0.750	0.0	0.0	+3.0	+0.542
M	$3s$	+0.130	+0.250	−1.5000	+2.400	+3.220	−3.667	0.0	0.0	+3.0	+1.270
	$3p$	+0.388	−0.200	−0.2356	+0.5355	+3.150	−8.500	+5.05	+0.37	+3.0	+0.542
	$3d$	+0.350	+1.600	−3.0000	+4.000	+2.000	−5.000	−1.50	+3.50	+3.0	+0.950

For the XCVTS model, the parameter $A_\xi(Z)$ in Eq. (9) has been redefined as

$$A_\xi(Z) = C_\xi Z^{\lambda_\xi} \tag{12}$$

in terms of shell-dependent but species-independent new parameters, C_ξ and λ_ξ. The form of $A_\xi(Z)$ with its two parameters in Eq. (12) leads to the redundancy of the parameter $B_\xi(Z)$ in Eq. (9). Consideration of Eqs. (10–12) leads to the expression for EISICS in the XCVTS model of Ref. [48] as

$$\sigma_{\mathrm{XCVTS}}(U) = \sum R(U)F_{\mathrm{ion}}(U)A_\zeta(Z)N_\zeta \frac{1}{U}\ln(U). \tag{13}$$

Here, N_ξ is the number of electrons in each subshell ξ contributing to total ionization. For the *L*- and *M*-shell ionization, the total EISICS is obtained by summing the contributions from the subshells composing the shell.

The relativistic parameters δ_1, δ_2, and δ_3 in Eq. (10), the ionic parameters ζ and η in Eq. (11), and the parameters C_ξ and λ_ξ in Eq. (12) have been optimized by minimizing the chi-square, shown in Eq. (8), for fitting the experimental data with the criteria specified earlier. The optimization procedure is similar to that followed for the MBELL model excepting that the repetition over the number of targets is to be done for the same ionizing shell in place of orbit for seeking the convergence of the parameter values. The optimum values thus obtained for all parameters of the XCVTS model are tabulated in Table 6.2.

2.3. GKLV model

The total cross section in the generalized Kolbenstvedt (GKLV) model [50, 51], for *K*-, *L*-, and *M*-shell ionization after summing the contributions over all ionized orbits, can be written as

$$\sigma_{\mathrm{GKLV}} = \sum N_{nl}R_{\mathrm{F}}(F_{\mathrm{M}}\sigma_{\mathrm{ph}} + \sigma_M), \tag{14}$$

where N_{nl} is again the number of electrons in the ionized nl-orbit. σ_{ph} and σ_{M} representing, respectively, the cross section contributions from the distant

Table 6.2 The parameter $A_\xi(Z) = C_\xi Z^{\lambda_\zeta}$ in Eq. (12) as the function of the atomic number Z, the ionic parameters ζ and η, and the relativistic parameters δ_1, δ_2, and δ_3 for *K*-, *L*-, and *M*-shell ionization

Shell	C_ξ	λ_ξ	A_ξ	ζ	η	δ_1	δ_2	δ_3
K	11.5	−4.35	$11.5 \times Z^{-4.35}$	0.01	1.0	2.02	0.22	0.27
L	5500	−4.95	$5500 \times Z^{-4.95}$	0.01	1.0	2.02	0.22	0.27
M	5700	−4.25	$5700 \times Z^{-4.25}$	0.01	1.0	2.02	0.22	0.27

and close collisions, are expressed as

$$\sigma_{\rm ph} = \frac{0.141(E+1)^2}{I_{nl}E'_{nl}(E'_{nl}+2)} \times \left[\ln\frac{1.243E(E+2)}{I_{nl}} - \frac{E(E+2)}{(E+1)^2}\right] \text{ barns}, \qquad (15)$$

and

$$\sigma_M = \frac{\eta_{nl}(E+1)^2}{I_{nl}E(E+2)} \times \left[1 - \frac{I_{nl}}{E}\left(1 - \frac{E^2}{2(E+1)^2} + \frac{2E+1}{(E+1)^2}\ln\frac{E}{I_{nl}}\right)\right] \text{ barns}, \quad (16)$$

with E', the effective kinetic energy (with details given in Ref. [61]) as seen by the bound electron, is

$$E' = E + \frac{\varepsilon_{nl}(\chi_{nl} + I_{nl})}{(q+1)^{1/2}}. \qquad (17)$$

Here, q is the effective charge of the target as seen by the incident electron, ε_{nl} is the ionic parameter for the relevant orbit, and χ_{nl} is the kinetic energy of an electron in the relevant ionized orbit. While ε_{nl} influences both the peak position and magnitude, η_{nl} controls only the magnitude. The KLV model of Kolbenstvedt [23] fixes $\eta_{1s} = 0.499$ for the K-shell ionization, such that N_{1s} $\eta_{nl} = 0.998$ with $N_{1s} = 2$. The appropriate forms of the relativistic factor $R_{\rm F}$ and the scaling factor $F_{\rm M}$, which are detailed in Ref. [50], are, respectively, given by

$$R_{\rm F} = \left(1 + mU_{nl}^{\lambda}\right), \qquad (18)$$

where $U_{nl} = T/I_{nl}$ is the reduced energy for the nl-orbit, and m and λ are the relativistic parameters, and

$$\begin{aligned} F_{\rm M} &= 2.5\left(1 - \frac{1}{U_{nl}}\right) \quad \text{for} \quad U_{nl} \le 1.70, \\ &= 1.0 \quad \text{for} \quad U_{nl} > 1.70. \end{aligned} \qquad (19)$$

With $\eta_{1s} = 0.499$ fixed, the parameters ε_{nl}, m, and λ have been optimized through the χ^2 minimization on the experimental K-shell EIICS data for ionic targets, as done in Ref. [61], leading to $\varepsilon_{1s} = 2.0$, $m = 0.054$, and $\lambda = 0.067$. Keeping these optimized values fixed for both m and λ, the ε_{nl} and η_{nl} are obtained by minimizing the chi-square in Eq. (8) over for experimental EIICS data sets of Be^+, C^{2+}, $N^{3+,4+}$, O^{4+}, Ne^{7+}, and U^{89+} ionic targets for the 2s-orbit; of C^+, N^{2+}, $O^{+,3+}$, F^{2+}, $Ne^{2+,3+,4+,5+}$, and U^{82+} for the 2p-orbit; of Si^{3+}, S^{4+}, and Cl^{5+} for the 3s-orbit; of $Ar^{3+,5+}$, Cr^{8+}, and Fe^{9+} for the 3p-orbit; and of Ti^{2+}, $Ni^{4+,5+}$, and Kr^{9+} for the 3d-orbit with details in Ref. [61]. The best-fitting parameters ε_{nl} and η_{nl} for various orbits are given in Table 6.3.

Table 6.3 Values of the parameters ε_{nl} and η_{nl} for the inner shell ionization in the 1*s*, 2*s*, 3*s*, 3*p*, and 3*d* orbits

	Orbits					
Parameter	1*s*	2*s*	2*p*	3*s*	3*p*	3*d*
ε_{nl}	2.0	1.0	1.0	2.0	0.3	0.1
η_{nl}	0.499	0.40	0.57	0.65	0.70	1.15

2.4. Outline of the MUIBED Model

For an ionized shell, according to Patoary et al. [58], the cross section for the *K*-shell ionization in the MUIBED model is

$$\sigma_{\text{MUIBED}} = \sum F(Z)\left(R_{\text{M}} S' H + R_{\text{B}} F G\right). \tag{20}$$

Here, the summation is taken over all the contributing orbits in a shell. $F(Z)$, the generalized scaling factor for the *K*-, *L*-, and *M*-shell ionization, following [54], is given by

$$F(Z) = 1 + mZ^{\lambda}, \tag{21}$$

For filled 1*s*-orbit $m = 0.0$ and $\lambda = 0.0$ and they have nonzero values for other cases including a filled configuration of *L*- and *M*-shell ionization.

The term S' in Eq. (20) is given as

$$S' = \frac{4\pi N_{nl}}{k_0^2 + (k_{\text{b}}^2 + \alpha_0^2)/(q+1)}. \tag{22}$$

N_{nl} is the number of electrons in the ionizing nl-orbit, and q denotes the effective charge as seen by the incident electron.

The terms H, F, and G is given in Ref. [58] as

$$H = \left[\frac{k_0^2 - \alpha_0^2}{k_0^2 \alpha_0^2} - \frac{\ln\left(k_0^2/\alpha_0^2\right)}{k_0^2 + \alpha_0^2}\right], \tag{23}$$

$$F = \frac{64\,\alpha_0^3 N_{nl}}{k_0^2}, \tag{24}$$

and

$$G = \int_0^{\left(k_0^2 - \alpha_0^2\right)/2} k_{\text{p}}\left(k_{\text{p}}^2 + \alpha_0^2\right) \mathrm{d}E_{\text{p}} \times \int_{K_{\min}}^{K_{\max}} \frac{1 + d_1 t + d_2 t^2}{K\left[\left(K + k_{\text{p}}\right)^2 + \alpha_0^2\right]^3 \left[\left(K - k_{\text{p}}\right)^2 + \alpha_0^2\right]^3} \mathrm{d}K. \tag{25}$$

Using atomic units in the above Eqs. (22–25), $k_0^2/2$ is the energy of the incident electron; $k_b^2/2$ is the kinetic energy of the bound electron; $I = \alpha_0^2/2$ is the ionization potential of the relevant shell electron; and $k_p^2/2$ is the energy of the ejected electron with k_p having the dimension of momentum [53]. $\vec{K} = \vec{k}_0 - \vec{k}_1$, denotes the momentum transfer vector with k_1 being the momentum of the incident electron after a collision. The values of K_{max} and K_{min} are given in Ref. [62]. The parameters d_1 and d_2 in Eq. (25) determine, respectively, the EISICS peak and EISICS values at higher energies [55]. The EISICS data on most atomic targets favor $d_1 = 0.0$ [55–57] and, with the inclusion of relativistic factors, d_2 is also set to $d_2 = 0.0$.

With R_B and R_M in Eq. (20), the relativistic factors for the K-shell ionization [58] in line with Gryzinski's relativistic factor [22] are as follows:

$$R_B = \left[\frac{(1+U)(U+2J)(1+J)^2}{J^2(1+2J)+U(U+2J)(1+J)^2}\right]^{1.5}, \tag{26}$$

and

$$R_M = \left(\frac{1+2J}{0.5U+2J}\right)\left(\frac{U+J}{1+J}\right)^{2.11}. \tag{27}$$

We adopt the generalized expression (20) for EISICS to the L- and M-shell ionization, it has been found necessary to modify the factor R_M, associated with the relativistic effect in the Mott part of Eq. (20). The fitting of the experimental EISICS data for L- and M-shell leads to the optimized forms for R_M as follows:

1. For L-shell ionization,

$$R_M = \left(\frac{1+2J}{0.34U+J}\right)\left(\frac{U+J}{1+J}\right)^{2.11}. \tag{28}$$

2. For M-shell ionization,

$$R_M = \left(\frac{1+2J}{0.3U+J}\right)\left(\frac{U+J}{1+J}\right)^{2.11}. \tag{29}$$

With $d_1 = d_2 = 0.0$ and the relativistic factor R_B in Eq. (26) for all cases, and the form of the factor R_M in Eq. (27), Eq. (28), or Eq. (29), chosen respectively, for the K-, L-, or M-shell ionization, Eq. (20) generates the total EISICS in the MUIBED model. The fitting parameters of the MUIBED model are m and λ in Eq. (21). In conjunction with the relativistic factor R_M in Eq. (27) for the

Table 6.4 Values of the parameters m and λ and for K-, L-, and M-shell ionization

	Parameters	
Shell	M	λ
Filled K	0.000	0.000
Unfilled K	+0.365	+0.050
L	−0.605	+0.060
M	−0.890	+0.015

K-shell ionization, these are determined from optimizing the overall fits of the experimental EIICS data for H-isoelectronic sequence with an unfilled configuration, as done in Ref. [54] and He-like targets with a filled configuration. The optimized values of m and λ for the K-shell are listed in Table 6.4. The optimized m and λ for the L-shell with R_M in Eq. (28) and the M-shell with R_M in Eq. (29) have been obtained using the respective inner-shell EIICS data of Au, Pb, and Bi and are listed in Table 6.4.

3. EXPERIMENTAL DATA SOURCES

Excellent reviews on various techniques of measuring the inner-shell ionization cross sections have been provided by C. J. Powell [63–65]. Three techniques are usually used for measuring K-, L-, and M-inner-shell ionization cross sections. These are (1) X-ray fluorescence, (2) Auger electron spectroscopy, and (3) transmission electron energy loss spectroscopy. In the X-ray spectroscopy technique, cross sections are obtained from the measurement of fluorescence yield from X-rays emission resulting from the filling up of vacancies created by the electron impact ionization in the inner shells. Auger electron spectroscopy, however, involves measurements of yields of characteristic Auger electrons for determination of EIICS. Inner-shell ionization cross sections are also derived from the transmission electron energy loss experiments. The experimental data used for comparison with our calculated cross sections are derived from one or another of these three techniques.

4. DISCUSSION AND CONCLUSIONS

The calculated EISICS from the MBELL, XCVTS, GKLV, and MUIBED models are compared with available experimental data: the K-shell ionization

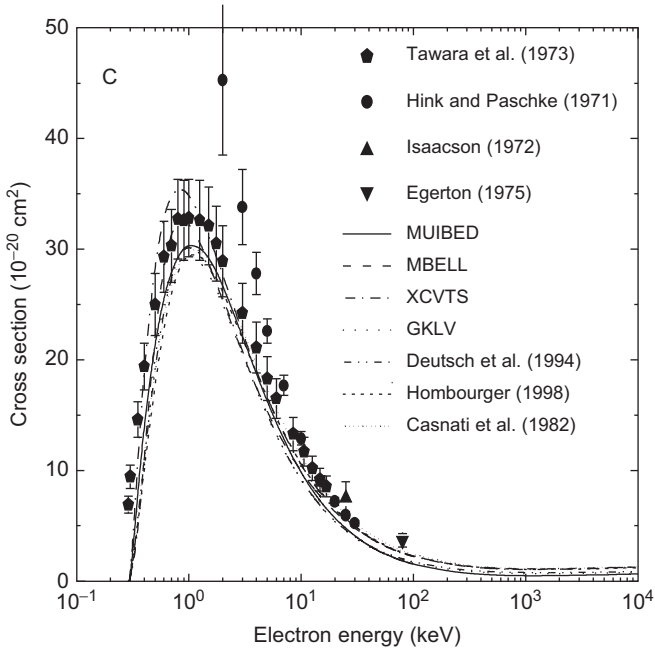

Figure 6.1 Electron impact ionization cross sections (in square centimeter) for the *K*-shell in C are plotted as a function of the incident electron energy (in kiloelectron volt). The sources of experimental EIICS data in solid symbols are given in Refs. [66–69]. Solid line (—), dashed line (- - - -), dash-dotted line (-·-·-), and dotted line (· · · · ·) represent the calculated results using the MUIBED, MBELL, XCVTS, and GKLV models, respectively. Predicted cross sections from the models of Deutsch et al. [28], Casnati et al. [59], and Hombourger [60] are also displayed.

cross sections for C to U in Figures 6.1–6.51, the *L*-shell ionization cross sections for Ar to U in Figures 6.52–6.80, and the *M*-shell ionization cross sections for Au to U atoms in Figures 6.81–6.84. The quantal results for the *K*-shell ionization are shown in Figure 6.10 for Ar, Figure 6.16 for Cr, Figure 6.17 for Mn, Figure 6.20 for Ni, Figure 6.21 for Cu, Figure 6.29 for Y, Figure 6.34 for Ag, Figure 6.36 for Sn, Figure 6.40 for Ba, Figure 6.42 for Ho, Figure 6.47 for Au, Figure 6.48 for Hg, Figure 6.49 for Pb, Figure 6.50 for Bi, and Figure 6.51 for U. For the *L*-shell ionization, the quantal cross sections are plotted in Figure 6.52 for Ar, Figure 6.53 for Ni, Figure 6.57 for Y, Figure 6.60 for Ag, Figure 6.63 for Ba, Figure 6.71 for Ho, Figure 6.74 for Ta, Figure 6.77 for Au, Figure 6.78 for Pb, Figure 6.79 for Bi, and Figure 6.80 for U. For the *M*-shell ionization, the only available PWBA results [1] are shown in Figures 6.82, 6.83, and 6.84 for Pb, Bi, and U target atoms, respectively. The relative performances of the four models depend on the species and the

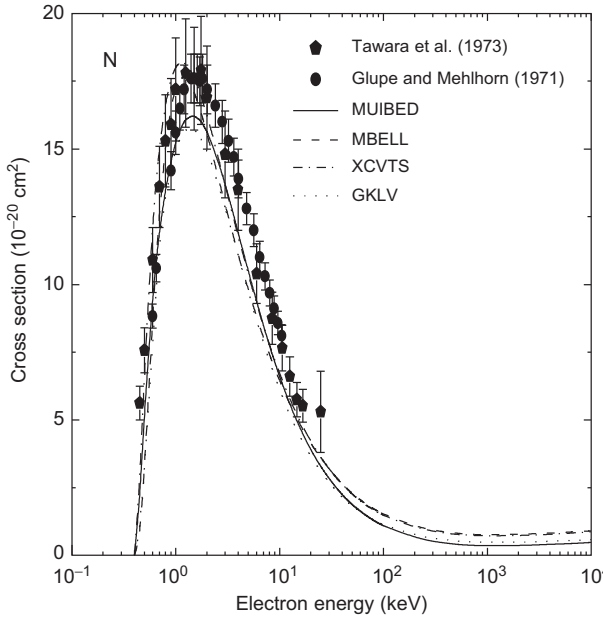

Figure 6.2 Same as in Figure 6.1 for the *K*-shell in N without the predictions from the models in Refs. [28, 59, 60]. The EIICS data are from Refs. [66, 70].

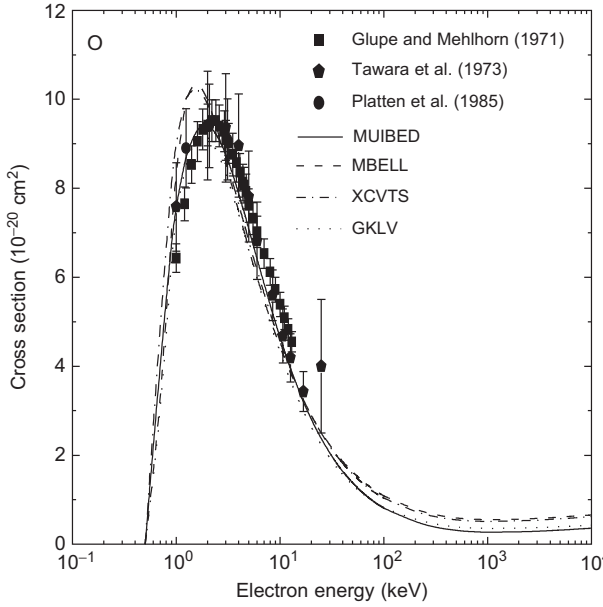

Figure 6.3 Same as in Figure 6.2 for the *K*-shell in O. The EIICS data are from Refs. [66, 70, 71].

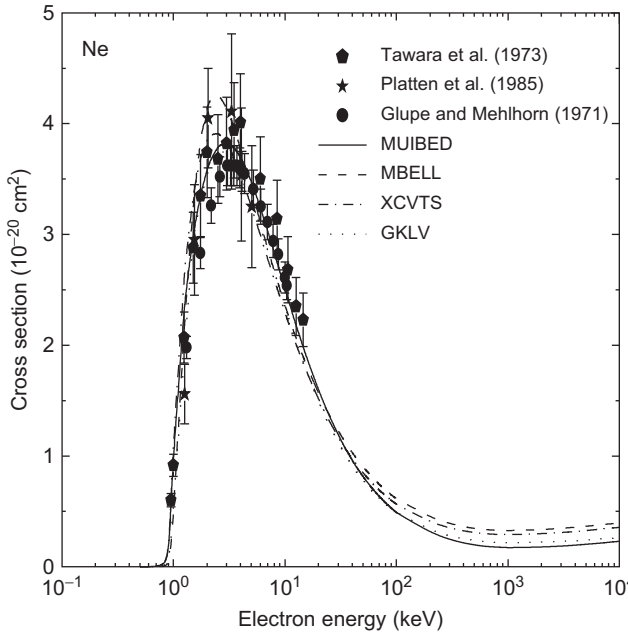

Figure 6.4 Same as in Figure 6.2 for the *K*-shell in Ne. The EIICS data are from Refs. [68, 72, 73].

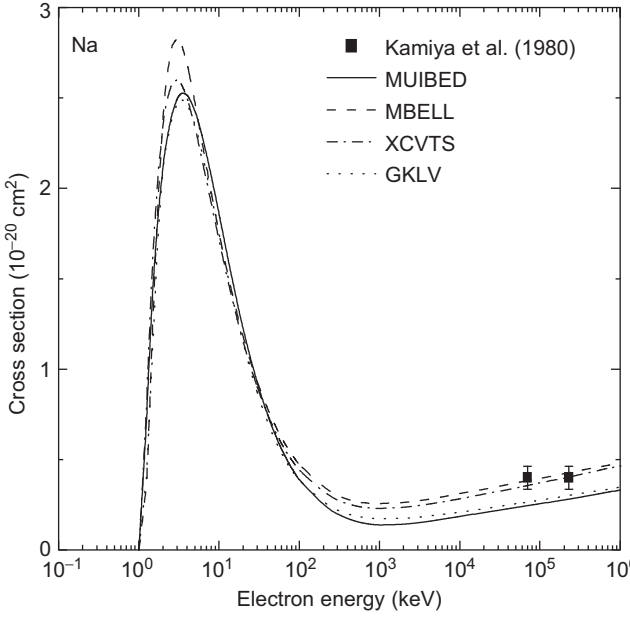

Figure 6.5 Same as in Figure 6.2 for the *K*-shell in Na. The EIICS data are from Refs. [72].

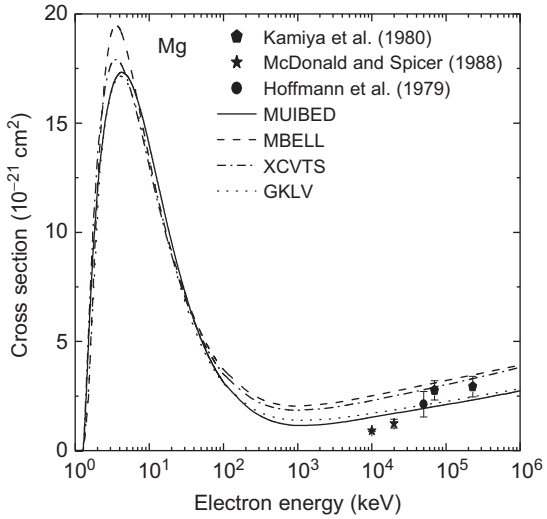

Figure 6.6 Same as in Figure 6.2 for the *K*-shell in Mg. The EIICS data are from Refs. [72–74].

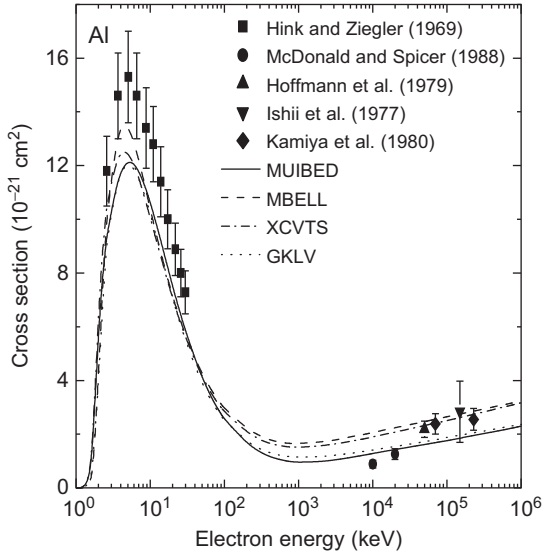

Figure 6.7 Same as in Figure 6.2 for the *K*-shell in Al. The EIICS data are from Refs. [72–76].

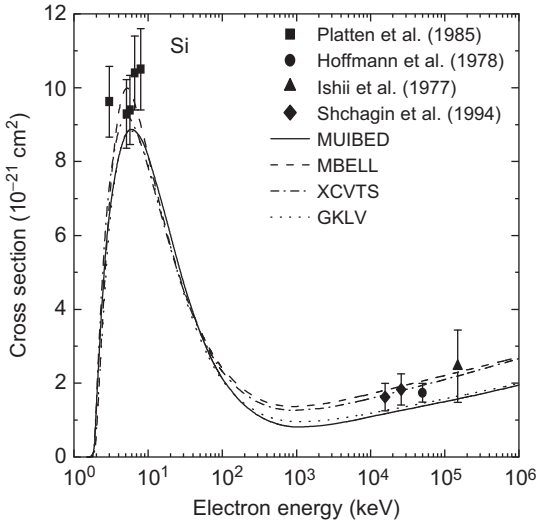

Figure 6.8 Same as in Figure 6.2 for the *K*-shell in Si. The EIICS data are from Refs. [71, 74, 76, 77].

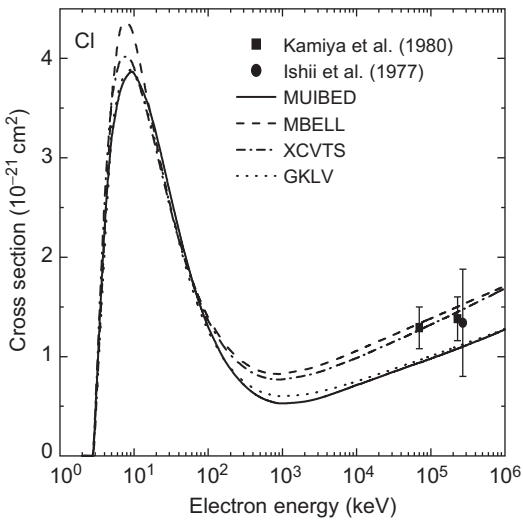

Figure 6.9 Same as in Figure 6.2 for the *K*-shell in Cl. The EIICS data are from Refs. [72, 76].

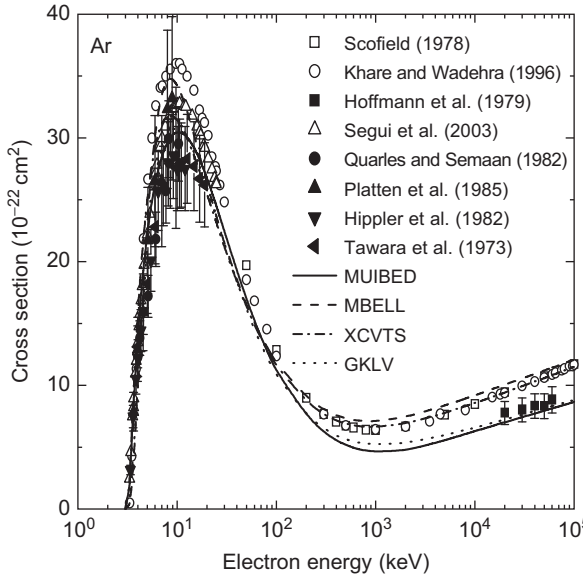

Figure 6.10 Same as in Figure 6.2 for the *K*-shell in Ar. The EIICS data are from Refs. [66, 71, 74, 78, 79]. The open circles, squares, and triangles are the quantum results from Refs. [1, 2, 8].

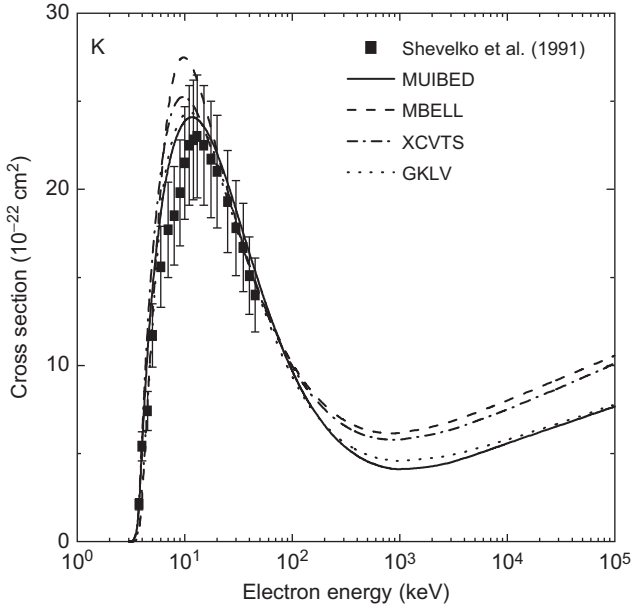

Figure 6.11 Same as in Figure 6.2 for the *K*-shell in K. The EIICS data are from Ref. [80].

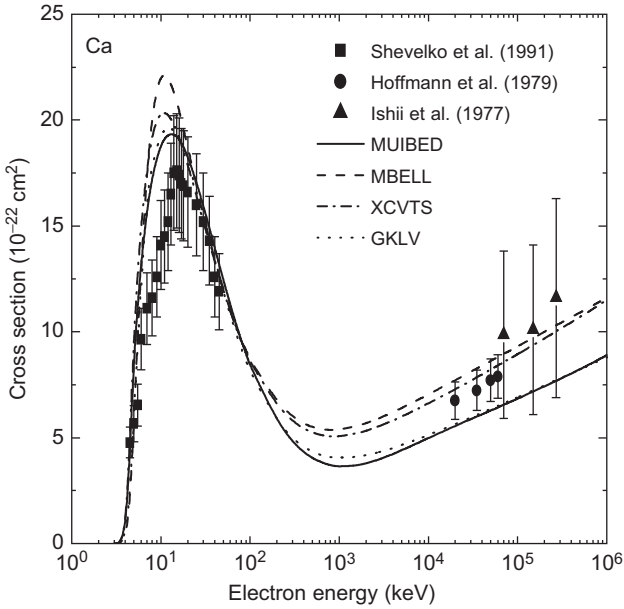

Figure 6.12 Same as in Figure 6.2 for the *K*-shell in Ca. The EIICS data are from Refs. [74, 76, 80].

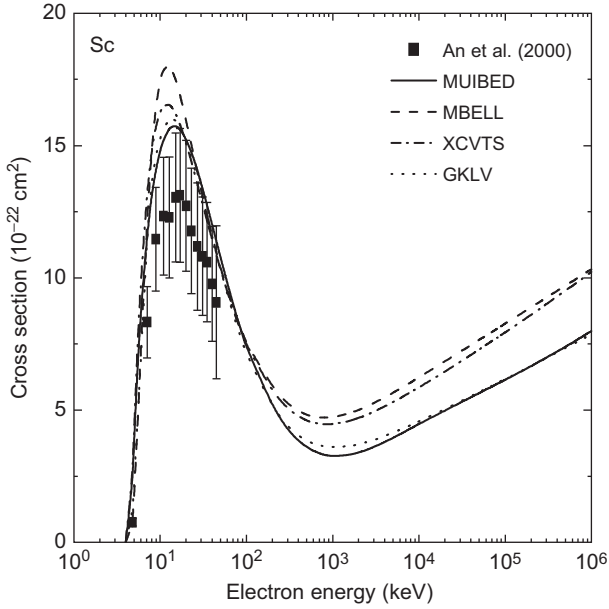

Figure 6.13 Same as in Figure 6.2 for the *K*-shell in Sc. The EIICS data are from Ref. [81].

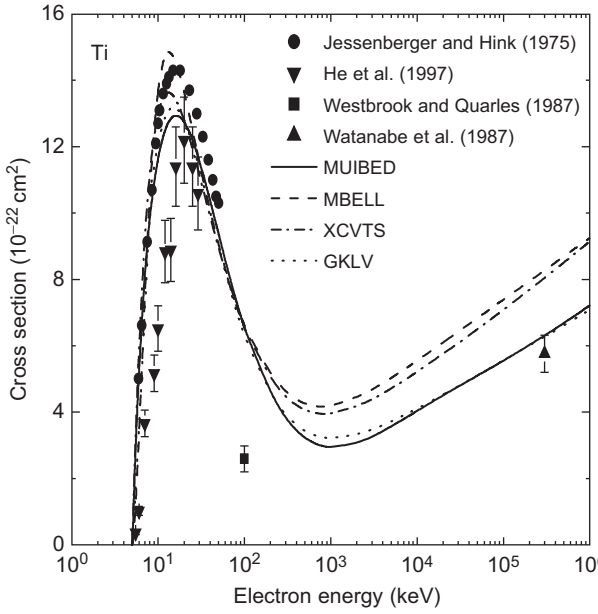

Figure 6.14 Same as in Figure 6.2 for the *K*-shell in Ti. The EIICS data are from Refs. [82–85].

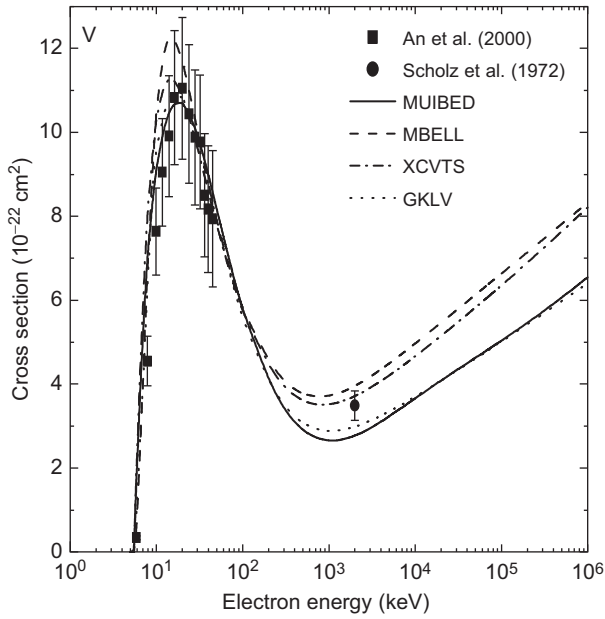

Figure 6.15 Same as in Figure 6.2 for the *K*-shell in V. The EIICS data are from Refs. [81, 86].

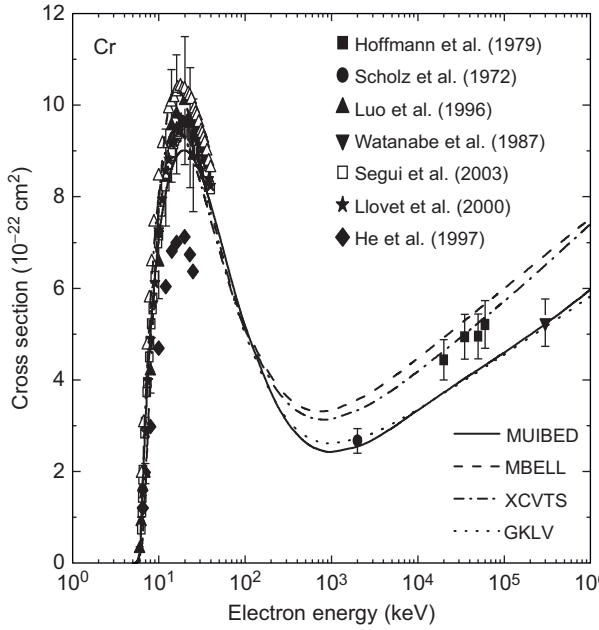

Figure 6.16 Same as in Figure 6.2 for the *K*-shell in Cr. The EIICS data are from Refs. [74, 83, 85–88]. The open squares are the quantum results from Ref. [8].

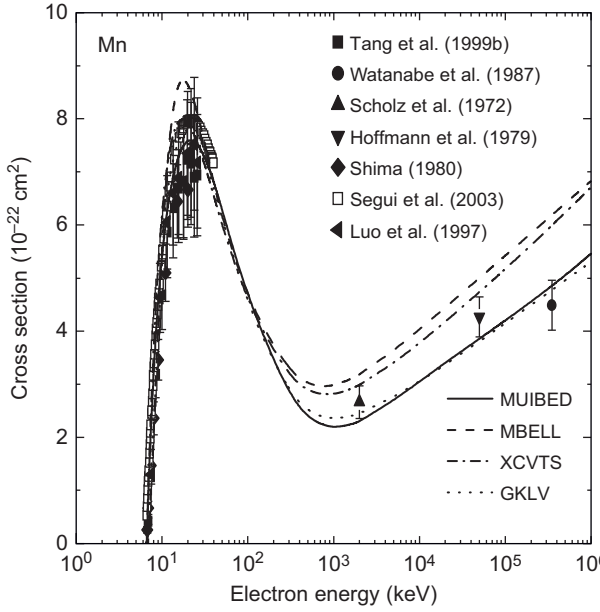

Figure 6.17 Same as in Figure 6.2 for the *K*-shell in Mn. The EIICS data are from Refs. [74, 85, 86, 89–91]. The open squares are the quantum results from Ref. [8].

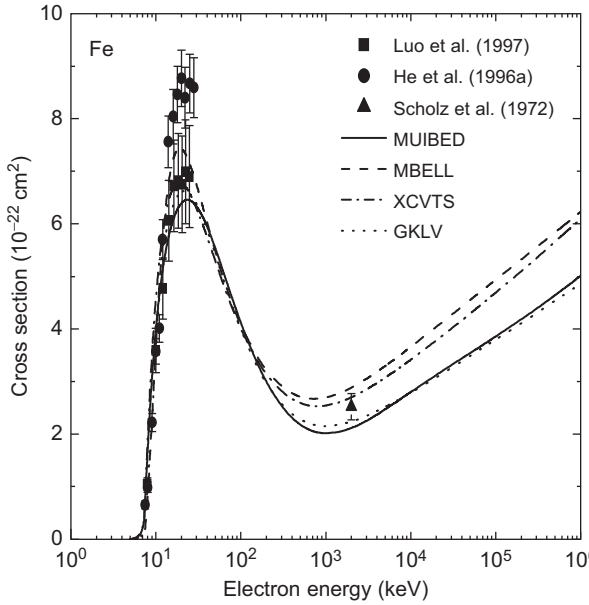

Figure 6.18 Same as in Figure 6.2 for the *K*-shell in Fe. The EIICS data are from Refs. [86, 91, 92].

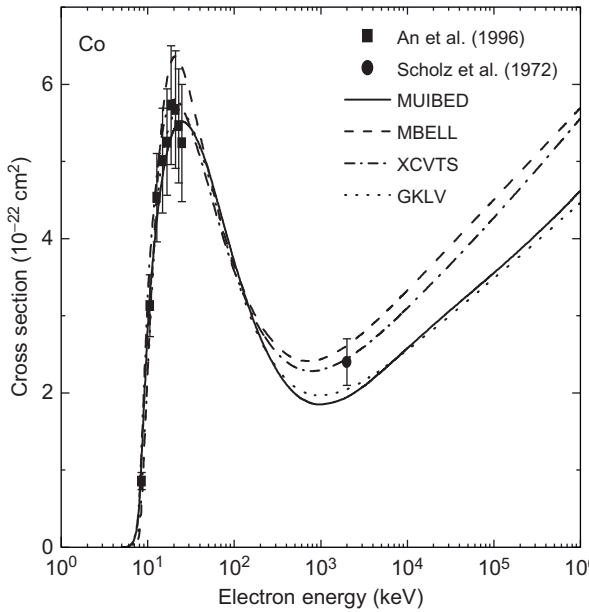

Figure 6.19 Same as in Figure 6.2 for the *K*-shell in Co. The EIICS data are from Refs. [86, 93].

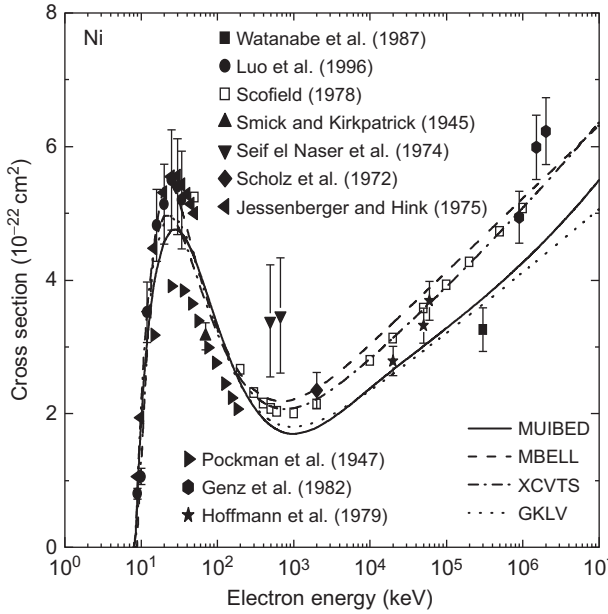

Figure 6.20 Same as in Figure 6.2 for the *K*-shell in Ni. The EIICS data are from Refs. [74, 82, 85–87, 94–97]. The squares are the quantum results from Ref. [2].

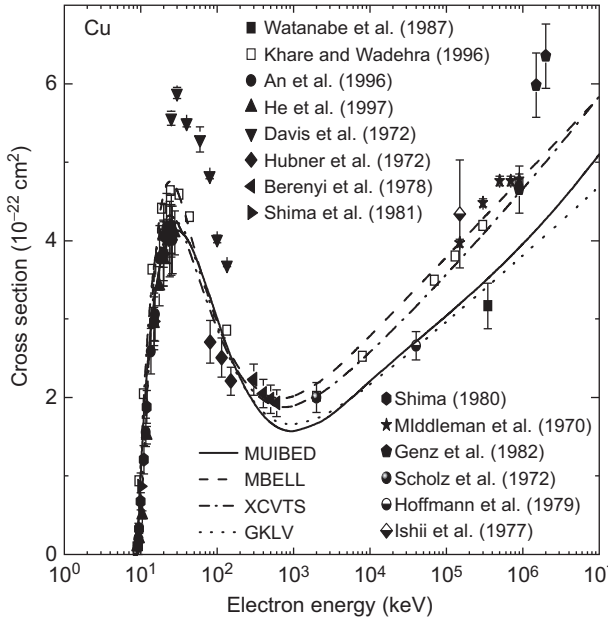

Figure 6.21 Same as in Figure 6.2 for the *K*-shell in Cu. The EIICS data are from Refs. [74, 76, 83, 85, 86, 90, 93, 97–102]. The squares are the quantum results from Ref. [1].

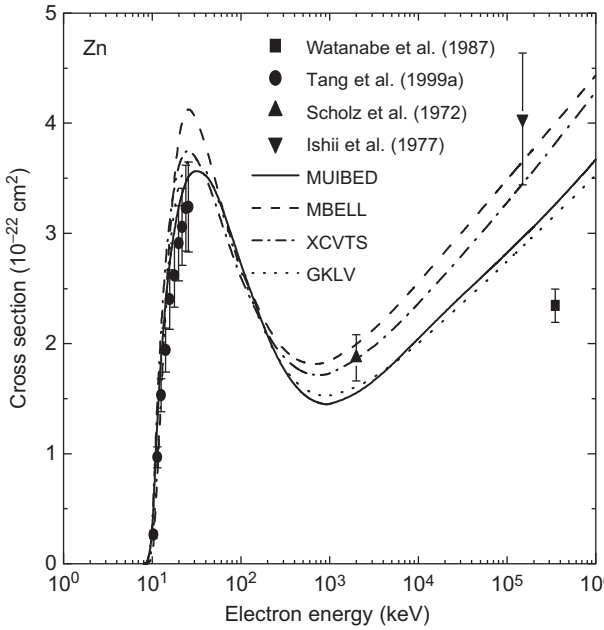

Figure 6.22 Same as in Figure 6.2 for the *K*-shell in Zn. The EIICS data are from Refs. [76, 85, 86, 103].

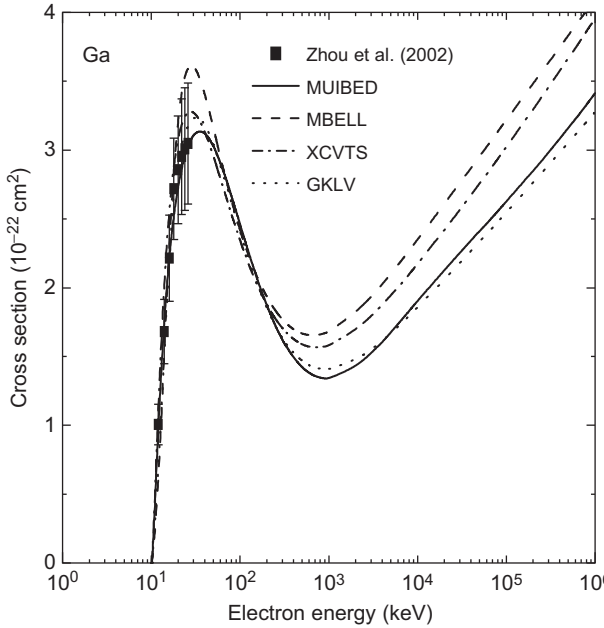

Figure 6.23 Same as in Figure 6.2 for the *K*-shell in Ga. The EIICS data are from Ref. [104].

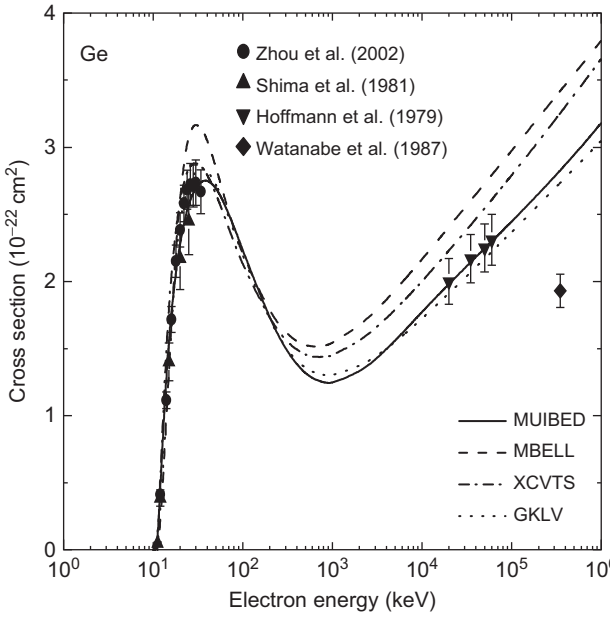

Figure 6.24 Same as in Figure 6.2 for the *K*-shell in Ge. The EIICS data are from Refs. [74, 85, 101, 104].

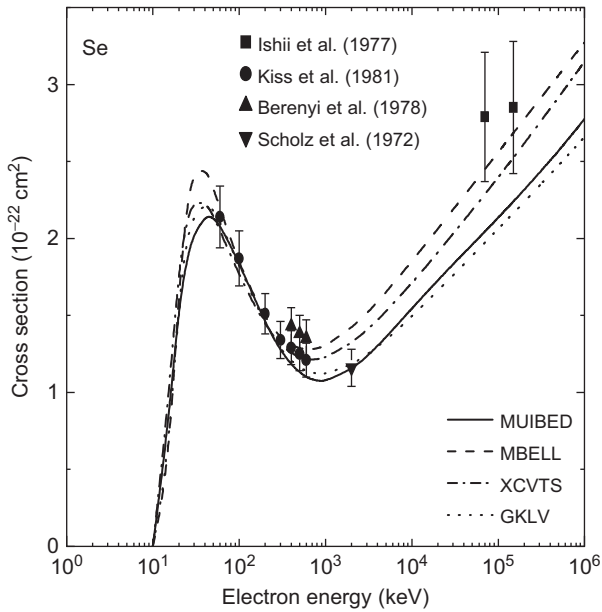

Figure 6.25 Same as in Figure 6.2 for the *K*-shell in Se. The EIICS data are from Refs. [76, 86, 100, 105].

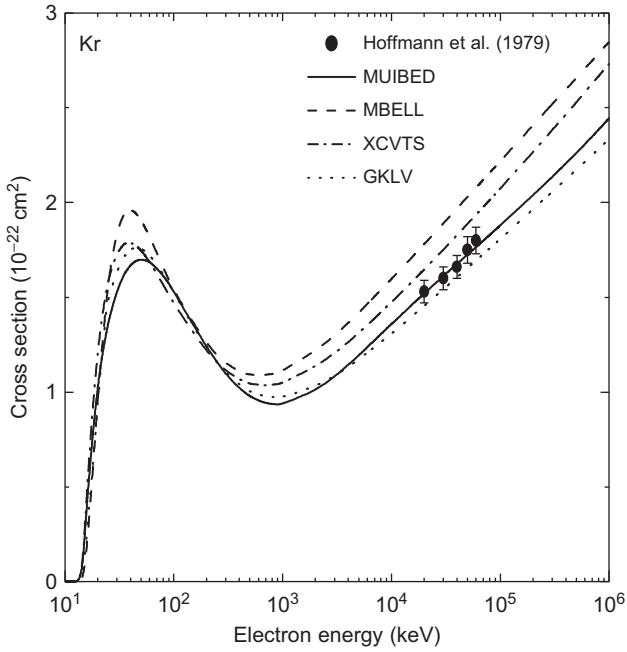

Figure 6.26 Same as in Figure 6.2 for the *K*-shell in Kr. The EIICS data are from Ref. [74].

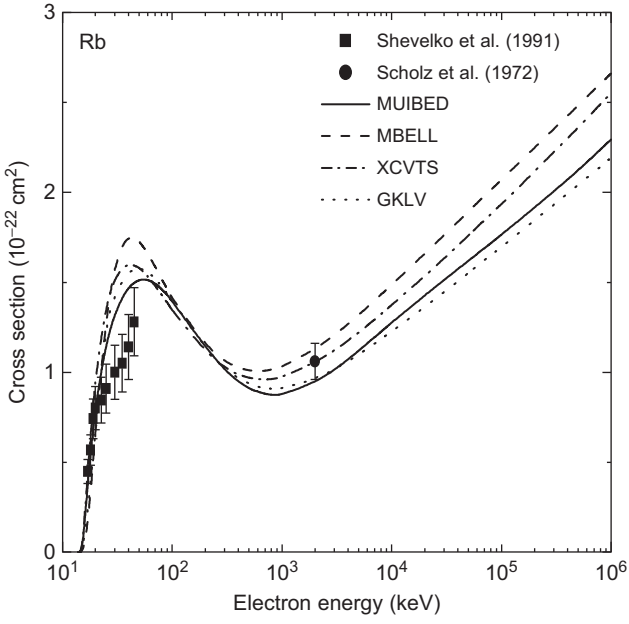

Figure 6.27 Same as in Figure 6.2 for the *K*-shell in Rb. The EIICS data are from Refs. [80, 86].

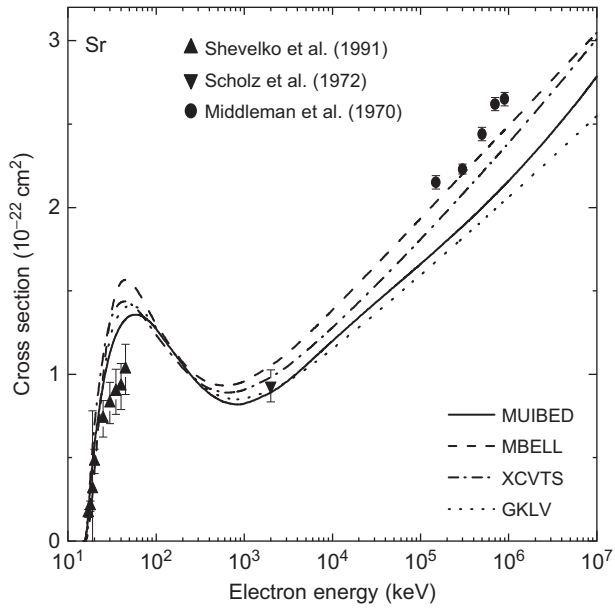

Figure 6.28 Same as in Figure 6.2 for the *K*-shell in Sr. The EIICS data are from Refs. [80, 86, 102].

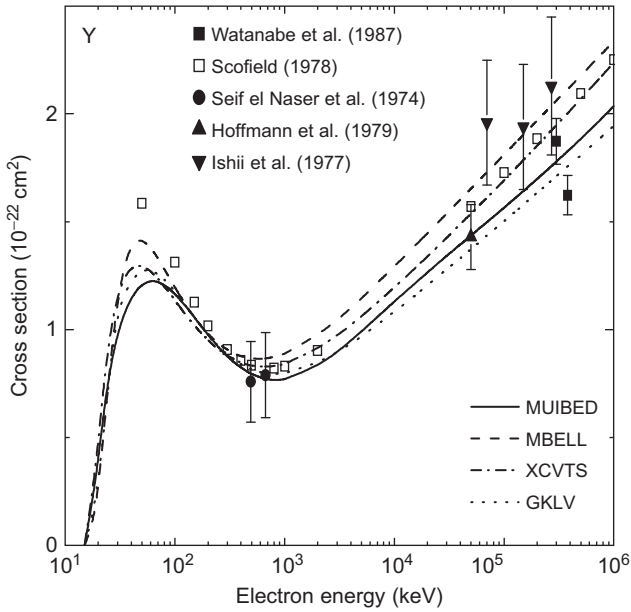

Figure 6.29 Same as in Figure 6.2 for the *K*-shell in Y. The EIICS data are from Refs. [74, 76, 85, 95]. The open squares are the quantum results from Ref. [2].

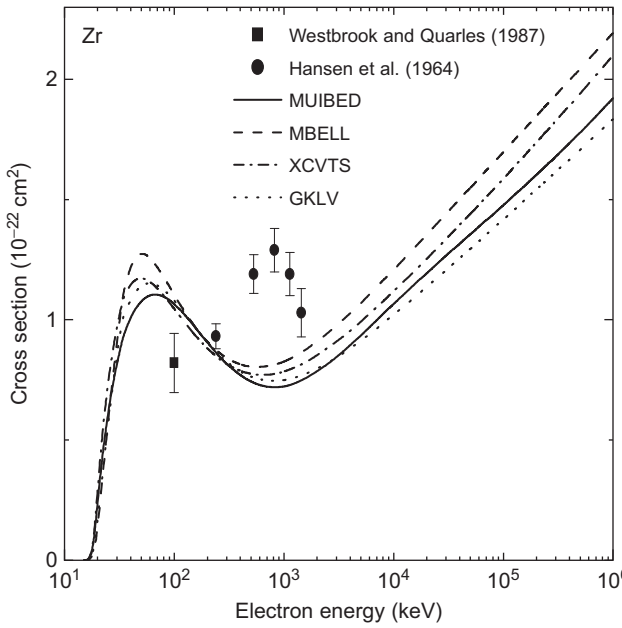

Figure 6.30 Same as in Figure 6.2 for the *K*-shell in Zr. The EIICS data are from Refs. [84, 106].

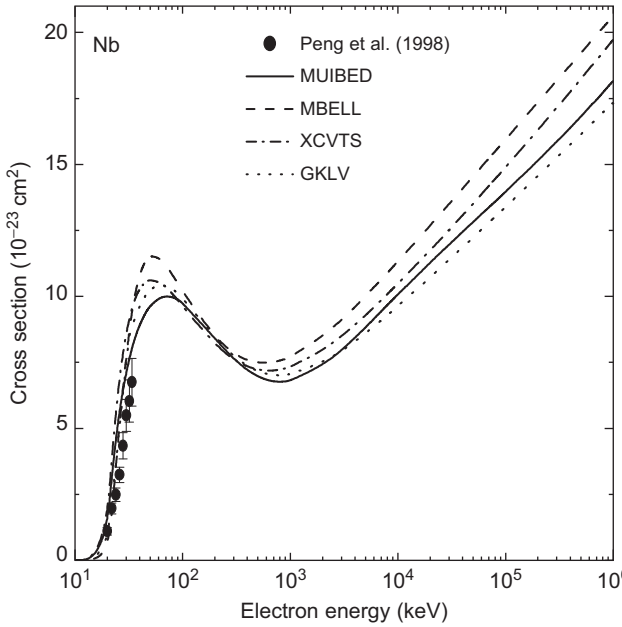

Figure 6.31 Same as in Figure 6.2 for the *K*-shell in Nb. The EIICS data are from Ref. [107].

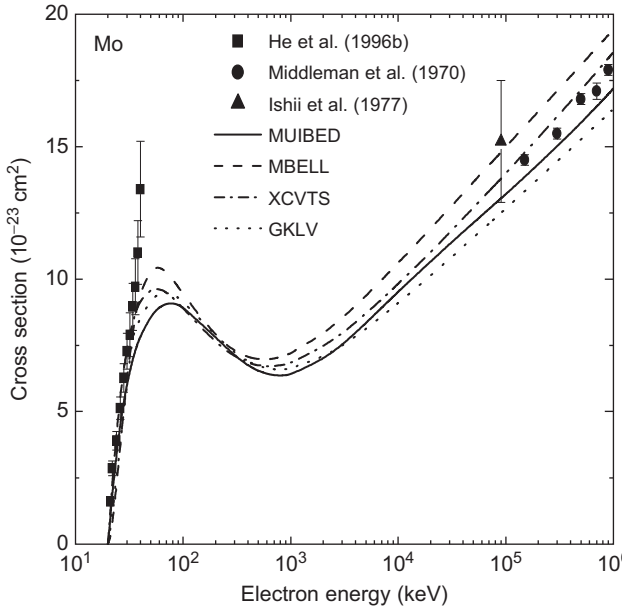

Figure 6.32 Same as in Figure 6.2 for the *K*-shell in Mo. The EIICS data are from Refs. [76, 102, 108].

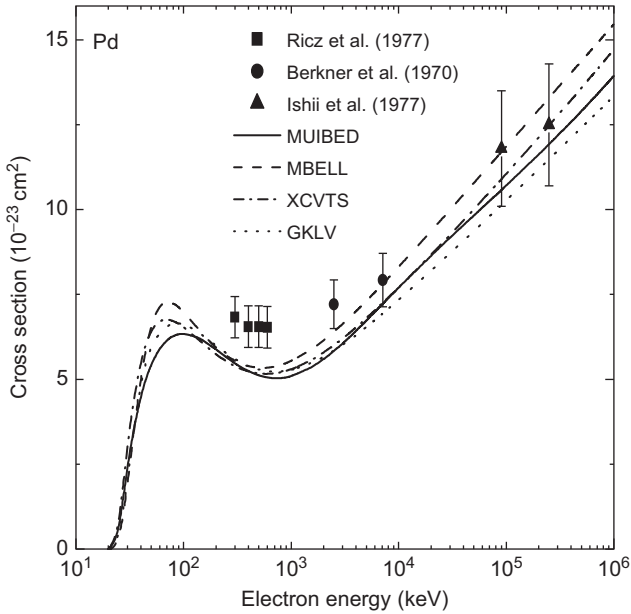

Figure 6.33 Same as in Figure 6.2 for the *K*-shell in Pd. The EIICS data are from Refs. [76, 109, 110].

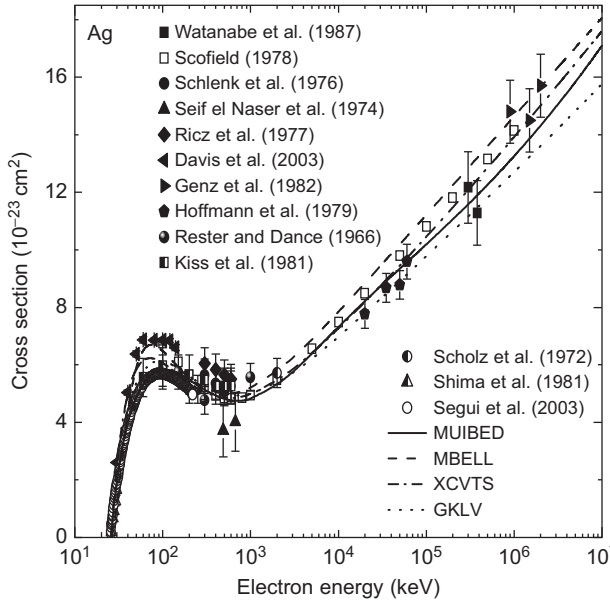

Figure 6.34 Same as in Figure 6.2 for the *K*-shell in Ag. The EIICS data are from Refs. [74, 85, 86, 95, 97, 98, 101, 105, 109, 111, 112]. The open squares and circles are the quantum results from Refs. [2, 8].

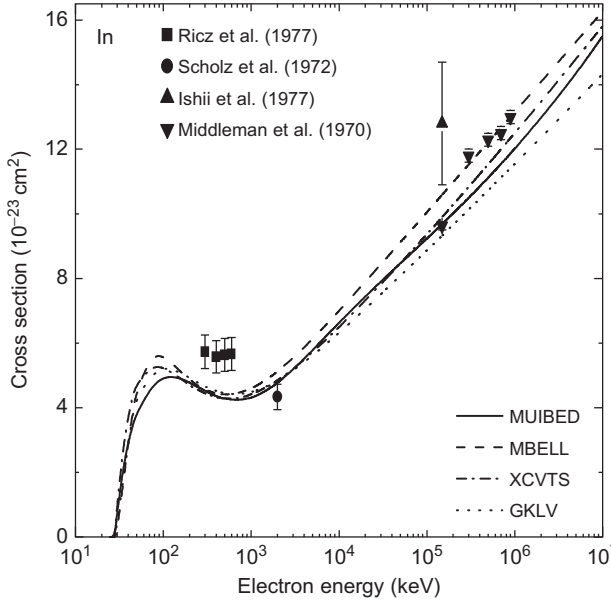

Figure 6.35 Same as in Figure 6.2 for the *K*-shell in In. The EIICS data are from Refs. [76, 86, 102, 109].

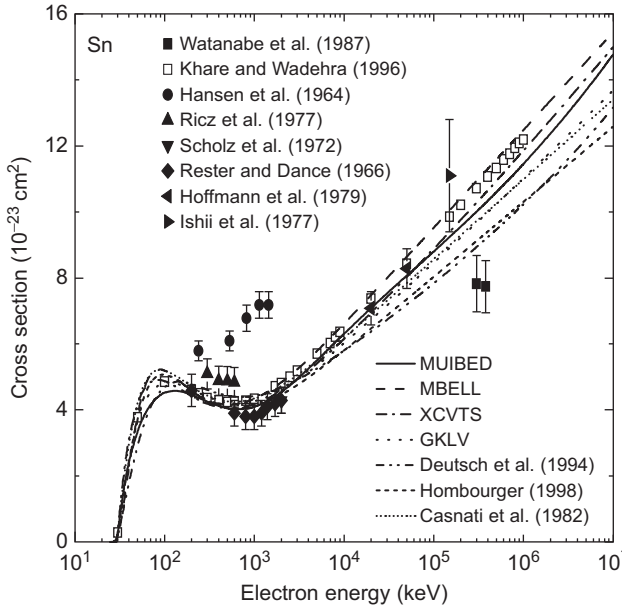

Figure 6.36 Same as in Figure 6.1 for the *K*-shell in Sn. The EIICS data are from Refs. [74, 76, 85, 86, 106, 109, 112]. The open squares are the quantum results from Ref. [1].

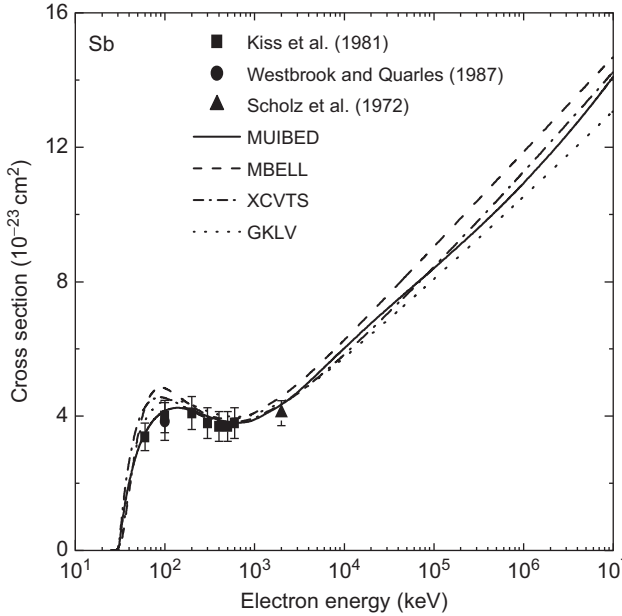

Figure 6.37 Same as in Figure 6.2 for the *K*-shell in Sb. The EIICS data are from Refs. [84, 86, 105].

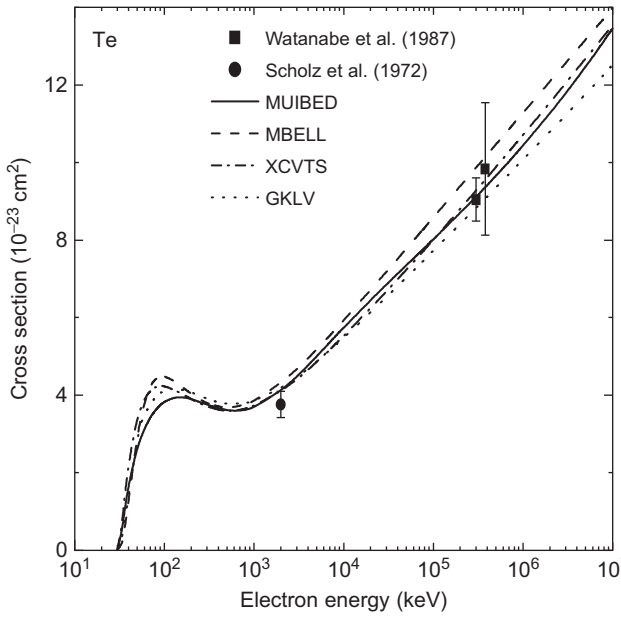

Figure 6.38 Same as in Figure 6.2 for the *K*-shell in Te. The EIICS data are from Refs. [85, 86].

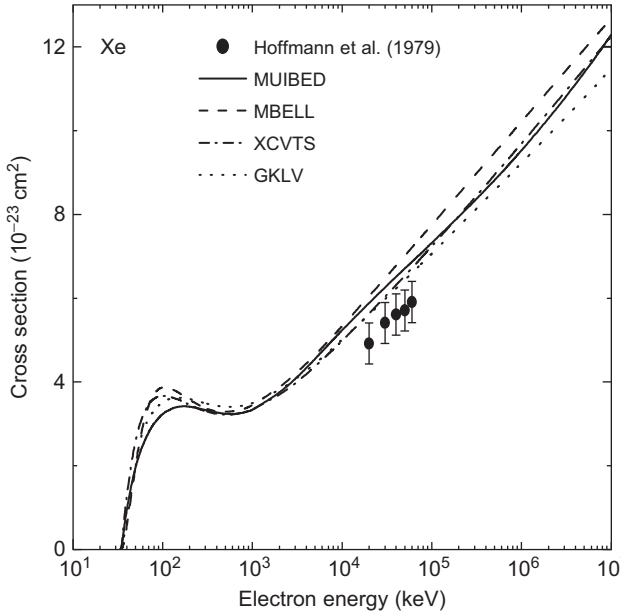

Figure 6.39 Same as in Figure 6.2 for the *K*-shell in Xe. The EIICS data are from Ref. [74].

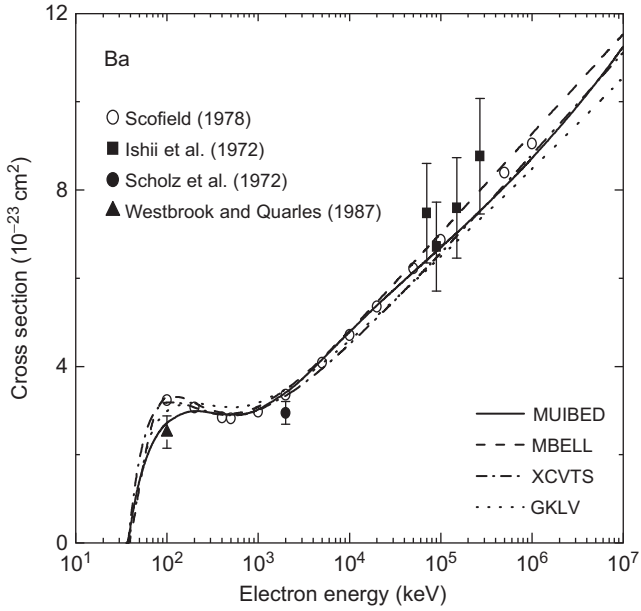

Figure 6.40 Same as in Figure 6.2 for the *K*-shell in Ba. The EIICS data are from Refs. [76, 84, 86]. The open circles are the quantum results from Ref. [2].

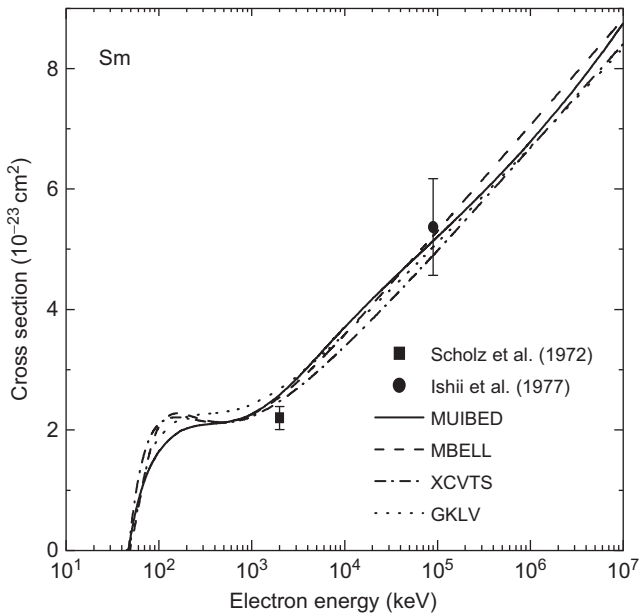

Figure 6.41 Same as in Figure 6.2 for the *K*-shell in Sm. The EIICS data are from Refs. [76, 86].

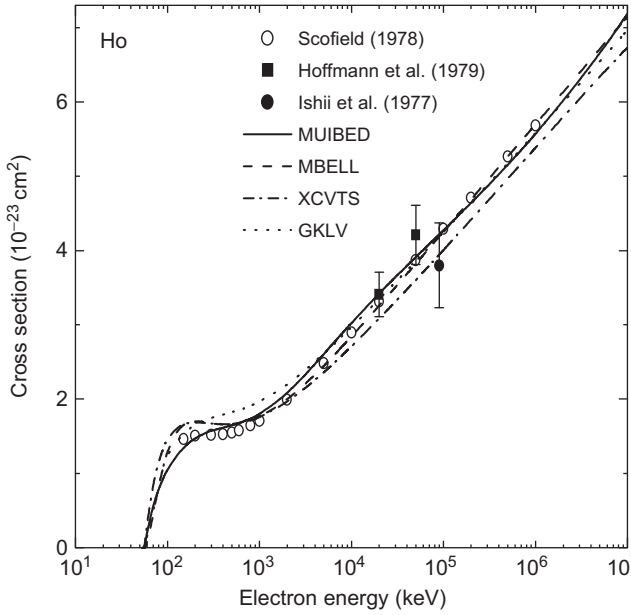

Figure 6.42 Same as in Figure 6.2 for the *K*-shell in Ho. The EIICS data are from Refs. [74, 76]. The open circles are the quantum results from Ref. [2].

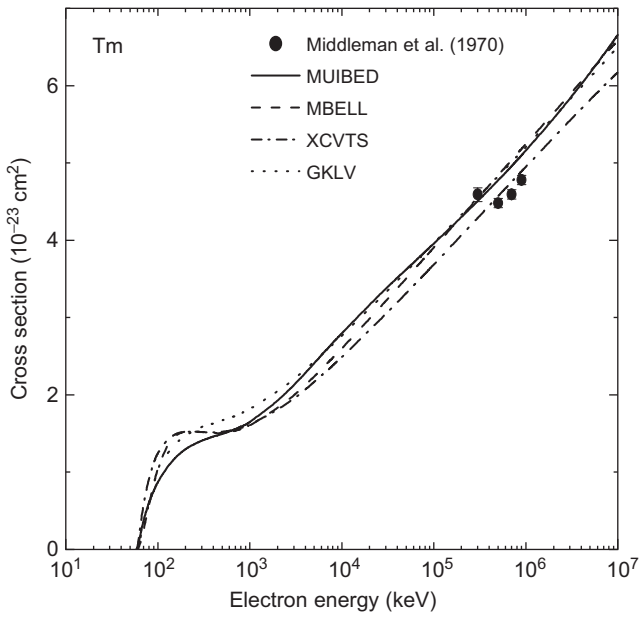

Figure 6.43 Same as in Figure 6.2 for the *K*-shell in Tm. The EIICS data are from Ref. [102].

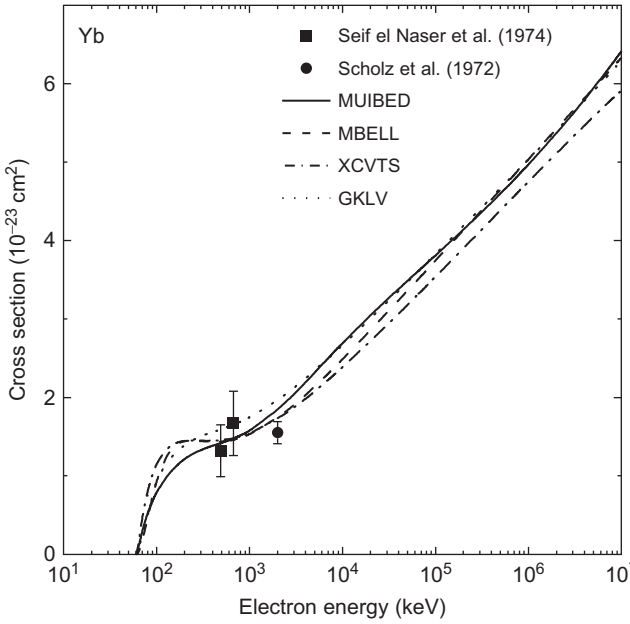

Figure 6.44 Same as in Figure 6.2 for the *K*-shell in Yb. The EIICS data are from Refs. [86, 95].

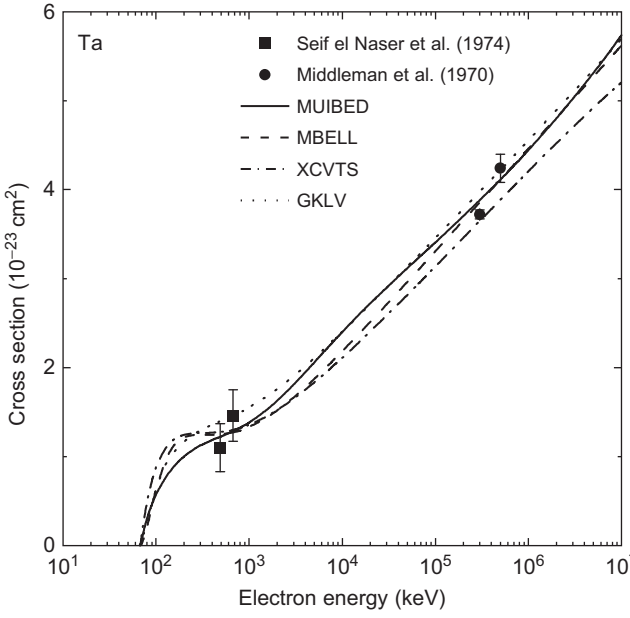

Figure 6.45 Same as in Figure 6.2 for the *K*-shell in Ta. The EIICS data are from Refs. [95, 102].

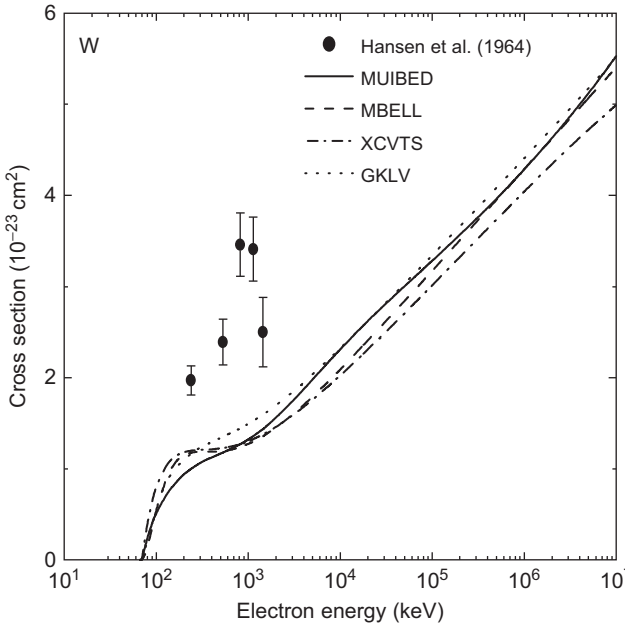

Figure 6.46 Same as in Figure 6.2 for the *K*-shell in W. The EIICS data are from Ref. [106].

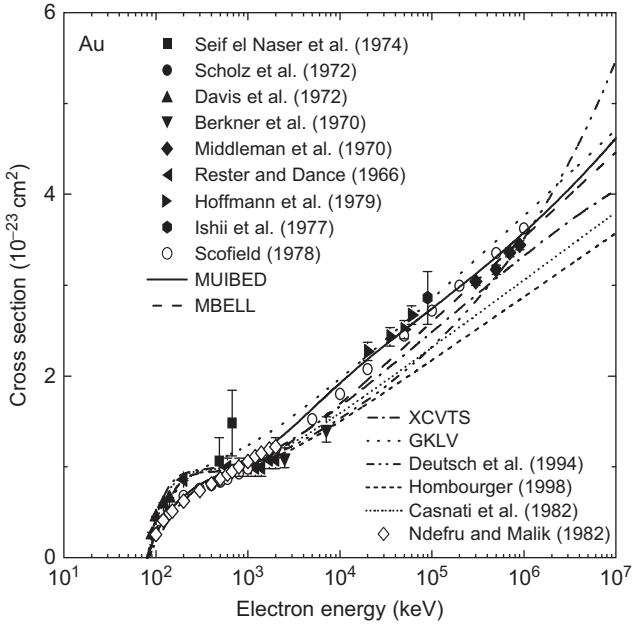

Figure 6.47 Same as in Figure 6.1 for the *K*-shell in Au. The EIICS data are from Refs. [74, 76, 86, 95, 98, 102, 110, 112]. The open circles are the quantum results from Refs. [2, 4].

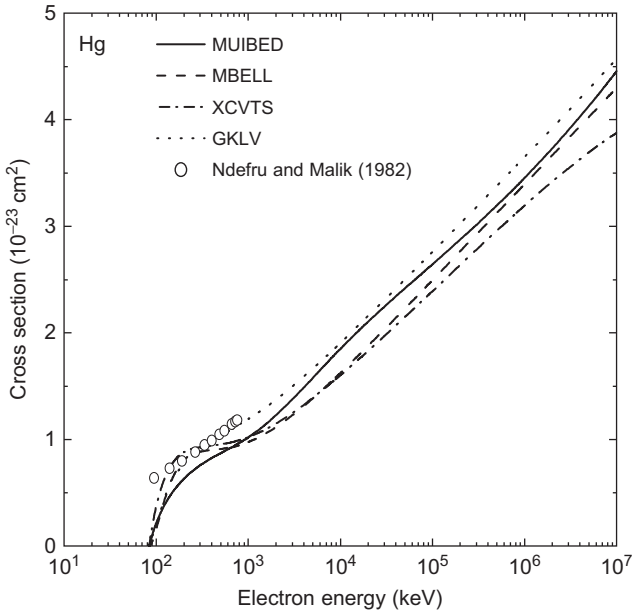

Figure 6.48 Same as in Figure 6.2 for the *K*-shell in Hg without EIICS data. The open circles are the quantum results from Ref. [4].

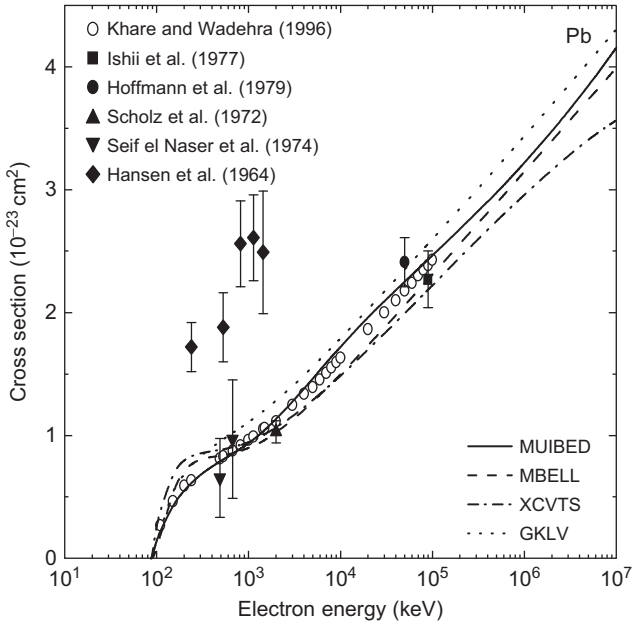

Figure 6.49 Same as in Figure 6.2 for the *K*-shell in Pb. The EIICS data are from Refs. [74, 76, 86, 95, 106]. The open circles are the quantum results from Ref. [1].

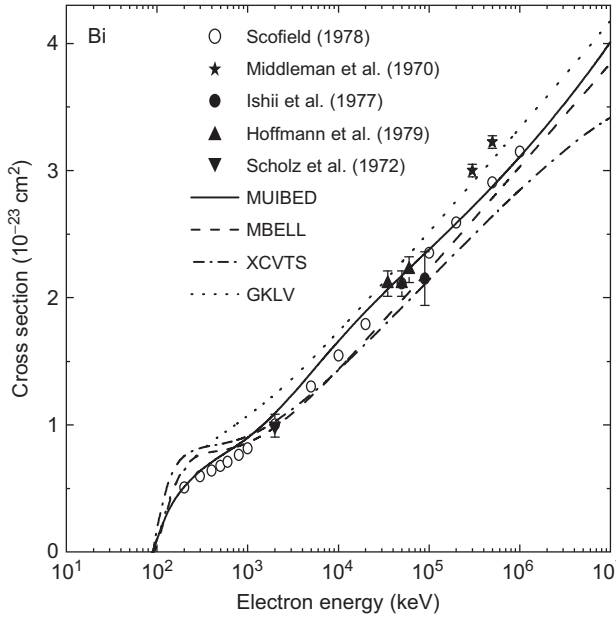

Figure 6.50 Same as in Figure 6.2 for the *K*-shell in Bi. The EIICS data are from Refs. [74, 76, 86, 102]. The open circles are the quantum results from Ref. [2].

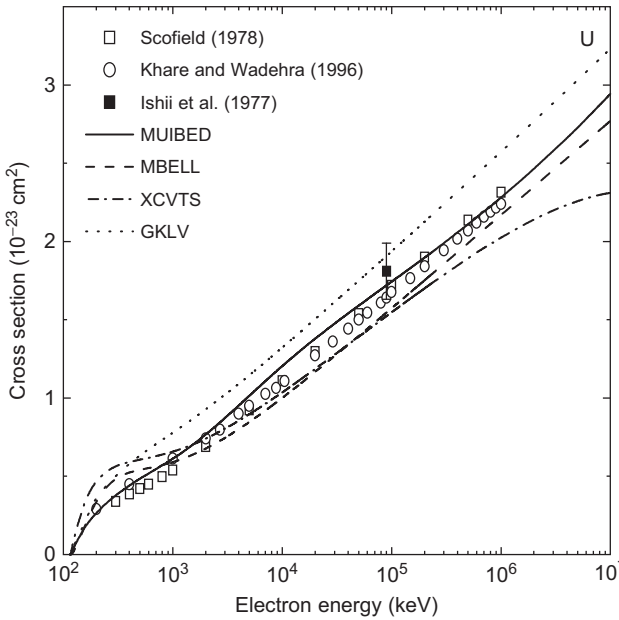

Figure 6.51 Same as in Figure 6.1 for the *K*-shell in U. The EIICS data are from Ref. [76]. The open circles and square are the quantum results from Refs. [1, 2].

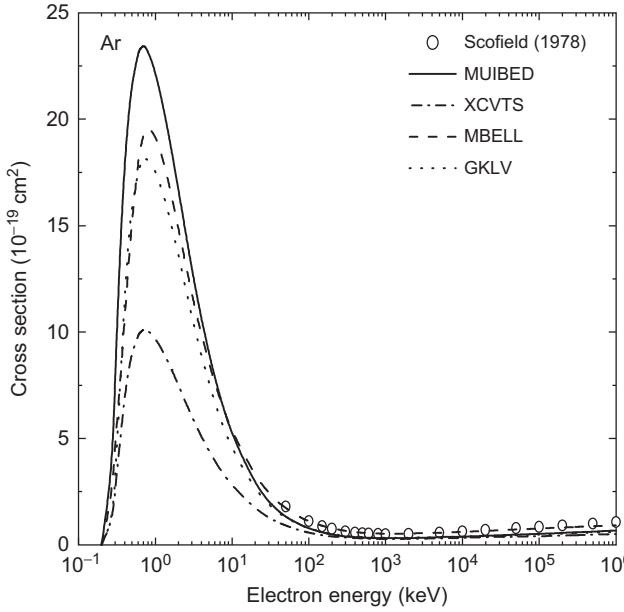

Figure 6.52 Same as in Figure 6.2 for the *L*-shell in Ar without EIICS data. The open circles are the quantum results from Ref. [2].

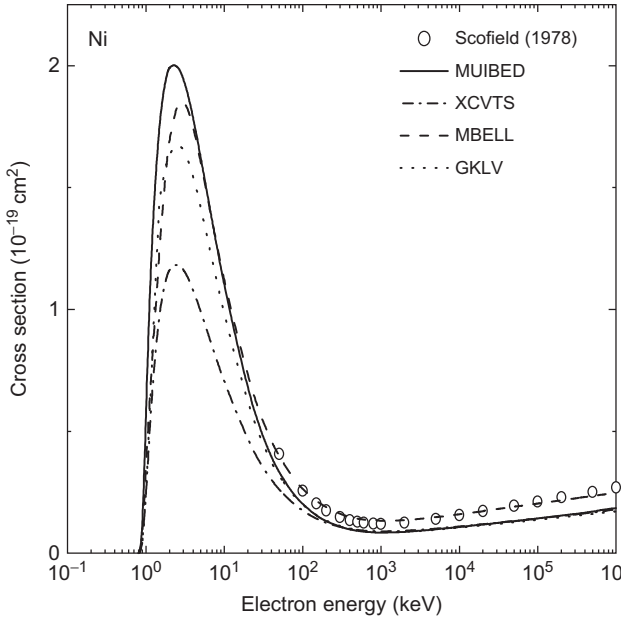

Figure 6.53 Same as in Figure 6.2 for the *L*-shell in Ni without EIICS data. The open circles are the quantum results from Ref. [2].

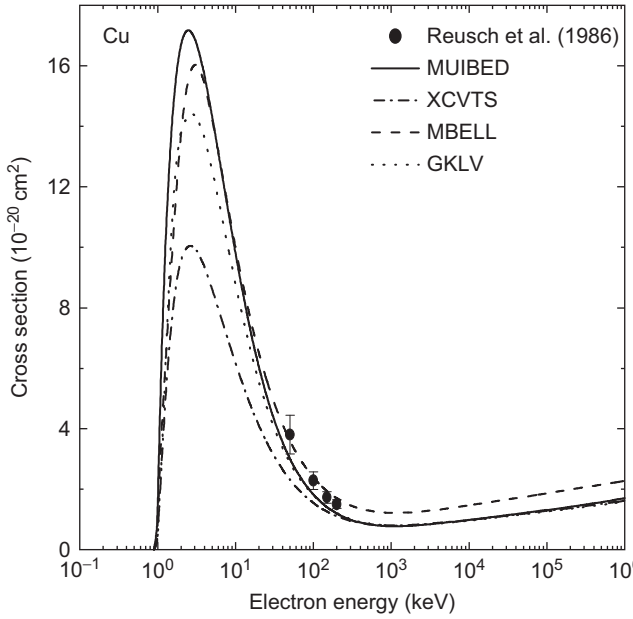

Figure 6.54 Same as in Figure 6.2 for the *L*-shell in Cu. The EIICS data are from Ref. [113].

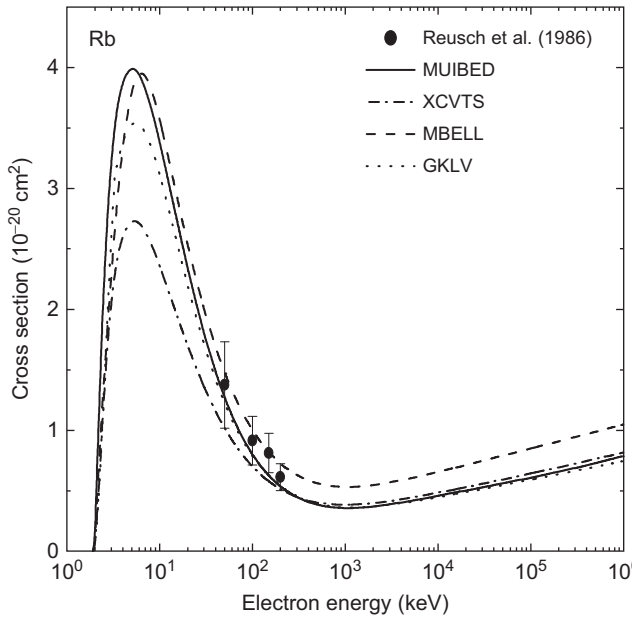

Figure 6.55 Same as in Figure 6.2 for the *L*-shell in Rb. The EIICS data are from Ref. [113].

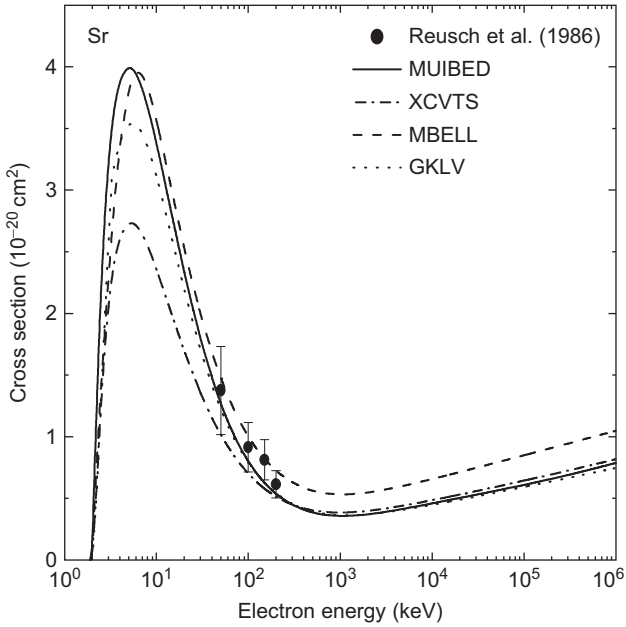

Figure 6.56 Same as in Figure 6.2 for the *L*-shell in Sr. The EIICS data are from Ref. [113].

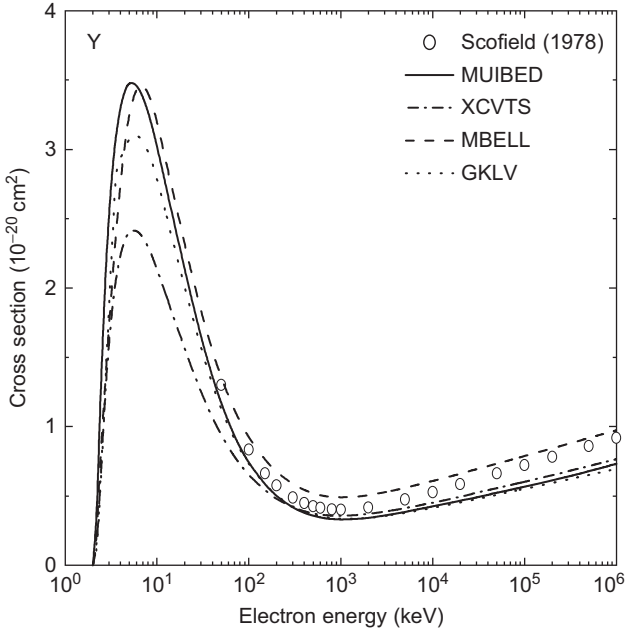

Figure 6.57 Same as in Figure 6.2 for the *L*-shell in Y without EIICS data. The open circles are the quantum results from Ref. [2].

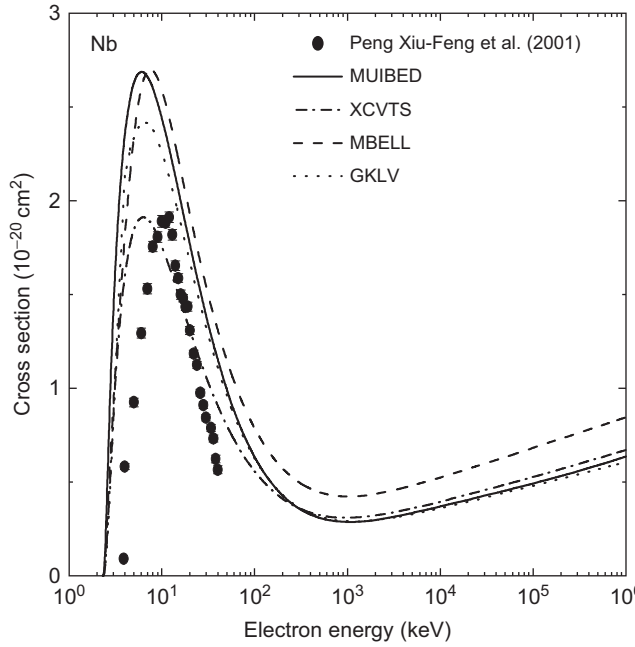

Figure 6.58 Same as in Figure 6.2 for the *L*-shell in Nb. The EIICS data are from Ref. [114].

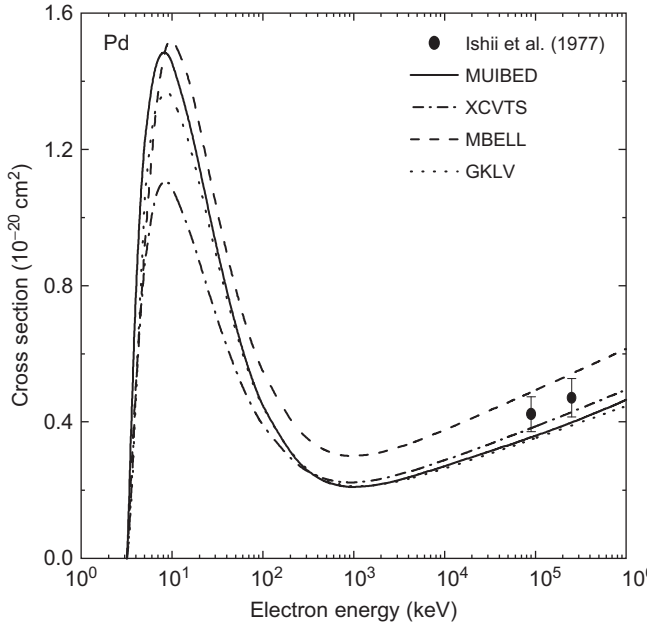

Figure 6.59 Same as in Figure 6.2 for the *L*-shell in Pd. The EIICS data are from Ref. [76].

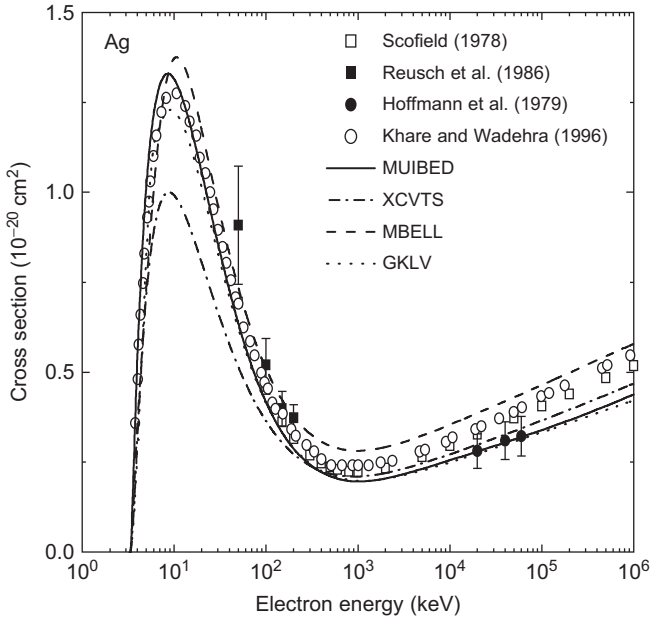

Figure 6.60 Same as in Figure 6.2 for the *L*-shell in Ag. The EIICS data are from Refs. [74, 113]. The open circles and squares are the quantum results from Refs. [1, 2].

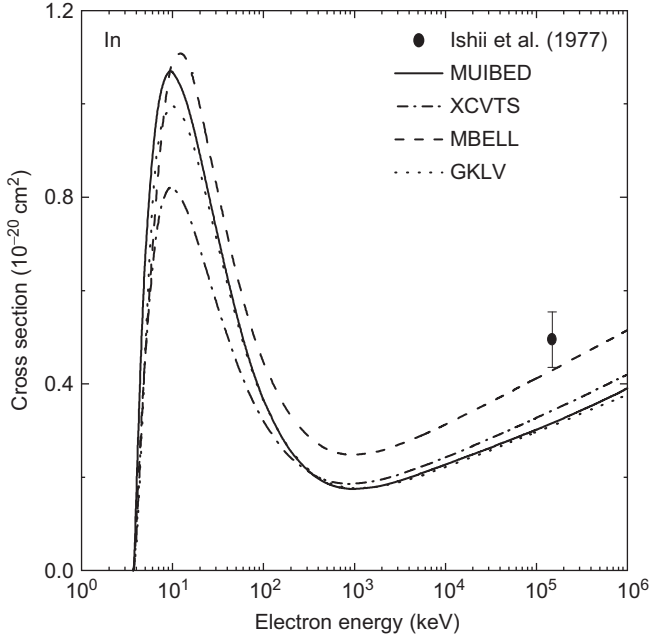

Figure 6.61 Same as in Figure 6.2 for the *L*-shell in In. The EIICS data are from Ref. [76].

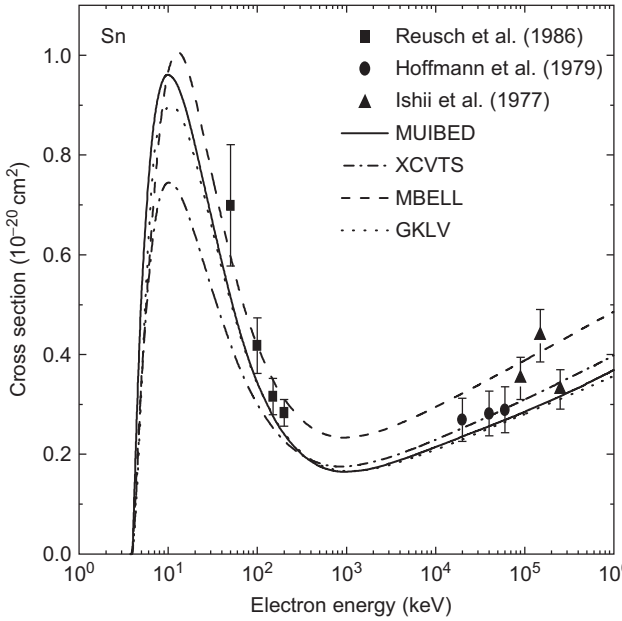

Figure 6.62 Same as in Figure 6.2 for the *L*-shell in Sn. The EIICS data are from Refs. [74, 76, 113].

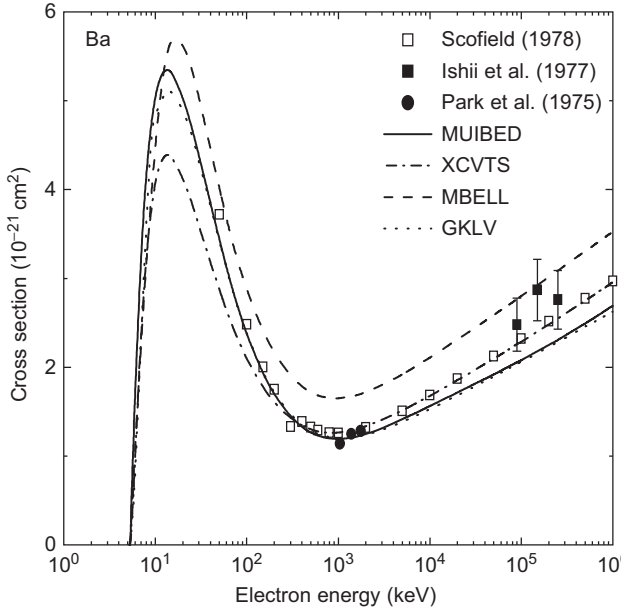

Figure 6.63 Same as in Figure 6.2 for the *L*-shell in Ba. The EIICS data are from Refs. [76, 115]. The open squares are the quantum results from Ref. [2].

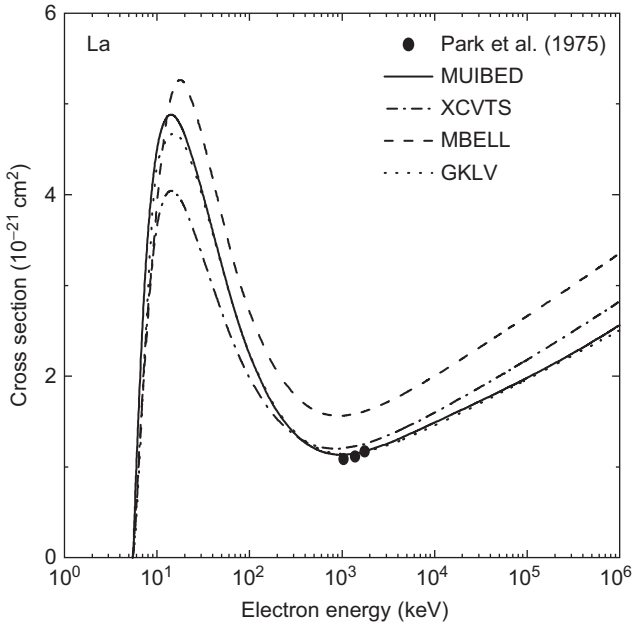

Figure 6.64 Same as in Figure 6.2 for the *L*-shell in La. The EIICS data are from Ref. [115].

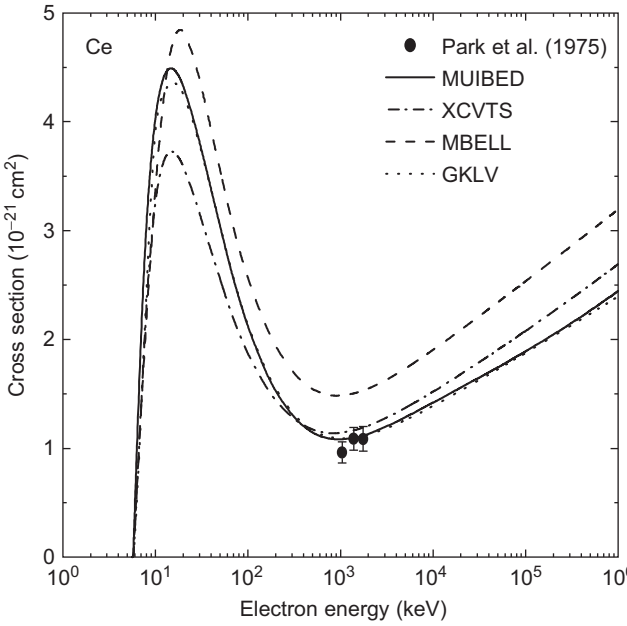

Figure 6.65 Same as in Figure 6.2 for the *L*-shell in Ce. The EIICS data are from Ref. [115].

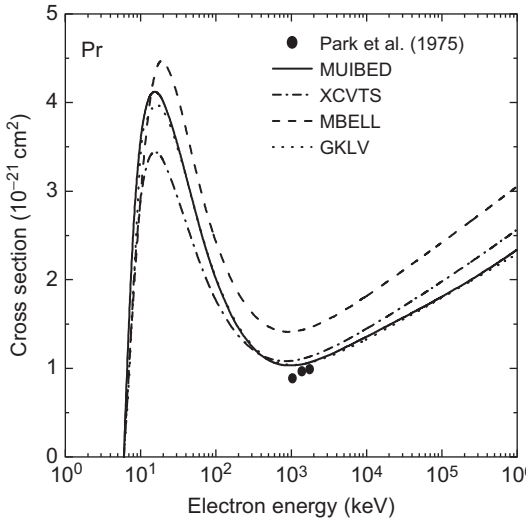

Figure 6.66 Same as in Figure 6.2 for the *L*-shell in Pr. The EIICS data are from Ref. [115].

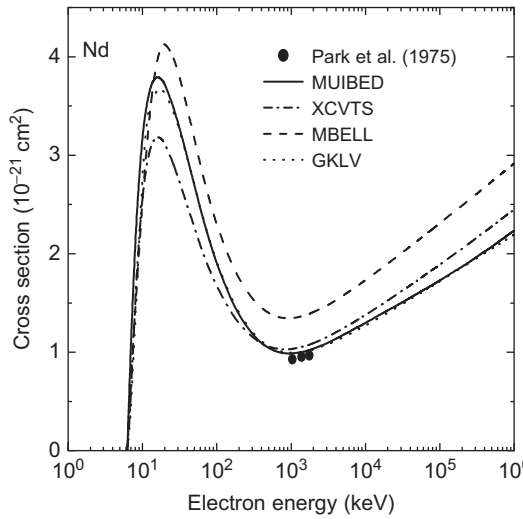

Figure 6.67 Same as in Figure 6.2 for the *L*-shell in Nd. The EIICS data are from Ref. [115].

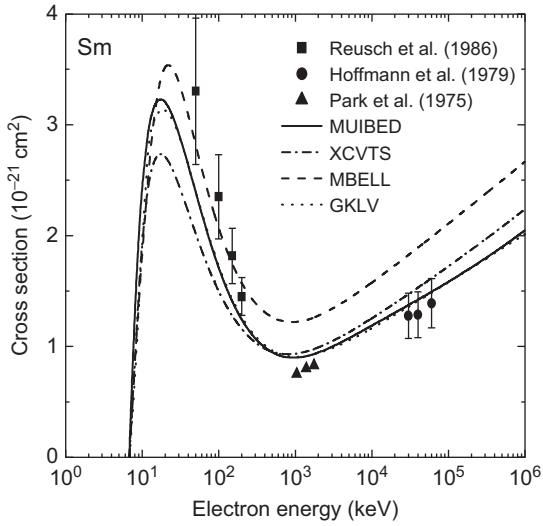

Figure 6.68 Same as in Figure 6.2 for the *L*-shell in Sm. The EIICS data are from Refs. [74, 113, 115].

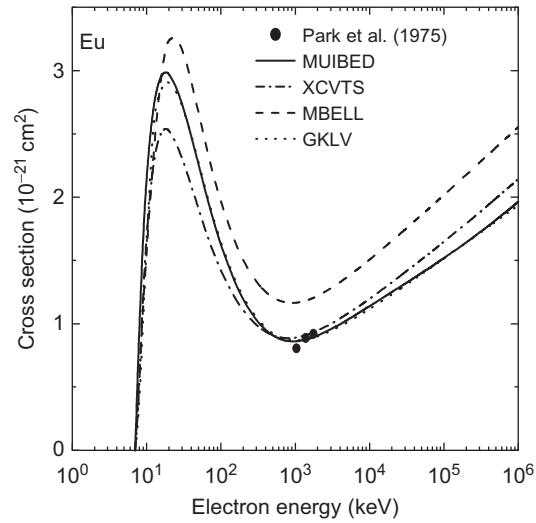

Figure 6.69 Same as in Figure 6.2 for the *L*-shell in Eu. The EIICS data are from Ref. [115].

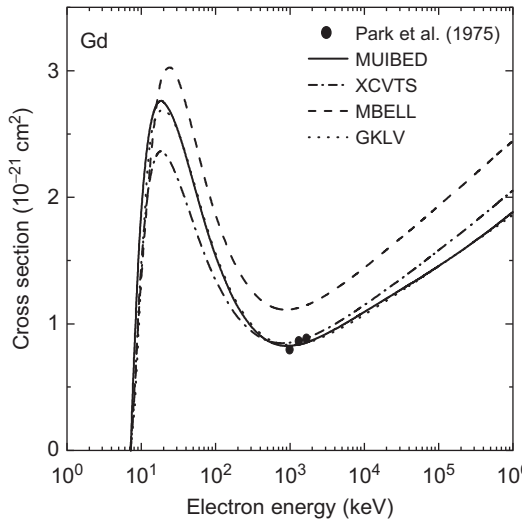

Figure 6.70 Same as in Figure 6.2 for the *L*-shell in Gd. The EIICS data are from Ref. [115].

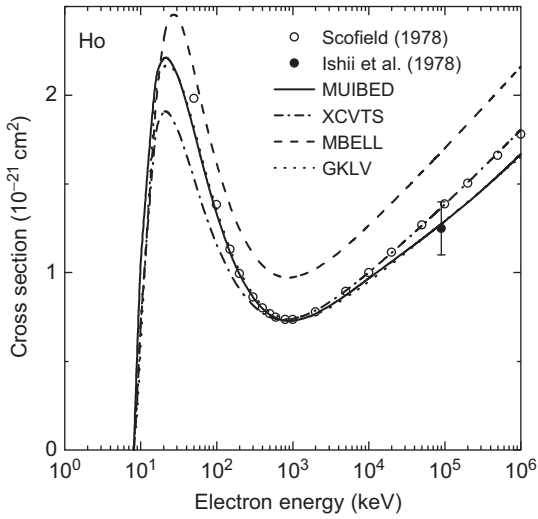

Figure 6.71 Same as in Figure 6.2 for the *L*-shell in Ho. The EIICS data are from Ref. [76]. The open squares are the quantum results from Ref. [2].

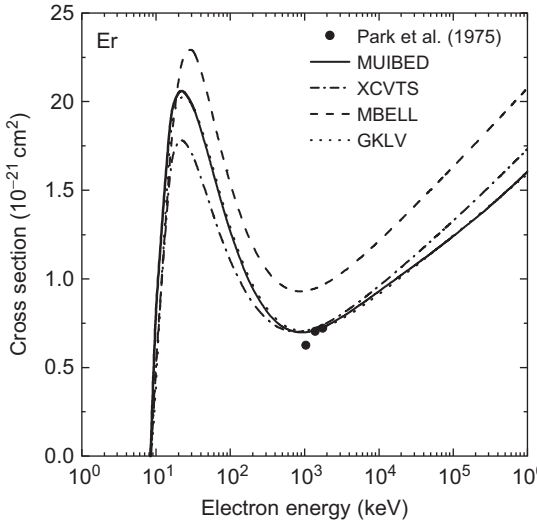

Figure 6.72 Same as in Figure 6.2 for the *L*-shell in Er. The EIICS data are from Ref. [115].

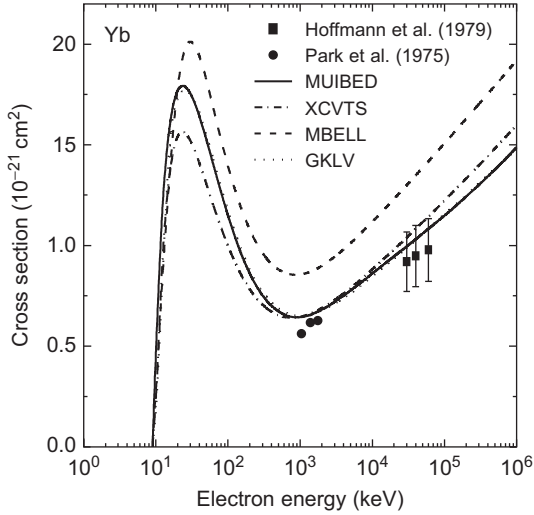

Figure 6.73 Same as in Figure 6.2 for the *L*-shell in Yb. The EIICS data are from Refs. [74, 115].

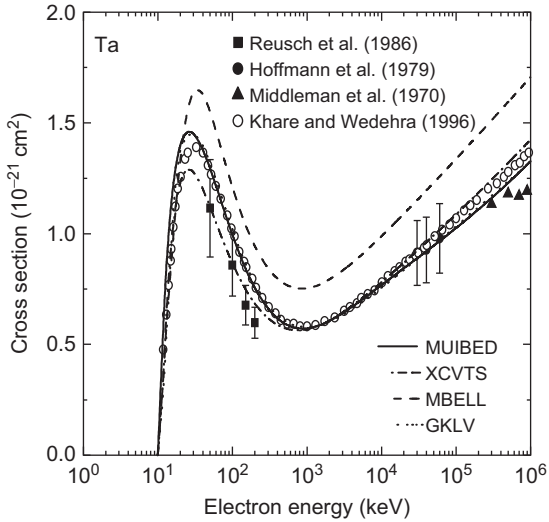

Figure 6.74 Same as in Figure 6.2 for the *L*-shell in Ta. The EIICS data are from Refs. [74, 102, 113]. The open circles are the quantum results from Ref. [1].

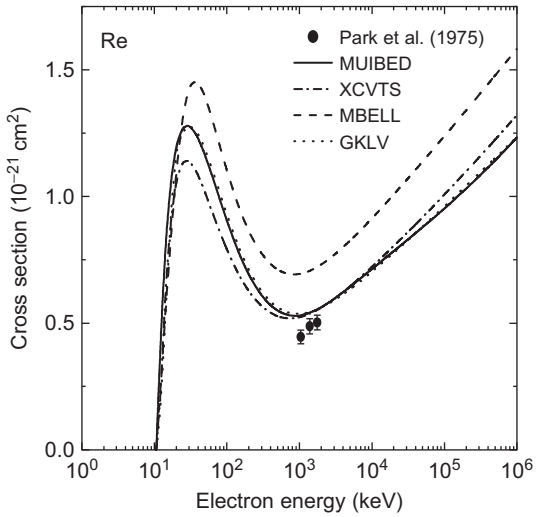

Figure 6.75 Same as in Figure 6.2 for the *L*-shell in Re. The EIICS data are from Ref. [115].

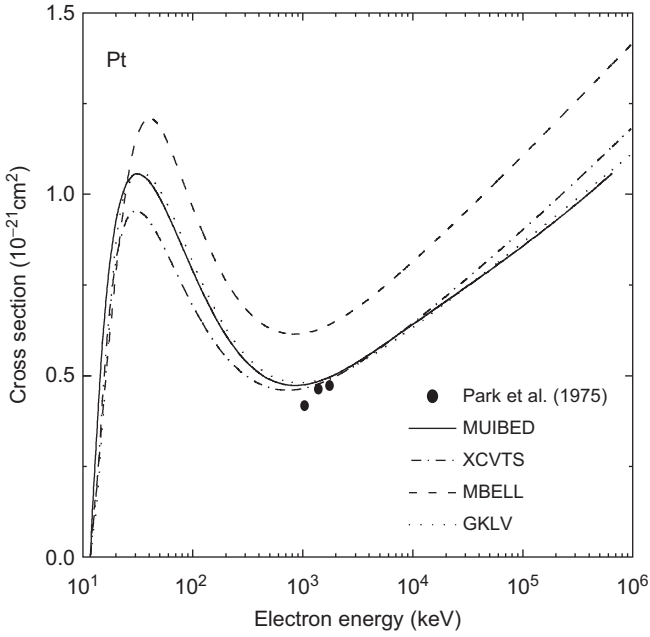

Figure 6.76 Same as in Figure 6.2 for the *L*-shell in Pt. The EIICS data are from Ref. [115].

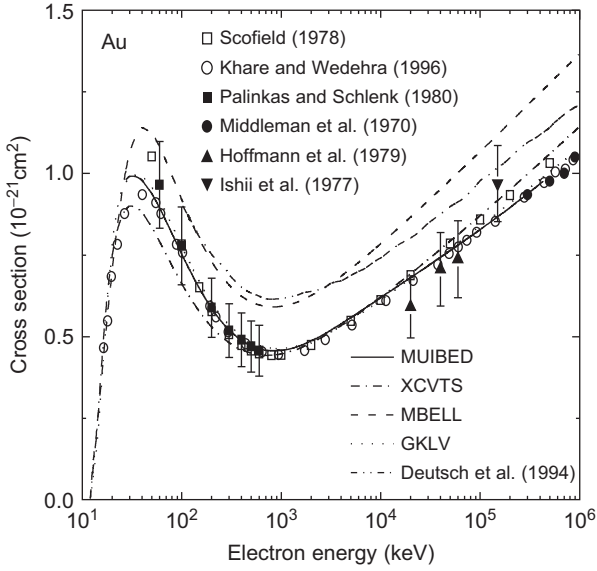

Figure 6.77 Same as in Figure 6.1 for the *L*-shell in Au along with the predictions from the DM model [28]. The EIICS data are from Refs. [74, 76, 102, 116]. The open circles and squares are the quantum results from Refs. [1, 2].

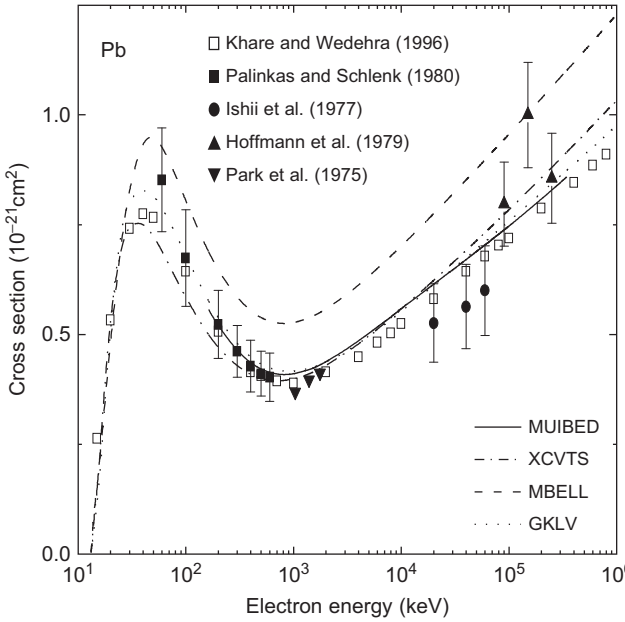

Figure 6.78 Same as in Figure 6.2 for the *L*-shell in Pb. The EIICS data are from Refs. [74, 76, 115, 116]. The open squares are the quantum results from Ref. [1].

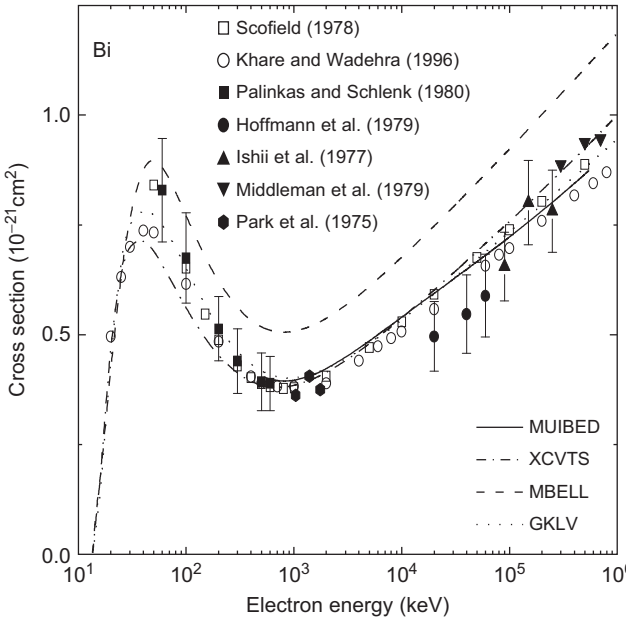

Figure 6.79 Same as in Figure 6.2 for the *L*-shell in Bi. The EIICS data are from Refs. [74, 76, 102, 115, 116]. The open circles and squares are the quantum results from Refs. [1, 2].

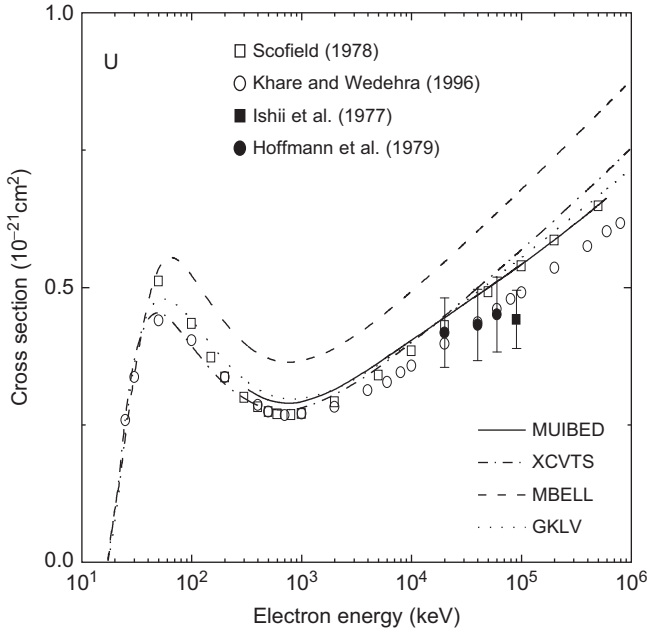

Figure 6.80 Same as in Figure 6.2 for the *L*-shell in U. The EIICS data are from Refs. [74, 76]. The open circles and squares are the quantum results from Refs. [1, 2].

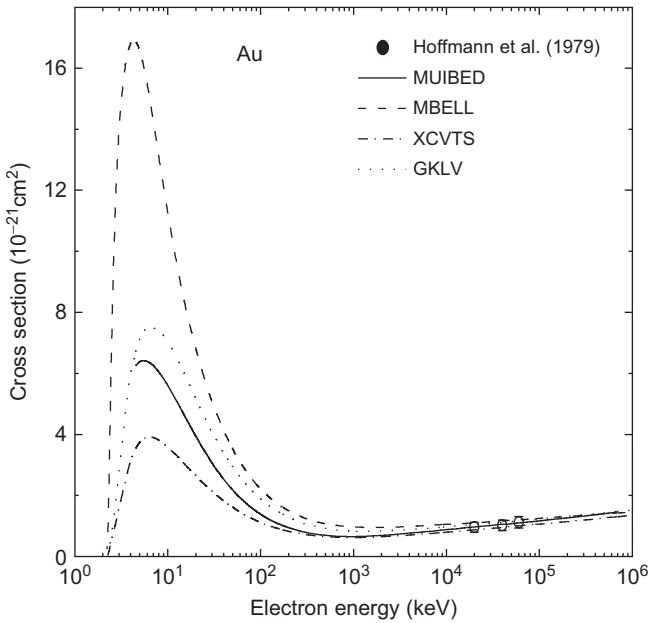

Figure 6.81 Same as in Figure 6.2 for the *M*-shell in Au. The EIICS data are from Ref. [74].

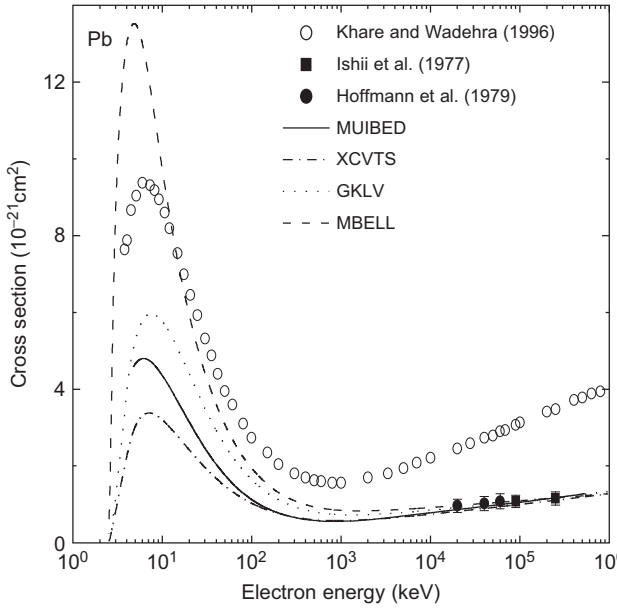

Figure 6.82 Same as in Figure 6.2 for the *M*-shell in Pb. The EIICS data are from Refs. [74, 76]. The open circles are the quantum results from Ref. [1].

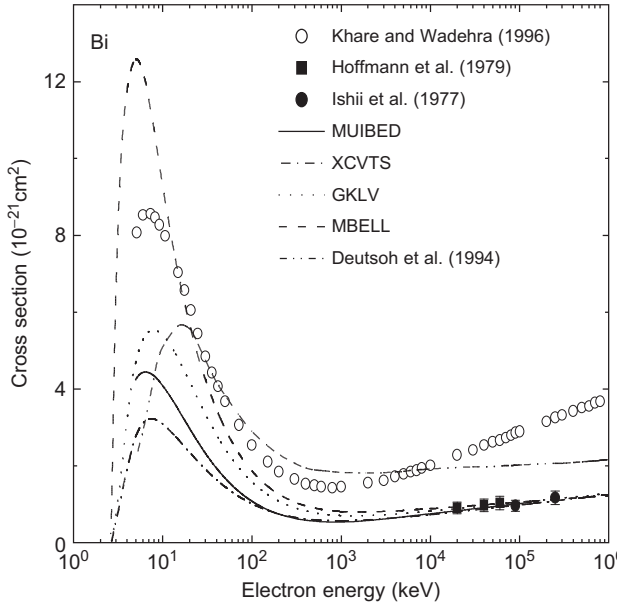

Figure 6.83 Same as in Figure 6.1 for the *M*-shell in Bi along with the predictions from the DM model [28]. The EIICS data are from Refs. [74, 76]. The open circles are the quantum results from Ref. [1].

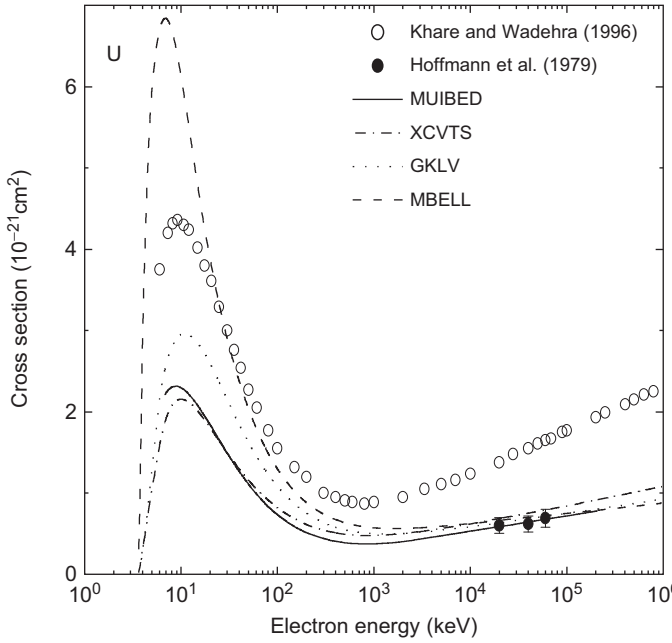

Figure 6.84 Same as in Figure 6.2 for the *M*-shell in U. The EIICS data are from Ref. [74]. The open circles are the quantum results from Ref. [1].

energy region apart from the ionization shell. They are based on different inherent structures, for example:

1. The MBELL model combines the Bethe asymptotic form and the low-energy behavior of collision, respectively, through the first and series terms in Eq. (5) and contains nine shell-dependent parameters shown in Table 6.1 excluding the fixed parameter m.
2. The XCVTS model is simulation of DWBA calculations, through its parent CVTS [47] model, in terms of the two fitting parameters C_ξ and λ_ξ shown in Eq. (12) apart from other shell-independent parameters depicted in Table 6.2.
3. The GKLV model is based on the Kolbenstvedt model [23], which has its root in the quantum electrodynamics, with two orbit-dependent fitting parameters ε_{nl} and η_{nl} tabulated in Table 6.3.
4. The MUIBED model, through its parent siBED [53], replaces the Bethe part of the BED model with a two-parameter Born term through Eq. (25) leading to ultimately two shell-dependent fitting parameters m and λ in Eq. (21), noted in Table 6.4 after both the parameters d_1 and d_2 are set to zero.

In spite of the structural differences in the four models, they all generate almost identical results in the energy region of available experimental

data for C, N, Ne, Ar, Ag, Sb, Te, Ba, Sm, Ho, Tm, Ta, and U atoms in the *K*-shell ionization; for Cu, Rb, Sr, Pd, Ag, Sn, and Ba atoms in the *L*-shell ionization, and for Au, Pb, Bi, and U atoms in the *M*-shell ionization, where there remain large differences in the predictions around the peak region. In few cases, these models perform differently in describing the experimental data in distinct energy regions with examples of Cr, Cu, and Ag atoms for the *K*-shell, and Sm, Pb, and Bi atoms for the *L*-shell ionization. Excepting the cases of Ti, Zr, W, and Pb atoms in the *K*-shell and atomic Nb target in the *L*-shell ionization, the experimental data are well described by three or two of the models.

For the *K*-shell ionization, all four models have produced almost similar cross sections over the entire energy domain for atoms in the ranges $Z = 6$ (C)–10 (Ne), 47 (Ag)–60 (Nd), and 61 (Pm)–67 (Ho). These also include the cases: (1) for F, I, Cs, Pm, Tb, and Dy atoms with no experimental EIICS data available to the best of our knowledge, (2) for As, Br, Cd, Ce, Nd, Eu, Gd, Er, Pt [86] and U [76] atoms with only one-point EIICS datum [86], and (3) for Na, La, Pr, Sm, and Na atoms with two available data points [79, 82, 103]. However, the predicted EISICS for the atoms in the first case are not displayed in figures. For the latter two cases, the comparison between the experimental results and model predictions are shown only for typical cases of Na and U targets (Figures 6.5, 6.51). It is observed that from atomic C to O ($Z = 6$–8) and also from Gd to U atoms ($Z = 64$–92), the MBELL model overestimates the cross sections for all *K*-, *L*-, and *M*-shell ionizations throughout the studied energy range except for the *M*-shell ionization in the relativistic domain. For the *M*-shell ionization in the peak region, where experimental data are yet unavailable, the EISICS predictions due to MBELL remain by far the largest as compared with those calculated by the other three reported models. The above-mentioned aspect of MBELL for the *L*- and *M*-shell ionization, apply to the cases of K, Ca, Sc, Ti, V, Cr, Mn, Fe, Co, Zn, Ga, Ge, As, Se, Br, Kr, Zr, Mo, Tc, Ru, Rh, Cd, Sb, Te, I, Xe, Cs, Pm, Tb, Dy, Tm, Lu, Hf, W, Os, Ir, Hg, Tl, Po, At, Rn, Fr, Ra, Ac, Th, and Pa atoms for the *L*-shell, and Hg, Tl, Po, At, Rn, Fr, Ra, Ac, Th, and Pa atoms for the *M*-shell ionization, where EIICS data are not available as far as we know. The MBELL model nevertheless performs best for the *L*-shell ionization in describing the experimental data of Tin (Sn) and Samarium (Sm) just beyond the peak region and for Iodine (I) in the relativistic region. Moreover, MBELL produces reasonable to excellent fits to most of the available data for the *K*-, *L*-, and *M*-shell ionization.

In most cases of the *L*- and *M*-shell ionization, the predicted results resulting from XCVTS, GKLV, and MUIBED models agree nicely and produce excellent account of the available experimental data. Even in the peak region, these three models perform quite well as compared with the measured data for the *L*-shell ionization of Au and Pb. But all of them fail to reproduce the *L*-shell ionization EIICS data for Nb target, where the available experimental data cover the whole peak region. The quantal results due to the plane-wave BA (PWBA) [1], relativistic PWBA (RPWBA) [2] and [4], or

the relativistic DWBA (RDWBA) [8] for the *K*-shell and *L*-shell ionization agree remarkably well by most of these models. However, for the *M*-shell ionization, the findings of the PWBA [1] model fail to describe the EIICS data, which are very well accounted for by our model calculations, considered herein.

To adjudge the effectiveness of the MBELL, XCVTS, GKLV, and MUIBED models, the predictions of these models are compared with those of the other successful models [28, 59, 60] along with the available EIICS data for few typical species. For the *K*-shell ionization, the calculated cross sections from the relativistic DM model [28] as well as empirical models of Casnati et al. [59] and Hombourger [60] are shown in Figures 6.1, 6.36, 6.47, and 6.51, respectively, for C, Sn, Au, and U. Although the latter three models work pretty well for C and Sn targets, they perform very poorly at relativistic energies beyond 10 MeV for heavier targets, such as Au and U atoms. For Au (Figure 6.47), the DM model [28] provides underestimated cross sections in the energy region $20 \leq E \leq 300$ MeV, and both the empirical models [59, 60] follow the same trend at all energies beyond 10 MeV. At $E \geq 300$ MeV, the findings of the DM model, however, manage to agree with the experimental EIICS data. The DM and both the empirical models [59, 60] perform even worse to reproduce the experimental point for U atom (Figure 6.51) at about $E = 80$ MeV. For the *L*- and *M*-shell ionization, the DM results [28] greatly overestimate the experimental findings, respectively, on Au (Figure 6.77) over the entire energy range and on Bi (Figure 6.83) in the energy range $20 \leq E \leq 250$ MeV.

In conclusion, this review presents the calculated results from the MBELL, XCVTS, GKLV, and MUIBED models embodying the single one-step ionization dynamics. In the overall picture, these four models are found successful in describing the most of the available experimental EIICS data for the *K*-, *L*-, and *M*-shell ionization of the atomic targets, ranging from C to U atoms and for incident energies *E* up to 2 GeV. These four models can easily be used to generate accurate EISICS results for the species and energies, where the experimental data are either sparse or even nil. The differences found among the predicted results may, however, be considered as the limiting values for use in various modeling applications.

ACKNOWLEDGMENTS

Authors are thankful to Professor F. B. Malik, Southern Illinois University at Carbondale, IL, for his encouragements and suggestions for improving the manuscript. This work was completed within the framework of the Associateship Scheme of the Abdus Salam International Centre for Theoretical Physics (ICTP), Trieste, Italy. A. K. Fazlul Haque would like to thank ICTP for their kind hospitality and support, and Bidhan C. Saha gratefully acknowledges the support from the National Science Foundation via the NSF-CREST project (grant # 0630370).

REFERENCES

[1] S.P. Khare, J.M. Wadehra, *K*-, *L*- and *M*-shell ionization of atoms by electron and positron impact, Can. J. Phys. 74 (1996) 376.

[2] J.H. Scofield, *K*- and *L*-shell ionization of atoms by relativistic electrons, Phys. Rev. A 18 (1978) 963.

[3] J.T. Ndefru, F.B. Malik, Calculations of the Li ionization cross sections of elements between 56 and 83 by 1.04, 1.39 and 1.76 MeV in relativistic plane wave Born approximation, J. Phys. B At. Mol. Opt. Phys. 13 (1980) 2117.

[4] J.T. Ndefru, F.B. Malik, Relativistic effects in the *K*-shell ionization of Au and Hg by electron impact, Phys. Rev. A 25 (1982) 2407.

[5] F.B. Malik, E. Trefftz, Ionizations quershnitt von OV gegenuber electrons toss unter teilweiser Berucksichtigug des Austausches, Zeitsch. Fur Naturforsch. 16a (1961) 583.

[6] D.L. Moores, K.J. Reed, Effect of Møller interaction on electron-impact of high-Z hydrogen-like ions, Phys. Rev. A 51 (1995) R9.

[7] D.L. Moores, K.J. Reed, Electron impact ionization of highly charged uranium ions, J. Phys. B At. Mol. Opt. Phys. 28 (1995) 4861.

[8] S. Segui, M. Dingfelder, F. Salvat, Distorted-wave calculation of cross sections for inner-shell ionization by electron and positron impact, Phys. Rev. A 67 (2007) 062710.

[9] S.M. Younger, Distorted-wave electron-impact ionization cross sections for the argon electronic sequence, Phys. Rev. A 26 (1982) 3177.

[10] C.J. Fontes, D.H. Sampson, H.L. Zhang, Fully relativistic calculations of and fits to 1s ionization cross sections, Phys. Rev. A 59 (1999) 1329.

[11] M.S. Pindzola, D. Mitnik, F. Robicheaux, T-matrix calculation for the electron-impact ionization of hydrogen in the Tempkin-poet model, Phys. Rev. A 62 (2000) 062718.

[12] P. Burke, K. Berrington, Atomic and Molecular Processes: An R-Matrix Approach, IOP Publishing, Bristol, 1993.

[13] I. Bray, A.T. Stelbovics, Calculation of electron scattering on hydrogenic targets, Adv. At. Mol. Opt. Phys. 35 (1995) 209.

[14] I. Bray, Convergent close-coupling method for calculation of electron scattering on hydrogenlike targets, Phys. Rev. A 49 (1994) 1066.

[15] P. Bartllet, A.T. Stelbovics, I. Bray, Threshold ionization laws for electron-hydrogen scattering and their dominant region of configuration space, Phys. Rev. A 68 (2003) 030701.

[16] M. Baertschy, T.N. Reseigno, W.A. Isaacs, X. Li, C.W. McCurdy, Electron-impact ionization of atomic hydrogen, Phys. Rev. A 63 (2001) 022712.

[17] F. Robicheaux, M.S. Pindzola, D.R. Plante, Time-dependent quantal calculations for $L = 0$ models of the electron-impact ionization of hydrogen near threshold, Phys. Rev. A 55 (1997) 3573.

[18] A.S. Kadyrov, A.M. Mukhamedzhanov, A.T. Stelbovics, Asymptotic form of the electron-hydrogen scattered wave, Phys. Rev. A 67 (2003) 024702.

[19] D.L. Moores, K.J. Reed, Indirect processes in electron impact ionization of positive ions, Adv. At. Mol. Opt. Phys. 34 (1994) 301.

[20] H. Deutsch, K. Becker, S. Matt, T.D. Märk, Theoretical determination of absolute electron-impact ionization cross sections of molecules, Int. J. Mass Spectrom. 197 (2000) 37.

[21] J.J. Thomson, Ionization by moving electrified particles, Philos. Mag. London 23 (1912) 449.

[22] M. Gryzinski, Classical theory of atomic collisions: I. Theory of inelastic collisions, Phys. Rev. 138 (1965) A 336.

[23] H. Kolbenstvedt, Simple theory for *K*-ionization by relativistic electrons, J. Appl. Phys. 38 (1967) 4785.

[24] W. Lotz, Electron impact ionization cross sections for atoms up to $Z = 108$, Z. Phys. 232 (1970) 101.

[25] V.A. Bernshtam, Y.V. Ralchenco, Y. Maron, Empirical formula for cross section of direct electron-impact ionization of ions, J. Phys. B At. Mol. Opt. Phys. 33 (2000) 5025.
[26] H. Deutsch, T.D. Märk, Calculation of absolute electron impact ionization cross section functions for single ionization of He, Ne, Ar, Kr, Xe, N and F, Int. J. Mass Spectrom. Ion Processes 79 (1987) R1.
[27] H. Bethe, Zur Theorie des Durchgangs schneller Korpuskularstrahlen durch Materie, Ann. Phys. (Leipzig) 5 (1930) 325.
[28] H. Deutsch, K. Becker, B. Gstir, T.D. Märk, A semi-empirical approach to the calculation of absolute inner-shell electron impact ionization cross sections, Z. Phys. D 29 (1994) 31.
[29] H. Deutsch, P. Scheier, K. Becker, T.D. Märk, Revised high energy behavior of the Deutsch-Märk (DM) formula for calculation of electron impact cross sections of atoms, Int. J. Mass Spectrom. 233 (2004) 13.
[30] A.K.F. Haque, M.S.I. Sarker, M.A.R. Patoary, M. Shahjahan, M. Ismail Hossain, M.A. Uddin, et al., Modified version of revised Deutsch-Märk model for electron impact *K*-shell ionization cross sections of atoms at relativistic energies, Int. J. Quantum Chem. 109 (2009) 1442.
[31] Y.-K. Kim, M.E. Rudd, Binary-encounter-dipole model for electron-impact ionization, Phys. Rev. A 50 (1994) 3954.
[32] N.F. Mott, The collision between two electrons, Proc. R. Soc. (Lond.) A 126 (1930) 259.
[33] K.L. Bell, H.B. Gilbody, J.G. Hughes, A.E. Kingston, F.J. Smith, Recommended data on the electron impact ionization of light atoms and ions, J. Phys. Chem. Ref. Data 12 (1983) 891.
[34] A.I. Godunov, P.B. Ivanov, On analytical fits for electron impact ionization cross sections, Phys. Scr. 59 (1999) 277.
[35] A.K.F. Haque, M.A. Uddin, A.K. Basak, K.R. Karim, B.C. Saha, Empirical model for the electron-impact *K*-shell-ionization cross section, Phys. Rev. A 73 (2006) 012708.
[36] A.K.F. Haque, M.A. Uddin, A.K. Basak, K.R. Karim, B.C. Saha, F.B. Malik, Electron-impact ionization of *L*-shell atomic species, Phys. Rev. A 73 (2006) 052703.
[37] A.K.F. Haque, M.A. Uddin, A.K. Basak, K.R. Karim, B.C. Saha, F.B. Malik, Electron impact ionization of *M*-shell atoms, Phys. Scr. 74 (2006) 377.
[38] A.K.F. Haque, M.A. Uddin, A.K. Basak, K.R. Karim, B.C. Saha, F.B. Malik, Relativistic effects in electron impact ionization from the p-orbital, Phys. Lett. A 354 (2006) 449.
[39] M.A.R. Patoary, M.A. Uddin, A.K.F. Haque, M. Shahjahan, A.K. Basak, M.R. Talukder, et al., Empirical model for the electron impact K-shell ionization cross section of atoms, Int. J. Quantum Chem. 109 (2009) 897.
[40] M.R. Talukder, S. Bose, M.A.R. Patoary, A.K.F. Haque, M.A. Uddin, A.K. Basak, et al., Empirical model for electron impact ionization cross sections of neutral atoms, M. Eur. Phys. J D 46 (2008) 281.
[41] L. Vriens, Electron exchange in binary encounter collision theory, Proc. Phys. Soc. (London) 89 (1966) 13.
[42] B.N. Roy, D.K. Rai, Electron-impact ionization of Alkali metals, Phys. Rev. A 8 (1973) 849.
[43] B.N. Roy, D.K. Rai, Electron impact ionisation of alkaline earths, J. Phys. B 16 (1983) 4677.
[44] M.A. Uddin, M.N.A. Abdullah, M.S. Mahbub, A.K. Basak, Electron impact ionization of hydrogenic atoms, Phys. Scr. 68 (2003) 192.
[45] M. Alfaz Uddin, A.K. Basak, B.C. Saha, Electron impact single ionization cross-sections of helium isoelectronic systems, Int. J. Quantum Chem. 100 (2004) 184.
[46] M.A.R. Patoary, M.A. Uddin, A.K.F. Haque, M. Shahjahan, A.K. Basak, B.C. Saha, Binary encounter model for the electron impact *K*-shell ionization of atoms, Int. J. Quantum Chem. 108 (1008) 1326.
[47] C.S. Campos, M.A.Z. Vasconcellos, J.C. Trincavelli, S. Segui, Analytical expression for *K*- and *L*-shell cross sections of neutral atoms near ionization threshold by electron impact, J. Phys. B At. Mol. Opt. Phys. 40 (2007) 3835.

[48] A.K.F. Haque, M.R. Talukder, M. Shahjahan, M.A. Uddin, A.K. Basak, B.C. Saha, An extended empirical formula for inner-shell ionization of atoms, J. Phys. B At. Mol. Opt. Phys. 43 (2010) 115201.
[49] C. Møller, Über den stoß zweier Teilchen unter Berücksichtigung der Retardation der Kräfte, Z. Phys. 70 (1931) 786.
[50] M.A. Uddin, A.K.F. Haque, K.R. Karim, A.K. Basak, F.B. Malik, Modified Kolbenstvedt model for the electron impact *K*-shell ionization cross sections of atoms and ions, Eur. Phys. J. D 37 (2006) 361.
[51] A.K.F. Haque, M.A. Uddin, M.A.R. Patoary, A.K. Basak, M.R. Talukder, B.C. Saha, et al., Generalized Kolbenstvedt model for electron impact ionization of *K*-, *L*- and *M*-shell atoms, Eur. Phys. J. D 42 (2007) 203.
[52] M.A. Uddin, A.K. Basak, A.K.M.A. Islam, F.B. Malik, Electron impact single ionization of light ionic targets with charge $q > 2$, J. Phys. B At. Mol. Opt. Phys. 37 (2004) 1909.
[53] W.M. Huo, Convergent series representation for the generalized oscillator strength of electron-impact ionization and an improved binary-encounter-dipole model, Phys. Rev. A 64 (2001) 042719.
[54] M.A. Uddin, A.K.F. Haque, A.K. Basak, K.R. Karim, B.C. Saha, Electron-impact ionization of hydrogen and lithiumlike systems, Phys. Rev. A 72 (2005) 032715.
[55] M.A. Uddin, A.K.F. Haque, M.M. Billah, A.K. Basak, K.R. Karim, B.C. Saha, Computation of electron-impact K-shell ionization cross sections of atoms, Phys. Rev. A 71 (2005) 032715.
[56] M.A. Uddin, M.A.K.F. Haque, A.K. Basak, B.C. Saha, Calculations of electron-impact single-ionization cross sections of helium isoelectronic systems, Phys. Rev. A 70 (2004) 032706.
[57] M.A. Uddin, A.K.F. Haque, M.S. Mahbub, K.R. Karim, A.K. Basak, B.C. Saha, Electron impact ionization of beryllium isoelectronic ions, Int. J. Mass Spectrom. 244 (2005) 76.
[58] M.A.R. Patoary, M.A. Uddin, A.K.F. Haque, A.K. Basak, M.R. Talukder, K.R. Karim, et al., Electron impact *K*-shell ionization cross sections of atoms at relativistic energies, Int. J. Quantum Chem. 108 (2008) 1023.
[59] E. Casnati, A. Tartari, C. Baraldi, An empirical approach to *K*-shell ionization cross section by electrons, J. Phys. B At. Mol. Opt. Phys. 15 (1982) 155.
[60] C. Hombourger, An empirical expression for *K*-shell ionization cross section by electron impact, J. Phys. B At. Mol. Opt. Phys. 31 (1998) 3693.
[61] A.K.F. Haque, M. Shahjahan, M.A. Uddin, M.A.R. Patoary, A.K. Basak, B.C. Saha, et al., Generalized Kolbenstvedt model for electron impact ionization of *K*-, *L*- and *M*-shell ions, Phys. Scr. 81 (2010) 045301.
[62] M. Inokuti, Inelastic collisions of fast charged particles with atoms and molecules – the Bethe theory revisited, Rev. Mod. Phys. 43 (1971) 297.
[63] C.J. Powell, Cross-sections for ionization of inner-shell electrons by electrons, Rev. Mod. Phys. 48 (1976) 33.
[64] C.J. Powell, Inner-shell ionization cross sections, in: T.D. Märk, D.H. Dunn (Eds.), Electron Impact Ionization, Springer, Berlin, 1985, p. 198.
[65] C.J. Powell, Inner-shell Ionization cross-sections, in: J.R. Michael, P. Ingram (Eds.), Microbeam Analysis, Sun Francisco Press, San Francisco, 1990, pp. 13–20.
[66] H. Tawara, K.G. Horrison, F.G. De Heer, X-ray emission cross sections and fluorescence yields for light atoms and molecules by electron impact, Physica 63 (1973) 351.
[67] W. Hink, H. Paschke, *K*-shell-fluorescence yield for carbon and other light elements, Phys. Rev. A 4 (1971) 507; W. Hink, H. Paschke, Der Wirkungsquerschnitt für die Ionisierung derK-Schale von Kohlenstoff durch Elektronenstoß (2–30 keV), Z. Phys. 244 (1971) 140.
[68] M. Isaacson, Interaction of 25 keV electrons with the nucleic acid bases, Adenine, Thymine, Uracil. II. Inner shell excitation and inelastic scattering cross sections, J. Chem. Phys. 56 (1972) 1813.

[69] R.F. Egerton, Inelastic scattering of 80 keV electrons in amorphous carbon, Philos. Mag. 31 (1975) 199.
[70] G. Glupe, W. Mehlhorn, Absolute electron impact ionization cross sections of N, O and Ne, J. Phys. Suppl. 32 (1971) C4–40; G. Glupe, W. Mehlhorn, A new method for measuring electron impact ionization cross sections of inner shells, Phys. Lett. A 25 (1967) 274.
[71] H. Platten, G. Schiwietz, G. Nolte, Cross sections for K-shell ionization of Si and Ar by 4 keV to 10 keV electron impact, Phys. Lett. A 107 (1985) 83.
[72] M. Kamiya, A. Kuwako, R. Ishii, S. Morita, M. Oyamada, Density effect in *K*-shell ionization by ultrarelativistic electrons, Phys. Rev. A 22 (1980) 413.
[73] S.C. McDonald, B.M. Spicer, Density effect in K-shell ionization by relativistic electron impact, Phys. Rev. A 37 (1988) 985.
[74] D.H.H. Hoffmann, C. Brendel, H. Genz, W. Low, S. Muller, A. Richter, Inner-shell ionization by relativistic electron impact, Z. Phys. A 293 (1979)187; D.H.H. Hoffmann, H. Genz, W. Low, A. Richter, Z and E dependence and scaling behaviour of the K-shell ionization cross section for relativistic electron impact, Phys. Lett. A 65 (1978) 304.
[75] W. Hink, A. Ziegler, Der Wirkungsquerschnitt für die Ionisierung der K-Schale von Aluminium durch Elektronenstoß (3–30 keV), Z. Phys. 226 (1969) 222.
[76] K. Ishii, M. Kamiya, K. Sera, S. Morita, H. Tawara, H. Oyamada, et al., Inner-shell ionization by ultrarelativistic electrons, Phys. Rev. A 15 (1977) 906.
[77] A.V. Shchagin, V.I. Pristupa, N.A. Khizhnyak, *K*-shell ionization cross section of Si atoms by relativistic electrons, Nucl. Instrum. Methods B 84 (1994) 9.
[78] C. Quarles, M. Semaan, Characteristic x-ray production by electron bombardment of argon, krypton, and xenon from 4 to 10 keV, Phys. Rev. A 26 (1982) 3147.
[79] R. Hippler, K. Saeed, I. McGregor, H. Kleinpoppen, Energy dependence of characteristic and bremsstrahlung cross sections of argon induced by electron bombardment at low energies, Z. Phys. A 307 (1982) 83.
[80] V.P. Shevelko, A.M. Solomon, V.S. Vukstich, *K*-shell ionization of free metal atoms K, Ca, Rb and Sr by electron impact, Phys. Scr. 43 (1991) 158.
[81] Z. An, C.H. Tang, C.G. Zhou, Z.M. Luo, Measurement of scandium and vanadium *K*-shell ionization cross sections by electron impact, J. Phys. B 33 (2000) 3677.
[82] J. Jessenberger, W. Hink, Absolute electron impact *K*-ionization cross sections of titanium and nickel (50 keV), Z. Phys. A 275 (1975) 331.
[83] F.Q. He, X.F. Peng, X.G. Long, Z.M. Luo, Z. An, *K*-shell ionization cross sections by electron bombardment at low energies, Nucl. Instrum. Methods B 129 (1997) 445.
[84] G.L. Westbrook, C.A. Quarles, Total cross sections for ionization of the k-shell by electron bombardment, Nucl. Instrum. Methods B 24–25 (1987) 196.
[85] Y. Watanabe, T. Kubozoe, T. Tomimasu, T. Mikado, T. Yamazaki, *K*-shell ionization by relativistic electron impact, Phys. Rev. A 35 (1987) 1423.
[86] W. Scholz, A. Li-Scholz, R. Collé, I.L. Preiss, *K*-shell ionization cross sections for 2.04-MeV electrons, Phys. Rev. Lett. 29 (1972) 761; A. Li-Scholz, R. Collé, I.L. Preiss, W. Scholz, Cross sections for *K*-shell ionization by 2-MeV-Electron impact, Phys. Rev. A 7 (1973) 1957.
[87] Z.M. Luo, Z. An, F.Q. He, T.H. Li, X.G. Long, X.F. Peng, Correction of the influence of the substrate upon the measurement of K-shell ionization cross sections, J. Phys. B 29 (1996) 4001.
[88] X. Llovet, C. Merlet, F. Salvat, Measurements of *K*-shell ionization cross sections of Cr, Ni and Cu by impact of 6.5-40 keV electrons, J. Phys. B At. Mol. Opt. Phys. 33 (2000) 3761.
[89] C.H. Tang, Z. An, T.H. Li, Z.M. Luo, Measurement of zinc and manganese K-shell ionization cross-sections by electron impact, Nucl. Instrum. Methods B 155 (1999) 1.
[90] K. Shima, Mn and Cu K-shell ionization cross sections by slow electron impact, Phys. Lett. A 77 (1980) 237.
[91] Z.M. Luo, Z. An, T.H. Li, L.M. Wang, Q. Zhu, X.Y. Xia, Measurement of *K*-shell ionization cross sections of Fe and Mn by electron impact, J. Phys. B 30 (1997) 2681.

[92] F.Q. He, X.G. Long, X.F. Peng, Z.M. Luo, Z. An, *K*-shell ionization of iron by electron bombardment, Acta Phys. Sinica 5 (1996) 499.
[93] Z. An, T.H. Li, L.M. Wang, X.Y. Xia, Z.M. Luo, Correction of substrate effect in the measurement of 8–25-keV electron-impact *K*-shell ionization cross sections of Cu and Co elements, Phys. Rev. A 54 (1996) 3067.
[94] A.E. Smick, P. Kirkpatrick, Absolute *K*-ionization cross section of the nickel atom under electron bombardment at 70 kv, Phys. Rev. 67 (1945) 153.
[95] S.A.H. Seif el Naser, D. Berenyi, G. Bibok, Inner shell ionization cross sections for relativistic electrons, Z. Phys. 267 (1974) 169.
[96] L.T. Pockman, D.L. Webster, P. Kirkpatrick, K. Harworth, The probability of K ionization of nickel by electrons as a function of their energy, Phys. Rev. 71 (1947) 330.
[97] H. Genz, C. Brendel, P. Eschwey, U. Kuhn, W. Low, A. Richter, et al., Search for the density effect in inner-shell lonization by ultra relativistic electron impact, Z. Phys. 305 (1982) 9.
[98] D.V. Davis, V.D. Mistry, C.A. Quarles, Inner shell ionization of copper, silver and gold by electron bombardment, Phys. Lett. 38A (1972) 169.
[99] H. Hubner, K. Ilgen, K.-W. Hoffmann, Messung des Wirkungsquerschnitts für Ionisierung in der *K*-Schale durch Elektronenstoß, Z. Phys. 255 (1972) 269.
[100] D. Berenyi, G. Hock, S. Ricz, B. Schlenk, A. Valek, K_α/K_β X-ray intensity ratios and *K*-shell ionisation cross sections for bombardment by electrons of 300-600 keV, J. Phys. B 11 (1978) 709.
[101] K. Shima, T. Nakagawa, K. Umetani, T. Mikumo, Threshold behavior of Cu-, Ge-, Ag-K-, and Au-L_3-shell ionization cross sections by electron impact, Phys. Rev. A 24 (1981) 72.
[102] L.N. Middleman, R.L. Ford, R. Hofstadter, Measurement of cross sections for X-ray production by high-energy electrons, Phys. Rev. A 2 (1970) 1429.
[103] C.H. Tang, Z.M. Luo, Z. An, T.H. Li, Measurement of zinc *K*-shell ionization cross sections by electron impact, Chin. Phys. Lett. 16 (1999) 505.
[104] C. Zhou, Z. An, Z. Luo, Measurement of *K*-shell production cross sections for Ga, Ge and Zr elements by electron impact, J. Phys. B At. Mol. Opt. Phys. 35 (2002) 841.
[105] K. Kiss, G. Kalman, J. Palinkas, B. Schlenk, Investigation of inner-shell ionization by electron impact in the 60–600 keV energy region, Acta Phys. Hung. 50 (1981) 97.
[106] H. Hansen, H. Weigmann, A. Flammersfeld, Messung des wirkungsquerschnitts für K-ionisierung durch negatonen- und positonenstoß, Nucl. Phys. 58 (1964) 241.
[107] X.F. Peng, F.Q. He, X.G. Long, Z.M. Luo, Z. An, Cross sections for *K*-shell ionization of niobium by electron impact, Phys. Rev. A 58 (1998) 2034.
[108] F.Q. He, X.G. Long, X.F. Peng, Z.M. Luo, Z. An, *K*-shell ionization of molybdenum by electron bombardment, Nucl. Instrum. Methods B 114 (1996) 213.
[109] S. Ricz, B. Schlenk, D. Berenyi, G. Hock, A. Valek, *K*-shell ionization cross sections of Pd, Ag, In and Sn for relativistic electrons, Acta Phys. Hung. 42 (1977) 269.
[110] K.H. Berkner, S.N. Kaplan, R.V. Pyle, Cross sections for *K*-shell ionization of Pd and Au by 2.5 and 7.1 MeV electrons, Bull. Am. Phys. Soc. 15 (1970) 786.
[111] B. Schlenk, D. Berenyi, S. Ricz, A. Valek, G. Hock, Inner-shell ionization by electrons in the 300–600 keV region, Acta Phys. Hung. 41 (1976) 159.
[112] D.H. Rester, W.E. Dance, *K*-shell ionization of Ag, Sn, and Au from electron bombardment, Phys. Rev. 152 (1966) 1.
[113] S. Reusch, H. Genz, W. Low, A. Richer, A method to determine *L*-subshell ionization cross sections for medium and heavy elements, Z. Phys. D 3 (1986) 379.
[114] X.-F. Peng, F.-Q. He, X.-G. Long, A. Zhu, Z.-M. Luo, Measurement of L-shell ionization cross sections for niobium by electron impact, Chin. Phys. 10 (2001) 31.
[115] Y.K. Park, M.T. Smith, W. Scholz, Cross sections for *L* X-ray production and *L*-subshell ionization by MeV electrons, Phys. Rev. A 12 (1975) 1358.
[116] J. Palinkas, B. Schlenk, *L*-subshell ionization cross sections for Au, Pb, and Bi by 60–600 keV electron impact, Z. Phys. A 297 (1980) 29.

INDEX

Note: The letters '*f*' and '*t*' following locators denote figures and tables respectively

A
Absorption component shape spectra, 248*f*
Absorption total shape spectra, 248*f*
Abstract configuration space, role of, 54
Ahlström force field, 135, 138
AIM, *see* Atoms-in-molecules
Allyl π-electron system, 30
AO, *see* Atomic orbital
ARMA model, *see* Autoregressive moving average model
Atomic orbital (AO), 3, 131
  fragment-normalized probabilities, 38
  populational decoupling of
    chemical bonds, 23
    Hückel approximation, 26
    MO, 21–24
    molecular information channel, 25
    population-weighting procedure, 25
    probability scattering, 27–28
    quantum-mechanical CBO matrix, 21
Atomic output reduction, 37
Atoms-in-molecules (AIM), 3
Auger electron spectroscopy, 330
Autocorrection, 175
Autocorrelation function, 151
  equivalence of, 157–161
Autoregressive moving average (ARMA) model, 161
Average entropic descriptors, 40

B
BA, *see* Born approximations
Baker-Campbell-Hausdorff (BCH) expansion, 120, 123, 127
Beam splitter (BS), 83–84
BED model, *see* Binary-encounter-dipole model
Belfast ionization (BELI), 319
BELL parameters, 322, 323, 325*t*
1,4-benzenedithiol (BDT), 288
Binary entropy function, 11
Binary-encounter-Bethe, 319
Binary-encounter-dipole (BED) model, 319
Bonding
  and antibonding, 24, 27, 29, 36, 44, 45
  CTCB, 3
  hydrogen, 138
  MO, 10–12, 14, 22
  probabilities of AO, 39
  two-electron system, 21
Born approximations (BA), 318
Born–Bethe theory, 318, 319
BS, *see* Beam splitter
Butadiene, 33

C
Cartesian coordinate system, 34
Cauchy integral, 183–184
Cayley-Hamilton theorem, 174, 192
CBO, *see* Charge and bond order
CCF, *see* Contracted continued fraction
Cell surviving fractions
  after irradiation, PQL model, 254–256
  radiobiological modelings, 225–226
CF, *see* Continued fraction
CG, *see* Contragradience
Charge and bond order (CBO), 6
  matrix, 11, 14
Chemical shifts, 228, 257
  NMR, 137–138
Christoffel-Darboux formula, 186
Closed-shell (CS), 6
  and MO, 8
  molecular systems, 38
  normalization constant, 7
Coherence, lost and regained, 87
Communication theory of the chemical bond (CTCB), 3

Companion matrix, *see* Hessenberg matrix
Condensed conditional probabilities, 37
Conditional entropy, 9, 18
Continued fraction (CF), 203
  coefficients, analytical expressions, 208–209
  contracted, 214–215
  equations for eigenvalues via, 205–206
Contracted continued fraction (CCF), 214–215
Contragradience (CG), 3
Convergence
  rate, 239*f*
  regions, 242*f*
Convergent close-coupling method, 318
Copenhagen interpretation, 55
Copenhagen view, 57–60, 101
Coulombic interactions, 112, 273
Coupled-perturbed Kohn-Sham (CPKS) equations, 131
Covalency, 3, 9
Covalent promolecule, 11
CS, *see* Closed-shell
CTCB, *see* Communication theory of the chemical bond
Cubic response function, 127–130
CVTS model, 320, 321, 324
Cyclohexatriene, 28

D
Decimated signal diagonalization (DSD), 200
Decoupled bonds, 11–15
Density functional theory (DFT), 108
Detector function, 91–94
Deutsch and Märk (DM) model, 318, 369*f*–372*f*, 375
DFT, *see* Density functional theory; Discrete Fourier transform
Diagonalization
  of Hessenberg/companion matrix, 182
  of Jacobi matrix, 171–173
Diatomic chemical interactions, average entropic descriptors, 40–44
Diatomic molecules, 39
Diatomic Wiberg, 42
Diffraction quantum state, 65–66
Diminished bond multiplicity, 25
Dirac function, 184
Dirac-Lebesgue measure for discretization, 183–184
Discrete Fourier transform (DFT), 157
Dithiol molecules, 272*f*
Double-slit case, 60–66
DSD, *see* Decimated signal diagonalization
Dual Lanczos representation via state vectors, 189–190
Dyson equations, 273, 277*f*, 305*f*
Dyson orbital 40, 290
Dyson pole strengths, 284

E
Ehrenfest theorem, 122, 123, 127
EI ionization cross sections (EIICS) data, 318
EI single ionization cross sections (EISICS), 318, 329
Eigenvalues, 209–212
EIICS data, *see* EI ionization cross sections data
Einstein–Podolsky–Rosen (EPR) experiment, 78–83, 102
Electric field, transformed, 129, 130
Electron impact ionization cross section, 331*f*
Electron localization function, 3
Electron propagator, 284–287
Electron transfer, 300
Electron-phonon
  correction, 308
  interaction, 307–309
Electro-optic shutters, 88
Electrostatic energy, definition of, 114
Embedded molecules, nuclear magnetic shielding tensors, 130–132
Entanglement issues, 98–100
EPR experiment, *see* Einstein–Podolsky–Rosen experiment
Excitation energies, 136–137
Excitation operator, 52
Explicit Lanczos wave packet propagation, 192–193
Explicit Padé approximant, 206–207
External quantum state, 53

F
Fast Fourier transform (FFT), 148, 161
Fast Padé transform (FPT), 148, 149, 222–224
Fence
  double-slit case, 60–66
  recording screens, 66–70
  Tonomura's experiment, 71–73
FFT, *see* Fast Fourier transform
FID curve, *see* Free induction decay curve
Field-effect transistor, 292
Filter diagonalization (FD) method, 192
Finite field (FF) techniques, 139
Finite-rank Green function, 222
Flexible-input generalization, 15–21

Force fields, hierarchy of, 133–136
Forward and root-reflected backward linear predictor (FB-LP), 253
Fourier transformation, 121, 123
FPT, *see* Fast Padé transform
Fragment Hamiltonians, 110
Free induction decay (FID) curve, 226
Free-photon state, 95
Froissart doublets, 251*f*, 252*f*

G
Gas-to-aqueous solution shifts, 138
Gauge-including atomic orbitals (GIAOs), 109, 131, 132
Gaussian elimination method, 215–217
Gaussian software, 288
GKLV model, 326–328, 373
Gold electrodes, 272
Gram-Schmidt orthogonalization (GSO), 166
Green function, 152, 160–161, 172, 202, 204
Gryzinski's relativistic factor, 323, 329
GSO, *see* Gram-Schmidt orthogonalization

H
Hamiltonian, 300–302
  fragment, 110
  time-dependent KS, 119, 1222
Hankel determinant, 160
Hankel matrix, 160
Harmonic inversion problem (HIP), 159
Hartree-Fock
  calculations, 36–37
  exchange, 282*f*
  wavefunctions, 110
Heisenberg representation, 266
Hessenberg matrix, diagonalization of, 182
High-degree polynomials, rooting, 180–182
Hilbert space, 52, 53, 101
  EPR experiment, 78–83
  recording screens, 66, 67
  Tonomura's experiment, 72
HIP, *see* Harmonic inversion problem
HOs, *see* Hybrid orbitals
Hückel π-MO channels, 27
Hückel theory, 26, 28
Hybrid orbitals (HOs), 10
Hyperpolarizabilities, second, 138–140

I
ICRMS, *see* Ion cyclotron resonance mass spectroscopy
IDFT, *see* Inverse discrete Fourier transform
I-frame system, 53, 78
Information theory (IT), 3
Inner-shell ionization
  cross sections
    techniques for measuring, 330
  in MUIBED model, 328
Interaction Hamiltonian, 110, 115
  Taylor series, 112–113
Interference effects, 63
Internal quantum state, 53
Inverse discrete Fourier transform (IDFT), 158
Ion cyclotron resonance mass spectroscopy (ICRMS), 157
Ionicity, 9
IT, *see* Information theory

J
Jacobi
  eigenvalue problem, 164–169
  matrix, 163–164, 173–174
  method, 117
  state vectors, 171–173

K
Kadanoff-Baym equations, 270–272
Keldysh contour, 264–267
Keldysh function, Fourier transform for, 277
Keldysh space, 269
Kohn-Sham (KS) operator, 118
  time-dependent equations, 119, 122
Kolbenstvedt model, 321, 373
Krylov basis, 158
Krylov-Schrödinger
  general matrix, inversion of, 200–203
  mapping, Lanczos states, 195–197
  overlap determinant, closed expression for, 190
KS operator, *see* Kohn-Sham operator
K-shell ionization cross sections, 319, 320, 328, 331, 374, 375

L
Laboratory space, 53
Lanczos algorithm
  explicit solution of, 190–192
  for state vectors, 162–163
  of tridiagonalization, 169
Lanczos continued fractions (LCF), 203–205
Lanczos coupling constants, analytical expressions, 212–214
Lanczos orthogonal polynomials, 169–174
  three-term recursion, 169–171

Lanczos phenomenon, 165
Lanczos polynomials
  completeness of, 185–188
  matrix, 173–174
  matrix elements of evolution operator, 189–190
  monomials, mapping, 193–195
  power series, 178–180
  recursions for derivatives of, 175
Lanczos states
  Krylov-Schrödinger, mapping, 195–197
  matrix elements of evolution operator, 189
Lanczos vector space, 183–184
Lanczos wave packet propagation, explicit, 192–193
Langreth's mapping procedure, 277
LCAO-MO approach, 6
LCF, *see* Lanczos continued fractions
Lehmann representation, 284
Linear equations, 173–174
  tridiagonal inhomogeneous systems, 215–222
Linear response function, 123–124
Linear scaling techniques, 108
Linear superposition, 61
  principle of, 54
  Scully et al. double-slit setup, 77
Linear-quadratic (LQ) model, 225, 254
Line-broadening matrices, 279
LMO, *see* Localized MO
Localized bonds, 11–15
Localized MO (LMO), 10
LoProp force field, 133, 135
LQ model, *see* Linear-quadratic model
L-shell ionization cross sections, 329, 331, 357*f*–371*f*, 374

M

Maclaurin series, 161
Magnetic resonance spectroscopy (MRS), 222–224
  absorption
    component shape spectra, 248*f*
    total shape spectra, 248*f*
  chemical shifts, 228
  convergence
    rate, 239*f*
    regions, 242*f*
  FB-LP, 253
  FID curve, 226
  Froissart doublets, 251*f*, 252*f*
  residual/error spectra, 249*f*–250*f*
  root reflection, 253
  signal-noise separation, 247
  signal process time and frequency domain data, 235*f*–236*f*
  spectral parameters
    convergence of, 230*t*–231*t*, 232*t*–233*t*
    reconstructed, configurations of, 243*f*, 246*f*–247*f*
  time signal, 237*f*
Malin principles, 57
Matrix-vector multiplication, 117
Matsubara component, 270
MBELL model, 322–324, 373
Micromaser cavities, 76
Migdal's theorem, 309
Molecular dynamics (MD) simulations, 109
Molecular Dyson orbital, 292*f*
Molecular electron propagators, 273
Molecular electrostatic potential, 134–135
Molecular mechanics (MM), 108
Molecular nonlinear optical (NLO) properties, 139
Molecular normalization, 16
Molecular orbital (MO), 3, 21–24, 298
  bonding, 10–12, 14, 22
  CS and, 8
  populational decoupling of AO, 21–24
Molecular partial information channels, 30
Molecular π-electron information systems, 25
Molecular transistors, 292
Molecular wire
  Au-nitro-BDT-Au, 298*f*, 299*t*
  numerical calculations, 287–289
    negative differential resistance, 289–292
Monomials to Lanczos polynomials, mapping, 193–195
Moving average (MA) model, 161
MRDM model, 319
MRIBED model, 322
M-shell ionization cross sections, 331, 372*f*–373*f*
MUIBED model, 328–330, 373

N

Newton-Raphson algorithm, 180–182
2-nitro-1,4-benzenedithiol (nitro-BDT), 293*f*
NMR, *see* Nuclear magnetic resonance
Nonequilibrium Green's function
  formalism
    Kadanoff-Baym equations, 270–272
    Keldysh contour, 264–267
  for interacting bridge electrons, 280–283
Nonstationary quantum-mechanical spectral analysis, 149

Nuclear magnetic resonance (NMR), 130
  chemical shifts, 137–138
Nuclear magnetic shielding tensors, calculation, 130–132

O
OCT, *see* Orbital-communication theory
One-electron approaches, 4
Open-shell configuration, 8, 36
Orbital and condensed atom, 37
Orbital-communication channels, 36
Orbital-communication theory (OCT), 4–5, 8, 15
  bond differentiation in, 29
  entropy, 28

P
Padé approximant, 153
  for cell surviving fractions, 225–226
  explicit, 206–207
Padé via Lanczos (PVL) method, 198
Padé-Lanczos approximant (PLA), 197–200
Pade linear quadratic (PLQ) model, 254–256, 255*f*
Padé mythologies, 222
Parkinson group (UW), 299
Particle model, 59, 80
Particle picture and delayed-choice experiment, 86–87
PE, *see* Polarizable embedding
Peripheral carbon atoms, 25
Phase shift (PS), 85
Photocurrent, 302–303
  correlated QD electrons, 306–307
  electron–phonon interaction in semiconductor, 307–309
  Hamiltonian, 300–302
  in QDSSC, 299–300
  uncorrelated electrons in quantum dot, 303–306
Photoelectric current, *see* Photocurrent
PLA, *see* Padé-Lanczos approximant
Planck's law, 62
PLQ model, *see* Pade linear quadratic model
Polarizable embedding (PE), 108
  accuracy of potentials, 133–136
  response theory, *see* Response theory
  theoretical basis for, 109–118
Polarizable embedding-density functional theory (PE-DFT) method, 118
  applications of, 132–140
    accuracy of embedding potential, 133–136
    excitation energies, 136–137
    NMR chemical shifts, 137–138
    second hyperpolarizabilities, 138–149
Polynomials
  high-degree, 180–182
  Lanczos, *see* Lanczos polynomials
Power moment problem, 217–218
Power series, two Lanczos polynomials, 178–180
Probabilistic model, 21
Pyridine, 138

Q
Quadratic response function, 124–127
Quadrupole moments, 135
Quantum dot-sensitized solar cells (QDSSC), 299
  correlated QD electrons, 306–307
  electron transfer in, 300, 300*f*
  photocurrent in, 299–300
  uncorrelated electrons in, 303–306
Quantum eraser, 96–97
Quantum mechanical treatments, 318
Quantum mechanics (QM), 108, 138
Quantum states
  double-slit case, 60–66
  for quantum measurement
    coherence, 87
    EPR experiment, 78–83
    particle picture and delayed-choice experiment, 86–87
    Scully et al. double-slit setup, 73–78
    Wheeler's delayed-choice experiment, 83–85
  for quantum probing, 51–55
    entanglement issues, 98–100
    quantum eraser, 96–97
    Scully et al. atom interferometer, 88–94
    welcher Weg setup, 95–96
  recording screens, 66–70
Quantum-mechanical spectral analysis, 152
  nonstationary, 149
  time-independent, 154–157
QZ algorithm, 165

R
Rayleigh-Schrödinger perturbation treatment, 112
Recursion method, 203
Recursive residue generation method, 203
Residual/error spectra, 249*f*–250*f*
Response theory, 118–122
  cubic response function, 127–130

Response theory (*continued*)
linear response function, 123–124–130
quadratic response function, 124–127
Restricted Hartree–Fock (RHF), 6
Root mean square deviation (RMSD), 134, 135
Root mean square (RMS) noise, 228
Root reflection, 253
Rooting high-degree polynomials, 180–182

S
Scattered quantum states (SQS), 54, 59
Schrödinger equation, 149, 150
Scully et al. atom interferometer, 88–94
Scully et al. double-slit setup, 73–78
Secular equation, 176
and characteristic polynomial, 176–178
Self consistent field (SCF) iteration, 118
Self-energy, 271
Shockley-Queisser limit, 263
Signal process time and frequency domain data, 235*f*–236*f*
Signal-noise separation (SNS), 247
Singular eigenvalues, 165
Singular value decomposition (SVD), 165
SNS, *see* Signal-noise separation
Solute-solvent systems, 132
Special relativity (SR), 50, 104
Spectral analysis
problem of, 218–222
quantum-mechanical
nonstationary, 149
time-independent, 154–157
Spectral parameters
convergence of, 230*t*–231*t*, 232*t*–233*t*
reconstructed, configurations of, 243*f*, 246*f*–247*f*
Spectral shapes, 148
Spontaneous emission, 67, 99
SQS, *see* Scattered quantum states
SR, *see* Special relativity
Standard quantum measurement model
aspects of
Copenhagen view, 57–60
preparing and recording quantum state, 55–57
orthodox and, 70
State vectors
Jacobi, 171–173
Lanczos algorithm for, 162–163
Statistical interpretation, 55
Stieltjes integral, 183
SVD, *see* Singular value decomposition
System chemical bonds, 23
System electron density, 6

T
Taylor expansion, 266
Taylor series, interaction Hamiltonian, 112–113
Tensors
interaction, 113
nuclear magnetic shielding, 130–132
Third harmonic generation (THG), 139, 140
Time signal, 237*f*
equivalence of, 157–161
Time-contour variables, 268
Time-dependent density functional theory (TD-DFT), 108
Time-dependent KS Hamiltonian, 119
Time-dependent quantum-mechanical spectral analysis, 149–154
Time-evolution operator, 120
Time-independent quantum-mechanical spectral analysis, 154–157
Tonomura's experiment, 71–73
Transmission electron energy loss spectroscopy, 330
Tridiagonal inhomogeneous systems, linear equations, 215–222
Tridiagonalization, Lanczos algorithm of, 169
Tunneling junctions
Keldysh functions for noninteracting bridge electrons, 274
molecular transistors, 292
noncrossing approximation, 283–284
renormalized zeroth Green's functions, 277–280
transport in, 272–274
uncorrelated electrons in, 274–277
Two-electron approaches, 4

V
Valence Bond (VB) theory, 3–4

W
Welcher Weg setup, 95–96
Wheeler's delayed-choice experiment, 83–85

X
XCVTS model, 324–326, 373
X-ray spectroscopy technique, 330